

# THIS WEEK

## EDITORIALS

**WORLD VIEW** Pakistan and the new future for science and technology p.7

**SQUASHED** Quirky metamaterial gets narrower under pressure p.8



**HOT STUFF** Baby bird beaks extend when temperature soars p.9

## The test for Abenomics

*Japanese Prime Minister Shinzo Abe has been buoyed by election success, but he must show that his science policies take the opinions of researchers into account.*

The Japanese Liberal Democratic Party's decisive win in last Sunday's upper-house election was an impressive show of support for a sitting prime minister in a country that tends to chew its political leaders up and spit them out in short order. Especially popular with voters are Prime Minister Shinzo Abe's programmes for financial stimulus, which have started to breathe life into a country in a state of economic paralysis.

So what does the re-election mean for research and science? Abe, who took office last September, has been relatively generous with the scientific purse strings so far, and a prime minister who stays in power for more than a year might bring some stability to vacillating science policies. For example, the country's Council for Science and Technology Policy, once a strong body that set and streamlined science priorities, has in the past three years been reduced to rubber-stamping the decisions of others. Now it is set to resurge.

Abe has political capital to spend. But he may yet choose to use it to push positions that are unpopular with both scientists and the public.

First among them is his stand in favour of nuclear power. All polls show that most people in Japan do not want the country's reactors — shut down after the 2011 Fukushima accident — to be restarted. Yet Abe is pushing for that. The prime minister has tried to press the idea that the dysfunctional nuclear regulatory system that exacerbated the Fukushima accident has been fixed, but events in the past few weeks have shown that neither Fukushima's ominously steaming reactors nor the country's regulatory system are yet working correctly. The latest event to draw outrage was the discovery that Fukushima's operator, the Tokyo Electric Power Company, this year waited for more than a month before admitting that radioactive water from the plant was leaking into

the sea. The Japanese Nuclear Regulation Authority actually did its job, drawing public attention to the contamination weeks ago. But what power does the regulatory system have if the nuclear operator can be so slow to respond? Suspicious observers are already suggesting that it waited until after the election to confirm the bad news.

Abe's support for science is also getting mixed reviews. His emphasis on technology transfer has hit a popular chord with industrialists, as have his plans to merge biomedical research funding under a

**"For now, most scientists see the proposals as a threat."**

body inspired by the US National Institutes of Health (NIH). But the planned Japanese NIH is quite different from its namesake — it is intended to focus on applied science, and will be supervised mostly by Abe and bureaucrats, rather than by scientists (see *Nature* 499, 136–137; 2013).

This could send science off course. Already, Japan has focused too optimistically on induced pluripotent stem cells, and funding is set to increase further. The country should give more thought to what science and clinical applications are likely to emerge. Scientists in other fields feel they are being shunned. Is the Japanese NIH going to provide balance? It should, but Abe's proposal does not promise to do so.

A genuine copy of the US NIH — one that seeks and takes into account the opinions of scientists — could be a real boon in Japan. Yet for now, most scientists see the proposals as a threat, especially given that they are being implemented from the top down.

As the election results show, Abe is doing something right. Introducing more science and less politics to the operation of this NIH-like agency would be an early way to show that he can listen as well as lead. ■

## Forensics fiasco

*Inconsistent standards and a lack of research investment have left UK legal science in chaos.*

This publication is steadfast in promoting the benefits of funding for research, but even we might not say that reductions in cash for science could be allowing murderers and rapists to roam our streets. We don't have to: Andrew Miller has said it for us.

Miller leads the combative but respected (and cross-party) science select committee in the UK House of Commons. The committee last week produced a damning report — its second in just over three years — on the state of forensic science in the country. In his alarming sound bite, Miller neatly summarized the need for urgent government action, including dedicated funds for research into better sleuthing methods.

The British system is a perfect case study of a wider forensics malaise. The Forensic Science Service, which provided services to police forces across the nation, was subjected to a disastrous attempt at privatization before being closed in March 2012. Police laboratories have inconsistent standards, and private companies have been asked to fill the gap.

The problems that Miller's committee identifies are long-standing. But this time the politicians have upped the rhetorical ante, expressing concern that the minister responsible for forensic science "appeared to have so little understanding of the subject".

The shortcomings in this field are not restricted to the United Kingdom. In February, the US Department of Justice announced a new National Commission on Forensic Science that will develop guidance across the spectrum of forensics, from courtroom to laboratory, on matters such as professional codes. It is sorely needed: just last month, the Department of Justice announced that more than 2,000 criminal cases were being reviewed because of problems with hair-sample analysis. Forensic science holds great power over the lives and liberty of individuals. Now it must reclaim its great responsibility. ■



## Pakistan must seize the chance to revive its science

*The government of Nawaz Sharif needs to appoint a tough leader to deliver on its election promise of a research renaissance, says Ehsan Masood.*

Few general-election manifestos devote an entire chapter to promises in science and technology, so the campaign documents from the centre-right Pakistan Muslim League stood out. In its bid for power earlier this year, this party of landowners and industrialists did something unexpected: it pledged to put science and technology at the heart of its governing strategy.

It promised one million new high-tech jobs in the next five years. It talked of new funding agencies for biotechnology and nanotechnology, of new programmes in fuel cells and small satellites, and of revamping agricultural research. And it included a promise that the state would not interfere in the appointment of university vice-chancellors.

If kept, the promises would mark a step in the right direction for Pakistan, helping it to shed its reliance on international aid and edge towards economic independence and stability. But they seemed a little too good to be true.

The Muslim League is now in power after beating the ruling Pakistan People's Party in May's elections. And already, the glittering future it promised for research is in doubt. It is not too late for the pledges to be realized, and science can still play a pivotal part in the development of the country, but it will require strong and committed leadership to see the changes through.

The poor performance of science in Pakistan is a reflection of the discipline's traditionally low political standing. So often in the country's 66-year history, the science ministry has been accorded the status of backwater, or has been used as a political football at the whim of party leaders for reasons that have little to do with science or technology policy. In Pakistan, 'science minister' is not seen as a proper job.

Sometimes, the post has even been left vacant. In the 1990s, the centre-left government of Prime Minister Benazir Bhutto, for example, chose not to appoint a dedicated science minister during her second term. At other times, appointments have been questionable. One former science minister, the landowner Syeda Abida Hussain, was censured last year by the Press Council of Pakistan for promoting smoking in an article for *Newsweek Pakistan*.

The latest incumbent, Zahid Hamid, is an unpromising choice for science minister. The position was his reward from the Muslim League for switching political sides — and it is questionable whether he has the vision or the experience to effect the changes promised by the league.

Hamid also faces a political challenge that could see him exit the ministry as quickly as he arrived. He once was loyal to the former military dictator General Pervez Musharraf, who is now awaiting trial and may be charged with treason. If Musharraf goes down, it would undermine Hamid and leave him ripe for replacement.

There is no shortage of candidates to take his

place — people who have a record of building successful institutions at the interface of knowledge and commerce, despite the poor track record of Pakistan's science ministry. Any one of these would be well placed to turn the promises of the manifesto into reality.

Science does have the ear of the new prime minister, Nawaz Sharif. The man who was instrumental in placing science at the heart of the league's manifesto, Ahsan Iqbal, is minister for planning and development and a member of Sharif's inner circle. Should Hamid depart, Iqbal would have a golden opportunity to push for a widely respected and heavy-hitting science minister.

The country has had such a science minister before. Although most Pakistanis have nothing good to say about Musharraf, young and old are in awe of the science minister he appointed, the University of Karachi chemistry professor Atta-ur-Rahman. Rahman secured a large budget increase and spent much of the funds hiring senior faculty members and boosting early-career programmes. As Rahman's association with the general effectively rules out a return to a political role, who else is suitable?

One candidate is plant geneticist Kauser Malik, founding director of the National Institute for Biotechnology and Genetic Engineering in Faisalabad and one-time chairman of the Pakistan Agricultural Research Council. Malik has experience as both bench scientist and high-level administrator. He also has plenty of international connections and a record of delivering results. Alternatively, the government could look to the next generation and appoint Muhammad Iqbal Choudhary,

director of the HEJ Research Institute of Chemistry at the University of Karachi, which is among the largest such facilities in Asia.

A wild card would be Asad Umar, former chief executive of Engro, which he grew from a mid-size company to one of the continent's largest conglomerates, spanning agrochemicals to energy. Young, cricket-mad and popular with the public, Umar quit his job to join former cricketer Imran Khan's political party, Tehreek-e-Insaf, which in May came from nowhere to become the country's third electoral force.

Umar's decision to leave business for politics is part of a bigger trend among younger, middle-class and highly networked voters to become politically active. Unusually for Pakistan, many queued for the best part of a day to cast their votes in May's elections. Even if Hamid stays in his post, the government might consider appointing a heavy-hitter to take charge of the science-for-growth strategy, and have him or her report to Iqbal in the Planning Commission. That person could then get on with the task of dragging Pakistan into the twenty-first century. ■

### IN PAKISTAN 'SCIENCE MINISTER' IS NOT SEEN AS A PROPER JOB.

© NATURE.COM  
Discuss this article  
online at:  
[go.nature.com/y6ncnk](http://go.nature.com/y6ncnk)

**Ehsan Masood** is editor of Research Fortnight and teaches science policy at Imperial College London.  
e-mail: [news@researchresearch.com](mailto:news@researchresearch.com)

# RESEARCH HIGHLIGHTS

Selections from the scientific literature

## ZOOLOGY

### Bee trade spreads parasites

The international trade in beehives distributes dangerous parasites around the world.

William Hughes at the University of Sussex, UK, and his colleagues investigated 48 commercially produced hives of buff-tailed bumblebees (*Bombus terrestris*). Despite being certified as parasite-free by their producers, more than 75% of the hives carried microbial parasites. Uninfected bees that were fed faeces or pollen collected from the commercial hives subsequently tested positive for parasites and had shorter lifespans.

Worldwide, more than one million bumblebee hives are shipped every year, and the authors suggest that imported hives could infect native pollinators.

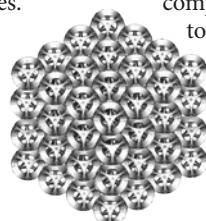
*J. Appl. Ecol.* <http://dx.doi.org/10.1111/1365-2664.12134> (2013)

## MATERIALS SCIENCE

### Odd performance under pressure

When squashed down, most materials expand outwards, but one class of 'metamaterials' gets narrower instead.

Katia Bertoldi at Harvard University in Cambridge, Massachusetts, and her colleagues crafted several structures using arrangements of spherical shells with regularly spaced holes. Whereas most structures are engineered to avoid mechanical instabilities, this metamaterial exploits them



by buckling and folding to become narrower under compression before returning to its original shape after the pressure is removed. X-ray images and numerical simulations showed how the holes in the structures (one example pictured)

distort under increasing strain.

These reversible architectures could be useful in applications such as energy-absorbing materials or acoustic dampeners, the authors suggest. *Adv. Mater.* <http://dx.doi.org/10.1002/adma.201301986> (2013)

## REMOTE SENSING

### Counting carbon from above

An airborne method for measuring biomass in forests and other ecosystems is as accurate as ground-based studies and can be used to create a national carbon map.

Gregory Asner at the Carnegie Institution for Science in Stanford, California, and his colleagues measured vegetation across 2.4% of Panama using an aeroplane equipped with a laser-based surface-detection system. They calibrated results by comparing data with 228 field plots and scaled up their analysis using satellite observations.

This produced the first high-fidelity map of carbon stocks across an entire country. The map has an uncertainty of 10% in areas measured from the plane, and 20% on average in other areas. The authors suggest that laser-based data can fill in gaps where there are no field data.

*Carbon Balance Mgmt.* 8, 7 (2013)

## IMMUNOLOGY

### Antibody tutors travel

A group of specialized white blood cells migrates back and forth through lymph nodes to teach other immune cells how to make a greater variety of antibodies against invading bacteria and viruses.

A team led by Michel Nussenzweig at the Rockefeller University in New York City and Gabriel Victora at the Whitehead Institute for Biomedical Research in Cambridge, Massachusetts, used fluorescence microscopy to monitor the behaviour of specialized T cells in lymph



## FISHERIES

### Hazard lights for turtles

Nets that are lit by ultraviolet lights deter turtles but catch just as many fish as unlit nets.

Vulnerable sea-turtle species are often caught unintentionally in nets set out by fisheries (pictured). Many commercial fish species cannot see ultraviolet light, but several types of sea turtle can, so a team of researchers led by John Wang at the University of Hawaii in Honolulu tested whether visual cues stopped turtles from being trapped. The group placed ultraviolet lights every 5 metres along net floatlines and compared catches to those from unlit nets. The lights reduced the capture rate of green sea turtles (*Chelonia mydas*) by 40% and, in separate studies in a commercial fishery, did not significantly alter the value or number of marketable fish caught.

*Biol. Lett.* 9, 20130383 (2013)

nodes in live mice. These T cells guide other white blood cells, known as B cells, to manufacture antibodies. The team found, unexpectedly, that the specialized T cells continually travelled between the structures in which B cells mature. This constant movement exposes stationary B cells to diverse T cells and might result in B cells producing a wider range of pathogen-specific antibodies, the authors say.

*Science* <http://dx.doi.org/10.1126/science.1241680> (2013)

#### PALAEONTHROPOLOGY

## Sex determination for the Stone Age

A DNA-sequencing method reliably reveals the sex of ancient human remains.

A team led by Pontus Skoglund at Uppsala University in Sweden analysed high-throughput-sequencing data from 14 modern humans and from the remains of 16 individuals up to 70,000 years old. By comparing the number of sequences that matched the X or Y chromosome, the team could identify males and females. This approach worked even when the sequence data were deliberately 'contaminated' by adding present-day DNA sequences of the opposite sex.

The technique determined the sex of 14 out of 16 ancient individuals studied, including several Neanderthals and a 5,300-year-old mummy (pictured). Two Neolithic individuals who had been classified as females on the basis of their morphology were identified as males.

JANE BURTON/DORLING KINDERSLEY/GETTY

WOLFGANG NEEB/THE BRIDGEMAN ART LIBRARY

The method could be useful for determining the sex of juvenile or highly degraded specimens, the researchers say. *J. Archaeol. Sci.* <http://dx.doi.org/10.1016/j.jas.2013.07.004> (2013)

#### OPTICAL PHYSICS

## Images on a subatomic scale

High-speed videos of nuclear reactions with frames lasting less than one-billionth of one-billionth of a second may eventually be possible, owing to a theoretical scheme for making ultrashort laser pulses.

Longer pulses of light lasting several attoseconds ( $10^{-18}$  seconds) are already used to capture high-resolution films of atomic and electronic processes. The pulses are typically generated from X-rays that are emitted when electrons are scattered by infrared lasers and then recombine with parent atoms.

Carlos Hernández-García of the University of Colorado Boulder and his colleagues suggest an even more sensitive technique that involves measuring the interference pattern between X-ray pulses emitted from electrons that have been scattered and recombined multiple times, potentially generating pulses that last only hundreds of zeptoseconds (1 zeptosecond is  $10^{-21}$  seconds). Such a timescale could be used to image subatomic processes. *Phys. Rev. Lett.* 111, 033002 (2013)

#### BIOLOGICAL MATERIALS

## How mussels flex for impact

The thin threads that attach mussels to rocks and fast-moving ships have the perfect ratio of components to absorb the battering forces of the sea.

Civil engineers Markus Buehler and Zhao Qin of the Massachusetts Institute of Technology in Cambridge measured the strength of the mollusc's 'byssal threads',



## COMMUNITY CHOICE

The most viewed papers in science

#### GENETICS

## Mice screened gene by gene

★ HIGHLY READ  
on www.cellpress.com in July

A systematic screen of engineered mouse lines found that mutations in previously unstudied genes were just as likely to produce effects as those in genes that had already been explored in other scientific publications.

Karen Steel at the Wellcome Trust Sanger Institute in Cambridge, UK, and her colleagues analysed 489 genes by systematically disabling each one in a separate mouse line. More than 40% of these genes were found to be essential for survival.

Adult mice from 250 of the lines were run through a wide range of tests, revealing traits such as reduced grip strength, fused joints, delayed response to heat, impaired hearing and altered blood chemistry.

Many results were unexpected: for example, disabling a gene that is thought to be involved in hearing led instead to increased body weight. Both the data and mutants are publicly available, and multiple groups are working together to perform similar tests on thousands more genes.

*Cell* 154, 452–464 (2013)

secreted protein fibres that extend from its shell to a hard surface. Using computer simulations, they found that the 4:1 ratio of soft to stiff material in natural threads minimizes the force experienced where threads join the shell, allowing the attachment to withstand crashing wave forces up to nine times the strength of the threads as measured with a stationary load.

The authors suggest that the insights could help researchers to design earthquake-resistant buildings, which, like mussels, must withstand fluctuating forces.

*Nature Commun.* 4, 2187 (2013)

#### PHYSIOLOGY

## Temperature fits the bill

In baby birds, ambient temperature can set beak size.

Gary Burness of Trent University in Peterborough, Canada, and his colleagues raised 40 Japanese quail hatchlings (*Coturnix*



*japonica*; pictured) at high (30 °C) or low (15 °C) temperatures. After 51 days, the hatchlings raised in warm conditions had longer bills than the chilled chicks. Beak growth in cold-reared chicks caught up after all birds were moved to an intermediate temperature, but the surface temperature of their beaks was, on average, 7.4 °C lower than that of birds reared at warmer temperatures, suggesting less blood flow.

Cold conditions soon after hatching may irreversibly inhibit blood flow or blood-vessel development in beaks. *Proc. R. Soc. B.* 280, 20131436 (2013)

#### NATURE.COM

For the latest research published by *Nature* visit: [www.nature.com/latestresearch](http://www.nature.com/latestresearch)

POLICY

## Carp invasion

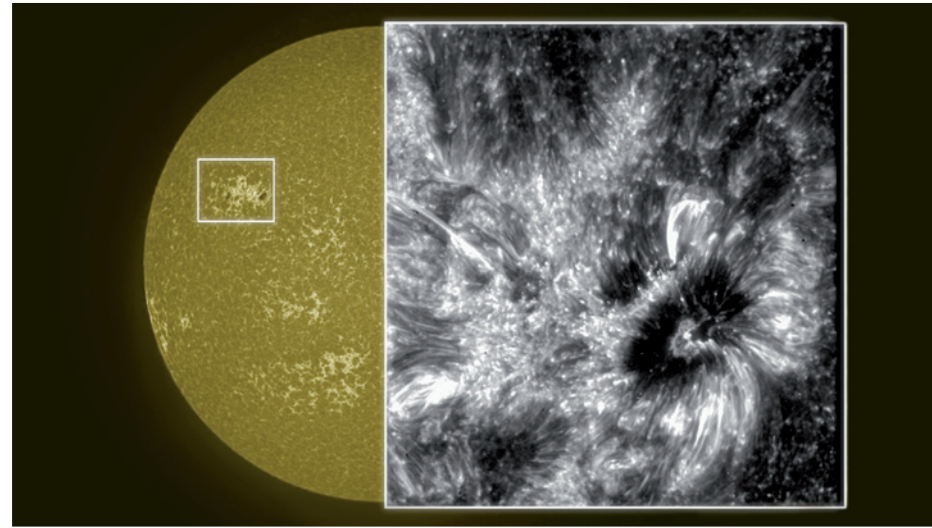
Adding electrified barriers and developing high-power water guns are part of a US plan announced on 24 July to prevent invasive Asian carp from reaching the Great Lakes. The carp, now abundant in the connecting Mississippi River, are crowding out fish native to the region such as the gizzard shad (*Dorosoma cepedianum*). The powerful jumpers have also injured humans and damaged boats. So far, the government has spent more than US\$200 million to keep the carp out of the Great Lakes.

## Publishing block

A court order is preventing the publication of work that identified security weaknesses in software used to immobilize cars, it emerged last week. Researchers at the University of Birmingham, UK, and Radboud University Nijmegen, the Netherlands, were due to present the findings this month at the USENIX Security Symposium in Washington DC. But they have pulled out after Volkswagen's parent company obtained an interim injunction from the British High Court on 25 June. On 29 July, Radboud said it found the ban "incomprehensible" but would respect the ruling; Birmingham also said it would defer publication of the paper.

## Drug import block

On 23 July, a US appeals court ruled that the Food and Drug Administration (FDA) cannot allow imports of an unapproved drug used as an anaesthetic for the execution of prisoners. The drug, sodium thiopental, is no longer available from authorized US manufacturers, forcing state officials to order the drug from sources abroad (see *Nature* <http://doi.org/ds64d9>; 2011).



NASA/SDO/IRIS

## Sun-scope opens its eyes

NASA has revealed the first images from its latest solar observatory, the Interface Region Imaging Spectrograph (IRIS). The instrument was launched into orbit in June (see *Nature* **498**, 279–280; 2013) to watch the flow of matter and energy in the Sun's chromosphere, a 1,700-kilometre-thick region between its

surface, known as the photosphere, and its outer atmosphere, called the corona. It takes much higher-resolution pictures than those captured by NASA's Solar Dynamic Observatory (pictured, yellow sphere), with features as small as 240 kilometres across made visible (pictured, black and white).

The FDA had argued that it has the discretion to allow the import of unapproved drugs, noting that it also uses this discretion to alleviate shortages of other drugs.

## Wetlands suit

A state board that oversees flood-protection efforts in Louisiana is suing some 100 energy companies, alleging that pipelines and access canals have damaged coastal wetlands. The Southeast Louisiana Flood Protection Authority–East filed the lawsuit on 24 July, arguing that the wetlands serve as a buffer zone that provides vital protection against flooding. On 23 July, a natural-gas well being drilled by the Walter Oil & Gas Corporation of Houston, Texas, exploded

in the Gulf of Mexico off the Louisiana coast.

BUSINESS

## Open clinical data

The pharmaceutical industry signalled its willingness last week to open vast stores of clinical-research data to scientists. In a statement on 24 July, the European Federation of Pharmaceutical Industries and Associations and the Pharmaceutical Research and Manufacturers of America — two of the world's leading trade bodies — said that they would "dramatically increase" the amount of information released by companies, including patient-level data and detailed clinical-study reports. Some campaigners

for greater openness in clinical trials said that the statement did not go far enough. See [go.nature.com/83ww6h](http://go.nature.com/83ww6h) for more.

## Pharma buyout

Health-care supplier Perrigo will buy Elan, a pharmaceutical company based in Dublin, for US\$8.6 billion, Perrigo announced on 29 July. Elan is best known for developing the multiple-sclerosis drug Tysabri (natalizumab), but spun off its research and development arm last year. It placed itself on the market after fending off a hostile takeover attempt earlier this year. Perrigo, which is based in Allegan, Michigan, and specializes in selling over-the-counter drugs, will receive a tax break for relocating its base to Ireland.

## PEOPLE

**Scripps head**

Margaret Leinen will take the helm of the Scripps Institution of Oceanography at the University of California, San Diego (UCSD), the university announced on 25 July. She will replace former director Tony Haymet on 1 October. Leinen, an oceanographer and president-elect of the American Geophysical Union, ran the geosciences directorate at the US National Science Foundation for seven years, and most recently led the Harbor Branch Oceanographic Institute in Fort Pierce, Florida. She says that her priorities as director will include strengthening academic partnerships between Scripps and the rest of UCSD in the face of tightening budgets.

**Sexologist dies**

Pioneering sex researcher Virginia Johnson (pictured) died last week aged 88, news outlets reported on 25 July. Johnson and her long-time collaborator William Masters were known for their landmark studies of the human sexual response, including filming changes inside the vagina during female arousal and orgasm. On the basis of observations that the vagina conforms to the penis, Johnson and Masters posited that



penis size should not be a prime determinant of female satisfaction (see *Nature* <http://doi.org/m92>; 2013).

**NASA top scientist**

Planetary geologist Ellen Stofan will be NASA's next chief scientist, the agency announced on 29 July. An honorary professor at University College London and vice-president of Proxemy Research in Laytonsville, Maryland, Stofan held various senior positions at NASA from 1991 to 2000. Replacing Waleed Abdalati as the agency's lead adviser on science programmes, Stofan will have to deal with severe budget cuts that have been proposed for the planetary sciences division.

**EFSA resignation**

The European Food Safety Authority (EFSA) announced the resignation of its executive

director on 24 July. Catherine Geslain-Lanéelle, who has led the agency since 2006, will take up a new post on 1 September as France's director general for agricultural, agri-food and territorial policies at the Ministry of Agriculture, Food and Forestry. Under her leadership, the EFSA introduced tougher conflict-of-interest policies for staff and outside experts. In January, the agency also announced a transparency initiative to make the data underlying its risk assessments publicly available.

## RESEARCH

**Big data satellite**

Alphasat, the most massive telecommunications satellite ever built in Europe, was launched on 25 July. Operated jointly by the European Space Agency and satellite company Inmarsat, the 6.6-tonne spacecraft will test an experimental device to relay messages between satellites using laser beams, which could vastly increase the rate at which data are communicated. The satellite will primarily communicate with Earth using radio waves in the commonly used L band of the electromagnetic spectrum, but it also carries an experiment for broadcasting in the less-crowded, high-frequency Q-V band. See [go.nature.com/wje1s](http://go.nature.com/wje1s) for more.

**COMING UP****4–9 AUGUST**

The Ecological Society of America discusses managing sustainable ecosystems and data-intensive research at its annual meeting in Minneapolis.

[www.esa.org/minneapolis](http://www.esa.org/minneapolis)

**Stem-cell network**

The California Institute for Regenerative Medicine (CIRM), based in San Francisco, approved plans on 25 July for a US\$70 million network of clinics to test stem-cell therapies. The 'Alpha Clinics' network will consist of up to five sites and a coordinating centre and will focus on therapies that involve transplanting or infusing stem cells. CIRM says that the network could help researchers to resolve technical and regulatory issues involved in early cellular therapy trials and educate patients who might otherwise turn to untested and risky treatments.

**Cigarette appeal**

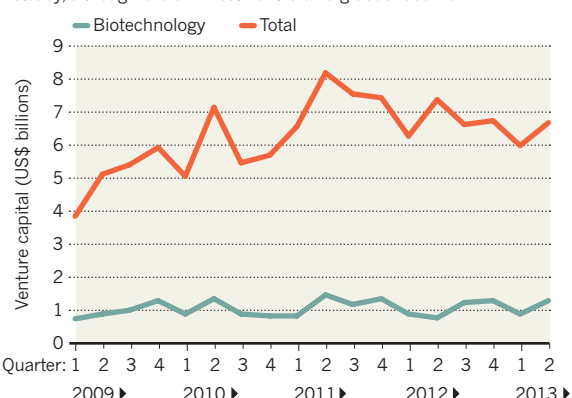
Flavour additives and cigarette packaging may influence smoking habits, according to two reports released last week. In a preliminary scientific evaluation, the US Food and Drug Administration said on 23 July that cigarettes containing menthol may pose a greater public-health risk than non-mentholated cigarettes, probably by increasing the take-up of smoking and reducing success in quitting. On 22 July, researchers in Australia reported that plain packaging for cigarettes is associated with lower smoking appeal and a greater urgency to quit (M. A. Wakefield *et al.* *BMJ Open* **3**, e003175; 2013).

**TREND WATCH**

Worldwide investment in the US biotechnology industry rose in the second quarter of this year, according to a report from PricewaterhouseCoopers and the US National Venture Capital Association. Venture capitalists pumped US\$1.3 billion into the sector, an increase of 68% over the same period last year. Meanwhile, investment in medical devices declined by 20%, and overall venture-capital investment across industries fell by 9% relative to the second quarter of 2012.

**BIOTECH BUCKS DOWNWARD TREND**

Venture-capital funding for US biotechnology firms has remained steady, although overall investment is on a gradual decline.

**NATURE.COM**

For daily news updates see:  
[www.nature.com/news](http://www.nature.com/news)

# NEWS IN FOCUS

**BIOMEDICINE** NIH considers rules to ramp up reproducibility **p.14**

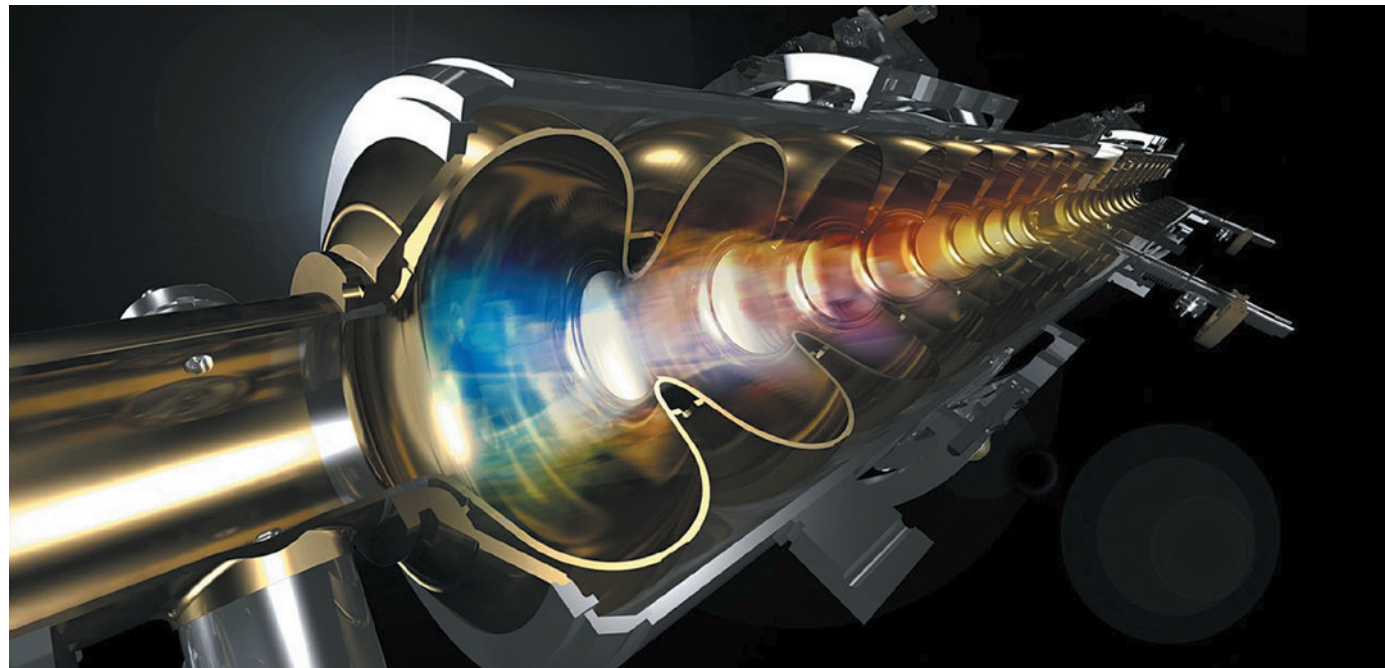
**MICROBIOLOGY** Effort to catalogue bacteria loses its home **p.16**

**CLIMATE** Solid rock could be dustbin for Earth-warming CO<sub>2</sub> **p.18**



**ARCHAEOLOGY** How the dawn of dairying upended Europe **p.20**

NGS/LAWRENCE BERKELEY NATL LAB



Superconducting cavities in the Next Generation Light Source (artist's impression) would accelerate electrons and then extract laser-like X-ray light from them.

## PHYSICS

# Labs vie for X-ray source

*California facilities respond to US panel's call for a powerful free-electron laser.*

BY EUGENIE SAMUEL REICH

**T**he competition to build the world's most powerful source of X-rays is becoming as intense as the light pulses it might one day emit, with two US Department of Energy (DOE) laboratories vying to host the proposed machine. The two California labs — the Lawrence Berkeley National Laboratory in Berkeley and the SLAC National Accelerator Laboratory in Menlo Park — each had hopes of getting its own project funded. But on 25 July, advisers to the DOE said that building just one, cutting-edge light source would be better.

"Instead of an argument, we'd like to have a unified proposal," says William Barletta, a physicist at the Massachusetts Institute of Technology in Cambridge who served on the DOE advisory committee, which met last week in Bethesda, Maryland, to put forward the light-source

recommendations. "You want to make a revolutionary machine that really stands out."

X-ray light sources provide an imaging technology that serves a wide range of scientists, including biologists, chemists and materials scientists. The DOE has led the area in recent decades, building four powerful synchrotrons, which produce intense X-rays as electrons zip around circular paths. The department has also built a pioneering free-electron laser, which uses special undulator magnets to wiggle an electron beam so that it emits intense, laser-like pulses of X-ray light. A European collaboration is constructing a free-electron laser in Germany, and Sweden, Japan and Brazil are working on designs for synchrotrons that would compete with the US machines. In January, the DOE commissioned a review to try to sustain US leadership in the field.

The panel's resulting report throws down the

gauntlet to light-source designers at the two competing labs to cooperate on a design for a single free-electron laser. In 2011, the Berkeley lab won initial approval from the DOE to begin work on a free-electron laser called the Next Generation Light Source (NGLS), whereas SLAC had hoped to upgrade its Linac Coherent Light Source (LCLS), the free-electron laser that it currently operates.

Managers at the labs had said that there was room for two complementary machines. The NGLS would produce lower-energy, 'soft' X-rays — ideal for imaging biological matter, chemical reactions and electron movement in the outer shells of atoms. Its particular strength would be a high repetition rate for its X-ray pulses, which would enable multiple snapshots of electron motion and the creation of 'molecular movies' of chemical processes. By contrast, the LCLS upgrade would extend

## SHINING LIGHTS

Individually, proposals for the Linac Coherent Light Source (LCLS) and the Next Generation Light Source (NGLS) do not meet the specifications called for by a panel that advises the US Department of Energy.

Proposed project	Repetition rate	Upper energy limit
LCLS upgrade	1 kHz	25,000 eV
NGLS	1,000 kHz	720 eV
Panel recommendation	100 kHz	5,000 eV

Kilohertz (kHz); electronvolts (eV)

► the machine's capability to produce higher-energy, 'hard' X-rays, which could image the arrangement of atoms and penetrate deep into heavier elements. But its intense pulses would come at a lower repetition rate, ruling out movies of dynamic processes.

Both approaches would be likely to attract users. Lou DiMauro, an atomic physicist at Ohio State University in Columbus, is keen to run 'pump-probe' experiments, in which an initial X-ray pulse is used to excite an atom, and the next pulse is used to probe the atom's state. The closely spaced pulses of the NGLS design would be ideal for that. But Phil Bucksbaum, an atomic physicist at Stanford University in California, who uses the SLAC light source, says that the NGLS would not be able to probe heavier elements because it operates at too low an energy compared with an upgraded LCLS.

The DOE advisory group found that the broadest science case could be met by a single facility that combines the strengths of both the NGLS and the LCLS (see 'Shining lights'). The committee's recommendations will help the energy department to respond to members of the US Congress who have asked for a more compelling case for a future free-electron laser.

Building two, smaller, less-capable machines "is not the best science per dollar", says Barletta.

In response to the panel's recommendation, the Berkeley lab and SLAC have been scrambling to extend the reach of their proposals, and jockeying to be the front-runner to host a single site. Paul Alivisatos, director of the Berkeley lab, says that the NGLS design had

**"You want to make a revolutionary machine that really stands out."**

an upper energy limit of 720 electron-volts (eV) to keep project costs below US\$700 million. Increasing the budget to \$1.2 billion would allow the electron-beam accelerator to be lengthened and would boost the upper energy limit to 3,000 eV, not far from the advisory panel's desired level of 5,000 eV. "It's a straightforward extension of our proposal," he says.

Uwe Bergmann, associate director of the LCLS, says that an upgrade to his machine could get it to a repetition rate of 10 kilohertz (kHz), but the current proposal boosts it to only 1 kHz. To get near the panel's recommendation of 100 kHz, he acknowledges that his facility

would need to replace its accelerator with a superconducting one — a key feature of the Berkeley lab's proposal. But ultimately, he says, the idea of upgrading an existing machine may be more realistic in a cost-constrained environment than the advisory panel's ambitious vision. "A committee suggests something — but the committee doesn't foot the bill."

The tight fiscal climate has exacerbated competition between the two proposals, says accelerator physicist Michael Borland of Argonne National Laboratory in Illinois. "There is limited funding, and government agencies need to decide which machine to build first," he says. But he sees at least one way to combine the two projects: the electron source and superconducting linear accelerator from the NGLS proposal could be put in the existing LCLS tunnel to take advantage of its undulator magnets. "This seems to make more sense than starting from scratch with a higher-energy NGLS."

For users, a new plan cannot come too soon, says Thomas Russell, a polymer scientist at the University of Massachusetts Amherst. Russell wants to use a fast-repeating X-ray source to watch the crystallization of photoactive materials used in solar cells. The current LCLS is not fast enough to make the movies he wants, and moreover, as the premier free-electron laser in the United States, the LCLS turns away four scientists for every one that is granted time. He has visited all four of the US X-ray synchrotrons, but the diffuse nature of their light would make it impossible for him to understand his crystal structures. "You reach a certain limit and you just can't do the experiment you want to do," he says. "The light sources that exist just don't provide enough oomph." ■

## BIOMEDICINE

# NIH mulls rules for validating key results

*US biomedical agency could enlist independent labs for verification.*

BY MEREDITH WADMAN

In biomedical science, at least one thing is apparently reproducible: a steady stream of studies that show the irreproducibility of many important experiments.

In a 2011 internal survey, pharmaceutical firm Bayer HealthCare of Leverkusen, Germany, was unable to validate the relevant preclinical research for almost two-thirds of 67 in-house projects. Then, in 2012, scientists at Amgen, a drug company based in Thousand

Oaks, California, reported their failure to replicate 89% of the findings from 53 landmark cancer papers. And in a study published in May, more than half of the respondents to a survey at the MD Anderson Cancer Center in Houston, Texas, reported failing at least once in attempts at reproducing published data (see 'Make believe').

The growing problem is threatening the reputation of the US National Institutes of Health (NIH) based in Bethesda, Maryland, which funds many of the studies in question.

Senior NIH officials are now considering adding requirements to grant applications to make experimental validations routine for certain types of science, such as the foundational work that leads to costly clinical trials. As the NIH pursues such top-down changes, one

company is taking a bottom-up approach, targeting scientists directly to see if they are willing to verify their experiments. [go.nature.com/zqfrnp](http://go.nature.com/zqfrnp)

There is the looming

## SHINING LIGHTS

Individually, proposals for the Linac Coherent Light Source (LCLS) and the Next Generation Light Source (NGLS) do not meet the specifications called for by a panel that advises the US Department of Energy.

Proposed project	Repetition rate	Upper energy limit
LCLS upgrade	1 kHz	25,000 eV
NGLS	1,000 kHz	720 eV
Panel recommendation	100 kHz	5,000 eV

Kilohertz (kHz); electronvolts (eV)

► the machine's capability to produce higher-energy, 'hard' X-rays, which could image the arrangement of atoms and penetrate deep into heavier elements. But its intense pulses would come at a lower repetition rate, ruling out movies of dynamic processes.

Both approaches would be likely to attract users. Lou DiMauro, an atomic physicist at Ohio State University in Columbus, is keen to run 'pump-probe' experiments, in which an initial X-ray pulse is used to excite an atom, and the next pulse is used to probe the atom's state. The closely spaced pulses of the NGLS design would be ideal for that. But Phil Bucksbaum, an atomic physicist at Stanford University in California, who uses the SLAC light source, says that the NGLS would not be able to probe heavier elements because it operates at too low an energy compared with an upgraded LCLS.

The DOE advisory group found that the broadest science case could be met by a single facility that combines the strengths of both the NGLS and the LCLS (see 'Shining lights'). The committee's recommendations will help the energy department to respond to members of the US Congress who have asked for a more compelling case for a future free-electron laser.

Building two, smaller, less-capable machines "is not the best science per dollar", says Barletta.

In response to the panel's recommendation, the Berkeley lab and SLAC have been scrambling to extend the reach of their proposals, and jockeying to be the front-runner to host a single site. Paul Alivisatos, director of the Berkeley lab, says that the NGLS design had

**"You want to make a revolutionary machine that really stands out."**

an upper energy limit of 720 electron-volts (eV) to keep project costs below US\$700 million. Increasing the budget to \$1.2 billion would allow the electron-beam accelerator to be lengthened and would boost the upper energy limit to 3,000 eV, not far from the advisory panel's desired level of 5,000 eV. "It's a straightforward extension of our proposal," he says.

Uwe Bergmann, associate director of the LCLS, says that an upgrade to his machine could get it to a repetition rate of 10 kilohertz (kHz), but the current proposal boosts it to only 1 kHz. To get near the panel's recommendation of 100 kHz, he acknowledges that his facility

would need to replace its accelerator with a superconducting one — a key feature of the Berkeley lab's proposal. But ultimately, he says, the idea of upgrading an existing machine may be more realistic in a cost-constrained environment than the advisory panel's ambitious vision. "A committee suggests something — but the committee doesn't foot the bill."

The tight fiscal climate has exacerbated competition between the two proposals, says accelerator physicist Michael Borland of Argonne National Laboratory in Illinois. "There is limited funding, and government agencies need to decide which machine to build first," he says. But he sees at least one way to combine the two projects: the electron source and superconducting linear accelerator from the NGLS proposal could be put in the existing LCLS tunnel to take advantage of its undulator magnets. "This seems to make more sense than starting from scratch with a higher-energy NGLS."

For users, a new plan cannot come too soon, says Thomas Russell, a polymer scientist at the University of Massachusetts Amherst. Russell wants to use a fast-repeating X-ray source to watch the crystallization of photoactive materials used in solar cells. The current LCLS is not fast enough to make the movies he wants, and moreover, as the premier free-electron laser in the United States, the LCLS turns away four scientists for every one that is granted time. He has visited all four of the US X-ray synchrotrons, but the diffuse nature of their light would make it impossible for him to understand his crystal structures. "You reach a certain limit and you just can't do the experiment you want to do," he says. "The light sources that exist just don't provide enough oomph." ■

## BIOMEDICINE

# NIH mulls rules for validating key results

*US biomedical agency could enlist independent labs for verification.*

BY MEREDITH WADMAN

In biomedical science, at least one thing is apparently reproducible: a steady stream of studies that show the irreproducibility of many important experiments.

In a 2011 internal survey, pharmaceutical firm Bayer HealthCare of Leverkusen, Germany, was unable to validate the relevant preclinical research for almost two-thirds of 67 in-house projects. Then, in 2012, scientists at Amgen, a drug company based in Thousand

Oaks, California, reported their failure to replicate 89% of the findings from 53 landmark cancer papers. And in a study published in May, more than half of the respondents to a survey at the MD Anderson Cancer Center in Houston, Texas, reported failing at least once in attempts at reproducing published data (see 'Make believe').

The growing problem is threatening the reputation of the US National Institutes of Health (NIH) based in Bethesda, Maryland, which funds many of the studies in question.

Senior NIH officials are now considering adding requirements to grant applications to make experimental validations routine for certain types of science, such as the foundational work that leads to costly clinical trials. As the NIH pursues such top-down changes, one

company is taking a bottom-up approach, targeting scientists directly to see if they are willing to verify their experiments. [go.nature.com/zqfrnp](http://go.nature.com/zqfrnp)

There is the looming



## MAKE BELIEVE

Reproducibility problems have led the National Institutes of Health to consider verification rules for some experiments.

**SEPTEMBER 2011** Bayer HealthCare finds inconsistencies between in-house and published data in almost two-thirds of 67 projects.

**MARCH 2012** Amgen publication shows that the findings from only 11% of 53 landmark papers can be replicated by company scientists.

**JANUARY 2013** Elizabeth Iorns (pictured), chief executive of Science Exchange, asks more than 22,000 study authors if they want her company to arrange verification of their experiments; nearly 2,000 say yes.

**MAY 2013** A survey at the MD Anderson Cancer Center finds that more than half of its respondents have tried and failed to reproduce published data.

**JULY 2013** Science Exchange launches a verification programme for commercially sold antibodies.

question, however, of who will pay for it all. Independently validating the results of a major paper that has *in vitro* and animal experiments can cost US\$25,000, says Elizabeth Iorns, chief executive of Science Exchange, a company in Palo Alto, California, that matches scientists with verification service providers.

Last year, the NIH convened two workshops that examined the issue of reproducibility, and last October, the agency's leaders and others published a call for higher standards in the reporting of animal studies in grant applications and journal publications. At a minimum, they wrote, studies should report on whether and how animals were randomized, whether

investigators were blind to the treatment, how sample sizes were estimated and how data were handled.

The NIH is just beginning to take active measures, says Lawrence Tabak, the agency's principal deputy director. "There is certainly sufficient information now that the NIH feels it's appropriate to look at this at a central-agency level," he says. This summer, he and other senior NIH officials, including Story Landis, director at the neurology institute, and Harold Varmus, director at the cancer institute, are assessing input gathered from the directors of the agency's 27 institutes and centres. They will then confer with NIH director Francis Collins, who will decide what steps to take.

Proposals under consideration include modifying peer review to bring greater scrutiny to the work a grant application is based on — perhaps just for applications that are likely to lead to clinical trials. In a June meeting of Collins's advisory committee, Tabak imagined implementing such a scenario. "If the premise isn't validatable, then we're done; it doesn't matter how well you wrote the grant," he said. Agency officials are also considering a requirement that independent labs validate the results of important preclinical studies as a condition of receiving grant funding.

The very idea of a validation requirement makes some scientists queasy. "It's a disaster," says Peter Sorger, a systems biologist at Harvard Medical School in Boston, Massachusetts. He says that frontier science often relies on ideas, tools and protocols that do not exist in run-of-the-mill labs, let alone in companies that have been contracted to perform verification. "It is unbelievably difficult to reproduce cutting-edge science," he says.

But others say that independent validation is a must to counteract the pressure to publish positive results and the lack of incentives to publish negative ones. Iorns doubts that tougher reporting requirements will make any real impact, and thinks that it would be better to have regular validations of results, either through random audits or selecting the highest-profile papers.

Science Exchange would clearly benefit from a new flow of business should the NIH impose such a mandate on even some studies. The company's Reproducibility Initiative, launched last year, arranges for the independent replication of study results for authors who request the service — and the first batch of academic validations began in May. In January, Iorns asked more than 22,000 corresponding authors of original biomedical papers published in 2012 if they would allow the experiments in their reports to be independently verified, should funding be made available. Of those who responded, 1,892 scientists said yes and 416 declined.

Iorns says that there are plenty of important papers among those published by the 1,892 — they had a readership that was, on average, an order of magnitude higher than that of ▶

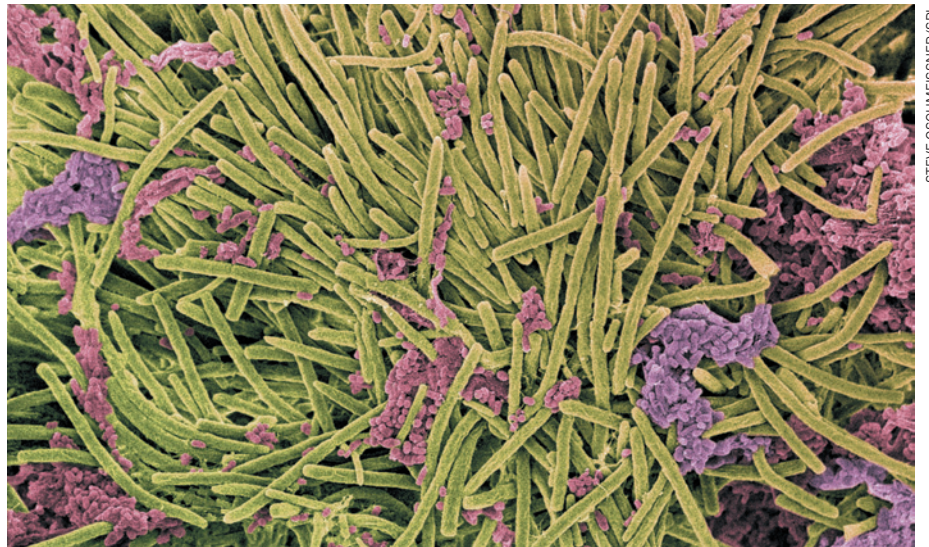
► the papers whose authors declined, as measured by downloads to a free online reference manager, Mendeley. The Laura and John Arnold Foundation, based in Houston, Texas, says that it is actively considering funding Science Exchange to validate cancer-cell biology papers within Iorns' cohort.

Some at the NIH are coming round to the idea that validation is best contracted out. Shai Silberberg, who is responsible for reproducibility issues at the agency's neurology institute, has almost finished a pilot study in which several academic labs tried to reproduce findings from studies aiming to move drugs to a stage at which they are ready to be tested in humans. He points out that it has already taken two and a half years. "It's too slow," he says. He now favours speedier contract-research organizations.

Iorns, for her part, is not waiting for the NIH to take action. On 30 July, Science Exchange launched a programme with reagent supplier antibodies-online.com, based in Aachen, Germany, to independently validate research antibodies. These are used, for example, to probe gene function in biomedical experiments, but their effects are notoriously variable. "Having a third party validate every batch would be a fabulous thing," says Peter Park, a computational biologist at Harvard Medical School. He notes that the consortium behind ENCODE — a project aimed at identifying all the functional elements in the human genome — tested more than 200 antibodies targeting modifications to proteins called histones and found that more than 25% failed to target the advertised modification.

With antibodies, the companies that make them have an incentive to prove the quality of their products, and Iorns hopes that they will pay the thousands of dollars that such validation costs. Antibodies that pass muster will receive an 'independently validated' green tick in the antibodies-online.com catalogue.

But with budgets stretched thin — and with Congress well aware of the reproducibility issues — the NIH also has an incentive to make sure that its \$29-billion budget is spent on verifiable science. "We are obliged to consider how we want to address this," says Tabak. ■



STEVE GSCHMEISSNER/SPL

The tongue is one of many sites to have its bacteria catalogued by the Human Microbiome Project.

#### MICROBIOLOGY

# Microbiome research goes without a home

Scientists say core tools and expertise remain necessary.

BY BETH MOLE

**T**rillions of microorganisms call the human body home. But 'home' for many US scientists studying these microscopic squatters is about to change, as funding for human microbiome research scatters across 16 of the 27 centres of the US National Institutes of Health (NIH).

Last year, researchers completed the \$US173-million Human Microbiome Project, which took five years and generated a slew of reference data, mostly genetic sequences of all the microbes that dwell on and inside humans. But the project's scientists fear that a lack of standards and expertise in data-gathering and analysis are hampering efforts to extract meaning from this information.

At a meeting last week in Bethesda, Maryland, they reiterated that identifying the

microbes is just the first step. Researchers must also focus on how bacteria interact with each other and the human body to cause — or prevent — disease. Yet these calls for action are coming as the project faces significant downsizing: by the beginning of 2014, microbiome researchers will no longer be able to depend on centralized resources based at the NIH's National Human Genome Research Institute (NHGRI) in Bethesda.

"The microbiome has so much appeal," says Christian Jobin, an immunologist at the University of Florida in Gainesville, who studies the interplay between gut microbes, inflammation and cancer. "But we're lacking direction right now."

In 2012, the project culminated with a flurry of publications (D. A. Relman *Nature* **486**, 194–195; 2012). But, says Lita Proctor, the project's programme director, some efforts still seem too

## MORE ONLINE

### TOP STORY



Incan mummies' hair shows that ritual sacrifice victims had ingested alcohol and coca [go.nature.com/2cm5ec](http://go.nature.com/2cm5ec)

### MORE NEWS

- Pilot projects bury carbon dioxide in porous basalt layers [go.nature.com/zop2ew](http://go.nature.com/zop2ew)
- Conflicting studies rekindle debate on why monogamy evolved in primates [go.nature.com/9efog](http://go.nature.com/9efog)
- An artificial-intelligence algorithm for quantum computers [go.nature.com/vt08pf](http://go.nature.com/vt08pf)

### NATURE PODCAST



Lactose tolerance in ancient Europeans, nanodiamonds inside cells, and Middle East science [nature.com/nature/podcast](http://nature.com/nature/podcast)

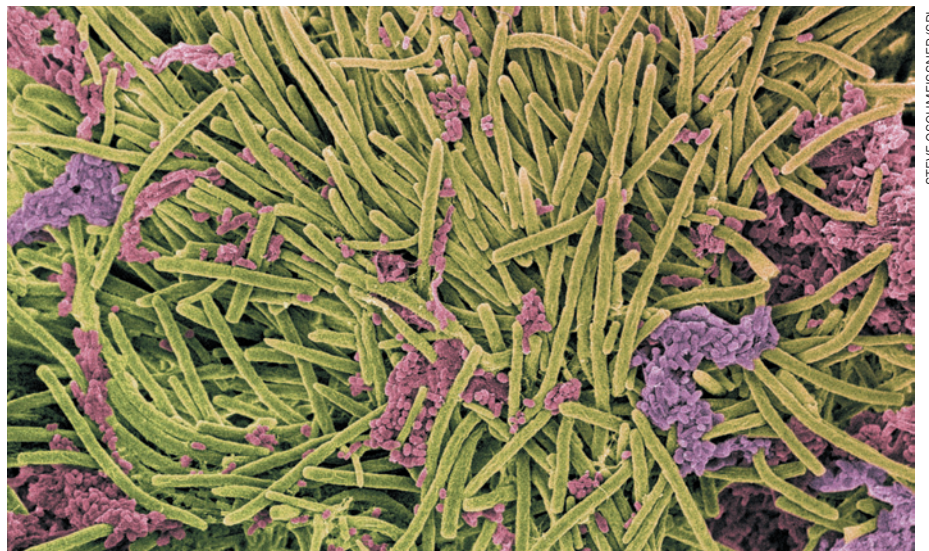
► the papers whose authors declined, as measured by downloads to a free online reference manager, Mendeley. The Laura and John Arnold Foundation, based in Houston, Texas, says that it is actively considering funding Science Exchange to validate cancer-cell biology papers within Iorns' cohort.

Some at the NIH are coming round to the idea that validation is best contracted out. Shai Silberberg, who is responsible for reproducibility issues at the agency's neurology institute, has almost finished a pilot study in which several academic labs tried to reproduce findings from studies aiming to move drugs to a stage at which they are ready to be tested in humans. He points out that it has already taken two and a half years. "It's too slow," he says. He now favours speedier contract-research organizations.

Iorns, for her part, is not waiting for the NIH to take action. On 30 July, Science Exchange launched a programme with reagent supplier antibodies-online.com, based in Aachen, Germany, to independently validate research antibodies. These are used, for example, to probe gene function in biomedical experiments, but their effects are notoriously variable. "Having a third party validate every batch would be a fabulous thing," says Peter Park, a computational biologist at Harvard Medical School. He notes that the consortium behind ENCODE — a project aimed at identifying all the functional elements in the human genome — tested more than 200 antibodies targeting modifications to proteins called histones and found that more than 25% failed to target the advertised modification.

With antibodies, the companies that make them have an incentive to prove the quality of their products, and Iorns hopes that they will pay the thousands of dollars that such validation costs. Antibodies that pass muster will receive an 'independently validated' green tick in the antibodies-online.com catalogue.

But with budgets stretched thin — and with Congress well aware of the reproducibility issues — the NIH also has an incentive to make sure that its \$29-billion budget is spent on verifiable science. "We are obliged to consider how we want to address this," says Tabak. ■



STEVE GSCHMEISSNER/SPL

The tongue is one of many sites to have its bacteria catalogued by the Human Microbiome Project.

#### MICROBIOLOGY

# Microbiome research goes without a home

Scientists say core tools and expertise remain necessary.

BY BETH MOLE

**T**rillions of microorganisms call the human body home. But 'home' for many US scientists studying these microscopic squatters is about to change, as funding for human microbiome research scatters across 16 of the 27 centres of the US National Institutes of Health (NIH).

Last year, researchers completed the \$US173-million Human Microbiome Project, which took five years and generated a slew of reference data, mostly genetic sequences of all the microbes that dwell on and inside humans. But the project's scientists fear that a lack of standards and expertise in data-gathering and analysis are hampering efforts to extract meaning from this information.

At a meeting last week in Bethesda, Maryland, they reiterated that identifying the

microbes is just the first step. Researchers must also focus on how bacteria interact with each other and the human body to cause — or prevent — disease. Yet these calls for action are coming as the project faces significant downsizing: by the beginning of 2014, microbiome researchers will no longer be able to depend on centralized resources based at the NIH's National Human Genome Research Institute (NHGRI) in Bethesda.

"The microbiome has so much appeal," says Christian Jobin, an immunologist at the University of Florida in Gainesville, who studies the interplay between gut microbes, inflammation and cancer. "But we're lacking direction right now."

In 2012, the project culminated with a flurry of publications (D. A. Relman *Nature* **486**, 194–195; 2012). But, says Lita Proctor, the project's programme director, some efforts still seem too

## MORE ONLINE

### TOP STORY



Incan mummies' hair shows that ritual sacrifice victims had ingested alcohol and coca [go.nature.com/2cm5ec](http://go.nature.com/2cm5ec)

### MORE NEWS

- Pilot projects bury carbon dioxide in porous basalt layers [go.nature.com/zop2ew](http://go.nature.com/zop2ew)
- Conflicting studies rekindle debate on why monogamy evolved in primates [go.nature.com/9efog](http://go.nature.com/9efog)
- An artificial-intelligence algorithm for quantum computers [go.nature.com/vt08pf](http://go.nature.com/vt08pf)

### NATURE PODCAST



Lactose tolerance in ancient Europeans, nanodiamonds inside cells, and Middle East science [nature.com/nature/podcast](http://nature.com/nature/podcast)

focused on data-gathering and do not account for the complex ways in which microbes interact with one another and their hosts. Some scientists are “struggling to figure out how to think about the microbiome”, she says.

There are several problems, says Rob Knight, a microbial ecologist at the University of Colorado Boulder. First, scientists need to forge standards on matters such as how long to wait after a person has a shower before swabbing their skin for microbes, or what a person ate before collecting a stool sample. Although researchers who gathered the reference data sets from healthy individuals tried to establish such standards, some of these have been ignored, and there is also wide variation in the way that microbiome samples are amassed from people with diseases.

Second, collecting, sequencing and analysing DNA from thousands of microbial species living in and on humans requires an interdisciplinary team with knowledge of clinical ethics, engineering and bioinformatics — expertise that can be tricky to assemble.

Last, it remains difficult to establish whether a microbial trend associated with a disease is the cause or a result of that disease. One solution, Knight says, would be to track people over time, to allow researchers to detect microbial changes that occur before or after someone becomes ill. Soon, he hopes,

microbiome information could help doctors to predict a patient’s risk of developing various diseases, and conditions such as obesity.

Jobin says few microbiologists are trying to understand what the microbes are doing and how they might be controlled. This year, he

**“Scientists are struggling to figure out how to think about the microbiome.”**

sat on a review panel for grant applications proposing to explore the microbiome’s connection to gastrointestinal cancers, and noted that many

planned simply to sequence microbial communities. They were swiftly rejected. “There are very few mechanism-driven studies,” he says.

Expectations are higher now than they were in 2003, when the Human Genome Project wrapped up, says Owen White, a bioinformatics researcher at the University of Maryland School of Medicine in Baltimore. “When you were sequencing the human genome, or the next mammalian genome, everyone knew that that was relatively hypothesis-free — and that was fine,” he says.

The Human Genome Project was overseen by the NHGRI, which continues to lead genome-related work. By contrast, the Human Microbiome Project does not have a place to call home for its second phase. Over its first five years, it received \$146 million from the NIH common

fund, money that was managed by the NHGRI and that contributed to the development of field-wide tools. But in its second phase, from 2014 to 2016, only \$15 million in common-fund money will flow through the NHGRI. Microbiome research will instead be largely supported by 16 individual NIH institutes.

The project’s leaders say that the effort still needs a base to provide resources such as standardized sampling protocols, technical support, and microbiome samples and data from specific patient groups that researchers can mine. Many had assumed that the NHGRI would take on this role, because the microbiome project was initially seen as an extension of the Human Genome Project. But the NHGRI “has been less enthusiastic than expected”, Knight says. Jane Peterson, a senior adviser to the NHGRI director’s office, says that the future of human microbiome research will be in clinical applications, which does not fit with the NHGRI’s mission.

But Heidi Kong, a dermatologist and microbiome researcher at the National Cancer Institute in Bethesda, says that the project’s basic science needs to be nurtured further before it will be ready for the clinic. Scientists need first to pin down the function of individual microbes and the body’s response to them, and should only then begin testing treatments on those interactions. “There is a bit more work we need to do,” Kong says. ■

# Pilot projects bury carbon dioxide in basalt

Two experiments test viability of sequestering emissions in porous layers of hard rock.

BY JEFF TOLLEFSON

**B**y early August, scientists will have pumped 1,000 tonnes of pure carbon dioxide into porous rock far below the northwestern United States. The goal is to find a permanent home for the carbon dioxide generated by human activities.

Researchers at the US Department of Energy's Pacific Northwest National Laboratory (PNNL) in Richland, Washington, began the injections into the Columbia River Basalt formation near the town of Wallula on 17 July. The rock contains pores created as many as 16 million years ago, when magma flowed across what is now the Columbia River Basin. Bubbles of CO<sub>2</sub> migrated to the edges of the magma as it cooled, forming layers of holes sandwiched between solid rock (see 'Rock steady').

In pumping emissions back underground, "we are returning the carbon dioxide from whence it came", says Pete McGrail, an environmental engineer at the PNNL who is heading the experiment, part of a larger energy-department programme on ways to sequester carbon.

The Wallula project is the second of two worldwide to target basalt formations, which scientists hope can hold — and permanently mineralize — vast quantities of gas. In basalt, dissolved CO<sub>2</sub> should react with calcium and magnesium to form limestone over the course of decades. Until the gas is locked away, the porous basalt layers are capped by solid rock that will prevent leaking. That should eliminate concerns about leakage that have dogged other proposals to store CO<sub>2</sub> deep underground, often in sandstone reservoirs.

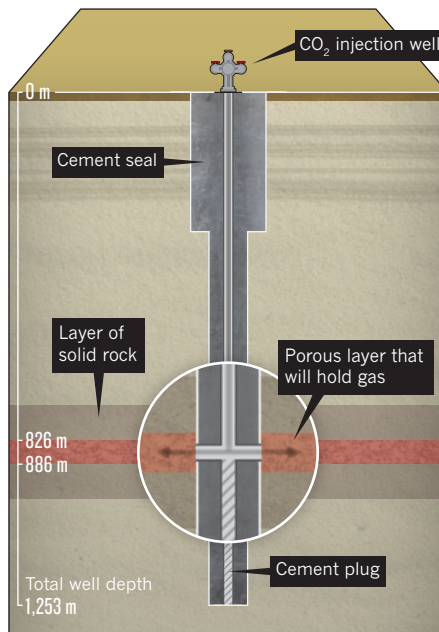
The basalt reactions are part of a natural weathering process that has helped to regulate atmospheric CO<sub>2</sub> levels throughout geological time. Scientists have analysed mineralization in the lab, but it is only now being tested in the field.

Researchers working on the other basalt project, based in Iceland and run by a consortium of US and European scientists along with Reykjavik Energy, made their first CO<sub>2</sub>

**"We are returning the carbon dioxide from whence it came."**

## ROCK STEADY

A carbon dioxide sequestration project in Washington state is testing whether chemical reactions in porous basalt will help to trap gas injected into the rock.



injections last year and will conduct another round this year. Early results look promising, says Juerg Matter, a geochemist at Columbia University's Lamont-Doherty Earth Observatory in Palisades, New York, who is working on the Iceland project. "The mineralization reaction is most likely faster than what we in the community had thought," says Matter, who has also contributed to the Wallula project. Assuming that holds true for basalt generally, "you reduce the risk of leakage, and you can pretty much walk away from your storage reservoirs".

In Wallula, researchers are already monitoring a series of shallow wells around the injection site for signs of CO<sub>2</sub> leaking into the soil and groundwater. Once the injection is finished, they will start taking samples from the injection well to monitor water chemistry, track changes in carbon isotopes and check for other evidence of reactions. Lab tests and computer simulations suggest that in general, around 20% of the CO<sub>2</sub> should be mineralized within 10–15 years, says McGrail.

The pilot project, however, is operating on a

shorter timescale. Fourteen months after the end of injection, the team plans to drill another well and pull up a core of rock to assess the results, says McGrail. "At that point, we are hoping to have some carbonized rock in our hands."

But achieving sequestration is only half the battle: scientists and engineers must still work out how to capture CO<sub>2</sub> from industrial facilities and transport it to the sequestration site cost-effectively. And even if a carbon-mineralization industry took off, establishing it on a global level would require an undertaking on the scale of rebuilding the oil industry.

Scientific opinions differ over whether it would be more desirable to stop burning fossil fuels than to undertake massive carbon-sequestration ventures — but if sequestration were to be favoured, many think that basalt could be important. And although backers of large-scale basalt sequestration have so far explored formations in the US northwest and southeast as well as in India, many are also looking offshore, where the sea floor could accommodate CO<sub>2</sub> emissions for centuries to come.

Carbon-sequestration research has until now tended to focus on sandstone reservoirs rather than basalt. There are two main reasons, says David Goldberg, a marine geologist at Lamont-Doherty. The oil industry is used to working with sandstone, and such formations are relatively common — making it easier to transport CO<sub>2</sub> from a power plant or other source to a sequestration site. That might mean that sandstone is more economically viable than ocean basalt, at least in the short term. But Goldberg says that the best place to bury globally significant volumes of CO<sub>2</sub> is offshore, where they will be safely capped by sediments and sea water.

A single formation off the US west coast, with an estimated storage volume of 685 cubic kilometres, has the potential to hold all the CO<sub>2</sub> emissions the country produces in a century, Goldberg notes. "If we can make it work," he says, "the oceans have a lot of advantages."

But none of this will be cheap, says Kevin Johnson, a geochemist at the University of Hawaii in Honolulu who has worked on lab experiments with McGrail's team. "It's a question of social importance — and whether the climate situation gets dire enough to justify the cost." ■



# The milk revolution

*When a single genetic mutation first let ancient Europeans drink milk, it set the stage for a continental upheaval.*

BY ANDREW CURRY

In the 1970s, archaeologist Peter Bogucki was excavating a Stone Age site in the fertile plains of central Poland when he came across an assortment of odd artefacts. The people who had lived there around 7,000 years ago were among central Europe's first farmers, and they had left behind fragments of pottery dotted with tiny holes. It looked as though the coarse red clay had been baked while pierced with pieces of straw.

Looking back through the archaeological literature, Bogucki found other examples of ancient perforated pottery. "They were so unusual — people would almost always include them in publications," says Bogucki, now at Princeton University in New Jersey. He had seen something similar at a friend's house that was used for straining cheese, so he speculated that the pottery might be connected with cheese-making. But he had no way to test his idea.

The mystery potsherds sat in storage until 2011, when Mélanie Roffet-Salque pulled them out and analysed fatty residues preserved in the clay. Roffet-Salque, a geochemist at the University of Bristol, UK, found signatures of abundant milk fats — evidence that the early

farmers had used the pottery as sieves to separate fatty milk solids from liquid whey. That makes the Polish relics the oldest known evidence of cheese-making in the world<sup>1</sup>.

Roffet-Salque's sleuthing is part of a wave of discoveries about the history of milk in Europe. Many of them have come from a €3.3-million (US\$4.4-million) project that started in 2009 and has involved archaeologists, chemists and geneticists. The findings from this group illuminate the profound ways that dairy products have shaped human settlement on the continent.

During the most recent ice age, milk was essentially a toxin to adults because — unlike children — they could not produce the lactase enzyme required to break down lactose, the main sugar in milk. But as farming started to replace hunting and gathering in the Middle East around 11,000 years ago, cattle herders learned how to reduce lactose in dairy prod-

ucts to tolerable levels by fermenting milk to make cheese or yogurt. Several thousand years later, a genetic mutation spread through Europe

that gave people the ability to produce lactase — and drink milk — throughout their lives. That adaptation opened up a rich new source of nutrition that could have sustained communities when harvests failed.

This two-step milk revolution may have been a prime factor in allowing bands of farmers and herders from the south to sweep through Europe and displace the hunter-gatherer cultures that had lived there for millennia. "They spread really rapidly into northern Europe from an archaeological point of view," says Mark Thomas, a population geneticist at University College London. That wave of emigration left an enduring imprint on Europe, where, unlike in many regions of the world, most people can now tolerate milk. "It could be that a large proportion of Europeans are descended from the first lactase-persistent dairy farmers in Europe," says Thomas.

## ON NATURE.COM

To hear Mark Thomas discuss the milk revolution, visit: [go.nature.com/aleyte](http://go.nature.com/aleyte)

## STRONG STOMACHS

Young children almost universally produce lactase and can digest the lactose in their mother's milk. But as they mature, most switch off the lactase gene. Only 35% of the human

population can digest lactose beyond the age of about seven or eight (ref. 2). “If you’re lactose intolerant and you drink half a pint of milk, you’re going to be really ill. Explosive diarrhoea — dysentery essentially,” says Oliver Craig, an archaeologist at the University of York, UK. “I’m not saying it’s lethal, but it’s quite unpleasant.”

Most people who retain the ability to digest milk can trace their ancestry to Europe, where the trait seems to be linked to a single nucleotide in which the DNA base cytosine changed to thymine in a genomic region not far from the lactase gene. There are other pockets of lactase persistence in West Africa (see *Nature* 444, 994–996; 2006), the Middle East and south Asia that seem to be linked to separate mutations<sup>3</sup> (see ‘Lactase hotspots’).

The single-nucleotide switch in Europe happened relatively recently. Thomas and his colleagues estimated the timing by looking at genetic variations in modern populations and running computer simulations of how the related genetic mutation might have spread through ancient populations<sup>4</sup>. They proposed that the trait of lactase persistence, dubbed the LP allele, emerged about 7,500 years ago in the broad, fertile plains of Hungary.

#### POWERFUL GENE

Once the LP allele appeared, it offered a major selective advantage. In a 2004 study<sup>5</sup>, researchers estimated that people with the mutation would have produced up to 19% more fertile offspring than those who lacked it. The researchers called that degree of selection “among the strongest yet seen for any gene in the genome”.

Compounded over several hundred generations, that advantage could help a population to take over a continent. But only if “the population has a supply of fresh milk and is dairy-ing”, says Thomas. “It’s gene–culture co-evolution. They feed off of each other.”

To investigate the history of that interaction, Thomas teamed up with Joachim Burger, a palaeogeneticist at the Johannes Gutenberg University of Mainz in Germany, and Matthew Collins, a bioarchaeologist at the University of York. They organized a multidisciplinary project called LeCHE (Lactase Persistence in the early Cultural History of Europe), which brought together a dozen early-career researchers from around Europe.

By studying human molecular biology and the archaeology and chemistry of ancient pottery, LeCHE participants also hoped to address a key issue about the origins of modern Europeans. “It’s been an enduring question in archaeology — whether we’re descended from Middle Eastern farmers or indigenous hunter-gatherers,” says Thomas. The argument boils down to evolution versus replacement. Did native populations of hunter-gatherers in Europe take up farming and herding? Or was there an influx of agricultural colonists who outcompeted the locals, thanks to a combination of genes and technology?

One strand of evidence came from studies of animal bones found at archaeological sites. If cattle are raised primarily for dairy-ing, calves are generally slaughtered before their first birthday so that their mothers can be milked. But cattle raised mainly for meat are killed later, when they have reached their full size. (The pattern, if not the ages, is similar for sheep and goats, which were part of the dairy-ing revolution.)

On the basis of studies of growth patterns in bones, LeCHE participant Jean-Denis Vigne, an archaeozoologist at the French National Museum of Natural History in Paris, suggests

that dairy-ing in the Middle East may go all the way back to when humans first started domesticating animals there, about 10,500 years ago<sup>6</sup>. That would place it just after the Middle Eastern Neolithic transition — when an economy based on hunter-gathering gave way to one devoted to agriculture. Dairy-ing, says Roz Gillis, also an archaeozoologist at the Paris museum, “may have been one of the reasons why human populations began trapping and keeping ruminants such as cattle, sheep and goats”. (See ‘Dairy-ing diaspora’.)

Dairy-ing then expanded in concert with

MAP SOURCE: REF. 2; POT PHOTOGRAPH: REF. 1

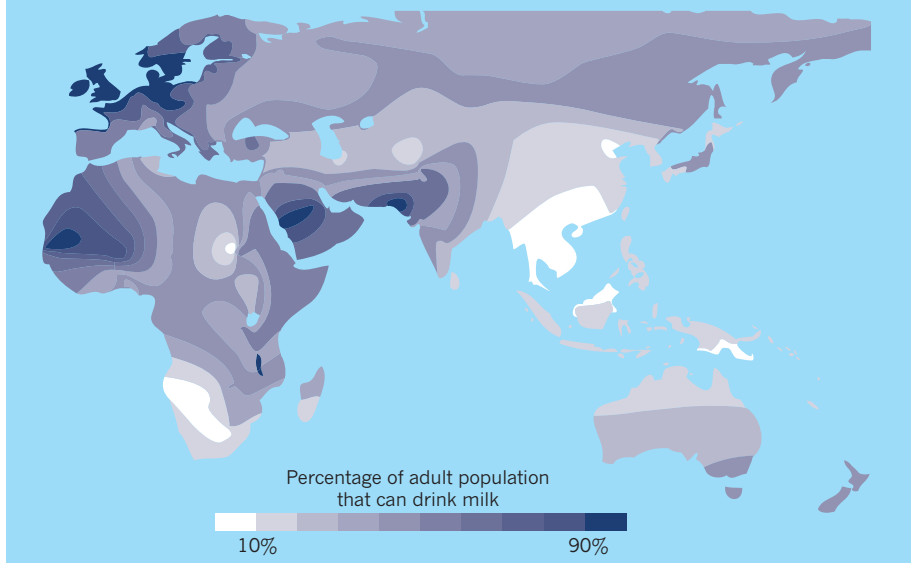
#### DAIRY DIASPORA

Dairy-ing practices spread from the Middle East to Europe as part of the Neolithic transition from hunting and gathering to agriculture.



#### LACTASE HOTSPOTS

Only one-third of people produce the lactase enzyme during adulthood, which enables them to drink milk.



the Neolithic transition, says Gillis, who has looked at bone growth at 150 sites in Europe and Anatolia (modern Turkey). As agriculture spread from Anatolia to northern Europe over roughly two millennia, dairying followed a similar pattern.

On their own, the growth patterns do not say whether the Neolithic transition in Europe happened through evolution or replacement, but cattle bones offer important clues. In a precursor study<sup>7</sup>, Burger and several other LeCHE participants found that domesticated cattle at Neolithic sites in Europe were most closely related to cows from the Middle East, rather than indigenous wild aurochs. This is a strong indication that incoming herders brought their cattle with them, rather than domesticating locally, says Burger.

A similar story is emerging from studies of ancient human DNA recovered at a few sites in central Europe, which suggest that Neolithic farmers were not descended from the hunter-gatherers who lived there before<sup>8</sup>.

Taken together, the data help to resolve the origins of the first European farmers. "For a long time, the mainstream of continental European archaeology said Mesolithic hunter-gatherers developed into Neolithic farmers," says Burger. "We basically showed they were completely different."

#### MILK OR MEAT

Given that dairying in the Middle East started thousands of years before the LP allele emerged in Europe, ancient herders must have found ways to reduce lactose concentrations in milk. It seems likely that they did so by making cheese or yogurt. (Fermented cheeses such as feta and cheddar have a small fraction of the lactose found in fresh milk; aged hard cheeses similar to Parmesan have hardly any.)

To test that theory, LeCHE researchers ran chemical tests on ancient pottery. The coarse, porous clay contains enough residues for chemists to distinguish what type of fat was absorbed during the cooking process: whether it was from meat or milk, and from ruminants such as cows, sheep and goats or from other animals. "That gave us a way into saying what types of things were being cooked," says Richard Evershed, a chemist at the University of Bristol.

Evershed and his LeCHE collaborators found milk fat on pottery in the Middle Eastern Fertile Crescent going back at least 8,500 years<sup>9</sup>, and Roffet-Salque's work on the Polish pottery<sup>1</sup> offers clear evidence that herders in Europe were producing cheese to supplement their diets between 6,800 and 7,400 years ago. By then, dairy had become a component of the Neolithic diet, but it was not yet a dominant part of the economy.

That next step happened slowly, and it seems

to have required the spread of lactase persistence. The LP allele did not become common in the population until some time after it first emerged: Burger has looked for the mutation in samples of ancient human DNA and has found it only as far back as 6,500 years ago in northern Germany.

Models created by LeCHE participant Pascale Gerbault, a population geneticist at University College London, explain how the trait might have spread. As Middle Eastern Neolithic cultures moved into Europe, their farming and herding technologies helped them to out-compete the local hunter-gatherers. And as the southerners pushed north, says Gerbault, the LP allele 'surfed' the wave of migration.

Lactase persistence had a harder time

## “It’s been an enduring question in archaeology – whether we’re descended from Middle Eastern farmers or indigenous hunter-gatherers.”

becoming established in parts of southern Europe, because Neolithic farmers had settled there before the mutation appeared. But as the agricultural society expanded northwards and westwards into new territory, the advantage provided by lactase persistence had a big impact. "As the population grows quickly at the edge of the wave, the allele can increase in frequency," says Gerbault.

The remnants of that pattern are still visible today. In southern Europe, lactase persistence is relatively rare — less than 40% in Greece and Turkey. In Britain and Scandinavia, by contrast, more than 90% of adults can digest milk.

#### CATTLE CONQUEST

By the late Neolithic and early Bronze Age, around 5,000 years ago, the LP allele was prevalent across most of northern and central Europe, and cattle herding had become a dominant part of the culture. "They discover this way of life, and once they can really get the nutritional benefits they increase or intensify herding as well," says Burger. Cattle bones represent more than two-thirds of the animal bones in many late Neolithic and early Bronze Age archaeological sites in central and northern Europe.

The LeCHE researchers are still puzzling out exactly why the ability to consume milk offered such an advantage in these regions. Thomas suggests that, as people moved north, milk would have been a hedge against famine. Dairy products — which could be stored for longer in colder climates — provided rich sources of calories that were independent of growing seasons or bad harvests.

Others think that milk may have helped, particularly in the north, because of its relatively high concentration of vitamin D, a nutrient that can help to ward off diseases such as rickets. Humans synthesize vitamin D

naturally only when exposed to the sun, which makes it difficult for northerners to make enough during winter months. But lactase persistence also took root in sunny Spain, casting vitamin D's role into doubt.

The LeCHE project may offer a model for how archaeological questions can be answered using a variety of disciplines and tools. "They have got a lot of different tentacles — archaeology, palaeoanthropology, ancient DNA and modern DNA, chemical analysis — all focused on one single question," says Ian Barnes, a palaeogeneticist at Royal Holloway, University of London, who is not involved in the project. "There are lots of other dietary changes which could be studied in this way."

The approach could, for example, help to tease apart the origins of amylase, an enzyme that helps to break down starch. Researchers have suggested that the development of the enzyme may have

followed — or made possible — the increasing appetite for grain that accompanied the growth of agriculture. Scientists also want to trace the evolution of alcohol dehydrogenase, which is crucial to the breakdown of alcohol and could reveal the origins of humanity's thirst for drink.

Some of the LeCHE participants are now probing further back in time, as part of a project named BEAN (Bridging the European and Anatolian Neolithic), which is looking at how the first farmers and herders made their way into Europe. Burger, Thomas and their BEAN collaborators will be in Turkey this summer, tracing the origins of the Neolithic using computer models and ancient-DNA analysis in the hope of better understanding who the early farmers were, and when they arrived in Europe.

Along the way, they will encounter beyaz peynir, a salty sheep's-milk cheese eaten with nearly every Turkish breakfast. It is probably much like the cheese that Neolithic farmers in the region would have eaten some 8,000 years ago — long before the march of lactase persistence allowed people to drink fresh milk. ■

**Andrew Curry** is a freelance writer in Berlin.

1. Salque, M. et al. *Nature* **493**, 522–525 (2013).
2. Leonardi, M., Gerbault, P., Thomas, M. G. & Burger, J. *Int. Dairy J.* **22**, 88–97 (2012).
3. Gerbault, P. et al. *Phil. Trans. R. Soc. B* **366**, 863–877 (2011).
4. Itan, Y., Powell, A., Beaumont, M. A., Burger, J. & Thomas, M. G. *PLoS Comp. Biol.* **5**, e1000491 (2009).
5. Bersaglieri, T. et al. *Am. J. Hum. Genet.* **74**, 1111–1120 (2004).
6. Vigne, J.-D. in *The Neolithic Demographic Transition and its Consequences* (eds Bocquet-Appel, J.-P. & Bar-Yosef, O.) 179–205 (Springer, 2008).
7. Edwards, C. J. et al. *Proc. R. Soc. B* **274**, 1377–1385 (2007).
8. Bramanti, B. et al. *Science* **326**, 137–140 (2009).
9. Evershed, R. P. et al. *Nature* **455**, 528–531 (2008).

# COMMENT



**ORNITHOLOGY** On the enduring relationship between birds and people **p.25**

**ENVIRONMENT** Psychological dissociation plagues our relationship with nature **p.26**

**GENOMICS** High-tech Smithsonian exhibition celebrates double helix **p.28**

**OBITUARY** Kenneth Wilson, physics revolutionary, remembered **p.30**

ILLUSTRATIONS BY EVA BEE



## Cell sex matters

Male and female cells can behave differently — it is time that researchers, journals and funders took this seriously, says **Elizabeth Pollitzer**.

Transplanting muscle-derived stem cells into diseased muscle regenerates it — a phenomenon that holds major potential for human therapies. But for years, researchers were puzzled by the unpredictability of these cells — sometimes they would promote fast regeneration, at other times none at all. Then, in 2007, a group led by Johnny Huard, a stem-cell researcher at the University of Pittsburgh in Pennsylvania, hit

on the rather surprising explanation — sex<sup>1</sup>. Muscle stem cells taken from female mice regenerate new muscle much faster than those from male mice when transplanted into diseased muscle of mice of either sex.

Researchers have also found that cells taken from male and female mice respond differently to stress<sup>2</sup>, and that human cells exhibit wildly different concentrations of many metabolites across the sexes<sup>3</sup>. Evidence

is mounting that cells differ according to sex, irrespective of their history of exposure to sex hormones. These differences could have major implications for the susceptibility to and course of many diseases, their diagnosis and treatment. However, most cell biologists do not note whether the cells they are using come from males or females<sup>4</sup>.

Between 1997 and 2001, ten prescription drugs were withdrawn from the

► market by the US Food and Drug Administration (FDA), eight of which were more dangerous to women than to men (see [go.nature.com/ksindo](http://go.nature.com/ksindo)). The ingredients used in non-prescription drugs can also pose greater health risks to women. In 2000, for instance, the FDA took steps to remove phenylpropanolamine, a component of many over-the-counter medications, from all drug products because of a reported increased risk of bleeding into the brain or into tissue around the brain in women but not in men. Such drug therapies are developed through basic research — but what if sex-related differences in studied cells contribute in a significant way to the observed effects?

This major potential problem has a relatively easy solution. Researchers, journals and peer reviewers must simply pay attention to cell sex, and whether it could affect findings.

#### YOU'VE GOT MALE

As a computing expert, the sex of cells has never had a direct influence on my research. I learned about the problem as director of genSET, a project funded by the European Union that looked at how gender issues are, or should be, addressed in science (see [www.genderinscience.org](http://www.genderinscience.org)). The biggest concern turned out to be not inequities in hiring or funding, but the absence of gender considerations in the design, analysis and reporting of bench experiments.

In 2010, genSET convened a panel of 14 experts who reviewed more than 120 papers from a range of fields — not just cell biology — and produced a consensus report with 13 recommendations (see [go.nature.com/kxnpfn](http://go.nature.com/kxnpfn)). They call for more thorough and systematic inclusion of sex and gender

analysis in study design, in the research process and in the training of scientists and lab managers.

The fact that sex and gender do matter has been recognized for years in clinical research, a field in which researchers have often disproportionately sampled men. For instance, a 2009 review<sup>5</sup> of hundreds of clinical studies in cancer revealed that 75% of them under-represented women, suggesting that women have less access to experimental medicine than men, and might respond less effectively to approved drugs.

The imbalances extend to basic research. When the journal *Pain* reviewed its publication record in 2007, it found that at least 79% of animal studies published in the journal over the preceding ten years used male subjects only, with just 8% of studies on females only. Another 4% were designed explicitly to test for sex differences and the rest did not specify<sup>6</sup>.

Hormones do not provide the entire explanation for these sex differences — embryonic neurons isolated from male and female rats before being exposed to sex hormones have different cellular responses to stress. Female cells are more sensitive to agents that induce programmed cell death (apoptosis), whereas male cells react more to oxygen deprivation, ischaemia and other forms of stress<sup>7</sup>. Female cells also show greater sensitivity to ethanol than do male cells — again, independent of hormonal effects<sup>2</sup>.

These dimorphisms in cellular behaviour may be because of different metabolic pathways. Sex-stratified analyses of genomic data that look at the location and expression of the genes controlling key enzymes (such as the *CPS1* gene, involved in protein and nitrogen metabolism) have revealed significant differences between females and males<sup>3</sup>. The products of metabolic reactions may be used as biomarkers for diseases such as diabetes and Alzheimer's, but clinicians might not always realize that they should expect different metabolite levels in men and women.

#### WAY FORWARD

My appreciation of the importance of this issue is helped by the fact that in my first degree, I took courses on molecular and cell biology, biochemistry, genetics and physics. I was introduced to the topic of social responsibility in science by the molecular biologist and physicist Maurice Wilkins, then head of the newly created biophysics department at King's College London. The

topic of gender in science has since taken an exciting form, opening up new directions for research, while improving its quality and efficacy.

In November, the third Gender Summit will take place in Washington DC under the leadership of the US National Science Foundation ([www.gender-summit.com](http://www.gender-summit.com)). The summit will feature discussions about understanding and addressing sex and gender issues in basic and applied science.

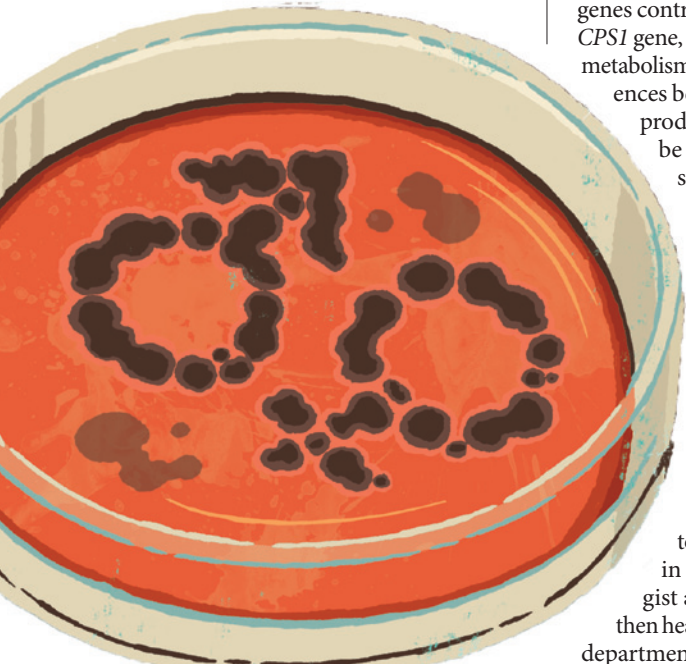
The three-day programme includes a wide range of topics delivered by more than 100 speakers. Attendees will be able to learn about the effects that sex differences have at the fundamental level of biochemical processes involved in cell regulation; about dimorphic effects in the regenerative properties of stem cells; and about how insights into the differences between the metabolic profiles of women and men can transform diagnosis, therapy and health economics. This is timely: when I attended the 38th Federation of European Biochemical Societies Congress in St Petersburg, Russia, a few weeks ago, I was surprised to see no mention of sex and gender differences in the titles of programmed talks.

The most important thing that scientists can do is to acknowledge that there are differences between male and female cells, and design experiments with this in mind. Do not combine male and female cells — separate them out, ideally performing the same experiment in each group. If working with only one sex or gender, then specify that, and explain why. Animal and human studies should abide by the same rules.

Peer reviewers, editors and funders can help to bring about this change by insisting that researchers determine whether and how sex and gender could influence their findings. After its 2007 analysis, *Pain* released guidelines that state medication trials must include sufficient numbers of men and women. In March 2012, the American Physiological Society issued a policy requiring identification of sex or gender in papers on animal or human studies (see [go.nature.com/bmvgiz](http://go.nature.com/bmvgiz)). Every member of the scientific community has the power and responsibility to do the same for cells. ■

**Elizabeth Pollitzer** is director of Portia in London. Portia is a non-profit organization that addresses gender issues in science. e-mail: [elizabeth@portiaweb.org.uk](mailto:elizabeth@portiaweb.org.uk)

1. Deasy, B. M. et al. *J. Cell Biol.* **177**, 73–86 (2007).
2. Penalosa, C. et al. *FASEB J.* **23**, 1869–1879 (2009).
3. Mittelstrass, K. et al. *PLoS Genet.* **7**, e1002215 (2011).
4. Wizemann, T. M. & Pardue, M.-L. (eds) *Exploring the Biological Contributions to Human Health: Does Sex Matter?* (National Academy Press, 2001).
5. Jaggi, R. et al. *Cancer* **115**, 3293–3301 (2009).
6. Greenspan, J. D. et al. *Pain* **132**, S26–S45 (2007).
7. Du, L. et al. *J. Biol. Chem.* **279**, 38563–38570 (2004).





A golden eagle perches on the glove of a Kazakh hunter in the Altai Mountains, western Mongolia.

## ORNITHOLOGY

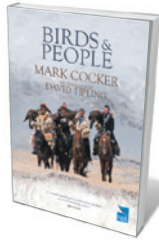
# Feathered encounters

Nicky Clayton enjoys a tribute to the enduring relationship between birds and humanity.

**B**irds and People is a delightful duet between nature writer Mark Cocker and wildlife photographer David Tipling. This monumental compendium is a reference book on the relationship between the class Aves and humanity — told in part through the personal stories of more than 650 people from 81 countries. But it is also a coffee-table collection of gorgeous images detailing that relationship, captured in 39 countries across 7 continents. At its core is our fascination with birds, and their enchanting and elaborate acoustic, visual and aerial displays.

Cocker vividly depicts how birds have become embodied in our arts and science, entwined in our philosophy and politics, and embedded in our cultures, from folklore to costume and cuisine. The eggs of the common ostrich (*Struthio camelus*), for example, have been used as water carriers, and birds are a central inspiration in Western art: think of the ballet *Swan Lake* or Constantin Brancusi's 1920s sculptural masterpiece *Bird in Space*.

Part natural history, part cultural anthology, the book describes how and why birds have colonized our imagination and become an integral part of the everyday, from back-garden birdwatching to feather duvets and boiled eggs. Images of penguins seem to be ubiquitous, appearing on everything from



**Birds and People**  
MARK COCKER  
Jonathan Cape: 2013.

publisher Allen Lane's famous paperbacks to Brazil's Antarctica beer. As a devotee of crows, ravens and other corvids — justly celebrated for their intelligence in the art of Pacific Northwest Native Americans — I was pleased to see behavioural ecologist

Tim Birkhead puncturing the persistent myth that magpies are responsible for the decline of some garden bird species.

There are some 10,500 species of bird and they inhabit every continent and almost every environment: land, water and the air (swifts, for instance, land only to breed). The book is organized by avian family, following the taxonomic-order classification and nomenclature of ornithologists Frank Gill and Minturn Wright. The science on each is beautifully plaited into the stories on birds' places in human cultures.

These stories are staggering in their diversity and as gripping for neophytes as for ornithologists. Cocker tells us that the domestic chicken, derived from the red junglefowl (*Gallus gallus*), is the biggest single

source of protein we consume. I shed a tear over how the black robin (*Petroica traversi*) of the Chatham Islands off New Zealand was pulled back from extinction, thanks to the dedication of scientist Don Merton and Old Blue, once the last remaining fertile female, which Merton found. Human–bird cooperation is an ancient phenomenon, of course: in East Asia, some fishermen encourage free-flying cormorants to catch fish. The birds deposit these on their 'owner's' boat, and are fed with some of the fish as a reward.

Numerous books have been written on the interactions between animals and humankind; few investigate cultural perspectives. Of those that do, the tendency is to focus on a species or family. *Birds and People* is refreshing in not being speciesist. Cocker and Tipling explore a relationship that lies at the heart of human experience and that has inspired great science and art, from Charles Darwin's groundbreaking findings on the Galapagos finches to Percy Bysshe Shelley's soaring 1820 poem *To a Skylark*. ■

**Nicky Clayton** is the professor of comparative cognition in the Psychology Department at the University of Cambridge, UK, and scientist in residence at Rambert, the UK's flagship contemporary dance company. e-mail: nsc22@cam.ac.uk



Rubbish piled up on the tundra outside Ilulissat in Greenland.

ENVIRONMENT

# Blanking out the mess

**Edward Humes** explores a study of the psychological dissociation plaguing our relationship with nature.

“Why do people make choices harmful to the environment even when they truly care about it?” This is the deceptively simple premise of *Invisible Nature*, in which environmental researcher Kenneth Worthy offers psychological, cultural and philosophical explanations for our curious and contradictory relationship with nature.

It is a thought-provoking, if frustrating, exploration. Like many of us who write on the environment, Worthy has an easier time diagnosing the ailment than prescribing a plausible cure. Still, his book offers readers concerned about humanity’s anaemic response to the crises of climate, waste and pollution a fresh starting point from which to consider another vital question: what next?

Worthy points to ‘dissociation’ as the key malady, particularly in the West. Modern economies, societies and lifestyles, he argues, put time, distance and disinformation between our everyday choices and their environmental consequences, such as acid rain caused by factory emissions. That consumer choices are destroying vital natural resources

is a factor rarely experienced directly and viscerally. We roll our rubbish to the kerb and it ‘magically’ disappears, never requiring us to smell a refuse dump or see the accumulation of plastic in oceans. Our experience of nature is limited to curated parks and street trees. Therein, Worthy writes, lies our downfall.

He offers eye-opening illustrations of the harm enabled by dissociation. Many consumers know that the silicon ‘brains’ inside their beloved smartphones are produced in clean, airtight rooms by workers wearing immaculate protective suits. Few realize that those suits are designed to protect the chips, not the workers. Toxic chemicals soak through, causing myriad health problems.

In the most fascinating part of *Invisible Nature*, Worthy takes his enquiry in a more original direction by examining the psychology of dissociation. He draws environmental lessons from the landmark 1960s experiments of social psychologist Stanley Milgram, in which students administered what they believed were powerful electric shocks to a person in the next room when urged to do so by an authority figure, despite

hearing the person’s screams and pleas. The students’ destructive obedience has been partly attributed to dissociation. The percentage of students willing to administer the largest shocks plummeted when they were in the same room as their victims, and fell even lower when they had to force their victims’ hands against a shock plate. The tendency of people acting as agents of a trusted authority

to commit acts they might never perform alone is another sort of dissociation: of action from responsibility.

Worthy contends that Milgram’s results — and those of the 20 subsequent obedience experiments modelled on his work — provide a psychological explanation for why people knowingly make environmentally destructive choices. He also draws



**Invisible Nature:**  
Healing the  
Destructive  
Divide Between  
People and the  
Environment  
KENNETH WORTHY  
*Prometheus: 2013.*

ASHLEY COOPER/VISUALS UNLIMITED, INC.

on the genocide studies of psychologist Ervin Staub, who suggests that psychological barriers to admitting that past acts were wrong encourage further destructive choices.

Worthy's argument begs many questions. Which variables lead to fewer destructive choices? Is detailed knowledge of environmental destruction enough, or is direct experience needed? Can trusted authority figures enforce 'constructive obedience', prodding people toward environmentally benign policies? This approach has worked in numerous communities worldwide, where consumers have abandoned disposable plastic shopping bags, urged on by civic leaders, elected officials and celebrity spokespeople. Most of all, I wanted Worthy to relate the thoughts and rationale of real people who chose a hybrid car or a gas guzzler, a reusable bag or a plastic sack. Why did they make those choices, and what would it take to alter them?

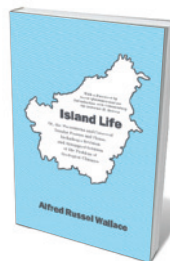
Instead, *Invisible Nature* switches to a lengthy, dry attack on Plato, Aristotle and Descartes as the philosophical fathers of our estrangement from nature. Oddly, these historical figures are the book's only fully developed characters. The sole modern human is Worthy's fictional character, Joe the accountant, a "typical office worker" who "spends most of his time with symbols, concepts, and figures that are abstractions of material-world things". Joe pops up now and then when the author needs a character who drinks from plastic water bottles or who is overly proud of his smartphone. But, being a caricature, he can't explain his choices — and that's too bad.

The book concludes with a disappointingly familiar list of ways to enhance our engagement with nature: cycling more; planting a vegetable garden; and embracing Eastern philosophies that depict nature and humanity in a mutually dependent context.

*Invisible Nature* could have been a great book had Worthy focused more on the psychology of dissociation and less on long-dead philosophers. Modern thinking on marketing, globalism and consumerism is more relevant to current environmental problems than ruminations on mind–body dualism. After all, it was J. Gordon Lippincott, father of corporate branding, who in 1947 set out the axiom of modern, environmentally destructive consumerism: "Our willingness to part with something before it is completely worn out is a phenomenon noticeable in no other society in history ... It must be further nurtured even though it runs contrary to one of the oldest inbred laws of humanity, the law of thrift." ■

**Edward Humes** is a Pulitzer prizewinning journalist and the author of 12 non-fiction books. His most recent is *Garbology: Our Dirty Love Affair With Trash*.

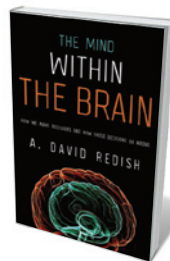
# Books in brief



## Island Life: Or, the Phenomena and Causes of Insular Faunas and Floras, Including a Revision and Attempted Solution of the Problem of Geological Climates

Alfred Russel Wallace, with Lawrence R. Heaney UNIVERSITY OF CHICAGO PRESS (2013)

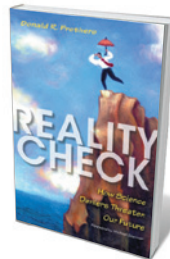
Co-discoverer of natural selection Alfred Russel Wallace pioneered island biogeography — the study of how organisms are distributed on isolated land masses. In fact, he was the field's Kepler, Linnaeus and even Chuck Berry, avers David Quammen in his foreword to this facsimile of Wallace's landmark 1880 study (see also *Nature* **496**, 165–166; 2013). Includes a commentary by Lawrence R. Heaney.



## The Mind Within the Brain: How We Make Decisions and How Those Decisions Go Wrong

A. David Redish OXFORD UNIVERSITY PRESS (2013)

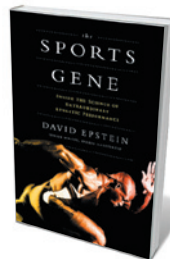
From drinking that fifth Martini to choosing a career, decisions shape our lives. In his study of the science of decision-making, neuroscientist David Redish keeps a cool head in an overheated theoretical arena. Synthesizing findings in psychology, robotics and more, he takes us from brain physiology to aspects of mind. His own decision-making model involves multiple 'action-selection' systems, failures in which can lead to behaviours such as compulsive gambling. Well researched and delivered with a light touch.



## Reality Check: How Science Deniers Threaten Our Future

Donald R. Prothero INDIANA UNIVERSITY PRESS (2013)

The shabby tactics of science denialists sparked this astute exposition of what we lose when science is sidelined. Palaeontologist Donald Prothero lays out key cases, such as former US President Ronald Reagan's misbegotten Strategic Defense Initiative and the demonization of biologist Rachel Carson for her work on pesticides. The usual suspects — from creationists to anti-vaccinationists — are examined too. Ultimately, Prothero argues, by claiming that clear findings on climate change, biodiversity loss and overpopulation are false, deniers inch us closer to catastrophic planetary tipping points.



## The Sports Gene: Inside the Science of Extraordinary Athletic Performance

David Epstein CURRENT (2013)

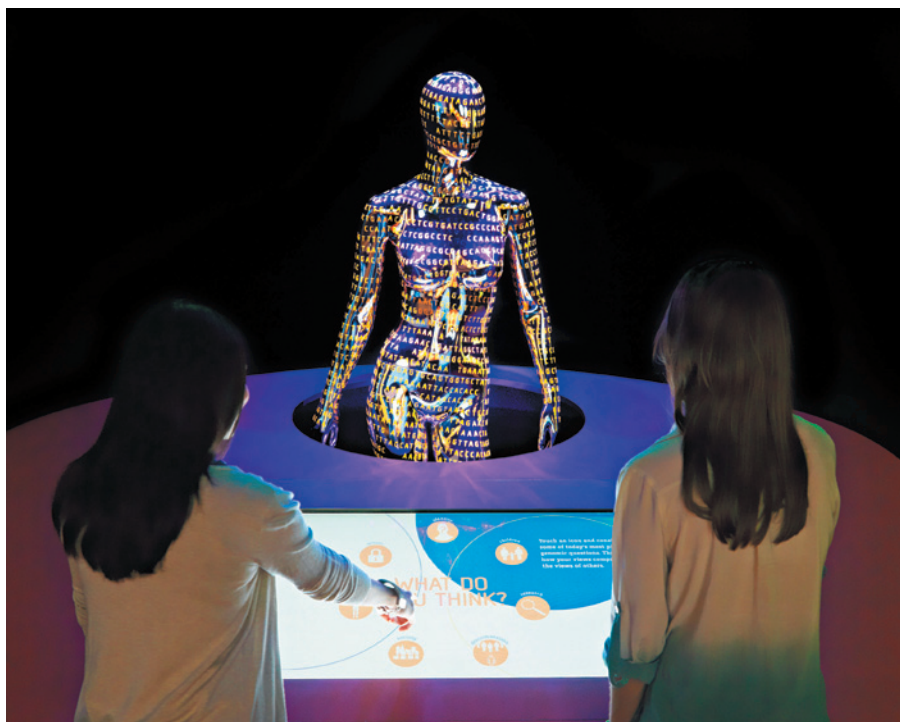
Sports-science writer David Epstein enters the nature–nurture debate on elite sporting ability. Drawing on interviews with sports scientists and leading athletes, Epstein looks at psychologist Anders Ericsson's '10,000-hour' study on how practice can masquerade as innate talent; gender testing and chromosomal anomalies; the heritability of height; and more. His conclusion that sporting excellence is down to the interplay of luck, intent and effort hardly surprises, but this is a rollicking ride through the latest science.



## The Making of the Mind: The Neuroscience of Human Nature

Ronald T. Kellogg PROMETHEUS (2013)

The genetic overlap between *Homo sapiens* and the chimpanzee is a biological conundrum. Some primatologists focus on what we share; cognitive psychologist Ronald Kellogg looks at what makes the human brain distinct. He argues that it is the interaction of cognitive elements such as our complex social intelligence and comprehension of others' mental intentions; symbolic thought and language; and a sense of time. Kellogg ends by speculating about the shaping of a "post-literate, Internet mind". **Barbara Kiser**



A mannequin covered in letters denoting DNA bases draws visitors to an interactive exhibit in *Genome*.

## GENOMICS

# The big blueprint

**Gene Russo** surveys a high-tech exhibition celebrating the double helix and the human genome sequence.

Two landmark dates in biology sparked *Genome: Unlocking Life's Code* — the completion of the human genome 10 years ago, and the unveiling of the double helix by James Watson and Francis Crick 60 years ago. The exhibition, currently at the Smithsonian National Museum of Natural History in Washington DC, has a tough task: to render the abstractions and complexities of genomics a feast for the senses. That microscopic, interiorized world presents a curatorial challenge light years away from displaying *Tyrannosaurus rex* skeletons.

Yet *Genome* — a Smithsonian Institution collaboration with the US National Human Genome Research Institute in Bethesda, Maryland — does engage, even if the content is sometimes a bit dense. Videos, genomics trivia and interactive screens navigated by track pad help to explore everything from bioethical quandaries to genomic testing. One section marks the two big anniversaries with films featuring, among others, Watson recalling the 1953 discovery and National Institutes

► **NATURE.COM**  
For a PastCast on the 'other' DNA papers:  
[go.nature.com/lizfik](http://go.nature.com/lizfik)

**Genome: Unlocking Life's Code**  
Smithsonian National Museum of Natural History, Washington DC.  
Until 1 September 2014, then on tour.

of Health director Francis Collins touting the importance of making genomic data freely available. As lead curator Meg Rivers puts it, the idea is to reveal to visitors that genomics is 'all about them'. "The biggest challenge is saying what a genome is, and making it meaningful," she says.

There are three thematic areas, covering genomics' influence on health and medicine, genes and ancestry, and genomic connections among living things. Any one of these could make an entire exhibition on its own.

An animation on a large LCD screen nicely explains the inner workings of DNA, genes and proteins. Factoids flash on-screen. "Unfolded, DNA is six feet long," we're told. "Yet it's 30,000 times thinner than a strand of human hair." A section on next-generation genomic medicine focuses on combating disease, personalized drug treatments and DNA sequencing's role in halting the spread of deadly infections. "How much do you want to know about your family's genetic

make up?" asks one interactive panel.

To learn about ancestry, you can drag an arrow across a timeline on a touch-screen world map to see how humankind migrated and how genetic diversity has changed over tens of thousands of years. Humans started out in Africa, but migrants took along only a portion of the genetic diversity — today, Africans harbour a more diverse gene pool than other populations.

Another section asks what we can glean from the genomes of other life forms. Selecting the horseshoe crab on a screen reveals that the species has not changed for 200 million years. 'Is it a living fossil?' it asks. No, we discover: only a small part of the genome controls body shape; the rest of the genome has continued to evolve.

Questions posted on the wall at the entrance ask visitors to describe their physical features and then reveal what proportion of people share their particular combination. 'Do you have dimples?' No. 'Are the lobes of your ears attached?' Yes. 'Can you curl your tongue?' No. 'Is your hairline pointed in the center?' No. Conclusion: '4% of 292 people polled share these four physical traits with you.' Another part of the exhibit probes thorny ethical dilemmas. For example, should we place limits on genomic research? A touch-screen prompt then asks the user to consider factors such as facilitating faster cures and getting permission from subjects.

To keep the show feeling fresh, a news ticker scrolls the most recent genetics-related stories onto a wall. On the day of the press preview, for example, the Supreme Court had just come down with its ruling against Myriad Genetics on patenting genes.

My main quibble is that *Genome* offers little to younger children, in a museum receiving 7 million visitors annually. The omission is even odder given that another exhibition has already shown the way. In 2001, the American Museum of Natural History in New York staged *The Genomic Revolution*. It featured a stack of 180 Manhattan telephone books, 1,646 pages each, in the shape of a double helix; the number of characters in them roughly equals the number of base pairs in DNA. Smaller children also loved the 'mutation station', where you could 'change a gene' by turning a rung on a giant plastic double helix. A television screen showed the physical effects in a fruit fly.

In this age of iPads and touch-screen technology, one might have expected a more creative approach than *Genome*'s final draft — perhaps a big touch screen allowing users to drag and match 'As' with 'Ts' and 'Cs' with 'Gs' on an animated double helix. Such a presentation might have prompted young and old alike to think about this thing in all of us called a 'genome'. ■

**Gene Russo** is editor of *Nature Careers*.

# Correspondence

## Reward research outreach in Japan

The Japan Science and Technology Agency last month reported that only 64% of almost 9,000 surveyed Japanese scientists communicate results outside the scientific community. This is surprising: since 2010, the government has urged the researchers it funds to improve communication with the tax-paying public — particularly after the March 2011 tsunami and nuclear accident at Fukushima.

Of the 36% of researchers who did not participate in outreach, many cited administrative overload and a lack of resources and time. The biggest issue among these scientists was that they felt there was no personal advantage in communicating their results to the public. This is because researcher performance in Japan is evaluated solely on the number of journal publications, so time and effort spent on science communication will not help scientists to secure funding, promotion or employment.

The government needs to recognize that scientific outreach activities are valid experiences for funding and job applications. Japan's researchers, in turn, should recognize that communicating with the public provides its own reward in the form of society's acknowledgement of their work.

**Amane Koizumi** National Institute for Physiological Sciences, Aichi, Japan.  
[amane@nips.ac.jp](mailto:amane@nips.ac.jp)

**Yuko Morita** National Museum of Emerging Science and Innovation (Miraikan), Tokyo, Japan.

**Shishin Kawamoto** Hokkaido University, Hokkaido, Japan.

## Flanders overrates impact factors

A renewed decree on research funding last year by the government of Flanders in northern Belgium advised that 40% of research evaluation

should be based on bibliometric data. This involves a complex calculation that includes the number of publications and citations, and the impact factors for the journals of publication (see [go.nature.com/mt9srg](http://go.nature.com/mt9srg); in Dutch). We question the merits of this strategy, given the debatable value of impact factors in gauging research quality (see, for example, B. Alberts *Science* **340**, 787; 2013).

The Flemish Interuniversity Council in fact advised Flemish universities in 2010 to reduce the importance of bibliometric data when weighing up researchers for appointment or promotion. In practice, however, such data have become even more important.

It is time to heed the widely recognized risk of overrating the quantity of scientific publications, which can compromise research quality and integrity.

**Karen Stroobants, Simon Godecharle** Research Foundation Flanders (FWO) and University of Leuven, Belgium.  
[karen.stroobants@chem.kuleuven.be](mailto:karen.stroobants@chem.kuleuven.be)

**Sofie Brouwers** FWO and Vrije Universiteit Brussel, Belgium.

## Time-lapsed awards for excellence

The number of scientific prizes has proliferated in the past 20 years (see *Nature* **498**, 152–154; 2013). But once a scientist has published a seminal contribution, how long is it before these glittering symbols of recognition come through?

Occasionally, recognition comes early in a scientific career. For example, the biologist Thomas Henry Huxley was elected as a fellow of the Royal Society in London in 1851 at age 26, and William Lawrence Bragg won the Nobel Prize in Physics in 1915 when he was just 25. But these may be exceptions.

We looked at 466 recipients of Nobel prizes in physics, chemistry, and physiology or medicine, awarded from 1901 to 2000, using a biographical encyclopedia that also lists

all other major institutional awards won by an individual (G. T. Kurian *The Nobel Scientists*, Prometheus; 2002). These include prizes such as the Davy Medal, the Max Planck Medal and the Canada Gairdner International Award.

Using the year in which laureates produced their Nobel-prizewinning work as an indicator for the timing of their peak scientific achievement, we calculated the average lag time in each field between this and the timing of the Nobel prize and other major awards.

Our investigations indicate that recognition is conferred relatively rapidly. In physics, the lag was just 5 years; in chemistry, 9 years; and in physiology or medicine, it was 11 years. It seems that important discoveries in physics, and perhaps in chemistry, are more easily defined than in physiology or medicine, so their merits are more swiftly recognized.

**Ho Fai Chan, Benno Torgler** Queensland University of Technology, Brisbane, Australia.  
[benno.torgler@qut.edu.au](mailto:benno.torgler@qut.edu.au)

maintain meta-populations.

In response, the state government is actively linking tiger populations by identifying ecologically important habitats and designating them as protected areas to ensure long-term habitat protection.

For example, in May 2013 it established the 906-square-kilometre Malai Mahadeshwara Wildlife Sanctuary, creating a 6,500-km<sup>2</sup> contiguous network of protected areas — the largest in the country. Over the past 19 months, the state government has added nearly 3,000 km<sup>2</sup> of tiger habitat to the network.

This extended landscape should be able to host a connected population of some 500 tigers.

**Sanjay Gubbi** *Panthera*, New York, USA; and *Nature Conservation Foundation*, Mysore, India.  
[sanjaygubbi@gmail.com](mailto:sanjaygubbi@gmail.com)

**H. C. Poornesha** *Nature Conservation Foundation*, Mysore, India.

## Comparing science and music is unsound

Stephane Detournay suggests that both scientific research and music composition undergo phases of “onset, development, refinement and exposition” (*Nature* **499**, 245; 2013). But so do hedge-fund management and tomato farming.

One thing that binds music and science is the idea that sincere, personal investment in one's work is good. Yet music is mainly about evoking, interpreting and savouring emotions, whereas science is essentially the pursuit of truth.

**Justin Jee** New York University, New York, USA.  
[justin.jee@med.nyu.edu](mailto:justin.jee@med.nyu.edu)

### CONTRIBUTIONS

Correspondence may be sent to [correspondence@nature.com](mailto:correspondence@nature.com) after consulting [go.nature.com/cmchno](http://go.nature.com/cmchno).

# Kenneth Geddes Wilson

## (1936–2013)

Nobel-prizewinning physicist who revolutionized theoretical science.

**B**efore Kenneth Wilson's work, calculations in particle physics were plagued by infinities. Results came from a workaround called renormalization, dubbed "ugly" even by one of its inventors, theoretical physicist Paul Dirac. In the 1970s, Wilson reformulated this method. Almost immediately, renormalization became a respectable and widely used tool, forming the basis of thousands of papers in condensed-matter and particle physics. It is now our primary method for seeing the connections among different theories in the physical sciences.

Wilson died on 15 June 2013. Born in 1936 in Waltham, Massachusetts, he started life amid theoretical science. His grandfather taught engineering at the Massachusetts Institute of Technology in Cambridge; his father was a theoretical chemist at Harvard University, also in Cambridge. Like his father, Kenneth Wilson was appointed to the Society of Fellows at Harvard, a group of young scholars picked for their exceptional promise and then given no responsibilities whatsoever.

Ken got his PhD in particle physics under Murray Gell-Mann at the California Institute of Technology in Pasadena. Appointed to the junior faculty at Cornell University in Ithaca, New York, in 1963, Wilson initially proved a disappointment, at least to those who vet promotions by bean counting. Despite having no journal publications before 1969, Wilson's exceptional promise brought him promotion to tenure at Cornell after just two years. Then, in 1971, Wilson revolutionized the mathematical sciences.

Both particle and condensed-matter physics describe observations at length scales set by the experimental apparatus, but depend on processes occurring at much shorter distances. So observation-based theories, whether they are about the elasticity of materials or the collisions of observable 'elementary' particles, cannot accurately describe natural forces acting at small scales.

This weakness showed up in mid-twentieth-century particle physics through the generation of infinities in most calculations. Before Wilson's work, the renormalization method achieved finite results by replacing the infinite quantities in the theory with empirically derived, finite quantities.

During the 1960s, Wilson noted the close analogy between particle physics and phase

transitions. (A phase transition is the change of matter from one form to another, such as the boiling of liquid water to produce steam.) Phase transitions had a rich experimental, analytical and numerical tradition, based on well-known science at the atomic

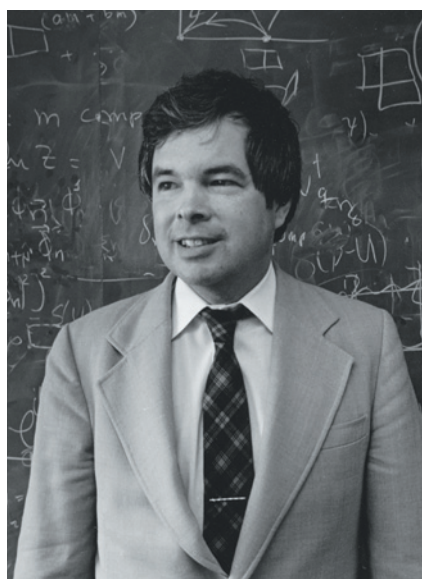
quarks that underlie a substantial portion of high-energy theory. He pointed out that these quarks can fall into several thermodynamic phases, differing in behaviour. In the phase that is found all around us, quarks become hard to observe because they are closely bound to one another. This work was important for understanding the basic theory of quantum chromodynamics and its realization in numerical computations, described as lattice gauge theory. This work founded a subfield of science, now practised at many centres.

In 1982, Wilson won a Nobel prize for his work on phase transitions. However, his renormalization has had an impact that is substantially beyond any single area of science. One might argue, as I do, that the connections among 'laws of nature' at different scales of energy, length or aggregation is the root subject of physics. It could then be said that Wilson has provided scientists with the single most relevant tool for understanding the basis of physics.

That was Wilson's main accomplishment. But it was not all. His work drove us to develop different work styles and new scientific areas. He implicitly encouraged us to emulate computers and computer programs in order to track all the different processes that arise in changing length scales. Wilson was influential in his championing of supercomputers and the National Science Foundation's national scientific supercomputing centres, one of which was established at Cornell in 1985. He constructed computer programs to enable the flexible use of very large computers for research. This work was, in part, carried out with his wife, computer scientist Alison Brown.

Ken was unfailingly generous to those working in his area. For example, he gave very careful credit in his papers to previous workers. I note Ken's kind (and almost unprecedented) inclusion of my name in the title of his first, great, renormalization paper.

The brilliance of Kenneth G. Wilson was dazzling, but he never tried to outshine those about him. He was all quiet competence and deep accomplishments. ■



or molecular level. As a result, a theory in this area could be verified or disproved by comparison with known results. But a theory was needed to bridge the gap between basic forces at one length scale and observations at a very different scale.

Ken built a new form of analysis for phase transitions. He focused on theories defined at different length scales, broadening the renormalization calculation of the connection between the scales to include all physical processes, not just the few that might show infinities. He added an analysis in which the eventual result of many changes in length would be a 'fixed point'. This result was easy to analyse because of its scale-independent behaviour.

Soon after Wilson first described his ideas, he worked with Michael Fisher, also at Cornell, to calculate the mathematical form of the interrelation among density, pressure and temperature for a fluid hovering close to its transition from liquid to vapour. The amazingly close agreement of their results with experimental findings helped to accelerate the acceptance of the new renormalization theory.

Wilson also applied his ideas to the

SOL GOLDBERG, CORNELL UNIV. PHOTOGRAPHY

**Leo P. Kadanoff** is a theoretical physicist and applied mathematician at the Perimeter Institute, Waterloo, Ontario, Canada; and at the James Franck Institute, University of Chicago, Illinois, USA.  
e-mail: leop@uchicago.edu

## On with their heads

Data from three teams show that alteration of a single cell-signalling mechanism can unlock the latent head-regeneration potential in normally regeneration-deficient species of flatworm. **SEE LETTERS P.73, P.77 & P.81**

ANDRÁS SIMON

Voltaire was not only a leading philosopher of his time but, inspired by natural scientists, he also carried out intriguing experiments that showed that decapitated snails could regenerate their heads. On the basis of these observations, Voltaire was said to be optimistic about humans being able to do the same one day<sup>1</sup>. Although the arrival of that day is apparently not imminent, clues to how to unlock a latent potential for head regrowth are presented in three papers\* in this issue<sup>2–4</sup>.

Some animals regenerate organs and even body parts following major injuries. The distribution of species with these abilities is seemingly random: representatives range from relatively simple organisms, such as hydra, to the more complex flatworms, and on to vertebrates such as salamanders<sup>5</sup>. The regenerative capacity of these organisms is quite remarkable. For example, some flatworms can be sectioned into small pieces, each of which will give rise to a new, complete worm<sup>6</sup>. And salamanders, after amputation, regrow entire limbs that are fully functional, perfect copies of the original extremity<sup>7</sup>.

Why some animals but not others respond to injury with such extensive regeneration is an outstanding question both from an evolutionary perspective and when considering possible interventions to enhance regenerative capacity. One way to address this question is to compare closely related species with differing injury responses. The three new papers all take this approach, by studying highly regenerative and regeneration-deficient flatworms. Two flatworm species, *Dugesia japonica* and *Schmidtea mediterranea*, can regenerate all missing body parts after transection, irrespective of how many times or where they are cut along the head-to-tail (anterior-to-posterior) axis. By contrast, the three non-regenerative species investigated in the studies reported here — *Phagocata kawakatsu* by Umesono *et al.*<sup>2</sup> (page 73), *Proctotyla fluviatilis* by Sikes and Newmark<sup>3</sup> (page 77) and *Dendrocoelum lacteum* by Liu *et al.*<sup>4</sup> (page 81) — all fail to regenerate heads from the tail fragment left after transection through the most posterior third of their bodies (Fig. 1).

\*This article and the papers under discussion<sup>2–4</sup> were published online on 24 July 2013.



WILLEM KOLVOORT/NATUREPL.COM

**Figure 1 |** *Dendrocoelum lacteum*. These flatworms, the subjects of Liu and colleagues' study<sup>4</sup>, are unable to regenerate a head from a tail fragment.

What mechanisms underlie these differences? Regeneration normally starts by wound healing and involves the proliferation of stem cells called neoblasts. These cells give rise to a cell mass called a blastema, which subsequently grows and differentiates into a fully patterned new body part. It seems that regeneration-deficient species respond to an injury with normal wound healing and cell-proliferation dynamics. This extended to blastema formation in the tail fragments of *D. lacteum*<sup>4</sup>, but this was not observed in *P. fluviatilis*<sup>3</sup>. Thus, the regenerative process seems to stop at or just before blastema formation. However, given the paucity of biological markers for blastemas, some caution about these conclusions may be warranted.

Importantly, the papers converge on the identity of a molecular signalling pathway that should be targeted to evoke head regeneration from tail fragments in all three regeneration-deficient species — the Wnt/β-catenin pathway, which plays a key part in several processes during embryonic development and adult homeostasis in multicellular organisms. Wnt proteins cause accumulation of β-catenin, which in turn regulates gene expression<sup>8</sup>, and perturbation of Wnt/β-catenin signalling is associated with developmental malformations, inappropriate cell turnover during adult homeostasis and tumour formation<sup>9</sup>. The common conclusion of the present studies is that downregulating the activity of this pathway by reducing β-catenin levels leads to head regeneration from otherwise regeneration-deficient tail fragments. Heads regenerated through this approach had

morphologically normal brains and contained photoreceptors — the 'simple eyes' of these animals. Furthermore, regenerated animals displayed normal behavioural responses to light and reacquired feeding ability.

The significance of Wnt/β-catenin signalling in regeneration has previously been highlighted in regeneration-competent flatworms. In these animals, reduced activity of this pathway leads to outgrowth of a head instead of a tail from posterior-facing wounds (resulting in a two-headed animal) and, conversely, enhanced activation of the pathway by stabilization of β-catenin leads to tail instead of head outgrowth from anterior-facing wounds (giving a two-tailed animal)<sup>10</sup>. In agreement with these observations, two of the present studies<sup>3,4</sup> found that stabilization of β-catenin also results in tail outgrowth from tail fragments in the normally non-regenerative *P. fluviatilis* and *D. lacteum*.

A possible interpretation of these combined findings is that achieving polarity along the head-to-tail axis is required for injury responses to proceed to the creation of a new body part, and that the inability to progress past blastema formation to regenerate a head is the result of insufficient polarity in Wnt/β-catenin signalling (Table 1). The next question is how Wnt/β-catenin signalling creates axial polarity. Data from Umesono and colleagues' study<sup>2</sup> indicate that another pathway, ERK signalling, normally forms an activity gradient that decreases from head to tail, and the authors suggest that the Wnt/β-catenin pathway exerts its effects by suppressing ERK signalling. According to their

**TABLE 1 | SIGNALLING AND REGENERATION**

Effects of altered Wnt/β-catenin signalling in regeneration-deficient flatworms

Wnt/β-catenin signalling	Axial polarity	Regeneration from tail fragment
Natural (deficient) regulation	Insufficient	None
Downregulated signalling	Correct	Head regeneration
Upregulated signalling	Reversed	Tail regeneration

model, *P. kawakatsui* fails to regenerate a head from tail fragments because head regeneration requires high levels of ERK signalling and this is prevented by Wnt/β-catenin activity. It will be interesting to further dissect these putative molecular interactions and determine whether the model also holds true for other regeneration-deficient worms.

How should we consider the evolutionarily uneven distribution of regenerative ability, and what are the implications of the current findings for regeneration in mammals? Is it possible, as these studies might indicate, that regeneration is an inherent trait that is manifest in some organisms but silent in others, such that reshuffling the interactions of

existing molecular components is sufficient for its awakening? Alternatively, is regeneration a capability that has been acquired by some species, possibly in a process that requires species-specific molecular components<sup>11</sup>?

Inducing regeneration of a body part in a species that cannot undergo full regeneration but is in many aspects regeneration-competent is quite different from achieving something comparable in largely non-regenerative organisms, which include most mammals. Nevertheless, the new studies highlight the importance of cross-species comparisons for understanding the molecular mechanisms of regeneration and identifying processes that prevent it from occurring. Moreover, the finding that manipulation

of a single major signalling pathway is sufficient to induce regeneration of a body part gives hope for the future that we will be able at least to improve regenerative responses in humans. ■

**András Simon** is in the Department of Cell and Molecular Biology, Karolinska Institute, 17177 Stockholm, Sweden.  
e-mail: andras.simon@ki.se

1. Goss, R. J. in *A History of Regeneration Research. Milestones in the Evolution of a Science*. (ed. Dinsmore, C. E.) 7–23 (Cambridge Univ. Press, 1991).
2. Umesono, Y. et al. *Nature* **500**, 73–76 (2013).
3. Sikes, J. M. & Newmark, P. A. *Nature* **500**, 77–80 (2013).
4. Liu, S.-Y. et al. *Nature* **500**, 81–84 (2013).
5. Brookes, J. P. & Kumar, A. *Annu. Rev. Cell Dev. Biol.* **24**, 525–549 (2008).
6. Newmark, P. A. & Sánchez Alvarado, A. *Nature Rev. Genet.* **3**, 210–219 (2002).
7. Simon, A. & Tanaka, E. M. *Wiley Interdiscip. Rev. Dev. Biol.* **2**, 291–300 (2013).
8. Valente, T., Hausmann, G. & Basler, K. *EMBO J.* **31**, 2714–2736 (2012).
9. Clevers, H. *Cell* **127**, 469–480 (2006).
10. Reddien, P. *Trends Genet.* **27**, 277–285 (2011).
11. Garza-Garcia, A. A., Driscoll, P. C. & Brookes, J. P. *Integr. Comp. Biol.* **50**, 528–535 (2011).

## CLIMATE SCIENCE

# Unequal equinoxes

**Innovative measurements of ocean turbulence show that mixing of cold water from below makes the surface of the equatorial Pacific much colder in September than in March. SEE LETTER P.64**

SHANG-PING XIE

Equatorial countries such as Indonesia and Ecuador are associated with thunder showers and lush rainforests. In September 1835, when Charles Darwin set foot on the Galapagos Islands, an archipelago on the Equator some 1,000 kilometres west of the Ecuadorian coast, he found none of these. Instead, he saw very dry land and leafless trees “in an intertropical region, but without the beauty which generally accompanies such a position”<sup>1</sup>. The cold surface sea water that keeps the Galapagos dry is part of a basin-scale structure called the equatorial cold tongue, and is known to originate from beneath the surface. But how the cold deep water reaches the surface has never been satisfactorily measured through a seasonal cycle, because of the prohibitive costs of operating ships in this remote ocean.

On page 64 of this issue, Moum *et al.*<sup>2</sup> report multi-year measurements of ocean turbulence using a revolutionary instrument called an  $\chi$ -pod, which is moored in the ocean (Fig. 1)\*. They show that small ocean eddies of diameter less than 1 metre bring cold water from the

thermocline layer (the ocean layer that separates the warm upper part of the ocean from the cold deeper part) to the sea surface. The new instrument has finally clinched the connection between turbulence and climate, and holds the promise of improving global climate models.

In explaining the absence of coral reefs around the Galapagos Islands, Darwin calculated that sea surface temperature (SST) was 20°C during his 35-day stay<sup>3</sup>, close to the modern September climatology (21°C) for this region, but much lower than in the western Pacific (29°C) at this time of the year. Had Darwin come to the islands in March, he would have been welcomed by trees covered with green leaves. SST in March reaches nearly 27°C, warm enough to permit rain showers. The pronounced annual cycle in SST is a mystery given our experience that the seasonal change in temperature is caused by the local change in solar radiation. The Sun marches across the Equator twice a year, at the March and September equinoxes, yet the SSTs between the two months differ by a whopping 6°C. What makes September cooler than March in the Galapagos?

Because of Earth’s rotation, easterly winds force upward motion in the Pacific Ocean on

the Equator that brings the cold water from the thermocline close to the surface, a process called upwelling. Likewise, southerly winds cause upwelling slightly (100–200 km) south of the Equator<sup>4</sup>. The climatic axis of symmetry turns out not to be on the geographic Equator, but 1,000 km to the north in the intertropical convergence zone where the southern and northern trade-wind systems converge to produce frequent thunder showers. Because the intertropical convergence zone is displaced north of the Equator, the Equator belongs to the Southern Hemisphere from a climatic perspective, being warm in March and cold in September<sup>5</sup>. In September, the seasonal warming of the Northern Hemisphere and cooling of the Southern Hemisphere accelerate the southeast trade winds, intensifying ocean upwelling. In March, the seasonal warming of the Southern Hemisphere weakens, but does not reverse the direction of the southeasterly cross-equatorial winds, suppressing ocean upwelling. Thus, the southeast trade winds attain an annual cycle in speed that drives annual variations in ocean upwelling and SST near the Equator<sup>6</sup>.

Upwelling pushes the thermocline close to the surface but it takes turbulence at sub-metre scales to mix the cold thermocline water into the surface layer. Conventionally, measurements of such ocean mixing are made by dropping microstructure profilers from ships, but nobody can afford to station a research vessel on the Equator for a year — the minimum length of time needed to unlock the mystery of the equatorial annual cycle. Moum and colleagues invented  $\chi$ -pods for deployment on moored buoys<sup>7</sup> to measure the dissipation rate of turbulent temperature variance ( $\chi_T$ ) for up to a year at a time.  $\chi_T$  is a measure of turbulent

\*This article and the paper under discussion<sup>2</sup> were published online on 24 July 2013.

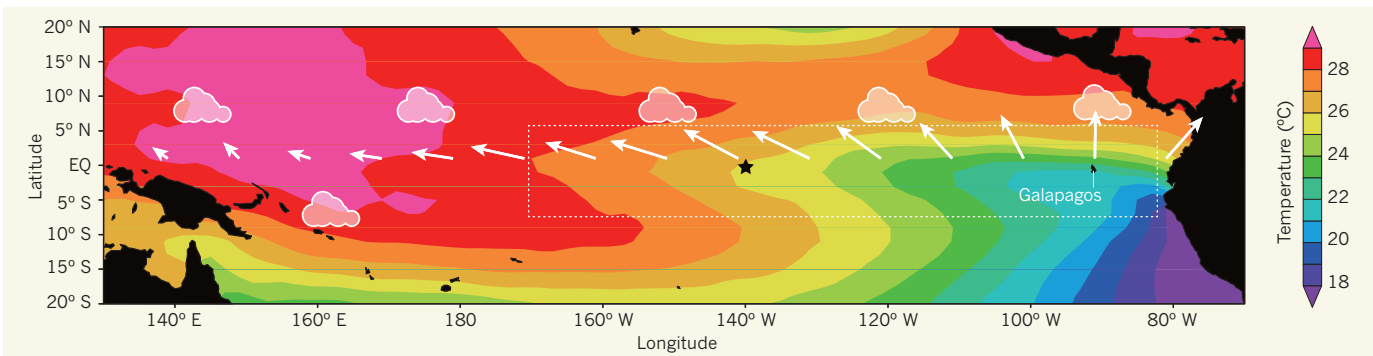


**Figure 1 | Tropical Pacific climate.** The image shows the September sea-surface temperature of the tropical Pacific, along with wind velocity (white arrows) on the equator and the location of atmospheric convection (cloud

symbols). The black star marks the mooring site where Moum *et al.*<sup>2</sup> carried out measurements of ocean turbulence. The dotted rectangle indicates the tongue-like structure of cold temperature on the Equator (EQ).

mixing intensity, from which one can calculate turbulent heat flux in the vertical direction. Their data, which span 6 years on the Equator at 140°W, show that the turbulent heat flux from below peaks in August and is the dominant mechanism for the rapid surface cooling, finally confirming a long-held hypothesis that ocean mixing drives the equatorial annual cycle.

Thus, the equatorial cold tongue (Fig. 1) is a tale of remarkable interactions across eight orders of magnitude, from turbulence ( $10^{-1}$  m) to the size of the vast Pacific Ocean ( $10^7$  m). Local and basin-scale winds set up the temperature and current structures that create sub-metre turbulence, and the turbulent mixing enables subsurface changes to affect SST and the atmosphere. Climate models do not do very well in the tropical Pacific, producing a cold tongue that is too cold and extends too far westwards<sup>8</sup>. Ocean mixing is considered one of the culprits for this. Over time, moored  $\chi$ -pods will sample the oscillations between the El Niño and La Niña phases of ocean state, and reveal how large-scale ocean variations modulate turbulent mixing. Such observations are invaluable for validating and improving models.

Deploying  $\chi$ -pods at other mooring sites across the equatorial Pacific is a natural next step. At the dateline, which marks the western terminus of the equatorial cold tongue, ocean-mixing observations can shed light on why the cold tongue in models extends too far westwards. Moum and colleagues'  $\chi$ -pod deployment at 140°W is in an easterly wind regime with the upwelling centred on the Equator. By contrast, the eastern Pacific at 95°W is in a southerly wind regime, where the upwelling occurs south of the Equator (Fig. 1). A cross-equatorial array will reveal how ocean mixing responds to the southerly winds and displaces the cold tongue south of the Equator. Therefore,  $\chi$ -pods fill a crucial gap by enabling a close look at how ocean mixing and climate co-vary and interact. ■

Shang-Ping Xie is at the Scripps Institution of Oceanography, University of California at San Diego, La Jolla, California 92093–0230, USA. e-mail: sxie@ucsd.edu

1. Keynes, R. D. (ed.) *Charles Darwin's Beagle Diary* 361–362 (Cambridge Univ. Press, 2001).
2. Moum, J. N., Perlin, A., Nash, J. D. & McPhaden, M. J. *Nature* **500**, 64–67 (2013).
3. Sponsel, A. *Coral Reef Formation and the Sciences of Earth, Life, and Sea, c. 1770–1952* PhD thesis, Princeton Univ. (2009).
4. Philander, S. G. H. & Pacanowski, R. C. *Tellus* **33**, 201–210 (1981).
5. Xie, S.-P. in *The Hadley Circulation: Past, Present and Future* (eds Diaz, H. F. & Bradley, R. S.) 121–152 (Kluwer, 2004).
6. Mitchell, T. P. & Wallace, J. M. J. *Clim.* **5**, 1140–1156 (1992).
7. Moum, J. N. & Nash, J. D. *J. Atmos. Oceanic Technol.* **26**, 317–336 (2009).
8. Zheng, Y., Lin, J.-L. & Shinoda, T. J. *Geophys. Res.* **117**, C05024 (2012).

#### ALZHEIMER'S DISEASE

# From big data to mechanism

**The gene variant APOE4 is the most common genetic risk factor associated with late-onset Alzheimer's disease. A comprehensive, multilayer study reveals the molecular and cellular signatures of APOE4 in humans. SEE ARTICLE P.45**

VIVEK SWARUP & DANIEL H. GESCHWIND

**A**lzheimer's disease is a genetically complex neurodegenerative condition typically associated with ageing. Reporting in this issue, Rhinn *et al.*<sup>1</sup> (page 45) use an integrative genomic approach based on analysis of transcriptional networks in human brain to uncover new relationships between this disorder, ageing, and the gene apolipoprotein E, or *APOE*, shedding light on molecular mechanisms that connect this gene to the processing and transport of amyloid precursor protein — considered to be a primary effector of the disease. To validate their hypotheses, the authors follow bioinformatic analyses with multiple levels of experimentation, impressively demonstrating the power of network biology\*.

Recent genome-wide association studies (GWAS) and transcriptomic studies have implicated<sup>2,3</sup> a wide set of pathophysiological mechanisms in Alzheimer's disease, including innate immunity, cellular uptake of molecules by the process of endocytosis and their

intracellular trafficking. However, a variant of *APOE* called *APOE4* remains the most common genetic risk factor, with the largest effect in late-onset Alzheimer's disease (LOAD)<sup>4</sup>. Therefore, understanding how *APOE4* conveys disease risk and its relationship with ageing remains a research imperative.

Rhinn *et al.* start with a simple, but previously unexplored, set of comparisons using published data on gene expression in the cerebral cortex region of the human brain to address a question widely debated in the field: do the molecular mechanisms underlying LOAD differ between those who carry *APOE4* and those who do not?

To discern the independent effects of disease and *APOE* status, the authors compare *APOE4*-negative healthy individuals with both *APOE4*-negative LOAD patients and *APOE4*-positive healthy individuals. Remarkably, they find that the total cellular transcript (transcriptome) profile of healthy *APOE4* carriers overlaps to a large extent with that of LOAD patients, and that the overlapping set of transcripts (designated A/E) most closely resembles the changes in transcript profile observed during the transition from

\*This article and the paper under discussion<sup>1</sup> were published online on 24 July 2013.

normal to incipient LOAD — an early phase of Alzheimer's disease. These data indicate that the *APOE4* status of an individual reflects a prodromal, or 'primed', state for developing LOAD.

Notably, transcriptional changes observed during normal ageing (through comparison of those under 75 years of age with those over 85) overlapped significantly with LOAD, but not with changes specific to *APOE4* carriers. That certain transcriptional alterations in LOAD are seen either with ageing or with *APOE4* status suggests that the contributions of *APOE4* to LOAD are mechanistically distinct from those of ageing. A potential caveat of this analysis, however, is the use of a hard categorical cut-off of age 75, rather than, for example, 65 — the age below which Alzheimer's disease is considered early onset. In this regard, a non-categorical quantitative analysis of transcripts associated with ageing should provide maximum analytical power.

Network-level co-expression analyses have been used successfully before to investigate disease-related molecular pathways in various neuropsychiatric<sup>5,6</sup> and neurodegenerative disorders, including Alzheimer's disease<sup>3,7</sup>; such analyses permit an unbiased, systems-level understanding of disease mechanism. Rhinn and colleagues' work differs from other network-based co-expression approaches in focusing on differential co-expression — that is, on changes in co-expression patterns observed between control and disease samples. The authors, who used a transcriptome-wide network-analysis tool called differential co-expression correlation analysis (DCA), provide extensive experimental support for the targets identified, which adds an unprecedented level of validation.

Of the 215 differentially expressed genes Rhinn *et al.* found by comparing *APOE4* carriers and non-carriers, 20 are top candidate 'network node' genes on the basis of their DCA ranking. Many of the node genes had been previously implicated in regulating amyloid precursor protein (APP) processing and intracellular sorting<sup>8</sup>, supporting their relevance.

The authors performed various *in vitro* experiments to validate several of the node genes, in particular SV2A and *RNF219*. In cell lines and in human induced neurons, obtained by the process of cellular reprogramming, they show that SV2A affects APP processing through the regulation of endocytosis and intracellular trafficking. They also find that *RNF219*, which had not been previously associated with APP processing or Alzheimer's disease, acts as a nuclear regulatory mediator of *APOE4*-induced APP endocytosis and its processing by the  $\beta$ -secretase enzyme.

The researchers muster and analyse multiple independent data sets, including published GWAS, which provide further support for the key role of the DCA hits in *APOE4*-mediated susceptibility to Alzheimer's disease, and make a case for further testing and replication studies

using this gene set. For example, they show that, together with the *APOE4* status, common genetic variants of *RNF219* and *FYN* — another node gene with a role in endocytosis — are correlated with age of LOAD onset. Indeed, using publicly available human positron-emission tomography imaging data from the Alzheimer's Disease Neuroimaging Initiative, Rhinn *et al.* find that variations in *RNF219* significantly affect APP processing in *APOE4*-negative healthy individuals — consistent with a prodromal role of this, and possibly other, A/E genes.

Overall, the present paper significantly advances our knowledge of molecular and genetic mechanisms that modify LOAD risk, further implicating defects in endocytosis and intracellular trafficking in Alzheimer's disease development<sup>9,10</sup>. The identification of key regulatory molecules and pathways involved in *APOE*-based risk for LOAD sets the stage for investigating their link to other deficits in this disorder, including immune function and metabolism of hyperphosphorylated tau protein, which forms the disease's characteristic neurofibrillary tangles. Ultimately, such investigations should lead to molecularly targeted therapeutics.

By demonstrating distinct mechanisms that depend on *APOE* status in LOAD, another implication of this work is that different genetic forms or subtypes of Alzheimer's disease may have specific underlying mechanisms and respond differently to treatment. If so, as with cancer, therapies based on genetic and genomic diagnostics may be most effective.

This work is also exemplary in demonstrating the extraordinary value of publicly available data resources. Published data on human gene expression, Alzheimer's disease GWAS and neuroimaging provide the pillars of Rhinn and collaborators' paper. Integrative analyses of these data by the authors, and previously by others<sup>3,7</sup>, weaken the view that substantive biological experimentation only takes place at the wet bench, and highlight the value of innovative re-analyses of existing data<sup>6</sup>. ■

**Vivek Swarup** is in the Department of Neurology, and **Daniel H. Geschwind** is in the Department of Neurology and the Semel Institute, David Geffen School of Medicine at UCLA, University of California Los Angeles, Los Angeles, California 90095-1761, USA.  
e-mail: [dhg@mednet.ucla.edu](mailto:dhg@mednet.ucla.edu)

1. Rhinn, H. *et al.* *Nature* **500**, 45–50 (2013).
2. Bettens, K., Sleegers, K. & Van Broeckhoven, C. *Lancet Neurol.* **12**, 92–104 (2013).
3. Zhang, B. *et al.* *Cell* **153**, 707–720 (2013).
4. Wijsman, E. M. *et al.* *PLoS Genet.* **7**, e1001308 (2011).
5. Voineagu, I. *et al.* *Nature* **474**, 380–384 (2011).
6. Geschwind, D. H. & Konopka, G. *Nature* **461**, 908–915 (2009).
7. Miller, J. A., Oldham, M. C. & Geschwind, D. H. *J. Neurosci.* **28**, 1410–1420 (2008).
8. Minami, S. S. *et al.* *Neurobiol. Aging* **33**, 825.e15–825.e24 (2012).
9. Ihara, Y., Morishima-Kawashima, M. & Nixon, R. *Cold Spring Harb. Perspect. Med.* **2**, a006361 (2012).
10. Small, S. A. & Gandy, S. *Neuron* **52**, 15–31 (2006).



## 50 Years Ago

'The Delhi Pillar' — The mystery which has enveloped this quite remarkable piece of metal should be once and for all removed as a result of three papers published in the ... *Journal of the National Metallurgical Laboratory of India* ... All that has been previously written is summarized and the theories propounded to explain its resistance to corrosion are collected ... Made by hammer-welding small balls of native iron ... its resistance to corrosion during the 1,600 years or so of its existence is ascribed to the combined influence of a number of normal, favourable factors. Among these are included the climate and freedom from pollution of the atmosphere. Secondly, to a progressively decreasing rate of attack due to the building up of a protective layer of oxide and scale during the early years of exposure. That in the past on ceremonial occasions the pillar was anointed appears to be probable ... This is supported by the X-ray analysis of a minute sample of the surface coating ... which contained no iron and only quartz and chalk providing another source of protection.

From *Nature* 3 August 1963

## 100 Years Ago

We have applied the new methods of investigation involving the use of X-rays to the case of the diamond, and have arrived at a result which seems of considerable interest. The structure is extremely simple. Every carbon atom has four neighbours at equal distances from it, and in directions symmetrically related to each other. The directions are perpendicular to the four cleavage or (111) planes of the diamond; parallel, therefore, to the four lines which join the centre of a given regular tetrahedron to the four corners. **W. H. Bragg & W. L. Bragg**

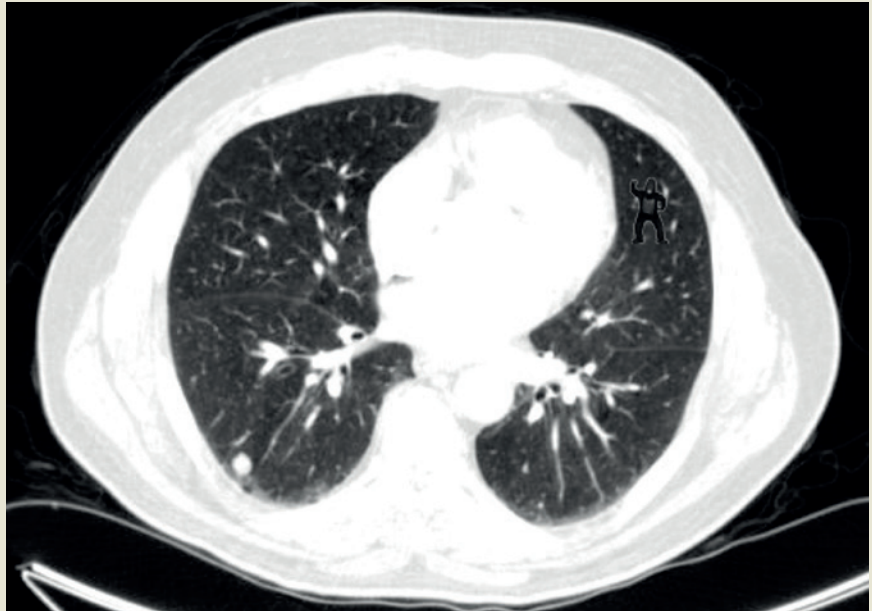
From *Nature* 31 July 1913

## PSYCHOLOGY

## Spot the gorilla

If it's not relevant you may miss it. This phenomenon of inattentional blindness is well documented; in a classic study, most observers asked to monitor a video of a ball game missed a gorilla on the court. But would experts also miss a gorilla? Yes, according to a study on the subject (T. Drew *et al.* *Psychol. Sci.* <http://doi.org/m9s>; 2013).

The authors asked 24 radiologists to search for lung nodules (small, bright circles) in several chest scans; the final scan (pictured) contained the image of a gorilla, 48 times larger than an average nodule. Surprisingly, and perhaps worryingly, 83% of the experts missed the gorilla. It is somewhat reassuring that the miss rate among non-medical observers performing the same task was even higher. **Sadaf Shadan**



PSYCHOLOGICAL SCIENCES

## NANOTECHNOLOGY

## Tiny thermometers used in living cells

**Nanometre-scale thermometers that operate with millikelvin sensitivity have now been made from diamond crystals. The devices have been used to measure temperature gradients in living cells. SEE LETTER P.54**

KONSTANTIN SOKOLOV

**D**espite many promising studies, taking temperature measurements of environments at nanometre-scale resolution remains a formidable challenge. On page 54 of this issue, Kucsko *et al.*<sup>1</sup> report a precious solution to this problem: a thermometer based on diamond nanocrystals, also known as nanodiamonds. This sensing tool could have many applications, ranging from studies of cell biology to measurements of nanoscale chemical reactions.

Temperature affects diverse physical phenomena. For example, changes in Earth's temperature patterns can lead to the formation of severe storms, droughts and floods. Temperature governs the kinetics, activation and equilibrium states of chemical reactions. And in humans, body temperature is precisely controlled, so that any deviation from the normal range triggers a cascade of biomolecular mechanisms to restore the body's equilibrium. Scientists have therefore developed a range of precise temperature-measuring tools — from satellites to infrared cameras, and a variety of

more familiar thermometers — to measure temperature over length scales from multiple kilometres to submillimetres. But how can we measure temperature at length scales of a few micrometres, or a few tens of nanometres?

Kucsko and co-workers' approach is to use the unique properties of electron spins associated with single-nitrogen-atom impurities in diamonds. The presence of a nitrogen atom in a diamond's carbon-atom lattice creates a point defect called a nitrogen vacancy (NV) centre, in which the nitrogen and a vacancy replace two neighbouring carbons. The ground state of an NV centre is split into two energy levels: the spin state of the lower level is 0, whereas that of the higher level is 1. The energy difference between the levels, known as the ground-state energy gap, is highly sensitive to temperature because it varies in response to thermally induced lattice strains. The principle of diamond thermometry is based on accurate measurement of changes in the transition frequency associated with this energy gap — the microwave frequency that corresponds to the energy difference between the lower and higher levels.

In their technique, Kucsko and colleagues

used green light to excite electrons in NV centres, which then decayed to the ground state by emitting red fluorescence. The intensity of the fluorescence depends on the spin state of the NV centres. The authors also irradiated their nanodiamonds with microwaves to modulate the electron occupancy of the ground spin states 0 and 1, and determined the occupancy of the states from the observed fluorescence. They then used this information to work out the changes in the ground-state energy gap that are associated with temperature variations.

The researchers first used an isotopically pure (carbon-12 isotope) bulk diamond sample to determine the ultimate sensitivity of their NV-based thermometry. In this system, they detected temperature changes with an accuracy of up to 1.8 millikelvins under ideal experimental conditions. Similar sensitivity has just been reported by other groups<sup>2,3</sup> using analogous experimental techniques and conditions.

However, Kucsko *et al.* went further by demonstrating how nanodiamond thermometers can measure the temperatures in living cells (Fig. 1). They used a clever nanowire-assisted delivery method<sup>4</sup> to position nanodiamonds and gold nanoparticles inside the cells. When excited by laser light, the gold nanoparticles acted as localized heat sources. By using their technique to measure sub-kelvin temperature changes inside a single cell, the authors directly monitored the amount of heat generated by a single gold nanoparticle that was required to kill the cell.

Kucsko and colleagues' nanodiamond temperature sensors have high spatial resolution together with sub-kelvin thermal sensitivity, chemical inertness, biocompatibility and the

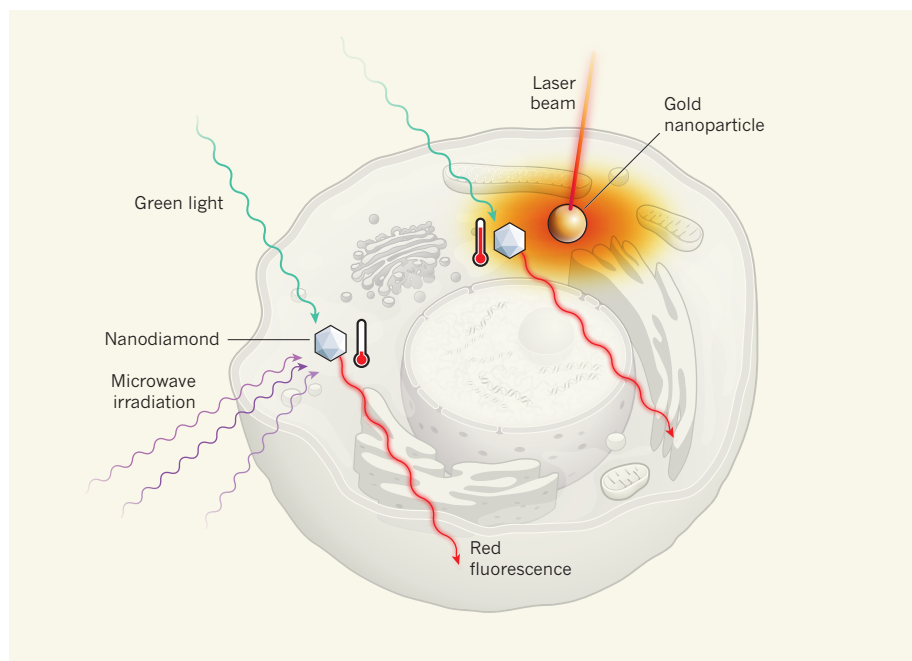


**Figure 1 | Temperature measurements in living cells.** When diamond-lattice defects known as nitrogen vacancy (NV) centres are excited by green light, they emit red fluorescence. Kucska *et al.*<sup>1</sup> inserted nanodiamonds into single living cells, and irradiated them with microwaves to modulate the electron occupancy of spin states in NV centres, and with green light. By measuring the fluorescence from these centres, the authors established the electron occupancy of the spin states, and so determined changes in the ground-state energy gap (the microwave frequency that corresponds to the energy difference between spin states) that are associated with temperature variations. In this way, they measured the temperature gradient generated when a gold nanoparticle in the cell was heated by a laser beam, achieving sub-kelvin sensitivity.

best-known thermal conductivity of all solid materials. This is an ideal blend for a nanothermometer. Furthermore, temperature sensing with nanodiamonds could be extended to *in vivo* applications if a different method for fluorescence excitation were adopted: microwave excitation of electronic spin states has already been carried out in animals<sup>5</sup>, and the use of ‘two-photon’ excitation would allow the analysis of deeper tissue than could be achieved with the present method.

Because nanodiamonds are discrete objects, however, the authors’ method can take measurements only at distinct locations, rather than taking continuous measurements of a temperature field. Furthermore, the method monitors temperature variations rather than absolute temperature. The authors suggest that this limitation could be overcome by using ensembles of nanodiamonds or diamond samples in which the lattices have low strain, either of which would reduce the experimental variations that currently limit absolute temperature from being measured. At present, the technique also has a fairly low temporal resolution of tens of seconds. This is sufficient for measurements of many biological processes, such as changes in gene expression, but is too slow for studies of temperature effects in faster processes, for example the initial steps of signal transduction, or neural activity.

How might this new tool further our understanding of human cell biology, or enable

biomedical advances? Most human cells are 10–20 micrometres in size and are highly compartmentalized by internal membranes that separate cellular organelles. These organelles create multiple micrometre-sized reactors in which a plethora of energy-producing and energy-absorbing reactions occur. The reactions generate intracellular temperature gradients on micrometre and submicrometre scales that, in turn, influence other cellular

biochemical reactions. Furthermore, external biochemical signalling and environmental changes activate molecular responses inside cells that can lead to corresponding changes in intracellular temperature gradients. The ability to measure intracellular temperature precisely would therefore provide an invaluable tool for cellular biophysicists, potentially allowing cellular behaviour and characteristics to be manipulated by controlling the temperature within, or close to, cellular organelles.

Kucska and co-workers’ technique could also open up many other intriguing topics for research, including the thermal modulation of immune responses<sup>6</sup>, molecular mechanisms of therapeutic tissue preservation induced by local cooling<sup>7</sup>, the role of subcellular temperature gradients in cell function<sup>8</sup>, and cell resistance to hyperthermia treatment<sup>9</sup> (deliberately induced elevated body temperature, used, for example, as anticancer therapy). When it comes to measuring temperature, it may be that diamonds are a scientist’s best friend. ■

**Konstantin Sokolov** is in the Department of Imaging Physics, The University of Texas MD Anderson Cancer Center, Houston, Texas 77030, USA.

e-mail: konstantin.sokolov@engr.utexas.edu

1. Kucska, G. *et al.* *Nature* **500**, 54–58 (2013).
2. Toyli, D. M., de las Casas, C. F., Christle, D. J., Dobrovitski, V. V. & Awschalom, D. D. *Proc. Natl. Acad. Sci. USA* **110**, 8417–8421 (2013).
3. Neumann, P. *et al.* *Nano Lett.* **13**, 2738–2742 (2013).
4. Shalek, A. K. *et al.* *Proc. Natl. Acad. Sci. USA* **107**, 1870–1875 (2010).
5. Han, J. Y., Hong, J. T. & Oh, K.-W. *Arch. Pharm. Res.* **33**, 1293–1299 (2010).
6. Frey, B. *et al.* *Int. J. Hyperthermia* **28**, 528–542 (2012).
7. Geva, A. & Gray, J. *Med. Decision Making* **32**, 266–272 (2012).
8. Yang, J.-M., Yang, H. & Lin, L. *ACS Nano* **5**, 5067–5071 (2011).
9. Rylander, M. N., Feng, Y., Zimmerman, K. & Diller, K. R. *Int. J. Hyperthermia* **26**, 748–764 (2010).

## CANCER

# Angiogenic awakening

**Metastatic tumour cells often remain dormant for years. New findings suggest that endothelial cells lining blood vessels have a central role in regulating the transition from dormancy to metastatic growth.**

## NETA EREZ

The primary cause of cancer-associated deaths is the metastasis of a tumour to distant organs. Advanced metastatic cancers are mostly incurable, and available therapies can only prolong life to a limited extent. In many tumour types there is a long lag between the arrival of cancerous cells at distant locations and their colonization of

an organ, such that the formation of clinically evident metastases can take months to decades. This prolonged dormancy suggests that disseminated tumour cells must overcome growth-inhibiting signals from their new local environment in order to take over the metastatic organ<sup>1,2</sup>. The role of the microenvironment in supporting tumour growth at the primary site is well documented<sup>3</sup>, but the role of the metastatic microenvironment

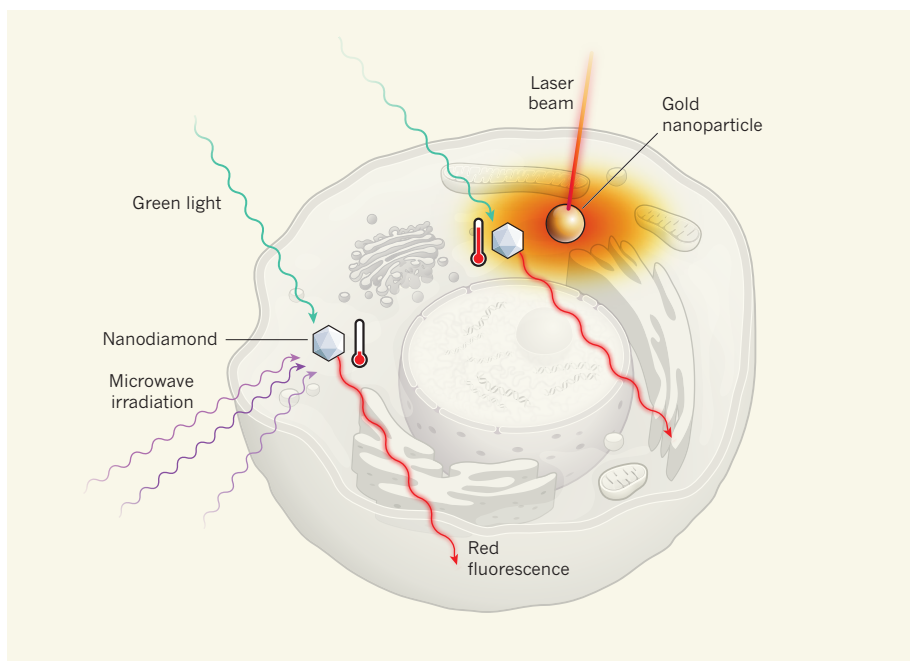


**Figure 1 | Temperature measurements in living cells.** When diamond-lattice defects known as nitrogen vacancy (NV) centres are excited by green light, they emit red fluorescence. Kucska *et al.*<sup>1</sup> inserted nanodiamonds into single living cells, and irradiated them with microwaves to modulate the electron occupancy of spin states in NV centres, and with green light. By measuring the fluorescence from these centres, the authors established the electron occupancy of the spin states, and so determined changes in the ground-state energy gap (the microwave frequency that corresponds to the energy difference between spin states) that are associated with temperature variations. In this way, they measured the temperature gradient generated when a gold nanoparticle in the cell was heated by a laser beam, achieving sub-kelvin sensitivity.

best-known thermal conductivity of all solid materials. This is an ideal blend for a nanothermometer. Furthermore, temperature sensing with nanodiamonds could be extended to *in vivo* applications if a different method for fluorescence excitation were adopted: microwave excitation of electronic spin states has already been carried out in animals<sup>5</sup>, and the use of ‘two-photon’ excitation would allow the analysis of deeper tissue than could be achieved with the present method.

Because nanodiamonds are discrete objects, however, the authors’ method can take measurements only at distinct locations, rather than taking continuous measurements of a temperature field. Furthermore, the method monitors temperature variations rather than absolute temperature. The authors suggest that this limitation could be overcome by using ensembles of nanodiamonds or diamond samples in which the lattices have low strain, either of which would reduce the experimental variations that currently limit absolute temperature from being measured. At present, the technique also has a fairly low temporal resolution of tens of seconds. This is sufficient for measurements of many biological processes, such as changes in gene expression, but is too slow for studies of temperature effects in faster processes, for example the initial steps of signal transduction, or neural activity.

How might this new tool further our understanding of human cell biology, or enable

biomedical advances? Most human cells are 10–20 micrometres in size and are highly compartmentalized by internal membranes that separate cellular organelles. These organelles create multiple micrometre-sized reactors in which a plethora of energy-producing and energy-absorbing reactions occur. The reactions generate intracellular temperature gradients on micrometre and submicrometre scales that, in turn, influence other cellular

biochemical reactions. Furthermore, external biochemical signalling and environmental changes activate molecular responses inside cells that can lead to corresponding changes in intracellular temperature gradients. The ability to measure intracellular temperature precisely would therefore provide an invaluable tool for cellular biophysicists, potentially allowing cellular behaviour and characteristics to be manipulated by controlling the temperature within, or close to, cellular organelles.

Kucska and co-workers’ technique could also open up many other intriguing topics for research, including the thermal modulation of immune responses<sup>6</sup>, molecular mechanisms of therapeutic tissue preservation induced by local cooling<sup>7</sup>, the role of subcellular temperature gradients in cell function<sup>8</sup>, and cell resistance to hyperthermia treatment<sup>9</sup> (deliberately induced elevated body temperature, used, for example, as anticancer therapy). When it comes to measuring temperature, it may be that diamonds are a scientist’s best friend. ■

**Konstantin Sokolov** is in the Department of Imaging Physics, The University of Texas MD Anderson Cancer Center, Houston, Texas 77030, USA.

e-mail: konstantin.sokolov@engr.utexas.edu

1. Kucska, G. *et al.* *Nature* **500**, 54–58 (2013).
2. Toyli, D. M., de las Casas, C. F., Christle, D. J., Dobrovitski, V. V. & Awschalom, D. D. *Proc. Natl. Acad. Sci. USA* **110**, 8417–8421 (2013).
3. Neumann, P. *et al.* *Nano Lett.* **13**, 2738–2742 (2013).
4. Shalek, A. K. *et al.* *Proc. Natl. Acad. Sci. USA* **107**, 1870–1875 (2010).
5. Han, J. Y., Hong, J. T. & Oh, K.-W. *Arch. Pharm. Res.* **33**, 1293–1299 (2010).
6. Frey, B. *et al.* *Int. J. Hyperthermia* **28**, 528–542 (2012).
7. Geva, A. & Gray, J. *Med. Decision Making* **32**, 266–272 (2012).
8. Yang, J.-M., Yang, H. & Lin, L. *ACS Nano* **5**, 5067–5071 (2011).
9. Rylander, M. N., Feng, Y., Zimmerman, K. & Diller, K. R. *Int. J. Hyperthermia* **26**, 748–764 (2010).

## CANCER

# Angiogenic awakening

**Metastatic tumour cells often remain dormant for years. New findings suggest that endothelial cells lining blood vessels have a central role in regulating the transition from dormancy to metastatic growth.**

## NETA EREZ

The primary cause of cancer-associated deaths is the metastasis of a tumour to distant organs. Advanced metastatic cancers are mostly incurable, and available therapies can only prolong life to a limited extent. In many tumour types there is a long lag between the arrival of cancerous cells at distant locations and their colonization of

an organ, such that the formation of clinically evident metastases can take months to decades. This prolonged dormancy suggests that disseminated tumour cells must overcome growth-inhibiting signals from their new local environment in order to take over the metastatic organ<sup>1,2</sup>. The role of the microenvironment in supporting tumour growth at the primary site is well documented<sup>3</sup>, but the role of the metastatic microenvironment

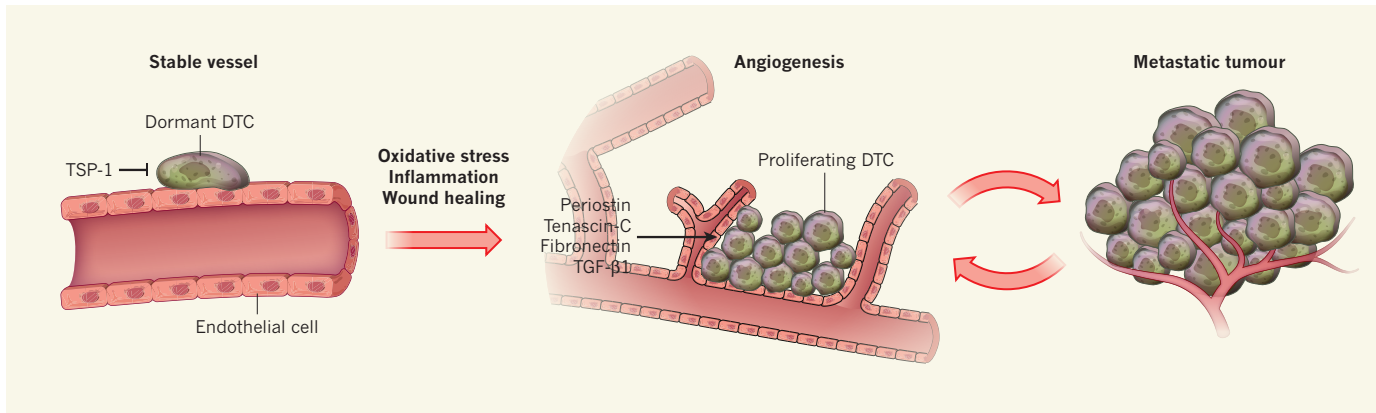


**Figure 1 | Instigation of angiogenesis enables tumour-cell exit from dormancy.** Ghajar *et al.*<sup>4</sup> show that expression of the protein TSP-1 by endothelial cells in stable blood vessels inhibits the proliferation of disseminated tumour cells (DTCs) residing on the blood vessels. By contrast, DTC proliferation is accelerated at the sprouting tips of new vessels, in part by endothelial-cell secretion of periostin,

tenascin-C, fibronectin and TGF- $\beta$ 1. Instigation of angiogenesis (the formation of new blood vessels), for example following oxidative stress, inflammation or wound healing, at a site to which tumour cells have metastasized but are dormant, might thus awaken these cells and enable the formation of metastatic tumours. Proliferating tumour cells will express pro-angiogenic signals that feed back to amplify this process.

and the molecular interactions between disseminated cancer cells and stromal cells at the metastatic organ are poorly characterized. Writing in *Nature Cell Biology*, Ghajar *et al.*<sup>4</sup> report a mechanism by which the endothelial cells that line blood vessels regulate the dormancy of disseminated breast cancer cells\*.

Using a mouse model of human breast cancer metastasis, the authors show that dormant disseminated tumour cells (DTCs) reside on the endothelium of the microvasculature in the lung, bone marrow and brain, which are common metastatic destinations of breast cancer. An *in vitro* three-dimensional model of microvasculature confirmed that this perivascular location of tumour cells is responsible for maintaining their quiescent state, and identified the protein thrombospondin-1 (TSP-1), secreted by endothelial cells, as a suppressor of tumour-cell growth.

Remarkably, this growth-suppressive microenvironment was found only around stable microvascular endothelium; the sprouting tips of newly forming vessels actually had an opposite, growth-accelerating effect on tumour cells. Unlike stable vessels, these growing tips were characterized by enhanced expression of the proteins periostin, tenascin-C, fibronectin and active tumour growth factor- $\beta$ 1 (TGF- $\beta$ 1), which have all previously been implicated in the formation of the metastatic niche<sup>5–7</sup> (Fig. 1).

These findings suggest that the vascular endothelium is an active participant in the formation of a growth-permissive microenvironment. The growth-accelerating effect could be seen *in vitro*: reducing the number of endothelial tips by targeting Notch1, a protein that regulates vessel sprouting, suppressed the proliferation of breast-tumour cells in the microvasculature models. And when the

authors injected the tumour cells into zebrafish that were genetically engineered to have excessive microvascular sprouting, they observed enhanced proliferation of the cells adjacent to new blood-vessel tips.

Angiogenesis — the growth of new blood vessels — is crucial to the ability of tumours and metastases to thrive<sup>8,9</sup>. Ghajar and colleagues' findings add a fascinating layer to this story by suggesting that metastatic propagation may rely on the induction of new vascular growth not only because such growth supports nutrient and oxygen supply to micrometastases, but also because it enables the exit of DTCs from dormancy.

But can solitary DTCs exhibit such pro-angiogenic signalling? Dormant tumours are metabolically active and sustain a balance between angiogenic inhibitors and stimulators, remaining dormant until this balance is shifted towards the stimulation of angiogenesis<sup>8,9</sup>. However, it is not clear whether single dormant DTCs can induce angiogenesis. Most previous studies on angiogenesis and tumour dormancy have focused on how tumour-cell characteristics determine the nature of the tumour vasculature. But the present findings imply that, in some cases, the order of events may be reversed, such that the awakening of the vasculature precedes metastatic growth and is independent of pro-angiogenic signalling from dormant DTCs.

In healthy adult tissues, the formation of blood vessels is a relatively infrequent event that is only triggered when certain signals lead to an increase in angiogenic activators — for example, following tissue-damaging events such as oxidative stress, inflammation or wound healing. If such events occurred in an organ in which DTCs reside, the resulting instigation of new vascular growth might inadvertently switch the balance from growth-suppressive to growth-accelerating signals and thereby facilitate the exit of DTCs from

dormancy. Thus, escape from dormancy may be, in some cases, secondary to the induction of angiogenesis at the metastatic site (Fig. 1).

The ability of tumour cells to exit dormancy and proliferate seems to be the rate-limiting step of metastasis. Ghajar and colleagues' results emphasize that to confront metastasis in a particular organ, the interactions of tumour cells with the microenvironment of that specific organ need to be elucidated.

Numerous studies have previously demonstrated the central role of innate and adaptive immune cells in the formation of a permissive metastatic environment<sup>1,2</sup>, and it is likely that immune cells and other cells at the metastatic site function together with the signals from endothelial cells to regulate tumour-cell dormancy. Ghajar *et al.* used immunodeficient mice in their experiments, but future studies in animal models with intact immunity may shed light on such interactions. Expanding our understanding of the early stages of metastatic growth will pave the way to new targeted therapeutics aimed at preventing, rather than trying to cure, metastatic disease. ■

**Neta Erez** is in the Department of Pathology, Sackler School of Medicine, Tel Aviv University, Tel Aviv, 69978 Israel.  
e-mail: netaerez@post.tau.ac.il

1. Joyce, J. A. & Pollard, J. W. *Nature Rev. Cancer* **9**, 239–252 (2009).
2. Erez, N. & Coussens, L. M. *Int. J. Cancer* **128**, 2536–2544 (2011).
3. Hanahan, D. & Coussens, L. M. *Cancer Cell* **21**, 309–322 (2012).
4. Ghajar, C. M. *et al.* *Nature Cell Biol.* **15**, 807–817 (2013).
5. Bhowmick, N. A. *Cancer Cell* **22**, 563–564 (2012).
6. Oskarsson, T. & Massagué, J. *EMBO J.* **31**, 254–256 (2012).
7. Peinado, H., Lavotshkin, S. & Lyden, D. *Semin. Cancer Biol.* **21**, 139–146 (2011).
8. Naumov, G. N., Akslen, L. A. & Folkman, J. *Cell Cycle* **5**, 1779–1787 (2006).
9. Berger, G. & Benjamin, L. E. *Nature Rev. Cancer* **3**, 401–410 (2003).

\*This News & Views article was published online on 24 July 2013.

# Myc-driven endogenous cell competition in the early mammalian embryo

Cristina Clavería<sup>1</sup>, Giovanna Giovinazzo<sup>1</sup>, Rocío Sierra<sup>1</sup> & Miguel Torres<sup>1</sup>

The epiblast is the mammalian embryonic tissue that contains the pluripotent stem cells that generate the whole embryo. We have established a method for inducing functional genetic mosaics in the mouse. Using this system, here we show that induction of a mosaic imbalance of Myc expression in the epiblast provokes the expansion of cells with higher Myc levels through the apoptotic elimination of cells with lower levels, without disrupting development. In contrast, homogeneous shifts in Myc levels did not affect epiblast cell viability, indicating that the observed competition results from comparison of relative Myc levels between epiblast cells. During normal development we found that Myc levels are intrinsically heterogeneous among epiblast cells, and that endogenous cell competition refines the epiblast cell population through the elimination of cells with low relative Myc levels. These results show that natural cell competition in the early mammalian embryo contributes to the selection of the epiblast cell pool.

Multicellular organisms have evolved tissue homeostasis mechanisms to ensure life-long fitness of their organs and systems. Among these mechanisms, those that regulate the elimination of unwanted cells are fundamental for tissue development and homeostasis<sup>1</sup>. Whereas overtly damaged or hyperproliferative cells usually trigger well-characterized cell-autonomous apoptotic pathways<sup>2</sup>, mechanisms that survey viable cell fitness to optimize a tissue's cell composition are less well understood. A candidate mechanism is the phenomenon of cell competition, first described in *Drosophila*<sup>3</sup>. Studies in flies have shown that the cells of growing organs are able to compare their fitness with that of neighbouring cells, and the less-fit but otherwise viable cells are eliminated (out-competed) when confronted with a fitter cell population (competitor)<sup>3–8</sup>. Cell competition for survival is an active process because, in addition to a contribution from differential proliferation<sup>9</sup>, it is executed through the apoptotic elimination of the less-fit population by cell non-autonomous mechanisms<sup>10</sup>. Cell parameters that trigger competition in flies include differences in protein synthesis capacity, growth factor receptivity and the expression level of *dMyc*<sup>3–5,10</sup>, a major activator of cell anabolism. Supercompetition is a variant of cell competition in which cells moderately overexpressing *dMyc* outcompete wild-type (WT) cells<sup>5</sup>. The replacement of cell populations through cell competition is phenotypically silent, because the competitor cells mostly conform to size-control mechanisms<sup>3–5</sup>. This process is potentially important for the long-term maintenance of tissue performance, as it might provide a mechanism for elimination of suboptimal cells from stem-cell niches and progenitor-cell pools (reviewed in refs 11, 12). In addition, cell competition for survival might serve to enhance tissue replacement during regeneration<sup>13</sup>. However, despite its potential importance, cell competition for survival has so far only been observed after experimental induction<sup>3–8,14–16</sup>, and its endogenous role has not been uncovered. Here we use a genetic mosaic approach to induce supercompetition in the mouse embryo conditionally, and identify endogenous cell competition in the epiblast as a mechanism for the selection of cells with higher anabolic activity (Supplementary Fig. 1).

## Myc-enriched cell expansion in embryos

To develop a methodology for analysing cell competition in mammals, we devised a recombinase-based system for producing inducible

random genetic mosaics (iMOS) (Supplementary Information). This system allows the conditional generation of random mosaics expressing two alternative transcripts, T1 or T2, from the ubiquitously expressed ROSA26 locus (Supplementary Fig. 2a). Once generated, the mosaic cell populations are stable (Supplementary Fig. 3) and can be independently tracked by the expression of *IRES-EYFP* inserted in T1 and *IRES-ECFP* in T2 (Supplementary Fig. 2a). Recombination of the *iMOS<sup>WT</sup>* allele in the epiblast using *Sox2-cre* (ref. 17) produced random mosaicism for the expression of the two reporter genes in all embryonic tissues (Supplementary Fig. 2b–i). Quantification by flow cytometry and confocal microscopy at embryonic day (E)9.5 showed a 1:3 ratio of enhanced cyan fluorescent protein (ECFP) to enhanced yellow fluorescent protein (EYFP) cells (Supplementary Fig. 2j, k).

To test whether increasing the dose of *Myc* expands cell populations in the mouse embryo, we generated an *iMOS* allele (*iMOS<sup>T1-Myc</sup>*) in which *Myc* was inserted before *IRES-EYFP* in T1 (Supplementary Fig. 4a). *Sox2-cre* recombination of the *iMOS<sup>T1-Myc</sup>* allele produced mosaic Myc expression at a similar level to a wild-type allele (Supplementary Fig. 5 and Supplementary Information) and resulted in significant rescue of the *Myc* null phenotype at E10.5 (Supplementary Fig. 4b–h), indicating that *Myc* overexpression occurs within a physiological range.

Rescued embryos had an elevated EYFP/ECFP expression ratio, suggesting an increase in the proportion of *Myc*-enriched cells (Supplementary Fig. 4i–n). We next induced *iMOS<sup>T1-Myc</sup>* mosaics in three *Myc* backgrounds: wild type, *Myc*<sup>+/–</sup> and *Myc*<sup>–/–</sup> (Fig. 1a). This strategy allowed *Myc*-enriched EYFP cells to be confronted with *Myc*-non-enriched ECFP cells at increasing ratios of relative *Myc* content (Fig. 1a). Compared with the *iMOS<sup>WT</sup>* mosaics, E10.5 *iMOS<sup>T1-Myc</sup>* mosaics showed a shift towards *Myc*-linked EYFP expression (Fig. 1b and Supplementary Fig. 4o). Moreover, increasing *Myc* dose imbalance between the two cell populations correlated with an increasing EYFP/ECFP signal ratio (Fig. 1b and Supplementary Fig. 4o). Quantification by confocal microscopy and flow cytometry at E10.5 showed that the proportion of *Myc*-non-enriched ECFP cells decreased in correlation with the imbalance in *Myc* dose (Fig. 1c), but that the changes in *Myc* dose did not affect cell size or embryo size (Supplementary Fig. 6). The shift in cell population proportions thus results from the replacement of

<sup>1</sup>Departamento de Desarrollo y Reparación Cardiovascular, Centro Nacional de Investigaciones Cardiovasculares (CNIC), Madrid E-28029, Spain.

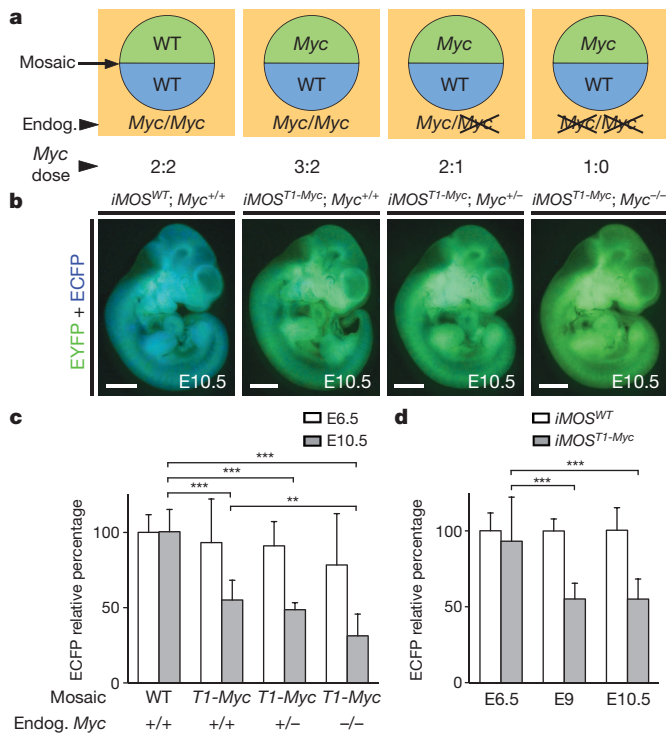


**Figure 1 | Myc overexpression promotes dose-dependent expansion of cell populations in mosaic embryos.** **a**, Myc gene doses in *Sox2-cre*-recombined *iMOS<sup>WT</sup>* and *iMOS<sup>T1-Myc</sup>* embryos in different endogenous Myc backgrounds. Myc dose indicates the numbers of Myc copies in EYFP and ECFP cells. **b**, Overlay views of EYFP and ECFP signals in E10.5 mosaics. Scale bars, 1 mm. **c, d**, ECFP cell relative percentages in confocal sections. Graphs show means  $\pm$  s.d. of cell percentages measured in individual embryos collected from various similar litters (biological replicates).  $n = 8, 7, 6, 11, 9, 5, 10, 6$  (from left to right) embryos in **c** and  $n = 8, 6, 7, 12, 7, 11$  embryos in **d**; \*\* $P < 0.01$ ; \*\*\* $P < 0.001$  by ANOVA followed by Tukey honestly significant difference (HSD) tests.

*Myc*-non-enriched cells by *Myc*-enriched cells. Notably, cells with wild-type levels of *Myc* are depleted when confronted with cells with higher *Myc* expression, but cells with absolute *Myc* levels similar to wild type (1 wild-type *Myc* + 1 *iMOS<sup>T1-Myc</sup>* alleles) or lower (1 *iMOS<sup>T1-Myc</sup>* allele) expand when confronted with cells with lower relative *Myc* levels, indicating that the key to this phenomenon is the *Myc* dose difference between cells. *iMOS<sup>WT</sup>* and *iMOS<sup>T1-Myc</sup>* mosaics in a wild-type background both survive to adulthood and display no evident phenotypic alterations ( $n > 150$  and  $n > 180$ , respectively). Enrichment in *Myc*-overexpressing cells thus results from a cell population replacement process that is phenotypically silent.

To track the depletion of wild-type cells in *iMOS<sup>T1-Myc</sup>* mosaics, we measured the proportion of ECFP cells at different stages. At E6.5, proportions did not differ significantly between *iMOS<sup>WT</sup>* and *iMOS<sup>T1-Myc</sup>* mosaics (Fig. 1d); but at E9, the frequency of wild-type cells was reduced by a half, and then remained unchanged at E10.5 (Fig. 1d). Wild-type cell depletion is thus not continuous within this period, but takes place in a short time window early in embryogenesis. The frequency of *Myc*-non-enriched cells in *iMOS<sup>T1-Myc</sup>* mosaics induced in *Myc<sup>+/-</sup>* and *Myc<sup>-/-</sup>* backgrounds already showed a tendency to reduce at E6.5 (Fig. 1c), indicating that the cell population replacement is active at early embryonic stages.

### Myc-induced expansion requires apoptosis

To explore how embryos become enriched in *Myc*-overexpressing cells, we first studied cell proliferation. ECFP and EYFP cell populations in *iMOS<sup>T1-Myc</sup>* mosaics showed no significant differences in  $\text{pH3}^+$  cell frequency at E6.5 or in 5-bromodeoxyuridine (BrdU) $^+$  cell

frequency at E6.5, E7.5 and E9.5 (Supplementary Fig. 7 and Supplementary Information).

To evaluate the contribution of cell death to the depletion of wild-type cells in *iMOS<sup>T1-Myc</sup>* mosaics, we generated a new *iMOS* allele (*iMOS<sup>T1-Myc/T2-p35</sup>*) incorporating *Myc* and *p35* in T1 and T2 (Fig. 2a). In these mosaics, the *Myc*-overexpressing cell population is confronted with a *Myc*-non-enriched cell population expressing the apoptosis inhibitor *p35* (Fig. 2a). *p35* expression in *iMOS<sup>T2-p35</sup>* mosaics inhibits apoptosis in the mouse embryo (Supplementary Fig. 8 and Supplementary Information). In *iMOS<sup>T1-Myc/T2-p35</sup>* mosaics, the higher proportion of EYFP signal seen in *iMOS<sup>T1-Myc</sup>* embryos at E9.5 was abolished (Fig. 2b–d). This was also evident on confocal sections and by flow cytometry (Fig. 2e–h). Quantitative confocal analysis showed that both the depletion of wild-type ECFP cells in *iMOS<sup>T1-Myc</sup>* mosaics and their rescue in *iMOS<sup>T1-Myc/T2-p35</sup>* mosaics were homogeneous in different tissues (Fig. 2i). *iMOS<sup>T1-Myc/T2-p35</sup>* mosaics survive to adulthood, and display no obvious phenotypic alteration ( $n > 50$ ). The inhibition of apoptosis in the wild-type cell population thus prevents its depletion and the concomitant expansion of the *Myc*-enriched cell population.

### Cell competition occurs in the epiblast

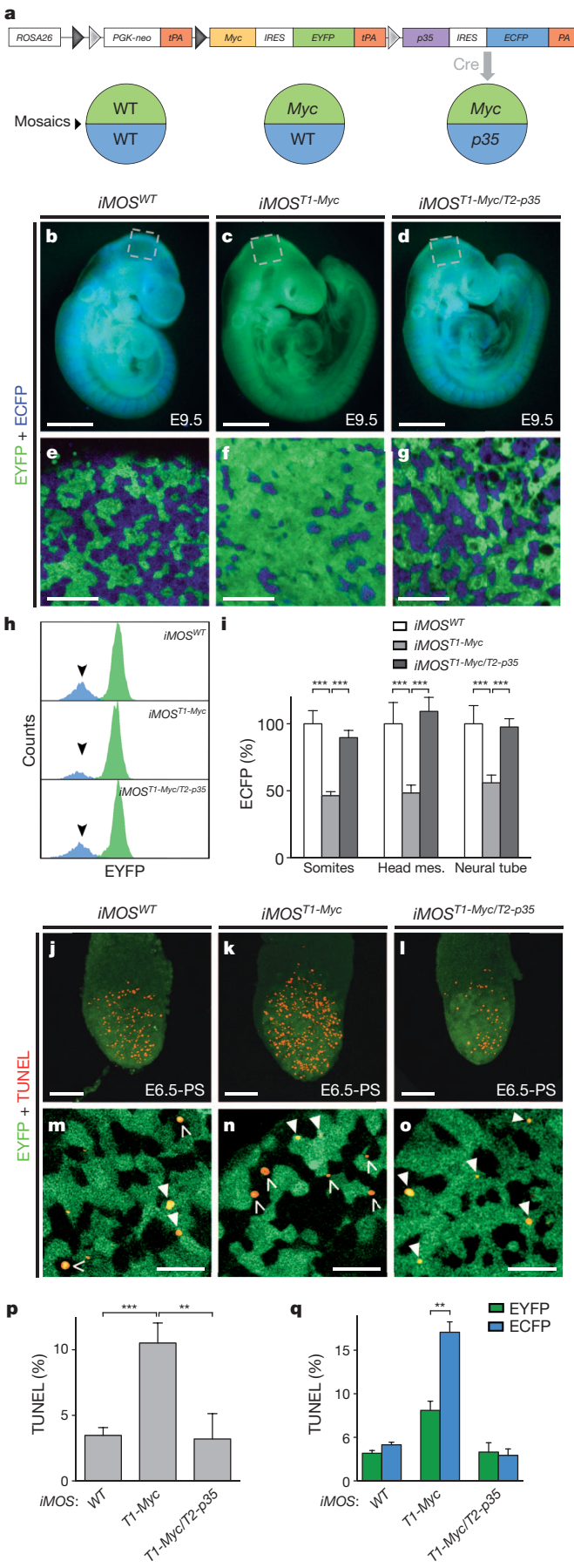
The fact that *Myc*-overexpressing cells do not increase between E9 and E10.5, together with the homogeneity of wild-type cell depletion and *p35* rescue in different embryonic tissues, suggests that wild-type cell depletion occurs earlier, in a homogeneous precursor population. We therefore analysed the epiblast, which contains all embryonic precursors. In agreement with previous studies<sup>18</sup>, the incidence of apoptosis in *iMOS<sup>WT</sup>* mosaics was high, and was restricted to the epiblast, without affecting extraembryonic regions (Fig. 2j). Mosaic *Myc* expression sharply increased cell death in the epiblast (Fig. 2k, p). Expression of *p35* in the complementary cell population completely rescued the increased cell death induced by mosaic *Myc* overexpression (Fig. 2l, p).

Scoring of TdT-mediated dUTP nick end labelling (TUNEL) staining in EYFP and ECFP populations (Fig. 2m–o, q) showed that the increased cell death in *iMOS<sup>T1-Myc</sup>* embryos mostly affects the wild-type ECFP population, with only a minor contribution from *Myc*-overexpressing EYFP cells (Fig. 2n, q). The increased incidence of TUNEL-positive ECFP cells was abolished in *iMOS<sup>T1-Myc/T2-p35</sup>* mosaics (Fig. 2o, q). Moreover, *iMOS<sup>T1-Myc/T2-p35</sup>* embryos lacked the moderate increase in cell death detected in the *Myc*-overexpressing EYFP cell population in *iMOS<sup>T1-Myc</sup>* mosaics (Fig. 2o, q).

We next quantified apoptosis in embryos homogenously overexpressing *Myc* and in embryos with reduced (*Myc<sup>+/-</sup>*) or absent (*Myc<sup>-/-</sup>*) *Myc* expression. In contrast with the results obtained with the mosaics, apoptosis was not modified in any of these conditions (Supplementary Fig. 9). These results exclude cell-autonomous induction of apoptosis by *Myc* overexpression or reduction. Wild-type cell depletion in *iMOS<sup>T1-Myc</sup>* mosaics is thus driven by a cell competition process implemented through non-autonomous induction of cell death in the mouse epiblast.

### Cell competition death mechanisms

Marker analysis in *iMOS<sup>T1-Myc</sup>* mosaics revealed activation of the intrinsic but not the extrinsic apoptotic pathway in epiblast cell death (Supplementary Fig. 10 and Supplementary Information). To dissect the mechanism of cell-competition-induced apoptosis further, we developed an *in vitro* drug-inducible *iMOS* model of *Myc* supercompetition in embryonic stem (ES) cells. *Myc* drives cell competition in this model in a manner similar to that observed in the mouse epiblast (Supplementary Information and Supplementary Fig. 11). To characterize the interactions required for cell competition, we induced recombination in homozygous *iMOS<sup>T1-Myc</sup>* ES cell cultures and scored apoptosis in wild-type cells residing in unrecombined colonies, wild-type cells in recombined colonies but not contacting EYFP cells, and wild-type cells contacting EYFP cells (Supplementary Fig. 12a and Fig. 3a–c). Increased



apoptosis with respect to uninduced cultures was observed only in wild-type cells in direct contact with Myc-overexpressing EYFP cells (Fig. 3d). A similar result was obtained for EYFP-cell-contacting and non-contacting wild-type cells in the *iMOS<sup>T1-Myc</sup>* embryonic epiblast (Fig. 3e, f and Supplementary Video 1). In addition, exposure of uninduced ES cell cultures to cell-competition-conditioned medium did not increase apoptosis or modify proliferation rates (Supplementary Fig. 12b-e). These results indicate that cell competition requires direct contact or very short-range interactions and that, under these experimental conditions, diffusible signals are not sufficient to induce it.

We next studied the mechanism by which apoptotic cells are eliminated in mammalian cell competition. Previous studies showed that dying cells in the mouse epiblast are removed through phagocytosis by neighbouring cells<sup>19</sup>. We found that cells showing apoptosis markers are engulfed by neighbouring cells in epiblasts and ES cell cultures undergoing cell competition (Supplementary Fig. 13a, c, d, f). Some phagocytic events take place in the absence of TUNEL staining, suggesting that engulfment by neighbours is an early event in epiblast and ES cell apoptosis (Supplementary Fig. 13b, e). These results indicate that mammalian cell competition involves phagocytosis by neighbouring cells, at least in situations in which there are no macrophages.

### Myc-driven endogenous competition

The high cell death rate in the epiblast and its sensitivity to induced supercompetition suggest that it might be a site of endogenous cell competition. We thus studied the distribution of endogenous Myc in the early mouse embryo. Up to E6.75, Myc mRNA and protein are expressed in the epiblast and extraembryonic tissues at levels that vary from cell to cell in an apparently random distribution (Supplementary Figs 14–16), contrasting with the homogenous expression of the epiblast marker *Oct4* (Supplementary Fig. 17). By E7.0 embryonic Myc expression ceases in the epiblast, restarting at E7.5 in a homogeneous distribution (Supplementary Figs 14 and 15). Embryonic Myc expression is thus heterogeneous until E6.75, in a pattern that is not regionally modulated but is instead intrinsic to individual cells. Myc mRNA and protein have a fast turnover and Myc protein abundance is predominantly regulated by mRNA availability<sup>20</sup>, indicating that the variable protein levels result from the variable mRNA levels. To confirm this, we performed per-cell quantification of Myc immunofluorescence (Methods and Supplementary Fig. 18) to determine the distribution of Myc levels in wild-type embryos and in *iMOS<sup>T1-Myc</sup>*; *Myc*<sup>−/−</sup> E6.5 embryos, in which Myc mRNA is exclusively produced from the *ROSA26* allele. Myc protein levels in *iMOS<sup>T1-Myc</sup>*; *Myc*<sup>−/−</sup> mosaics were more homogeneous than in wild-type embryos (2.2-fold higher residual variance in wild type;  $P < 0.001$ ) (Fig. 4a–h). The heterogeneity of endogenous Myc protein expression thus seems to result mostly from variable transcriptional activity of the *Myc* gene.

Further analysis indicated that the variability in Myc expression levels cannot be attributed to variations during the cell cycle (Supplementary

**Figure 2 | Expansion of Myc-overexpressing cells requires apoptosis of wild-type cells in the epiblast of early mosaic embryos.** **a**, *ROSA26*-targeted *iMOS<sup>T1-Myc/T2-p35</sup>* construct and the three mosaics studied. **b–d**, Overlay views of EYFP and ECFP signals in E9.5 mosaics. Scale bars, 1 mm. **e–g**, Confocal sections showing head mesenchyme corresponding to the boxed areas in **b–d**. Scale bars, 50 μm. **h**, Flow cytometry analysis of EYFP and ECFP cells in disaggregated representative E9.5 mosaics. Arrowheads indicate ECFP cell counts. **i**, ECFP proportion in confocal sections of E9.5 mosaics ( $n = 7, 8, 8$  (from left to right) embryos). **j–l**, TUNEL staining in whole E6.5 mosaics. **m–o**, Details of confocal sections. TUNEL-positive EYFP and ECFP cells are indicated by filled and open arrowheads, respectively. Scale bars, 100 μm (j–l), 25 μm (m–o). **p**, TUNEL-staining frequency in E6.5 mosaics. **q**, TUNEL-staining frequency in EYFP and ECFP populations in the E6.5 mosaics ( $n = 4, 4, 4$  embryos) in **i**, **p** and **q** were collected from various similar litters and represent biological replicates. Graphs show means  $\pm$  s.e.m. in **i** and **s.d.** in **p**, **q**; \*\* $P < 0.01$ ; \*\*\* $P < 0.001$  by unpaired two sample *t*-test.

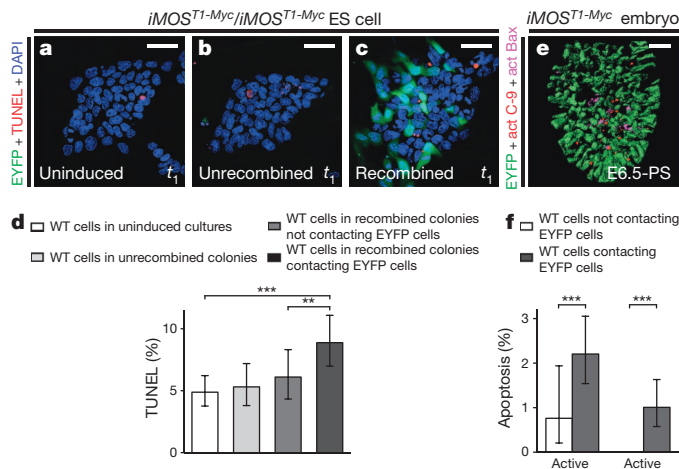


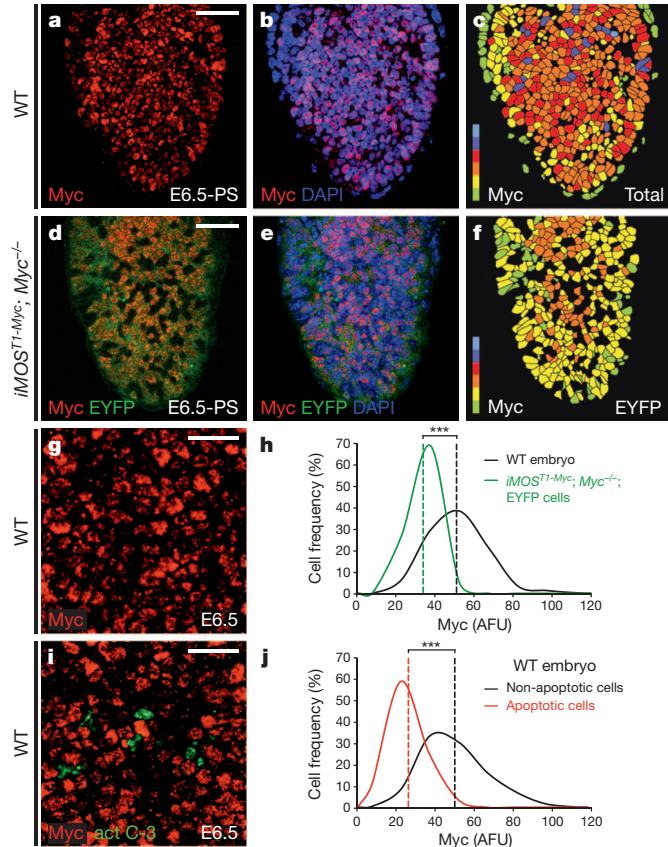
**Figure 3 | Myc-induced cell competition is triggered by short-range interactions.** **a–c**, Confocal sections showing TUNEL staining and EYFP in ES cell colonies. Scale bars, 50  $\mu$ m. **d**, TUNEL-staining percentage in wild-type (EYFP-negative) cells ( $n = 1,331, 773, 643, 858$  total cells from 5 different cultures). **e**, Confocal three-dimensional reconstruction of a representative E6.5 *iMOS<sup>T1-Myc</sup>* epiblast, showing EYFP, active caspase-9 and active Bax. Scale bar, 50  $\mu$ m. **f**, Percentages of apoptotic wild-type cells in **e** ( $n = 2,112$  total cells). Graphs show means and 95% confidence interval; \*\**P* < 0.01; \*\*\**P* < 0.001 by binomial test.

Information and Supplementary Fig. 19). We next measured Myc levels in non-apoptotic cells and in cells in the first phases of apoptosis (cells with active caspase-3 staining but still-intact nuclei) (Fig. 4i). Myc levels in non-apoptotic cells were on average >2 times higher than those in early apoptotic cells (Fig. 4j). This result is not due to Myc degradation during apoptosis (Supplementary Information and Supplementary Fig. 20), and thus suggests that intrinsically low levels of Myc protein correlate with natural apoptosis in the epiblast. Nonetheless, the detection of some apoptotic cells in the EYFP cell population of the *iMOS<sup>T1-Myc</sup>*; *Myc*<sup>−/−</sup> embryos (Supplementary Fig. 20) indicates that not all epiblast cell death correlates with heterogeneous Myc levels.

Endogenous Myc levels were also variable in wild-type ES cells (Fig. 5a, b), and pairs of engulfing–engulfed cells were abundantly detected in wild-type ES cell cultures (Supplementary Fig. 21). Analysis of TUNEL-negative engulfing–engulfed cell pairs in wild-type ES cell cultures revealed that Myc levels in engulfing cells were double those in their engulfed partners (Fig. 5c–e), again indicating a strong correlation between Myc levels and natural cell death.

Given that anabolic capacity is a major determinant of cell competition ability, we determined the relationship between endogenous Myc levels and anabolic status by measuring the protein synthesis rate in ES cell cultures *in situ* (Fig. 5f–h). Protein synthesis rate correlated positively with the natural variations in Myc levels (Fig. 5i). Furthermore, protein synthesis rate was enhanced by the extra Myc copies in *iMOS<sup>T1-Myc</sup>* ES cells (Fig. 5j), indicating that Myc is a ‘driver’ and not a ‘reader’ of cell anabolism. Scoring of protein synthesis rate in engulfing–engulfed pairs of cells showed higher rates in engulfing cells (Supplementary Fig. 22).

Our findings strongly suggest that endogenous cell competition eliminates cells with low relative Myc levels in wild-type epiblasts and in ES cell cultures. At least part of the natural epiblast cell death would thus be a consequence of endogenous cell competition. Supporting this view, wild-type embryos express the same apoptosis markers detected in *iMOS<sup>T1-Myc</sup>* mosaic embryos and also show phagocytosis between epiblast cells (Supplementary Fig. 21). We therefore used the *iMOS<sup>T2-p35</sup>* mosaics to study the consequences of inhibiting natural cell death in the mouse epiblast. TUNEL staining in the p35-expressing ECFP population was lower than in the wild-type EYFP population (Fig. 6a, b, e).



This reduction led to an enrichment in ECFP cell proportion at E9.5 (Fig. 6c, d, f), indicating that naturally dying cells in the epiblast can be rescued and contribute to the developing embryo. Moreover, *iMOS<sup>T2-p35</sup>* mosaics reared to adulthood showed no obvious phenotypic alteration ( $n > 40$ ). Thus, consistent with the idea of cell competition as a driver of epiblast apoptosis, naturally dying epiblast cells are viable and can be rescued to form part of the organism. Interestingly, whereas low Myc levels again correlated with apoptosis in the EYFP cell population of *iMOS<sup>T2-p35</sup>* mosaics, within the p35-expressing cell population Myc levels did not differ between the apoptotic and non-apoptotic cells (Fig. 6g). This result again shows that not all epiblast cell death results from Myc level heterogeneity, and that, in this setting, p35 can prevent the competition-driven death of viable cells but cannot rescue other types of epiblast cell death, presumably affecting non-viable cells.

Our findings predict that endogenous cell competition should select for cells with higher Myc levels and thus, that inhibition of cell competition should prevent this selection. Confirming this, mean Myc levels in the apoptosis-rescued p35-expressing ECFP population of *iMOS<sup>T2-p35</sup>* mosaics were 10% lower at E5.75 and 24% lower at E6.75 than in the wild-type EYFP population (Fig. 6h–l). Thus, prevention of natural epiblast cell death results in the progressive accumulation of cells with lower relative Myc content, which would have been eliminated in a

wild-type context. Conversely, when *iMOS<sup>T1-Myc</sup>* mosaics are induced on a *Myc<sup>+/−</sup>* background, Myc levels in the outcompeted cell population are significantly higher than those observed in *Myc<sup>+/−</sup>* embryos without induced cell competition, as predicted by the enhanced elimination of Myc-low cells in the mosaic embryos (Fig. 6m). These results show that endogenous cell competition selects for cells with higher Myc levels in the epiblast.

## Discussion

Our results show that cell competition is promoted by an imbalance in Myc dose between neighbouring cells in the mouse epiblast and ES cells. Crucially, it is not the absolute levels of Myc but rather the

relative levels among neighbouring cells that determine cell viability, and thus the natural cell competition detected in the mouse epiblast leads to the elimination of cells with lower Myc expression. These findings uncover a new mechanism for refining the epiblast cell population. We propose a model in which epiblast cells are subject to comparison with their neighbours, resulting in the elimination of cells with lower anabolic capacity, even though in the absence of more competitive cells they would contribute to the new organism (Supplementary Fig. 1). Such a mechanism, by ensuring that the most capable of the available precursor cells are selected to generate the new organism, would be especially relevant to long-lived organisms, in which somatic tissues need to maintain functionality for long

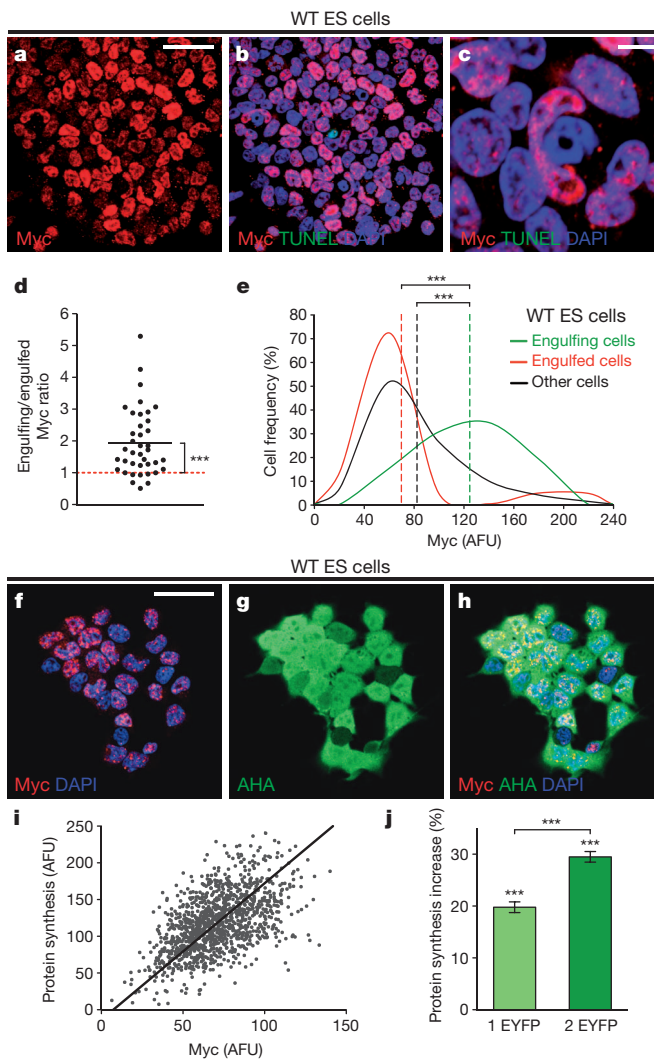


**Figure 5 | Cell death in ES cells correlates with low Myc levels and anabolic activity.** **a, b**, Confocal sections of uninduced (WT) *iMOS<sup>T1-Myc</sup>/iMOS<sup>T1-Myc</sup>* ES cells, showing endogenous Myc expression and TUNEL staining. Scale bar, 50 µm. **c**, Detail of cell engulfment. Scale bar, 10 µm. **d, e**, Myc level paired ratios (**d**) and global distributions (**e**) in engulfing and engulfed TUNEL-negative wild-type ES cells ( $n = 39$  pairs) and cells not involved in phagocytosis ('other';  $n = 1,193$  cells) in a representative culture. **f–h**, Confocal sections of wild-type ES cells showing Myc expression and protein synthesis labelling with L-azidohomoalanine (AHA). Scale bar, 50 µm. **i**, Correlation between endogenous Myc and protein synthesis in wild-type ES cells ( $n = 1,208$  cells) in a representative culture. **j**, Increase in protein synthesis in induced *iMOS<sup>T1-Myc</sup>/iMOS<sup>T1-Myc</sup>* mosaic ES cells expressing extra Myc copies (EYFP) ( $n = 568$  (left) and 589 (right) cells from a representative culture). Graph shows means and 95% confidence intervals. Horizontal bars in **d** indicate mean ratios. Dashed lines in **e** indicate mean value. \*\*\* $P < 0.001$  by one sample *t*-test  $P$  value (**d**), Gaussian linear model (**e**) and linear model (**j**).

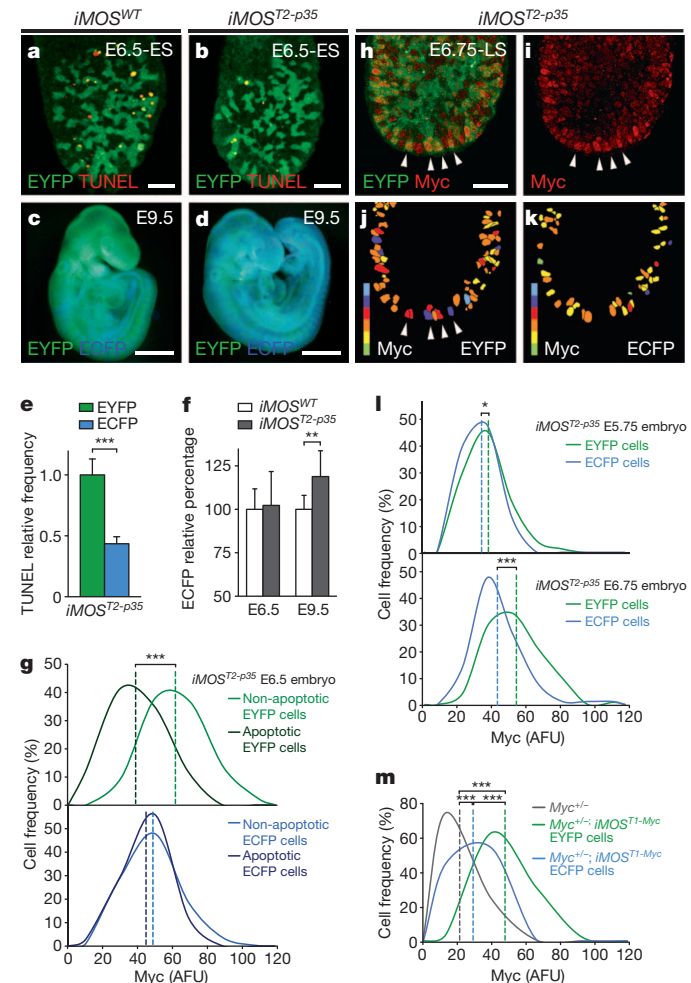


**Figure 6 | Endogenous cell competition in the mouse epiblast selects cells with higher relative Myc levels.** **a, b**, Confocal sections of TUNEL-stained E6.5 mosaics. Scale bars, 50 µm. ES, early streak. **c, d**, Overlay views of EYFP and ECFP in whole-mount E9.5 mosaics. Scale bars, 1 mm. **e, f**, Relative TUNEL-staining frequencies ( $n = 9$  embryos, 10,116 cells) (**e**) and relative ECFP cell percentage in confocal sections (**f**) ( $n = 8, 10, 7, 8$  (from left to right) embryos). Graphs show means  $\pm$  s.d. **g**, Distribution of Myc levels in cell populations of E6.5 mosaics ( $n = 3$  embryos, 2,112 cells). **h–k**, Confocal section showing EYFP and Myc (**h**, **i**) and corresponding colour coding of Myc levels in the EYFP (**j**) and ECFP (**k**) cells; arrowheads mark high Myc EYFP cells. LS, late streak. Scale bar, 50 µm. **l**, Distribution of Myc levels in representative mosaics at E6.75 ( $n = 3$  embryos, 485 cells) and E6.75 ( $n = 3$  embryos, 514 cells). **m**, Distribution of Myc levels in the indicated E6.5 embryo genotypes and cell populations ( $n = 494$  (grey), 354 (green) and 170 (blue) cells from representative embryos). Embryos in **e**, **f**, **g** and **l** were collected from various similar litters and represent biological replicates. \* $P < 0.05$ ; \*\* $P < 0.01$ ; \*\*\* $P < 0.001$  by one-sample *t*-test (**e** and **f**), mixed linear model (**g** and **l**) and generalized gamma lineal model (**m**).

periods. Under this interpretation, cell competition in the epiblast, which contains the precursors for the whole organism, would have the most far-reaching impact. These ideas are consistent with the finding that only epiblast cells have a high incidence of cell death, whereas extraembryonic tissues, which are short-lived, do not.

The description of endogenous cell competition in mammals opens the door to investigation of the role of this pathway in human diseases and processes in which tissue homeostasis is central, such as tumour formation, degenerative diseases and tissue regeneration. Our findings indicate that cell competition is a general feature of metazoans, thus suggesting that it represents a fundamental property of cell interaction within tissues.

## METHODS SUMMARY

DNA constructs, mouse strains, ES cell derivation and assays, three-dimensional embryo reconstruction, quantification of Myc protein and protein synthesis, and statistical analysis are detailed in the Methods. Confocal microscopy, flow cytometry, measurement of embryo total DNA content, immunofluorescence, TUNEL assay, BrdU labelling and *in situ* hybridization were conducted by standard procedures described in the Methods.

**Full Methods** and any associated references are available in the online version of the paper.

Received 5 July 2011; accepted 20 June 2013.

Published online 10 July 2013.

1. Jacobson, M. D., Weil, M. & Raff, M. C. Programmed cell death in animal development. *Cell* **88**, 347–354 (1997).
2. Vousden, K. H. & Lane, D. P. p53 in health and disease. *Nature Rev. Mol. Cell Biol.* **8**, 275–283 (2007).
3. Morata, G. & Ripoll, P. Minutes: mutants of *Drosophila* autonomously affecting cell division rate. *Dev. Biol.* **42**, 211–221 (1975).
4. de la Cova, C., Abril, M., Bellota, P., Gallant, P. & Johnston, L. A. *Drosophila* myc regulates organ size by inducing cell competition. *Cell* **117**, 107–116 (2004).
5. Moreno, E. & Basler, K. dMyc transforms cells into super-competitors. *Cell* **117**, 117–129 (2004).
6. Simpson, P. Analysis of the compartments of the wing of *Drosophila melanogaster* mosaic for a temperature-sensitive mutation that reduces mitotic rate. *Dev. Biol.* **54**, 100–115 (1976).
7. Simpson, P. Parameters of cell competition in the compartments of the wing disc of *Drosophila*. *Dev. Biol.* **69**, 182–193 (1979).
8. Simpson, P. & Morata, G. Differential mitotic rates and patterns of growth in compartments in the *Drosophila* wing. *Dev. Biol.* **85**, 299–308 (1981).
9. Martin, F. A., Herrera, S. C. & Morata, G. Cell competition, growth and size control in the *Drosophila* wing imaginal disc. *Development* **136**, 3747–3756 (2009).

10. Moreno, E., Basler, K. & Morata, G. Cells compete for decapentaplegic survival factor to prevent apoptosis in *Drosophila* wing development. *Nature* **416**, 755–759 (2002).
11. Díaz, B. & Moreno, E. The competitive nature of cells. *Exp. Cell Res.* **306**, 317–322 (2005).
12. Johnston, L. A. Competitive interactions between cells: death, growth, and geography. *Science* **324**, 1679–1682 (2009).
13. Oertel, M., Menthe, A., Dabeva, M. D. & Shafritz, D. A. Cell competition leads to a high level of normal liver reconstitution by transplanted fetal liver stem/progenitor cells. *Gastroenterology* **130**, 507–520 (2006).
14. Bondar, T. & Medzhitov, R. p53-mediated hematopoietic stem and progenitor cell competition. *Cell Stem Cell* **6**, 309–322 (2010).
15. Marusyk, A., Porter, C. C., Zaberezhnyy, V. & DeGregori, J. Irradiation selects for p53-deficient hematopoietic progenitors. *PLoS Biol.* **8**, e1000324 (2010).
16. Tamori, Y. et al. Involvement of Lgl and Mahjong/VprBP in cell competition. *PLoS Biol.* **8**, e1000422 (2010).
17. Hayashi, S., Lewis, P., Pevny, L. & McMahon, A. P. Efficient gene modulation in mouse epiblast using a Sox2Cre transgenic mouse strain. *Mech. Dev.* **119** (Suppl 1), S97–S101 (2002).
18. Heyer, B. S., MacAuley, A., Behrendtsen, O. & Werb, Z. Hypersensitivity to DNA damage leads to increased apoptosis during early mouse development. *Genes Dev.* **14**, 2072–2084 (2000).
19. Poelmann, R. E. Differential mitosis and degeneration patterns in relation to the alterations in the shape of the embryonic ectoderm of early post-implantation mouse embryos. *J. Embryol. Exp. Morphol.* **55**, 33–51 (1980).
20. Luscher, B. & Eisenman, R. N. Proteins encoded by the c-myc oncogene: analysis of c-myc protein degradation. *Princess Takamatsu Symp.* **17**, 291–301 (1986).

**Supplementary Information** is available in the online version of the paper.

**Acknowledgements** We thank S. Srinivas for pBigT and pROSA26PA vectors; I. Moreno de Alborán for *Myc*<sup>flox/flox</sup> mice; C. G. Arques for suggestions and patience; M. Manzanares for comments on the manuscript; L. M. Criado and S. Ortega for mouse generation; T. Córdoba, V. García, E. Escudero and S. Vela for mouse work; J. L. Ligos, M. Vítón and R. Nieto for help with flow cytometry; E. Arza and A. M. Santos for help with microscopy and three-dimensional reconstruction; F. Sánchez-Cabo and P. López-Romero for statistics; and S. Bartlett for text editing. The CNIC is supported by the Ministerio de Economía y Competitividad (MINECO) and the Pro-CNIC Foundation. This work was supported by a MINECO/ISCIII TerCel grant (RD06/0010/0008) and the Human Frontiers Science Program (RGP0008/2004). C.C. is supported by grants from the Madrid Regional Government (S-SAL-0190-2006 and P2010/BMD-2315).

**Author Contributions** C.C. designed the iMOS system, assembled the DNA constructs and performed the experiments and image acquisition; G.G. electroporated ES cells and screened them; G.G., C.C. and M.T. derived iMOS ES cells; R.S. genotyped the mice and embryos and performed histological processing; C.C. and M.T. designed the experiments, quantified and analysed the data and wrote the paper.

**Author Information** Reprints and permissions information is available at [www.nature.com/reprints](http://www.nature.com/reprints). The authors declare no competing financial interests. Readers are welcome to comment on the online version of the paper. Correspondence and requests for materials should be addressed to M.T. (mtorres@cnic.es).

## METHODS

**DNA constructs.** iMOS DNA constructs were assembled by standard cloning methods, starting from pBigT vector<sup>21</sup>. *loxP* sites were transformed into *lox2272* sites<sup>22</sup> using the QuickChange site-directed mutagenesis kit (Stratagene). *lox5171* sites<sup>22</sup> were inserted as annealed oligonucleotides. *IRES-EYFP* and *IRES-ECFP* were excised from pEYFP-N1 and pECFP-N1 vectors (Clontech), and were respectively inserted into the T1 and T2 units of iMOS constructs (Supplementary Fig. 2a). A triple SV40 polyadenylation sequence (tPA) was excised from pBigT and inserted 3' of *EYFP* (Supplementary Fig. 2a).

To ensure that T1 and T2 recombination frequencies were the same in all the iMOS mouse lines, a constant distance was maintained between *lox* site pairs in all constructs. In the *iMOS<sup>WT</sup>* construct (Supplementary Fig. 2a), the buffer sequences corresponded to non-translatable mutants of the ORFs for mouse *Myc* (T1) and baculovirus *p35* (T2). The mutated *Myc* ORF (*Myc<sup>stop</sup>*) was generated by PCR-mediated insertion of a T at the beginning of the fourth codon (<sub>10</sub>AAC<sub>12</sub>><sub>10</sub>TAA<sub>12</sub>). The mutated *p35* ORF (*p35<sup>stop</sup>*) was obtained by PCR-mediated T>A substitution of nucleotide six (<sub>4</sub>TGT<sub>6</sub>><sub>4</sub>TGA<sub>6</sub>). In the *iMOS<sup>T1-Myc</sup>* construct, the wild-type *Myc* ORF was inserted 5' to *IRES-EYFP*, in place of the T1 buffer sequence, and the *p35<sup>stop</sup>* ORF was used as the T2 buffer sequence (Supplementary Fig. 4a). In the *iMOS<sup>T2-p35</sup>* construct, the wild-type *p35* ORF was inserted 5' to *IRES-ECFP*, in place of the T2 buffer sequence, and the *Myc<sup>stop</sup>* ORF was used as the T1 buffer sequence (Supplementary Fig. 8a). In the *iMOS<sup>T1-Myc/T2-p35</sup>* construct, the wild-type *Myc* ORF was inserted 5' to *IRES-EYFP* and the wild-type *p35* ORF was inserted 5' to *IRES-ECFP*, replacing the T1 and T2 buffer sequences (Fig. 2a). The KpnI site in the pROSA26PA vector<sup>21</sup> was substituted by a SwaI site. pBigT-inserted iMOS constructs were cloned into PacI/Ascl sites of this modified pROSA26PA vector for gene targeting in ES cells. **Mouse strains.** To generate iMOS mice, the iMOS targeting vectors were linearized at the SwaI site and electroporated into ES cells<sup>23</sup>. ES cell clones were screened by Southern blot<sup>24</sup>. Chimaeric mice were generated by ES cell aggregation. Mice were genotyped by PCR<sup>24</sup>.

For mosaic induction, homozygous *iMOS* females (mixed C57BL/6 and R1 ESC background) were crossed with heterozygous *Sox2-cre* males (stock 004783, Jackson Laboratory)<sup>17</sup>. The stability of the iMOS system was tested by crossing homozygous *iMOS<sup>WT</sup>* males with *Sox2-cre* females (Supplementary Fig. 3a). Males derived from these crosses were used to establish a germ-line-recombined T1-expressing mouse line (*iMOS<sup>GLR-T1</sup>*) (Supplementary Fig. 3a). Females from this line were crossed with *Sox2-cre* males (Supplementary Fig. 3a).

To characterize the functionality of *Myc* expressed from the *iMOS<sup>T1-Myc</sup>* allele, *Sox2-cre* males were crossed with *Myc<sup>fl/fl</sup>* females<sup>25</sup> to obtain *Sox2-cre* mice with one *Myc* allele deleted (*Sox2-cre; Myc<sup>+/-</sup>*) (Supplementary Fig. 4b). Mouse lines homozygous for *Myc<sup>fl/fl</sup>* and *iMOS<sup>WT</sup>* or *iMOS<sup>T1-Myc</sup>* were generated, and females from these lines were crossed with *Sox2-cre; Myc<sup>+/-</sup>* males (Supplementary Fig. 4b). Once they are Cre-deleted, the *Myc<sup>fl/fl</sup>* alleles are represented as *Myc<sup>-/-</sup>*.

To test the effect of *Myc* expression from the *iMOS<sup>T1-Myc</sup>* allele under different *Myc* genetic backgrounds, we crossed homozygous *iMOS<sup>WT</sup>* and *iMOS<sup>T1-Myc</sup>* females with *Sox2-cre* males to obtain *iMOS<sup>WT</sup>; Sox2-cre* and *iMOS<sup>T1-Myc</sup>; Sox2-cre* mosaic embryos in a wild-type *Myc* background. In parallel, homozygous *iMOS<sup>T1-Myc</sup>; Myc<sup>fl/fl</sup>* females were crossed with *Sox2-cre; Myc<sup>+/-</sup>* males to obtain *iMOS<sup>T1-Myc</sup>; Sox2-cre* mosaic embryos in the *Myc<sup>+/-</sup>* and *Myc<sup>-/-</sup>* backgrounds. Embryos homogeneously overexpressing *Myc* (*iMOS<sup>GLR-T1-Myc</sup>*) were generated by crossing *iMOS<sup>T1-Myc</sup>; Sox2-cre* females with CD1 males. To generate *Myc<sup>+/-</sup>* and *Myc<sup>-/-</sup>* embryos, *Sox2-cre; Myc<sup>+/-</sup>* mice were crossed.

*iMOS<sup>T1-Myc</sup>/iMOS<sup>T1-Myc</sup>; Myc<sup>+/-fl/fl</sup>* crosses with *Sox2-cre; Myc<sup>+/-</sup>* males were used for the validation of *Myc* quantification (Supplementary Fig. 18) and for experiments in Fig. 6m.

Tamoxifen-inducible mosaics were generated by crossing homozygous iMOS mice with homozygous *RERT* mice, which express the inducible Cre-ERT<sup>2</sup> recombinase under the control of the large subunit of RNA polymerase II locus<sup>26</sup>.

Early embryos were staged as PS (pre-streak), ES (early streak), MS (mid-streak) and LS (late streak), according to ref. 27.

No randomization was used in any experiment and experiments were not blinded. No experiments were performed in adult animals.

All animal procedures have been reviewed and approved by the CNIC Animal Experimentation Ethics Committee, according to the National and European regulations.

**Confocal microscopy.** Whole embryos or histological sections and ES cell cultures were imaged with a Leica TCS SP5 confocal microscope at 405, 458, 488, 568 or 633 nm, with  $\times 20/0.7$  multi-immersion,  $\times 40/1.25$  oil,  $\times 63/1.4$  oil and  $\times 63/1.2$  water objectives. Areas occupied by EYFP and ECFP cells were quantified using the threshold detection and particle analysis tools in ImageJ (NIH, <http://rsb.info.nih.gov/ij>). To calculate the relative frequency of ECFP cells, the percentage of

ECFP cells in each embryo was divided by the average percentage in *iMOS<sup>WT</sup>; Sox2-cre* embryos.

**Flow cytometry.** To quantify EYFP- and ECFP-expressing cell populations, cells from E9.5 *Sox2-cre*-recombined *iMOS<sup>WT</sup>*, *iMOS<sup>T1-Myc</sup>* and *iMOS<sup>T1-Myc/T2-p35</sup>* embryos were suspended in PBS containing 1% fetal calf serum (FCS), 25 mM glucose and 25 mM HEPES by passing through 100  $\mu$ m cell strainers (BD Biosciences). Cells were stained with Hoechst 33258 (Sigma-Aldrich) to exclude dead cells. Because erythroid cells lose iMOS transgene expression as they differentiate (data not shown), they were excluded from the quantification by incubating cell suspensions with APC rat anti-mouse TER-119 antibody (BD Biosciences), which specifically reacts with cells of the erythroid lineage. Cell suspensions were analysed by flow cytometry in a BD FACSAria II SORP at 449, 488 and 633 nm. EYFP- and ECFP-expressing cells were quantified in the live, TER-119-negative population. Embryos were analysed separately.

To quantify cell size, cells from E9.5 *iMOS<sup>WT</sup>; Sox2-cre* embryos and *iMOS<sup>T1-Myc</sup>; Sox2-cre* embryos in wild-type, *Myc<sup>+/-</sup>* and *Myc<sup>-/-</sup>* backgrounds were suspended, stained and analysed as described. Forward scatter pulse area (FSC-A) of EYFP and wild-type cells was calculated for each mosaic and for wild-type littermates, and the mean ratio was calculated.

**Embryo total DNA content.** E9.5 *Sox2-cre*-recombined *iMOS<sup>T1-Myc</sup>* embryos and wild-type littermates were collected and individually stored at  $-80^{\circ}\text{C}$ . Total DNA was isolated and purified following standard protocols and measured in Nanodrop for each embryo.

**Immunofluorescence and TUNEL assay.** Embryos were obtained at different gestational stages, fixed overnight at  $4^{\circ}\text{C}$  in 2% paraformaldehyde (PFA) in PBS, and whole-mount stained or, when  $E \geq 10.5$ , gelatin-embedded and cryosectioned. Immunofluorescence was performed following standard protocols. Primary antibodies used were anti-phospho-histone H3 (Ser 10) 'mitosis marker' and biotin-conjugated anti-phospho-histone H3 (Ser 10) (both from Millipore); anti-BrdU antibody (Becton Dickinson); anti-Myc polyclonal antibody (Millipore); anti-p35 rabbit polyclonal antibody (Orbigen); anti-E-cadherin antibody (DECMA-1) (Abcam); anti-cleaved caspase-3 (Asp 175) (5A1E) rabbit antibody and Alexa Fluor 488-conjugated anti-cleaved caspase-3 (Asp 175) antibody (both from Cell Signaling); anti-Bax (ab10813) and anti-Bax (6A7) (ab5714) antibodies (both from Abcam); anti-cleaved caspase-9 (Asp 353) antibody (Cell Signaling); anti-Bcl-xL (54H6) rabbit antibody (Cell Signaling); and anti-cleaved caspase-8 (Asp387) (D5B2) rabbit antibody (Cell Signaling). Mitotic cells and cells in the G2/M transition were detected by pH3 staining. pH3-positive nuclei exhibiting a discrete punctate pattern and showing an interphase morphology were scored as G2/M cells.

TUNEL staining was performed on whole-mount embryos or sections using terminal deoxynucleotidyl transferase (TdT) and biotin-16-2'-deoxy-uridine-5'-triphosphate (biotin-16-dUTP) (both from Roche), and developed with several streptavidin fluorescent conjugates (Jackson ImmunoResearch).

**BrdU labelling.** To quantify cell proliferation of EYFP *Myc*-overexpressing and ECFP wild-type cells in *iMOS<sup>T1-Myc</sup>; Sox2-cre* mosaic embryos, pregnant females were intraperitoneally injected with 75 mg kg<sup>-1</sup> of BrdU (Sigma-Aldrich) at E6.5, E7.5 or E9.5, and embryos were extracted 1, 1 h 30 min or 3 h later, respectively. Embryos were fixed, treated with DNase I to cleave DNA and allow the binding of anti-BrdU antibody to BrdU, and immunostained as described above.

**ES cell derivation and assays.** ES cells were derived from E3.5 blastocysts homozygous for *iMOS<sup>T1-Myc</sup>* or *iMOS<sup>T1-Myc/T2-p35</sup>* and *RERT* and cultured on mitomycin-C-inactivated mouse embryonic fibroblast (MEF) feeder layers in serum replacement (SR)-ES medium<sup>28</sup>. Cell lines were checked negative for mycoplasma and for normal karyotype at their establishment. For *in vitro* assays, MEF-depleted ES cells were seeded on fibronectin-coated 3.5-mm glass bottom dishes (MatTek) and cultured in 2  $\times$  LIF SR-ES medium. Cells were treated with 20  $\mu$ M 4-hydroxytamoxifen (4-OHTAM) (Sigma-Aldrich) for 24 h to induce a high recombination rate, or 5  $\mu$ M 4-OHTAM for 4 h for a low recombination rate. Cells were fixed overnight at  $4^{\circ}\text{C}$  in 2% PFA in PBS at the time points detailed in each experiment. Immunofluorescence and TUNEL staining were performed as described.

For conditioned medium experiments, homozygous *iMOS<sup>T1-Myc</sup>; RERT* ES cells were induced as described in Supplementary Fig. 11b. Conditioned medium from these cultures was collected at  $t_1$ . For protein synthesis assays, we used the Click-iT detection of protein synthesis assay kit (Life Technologies). Metabolic labelling and detection was performed according to the manufacturer on untreated and 4-OHTAM-treated (10  $\mu$ M for 24 h at  $t_1$ ; Supplementary Fig. 11b) homozygous *iMOS<sup>T1-Myc</sup>; RERT* ES cells using Click-iT AHA (L-Azidohomoalanine), Click-iT cell reaction buffer kit and Alexa Fluor 647 alkyne triethylammonium salt. Myc immunofluorescence was performed after the Click-iT detection reaction. Myc protein and metabolic labelling were quantified on confocal sections using the Metamorph platform as described below.

**Three-dimensional embryo reconstruction.** Three-dimensional embryo reconstruction and analysis of apoptosis frequency were performed in *iMOS<sup>TI-Myc</sup>; Sox2-cre* E6.5 embryos using Imaris  $\times$ 64 software. Visceral endoderm was digitally removed to allow better visualization of the epiblast.

**In situ hybridization.** Whole-mount *in situ* hybridization was performed following standard protocols. The *Myc* probe was provided by T. Rodriguez and the *Oct4* probe by M. Manzanares.

**Quantification of Myc protein and protein synthesis.** Quantitative image analysis of confocal sections was performed with the Metamorph platform (Molecular Devices). To standardize quantification, we used medial confocal sections of E6.5 embryos, in which epiblast cells are mostly sectioned longitudinally and located in the embryo periphery. Several sections were quantified for each embryo. The nuclear area was defined from the DAPI image and Myc protein levels from the Cy3-developed Myc immunofluorescence image. Only nuclei showing an interphase morphology were scored, as Myc is delocalized during mitosis. Early apoptotic cells were defined by their cleaved caspase-3 or incipient TUNEL staining and the retention of normal cell and nucleus size. The DAPI images were signal-intensity thresholded, segmented and converted to 1-bit binary images using ImageJ. The DAPI mask was applied to the matching Myc image to obtain a combined image containing Myc fluorescence information for each nucleus. Myc fluorescence was measured as the 'average grey value' (the total grey value per nucleus) and expressed in arbitrary fluorescence units (AFU). Values were classified in regular linear intervals represented by a colour code. Myc fluorescence values were exported to Excel and frequency histograms, as well as curve interpolations, were generated.

To validate this quantification system, E6.5 embryos containing different *Myc* doses were analysed under the same confocal acquisition settings, and raw intensity data were quantified without post-processing (Supplementary Fig. 18). A similar procedure was used in all Myc quantifications in embryos and Myc and protein synthesis quantifications in ES cells.

**Statistical analysis.** The use of genetic mosaics, which allowed the comparison of randomly distributed cell populations within each embryo or ES cell colony, minimized usual sources of experimental variability between biological replicates. In experiments involving embryos we used a minimum of 4 embryos and scored a minimum of 1,000 cells per embryo, which allowed a minimum of 4 individual embryos for detection of at least 40% differences between population means at a power of 80% and a 0.05 alpha-level.

To compare average percentages of ECFP cells between more than two groups, we used the ANOVA test for normal distributions or the Kruskal–Wallis test for non-normal distributions. If there was a significant difference between the group means, the Tukey HSD test was used to test differences among each pair of means. For comparisons of only two groups we used a *t*-test for normal distributions or a Mann–Whitney *U*-test for non-normal distributions. Population mean differences from unity were tested with a one-sample *t*-test (normal distribution) or a Wilcoxon test (non-normal). All comparisons were made with Prism statistical software.

The significance of population changes in ES cell cultures over time and increases in Myc protein and total protein synthesis were compared by proportion

test. We also used these tests to determine percentages of apoptotic and proliferating cells in different ES cell populations. 95% confidence intervals from a binomial distribution are shown in all figures.

To compare the distribution of Myc and protein synthesis levels across different genotypes or cell populations, we used generalized mixed linear models. In Fig. 4 we used a mixed linear model in which we considered the condition (WT/ *iMOS<sup>TI-Myc</sup>*; *Myc*<sup>−/−</sup>, Fig. 4h; apoptotic/non-apoptotic, Fig. 4j) as fixed and the embryo as random factor. We used the same model to test Myc level differences between pH3-positive and -negative cells (Supplementary Fig. 19) and between apoptotic and non-apoptotic cells detected by TUNEL staining (Supplementary Fig. 20). In all cases, a variance function was used to model the variance structure of the errors within the experimental groups<sup>29</sup>. To compare Myc and protein synthesis levels in the cell populations shown in Fig. 5e and Supplementary Fig. 22e, we used a linear model with this characteristic as a factor. Additionally, in Fig. 5i we used Deming regression<sup>30</sup> to describe the correlation between Myc and protein synthesis. In Fig. 6l we analysed whether there was an interaction between differences in Myc levels in EYFP and ECFP populations and developmental stage. The fixed part of the model comprises the population effect, the developmental stage and the developmental stage interaction; the random part of the model is the embryo effect. A mixed model was also used to test differences between the distribution of Myc levels in apoptotic and non-apoptotic cells in ECFP and EYFP populations (Fig. 6g). In Fig. 6m and Supplementary Fig. 18, we tested the distribution of Myc levels between different genotypes using a general linear model of the gamma family. Standard diagnostics checks on the residuals from the fitted models were used to test assumptions of normality and heterogeneity of variance. All statistical analyses were performed using the open-source statistical scripting language R version 2.11.0 (R Development Core Team, 2006). Mixed linear model equations were fitted using the nlme R library<sup>31</sup>. The total number of embryos and/or cells scored in each analysis is provided in the figure legends.

21. Srinivas, S. *et al.* Cre reporter strains produced by targeted insertion of EYFP and ECFP into the ROSA26 locus. *BMC Dev. Biol.* **1**, 4 (2001).
22. Lee, G. & Saito, I. Role of nucleotide sequences of *loxP* spacer region in Cre-mediated recombination. *Gene* **216**, 55–65 (1998).
23. Torres, M. The use of embryonic stem cells for the genetic manipulation of the mouse. *Curr. Top. Dev. Biol.* **36**, 99–114 (1998).
24. Soriano, P. Generalized *lacZ* expression with the ROSA26 Cre reporter strain. *Nature Genet.* **21**, 70–71 (1999).
25. de Alboran, I. M. *et al.* Analysis of C-MYC function in normal cells via conditional gene-targeted mutation. *Immunity* **14**, 45–55 (2001).
26. Guerra, C. *et al.* Tumor induction by an endogenous K-ras oncogene is highly dependent on cellular context. *Cancer Cell* **4**, 111–120 (2003).
27. Downs, K. M. & Davies, T. Staging of gastrulating mouse embryos by morphological landmarks in the dissecting microscope. *Development* **118**, 1255–1266 (1993).
28. Bryja, V., Bonilla, S. & Arenas, E. Derivation of mouse embryonic stem cells. *Nature Protocols* **1**, 2082–2087 (2006).
29. Pinheiro, J. C. & Bates, D. M. *Mixed-Effects Models in S and S-PLUS* (Springer, 2000).
30. Deming, W. E. *Statistical Adjustment of Data* (Dover Publications edition, 1943).
31. Pinheiro, J. *et al.* nlme: Linear and nonlinear mixed effects models (2009).

# Integrative genomics identifies APOE $\epsilon$ 4 effectors in Alzheimer's disease

Herve Rhinn<sup>1,2\*</sup>, Ryousuke Fujita<sup>1,2\*</sup>, Liang Qiang<sup>1,2</sup>, Rong Cheng<sup>2</sup>, Joseph H. Lee<sup>2,3</sup> & Asa Abeliovich<sup>1,2</sup>

**Late-onset Alzheimer's disease (LOAD) risk is strongly influenced by genetic factors such as the presence of the apolipoprotein E  $\epsilon$ 4 allele (referred to here as *APOE4*), as well as non-genetic determinants including ageing. To pursue mechanisms by which these affect human brain physiology and modify LOAD risk, we initially analysed whole-transcriptome cerebral cortex gene expression data in unaffected *APOE4* carriers and LOAD patients. *APOE4* carrier status was associated with a consistent transcriptomic shift that broadly resembled the LOAD profile. Differential co-expression correlation network analysis of the *APOE4* and LOAD transcriptomic changes identified a set of candidate core regulatory mediators. Several of these—including *APBA2*, *FYN*, *RNF219* and *SV2A*—encode known or novel modulators of LOAD associated amyloid beta A4 precursor protein (APP) endocytosis and metabolism. Furthermore, a genetic variant within *RNF219* was found to affect amyloid deposition in human brain and LOAD age-of-onset. These data implicate an *APOE4* associated molecular pathway that promotes LOAD.**

Alzheimer's disease is the most common form of dementia worldwide, and is characterized by cognitive decline with distinctive brain pathology that includes regional neuron loss, amyloid plaques and neurofibrillary tangles<sup>1</sup>. Rare familial forms of Alzheimer's disease are early in onset and caused by mutations in specific genes<sup>2</sup>. In contrast, the aetiology of common, non-familial LOAD appears much more complex and includes many genetic and environmental factors. The major constituent of amyloid plaques is amyloid beta (A $\beta$ ), a proteolytic fragment derived from APP. The observation that familial-associated mutations typically modify A $\beta$  production has led to formulation of the so-called 'amyloid hypothesis', which posits that altered APP processing results in the generation of a toxic fragment that causes neurodegeneration.

Recent genome-wide association studies (GWAS) have implicated common variants at approximately 10 genetic loci in LOAD<sup>3–7</sup>. Individually, these variants have a modest effect on LOAD risk, with the notable exception of the *APOE*  $\epsilon$ 4 allele (*APOE4*): heterozygosity of *APOE4* is associated with a greater than threefold increase in LOAD risk, when compared to the common *APOE*  $\epsilon$ 3 allele (referred to here as *APOE3*), and *APOE4* homozygosity increases risk more than tenfold. A third and more rare allele, *APOE*  $\epsilon$ 2 (referred to here as *APOE2*), appears protective relative to *APOE3* in that carriers of this allele are at reduced risk of LOAD relative to non-carriers. The *APOE4* allele has been shown to modify the tertiary structure of *APOE* protein, but how this ultimately impacts LOAD is unclear. Various pathogenic mechanisms have been proposed for *APOE4*, including defects in the clearance and degradation of extracellular A $\beta$ , in lipid and cholesterol trafficking, in APP metabolism, in inflammation and in other aspects of neuronal function and survival<sup>8–13</sup>.

To pursue molecular pathways that underlie LOAD in an unbiased fashion, whole-transcriptome differential gene expression analyses have been used<sup>14–17</sup>. However, gene expression changes in diseased brain tissue often reflect processes that are secondary to the disease pathology, such as cell loss, rather than causative events. Network approaches, including differential co-expression analysis (DCA)<sup>18–21</sup>, have been developed to disentangle causative events from secondary changes within

transcriptome-wide gene expression data sets<sup>18,21</sup>. DCA is based on the notion that transcripts encoding causal 'nodes' or 'master regulators' of a disease process—whose activities are critically altered in a pathological state such as LOAD—can be identified by their co-expression correlation network properties, but not by simple differential gene expression analysis. We have broadened existing DCA tools to include consideration of genes other than those encoding known transcription factors<sup>21</sup>, with the rationale that DCA nodes would likely include upstream regulators of such factors. DCA ranks most highly those transcripts that are most altered in their co-expression correlation with the greatest number of differentially expressed transcripts in the context of a pathological state such as LOAD (Supplementary Fig. 1).

Here we apply DCA to uncover regulatory mechanisms that affect LOAD and LOAD risk. We first show by differential gene expression analysis that a transcriptome-wide pattern of change is associated with the presence of *APOE4* in disease-free brain tissue, and that this pattern overlaps with the transcriptomic changes that distinguish LOAD affected from unaffected brain tissue. Subsequent DCA identified candidate regulatory node genes predicted to mediate the common transcriptomic changes observed in *APOE4* carriers and LOAD patients. These genes include several known or novel modifiers of APP processing and endocytic trafficking such as *APBA2*, *ITM2B*, *FYN*, *RNF219* and *SV2A*, suggesting a shared mechanism of action. Genetic or pharmacological modulation of these candidate regulatory nodes suppressed altered APP processing in cell models, including *APOE4*-positive human induced neurons (hiNs). Furthermore, meta-analysis of LOAD genome-wide association data indicated that common genetic variants within two such candidate regulatory nodes, *FYN* and *RNF219*, are predictive of LOAD age-of-onset in an *APOE4*-dependent manner. Taken together, our findings reveal an *APOE4*-dependent molecular pathway to LOAD and LOAD risk.

## A pre-LOAD state in *APOE4* carriers

To broadly pursue a molecular correlate of the *APOE4* prodromal state in an unbiased manner, we initially re-evaluated publicly available

<sup>1</sup>Departments of Pathology, Cell Biology, and Neurology, Columbia University, 650 W. 168th Street, New York, New York 10032, USA. <sup>2</sup>Taub Institute for Alzheimer's Disease and the Aging Brain, Columbia University, 650 W. 168th Street, New York, New York 10032, USA. <sup>3</sup>Sergievsky Center and Department of Epidemiology, Columbia University, 630 W. 168th Street, New York, New York 10032, USA.

\*These authors contributed equally to this work.

transcriptome-wide gene expression data from cerebral cortex autopsy brain tissue of 185 individuals unaffected by LOAD, stratified by their *APOE* genotype (Supplementary Fig. 2, Gene expression omnibus (GEO) accession number GSE15222 (ref. 22)). Hierarchical clustering analysis revealed that the overall pattern of gene expression change associated with all *APOE* high-risk genotypes was closely related to the pattern of change associated with LOAD (relative to other neurological diseases; Fig. 1a).

We next sought to characterize in detail the specific gene expression changes affected by *APOE4* carrier status and to contrast these with changes seen in LOAD brain. To avoid potential confounding effects, LOAD associated changes in brain gene expression were quantified independently of *APOE* variability (by limiting the analysis of LOAD impact to individuals homozygous for *APOE3*); conversely, the transcriptomic effects of *APOE4* carrier status were evaluated independently of the LOAD analysis (by limiting the study to LOAD-unaffected individuals and excluding *APOE3* homozygous samples that were used in the LOAD analysis, Supplementary Fig. 3). Gene expression changes were highly correlated in the two comparisons ( $R = 0.62, P = 4 \times 10^{-16}$  by Wald statistics): out of 8,449 gene transcripts detected in all samples, 215 were found to be significantly altered in expression by either *APOE4* or LOAD status in the same direction, whereas 37 were significantly altered in opposite directions (Fig. 1b, c, Supplementary Fig. 4a and Supplementary Table 1). We note that similar analysis of the transcriptomic effect of ageing in LOAD-unaffected individuals (age  $>85$ , relative to age  $<75$ )—the major non-genetic risk factor for LOAD—revealed a high degree of overlap with LOAD-associated transcriptomic changes, but not with the changes associated with *APOE4* carrier status (Fig. 1c and Supplementary Figs 4b, c and 5). These data suggest that separate mechanisms underlie the effect of *APOE* status and ageing on LOAD risk.

Next, we hypothesized that the overlapping pattern of brain gene expression changes associated either with LOAD or with unaffected *APOE* high-risk status in brain tissue (termed the *APOE4*/LOAD

pattern; defined by a set of 215 transcripts) represented a signature of a pre-LOAD prodrome state (Fig. 1b, c and Supplementary Fig. 3b). Consistent with this, the *APOE4*/LOAD pattern was highly correlated with changes seen in transition from unaffected LOAD-free tissue to incipient-LOAD tissue in an independent data set of cortical tissue transcriptome expression profiles ( $R = 0.36, P = 9 \times 10^{-4}$  by Wald statistics; rather than the transition from incipient to moderate, or from moderate to severe disease,  $R = 0.04$  and  $0.02$ , respectively; Supplementary Fig. 4d).

### *APOE4* and LOAD differential co-expression analysis

Transcriptome-wide differential gene expression analyses, as described above for *APOE4* or LOAD, provide a broad and unbiased molecular perspective of a tissue. However, mechanistic interpretation of individual gene expression changes is challenging, as such changes may represent indirect, downstream consequences of pathology. To address this issue, we applied DCA—a tool for the identification of candidate regulatory node elements that play causal roles in the context of transcriptome-wide gene expression network changes—to the *APOE4*/LOAD pattern of change (Fig. 2a–c and Supplementary Figs 6–9). Among the 20 most highly ranked candidate node elements identified by DCA, we noted that several had previously been implicated in the processing and intracellular sorting of APP, including *APBA2* (ref. 23), *ITM2B* (ref. 24), *TMEM59L* (ref. 25) and *FYN* (ref. 26), suggesting a shared mechanism of action. Consistent with this notion, another top DCA hit, *SV2A*, encodes a well-described regulator of neuronal endocytosis. Furthermore, a selective *SV2A* inhibitor, the anti-epileptic levetiracetam<sup>27</sup>, was recently reported to suppress pathological neuronal hyperactivity in the hippocampus of individuals with mild cognitive impairment (MCI), which precedes LOAD<sup>28</sup>. The top-ranked DCA hit, *RNF219*, had not previously been linked to LOAD, but common genetic variants at the *RNF219* locus had been associated with alternations in lipid metabolism<sup>29</sup>, cognitive performance<sup>30</sup> and central nervous system ventricle volume<sup>31</sup>, akin to pathological associations ascribed to *APOE4*.

We sought to test whether DCA candidate node genes (Fig. 2b) may broadly function as regulators of APP processing in an *APOE4*-dependent manner. To functionally evaluate DCA-identified genes, we initially used a simple *in vitro* model system in which mouse neuroblastoma N2a cells that overexpress a human APP transgene (N2a-APP cells) were treated with exogenous *APOE* protein variants (100  $\mu$ g ml<sup>-1</sup> for 18 h). In this APP-N2a model system, treatment with recombinant human *APOE* ε4 variant protein (rhAPOE4), but not *APOE* ε2 or *APOE* ε3 protein (rhAPOE2 or rhAPOE3), significantly increased the levels of extracellular Aβ40 and Aβ42 (Supplementary Fig. 10a). Individual knockdown of several DCA hits by transfection of vectors encoding appropriate small hairpin RNAs (shRNAs; Supplementary Fig. 11a), including *RNF219*, *SV2A*, *HDLBP*, *ROGDI*, *CALU* and *PTK2B*, suppressed the induction of Aβ40 and Aβ42 levels in the context of rhAPOE4 treatment (Fig. 2d and Supplementary Figs 10b–d, 11b–h). With the exception of *HDLBP*, transfection of these knockdown vectors did not affect Aβ levels in the absence of rhAPOE4 (in rhAPOE2- or vehicle-only treated cultures). Thus, the DCA-identified node hits included many known or novel potential modifiers of *APOE4*-dependent Aβ accumulation.

### *RNF219* and *SV2A* modulate APP processing

We next investigated mechanisms by which DCA-identified genes may mediate the impact of *APOE4* on APP processing, and focused on the top two DCA hits: *RNF219* and *SV2A*. Cleavage of APP by the BACE1 β-secretase, a rate-limiting step in Aβ production<sup>32</sup>, generates both a soluble extracellular fragment, sAPPβ, and a transmembrane carboxy-terminal fragment (β-CTF), termed C99. rhAPOE4 treatment of N2a-APP cells increased levels of both sAPPβ in cell media and C99 fragment in cell lysates (Fig. 2e, f and Supplementary Fig. 12). Such effects were suppressed by knockdown of either *RNF219* or *SV2A*, pointing to

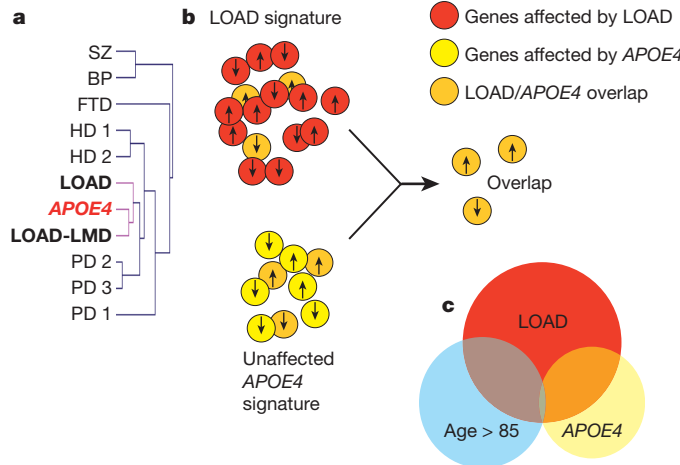


**Figure 1 | Transcriptomic evidence of a pre-LOAD state in unaffected *APOE4* brain tissue.** a, Schematic of the overlapping patterns of transcriptome-wide cerebral cortex gene expression changes associated with LOAD or with *APOE4* carrier status. b, Hierarchical clustering dendrogram demonstrates similarity between the transcriptome-wide gene expression changes associated with *APOE4* unaffected carrier status and with LOAD. Also presented are the differential expression profiles of LOAD laser-microdissected neurons (LOAD-LMD), bipolar disorder cerebral cortex (BD), schizophrenia cerebral cortex (SZ), fronto-temporal dementia cerebral cortex (FTD), Huntington's disease (in frontal cortex (HD 1) or in caudate nucleus (HD 2)) and Parkinson's disease (in substantia nigra (PD 1), in frontal cortex (PD 2), or in putamen (PD 3)). Analyses used Gene Expression Omnibus (GEO) data sets GSE15222, GSE5281, GSE12649, GSE13162, GSE3790 and GSE20295. c, Venn diagram illustrating the overlap in transcriptome-wide gene expression changes in the context of *APOE4*, advanced age ( $>85$  years old) or LOAD.

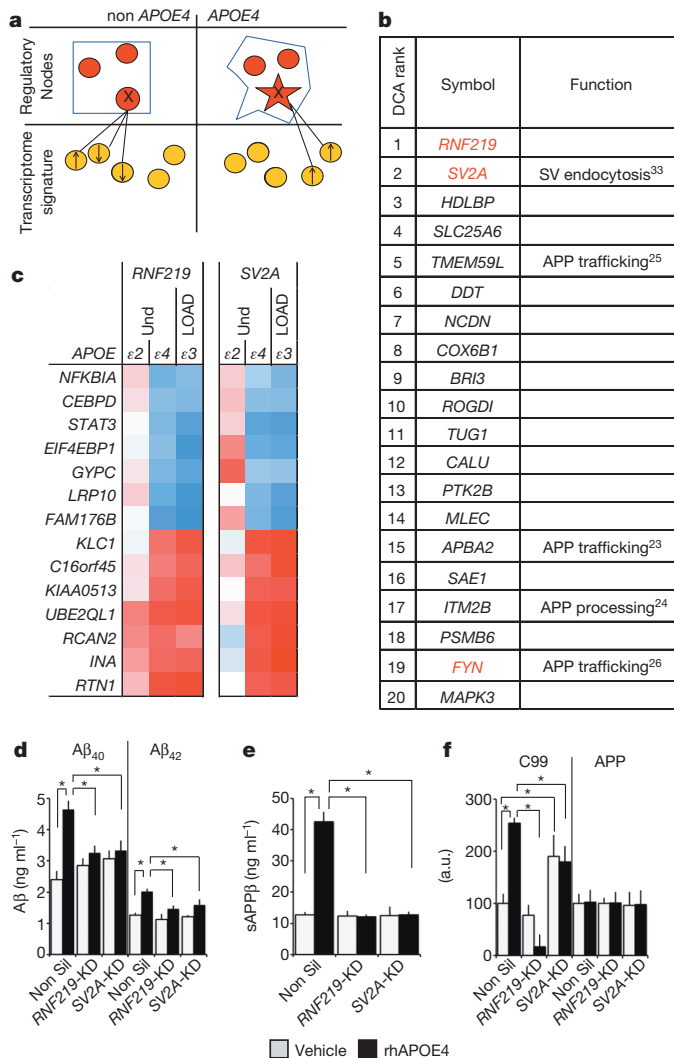


**Figure 2 | Differential co-expression correlation analysis of the APOE4 and LOAD-associated transcriptomic states.** **a**, Schematic of the DCA model. The pattern of node gene (red) co-expression with differentially expressed genes (yellow) is reconfigured in the context of APOE4 or LOAD tissue. **b**, Candidate node regulatory genes that underlie the APOE4/LOAD pattern of expression changes, rank-ordered by DCA. **c**, Heat maps representing the co-expression correlation coefficients for RNF219 or SV2A with representative genes from the APOE4/LOAD pattern set (in rows) as a function of *APOE* genotype and LOAD status (in columns; Und, LOAD-unaffected). High co-expression correlations are denoted in red, high anti-correlations in blue. **d–f**, rhAPOE4 treatment of N2a-APP cells induced the accumulation of APP metabolites including Aβ40, Aβ42 (**d**) and sAPPβ (**e**) in extracellular media, and C99 fragment (**f**) in cell lysates. Such accumulations were suppressed with transfection of shRNA vector-mediated knockdown of RNF219 or SV2A (RNF219-KD or SV2A-KD, respectively) (relative to non silencing vector control (Non Sil)). Error bars are s.e.m.;  $n = 12, 8$  and  $8$  (**d**, **e**), and  $6, 5$  and  $6$  (**f**) independent wells per group for the Non Sil, RNF219-KD and SV2A-KD groups, respectively.  $^*P < 0.05$ ; analyses by ANOVA followed by Student-Newman-Keuls (SNK) test.

increased BACE1 processing as a primary mechanism for the impact of APOE4 on Aβ accumulation, and a regulatory mediator role for SV2A and RNF219 in this context. Neither APP holoprotein nor BACE1 levels were altered in the context of rhAPOE4 treatment or knockdown of these DCA hits.

BACE1 cleavage of APP is most efficient in acidic intracellular compartments such as early and late endosomes<sup>32</sup>, and thus one potential mechanism for APOE4 action on APP processing would be through altered APP internalization<sup>11</sup>. We quantified the effect of DCA candidate node knockdown on APP and BACE1 subcellular co-localization

in the context of rhAPOE4 stimulation, using either immunocytochemistry (ICC), or by cell-surface protein analysis through selective biotinylation and fractionation. rhAPOE4 treatment of N2a-APP cells shifted both APP and BACE1 localization away from the cell surface and to a common endocytic compartment, leading to increased co-localization (Fig. 3a–d). Such rhAPOE4-induced endocytic co-localization of APP and BACE1 was suppressed by knockdown of the DCA node genes RNF219 or SV2A. Knockdown of RNF219 appeared to selectively inhibit the internalization of APP in the presence of rhAPOE4, whereas SV2A knockdown appeared to have a broader effect on APP internalization, even in the absence of rhAPOE4. Additionally, SV2A (but not RNF219) knockdown suppressed the internalization of BACE1 in an APOE4-dependent manner (Fig. 3a–d and Supplementary Figs 13, 14).

We further investigated the roles of SV2A and RNF219 in the context of overexpression studies. Transfection of N2a-APP cells with a vector encoding an SV2A enhanced green fluorescent protein fusion protein (SVA2-EGFP)<sup>33</sup> led to increased accumulation of sAPPβ, Aβ40 and Aβ42 species, regardless of the presence of rhAPOE4 (Fig. 3g and Supplementary Fig. 15d, e). Importantly, mutation of a critical tyrosine residue within the endocytosis motif of SV2A, Y46A (ref. 33), that selectively impairs SV2A association with clathrin adaptor proteins but does not affect other activities of SV2A (ref. 33), abrogated the effect of SV2A-EGFP overexpression on APP processing. Furthermore, whereas wild-type SV2A-EGFP co-localized with APP and BACE1, such co-localization was reduced with the Y46A mutant of SV2A-EGFP (Supplementary Fig. 15). These data support a direct role for SV2A-mediated endocytosis in the regulation of APP processing. In contrast with SV2A-EGFP, overexpression of wild-type RNF219-EGFP fusion protein in N2a-APP cells did not appear to significantly alter APP processing. However, overexpression of modified RNF219-EGFP forms that harbour RING-domain missense mutations at highly-conserved cysteines RNF219(C18A/C21A)-EGFP, or a RING-domain deletion RNF219(Δ1–77)-EGFP, suppressed the induction of Aβ40, Aβ42 and sAPPβ levels selectively in the context of rhAPOE4 (Fig. 3g, h and Supplementary Fig. 15). Such RNF219 mutants may act in a dominant-negative fashion to affect APP endocytosis and processing. Taken together, these data further implicate DCA candidate nodes in mediating the effect of APOE4 on APP processing through modified endocytosis.

## Levetiracetam corrects APOE4 phenotypes

We next hypothesized that treatment with levetiracetam, a selective SV2A inhibitor<sup>27</sup> used clinically to treat seizure disorders, could correct APOE4 related alteration in APP processing. Consistent with this, levetiracetam significantly decreased extracellular Aβ42 and Aβ40 levels in rhAPOE4 exposed N2a-APP cells (Supplementary Fig. 16a–c). To extend our analyses to a more physiological context, we next used a set of hiN cultures<sup>34</sup>, derived from human skin fibroblasts of APOE4 carriers or non-carriers. hiN cell cultures from APOE4 carriers displayed increased APP processing to Aβ42 and Aβ40 and increased APP co-localization with BACE1, relative to non-carriers (Fig. 4), consistent with the N2a studies above. Levetiracetam treatment suppressed the accumulation of Aβ40 or Aβ42 species, as well as APP co-localization with BACE1, selectively in the context of APOE4 carrier cultures. Thus, SV2A is required for the APOE4 mediated induction of APP processing in the context of human induced neurons that express endogenous levels of these proteins.

## RNF219 genetically interacts with APOE4

The above studies indicated that DCA-identified candidate node genes may function as effectors of APOE4, leading ultimately to LOAD. Thus, a prediction is that common human genetic variants at DCA gene loci may impact the association of APOE4 with LOAD risk or age-of-onset. To this end, single-nucleotide polymorphisms (SNPs) within 50 kilobases of the 20 top-ranking DCA identified genes were each evaluated for their genetic interaction with APOE4 in modulating LOAD age-of-onset, through a meta-analysis of 4 publicly available

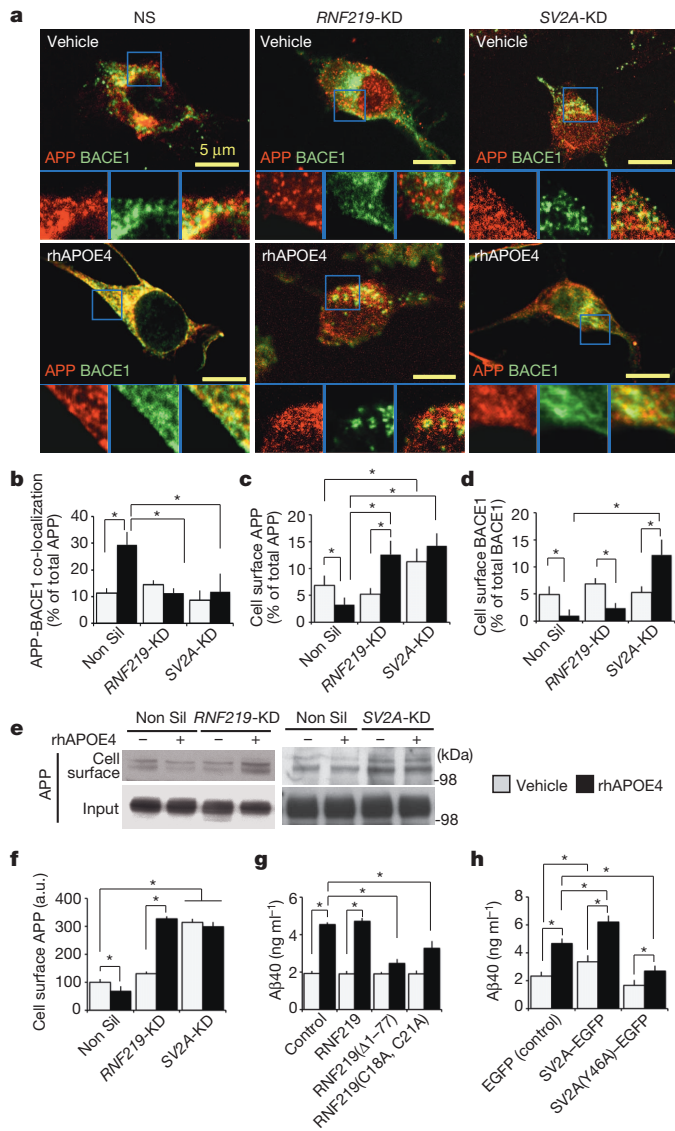


**Figure 3 | RNF219 and SV2A modulate APP proteolytic processing and localization in an APOE4-dependent manner.** **a–d**, ICC analysis of APP and BACE1 co-localization in N2a cells in the context of APOE4 or vehicle, and with transfection of knockdown (KD) vectors for RNF219, SV2A or non silencing vector control (Non Sil);  $n = 25, 24, 16, 18, 30$  and  $36$  cells in  $3$  independent wells per group, for the groups Non Sil plus vehicle; Non Sil plus rhAPOE4; RNF219-KD plus vehicle; RNF219-KD plus rhAPOE4; SV2A-KD plus vehicle, and SV2A-KD plus rhAPOE4, respectively. Scale bar,  $5\ \mu\text{m}$ . **e**, **f**, Biochemical quantification of cell-surface APP upon RNF219 or SV2A knockdown in rhAPOE4-treated N2a-APP cells. a.u., arbitrary units.  $n = 6, 5$  and  $6$  independent wells for the Non Sil, SV2A-KD and rhRNF219-KD groups, respectively. **g**, **h**, A $\beta$ 40 levels in media of N2a-APP cells in the context of RNF219 (**g**) or SV2A-EGFP (**h**) overexpression.  $n = 24, 22, 12, 12, 18$  and  $18$  independent wells for the groups Non Sil plus vehicle, Non Sil plus rhAPOE4, RNF219(wild-type) plus vehicle, RNF219(wild-type) plus rhAPOE4, RNF219( $\Delta 1-77$ ) plus vehicle, and RNF219( $\Delta 1-77$ ) plus rhAPOE4 respectively;  $n = 24, 22, 12, 12, 18$  and  $18$  independent wells for groups Non Sil plus vehicle, Non Sil plus rhAPOE4, SV2A-EGFP plus vehicle, SV2A-EGFP plus rhAPOE4, SV2A(Y46A)-EGFP plus vehicle, and SV2A(Y46A)-EGFP (**g**) respectively. For all figures, error bars are s.e.m.,  $*P < 0.05$  by ANOVA followed by Tukey HSD (**a**) or SNK test (**c, d, f–h**).

GWAS data sets: GenADA (875 LOAD cases and 850 controls<sup>35</sup>), TGEN Discovery (446 LOAD cases and 290 controls<sup>36</sup>), TGEN Replication (197 LOAD cases and 114 controls<sup>36</sup>), and ADNI (180 LOAD cases and 214 controls<sup>37</sup>). SNP variants at the FYN and RNF219 loci were associated with significantly decreased LOAD age-of-onset in APOE4

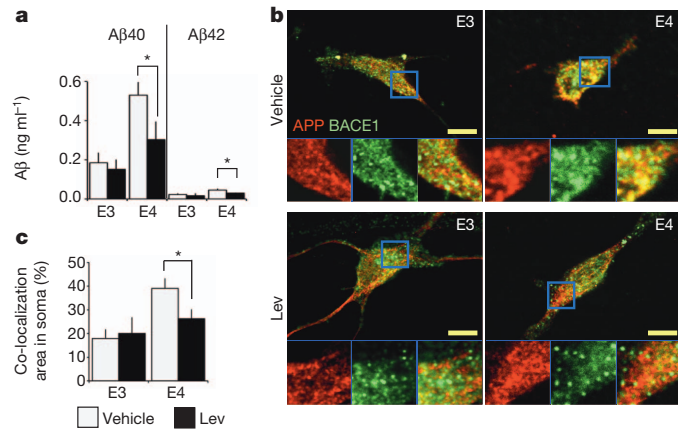


**Figure 4 | SV2A inhibition in human induced neurons modifies APP processing in an APOE4-dependent manner.** **a**, A $\beta$ 40 and A $\beta$ 42 quantification in media from APOE  $\varepsilon 3/\varepsilon 3$  (E3) or APOE  $\varepsilon 3/\varepsilon 4$  (E4) hiN cultures treated with levetiracetam (Lev;  $1\ \mu\text{M}$ ) or vehicle-only. Results represent the means  $\pm$  s.e.m. ( $n = 6$  and  $12$  independent wells for E3 and E4 groups, respectively).  $*P < 0.05$ . Analysis by ANOVA followed by post-hoc Tukey HSD. **b, c**, ICC analysis of APP and BACE1 co-localization in APOE3 and APOE4 hiN cultures treated with levetiracetam ( $1\ \mu\text{M}$ ) or vehicle-only. Insets show high-magnification images for visualization of BACE1 and APP co-localization. Means  $\pm$  s.e.m. are presented (**c**).  $n = 40$  (in  $4$  independent wells),  $46$  ( $6$  independent wells),  $35$  ( $3$  independent wells) and  $48$  ( $6$  independent wells) cells in the groups E3 plus vehicle, E3 plus levetiracetam, E4 plus vehicle and E4 plus levetiracetam, respectively.  $*P < 0.05$  by ANOVA followed by post-hoc analysis with Tukey HSD test. Scale bar,  $5\ \mu\text{m}$ .

non-carriers, but not in APOE4 carriers (Bonferroni corrected  $P$  values =  $2.93 \times 10^{-4}$  and  $6.03 \times 10^{-3}$ , respectively; Fig. 5a, b, Supplementary Fig. 17a and Supplementary Tables 2–4), consistent with a genetic interaction between these DCA hits and APOE4. More broadly, the set of genetic loci that encode DCA ‘hits’ was found to be enriched for genetic variants modulating LOAD age-of-onset in an APOE4-dependent fashion, as quantified using a gene-set enrichment algorithm (Supplementary Fig. 18 and ref. 38). We note that this was not the case for genes that were identified by simple differential gene expression analysis only, supporting the notion that DCA more efficiently identifies genes with a causal role.

Given the role of RNF219 in APP processing *in vitro*, we next hypothesized that genetic variants at RNF219 that are associated with LOAD, such as rs2248663, may also affect central nervous system A $\beta$  accumulation *in vivo* even in unaffected carriers. To this end, we analysed Florbetapir ( $^{18}\text{F}$ ) positron emission tomography (PET) imaging, which quantifies central nervous system A $\beta$  amyloid load<sup>39</sup>, in a data set of  $206$  genotyped unaffected elderly individuals (cognitively intact; within the Alzheimer’s Disease Neuroimaging Initiative; ADNI<sup>37,40</sup>). As previously described<sup>40</sup>, APOE4 carrier status was strongly associated with increased A $\beta$  amyloid load across multiple brain regions including cingulate, frontal, parietal and temporal cortex. Strikingly, the RNF219 rs2248663 minor allele was similarly associated with increased A $\beta$  amyloid load within many brain regions including cingulate, frontal, parietal and temporal cortex and brainstem, but not cerebellum ( $n = 177$ ; Supplementary Table 5). When stratified by APOE genotype, the RNF219 genotype significantly affected A $\beta$  load in unaffected APOE4 non-carriers ( $\varepsilon 3/\varepsilon 3$ ;  $n = 129$ ; Fig. 5d). Such an association was not apparent in APOE4 carriers ( $\varepsilon 3/\varepsilon 4$ ;  $n = 44$ ), but could not be entirely excluded due to the more limited power of analysis in the APOE4 carrier subset. In contrast to such positive findings in unaffected cognitively intact individuals, A $\beta$  amyloid load was not significantly associated with RNF219 genotype in affected individuals diagnosed with mild cognitive impairment (MCI;  $n = 382$  total from the ADNI cohort<sup>40</sup>, Supplementary Table 5), regardless of APOE genotype. This is consistent with a selective role for RNF219 that precedes the onset of

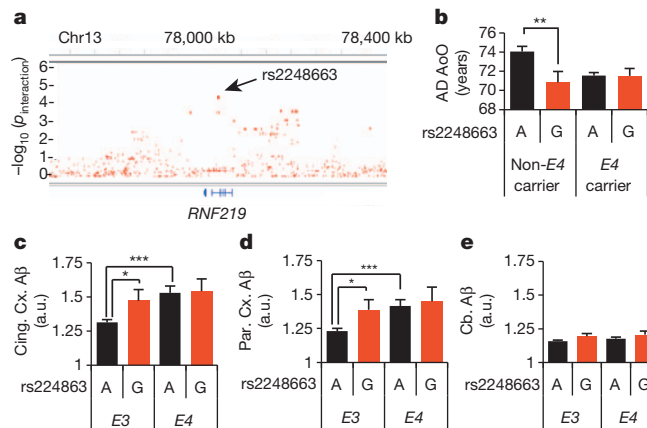


**Figure 5 | An RNF219 polymorphism modifies LOAD age-of-onset and amyloid deposition in human brain.** **a**, Manhattan plot of the RNF219 locus presenting the *P* value (log-scale, on *x*-axis) of the interaction between APOE4 and individual SNPs proximal to the RNF219 gene (in blue, vertical bars represent exons) in the LOAD age-of-onset meta-analysis. **b**, Mean LOAD age-of-onset across the TGEN, GenADA and ADNI data sets. Error bars represent s.e.m.; *n* = 339, 67, 530 and 102 individuals for the groups: non APOE4 carrier with RNF219 rs2248663(A); non APOE4 carrier with RNF219 rs2248663(G); APOE4 carrier with RNF219 rs2248663(A); and APOE4 carrier with RNF219 rs2248663(G). \*\**P* < 0.01 by ANOVA followed by Tukey HSD. **c–e**, Mean Aβ amyloid load in cognitively intact elderly individuals from the ADNI cohort, as quantified by florbetapir-PET within cingulate cortex (c), parietal cortex (d) or cerebellum (e). *n* = 129, 44, 41 and 7 individuals for the groups APOE3 carrier with RNF219 rs2248663(A); APOE3 carrier with RNF219 rs2248663(G); APOE4 carrier with RNF219 rs2248663(A); and APOE4 carrier with RNF219 rs2248663(G), respectively. Error bars represent s.e.m.; \**P* < 0.05, \*\**P* < 0.001 by ANOVA followed by Tukey HSD.

LOAD pathology. Taken together, these findings support a genetic interaction between RNF219 and APOE in the context of Aβ amyloid load in LOAD-unaffected human brain, as well as with respect to LOAD age-of-onset.

## Discussion

Using whole-transcriptome analysis of brain gene expression as a starting point, we describe molecular correlates of a prodromal pre-LOAD state present even in the context of unaffected APOE4 carriers. Such a prodromal molecular signature is consistent with reports that, even in LOAD-unaffected individuals, APOE4 is nonetheless associated with increased fibrillar Aβ accumulation in the brain<sup>41</sup>, decreased cerebrospinal fluid Aβ42 levels<sup>42</sup>, and accelerated cognitive decline<sup>43</sup>. As most APOE4 carriers do not go on to develop LOAD, it is likely that additional unknown ‘second hits’ are at play.

The candidate mediators identified by DCA herein show limited overlap with prior LOAD transcriptome network analyses, perhaps reflecting differences in experimental design<sup>15,44–47</sup>. For instance, most prior studies have used co-expression approaches primarily to identify clusters of functionally related genes, and subsequently compared the aggregated expression levels of such functional clusters in patient versus unaffected tissue. In contrast, DCA herein was used to identify individual candidate node genes that are highly altered in their patterns of co-expression with all other transcripts in affected tissue. Furthermore, we specifically pursued mechanisms that underlie the early causal events in LOAD, that would be apparent even in unaffected APOE4 carriers at high risk for LOAD; in contrast, prior network models have often pursued co-expression changes that correspond to disease progression<sup>47</sup>.

Levetiracetam was recently shown to improve cognition and reduce hippocampal hyperactivity in individuals with amnestic mild cognitive impairment (aMCI)<sup>28</sup>. Such increased hippocampal activation has also been described in asymptomatic individuals who carry the APOE4 allele<sup>48</sup>. Levetiracetam treatment of APP transgenic mice has similarly

been reported to improve cognitive function, whereas other antiepileptic agents fail to do so<sup>49</sup>. We note that in the absence of transgenic human APOE4, levetiracetam treatment did not modify APP processing in mice<sup>49</sup>, consistent with the *in vitro* findings herein. Although the therapeutic action of levetiracetam in patients with aMCI was ascribed to a general suppression of neuronal hyperactivity<sup>28</sup>, our data point to a more selective molecular mechanism of action for levetiracetam at SV2A. More broadly, it will be of interest to apply the integrative genomics approaches, as described here, to additional neurological and psychiatric brain disorders.

## METHODS SUMMARY

Differential expression and co-expression analysis were done using the R Bioconductor package essentially as described previously<sup>21</sup>. For knockdown experiments, N2a cells stably expressing human wild-type APP (N2a-APP) were transfected in Opti-MEM1 (Invitrogen) media containing 3 µl of Lipofectamine 2000 (Invitrogen) and an appropriate shRNA expression plasmid (1 µg). Cells were subsequently maintained in DMEM supplemented with 10% FBS, 500 µg ml<sup>-1</sup> puromycin (A.G. Scientific) and 500 µg ml<sup>-1</sup> geneticin (Invitrogen) for at least 1 week before phenotypic studies. Aβ quantification by enzyme-linked immunosorbent assay (ELISA) and APP-BACE1 ICC were performed as previously described<sup>34</sup>. Levels of APP holoprotein and BACE1 enzyme at the cell surface were quantified by cell surface biotinylation, fractionation and isolation with Avidin beads, using a Cell Surface Protein Isolation Kit (Pierce) followed by western blot. Human skin fibroblast cultures were obtained from de-identified, banked tissue samples (STC0022: Columbia University Institutional Review Board, IRB #AAAD3566; Primary Investigator Lawrence S. Honig; T-4560: Columbia University Taub Institute New York Brain Bank)<sup>34</sup>. Neurons were induced from the fibroblast cultures by transduction with replication-incompetent lentiviral particles encoding the neurogenic factors *Ascl1*, *Brn2*, *Zic1* and *Myt1l*, in fibroblast media containing polybrene (8 µg ml<sup>-1</sup>)<sup>34</sup>. hiNs were then cultured in glial-conditioned N2 media containing 20 ng ml<sup>-1</sup> BDNF (Peprotech) and supplemented with dorsomorphin (1 µM; Stemgent) for 4–6 days. Age-of-onset genetic analysis were done by linear regression of age-of-onset as a function of gender, APOE status and the queried SNP minor allele load using gPLINK<sup>30</sup> software. For human Aβ load analysis, Florbetapir (AV-45) PET-scan data was obtained from the ADNI consortium (<https://ida.loni.ucla.edu>), quantified as standardized uptake value ratio (SUVR)<sup>40</sup>. The effect of rs2248663 or APOE genotype on SUVR was evaluated using an additive model within the PLINK linear function, and adjusted for gender and age.

**Full Methods** and any associated references are available in the online version of the paper.

Received 14 August 2012; accepted 25 June 2013.

Published online 24 July 2013.

1. Selkoe, D. J. Toward a remembrance of things past: deciphering Alzheimer disease. *Harvey Lect.* **99**, 23–45 (2003).
2. Hardy, J. A hundred years of Alzheimer’s disease research. *Neuron* **52**, 3–13 (2006).
3. Bertram, L., McQueen, M. B., Mullin, K., Blacker, D. & Tanzi, R. E. Systematic meta-analyses of Alzheimer disease genetic association studies: the AlzGene database. *Nature Genet.* **39**, 17–23 (2007).
4. Harold, D. *et al.* Genome-wide association study identifies variants at CLU and PICALM associated with Alzheimer’s disease. *Nature Genet.* **41**, 1088–1093 (2009).
5. Lambert, J. C. *et al.* Genome-wide association study identifies variants at CLU and CR1 associated with Alzheimer’s disease. *Nature Genet.* **41**, 1094–1099 (2009).
6. Hollingworth, P. *et al.* Common variants at ABCA7, MS4A6A/MS4A4E, EPHA1, CD33 and CD2AP are associated with Alzheimer’s disease. *Nature Genet.* **43**, 429–435 (2011).
7. Naj, A. C. *et al.* Common variants at MS4A4/MS4A6E, CD2AP, CD33 and EPHA1 are associated with late-onset Alzheimer’s disease. *Nature Genet.* **43**, 436–441 (2011).
8. Castellano, J. M. *et al.* Human apoE isoforms differentially regulate brain amyloid-β peptide clearance. *Sci. Transl. Med.* **3**, 89ra57 (2011).
9. Koistinaho, M. *et al.* Apolipoprotein E promotes astrocyte colocalization and degradation of deposited amyloid-β peptides. *Nature Med.* **10**, 719–726 (2004).
10. Mahley, R. W. & Rall, S. C. Jr. Apolipoprotein E: far more than a lipid transport protein. *Annu. Rev. Genomics Hum. Genet.* **1**, 507–537 (2000).
11. He, X., Cooley, K., Chung, C. H., Dashti, N. & Tang, J. Apolipoprotein receptor 2 and X11 α/β mediate apolipoprotein E-induced endocytosis of amyloid-β precursor protein and β-secretase, leading to amyloid-β production. *J. Neurosci.* **27**, 4025–4040 (2007).
12. Ye, S. *et al.* Apolipoprotein (apo) E4 enhances amyloid β peptide production in cultured neuronal cells: apoE structure as a potential therapeutic target. *Proc. Natl. Acad. Sci. USA* **102**, 18700–18705 (2005).

13. Huang, Y. Apolipoprotein E and Alzheimer disease. *Neurology* **66**, S79–S85 (2006).
14. Pasinetti, G. M. Use of cDNA microarray in the search for molecular markers involved in the onset of Alzheimer's disease dementia. *J. Neurosci. Res.* **65**, 471–476 (2001).
15. Liang, D. et al. Concerted perturbation observed in a hub network in Alzheimer's disease. *PLoS ONE* **7**, e40498 (2012).
16. Gómez Ravetti, M., Rosso, O. A., Berretta, R. & Moscato, P. Uncovering molecular biomarkers that correlate cognitive decline with the changes of hippocampus' gene expression profiles in Alzheimer's disease. *PLoS ONE* **5**, e10153 (2010).
17. Bossers, K. et al. Concerted changes in transcripts in the prefrontal cortex precede neuropathology in Alzheimer's disease. *Brain* **133**, 3699–3723 (2010).
18. Hudson, N. J., Reverter, A. & Dalrymple, B. P. A differential wiring analysis of expression data correctly identifies the gene containing the causal mutation. *PLOS Comput. Biol.* **5**, e1000382 (2009).
19. Margolin, A. A. et al. ARACNE: an algorithm for the reconstruction of gene regulatory networks in a mammalian cellular context. *BMC Bioinformatics* **7** (suppl. 1), S7 (2006).
20. Presson, A. P. et al. Integrated weighted gene co-expression network analysis with an application to chronic fatigue syndrome. *BMC Syst. Biol.* **2**, 95 (2008).
21. Rhinn, H. et al. Alternative  $\alpha$ -synuclein transcript usage as a convergent mechanism in Parkinson's disease pathology. *Nature Commun.* **3**, 1084 (2012).
22. Webster, J. A. et al. Genetic control of human brain transcript expression in Alzheimer disease. *Am. J. Hum. Genet.* **84**, 445–458 (2009).
23. Sano, Y. et al. Enhanced amyloidogenic metabolism of the amyloid  $\beta$ -protein precursor in the X11L-deficient mouse brain. *J. Biol. Chem.* **281**, 37853–37860 (2006).
24. Fotinopoulou, A. et al. BRI2 interacts with amyloid precursor protein (APP) and regulates amyloid  $\beta$  ( $\beta$ A) production. *J. Biol. Chem.* **280**, 30768–30772 (2005).
25. Ullrich, S. et al. The novel membrane protein TMEM59 modulates complex glycosylation, cell surface expression, and secretion of the amyloid precursor protein. *J. Biol. Chem.* **285**, 20664–20674 (2010).
26. Hoe, H. S. et al. Fyn modulation of Dab1 effects on amyloid precursor protein and ApoE receptor 2 processing. *J. Biol. Chem.* **283**, 6288–6299 (2008).
27. Lynch, B. A. et al. The synaptic vesicle protein SV2A is the binding site for the antiepileptic drug levetiracetam. *Proc. Natl Acad. Sci. USA* **101**, 9861–9866 (2004).
28. Bakker, A. et al. Reduction of hippocampal hyperactivity improves cognition in amnestic mild cognitive impairment. *Neuron* **74**, 467–474 (2012).
29. Barber, M. J. et al. Genome-wide association of lipid-lowering response to statins in combined study populations. *PLoS ONE* **5**, e9763 (2010).
30. Cirulli, E. T. et al. Common genetic variation and performance on standardized cognitive tests. *Eur. J. Hum. Genet.* **18**, 815–820 (2010).
31. Furney, S. J. et al. Genome-wide association with MRI atrophy measures as a quantitative trait locus for Alzheimer's disease. *Mol. Psychiatry* **16**, 1130–1138 (2011).
32. Vassar, R. et al.  $\beta$ -secretase cleavage of Alzheimer's amyloid precursor protein by the transmembrane aspartic protease BACE. *Science* **286**, 735–741 (1999).
33. Yao, J., Nowack, A., Kensi-Hammes, P., Gardner, R. G. & Bajjalieh, S. M. Cotrafficking of SV2 and synaptotagmin at the synapse. *J. Neurosci.* **30**, 5569–5578 (2010).
34. Qiang, L. et al. Directed conversion of Alzheimer's disease patient skin fibroblasts into functional neurons. *Cell* **146**, 359–371 (2011).
35. Li, H. et al. Candidate single-nucleotide polymorphisms from a genome-wide association study of Alzheimer disease. *Arch. Neurol.* **65**, 45–53 (2008).
36. Reiman, E. M. et al. GAB2 alleles modify Alzheimer's risk in APOE epsilon4 carriers. *Neuron* **54**, 713–720 (2007).
37. Mueller, S. G. et al. Ways toward an early diagnosis in Alzheimer's disease: the Alzheimer's Disease Neuroimaging Initiative (ADNI). *Alzheimers Dement.* **1**, 55–66 (2005).
38. Voineagu, I. et al. Transcriptomic analysis of autistic brain reveals convergent molecular pathology. *Nature* **474**, 380–384 (2011).
39. Clark, C. M. et al. Use of florbetapir-PET for imaging  $\beta$ -amyloid pathology. *J. Am. Med. Assoc.* **305**, 275–283 (2011).
40. Ramanan, V. K. et al. APOE and BCHE as modulators of cerebral amyloid deposition: a florbetapir PET genome-wide association study. *Mol. Psychiatry* <http://dx.doi.org/10.1038/mp.2013.19> (in the press).
41. Reiman, E. M. et al. Fibrillar amyloid- $\beta$  burden in cognitively normal people at 3 levels of genetic risk for Alzheimer's disease. *Proc. Natl Acad. Sci. USA* **106**, 6820–6825 (2009).
42. Morris, J. C. et al. APOE predicts amyloid- $\beta$  but not tau Alzheimer pathology in cognitively normal aging. *Ann. Neurol.* **67**, 122–131 (2010).
43. Dik, M. G. et al. Memory complaints and APOE- $\epsilon$ 4 accelerate cognitive decline in cognitively normal elderly. *Neurology* **57**, 2217–2222 (2001).
44. Miller, J. A., Oldham, M. C. & Geschwind, D. H. A systems level analysis of transcriptional changes in Alzheimer's disease and normal aging. *J. Neurosci.* **28**, 1410–1420 (2008).
45. Ray, M. and Zhang, W. Analysis of Alzheimer's disease severity across brain regions by topological analysis of gene co-expression networks. *BMC Syst. Biol.* **4**, 136 (2010).
46. Soler-López, M., Zanzoni, A., Lluís, R., Stelzl, U. & Aloy, P. Interactome mapping suggests new mechanistic details underlying Alzheimer's disease. *Genome Res.* **21**, 364–376 (2011).
47. Zhang, B. et al. Integrated systems approach identifies genetic nodes and networks in late-onset Alzheimer's disease. *Cell* **153**, 707–720 (2013).
48. Bookheimer, S. Y. et al. Patterns of brain activation in people at risk for Alzheimer's disease. *N. Engl. J. Med.* **343**, 450–456 (2000).
49. Sanchez, P. E. et al. Levetiracetam suppresses neuronal network dysfunction and reverses synaptic and cognitive deficits in an Alzheimer's disease model. *Proc. Natl. Acad. Sci. USA* **109**, E2895–E2903 (2012).
50. Purcell, S. et al. PLINK: a tool set for whole-genome association and population-based linkage analyses. *Am. J. Hum. Genet.* **81**, 559–575 (2007).

**Supplementary Information** is available in the online version of the paper.

**Acknowledgements** We thank R. Mayeux, G. Di Paulo, S. Small and A. Rosenthal for comments on the manuscript; D. Holtzman and J. Cirrito for antibody reagents; and S. Bajjalieh and J. Yao for SV2A expression vectors. We are especially grateful to the many laboratories who contributed data sets included in this study. The work was supported by grants from the National Institutes of Health (NIH) (R01AG042317 and R01NS064433). J.H.L. and R.C. were partially funded by R37 AG015473 and R01MH084995. Additionally, data collection and sharing for this project was funded by the Alzheimer's Disease Neuroimaging Initiative (ADNI) (NIH grant U01 AG024904). ADNI is funded by the National Institute on Aging, the National Institute of Biomedical Imaging and Bioengineering, and through generous contributions from the following: Alzheimer's Association; Alzheimer's Drug Discovery Foundation; BioClinica; Biogen Idec; Bristol-Myers Squibb; Eisai; Elan Pharmaceuticals; Eli Lilly; F. Hoffmann-La Roche and its affiliated company Genentech; GE Healthcare; Innogenetics, NV; IXICO; Janssen Alzheimer Immunotherapy Research and Development; Johnson and Johnson Pharmaceutical Research and Development; Medpace; Merck; Meso Scale Diagnostics; NeuroRx Research; Novartis; Pfizer; Piramal Imaging; Servier; Synarc; and Takeda Pharmaceutical Company. The Canadian Institutes of Health Research is providing funds to support ADNI clinical sites in Canada. Private sector contributions are facilitated by the Foundation for the National Institutes of Health (<http://fnih.org>). The grantee organization is the Northern California Institute for Research and Education, and the study is coordinated by the Alzheimer's Disease Cooperative Study at the University of California, San Diego. ADNI data are disseminated by the Laboratory for Neuro Imaging at the University of California, Los Angeles. This research was also supported by NIH grants P30 AG010129 and K01 AG030514.

**Author Contributions** A.A., H.R. and R.F. designed studies, interpreted data and wrote the manuscript. H.R. performed the bioinformatics and genetic analysis. R.F. performed the cell culture and biochemistry experiments. L.Q. participated in the generation of hiNs. R.C. and J.H.L. provided support for the genetic analysis. Data used in preparation of this article were obtained from the Alzheimer's Disease Neuroimaging Initiative (ADNI) database (<http://adni.loni.ucla.edu>). As such, the investigators within the ADNI contributed to the design and implementation of ADNI and/or provided data but did not participate in analysis or writing of this report. A complete listing of ADNI investigators can be found at ([http://adni.loni.ucla.edu/wp-content/uploads/how\\_to\\_apply/ADNI\\_Acknowledgement\\_List.pdf](http://adni.loni.ucla.edu/wp-content/uploads/how_to_apply/ADNI_Acknowledgement_List.pdf)).

**Author Information** Reprints and permissions information is available at [www.nature.com/reprints](http://www.nature.com/reprints). The authors declare no competing financial interests. Readers are welcome to comment on the online version of the paper. Correspondence and requests for materials should be addressed to A.A. (aa900@columbia.edu).

## METHODS

**Materials.** Levetiracetam was obtained from LKT Laboratories, puromycin was purchased from AG Scientific. Recombinant human APOE2 (rhAPOE2), APOE3 (rhAPOE3), and APOE4 (rhAPOE4) were from BioVision. Antibodies obtained were anti-APP C terminus and anti-RNF219 (both rabbit polyclonals, Sigma-Aldrich), anti-APP N-terminal (mouse monoclonal, 22C11, Millipore), anti-APP C-terminal (mouse monoclonal, 2.F2.19B4; from Millipore, for detection of the exogenous human wild-type APP transgene and cleavage products), Anti-APP C-terminal (mouse monoclonal, c1/6.1; Covance, for detection of the endogenous murine APP and cleavage products), anti-beta amyloid (mouse monoclonals, 4G8, 6E10; Covance), anti-BACE1 (rabbit polyclonal; Invitrogen) and anti-RNF219 (rabbit polyclonal; Santa Cruz Biotechnology).

**Cell culture and shRNA expression vector transfection.** N2a cells stably expressing human APP wild type (N2a-APP) were maintained in DMEM supplemented with 10% FBS and 1% penicillin 1% streptomycin and 500–1,000 µg ml<sup>-1</sup> geneticin (Invitrogen). For knockdown experiments, cells grown overnight to 70–90% confluence in 24-well plates were transfected in Opti-MEM1 (Invitrogen) media containing 3 µl of Lipofectamine 2000 (Invitrogen) and 1 µg of shRNA expressing plasmid DNA and incubated in DMEM supplemented with 10% FBS and 500 µg ml<sup>-1</sup> puromycin (A.G. Scientific) and 500 µg ml<sup>-1</sup> geneticin (Invitrogen) at least for 1 week before further experiments. Validated shRNA plasmids were obtained from Open biosystems (pGIPZ backbone): SV2A (#1:V3LMM\_450995, 5'-TATTGTGCTAGGAACGTGCT-3'; #2: V3LMM\_450996, 5'-TGATGAACGTGCAAGTTCGCG-3'; #3:V3LMM\_451000, 5'-TGCAGGAAGAATGTGTTGCT-3'), RNF219 (V3LMM\_483077, 5'-ATCACTTCGTTCTAGAGCT-3') or Sigma (pLKO backbone): NCDN (TRCN0000119418, 5'-CGTAGGATCTTGATGCCGTT-3'), CALU (TRCN000114827, 5'-GCTCAGCGATAAAGTTCACAA-3'), FYN (TRCN0000023379, 5'-GCTCGGGTGTATTGAAGACAAT-3'), TMEM95L (TRCN0000178059, 5'-GCTTATTGACATTCTCACAT-3'), MAPK3 (TRCN0000023186, 5'-CCATGA GAATGTTATAGGCAT-3'), HDLBP (TRCN0000105171, 5'-GCTCGCATTAA GAAGATTAT-3'), RNF219 (TRCN0000125455, 5'-CCACGAGATGAGTGA AGATT-3'), ROGDI (TRCN0000012233, 5'-CCCTCCTCATTCCTGTGGTA-3'). **A $\beta$  ELISA.** A $\beta$  quantification was performed by ELISA as described previously<sup>34,51</sup>. Media was conditioned for 48 h before harvesting. Samples were analysed for A $\beta$ 40 or A $\beta$ 42 using specific sandwich ELISAs. Briefly, A $\beta$ 40, and A $\beta$ 42 were captured using monoclonal antibodies targeted against amino acids 35–40 (HJ2.0), or 33–42 (HJ7.4) of A $\beta$ , respectively. The antibodies HJ2.0, HJ5.1 and HJ7.4 were gifts from D. M. Holtzman. For A $\beta$ 40 and A $\beta$ 42 assays, a biotinylated central domain monoclonal antibody (HJ5.1) followed by streptavidin-poly-HRP-40 was used for detection (Sigma). All assays were developed using Super Slow ELISA TMB (Sigma) and read on a VersaMax ELISA Microplate Reader (Molecular Devices) at 650 nm. ELISA signals were reported as the mean  $\pm$  s.e.m. of three replica wells in ng of A $\beta$  per ml of supernatant, based on standard curves using synthetic human and mouse recombinant A $\beta$ 40 and A $\beta$ 42 peptides (rPeptide; Bogart, GA). Samples were optimized to detect A $\beta$ 40 and A $\beta$ 42 in the range of 1–3,000 and 0.03–30 ng ml<sup>-1</sup>, respectively<sup>34</sup>. The amount of A $\beta$  was normalized to total cell protein levels.

**Quantitative real time RT-PCR.** qRT-PCR was done as described previously<sup>52</sup>. mRNA levels were quantified using  $\Delta\Delta Ct$  methods, using GAPDH as a normalizing factors. Forward/reverse primers pairs used were 5'-AGGTGGTGTGAA CGGATTG-3'/5'-GGGGTCGTTGATGGCAACA-3' for GAPDH, 5'-GTGCCA CATTGCTGGGG-3'/5'-TCAGGAGTGATCGGGACTCTG-3' for RNF219, 5'-AGGTGAAAGGGACTCTGACTC-3'/5'-GCCAAGTGCAACAACCTGGT-3' for ROGDI, 5'-AATGCTGATGGGTCATTGATCT-3'/5'-GGTTCTTATCTC GAAACTCCACG-3' for CALU, 5'-ACAGTGCAGACAGAGATCCAG-3'/5'- CGGATTGAAAGGTCAACCTCCA-3' for PTK2B, 5'-CTCAGGTGTTTCAT GTACCCC-3'/5'-TCAAGGCAGATTTCGTTGCT-3' for HDLBP, 5'-GGT TCACCTTCCCAACCGA-3'/5'-GCTGGCTAGTTCAGGGTCG-3' for NCDN and 5'-TCCGCCATGAGAATGTTAGGC-3'/5'-GGTGGTGTGATAAAGC AGATTGG-3' for MAPK3.

**Immunohistochemistry.** Immunocytochemistry (ICC) was performed as previously described<sup>34</sup>. Cells were fixed with 4% paraformaldehyde for 10 min at room temperature, followed by rinsing 3 times with phosphate-buffered saline (PBS). Cells were then permeabilized with 0.3% Triton X-100 in 1× PBS for 2 min at room temperature. After rinsing three times with PBS, cells were incubated with blocking buffer containing 1% BSA and 1% normal goat serum at room temperature for 1 h. All primary antibodies were diluted in blocking buffer. Cells were incubated with primary antibodies (1:200 to 1,500) at 4 °C for 12–16 h, followed by the corresponding secondary antibody solutions at room temperature for 1 h. Cells were rinsed with 1× PBS three times followed by mounting on coverslips with Fluoro-Gel (Electron Microscopy Sciences). Detailed antibody sources and dilutions used can be found in the Supplementary Information. Imaging was conducted by laser-scanning confocal microscopy with a  $\times$ 63 (1.4 NA) objective (LSM510, Carl Zeiss). Cell counts and fluorescence intensities were quantified in

10 to 35 images of randomly selected views per well. Subsequently, images were analysed for cell counts and fluorescent intensity using Image J 1.42q software (National Institutes of Health).

**Immunoblotting.** Cells were suspended in RIPA buffer contained protease inhibitor cocktail (Sigma) and sonicated, then cells were incubated for 1 h at 4 °C. The lysates were cleared by centrifugation at 10,000g for 10 min at 4 °C. Protein concentration was determined by Bio-Rad Dc Protein assay kits (Bio-Rad), 5–30 µg of total protein lysate was resolved on a 4–12% SDS-PAGE gel. Protein samples were transferred onto nitrocellulose membranes using the semi-dry transfer unit (Owl Scientific) and blocked with 3% skimmed milk in Tris buffered saline with 0.1% Tween 20 for 1 h. The primary antibodies were incubated overnight at 4 °C, and primary antibody binding was detected using horseradish peroxidase conjugated anti-mouse IgG at 1:5,000 dilution (Jackson Immunoresearch Laboratories) or horseradish peroxides conjugated anti-rabbit IgG at 1:5,000 dilution (Jackson Immunoresearch Laboratories).

**Cell surface biotinylation.** Levels of APP holoprotein and BACE1 at the cell surface were quantified using cell surface biotinylation followed by fractionation and western blotting. Cell surface biotinylation was performed using a cell surface protein isolation kit following the manufacturer's instructions (Pierce). N2a cell cultures in two 10-cm dishes at 90–95% confluence were first rinsed three times with ice-cold culture medium and then incubated in PBS containing 1 mg ml<sup>-1</sup> of EZ-link Sulfo NHS-LC biotin (Pierce Chemical), or PBS alone, for 30 min at 4 °C. To quench any excess biotin, cell cultures were rinsed and then incubated in quenching solution for 10 min at 4 °C. Next, cells were gently scraped into conical tubes and centrifuged. Pellets were washed in cold PBS three times, and lysis buffer with protease inhibitor at 4 °C added as per manufacturer's instructions. Cells were sonicated for disruption and incubated 30 min on ice. After incubation, sample were centrifuged 10,000g for 2 min and supernatants were collected. Cell lysates from biotin-labelled and unlabelled samples were incubated with NeutrAvidin agarose beads (Pierce Chemical) for 60 min at room temperature. Subsequently, beads were washed with RIPA buffer containing protease inhibitor cocktail (Sigma), and total protein levels were determined using a BCA protein quantification assay kit (Bio-Rad). For western blot analysis, lysates were mixed with sample buffer, boiled for 10 min, and then resolved on an SDS-PAGE gel. Total protein, containing 15 µg of lysate was simultaneously resolved on the gel, transferred to PVDF membrane and probed for APP and BACE1 expression.

**Human skin fibroblasts.** Human skin fibroblast cultures used in this study were obtained from de-identified, banked tissue samples; there was no interaction with subjects, no intervention, and private, identifiable information was not collected. One fibroblast line was obtained from an unaffected individual homozygous for the APOE3 allele (STC0022 (female, 65 years old)), and a second line from an unaffected individual who carries one APOE4 and one APOE3 allele (T-4560 (male, 89+ years old)). STC0022 and T-4560 were obtained from de-identified, banked tissue samples (STC0022: Columbia University Institutional Review Board, IRB #AAAD3566; Primary Investigator, Lawrence S. Honig; T-4560: Columbia University Taub Institute New York Brain Bank)<sup>34</sup>. Human skin fibroblasts were cultured in standard fibroblast media (DMEM with 10% FBS).

**hIN cell induction and transfection.** Fibroblasts were plated at 20,000 cells per well in 24-well plates one day before infection. Culture plates and dishes were treated with poly-L-ornithine (Sigma) and laminin (Invitrogen) or poly-D lysine (Trevigen) and laminin before the application of the cells as per the manufacturer's instructions. Fibroblasts were transduced with replication-incompetent, VSVg-coated lentiviral particles encoding Ascl1, Brn2, Zic 1 and Myt1l, in fibroblast media containing polybrene (8 µg ml<sup>-1</sup>). Each lentiviral type was added at a multiplicity of infection  $\sim$ 2:1. Two day after transduction, the media was replaced with glial-conditioned N2 media containing 2 ng ml<sup>-1</sup> BDNF (Peprotech). For the first 4–6 days in N2 media, dorsomorphin (1 µM; Stemgent) was applied to the culture. Media was changed every 2–3 days for the duration of the culture period.

**Differential expression.** The microarray data set was downloaded from the Myers laboratory website. All subsequent data manipulations and analyses were done using R Bioconductor package. For each gene, differential expression between two conditions was assessed by a two-tailed *t*-test, using a threshold *P*-value of 0.05. For a gene to be considered affected by both APOE genotype and AD phenotype, its expression level has to be significantly changed in the same direction when comparing samples from unaffected APOE4 individuals to unaffected APOE2 individuals and when comparing samples from AD APOE3 patients to unaffected APOE3 individuals. Genes annotation enrichment were queried using GSEA<sup>53</sup> or the DAVID bioinformatics resources<sup>54,55</sup>.

**Differential wiring analysis.** The microarray data set was downloaded from the Myers laboratory website. All subsequent data manipulations and analyses were done using R Bioconductor package. Correlations between gene expression levels were assessed using cosine similarity on log-transformed levels; briefly, two genes whose expression levels are simultaneously high or low across many samples are

in phase and will have a correlation coefficient close to 1. On the contrary, if one gene shows high expression levels when another one shows low across many samples, those two genes are in anti-phase and will have a correlation coefficient close to -1. The absence of linear relationship between the expression levels of both genes will result in a correlation coefficient close to 0. Comparisons between correlations obtained in two independent groups were done using a Fisher's Z transformation followed by a statistical test using pnorm R function.

The principle underlying DW algorithms<sup>18,56</sup> is that for a given candidate 'master regulator' node gene X, the global DW score—when comparing two experimental conditions 1 and 2—is the sum of DW subscores between gene X and each of the other genes Gi queried. The subscore between the gene of interest X (for which the DW score is calculated) and a gene Gi is proportional to: (1) the extent of the shift in correlation between the expression levels of Gi and X when comparing conditions 2 and 1 (thus genes exhibiting a high number of strong shifts in correlation with many other genes are assumed to be relevant nodes in the differential gene expression network between conditions 1 and 2); (2) the extent of differential expression of Gi between conditions 1 and 2 (averaged across the panel of samples for each condition; thus, the more a gene is on average differentially expressed between 2 conditions, the more it is predicted to have a phenotypic impact); (3) the level of expression Gi (a more highly expressed gene is thought to have a higher phenotypic impact; this is to compensate for the fact that lowly expressed genes are more likely to exhibit strong shifts in expression between the two conditions).

The three main modifications we introduce to the previously described wiring algorithms<sup>18,56</sup> are: (1) We broadened the analysis of possible 'master regulator' genes from only annotated transcription factors to all genes. (2) We introduced significance threshold tests for the interactor genes: as we included all the genes as candidate 'master disease regulators', instead of only all the annotated transcription factors we wanted to avoid artificial results when working at a genome-wide scale than with hundreds of selected genes. Low-selective threshold ( $P$  value = 0.05) were however chosen to keep a high sensitivity. (3) We considered for differential expression as well as for differential correlation the intersection between 2 comparisons involving 4 independent groups. For a gene to be considered as differentially expressed, it has to be significantly differentially expressed in both conditions with the same orientation.

The differential wiring score for a gene X between for two comparisons each between two independent experimental groups (1 and 2 with  $n_1$  and  $n_2$  elements and A and B with  $n_A$  and  $n_B$  elements, respectively) was thus calculated as the sum over all the genes Gi of the absolute value of the product of: (1) The conditional Z-distance evaluating the difference observed between the two groups in each of the two comparisons for the correlation between the expression levels of genes X and Gi  $\langle \Delta_{Gi(1vs2) \cap (AvsB)} \rangle_p$  in the formal DW formula below. Thus, for a given threshold  $P$  value (0.05 here), it has a null value if the correlation shift is not significant. The amplitude of the Z-distance is proportional to the shift in correlation between the two experimental conditions. Fisher's Z-transformation corrects for the non-normal distribution of the correlation value (between -1 and 1). As a consequence, a shift in correlation from 0.7 to 0.9 will lead a Z-distance value higher than a shift from -0.1 to 0.1. (2) The conditional log-scaled amplitude of the differential expression of gene Gi  $\langle \delta(X, Gi)_{(1vs2) \cap (AvsB)} \rangle_p$  in the DW formula below. For a given threshold  $P$  value (0.05 here), it has a null value if the gene is found to not be differentially expressed between the two conditions. If the gene is differentially expressed for the chosen  $P$  value, the value will be the log of the ratio between the averaged gene expression levels in each group. (3) The averaged expression level of gene Gi among all samples  $\langle \overline{(E_{Gi})_{1 \cup 2 \cup A \cup B}} \rangle_p$  in the formula below.

As a consequence of the use of significance threshold tests, only those genes which are differentially expressed between the two experimental conditions, and that see their correlation with gene X significantly changed between the two experimental conditions, will participate in the DW score.

Formally, the DW score was thus calculated as:

Differential wiring score for gene X:

$$DW(X)_{1vs2} = \sum Gi \left| \langle \Delta_{Gi(1vs2) \cap (AvsB)} \rangle_p \right| \left| \langle \delta(X, Gi)_{(1vs2) \cap (AvsB)} \rangle_p \right| \left| \langle \overline{(E_{Gi})_{1 \cup 2 \cup A \cup B}} \rangle_p \right|$$

With:

Conditional Z-distance for a p-value p:

$$\langle \delta_{1vs2} \rangle_p = \begin{cases} \sqrt{\delta_{1vs2} \cdot \delta_{AvsB}} & \text{IF } pnorm(\delta_{1vs2}) < p \\ & \text{AND } pnorm(\delta_{AvsB}) < p \\ & \text{AND } \delta_{1vs2} \cdot \delta_{AvsB} \\ 0 & \text{OTHERWISE} \end{cases}$$

$$\delta(X, G)_{1vs2} = \frac{F_z(r(X, G)_1) - F_z(r(X, G)_2)}{\sqrt{\frac{1}{n_1 - 3} + \frac{1}{n_2 - 3}}} \text{ Z-distance between } r(X, G)_1 \text{ and } r(X, G)_2$$

$$\delta(X, G)_{AvsB} = \frac{F_z(r(X, G)_A) - F_z(r(X, G)_B)}{\sqrt{\frac{1}{n_A - 3} + \frac{1}{n_B - 3}}} \text{ Z-distance between } r(X, G)_A \text{ and } r(X, G)_B$$

$r(X, G)_1, r(X, G)_2, r(X, G)_A, r(X, G)_B$  correlation coefficient between the expression levels of genes X and G, evaluated in experimental groups 1 ( $n_1$  elements), 2 ( $n_2$  elements), A ( $n_A$  elements) B ( $n_B$  elements).

$$F_z(r) = \frac{1}{2} \log \left( \frac{1+r}{1-r} \right) \text{ Fisher's z transformation for a correlation coefficient } r$$

Conditional differential gene expression amplitude of Gi

$$\langle \Delta_{Gi(1vs2) \cap (AvsB)} \rangle_p = \begin{cases} \sqrt{\log \left( \frac{\langle \overline{(E_{Gi})_1} \rangle}{\langle \overline{(E_{Gi})_2} \rangle} \right) \cdot \log \left( \frac{\langle \overline{(E_{Gi})_A} \rangle}{\langle \overline{(E_{Gi})_B} \rangle} \right)} & \text{IF } p. \text{ value } (t.test((E_G)_1, (E_G)_2)) < p \\ & \text{AND } p. \text{ value } (t.test((E_G)_A, (E_G)_B)) < p \\ & \text{AND } \log \left( \frac{\langle \overline{(E_{Gi})_1} \rangle}{\langle \overline{(E_{Gi})_2} \rangle} \right) \cdot \log \left( \frac{\langle \overline{(E_{Gi})_A} \rangle}{\langle \overline{(E_{Gi})_B} \rangle} \right) > 0 \\ 0 & \text{OTHERWISE} \end{cases}$$

$(E_G)_i$ : collection of the expression level values for gene G among an experimental group i. All calculations were performed using the R statistical environment.

**GWAS epistasis analysis.** We used 4 publicly available GWAS data sets; GenADA study was downloaded from NCBI's dbGap repository<sup>57</sup> (Multi-Site Collaborative Study for Genotype–Phenotype Associations in Alzheimer's disease and Longitudinal follow-up of Genotype–Phenotype Associations in Alzheimer's disease and Neuroimaging component of Genotype–Phenotype Associations in Alzheimer's disease, dbGap phs000219.v1.p1), which includes 875 AD cases and 850 controls<sup>35</sup>. Two Tgen neuropathological data sets were obtained from the Translational Genomics Research Institute (<http://www.tgen.org>). The 'discovery cohort' includes 446 AD cases and 290 controls, the 'replication cohort' 197 AD cases and 114 controls<sup>36</sup>. The ADNI data sets were downloaded from the Alzheimer's Disease Neuroimaging Initiative website (<https://ida.loni.ucla.edu>) and includes 180 AD cases and 214 controls<sup>37</sup>. All subsequent genetic analysis were done using gPLINK<sup>50</sup> software. Interaction between different SNPs and APOE4 in each data set were evaluated using PLINK linear and interaction functions, applied to the following model  $AoO = a + b.APOE + c.Sex + d.SNP + e.SNP \times APOEbin$ , where  $AoO$  is the age-of-onset of Alzheimer's disease,  $APOE$  is the allelic load of  $APOE \varepsilon 4$  allele (= 0, 1 or 2),  $Sex$  is the gender (= 0 or 1),  $SNP$  the allelic load of the minor allele for the studied SNP (= 0, 1 or 2) and  $APOEbin$  a binary indicator for the presence or absence of at least one  $APOE4$  allele (= 0 or 1). The term  $e$  is considered as the interaction term in the current analysis. Rare  $APOE2$  allele carriers were not considered in the present study. Analysis was performed independently in each data set, and then combined in a meta-analysis using METAL (<http://www.sph.umich.edu/csg/abecasis/meta/>).

**AD age-of-onset GWAS set enrichment analysis.** GWAS enrichment analysis was performed essentially as previously described<sup>38</sup>, using the  $P$  value resulting from the  $APOE4$ -dependent AD age-of-onset association meta-analysis described above. For each gene present in the gene expression data set the associated  $P$  value corresponds to the lowest meta-analysis  $P$  value for a SNP located within 50-kb on either side of the gene, using the 286,178 SNPs present in at least 3 of the 4 studies used in the meta-analysis. A gene set enrichment score was calculated for the different groups of genes considered using a weighted Kolmogorov–Smirnov-like running-sum statistic as previously described<sup>38</sup>. For each gene set, a null distribution was generated by permuting 10,000 times the gene labels, and was used to evaluate an empirical  $P$  value for the enrichment score. All calculations were made using R statistical software.

**Florbetapir (AV-45) PET-scan epistasis analysis.** Data was downloaded from the Alzheimer's Disease Neuroimaging Initiative website (<https://ida.loni.ucla.edu>) and includes data from 177 cognitively intact and 338 mildly cognitively impaired elderly genotyped individuals. Briefly,  $A\beta$  load was evaluated by florbetapir-PET and quantified as a standardized uptake value ratio (SUVR)<sup>40</sup> in different brain regions (parietal cortex, cingulate cortex, frontal cortex, temporal cortex, brain-stem and cerebellum). The effect of rs2248663 minor allele (G) or  $APOE4$  allele

load on the SUVR was evaluated for each group using an additive model within the PLINK linear function, and adjusted for gender and age.

51. Cirrito, J. R. *et al.* *In vivo* assessment of brain interstitial fluid with microdialysis reveals plaque-associated changes in amyloid- $\beta$  metabolism and half-life. *J. Neurosci.* **23**, 8844–8853 (2003).
52. Rhinn, H. *et al.* Housekeeping while brain's storming Validation of normalizing factors for gene expression studies in a murine model of traumatic brain injury. *BMC Mol. Biol.* **9**, 62 (2008).
53. Subramanian, A. *et al.* Gene set enrichment analysis: a knowledge-based approach for interpreting genome-wide expression profiles. *Proc. Natl Acad. Sci. USA* **102**, 15545–15550 (2005).
54. Huang D. W., Sherman, B. T. & Lempicki, R. A. Bioinformatics enrichment tools: paths toward the comprehensive functional analysis of large gene lists. *Nucleic Acids Res.* **37**, 1–13 (2009).
55. Huang D. W., Sherman, B. T., Lempicki, R. & A. Systematic and integrative analysis of large gene lists using DAVID bioinformatics resources. *Nature Protocols* **4**, 44–57 (2009).
56. Reverter, A., Hudson, N. J., Nagaraj, S. H., Perez-Enciso, M. & Dalrymple, B. P. Regulatory impact factors: unraveling the transcriptional regulation of complex traits from expression data. *Bioinformatics* **26**, 896–904 (2010).
57. Mailman, M. D. *et al.* The NCBI dbGaP database of genotypes and phenotypes. *Nature Genet.* **39**, 1181–1186 (2007).

# An age difference of two billion years between a metal-rich and a metal-poor globular cluster

B. M. S. Hansen<sup>1</sup>, J. S. Kalirai<sup>2,3</sup>, J. Anderson<sup>2</sup>, A. Dotter<sup>4</sup>, H. B. Richer<sup>5</sup>, R. M. Rich<sup>1</sup>, M. M. Shara<sup>6</sup>, G. G. Fahlman<sup>7</sup>, J. R. Hurley<sup>8</sup>, I. R. King<sup>9</sup>, D. Reitzel<sup>1</sup> & P. B. Stetson<sup>7</sup>

**Globular clusters trace the formation history of the spheroidal components of our Galaxy and other galaxies<sup>1</sup>, which represent the bulk of star formation over the history of the Universe<sup>2</sup>.** The clusters exhibit a range of metallicities (abundances of elements heavier than helium), with metal-poor clusters dominating the stellar halo of the Galaxy, and higher-metallicity clusters found within the inner Galaxy, associated with the stellar bulge, or the thick disk<sup>3,4</sup>. Age differences between these clusters can indicate the sequence in which the components of the Galaxy formed, and in particular which clusters were formed outside the Galaxy and were later engulfed along with their original host galaxies, and which were formed within it. Here we report an absolute age of  $9.9 \pm 0.7$  billion years (at 95 per cent confidence) for the metal-rich globular cluster 47 Tucanae, determined by modelling the properties of the cluster's white-dwarf cooling sequence. This is about two billion years younger than has been inferred for the metal-poor cluster NGC 6397 from the same models, and provides quantitative evidence that metal-rich clusters like 47 Tucanae formed later than metal-poor halo clusters like NGC 6397.

The ages of globular clusters are most easily determined by modelling the properties of main-sequence and horizontal-branch stars<sup>5–9</sup>, but doing so leads to uncertainties caused by covariance between the measured age and the spectroscopic metallicity required to compare observed colours and magnitudes to theoretical models. The metals in the atmospheres of white dwarfs sediment out because of the strong stellar gravity, resulting in an age determination more robust with respect to metallicity correlations. In such cases, the age is based on the monotonic cooling of white dwarfs, because the luminosity function peak moves to fainter magnitudes for older populations. The consistency of the two approaches has been demonstrated with the determination of absolute ages for the globular clusters Messier 4 and NGC 6397 (refs 10–13). Our attempt to extend the application of this method (fitting the cooling sequence of the white dwarfs) to the metal-rich cluster 47 Tucanae is driven by the fact that the covariance between metallicity and age in the main-sequence fitting method becomes stronger with increasing metallicity, indicating the need for an independent determination.

We observed a field at roughly the half-mass radius of the cluster with the Hubble Space Telescope. The primary science observations were performed with the Advanced Camera for Surveys, with observations split between the wide F606W (total integration of 163.7 ks) and F814W (total integration of 172.8 ks) bandpasses. The field was also chosen to overlap with prior Hubble Space Telescope observations, so that the cluster motion results in positional shifts of cluster members with respect to background stars, and so cluster and non-cluster members can be separated. Details of the photometry, completeness and measurement of the proper motions is described in the Supplementary Information.

The white-dwarf population is isolated by both colour and proper motion, as shown in Fig. 1. The distribution of white dwarfs with luminosity (the luminosity function) can be compared (Fig. 2) with the white-dwarf luminosity function of a metal-poor, globular cluster with deep Hubble Space Telescope observations, called NGC 6397 (ref. 12). The abrupt truncation of these luminosity functions is a manifestation of the finite age of a population, as white dwarfs cool monotonically, and this cutoff moves to fainter magnitudes as a population ages. In Fig. 2 we have adjusted the magnitudes of the NGC 6397 population to correct for the different cluster distances, and so placed it on the same magnitude scale as the 47 Tucanae population. The 47 Tucanae luminosity function drops to half of the peak value at approximately 0.4 magnitudes brighter than that of NGC 6397, a direct demonstration that this cluster is younger. A comparison to a third cluster, Messier 4 (ref. 13), shows a similar age difference.

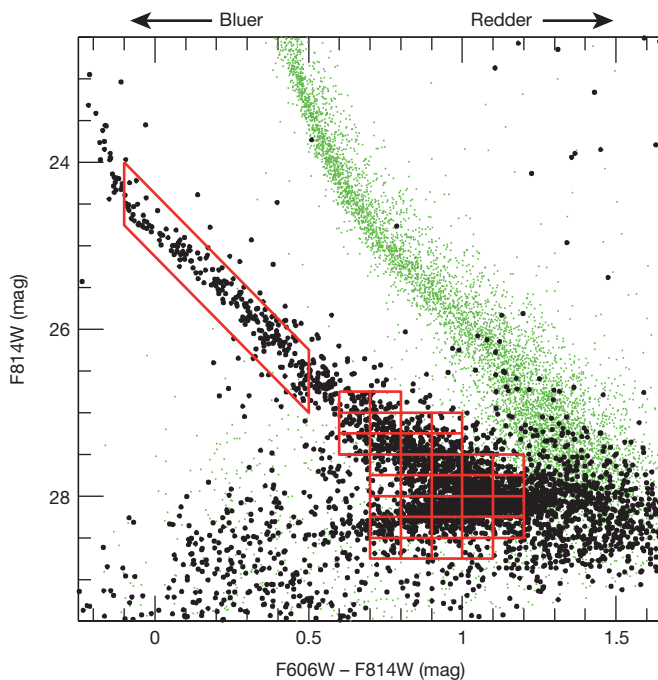


**Figure 1 | The 47 Tucanae white-dwarf cooling sequence.** The filled black points on the magnitude–colour plot are the proper-motion-selected white dwarfs of 47 Tucanae, and the small green points are those objects that fall outside the proper-motion cut. At brighter magnitudes (redder colours) these are members of the main-sequence population of the Small Magellanic Cloud, whereas at fainter magnitudes (bluer colours) they are mostly background galaxies. The grid outlined in red shows the binning used to compare the observations to the Monte Carlo populations.

<sup>1</sup>Division of Astronomy, University of California Los Angeles, Los Angeles, California 90095, USA. <sup>2</sup>Space Telescope Science Institute, 3700 San Martin Drive, Baltimore, Maryland 21218, USA. <sup>3</sup>Center for Astrophysical Sciences, Johns Hopkins University, Baltimore, Maryland 21218, USA. <sup>4</sup>Research School of Astronomy and Astrophysics, Australian National University, Weston Creek, Australian Capital Territory 2611, Australia. <sup>5</sup>Department of Physics and Astronomy, University of British Columbia, Vancouver, British Columbia, V6T 1Z1, Canada. <sup>6</sup>Department of Astrophysics, American Museum of Natural History, Central Park West and 79th Street, New York, New York 10024, USA. <sup>7</sup>NRC Herzberg, Victoria, British Columbia V9E 2E7, Canada. <sup>8</sup>Center for Astrophysics and Supercomputing, Swinburne University of Technology, Hawthorn, Victoria 3122, Australia. <sup>9</sup>Department of Astronomy, Box 351580, University of Washington, Seattle, Washington 98195, USA.

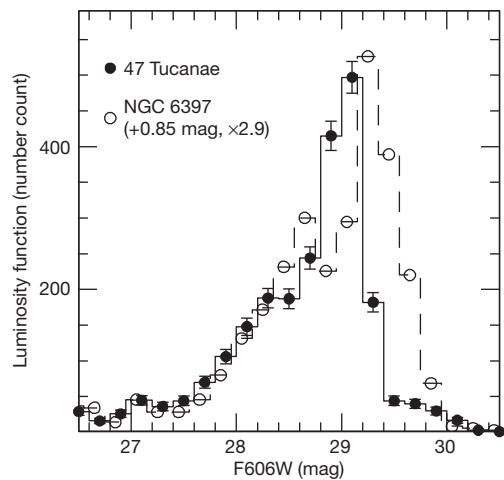


**Figure 2 | Luminosity function comparison between 47 Tucanae and NGC 6397.** The solid points and histogram show the white-dwarf luminosity function for 47 Tucanae, while the open circles and dashed histogram is the corresponding quantity for NGC 6397 (ref. 12), with error bars based on Poisson statistics. Each shows the characteristic behaviour of populations that result from a single burst of star formation, namely a sharp rise followed by a relatively abrupt truncation. In the case of NGC 6397 data, we have applied a horizontal shift of 0.85 magnitudes to correct for the different cluster distances and put them on the same magnitude scale, and the vertical scaling has been adjusted by a global multiplicative factor of 2.9 to correct for differences in the absolute numbers of the different populations. We see that the 47 Tucanae luminosity function clearly truncates at a brighter luminosity than that of NGC 6397, indicating that this cluster is younger.

To determine a quantitative measure of the age difference, we construct Monte Carlo models for the cooling of the cluster white-dwarf population, including a model for photometric shifts, scatter and incompleteness, based on artificial star tests. We fit these models, including the uncertainties in distance and extinction, to both the observed luminosity function and the two-dimensional distribution of the white-dwarf population in colour and magnitude (the Hess diagram). If we use the same models to fit the 47 Tucanae data as we did for NGC 6397 (ref. 12), we obtain an age of  $9.7 \pm 0.4$  billion years (Gyr) (at 95% confidence) for 47 Tucanae, compared to the corresponding value of  $11.7 \pm 0.3$  Gyr for NGC 6397. Therefore, the relative age difference is  $2.0 \pm 0.5$  Gyr.

The cluster 47 Tucanae has a metallicity<sup>14–16</sup> of  $[\text{Fe}/\text{H}] = -0.75$ , compared to  $[\text{Fe}/\text{H}] = -1.8$  for NGC 6397. Although white-dwarf atmospheres are not sensitive to overall metallicity, the cooling may be affected by changes in the nuclear burning history owing to different metallicities. To quantify any difference introduced by variations in progenitor behaviour, we have calculated new evolutionary models using progenitors of appropriate metallicity for 47 Tucanae. Using the MESA code<sup>17</sup>, we have calculated the evolution of solar-mass stars with  $[\text{Fe}/\text{H}] = -0.75$  and  $[\alpha/\text{Fe}] = +0.2$ , as well as with a range of helium enrichment Y (see Supplementary Information) seen in 47 Tucanae<sup>18</sup>. We have also verified that these calculations produce similar results to the models used to determine the age of the cluster from the main sequence<sup>19</sup>, to facilitate comparison with those earlier analyses. We find that the final age determination is not sensitive to either progenitor metallicity, helium fraction or which of the Schwarzschild or Ledoux criteria for convection is assumed when calculating the mixing of the progenitor core. Neither is the result sensitive to the use of different atmospheric models for correcting effective temperatures to observed colours. Details of this analysis are discussed in the Supplementary Information. Marginalizing over all these models results in an age of  $9.9 \pm 0.7$  Gyr for 47 Tucanae. Figure 3 shows the comparison between the best-fit model and the data, binned according to the grid in Fig. 1.

Estimates based on fitting main-sequence models to the main-sequence turnoff report ages between 10 Gyr and 13 Gyr, with the range

due to a variety of factors including differences in adopted models physics (such as nuclear reaction rates and gravitational settling) as well as different bandpasses employed in the observational data<sup>20–23</sup>. The most precise age so far obtained from the main sequence of 47 Tucanae comes from the detached, eclipsing binary star V69 (ref. 24). V69 comprises two stars that lie just above and below the main-sequence turnoff, meaning that the pair provides a particularly valuable age constraint. The resulting age is somewhat sensitive to the assumed metallicity of the stars. The original age estimate for V69 (ref. 24) was  $11.25 \pm 0.21 \pm 0.85$  Gyr, denoting random and systematic errors, respectively. This result is based on the assumption of  $[\text{Fe}/\text{H}] = -0.7$  and  $[\alpha/\text{Fe}] = +0.4$ . Adopting a chemical composition in accordance with more recent studies<sup>14–16</sup> and employing a more robust estimate of the systematic error implies that the age derived from the binary system is  $10.39 \pm 0.54$  Gyr, here citing only the systematic error. This estimate is fully consistent with the white-dwarf result given above, suggesting that consistency between the two age measurement techniques is possible, provided we also have accurate determination of extrinsic properties such as distance, reddening and metallicity.

The bimodality in the metallicity distribution of globular clusters appears to be ubiquitous among large galaxies<sup>1</sup>, and is held to reflect the sequence in which galaxies at high redshifts assemble their stellar mass. It is still disputed whether the two classes represent two distinct epochs of stellar assembly within a single dark matter halo, or whether some clusters are assembled early in smaller haloes and then later accreted<sup>25–27</sup>. Within this context, our result supports the idea that there is a measurable age difference between metal-poor and metal-rich globular clusters in the Milky Way. Figure 4 shows the relationship between white-dwarf-based age and metallicity for several Galactic populations. Including the uncertainties due to stellar models, 47 Tucanae has an

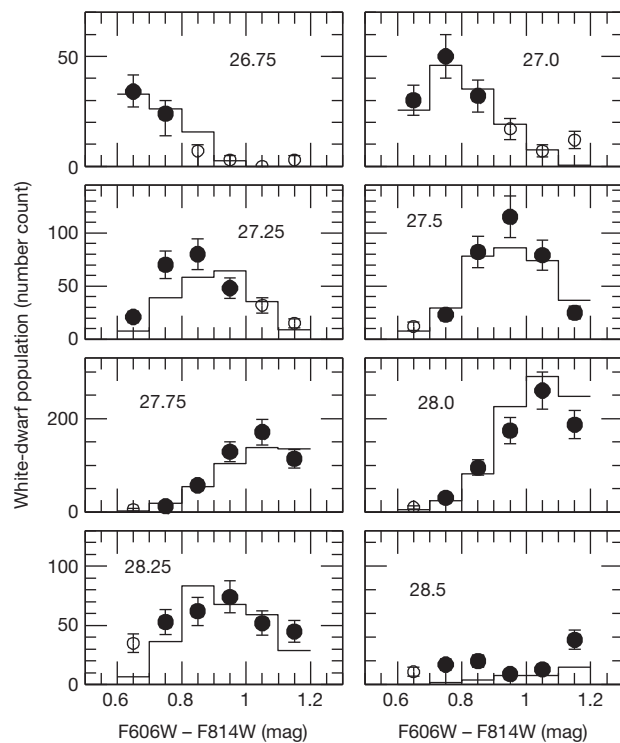


**Figure 3 | Model comparison to white-dwarf colour-magnitude distribution.** In each panel, the points show the number count of the white-dwarf population as a function of colour at fixed magnitude. Each panel is labelled with the corresponding central F814W magnitude. Filled circles are points that are included in the grid in Fig. 1, whereas open circles are not included, because they are expected to be dominated by residual contamination from background populations. Error bars are Poisson errors. The histogram is the model distribution binned in the same way, for an age of 9.7 Gyr and distance to the cluster  $\mu_{606W} = 13.38$  (see Supplementary Information).

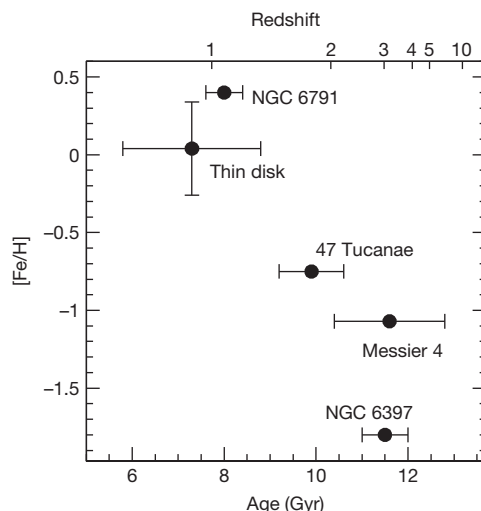


**Figure 4 | Age–metallicity relation based on white dwarfs.** Each point shows the age of a Galactic population as determined using the white-dwarf luminosity function, and the corresponding metallicity determined from main-sequence stars. The age of 47 Tucanae is determined here, while those of NGC 6397 (ref. 12), Messier 4 (ref. 13) and the open cluster NGC 6791 (ref. 28) are taken from the literature. The age of the thin disk is taken from an analysis of the white-dwarf population in the solar neighbourhood<sup>10</sup> and the metallicity error bar is determined from the range of metallicities measured for nearby stars<sup>29</sup>. The age uncertainties for all populations are quoted from the given references. The redshift axis uses the age–redshift relation appropriate to the WMAP (currently accepted) cosmology<sup>30</sup>. This demonstrates that the age difference derived here corresponds to the difference between  $z \approx 3$  and  $z \approx 2$ .

absolute age of  $9.9 \pm 0.7$  Gyr, which places its formation at a redshift of approximately two. This age is consistent with the model in which the metal-rich globular clusters are formed by the massive, star-forming events that are responsible for the peak in the global star-formation rate at this redshift, whether driven by mergers or in situ formation<sup>25–27</sup>.

Received 28 December 2012; accepted 17 May 2013.

1. Brodie, J. P. & Strader, J. Extragalactic globular clusters and galaxy formation. *Annu. Rev. Astron. Astrophys.* **44**, 193–267 (2006).
2. Fukugita, M., Hogan, C. J. & Peebles, P. J. E. The cosmic baryon budget. *Astrophys. J.* **503**, 518–530 (1998).
3. Zinn, R. The globular cluster system of the galaxy. IV—The halo and disk subsystems. *Astrophys. J.* **293**, 424–444 (1985).
4. Minniti, D. Metal-rich globular clusters with  $R \leq 3$  kpc: disk or bulge clusters. *Astron. J.* **109**, 1663–1669 (1995).
5. Salaris, M. & Weiss, A. Metal-rich globular clusters in the galactic disk: new age determinations and the relation to halo clusters. *Astron. Astrophys.* **335**, 943–953 (1998).
6. Rosenberg, A., Saviane, I., Piotto, G. & Aparicio, A. Galactic globular cluster relative ages. *Astron. J.* **118**, 2306–2320 (1999).
7. De Angeli, F. et al. Galactic globular cluster relative ages. *Astron. J.* **130**, 116–125 (2005).
8. Marin-Franch, A. et al. The ACS survey of galactic globular clusters. VII. Relative ages. *Astrophys. J.* **694**, 1498–1516 (2009).
9. Dotter, A., Sarajedini, A. & Anderson, J. Globular clusters in the Outer Galactic Halo: new Hubble Space Telescope/Advanced Camera for Surveys imaging of six

globular clusters and the Galactic Globular Cluster age–metallicity relation. *Astrophys. J.* **738**, 74–84 (2011).

10. Hansen, B. et al. The white dwarf cooling sequence of the globular cluster Messier 4. *Astrophys. J.* **574**, L155–L158 (2002).
11. Hansen, B. et al. Hubble Space Telescope observations of the white dwarf cooling sequence of M4. *Astrophys. J.* **155** (Suppl.), 551–576 (2004).
12. Hansen, B. et al. The white dwarf cooling sequence of NGC 6397, 2007. *Astrophys. J.* **671**, 380–401 (2007).
13. Bedin, L. R. et al. The end of the white dwarf cooling sequence in M4: An efficient approach. *Astrophys. J.* **697**, 965–979 (2009).
14. Koch, A. & McWilliam, A. A new abundance scale for the globular cluster 47 Tuc. *Astron. J.* **135**, 1551–1566 (2008).
15. McWilliam, A. & Bernstein, R. A. Globular cluster abundances from high-resolution integrated-light spectra. I. 47 Tuc. *Astrophys. J.* **684**, 326–347 (2008).
16. Carretta, E. et al. Intrinsic iron spread and a new metallicity scale for globular clusters. *Astron. Astrophys.* **508**, 695–706 (2009).
17. Paxton, B. et al. Modules for experiments in stellar astrophysics (MESA). *Astrophys. J.* **192** (Suppl.), 3–37 (2011).
18. Milone, A. et al. Multiple stellar populations in 47 Tucanae. *Astrophys. J.* **744**, 58–79 (2012).
19. Dotter, A. et al. The ACS survey of galactic globular clusters. II. Stellar evolution tracks, isochrones, luminosity functions, and synthetic horizontal-branch models. *Astron. J.* **134**, 376–390 (2007).
20. Gratton, R. G. et al. Distances and ages of NGC 6397, NGC 6752 and 47 Tuc. *Astron. Astrophys.* **408**, 529–543 (2003).
21. Vandenberg, D. A. Models for old, metal-poor stars with enhanced -element abundances. II. Their implications for the ages of the galaxy's globular clusters and field halo stars. *Astrophys. J.* **129** (Suppl.), 315–352 (2000).
22. Salaris, M. & Weiss, A. Homogeneous age dating of 55 Galactic globular clusters. Clues to the Galaxy formation mechanisms. *Astron. Astrophys.* **388**, 492–503 (2002).
23. Salaris, M. et al. Deep near-infrared photometry of the globular cluster 47 Tucanae. Reconciling theory and observations. *Astron. Astrophys.* **476**, 243–253 (2007).
24. Thompson, Y. B. et al. The Cluster AgeS Experiment (CASE). IV. Analysis of the eclipsing binary V69 in the globular cluster 47 Tuc. *Astron. J.* **139**, 329–341 (2010).
25. Muratov, A. L. & Gnedin, O. Y. Modeling the metallicity distribution of globular clusters. *Astrophys. J.* **718**, 1266 (2010).
26. Shapiro, K. L., Genzel, R. & Förster Schreiber, N. M. Star-forming galaxies at  $z \sim 2$  and the formation of the metal-rich globular cluster population. *Mon. Not. R. Astron. Soc.* **403**, L36–L40 (2010).
27. Tonini, C. The metallicity bimodality of globular cluster systems: a test of galaxy assembly and the evolution of the galaxy mass–metallicity relation. *Astrophys. J.* **762**, 39–50 (2013).
28. García-Berro, E. et al. A white dwarf cooling age of 8Gyr for NGC 6791 from physical separation processes. *Nature* **465**, 194–196 (2010).
29. Valenti, J. A. & Fischer, D. A. Spectroscopic properties of cool stars (SPOCS). I. 1040 F, G, and K Dwarfs from Keck, Lick, and AAT planet search programs. *Astrophys. J.* **159** (Suppl.), 141–166 (2005).
30. Wright, E. L. A cosmology calculator for the World Wide Web. *Pub. Astron. Soc. Pacif.* **118**, 1711–1715 (2006).

**Supplementary Information** is available in the online version of the paper.

**Acknowledgements** Support for the programme GO-11677 was provided by NASA through a grant from the Space Telescope Science Institute, which is operated by the Association of Universities for Research in Astronomy, Inc., under NASA contract NAS 5-26555. This work is supported in part by the Natural Science and Engineering Research Council of Canada.

**Author Contributions** B.M.S.H. and A.D. were primarily responsible for the modelling efforts. J.S.K. and J.A. were primarily responsible for the analysis of the data. H.B.R., R.M.R. and D.R. were responsible for the scheduling of the observations. All authors, including M.M.S., G.G.F., J.R.H., I.R.K. and P.B.S. were involved in the conception and planning of the project and in the writing of the paper.

**Author Information** Reprints and permissions information is available at [www.nature.com/reprints](http://www.nature.com/reprints). The authors declare no competing financial interests. Readers are welcome to comment on the online version of the paper. Correspondence and requests for materials should be addressed to B.M.S.H. (hansen@astro.ucla.edu).

# Nanometre-scale thermometry in a living cell

G. Kucsko<sup>1\*</sup>, P. C. Maurer<sup>1\*</sup>, N. Y. Yao<sup>1</sup>, M. Kubo<sup>2</sup>, H. J. Noh<sup>3</sup>, P. K. Lo<sup>4</sup>, H. Park<sup>1,2,3</sup> & M. D. Lukin<sup>1</sup>

Sensitive probing of temperature variations on nanometre scales is an outstanding challenge in many areas of modern science and technology<sup>1</sup>. In particular, a thermometer capable of subdegree temperature resolution over a large range of temperatures as well as integration within a living system could provide a powerful new tool in many areas of biological, physical and chemical research. Possibilities range from the temperature-induced control of gene expression<sup>2–5</sup> and tumour metabolism<sup>6</sup> to the cell-selective treatment of disease<sup>7,8</sup> and the study of heat dissipation in integrated circuits<sup>1</sup>. By combining local light-induced heat sources with sensitive nanoscale thermometry, it may also be possible to engineer biological processes at the subcellular level<sup>2–5</sup>. Here we demonstrate a new approach to nanoscale thermometry that uses coherent manipulation of the electronic spin associated with nitrogen–vacancy colour centres in diamond. Our technique makes it possible to detect temperature variations as small as 1.8 mK (a sensitivity of  $9 \text{ mK Hz}^{-1/2}$ ) in an ultrapure bulk diamond sample. Using nitrogen–vacancy centres in diamond nanocrystals (nanodiamonds), we directly measure the local thermal environment on length scales as short as 200 nanometres. Finally, by introducing both nanodiamonds and gold nanoparticles into a single human embryonic fibroblast, we demonstrate

temperature-gradient control and mapping at the subcellular level, enabling unique potential applications in life sciences.

Many promising approaches to local temperature sensing<sup>1</sup> are being explored at present. These include scanning probe microscopy<sup>1,9</sup>, Raman spectroscopy<sup>10</sup>, and fluorescence-based measurements using nanoparticles<sup>11,12</sup> and organic dyes<sup>13,14</sup>. Fluorescent polymers<sup>13</sup> and green fluorescent proteins<sup>14</sup> have recently been used for temperature mapping within a living cell. However, many of these existing methods are limited by drawbacks such as low sensitivity and systematic errors due to fluctuations in the fluorescence rate<sup>11,12</sup>, the local chemical environment<sup>13</sup> and the optical properties of the surrounding medium<sup>14</sup>. Moreover, although promising, methods based on green fluorescent proteins rely on cellular transfection<sup>14</sup> that proves to be difficult to achieve in certain primary cell types<sup>15</sup>. Our new approach to nanoscale thermometry uses the quantum mechanical spin associated with nitrogen–vacancy colour centres in diamond. As illustrated in Fig. 1b, in its electronic ground state each nitrogen–vacancy centre constitutes a spin-1 system. These spin states can be coherently manipulated using microwave pulses and efficiently initialized and detected by means of laser illumination (Supplementary Information). In the absence of an external magnetic field, the precise value of the transition frequency

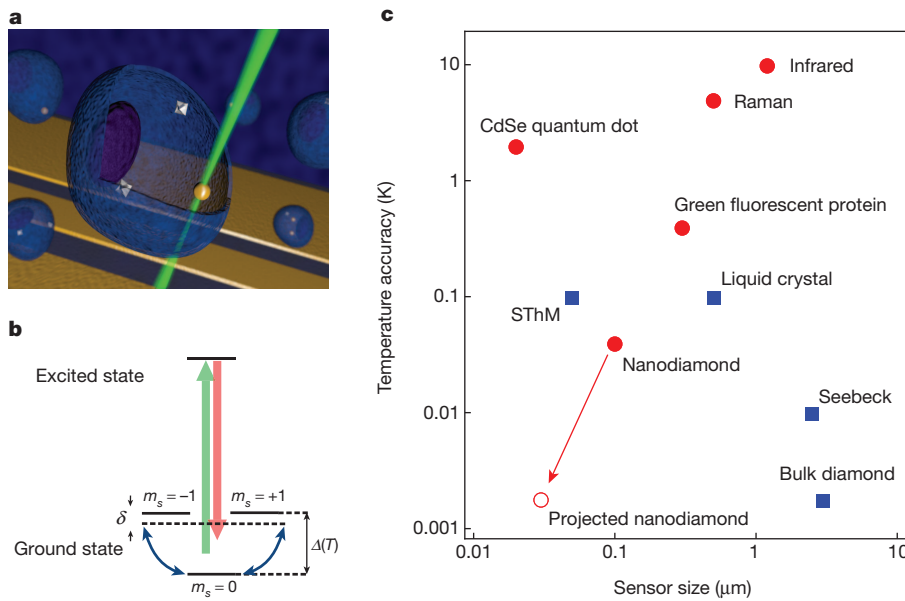


**Figure 1 | Nitrogen–vacancy-based nanoscale thermometry.** **a**, Schematic image depicting nanodiamonds (grey diamonds) and a gold nanoparticle (yellow sphere) within a living cell (central blue object; others are similar) with coplanar waveguide (yellow stripes) in the background. The controlled application of local heat is achieved by laser illumination of the gold nanoparticle, and nanoscale thermometry is achieved by precision spectroscopy of the nitrogen–vacancy spins in the nanodiamonds. **b**, Simplified nitrogen–vacancy level diagram showing a ground-state spin triplet and an

excited state. At zero magnetic field, the  $|\pm 1\rangle$  sublevels are split from the  $|0\rangle$  state by a temperature-dependent zero field splitting  $\Delta(T)$ . Pulsed microwave radiation is applied (detuning,  $\delta$ ) to perform Ramsey-type spectroscopy.

**c**, Comparison of sensor sizes and temperature accuracies for the nitrogen–vacancy quantum thermometer and other reported techniques. Red circles indicate methods that are biologically compatible. The open red circle indicates the ultimate expected accuracy for our measurement technique in solution (Methods).

<sup>1</sup>Department of Physics, Harvard University, Cambridge, Massachusetts 02138, USA. <sup>2</sup>Department of Chemistry and Chemical Biology, Harvard University, Cambridge, Massachusetts 02138, USA. <sup>3</sup>Broad Institute of MIT and Harvard University, 7 Cambridge Center, Cambridge, Massachusetts 02142, USA. <sup>4</sup>Department of Biology and Chemistry, City University of Hong Kong, Tat Chee Avenue, Kowloon, Hong Kong SAR, China.

\*These authors contributed equally to this work.

( $\Delta$ ) between the  $|m_s = 0\rangle$  and  $|m_s = \pm 1\rangle$  states ( $m_s$ , spin projection) has a temperature dependence ( $d\Delta/dT = -2\pi \times 77 \text{ kHz K}^{-1}$ ) due to thermally induced lattice strains<sup>16–18</sup>.

The operational principle of nitrogen–vacancy-based thermometry relies on the accurate measurement of this transition frequency, which can be optically detected with high spatial resolution (Fig. 1). For a sensor containing  $N$  colour centres, the temperature sensitivity is given by

$$\eta = \frac{1}{Cd\Delta/dT} \frac{1}{\sqrt{T_{\text{coh}}Nt}}$$

where  $T_{\text{coh}}$  is the nitrogen–vacancy spin coherence time and  $t$  is the integration time. Here we also introduce a factor,  $C$ , to account for imperfections in readout and initialization<sup>19</sup>. If  $T_{\text{coh}}$  is of the order of a few milliseconds and  $C \approx 0.03$  (ref. 19), then a single nitrogen–vacancy can potentially exhibit a sensitivity better than  $1 \text{ mK Hz}^{-1/2}$ . Apart from high sensitivity, nitrogen–vacancy-based thermometry also offers several distinct advantages over existing methods in biological and chemical temperature sensing. First, owing to diamond’s chemical inertness, it is generally robust to changes in the local chemical environment. Second, it can be applied over a wide range of temperatures (200–600 K; refs 17, 18), which is of particular interest in the study of nanoscale chemical reactions<sup>20</sup>.

As a benchmark experiment, we demonstrate the high temperature sensitivity of nitrogen–vacancy-based thermometry in a bulk diamond sample. Although the nitrogen–vacancy’s magnetic sensitivity has rendered it a competitive magnetometer<sup>21,22</sup>, to determine the temperature accurately it is necessary to decouple the nitrogen–vacancy electronic spin from fluctuating external magnetic fields. This is achieved using a modified spin-echo sequence that makes use of the spin-1 nature of the nitrogen–vacancy defect<sup>23</sup>, allowing us to eliminate the effects of an external, slowly varying magnetic field. Specifically, we apply a microwave pulse at frequency  $\omega$  (Fig. 1b) to create a coherent superposition  $(|0\rangle + |B\rangle)/\sqrt{2}$ , where  $|B\rangle = (|+1\rangle + |-1\rangle)/\sqrt{2}$ . After half the total evolution time,  $\tau$ , we apply a  $2\pi$  echo pulse that swaps the population of the  $|+1\rangle$  and  $|-1\rangle$  states (Fig. 2a). Following another period of free evolution for time  $\tau$ , quasistatic, magnetic-field-induced shifts of these  $|\pm 1\rangle$  levels are eliminated, allowing for accurate temperature sensing. In the experiment, we use a sample of isotopically pure diamond (99.99% spinless  $^{12}\text{C}$  isotope) grown by chemical vapour deposition<sup>24</sup> to further reduce magnetic field fluctuations originating from the intrinsic  $^{13}\text{C}$  nuclear spin bath. As shown in Fig. 2a, this allows us to observe coherence

fringes for up to 0.5 ms. Notably, for all nitrogen–vacancies tested, we observe a characteristic low-frequency beating of the fluorescence signal that varies from defect to defect, which is most probably due to locally fluctuating charge traps<sup>25</sup>. Despite this beating, for a fixed evolution time  $2\tau$ , the nitrogen–vacancy spin depends sensitively on the sample temperature (Fig. 2b). We observe a temperature sensitivity of  $\eta = (9 \pm 1.8) \text{ mK Hz}^{-1/2}$  for  $2\tau = 250 \mu\text{s}$ . For 30 s of integration, we achieve a measurement accuracy of  $\delta T = 1.8 \pm 0.3 \text{ mK}$  (Methods). Although the measurement sequence for a single value of  $2\tau$  allows us to determine the temperature only up to a multiple of  $(2d\Delta/dT2\tau)^{-1}$ , absolute temperature variations can be determined by repeating the measurement for  $2\tau' < 2\tau$ , as shown in Fig. 2b.

We now demonstrate the high spatial resolution of nitrogen–vacancy-based thermometry. This is achieved by using nanodiamonds. In most commercially available nanodiamonds, the nitrogen–vacancy coherence time is limited to approximately 1  $\mu\text{s}$  owing to additional paramagnetic impurities. Although this shortened coherence time reduces the intrinsic temperature sensitivity for a single defect, this decrease can be offset by using an ensemble of nitrogen–vacancies to enhance the signal-to-noise ratio by a factor of  $\sqrt{N}$ . We note that, unlike nitrogen–vacancy-based magnetometry, where the proximity to the source (often limited by the nanodiamond size) is critical to the maximum sensitivity, nitrogen–vacancy thermometry is not subject to such a constraint; in fact, the excellent thermal conductivity of diamond ensures that all nitrogen–vacancy centres within a nanocrystal are in thermal equilibrium with the local heat environment. To maximize the number of nitrogen–vacancy centres and to minimize the lattice strain, our measurements are performed on single-crystalline nanodiamonds containing approximately 500 nitrogen–vacancy centres (Adamas Nanotechnologies). The zero-field splitting,  $\Delta$ , of the nitrogen–vacancy ensemble, and, thus, the temperature, is determined by recording a continuous-wave electron spin resonance (ESR) spectrum. Specifically, we measure changes to the zero-field splitting by recording the fluorescence at four different frequencies centred around  $\Delta = 2\pi \times 2.87 \text{ GHz}$  (Fig. 3a). This procedure eliminates unwanted effects from fluctuations in the total fluorescence rate, ESR contrast, Rabi frequency and magnetic field, yielding a robust thermometer (Methods).

Combining our nanodiamond thermometer with the laser heating of a gold nanoparticle allows us to both monitor and control temperature at nanometre length scales (Fig. 3). Both nanodiamonds and gold nanoparticles (nominal diameter, 100 nm) are initially spin-coated on a microscope coverslip. Using a confocal microscope with two independent scanning beams, we co-localize gold nanoparticles and nanodiamonds

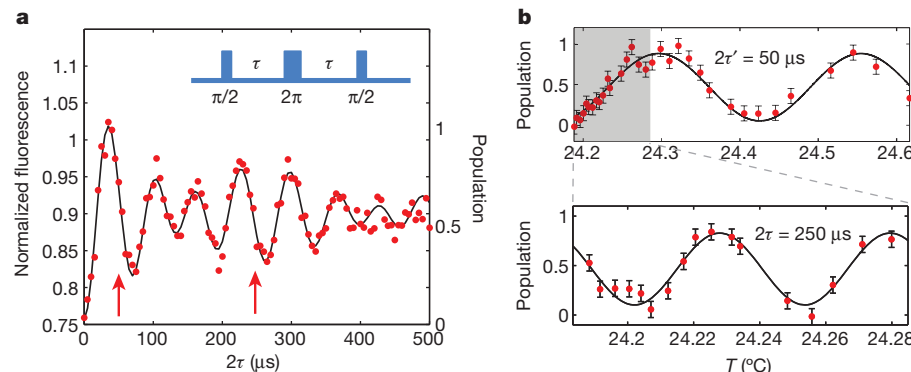


**Figure 2 | Sensitivity of single nitrogen–vacancy thermometer.** **a**, Measured fluorescence as a function of echo evolution time,  $2\tau$  (red points); the black solid line indicates a fit corresponding to a damped cosine function with two distinct frequencies. The characteristic beating can be explained by fluctuating proximal charge traps separated from the nitrogen–vacancy centre by a distance of about 50 nm. Inset, the microwave  $2\pi$  echo pulse sequence used to cancel unwanted external magnetic field fluctuations<sup>23</sup>. **b**, Measured fluorescence (red points) as a function of temperature for echo times of

$2\tau = 250 \mu\text{s}$  (bottom) and  $2\tau' = 50 \mu\text{s}$  (top). Black lines, best fits; errors,  $1\sigma$ . The fixed evolution times of  $2\tau$  and  $2\tau'$  are indicated in **a** by red arrows. The temperature is controlled by a Peltier element at the sample mount, and the (local)  $x$ -axis temperature is determined using a thermistor located immediately next to the sample. The fluorescence is converted to population by normalizing to two reference measurements where the spin is prepared with  $m_s = 0$  and, respectively,  $m_s = -1$ .

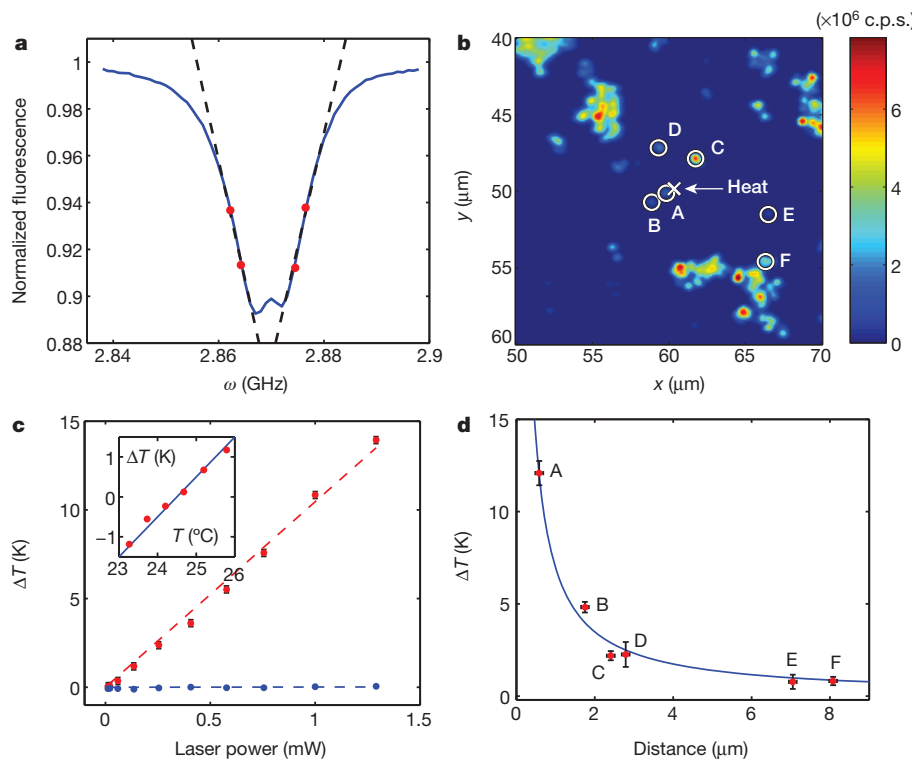


**Figure 3 | Submicrometre thermometry using nanodiamonds.** **a**, Frequency scan of a single nanodiamond containing approximately 500 nitrogen–vacancy centres. The four red points indicate the measurement frequencies used to extract the temperature as detailed in Methods. **b**, Two-dimensional confocal scan of nanodiamonds (circles) and a gold nanoparticle (cross) spin-coated onto a glass coverslip. The colour bar represents fluorescence, expressed in counts per second (c.p.s.). **c**, Temperature of a single nanodiamond as a function of laser power for two different laser focus locations. The red data points depict the pronounced heating of a nanodiamond as a result of laser illumination of a nearby gold nanoparticle. The blue data points depict the same measurement with the laser focus displaced by 0.8 μm from the nanoparticle location; this results in negligible heating of the nanodiamond as a function of laser power. Inset, the measured temperature change of a nanodiamond, when the surrounding temperature is controlled by a Peltier element. **d**, Temperature changes measured (red points) at the six nanodiamond locations in **b** as a function of distance from the illuminated gold nanoparticle (cross). The blue curve is the theoretical temperature profile based on a steady-state solution of the heat equation. All data in this figure were obtained on a glass coverslip, and all error bars correspond to  $1\sigma$ .

with a resolution of  $\sim 100$  nm (Supplementary Information). While locally heating the gold nanoparticles by continuous illumination with a variable-power green laser (focused to a diffraction-limited spot), we simultaneously measure the temperature at the nanodiamond location using ESR spectroscopy.

The ability to measure temperature with nanodiamonds is verified by heating the substrate temperature over a range of 2.5 K and simultaneously monitoring the zero-field splitting (Fig. 3c, inset). To demonstrate nanoscale temperature control, in Fig. 3c (red points) we show the temperature change recorded by the nanodiamond as a function of the green-laser power applied to the gold nanoparticle at a distance of  $0.8 \pm 0.1$  μm. To verify further that the temperature change results from local heating, we repeat the measurement with the excitation laser displaced from the nanodiamond by 0.8 μm in the opposite direction. In this case, the temperature measured by the nanodiamond remained constant as a function of laser power (Fig. 3c, blue points), thereby confirming the locality of the heat source. From a linear fit to the data, we estimate the accuracy of our nitrogen–vacancy sensor to be  $\delta T = 44 \pm 10$  mK. The measured temperature change agrees with the theoretically expected temperature profile based on a steady-state solution of the heat equation,  $\Delta T(r) = \dot{Q}/4\pi\kappa r$ , where  $\dot{Q}$  is the heat dissipation,  $\kappa$  is the thermal conductivity of glass and  $r$  is the distance between the nanodiamond and the gold nanoparticle. As shown in Fig. 3b, by recording the temperature of six nanodiamonds at different distances from the laser-heated gold nanoparticle we find that the measured temperature profile (Fig. 3d, points) is in excellent agreement with the theoretical steady-state prediction (solid line). This allows us directly to estimate the temperature change at the location of the gold nanoparticle to be  $72 \pm 6$  K.

To demonstrate that nanodiamond thermometry is compatible with living cells, we introduce nanodiamonds and gold nanoparticles into human embryonic fibroblast WS1 cells using nanowire-assisted delivery<sup>15</sup>. Just as in the control experiments described above, we probe the temperature at two different nitrogen–vacancy locations ( $NV_1$  and  $NV_2$ ) within a single cell while locally heating an individual gold nanoparticle

(Fig. 4a). As shown in Fig. 4b,  $NV_1$ , which is significantly closer to the heat source, has a stronger temperature dependence as a function of laser power than does  $NV_2$ . Varying the incident power allows us to generate controlled temperature differences of up to 5 K over distances of approximately 7 μm. To ensure that this temperature gradient is created by the controlled illumination of the nanoparticle and does not result from heating of the cellular cytoplasm, we displace the laser spot from the gold nanoparticle. This results in a negligible temperature change at the location of  $NV_1$  with  $\Delta T = -20 \pm 50$  mK (Fig. 4b, green square). The increased measurement uncertainty for larger laser powers is the result of heating fluctuations from drift of the gold nanoparticle.

The experiments shown in Fig. 4b demonstrate the submicrometre measurement of an intracellular heat gradient. However, the substantial heating induced by constant illumination for an extended period of time ultimately leads to the death of the cell, which is confirmed using a standard live/dead assay (calcein AM/ethidium homodimer-1). To demonstrate that our technique can be used within living cells, we increase the concentration of gold nanoparticles to allow for heat generation at different locations simply by moving the laser focus. Then we measure the temperature variation at a single nanodiamond (Fig. 4c, bar graph) while slightly heating the gold nanoparticles in two different locations (crosses). After our measurement, the viability of the cell is confirmed (Fig. 4c).

Finally, we demonstrate that our method can be used to control cell viability. To start, we heat the cell with 12 μW of laser power and measure a temperature change of  $0.5 \pm 0.2$  K at the nanodiamond location; this corresponds to a change of approximately 10 K at the position of the gold nanoparticle. At this point, the cell is still alive, as confirmed by the absence of ethidium homodimer-1 fluorescence inside the membrane (Fig. 4d). By increasing the laser power to 120 μW, we induce a temperature change of  $3.9 \pm 0.1$  K at the nanodiamond location (approximately 80 K at the location of the laser focus); in this case, the cell is flooded with fluorescence from the ethidium homodimer, signalling cell death. This proof-of-principle experiment indicates that

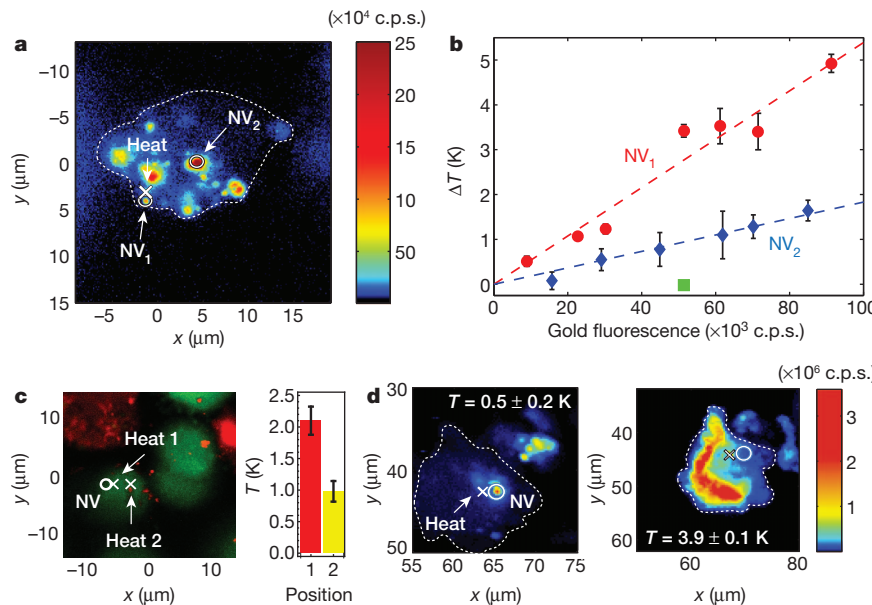


**Figure 4 | Nanoscale thermometry in cells.** **a**, Confocal scan of a single cell under laser excitation at a wavelength of 532 nm, with collection at wavelengths greater than 638 nm. The cross marks the position of the gold nanoparticle used for heating, and circles represent the location of the nanodiamonds ( $NV_1$  and  $NV_2$ ) used for thermometry. The dotted line provides a guide to the eye and outlines the cell membrane. Colour bars indicate the fluorescence in counts per second. **b**, Measured change in temperature at the positions of  $NV_1$  and  $NV_2$  relative to the incident laser power applied to the gold nanoparticle. Dashed lines are linear fits to the data. Each point consists of an average of five measurements, with each individual measurement taking 4 s. The error bars

( $1\sigma$ ) are set by fluctuations in the laser heating of the gold nanoparticle. **c**, Fluorescence scan of stained cells (live/dead assay) with excitation at 494 or 528 nm and emission at 515 nm (green; live cells) and 617 nm (red; dead cells). The bar graph shows the temperature of a single nanodiamond (circle) with local heat applied at two different locations (crosses). **d**, Confocal fluorescence scans of an individual cell under varying illumination power. Excitation occurs at 532 nm and collection is above 630 nm. Cell death is indicated by the penetration of ethidium homodimer-1 through the cell membrane, staining the nucleus. At low laser powers, the cell remains alive; cell death occurs as laser-induced heating is increased.

nanodiamond thermometry may enable the optimization of nanoparticle-based photothermal therapies<sup>8</sup>.

Our experiments demonstrate that nitrogen–vacancy centres in diamond can be used as robust temperature sensors that combine the virtues of submicrometre spatial resolution, subdegree thermal sensitivity and biocompatibility. The sensitivity of our current measurement can be enhanced by increasing the relevant coherence time or the number of nitrogen–vacancy centres within the nanocrystal, or both. Optimizing these factors should allow us to reach sensitivities of  $80 \mu\text{K Hz}^{-1/2}$  (Methods), yielding the ability to sense subkelvin temperature variations with millisecond time resolution. In solution, the ultimate accuracy of our method will probably be limited by residual heating during the measurement process. As discussed in the Methods, this limit is in the range of 0.05–5 mK, depending on experimental conditions. Although the present work focuses on monitoring temperature variations, the use of diamond samples with low strain, or, alternatively, ensembles of nanodiamonds, should allow for the realization of an absolute thermometer (Methods). The spatial resolution of our method can be further improved by using far-field subdiffraction techniques<sup>26</sup>.

The present observations raise a number of intriguing possibilities. For instance, the simultaneous measurement and control of a subcellular thermal gradient could enable the accurate control of gene expression<sup>27</sup>. Further improvements in sensitivity may allow for real-time observations of non-equilibrium subcellular processes in biological and medical applications<sup>11</sup>. The large dynamic range of our quantum thermometer and its intrinsic robustness may also allow for the direct microscopic monitoring and control of chemical reactions<sup>20</sup>. Moreover, combining our technique with two-photon microscopy<sup>28,29</sup> may enable *in vivo* identification of local tumour activity by mapping atypical thermogenesis at the single-cell level<sup>30</sup>. Finally the combination of thermoablative therapy with our temperature sensor could be a potent tool for the selective identification and killing of malignant cells without damaging surrounding tissue<sup>7,8</sup>.

## METHODS SUMMARY

**Nanodiamond measurement pulse sequence.** As indicated in Fig. 3a, we record the fluorescence at four different frequencies centred on  $\Delta = 2\pi \times 2.87 \text{ GHz}$ :

$$\begin{aligned} f^1 &\approx f(\omega_-) + \frac{\partial f}{\partial \omega} \Big|_{\omega_-} \left( -\delta\omega + \delta\beta + \delta T \frac{d\Delta}{dT} \right) \\ f^2 &\approx f(\omega_-) + \frac{\partial f}{\partial \omega} \Big|_{\omega_-} \left( \delta\omega + \delta\beta + \delta T \frac{d\Delta}{dT} \right) \\ f^3 &\approx f(\omega_+) + \frac{\partial f}{\partial \omega} \Big|_{\omega_+} \left( -\delta\omega - \delta\beta + \delta T \frac{d\Delta}{dT} \right) \\ f^4 &\approx f(\omega_+) + \frac{\partial f}{\partial \omega} \Big|_{\omega_+} \left( \delta\omega - \delta\beta + \delta T \frac{d\Delta}{dT} \right) \end{aligned}$$

This allows us to determine the change in temperature:

$$\delta T = \frac{\delta\omega}{d\Delta/dT} \frac{(f^1 + f^2) - (f^3 + f^4)}{(f^1 - f^2) + (f^3 - f^4)} \quad (1)$$

Here  $\omega_{\pm} \mp \delta\omega$  are the four microwave carrier frequencies and  $\delta\beta$  is an unknown static magnetic field. By using the fluorescence at these four frequencies as shown in equation (1), we are able to remove errors associated with changes in total fluorescence rate, ESR contrast, Rabi frequency and magnetic field.

**Full Methods** and any associated references are available in the online version of the paper.

Received 19 March; accepted 10 June 2013.

- Yue, Y. & Wang, X. Nanoscale thermal probing. *Nano Rev.* <http://dx.doi.org/10.3402/nano.v3i0.11586> (2012).
- Lucchetta, E., Lee, J., Fu, L., Patel, N. & Ismagilov, R. Dynamics of *Drosophila* embryonic patterning network perturbed in space and time using microfluidics. *Nature* **434**, 1134–1138 (2005).
- Kumar, S. V. & Wigge, P. A. H2A.Z-containing nucleosomes mediate the thermosensory response in *Arabidopsis*. *Cell* **140**, 136–147 (2010).
- Lauschke, V. M., Tsiairis, C. D., François, P. & Aulehla, A. Scaling of embryonic patterning based on phase-gradient encoding. *Nature* **493**, 101–105 (2012).

5. Kamei, Y. *et al.* Infrared laser-mediated gene induction in targeted single cells *in vivo*. *Nature Methods* **6**, 79–81 (2009).
6. Vreugdenburg, T., Willis, C., Mundy, L. & Hiller, J. A systematic review of elastography, electrical impedance scanning, and digital infrared thermography for breast cancer screening and diagnosis. *Breast Cancer Res. Treat.* **137**, 665–676 (2013).
7. Schroeder, A. *et al.* Treating metastatic cancer with nanotechnology. *Nature Rev. Cancer* **12**, 39–50 (2011).
8. O'Neal, D. P., Hirsch, L. R., Halas, N. J., Payne, J. D. & West, J. L. Photo-thermal tumor ablation in mice using near infrared-absorbing nanoparticles. *Cancer Lett.* **209**, 171–176 (2004).
9. Majumdar, A. Scanning thermal microscopy. *Annu. Rev. Mater. Sci.* **29**, 505–585 (1999).
10. Kim, S. H. *et al.* Micro-Raman thermometry for measuring the temperature distribution inside the microchannel of a polymerase chain reaction chip. *J. Micromech. Microeng.* **16**, 526 (2006).
11. Yang, J., Yang, H. & Lin, L. Quantum dot nano thermometers reveal heterogeneous local thermogenesis in living cells. *ACS Nano* **5**, 5067–5071 (2011).
12. Vetrone, F. *et al.* Temperature sensing using fluorescent nanothermometers. *ACS Nano* **4**, 3254–3258 (2010).
13. Okabe, K. *et al.* Intracellular temperature mapping with a fluorescent polymeric thermometer and fluorescence lifetime imaging microscopy. *Nature Commun.* **3**, 705 (2012).
14. Donner, J., Thompson, S., Kreuzer, M., Baffou, G. & Quidant, R. Mapping intracellular temperature using green fluorescent protein. *Nano Lett.* **12**, 2107–2111 (2012).
15. Shalek, A. K. *et al.* Vertical silicon nanowires as a universal platform for delivering biomolecules into living cells. *Proc. Natl. Acad. Sci. USA* **107**, 1870–1875 (2010).
16. Acosta, V. *et al.* Temperature dependence of the nitrogen-vacancy magnetic resonance in diamond. *Phys. Rev. Lett.* **104**, 070801 (2010).
17. Toyli, D. *et al.* Measurement and control of single nitrogen-vacancy center spins above 600 K. *Phys. Rev. X* **2**, 031001 (2012).
18. Chen, X.-D. *et al.* Temperature dependent energy level shifts of nitrogen-vacancy centers in diamond. *Appl. Phys. Lett.* **99**, 161903–161903 (2011).
19. Taylor, J. *et al.* High-sensitivity diamond magnetometer with nanoscale resolution. *Nature Phys.* **4**, 810–816 (2008).
20. Jin, C., Li, Z., Williams, R., Lee, K. & Park, I. Localized temperature and chemical reaction control in nanoscale space by nanowire array. *Nano Lett.* **11**, 4818–4825 (2011).
21. Maze, J. *et al.* Nanoscale magnetic sensing with an individual electronic spin in diamond. *Nature* **455**, 644–647 (2008).
22. Balasubramanian, G. *et al.* Nanoscale imaging magnetometry with diamond spins under ambient conditions. *Nature* **455**, 648–651 (2008).
23. Hodges, J. *et al.* Time keeping with electron spin states in diamond. *Phys. Rev. A* **87**, 032118 (2013).
24. Balasubramanian, G. *et al.* Ultralong spin coherence time in isotopically engineered diamond. *Nature Mater.* **8**, 383–387 (2009).
25. Dolde, F. *et al.* Electric-field sensing using single diamond spins. *Nature Phys.* **7**, 459–463 (2011).
26. Maurer, P. *et al.* Far-field optical imaging and manipulation of individual spins with nanoscale resolution. *Nature Phys.* **6**, 912–918 (2010).
27. Xu, G. *et al.* Identification of proteins sensitive to thermal stress in human neuroblastoma and glioma cell lines. *PLoS ONE* **7**, e49021 (2012).
28. Helmchen, F. & Denk, W. Deep tissue two-photon microscopy. *Nature Methods* **2**, 932–940 (2005).
29. Wee, T.-L. *et al.* Two-photon excited fluorescence of nitrogen-vacancy centers in proton-irradiated type Ib diamond. *J. Phys. Chem. A* **111**, 9379–9386 (2007).
30. Tsoli, M. *et al.* Activation of thermogenesis in brown adipose tissue and dysregulated lipid metabolism associated with cancer cachexia in mice. *Cancer Res.* **72**, 4372–4382 (2012).

**Supplementary Information** is available in the online version of the paper.

**Acknowledgements** We thank R. Walsworth, V. Denic, C. Latta, L. Jiang, A. Gorshkov, P. Cappellaro, A. Sushkov and I. Lovchinsky for discussions and help with experiments. This work was supported by the NSF, the Center for Ultracold Atoms, the Defense Advanced Research Projects Agency (QUASAR programme), the Army Research Office (MURI programme), the Packard Foundation, NIH Pioneer Awards (5DP1OD003893-03), the NHGRI (1P50HG006193-01) and the Swiss National Science Foundation (PBSKP2\_143918) (P.C.M.).

**Author Contributions** P.C.M., H.J.N., H.P. and M.D.L. developed the idea for the study. G.K., P.C.M. and N.Y.Y. designed and conducted the experiments and analysed the data. M.K., P.K.L. and H.P. prepared the biological samples. All authors participated in discussions and writing of the manuscript.

**Author Information** Reprints and permissions information is available at [www.nature.com/reprints](http://www.nature.com/reprints). The authors declare no competing financial interests. Readers are welcome to comment on the online version of the paper. Correspondence and requests for materials should be addressed to H.P. (hongkun\_park@harvard.edu) or M.D.L. (lukin@physics.harvard.edu).

## METHODS

**Experimental apparatus, sensitivity and accuracy.** Our experimental apparatus consists of a confocal microscope with two independent excitation–collection paths, allowing measurement and heating at two independent locations simultaneously. The experiments use either a Nikon Plan Fluor  $\times 100$ , oil immersion, NA = 1.3 objective (nanodiamonds) or a Nikon Plan Apo  $\times 100$ , air, NA = 0.95 objective (bulk sample), resulting in  $C \approx 0.03$ , which can be further improved by employing a solid immersion lens or diamond nanopatterning. Microwaves are delivered using a lithographically defined coplanar waveguide on top of a glass coverslip. For experiments with nanodiamonds, we use neutral-density filters in the collection path to avoid saturation of the avalanche photodiode. The temperature accuracy,  $\delta T$ , for bulk diamond is estimated from the measurement shown in Fig. 2b. Using the standard deviation  $\sigma$  (plotted error bars), we determine the accuracy to be  $\delta T = \sigma(2\tau c dA/dT)^{-1}$ , where  $c$  is the oscillation amplitude and  $2\tau$  is the free evolution time. We find that for integration times  $t < 30$  s (limited by temperature stability) the temperature accuracy increases in proportion to  $\sqrt{t}$ , giving a sensitivity of  $\eta = \delta T \sqrt{t}$ . A linear dependence of the dissipated heat on laser power (Fig. 3b) is used to determine the measurement accuracy for nanodiamonds. A linear function, with slope  $m$ , is fitted to the data (Fig. 3c, red dashed line) and the measurement accuracy is given by  $\delta T = \sqrt{\sum_{i=1}^N (T_i - m P_i)^2 / (N - 1)}$ , where  $T_i$  is the measured temperature and  $P_i$  is the corresponding laser power. The error bars are evaluated as

$$\sigma(\delta T) = \delta T \sqrt{1 - \frac{2}{N-1} \frac{\Gamma^2(n/2)}{\Gamma^2((n-1)/2)}}$$

where  $\Gamma(\cdot)$  is the Gamma distribution.

**Ultimate sensitivity.** The ultimate sensitivity of our method is limited by the nitrogen–vacancy coherence time and the number of defect centres. In our current experiment, we have demonstrated a sensitivity of  $9 \text{ mK Hz}^{-1/2}$  (with a free evolution time of  $250 \mu\text{s}$ ). Two natural extensions allow longer nitrogen–vacancy coherence: decreasing the  $^{13}\text{C}$  concentration to suppress the nuclear spin bath, and

further dynamical decoupling. These methods can, in principle, allow us to extend the evolution time to  $T_1/2 \approx 3$  ms. In combination with a nanocrystal that contains  $\sim 1,000$  nitrogen–vacancy centres, this could yield an ultimate sensitivity limit of  $80 \mu\text{K Hz}^{-1/2}$ . Further improvement may be possible by using spin-squeezed states. Finally, the determination of absolute temperature is limited by variations in the zero-field splitting due to spatially varying strain. For low-strain diamond samples, we find that the variation in the zero-field splitting is less than  $60 \text{ kHz}$ , allowing for subkelvin absolute-temperature determination. In addition, the use of an ensemble of nitrogen–vacancy centres in different nanodiamonds with uncorrelated strain values allows for a further increase in absolute sensitivity by a factor of  $\sqrt{n}$ , where  $n$  is the number of nanodiamonds.

**Ultimate accuracy in solution.** In cases where our method is used to probe a system that is in solution (for example cells and chemical reactions), the primary accuracy limit is set by heat dissipation during the measurement process. In particular, the microwave spectroscopy used to detect changes in the nitrogen–vacancy zero-field splitting also induces heating of the solution. In the present experiment, we use a lithographically fabricated microwave loop (diameter,  $200 \mu\text{m}$ ) to generate an a.c. magnetic field,  $B \approx 10 \text{ mG}$ , for spin manipulations. Estimating the effective dipole field created by the microwave loop shows that the solution (water) absorbs  $10^{-6} \text{ W}$  of power, yielding a temperature increase of  $5 \text{ mK}$  in the steady state. By using a smaller microwave loop ( $20 \mu\text{m}$ ) and reducing the duty cycle, it should be possible to decrease the heating of the solution to approximately  $50 \mu\text{K}$ .

**Injection of nanodiamonds into cells.** Nanodiamonds and gold nanoparticles were introduced into human embryonic fibroblast WS1 cells by means of silicon-nanowire-mediated delivery<sup>15</sup>. Silicon nanowires were treated with 3-amino-propyltrimethoxysilane to give  $\text{NH}_2$  functionality on the surface. Nanodiamonds and gold nanoparticles were subsequently attached by electrostatic binding. Afterwards, WS1 cells were plated on the silicon nanowire substrates and cultured overnight. The cells were removed by trypsin treatment and re-plated on a glass slide with lithographically defined strip lines for ESR measurements. The samples were stained with calcein AM and ethidium homodimer-1 for the live/dead assay.

# Stretchable nanoparticle conductors with self-organized conductive pathways

Yoonseob Kim<sup>1</sup>, Jian Zhu<sup>1</sup>, Bongjun Yeom<sup>1</sup>, Matthew Di Prima<sup>1</sup>, Xianli Su<sup>2</sup>, Jin-Gyu Kim<sup>3</sup>, Seung Jo Yoo<sup>3</sup>, Ctirad Uher<sup>2</sup> & Nicholas A. Kotov<sup>1</sup>

Research in stretchable conductors is fuelled by diverse technological needs. Flexible electronics, neuroprosthetic and cardiostimulating implants, soft robotics and other curvilinear systems require materials with high conductivity over a tensile strain of 100 per cent (refs 1–3). Furthermore, implantable devices or stretchable displays<sup>4</sup> need materials with conductivities a thousand times higher while retaining a strain of 100 per cent. However, the molecular mechanisms that operate during material deformation and stiffening make stretchability and conductivity fundamentally difficult properties to combine. The macroscale stretching of solids elongates chemical bonds, leading to the reduced overlap and delocalization of electronic orbitals<sup>5</sup>. This conductivity–stretchability dilemma can be exemplified by liquid metals, in which conduction pathways are retained on large deformation but weak interatomic bonds lead to compromised strength. The best-known stretchable conductors use polymer matrices containing percolated networks of high-aspect-ratio nanometre-scale tubes or nanowires to address this dilemma to some extent<sup>6–11</sup>. Further improvements have been achieved by using fillers (the conductive component) with increased aspect ratio, of all-metallic composition<sup>12</sup>, or with specific alignment (the way the fillers are arranged in the matrix)<sup>13,14</sup>. However, the synthesis and separation of high-aspect-ratio fillers is challenging, stiffness increases with the volume content of metallic filler, and anisotropy increases with alignment<sup>15</sup>. Pre-strained substrates<sup>16,17</sup>, buckled microwires<sup>18</sup> and three-dimensional microfluidic polymer networks<sup>19</sup>

have also been explored. Here we demonstrate stretchable conductors of polyurethane containing spherical nanoparticles deposited by either layer-by-layer assembly or vacuum-assisted flocculation. High conductivity and stretchability were observed in both composites despite the minimal aspect ratio of the nanoparticles. These materials also demonstrate the electronic tunability of mechanical properties, which arise from the dynamic self-organization of the nanoparticles under stress. A modified percolation theory incorporating the self-assembly behaviour of nanoparticles gave an excellent match with the experimental data.

Nanoparticles may initially appear as unfavourable candidates for the task of filling a polymer matrix. First of all, spherical nanoparticles have a percolation threshold  $V_c$  that is 10 to 100 times higher than high-aspect-ratio nanometre-scale components. The charge transport between nanoparticles involves a large number of nanoparticle–nanoparticle junctions, resulting in high contact resistance and charge carriers scattering. Additionally, nanoparticles with a strong attraction to polymers cause stiffening of the matrix. On the other hand, nanoparticles in a polymer matrix represent a more dynamic system that has greater freedom for reversible nanoscale restructuring, which is essential for stretchability. Although nanoparticle dynamics in a polymer matrix at high stress/strain levels is poorly understood, one should expect greater matrix mobility from nanoparticles than from nanotubes or nanowires. Therefore, the conducting pathways lost upon deformation could potentially be recovered in a different particle configuration. It is also important that the

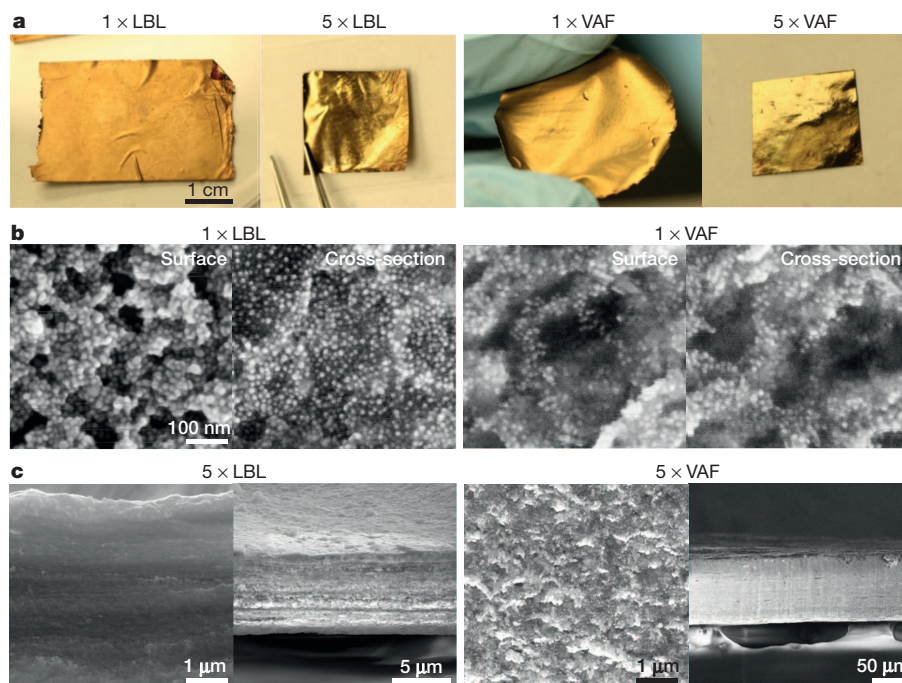


**Figure 1 | Preparation of polyurethane-nanoparticle nanocomposites.** **a**, Photographs of a free-standing film (PU/NP)<sub>500</sub>, a consolidated 5 × LBL stack, a free-standing film made by VAF, and a consolidated 5 × VAF stack. **b**, SEM images of 1 × LBL and 1 × VAF. **c**, Cross-sectional SEM images of 5 × LBL and 5 × VAF.

<sup>1</sup>Department of Chemical Engineering, University of Michigan, Ann Arbor, Michigan 48109-2136, USA. <sup>2</sup>Department of Physics, University of Michigan, Ann Arbor, Michigan 48109-1040, USA. <sup>3</sup>Division of Electron Microscopic Research, Korea Basic Science Institute (KBSI), 169-148 Gwahangno, Yuseong-gu, Daejeon 305-806, South Korea.

conductance between two nanoparticles does not depend on their mutual orientation.

As a model system, we chose citrate-stabilized gold nanoparticles  $13.0 \pm 0.3$  nm in diameter (Supplementary Fig. 1a). The thin citrate layer on the surface of the nanoparticles makes them negatively charged. Citrate coating is expected to present a minimal barrier for charge transfer between nanoparticles (Supplementary Fig. 1b). Polyurethane with two sets of 28 repeating units of ductile moieties (Supplementary Fig. 1c) was used as a polymeric partner for these particles (1.0% by volume in aqueous solution). Its strong positive charge is complementary to the negative charge of the nanoparticles and allowed us to use layer-by-layer (LBL) deposition to make corresponding composites<sup>20,21</sup>. The application of LBL allowed us to (1) reach high nanoparticle loadings, (2) maintain the uniformity of nanoparticle distribution throughout the material, and (3) make adequate comparisons between nanoparticle composites with different nanoscale fillers<sup>22</sup>. We also used an alternative method of construction, allowing us to generalize the properties of nanoparticle composites as stretchable conductors, in which the nanoparticle materials were obtained by vacuum-assisted flocculation (VAF).

Free-standing composite films were obtained after 500 LBL deposition cycles and the resulting polyurethane–nanoparticle film is denoted  $(\text{PU}/\text{NP})_{500}$ . Their thickness was determined by scanning electron microscopy (SEM) to be  $2.0 \pm 0.2$   $\mu\text{m}$ . The ellipsometric thickness for one to ten layer pairs gave a total thickness of  $1.97 \pm 0.1$   $\mu\text{m}$  for 500 layer pairs (Supplementary Fig. 2a). It is nearly identical to the SEM thickness, which indicates excellent thickness control of the LBL

growth<sup>23,24</sup>. Similar free-standing VAF sheets had an SEM thickness of  $30 \pm 3.0$   $\mu\text{m}$ . Both LBL and VAF sheets had an unmistakably metallic appearance (Fig. 1a). LBL and VAF composites were made to have the same volumetric fraction of fillers  $V_f$ , 21.7 vol.% (Supplementary Fig. 3). Experimentally determined values of  $V_c$  for the LBL and VAF composites were 16.2 vol.% and 17.5 vol.%, respectively. To transition to fully macroscopic materials as-prepared LBL and VAF free-standing films were laminated into stacks<sup>25</sup>. Hot-pressing 3–10 free-standing sheets together at  $120^\circ\text{C}$  and a pressure of 20 MPa for 1 h revealed a high degree of consolidation (Fig. 1c). The lamination temperature was chosen because no phase change was observed up to  $130^\circ\text{C}$  for all materials according to differential scanning calorimetry data (Supplementary Fig. 4). The laminated samples of five sheets were denoted  $5 \times \text{LBL}$  or  $5 \times \text{VAF}$  and had SEM thicknesses of  $6.5 \pm 0.7$   $\mu\text{m}$  and  $110 \pm 10$   $\mu\text{m}$ , respectively.

LBL and VAF films had different properties even when the gold content was the same. The LBL composites had better dispersed nanoparticles, leading to more efficient conducting pathways than did the VAF composites, whose nanoparticles were more aggregated. Simultaneously, the presence of larger polyurethane domains resulted in a higher stretchability of the VAF composites (Fig. 2h–k and Supplementary Fig. 5). The free-standing  $1 \times \text{LBL}$  and  $1 \times \text{VAF}$  had conductivities  $\sigma$  of  $6,800 \text{ S cm}^{-1}$  and  $510 \text{ S cm}^{-1}$  and maximum tensile strains  $\varepsilon_{\max}$  of 16% and 75%, respectively. Lamination increased the conductivity of both types of film and considerably improved stretchability. The conductivities of the  $5 \times \text{LBL}$  and  $5 \times \text{VAF}$  composites were  $11,000 \text{ S cm}^{-1}$

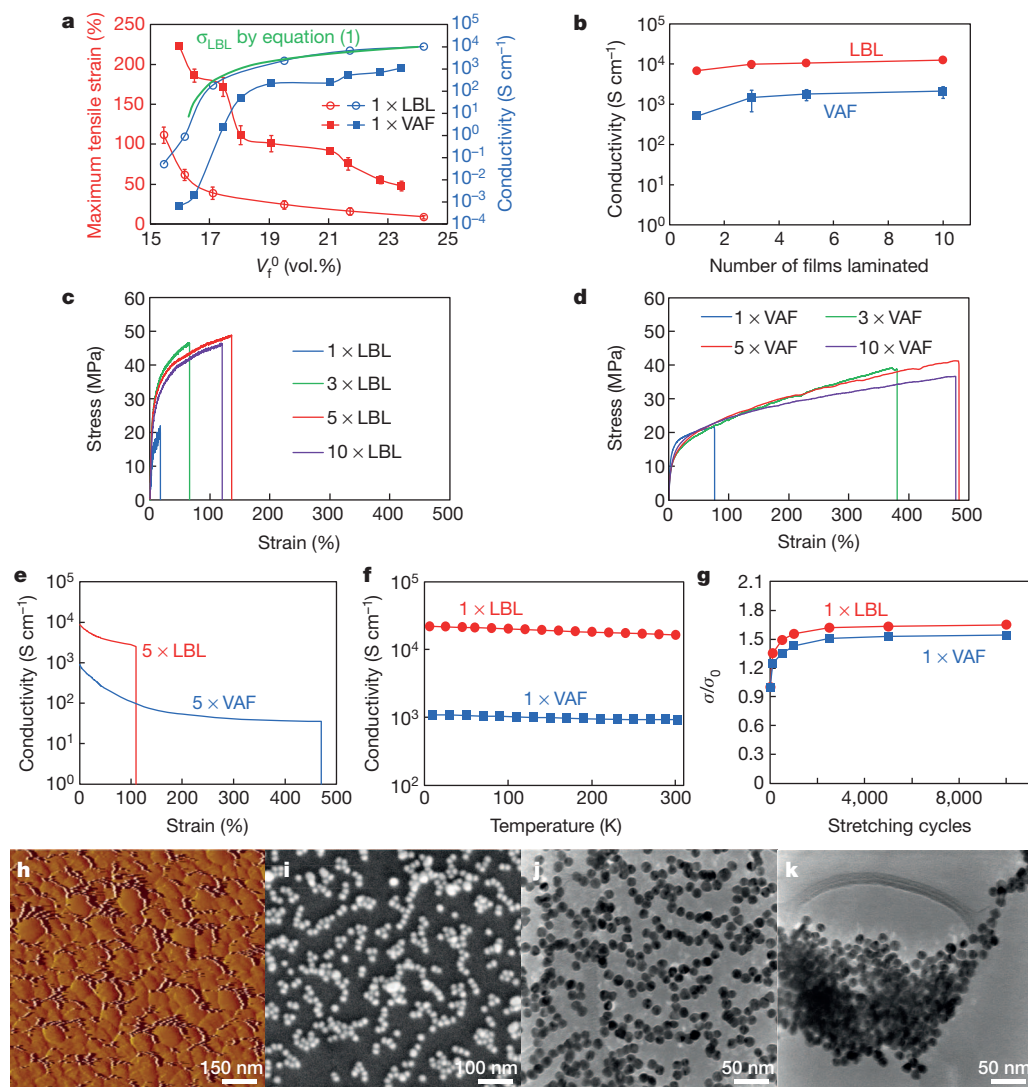


**Figure 2 | Mechanical and electrical properties of polyurethane–nanoparticle nanocomposites.** **a**, Dependence of strain and conductivity of  $1 \times \text{LBL}$  and  $1 \times \text{VAF}$  on the volumetric gold content at  $\varepsilon = 0\%$ ,  $V_f^0$ . The green line shows the calculated conductivity of the LBL composite based on the power-law relation in equation (1) and three-dimensional percolation theory. **b**, Conductivity data of laminated films composed of 1, 3, 5 and 10 consolidated films for LBL and VAF. Error bars in **a** and **b** are mean  $\pm$  s.d. ( $n = 3$ ). **c**, **d**, Stress–strain curves for consolidated LBL (**c**) and VAF (**d**) stacks composed of 1, 3, 5 and 10 films, respectively. **e**, Conductivity as a function of uniaxial strain of  $5 \times \text{LBL}$  and  $5 \times \text{VAF}$ . **f**, Temperature dependence of conductivity for  $1 \times \text{LBL}$  and  $1 \times \text{VAF}$ . **g**, Change in conductivity ( $\sigma/\sigma_0$ ) of  $1 \times \text{LBL}$  and  $1 \times \text{VAF}$  after recurrent stretching cycles,  $\varepsilon = 5\%$ . **h–j**, Atomic-force-microscopy amplitude, SEM and TEM images of  $(\text{PU}/\text{NP})_2$ , respectively. **k**, TEM image of a VAF nanocomposite.

and  $1,800 \text{ S cm}^{-1}$  for  $\varepsilon = 0\%$  (Fig. 2b). Compared to the conductivities of other LBL films from gold nanoparticles stabilized by longer capping agents<sup>23</sup>, those of our composites were more than  $10^5$  times better (see Supplementary Fig. 1 and Supplementary Table 1 for details). The  $\varepsilon_{\max}$  values for  $5 \times \text{LBL}$  and  $5 \times \text{VAF}$  were 115% and 486%, respectively (Fig. 2c and d). The conductivity of  $5 \times \text{LBL}$  and the stretchability of  $5 \times \text{VAF}$  are, to the best of our knowledge, the highest for previously studied composites.

As expected, the conductivity of LBL and VAF composites decreased with the increase of strain  $\varepsilon$  (Fig. 2e).  $\varepsilon = 60\%$  resulted in a reduction of conductivity to  $3,500 \text{ S cm}^{-1}$  for  $5 \times \text{LBL}$  and a reduction to  $210 \text{ S cm}^{-1}$  for  $5 \times \text{VAF}$ .  $\varepsilon = 110\%$  resulted in a reduction to  $2,400 \text{ S cm}^{-1}$  for  $5 \times \text{LBL}$  and a reduction to  $94 \text{ S cm}^{-1}$  for  $5 \times \text{VAF}$ . However, the conductivity values for high strain were slightly or considerably higher than similar values for carbon-nanotube-based materials<sup>4,9</sup>, despite the much smaller aspect ratio of the nanoparticles. Moreover, no other composites have displayed  $\sigma = 35 \text{ S cm}^{-1}$  at  $\varepsilon = 480\%$ , as  $5 \times \text{VAF}$  does.

It is thus essential to understand how these composites retain the capability to transport electrons efficiently at very high deformations. From the outset we knew that nanoparticles are capable of self-assembling in

solution into chains<sup>26</sup>. Atomic force microscopy, SEM and transmission electron microscopy (TEM) images indicated that nanoparticles in the LBL composites produced chains of 20–40 nanoparticles while they were being deposited (Fig. 2h–j). Such chains can behave similarly to high-aspect-ratio nanocomponents, reducing  $V_c$  (ref. 27) while displaying a high conductance similar to that of bulk gold. This ability to self-assemble at the time of LBL deposition was initially hypothesized to be the cause of such an unusual combination of properties. We, however, could not find evidence for nanoparticle-chain formation in the bulk from small-angle X-ray scattering (SAXS) data immediately after deposition at 0% strain (Fig. 3g, i, and l) or by using high-voltage electron microscopy (Supplementary Fig. 6) for the LBL and VAF composites. We next considered the possibility that although they may be almost fully disorganized initially, the nanoparticles can self-organize under stress. Some elements of self-organization have been seen for low filler concentrations and high-aspect-ratio nanomaterials<sup>21,28,29</sup>.

Indeed, we found clear evidence of stress-induced nanoparticle organization in both LBL and VAF composites from TEM images, SAXS data and SEM images (Fig. 3). First of all, TEM images of ultra-thin (130 nm) LBL films under tensile strain showed a high mobility of

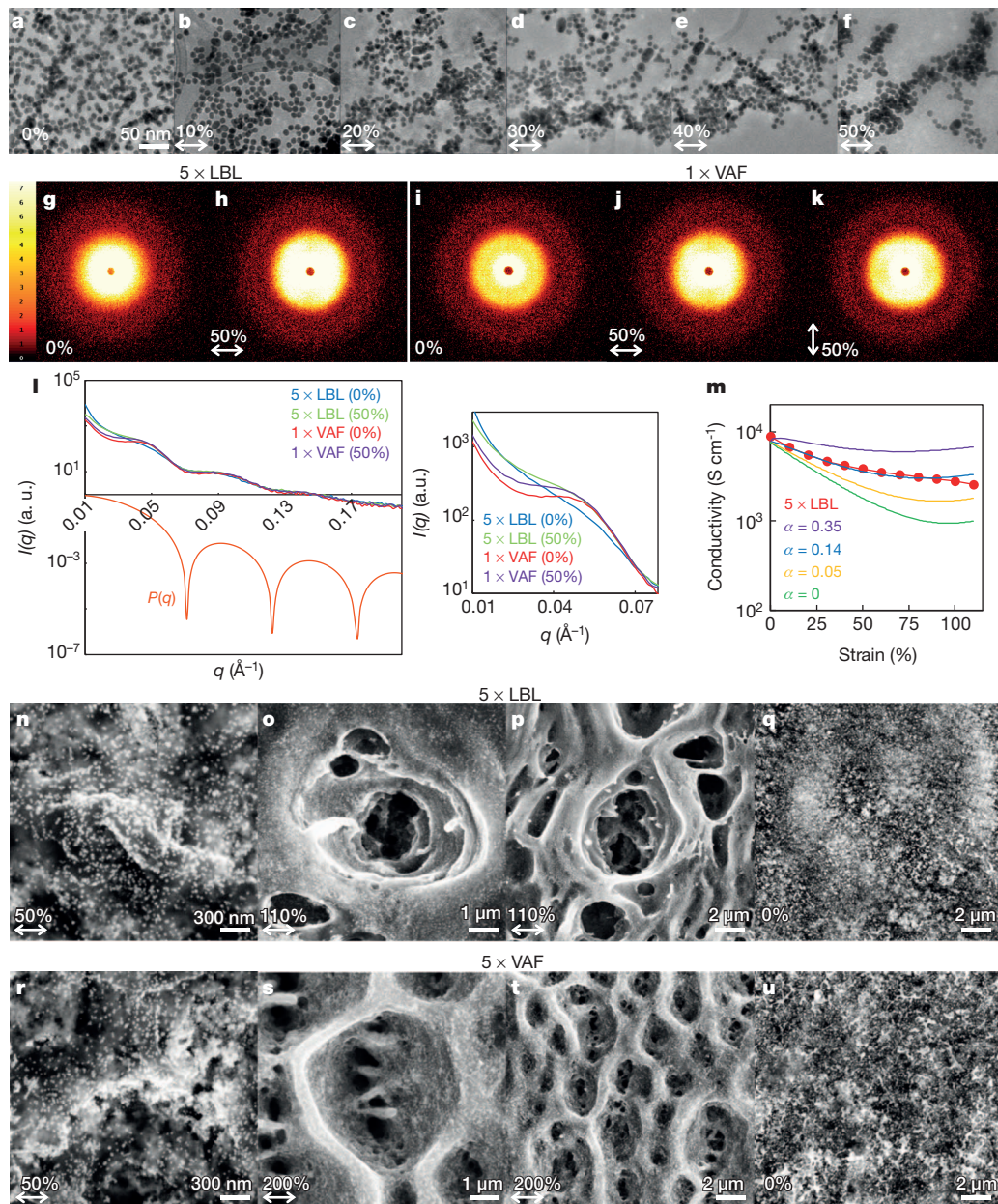


**Figure 3 | Reorganization of nanoparticles under stress.**

**a–f**, TEM images of  $(\text{PU}/\text{PAA})_2(\text{PU}/\text{NP})_4(\text{PU}/\text{PAA})_1$  under strains of 0%, 10%, 20%, 30%, 40% and 50%, respectively, where PAA is polyacrylic acid. **g–k**, SAXS beam images of  $5 \times \text{LBL}$  and  $1 \times \text{VAF}$  at various strains. **l**, SAXS diffraction curves for films at different strains.  $P(q)$  is form factor from the size and shape of nanoparticles. The diffraction curve segments around the peak at  $q = 0.045 \text{ \AA}^{-1}$  are given in the inset. **m**, Calculated conductivity dependence on strain for LBL composites described by percolation theory for self-assembling systems (equation (2)) with various self-assembly coefficients  $\alpha$  in comparison with actual data for  $5 \times \text{LBL}$ . **n–u**, SEM images of focused-ion-beam milled  $5 \times \text{LBL}$  and  $5 \times \text{VAF}$  at various strains. The images in **q** and **u** were taken after five consecutive stretches to 110% and 200%, respectively. Milling depths for samples in this study are 1  $\mu\text{m}$  for  $5 \times \text{LBL}$  and 2  $\mu\text{m}$  for  $5 \times \text{VAF}$ . Stretching directions are indicated by the double arrows.

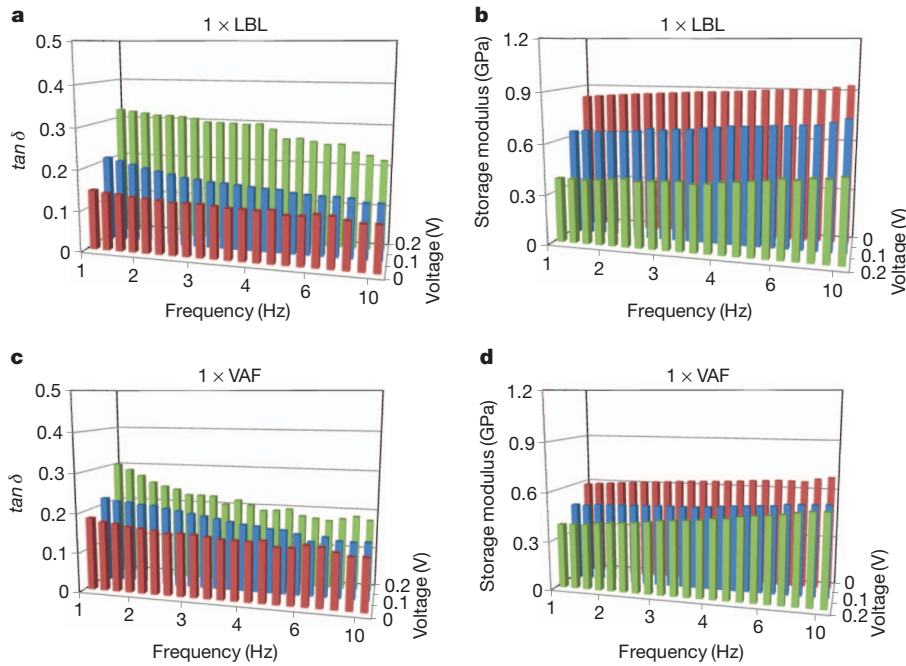


**Figure 4 | Viscoelastic properties of polyurethane–nanoparticle nanocomposites for different applied voltages. a, b, Damping parameter  $\tan\delta$  and storage modulus for  $1 \times \text{LBL}$ , respectively. c, d, Damping parameter  $\tan\delta$  and storage modulus of  $1 \times \text{VAF}$ , respectively.**

the nanoparticles in the polymer matrix. As the strain increased, the nanoparticles gradually re-organized into bands along the stretching direction (Fig. 3a–f). In the SAXS data the well developed hourglass-shaped scattering patterns were observed at higher elongations of  $\varepsilon = 50\%$  for both composites, confirming that nanoparticles were organized in elongated structures (Fig. 3h, j, and k). The intensity of the diffraction peak at scattering vector  $q = 0.045 \text{ \AA}^{-1}$  also substantially increased at  $\varepsilon = 50\%$  for both composites (Fig. 3l).

Unlike other stress-induced composite reorganization, the beam patterns and intensity plots of SAXS data that developed upon stretching disappeared when the tension was released. The self-assembled nanoparticle patterns observed here were remarkably different from other patterns observed in both solutions and solids<sup>26,28,29</sup>. To reveal the nanoparticle patterns in the bulk of the composites, focused-ion-beam milling was applied to a depth of 1–2  $\mu\text{m}$ . SEM images of such samples remaining under  $\varepsilon = 110\%$  for  $5 \times \text{LBL}$  and  $\varepsilon = 200\%$  for  $5 \times \text{VAF}$  revealed three-dimensional cellular self-organized patterns with characteristic dimensions of 1–5  $\mu\text{m}$  (Fig. 3o, p, s and t). These distinct nanoparticle networks can be the result of local phase separation of the nanoparticles in the polymer under high strain.

Importantly, when the tension was released, these cellular networks were not observed even after five consecutive stretches, indicating that the nanoparticle networks were reconfigurable (Fig. 3q and u). However, slight irreversible reconstruction of the material did occur on the surface, leading to formation of bands of nanoparticles running perpendicularly to the stress direction and decreased stiffness (Supplementary Fig. 7). With  $\varepsilon = 5\%$  (the elastic limit of both composites is considered to be less than  $\varepsilon = 10\%$ ), the films were repetitively stretched to observe changes in conductivity with deformation cycling. Interestingly, conductivity after 5,000 cycles increased substantially by 1.7-fold for  $1 \times \text{LBL}$  and 1.5-fold for  $1 \times \text{VAF}$  (Fig. 2g). The resistance of  $1 \times \text{LBL}$  and  $1 \times \text{VAF}$  films after 10,000 stretch cycles, measured parallel and perpendicular to the stretching direction, also confirmed the gradual internal rearrangement of the nanoparticles, which are completely isotropic without stress. Resistance in both directions decreased but decreased slightly more in the parallel direction than in the perpendicular direction. SAXS data for  $1 \times \text{LBL}$  and  $1 \times \text{VAF}$  films after 10,000 stretch cycles also confirmed the reorganization of nanoparticles (Supplementary Fig. 8).

The prepared composites presented an interesting case for percolation theory because of (1) the unusually high conductance of particles with minimal aspect ratio and (2) the extensive structural characterization

(Figs 1–3). We note that there are no examples of applications of percolation theory to self-organized systems. The classical power law relates the conductivity of an unstretched material  $\sigma$  to  $V_f$  as follows:

$$\sigma = \sigma_0 (V_f^0 - V_c^0)^s \quad (1)$$

where  $\sigma_0$  is the conductivity of the filler,  $V_f^0$ , and  $V_c^0$  are the volumetric fractions of the filler and percolation threshold at  $\varepsilon = 0\%$ , respectively, and  $s$  is the critical exponent. Unambiguous application of equation (1) to VAF composites is difficult owing to aggregation of nanoparticles (Fig. 2k and Supplementary Fig. 9). Also the existing method<sup>9</sup> is unable to describe percolation correctly at high strains, as is the case for VAF composites (see comments to Supplementary Fig. 9). Therefore, we restricted consideration of percolation theory to LBL composites, which represent an almost ideal case for this theory owing to the nearly uniform distribution of nanoparticles. Indeed,  $\sigma_{\text{LBL}}$  calculated from equation (1) showed excellent agreement with  $\sigma_{1 \times \text{LBL}}$  in the absence of strain at various  $V_f^0$  (Fig. 2a). The conductivities of the composites for different strains were calculated according to a recently developed method<sup>9</sup> but showed significant discrepancies. As strain increases, the calculated  $\sigma$  dropped faster than did the experimental data, despite the general tendency of the method to overestimate the conductance for large strains. This finding showed that the current percolation theory cannot explain the dynamic nature of conductive pathways under strain. The influence of stress-induced self-organization processes could be described as an apparent increase of the aspect ratio of the fillers, which reduced  $V_c$  and hence increased  $\sigma$ . Thus,  $V_c^0$  in equation (1) was modified by introducing a self-assembly coefficient  $\alpha$  with square-root dependency of  $\varepsilon$  as follows:

$$V_c(\varepsilon) = \frac{V_c^0}{1 + \alpha\sqrt{\varepsilon}} \quad (2)$$

When  $\alpha = 0.14$  the theoretical curve fitted the experimental data nearly perfectly (Fig. 3m). As the coefficient  $\alpha$  increases the ability of particles to reorganize to form conductive pathways becomes more pronounced. The numerical value of  $\alpha$  reflects the effects of both the ability of nanoparticles to form non-random associations in solids and their directionality.

An understanding of charge transport in these materials is academically and practically essential. Fitting the temperature dependence of conductivity from 2 to 300 K with variable-range charge transport equations revealed clear metallic behaviour via direct nanoparticle

contact (see Fig. 2f and Supplementary Fig. 10 for details), whereas the temperature dependence of conductivity from 2 to 300 K in the stretchable conductors from carbon nanotubes showed semiconducting behaviour and hopping electron transport<sup>13</sup>. Importantly, gold nanoparticle composites had high electron mobilities of  $1.75 \times 10^{-4} \text{ m}^2 \text{ V}^{-1} \text{ s}^{-1}$  for 1  $\times$  LBL and  $5.45 \times 10^{-5} \text{ m}^2 \text{ V}^{-1} \text{ s}^{-1}$  for 1  $\times$  VAF, and the carrier concentration of  $5.83 \times 10^{28} \text{ m}^{-3}$  for 1  $\times$  LBL at 300 K approached very closely to that for bulk gold,  $5.90 \times 10^{28} \text{ m}^{-3}$  (Supplementary Fig. 11).

As one of many possible demonstrations of the practical relevance of the new composites, we performed a dynamic mechanical analysis under small voltage to illustrate the electro-tunability of their viscoelastic properties. The relaxation of composites at a frequency of 1–10 Hz significantly increased when a small voltage of 0.2 V was applied, owing to repulsive transient charges on nanoparticles. As such, the damping parameter  $\tan \delta$  increased by 2.2-fold and 1.6-fold and the storage modulus decreased by 2.1-fold and 1.5-fold for 1  $\times$  LBL and 1  $\times$  VAF, respectively (Fig. 4 and Supplementary Fig. 13). Solid materials with electro-tunable mechanical properties are more practically viable than metallic structures filled with liquid electrolytes<sup>30</sup>.

From a fundamental perspective, these composites with high gold-nanoparticle loading displayed a previously unknown reorganization into cellular networks under stress. To some degree such restructuring imitates the behaviour of atoms in liquid metals, while retaining structural integrity and strong bonding. The nanoparticle dynamics in such composites can be described by a variation of classical percolation theory and can be extended to a variety of other nanoparticle–polymer systems. Further improvements can be achieved by the development of commercially affordable conducting fillers and new polyelectrolytes to optimize properties. Further fabrication of such composites could aim to meet the demands of applications in medicine, optoelectronics, and energy storage devices that require electro-tunable properties.

## METHODS SUMMARY

We used as-received cationic polyurethane aqueous dispersion (30 vol.%, molecular mass approximately 92,000, from Hepce Chem, South Korea) after diluting to 1 vol.% solutions in deionized water. Gold(III)chloride trihydrate, sodium citrate tribasic dihydrate (Sigma-Aldrich) were used as-received. Citrate-stabilized gold nanoparticles with diameter  $13 \pm 0.3 \text{ nm}$  were synthesized.

For LBL assembly, substrates were sequentially dipped into a diluted solution of polyurethane and a dispersion of concentrated gold nanoparticles, with each step followed by rinsing with deionized water and drying with compressed air. This deposition cycle constitutes a pair of layers, and can be repeated as many times  $n$  as necessary to obtain the desirable thickness. The desired gold content in the composites was acquired by controlling the dipping time of a substrate to achieve the required dispersion of gold nanoparticles.

For VAF film preparation, we stirred a mixture of as-prepared gold nanoparticles and a diluted solution of polyurethane, followed by filtration. The desired gold content in the composites was achieved by controlling the volume of a dispersion of as-prepared gold-nanoparticle solutions. Unless otherwise specified, LBL and VAF films had the same gold contents in all the tests. The described measurements were performed at room temperature and relative humidity of 20–30% for both LBL and VAF composites. See Methods for details of the synthesis of gold nanoparticles, preparation of LBL and VAF films, and their characterizations.

**Full Methods** and any associated references are available in the online version of the paper.

Received 15 October 2012; accepted 13 June 2013.

Published online 17 July 2013.

1. Rogers, J. A., Someya, T. & Huang, Y. Materials and mechanics for stretchable electronics. *Science* **327**, 1603–1607 (2010).
2. Fan, Z. *et al.* Toward the development of printable nanowire electronics and sensors. *Adv. Mater.* **21**, 3730–3743 (2009).
3. Nolfi, S. & Floreano, D. *Evolutionary Robotics: the Biology, Intelligence, and Technology of Self-Organizing Machines* (MIT Press, 2000).
4. Sekitani, T. *et al.* Stretchable active-matrix organic light-emitting diode display using printable elastic conductors. *Nature Mater.* **8**, 494–499 (2009).
5. Torquato, S., Hyun, S. & Donev, A. Multifunctional composites: optimizing microstructures for simultaneous transport of heat and electricity. *Phys. Rev. Lett.* **89**, 266601 (2002).

6. Baughman, R. H., Zakhidov, A. A. & de Heer, W. A. Carbon nanotubes—the route toward applications. *Science* **297**, 787–792 (2002).
7. Lee, P. *et al.* Highly stretchable and highly conductive metal electrode by very long metal nanowire percolation network. *Adv. Mater.* **24**, 3326–3332 (2012).
8. Hu, L. *et al.* Stretchable, porous, and conductive energy textiles. *Nano Lett.* **10**, 708–714 (2010).
9. Chun, K.-Y. *et al.* Highly conductive, printable and stretchable composite films of carbon nanotubes and silver. *Nature Nanotechnol.* **5**, 853–857 (2010).
10. Sekitani, T. *et al.* A rubberlike stretchable active matrix using elastic conductors. *Science* **321**, 1468–1472 (2008).
11. Lipomi, D. J. *et al.* Skin-like pressure and strain sensors based on transparent elastic films of carbon nanotubes. *Nature Nanotechnol.* **6**, 788–792 (2011).
12. Fuhrer, M. S. *et al.* Crossed nanotube junctions. *Science* **288**, 494–497 (2000).
13. Zhang, Y. Y. *et al.* Polymer-embedded carbon nanotube ribbons for stretchable conductors. *Adv. Mater.* **22**, 3027–3031 (2010).
14. Liu, K. *et al.* Cross-stacked superaligned carbon nanotube films for transparent and stretchable conductors. *Adv. Funct. Mater.* **21**, 2721–2728 (2011).
15. Mittal, V., Kim, J. K. & Pal, K. *Recent Advances in Elastomeric Nanocomposites (Advanced Structured Materials)* 258 (Springer, 2013).
16. Yu, C. J., Masarapu, C., Rong, J. P., Wei, B. Q. & Jiang, H. Q. Stretchable supercapacitors based on buckled single-walled carbon nanotube macrofilms. *Adv. Mater.* **21**, 4793–4797 (2009).
17. Xu, F., Wang, X., Zhu, Y. T. & Zhu, Y. Wavy ribbons of carbon nanotubes for stretchable conductors. *Adv. Funct. Mater.* **22**, 1279–1283 (2012).
18. Kim, D. H. *et al.* Materials and noncoplanar mesh designs for integrated circuits with linear elastic responses to extreme mechanical deformations. *Proc. Natl. Acad. Sci. USA* **105**, 18675–18680 (2008).
19. Park, J. *et al.* Three-dimensional nanonetworks for giant stretchability in dielectrics and conductors. *Nature Commun.* **3**, 916, doi:10.1038/ncomms1929 (2012).
20. Decher, G. Fuzzy nanoassemblies: toward layered polymeric multicomposites. *Science* **277**, 1232–1237 (1997).
21. Mamedov, A. A. *et al.* Molecular design of strong single-wall carbon nanotube/polyelectrolyte multilayer composites. *Nature Mater.* **1**, 190–194 (2002).
22. Hammond, P. T. Form and function in multilayer assembly: new applications at the nanoscale. *Adv. Mater.* **16**, 1271–1293 (2004).
23. Schlicke, H. *et al.* Freestanding films of crosslinked gold nanoparticles prepared via layer-by-layer spin-coating. *Nanotechnology* **22**, 305303 (2011).
24. Tang, Z. Y., Kotov, N. A., Magonov, S. & Ozturk, B. Nanostructured artificial nacre. *Nature Mater.* **2**, 413–418 (2003).
25. Podsiadlo, P. *et al.* LBL assembled laminates with hierarchical organization from nano- to microscale: high-toughness nanomaterials and deformation imaging. *ACS Nano* **3**, 1564–1572 (2009).
26. Reuter, T., Vidoni, O., Torma, V. & Schmid, G. Two-dimensional networks via quasi one-dimensional arrangements of gold clusters. *Nano Lett.* **2**, 709–711 (2002).
27. Li, J. *et al.* Correlations between percolation threshold, dispersion state, and aspect ratio of carbon nanotubes. *Adv. Funct. Mater.* **17**, 3207–3215 (2007).
28. Dirix, Y., Bastiaansen, C., Caseri, W. & Smith, P. Oriented pearl-necklace arrays of metallic nanoparticles in polymers: a new route toward polarization-dependent color filters. *Adv. Mater.* **11**, 223–227 (1999).
29. Pérez-Juste, J., Rodríguez-González, B., Mulvaney, P. & Liz-Marzan, L. M. Optical control and patterning of gold-nanorod-poly(vinyl alcohol) nanocomposite films. *Adv. Funct. Mater.* **15**, 1065–1071 (2005).
30. Jin, H. J. & Weissmuller, J. A material with electrically tunable strength and flow stress. *Science* **332**, 1179–1182 (2011).

**Supplementary Information** is available in the online version of the paper.

**Acknowledgements** We thank the STX foundation, Seoul, Korea, for partial funding of this research by providing a stipend to Y.K. The LBL/VAF preparation and low-temperature-conductivity studies were in part supported by the Center for Solar and Thermal Energy Conversion, an Energy Frontier Research Center (EFRC) funded by the US Department of Energy, Office of Science, Office of Basic Energy Sciences, under award number DE-SC0000957. The in-depth study of the self-assembly processes was funded by the Center for Photonic and Multiscale Nanomaterials (C-PHOM) as a part of the National Science Foundation Materials Research Science and Engineering Center programme DMR 1120923. We are also grateful to AFOSR, project FA9550-08-1-0382 and Game Changer programme for funding used for M.D.P.’s salary. The DARPA MATLOG project made possible the measurements of damping coefficients. We thank the University of Michigan’s Electron Microscopy and Analysis Laboratory (EMAL) for its assistance with electron microscopy, and for NSF grants (numbers DMR-0320740 and DMR-9871177), for funding the FEI Nova Nanolab Dualbeam Focused Ion Beam Workstation and Scanning Electron Microscope and the JEOL 2010F analytical electron microscope used in this work. We also thank EMAL and the College of Engineering for assistance with the Bruker NanoStar Small-Angle X-ray Scattering System. We also thank E. Arruda, J. Shaw and S. Daly for the use of mechanical facilities. We are grateful to Y. S. Huh for help with the high-voltage electron microscopy image.

**Author Contributions** N.A.K. conceived the project. Y.K., J.Z., M.D.P. and N.A.K. designed the experiments. Y.K., J.Z. and M.D.P. performed the experiments. X.S. and C.U. measured conductivities at low temperatures. J.G.K. and S.J.Y. conducted electron microscope with high voltages. B.Y. contributed to the mechanical characterization. Y.K., J.Z., M.D.P., X.S., J.G.K., S.J.Y., B.Y., C.U. and N.A.K. analysed data. Y.K. and N.A.K. co-wrote the paper. All authors discussed the results and commented on the manuscript.

**Author Information** Reprints and permissions information is available at [www.nature.com/reprints](http://www.nature.com/reprints). The authors declare no competing financial interests. Readers are welcome to comment on the online version of the paper. Correspondence and requests for materials should be addressed to N.A.K. (kotov@umich.edu).

## METHODS

**Synthesis of gold nanoparticles.** To ultrapure deionized water (950 ml) in a one-litre glass beaker equipped with a magnetic stir bar was added gold(III)chloride trihydrate (180.0 mg, 0.458 mmol). The mixture was heated to boiling under vigorous stirring followed by additional heating for 20 min. Subsequently, 50 ml of 34 mM sodium citrate solution was added to the mixture. The aqueous solution was heated for 20 min followed by cooling to room temperature. As-prepared aqueous solution was directly used for the preparation of VAF films. In some cases, it was further concentrated to be used as the dipping solution for LBL films. For the concentration process, the as-made aqueous gold nanoparticles dispersions were transferred into 50-ml centrifuge tubes and the concentration of the solutions was increased using a Sorvall Legend Mach 1.6R centrifuge (Thermoscientific, USA) at the speed of 10,000 r.p.m. for 1 h. Less than 5 ml of concentrated gold-nanoparticle solution was settled at the bottom of the tube. The supernatant (45 ml) was removed by suction pipettes, while taking special care to prevent disturbing the sedimented nanoparticles. Finally, the resultant nanoparticles were collected for the LBL process. **Preparation of LBL films.** Glass slides (25 mm × 75 mm, Fisher Scientific) cleaned by piranha solution (sulphuric acid and hydrogen peroxide, from Sigma-Aldrich, in a 3:1 volume ratio) overnight were dipped into a 1 vol.% solution of polyurethane, for 5 min, rinsed with deionized water for 1 min and gently dried with compressed air. Please note that the piranha solution is dangerous and extremely reactive with organic substances so appropriate handling precautions are essential. Then the slides were dipped into a dispersion of concentrated gold nanoparticles for several minutes, rinsed for 1 min, and again dried with compressed air. After achieving the desired thickness, free-standing films were isolated by etching of the glass slides with 1 vol.% hydrofluoric acid (Sigma-Aldrich) solution. Note that hydrofluoric acid solution, even diluted, is very toxic so extreme precautions must be taken at all times. After thorough rinsing with water, the detached films were dried in an oven at 60 °C overnight and then kept in ambient conditions (room temperature and relative humidity of 20–30%) for another night before measurement of properties.

Conditions and procedures for preparation of LBL films with various gold contents were the same except for the dipping time to achieve the dispersion of concentrated gold nanoparticles. LBL films containing 15.4 vol.%, 16.2 vol.%, 16.9 vol.%, 19.4 vol.%, 21.7 vol.%, and 24.0 vol.% of gold nanoparticles were prepared with dipping times of 1 min, 2 min, 3 min, 8 min, 14 min and 20 min, respectively. When the substrate is dipped into the gold-nanoparticle dispersion, tiny amounts of polyurethanes, which might be weakly bonded, are slowly diffused into the dispersion of gold nanoparticles. In the process of cyclic deposition, polyurethanes are accumulated in the dispersion of gold nanoparticles and when they exceed the specific threshold of concentration, gold nanoparticles are flocculated. To maintain the homogeneity of the LBL film, careful monitoring of flocculation is needed. If flocculation is observed, the dispersion of gold nanoparticles must be changed. An LBL thin film of  $(\text{PU}/\text{PAA})_2(\text{PU}/\text{NP})_4(\text{PU}/\text{PAA})_1$  was prepared for TEM experiments. Detailed methods for film preparation were exactly the same as the above typical process. The dipping time of the glass slide into PAA was 5 min.

**Preparation of VAF films.** To a one-litre glass beaker containing a litre of as-prepared gold-nanoparticle dispersion (no additional concentration steps were applied) equipped with a magnetic stir bar we slowly added 1 ml of 1.0 vol.% aqueous polyurethane. The mixture was stirred for 15 min followed by filtration. Filter papers of 0.8-μm pore size with 47 mm diameter, and the filtration assembly, were obtained from Fisher Scientific. The resultant gold-coloured film was peeled off the filter paper. We recommend drying the film completely before taking it out from the filtration assembly. Individual peeled-off films have some fibrous material

attached that comes from the filter paper, which can be removed by gentle scratching. Conditions and procedures for preparation of VAF films with various gold contents were the same except for the volumetric ratio of a dispersion of as-prepared gold-nanoparticle solutions. VAF films containing 15.9 vol.%, 16.4 vol.%, 17.3 vol.%, 18.0 vol.%, 19.1 vol.%, 21.0 vol.%, 21.7 vol.%, 22.8 vol.% and 23.4 vol.% of gold nanoparticles were prepared with 250 ml, 500 ml, 650 ml, 700 ml, 800 ml, 900 ml, 1,000 ml, 1,050 ml and 1,100 ml of as-prepared gold-nanoparticle dispersion, respectively. To make a 30-μm-thick VAF film, in total about 1,800 ml of solution needs to be filtered. **Characterizations.** The initial stages of LBL deposition were monitored using an 8453 ultraviolet–visual Chem Station spectrophotometer (Agilent Technologies, USA). The thickness of the initial assembly of the LBL film was calculated using a BASE-160 Spectroscopic Ellipsometer (J. A. Woollam, USA). Calculations were fitted using a Cauchy's model. The LBL film for ellipsometry was prepared on silicon wafers following the same procedure as described for the LBL film.

Stress–strain curves were obtained by testing ~1-mm-wide and 5–7-mm-long rectangular strips of samples with a mechanical strength tester 100Q (TestResources, USA). Tests were performed at a rate of 0.01 mm s<sup>-1</sup> for LBL films and 0.08 mm s<sup>-1</sup> for VAF films with a ~111-N range load cell. Five samples were tested for each film. The force measurements from the load cell were divided by the measured initial thickness and initial width of the sample gauge section to give nominal stress. This procedure results in a plot of nominal stress versus nominal strain. The cyclic tensile test (Fig. 2g) was performed by a Servopneumatic Axial/Torsion Test Instrument with custom-made grips (EnduraTEC, USA). Tests were performed at a rate of 0.01 mm s<sup>-1</sup>.

Conductivity measurements with two-probe and four-probe methods were obtained using an 34401A Digital Multimeter, 6½ Digit (Agilent Technologies, USA). Measurements of conductivity as a function of strain (Fig. 2g) were done using a custom four-probe setup, depicted in Supplementary Fig. 12. The measured resistance and applied tensile strain were recorded simultaneously by a video camera, and close-up images of the sample were photographed by a high-speed camera to calculate the thickness of the sample at some strain level with the assumption that the volume of sample was kept constant. The temperature dependence of conductivity was measured using the four-probe method with a Magnetic Property Measurement System (MPMS) (Quantum Design, USA). The MPMS is a cryogenic probe that integrates a superconducting magnet with a superconducting quantum interference device (SQUID) detection system and a temperature controller in a specially designed Dewar. These sophisticated configurations provide rapid precision measurements over a temperature range from 2 to 300 K.

Filler fraction of sample was determined by a Pyris 1 TGA (PerkinElmer, USA) with a temperature ramp from 25 °C to 800 °C at 10 °C per min under an air atmosphere at a flow rate of 20 ml per min. The differential scanning calorimetry analysis was performed using a Q200 (TA Instruments, USA). SEM images were obtained with an FEI Nova Nanolab dual-beam focused ion beam and scanning electron microscope. TEM images were obtained with a JEOL 2010F analytical electron microscope. High-voltage electron microscopy images were obtained with a high-voltage electron microscope (1,250 kV, JEOL, JEM-ARM 1300S). Atomic-force-microscopy imaging was performed with a Nanoscope III atomic force microscope (Digital Instruments/Veeco Metrology Group). X-ray scattering data were obtained with a Bruker NanoStar Small-Angle X-ray Scattering System equipped with Siemens Kristallogflex 770 X-Ray Generator, and a Cu K $\alpha$  radiation (0.1542 nm) X-ray tube with peak power of 1.5 kW on a Hi Star Area 2D detector with 1 min of exposure time. The damping parameter  $\tan\delta$  and the storage modulus of the samples were obtained with an RSA 3 dynamic mechanical analyser (TA Instruments) with applied  $\varepsilon = 0.5\%$  within the frequency range of 1–90 Hz. A load cell with a maximum capacity of 3.5 N and a resolution of 1  $\mu\text{N}$  was used.

# Seasonal sea surface cooling in the equatorial Pacific cold tongue controlled by ocean mixing

James N. Moum<sup>1</sup>, Alexander Perlin<sup>1,‡</sup>, Jonathan D. Nash<sup>1</sup> & Michael J. McPhaden<sup>2</sup>

Sea surface temperature (SST) is a critical control on the atmosphere<sup>1</sup>, and numerical models of atmosphere–ocean circulation emphasize its accurate prediction. Yet many models demonstrate large, systematic biases in simulated SST in the equatorial ‘cold tongues’ (expansive regions of net heat uptake from the atmosphere) of the Atlantic<sup>2</sup> and Pacific<sup>3</sup> oceans, particularly with regard to a central but little-understood feature of tropical oceans: a strong seasonal cycle. The biases may be related to the inability of models to constrain turbulent mixing realistically<sup>4</sup>, given that turbulent mixing, combined with seasonal variations in atmospheric heating, determines SST. In temperate oceans, the seasonal SST cycle is clearly related to varying solar heating<sup>5</sup>; in the tropics, however, SSTs vary seasonally in the absence of similar variations in solar inputs<sup>6</sup>. Turbulent mixing has long been a likely explanation, but firm, long-term observational evidence has been absent. Here we show the existence of a distinctive seasonal cycle of subsurface cooling via mixing in the equatorial Pacific cold tongue, using multi-year measurements of turbulence in the ocean. In boreal spring, SST rises by 2 kelvin when heating of the upper ocean by the atmosphere exceeds cooling by mixing from below. In boreal summer, SST decreases because cooling from below exceeds heating from above. When the effects of lateral advection are considered, the magnitude of summer cooling via mixing (4 kelvin per month) is equivalent to that required to counter the heating terms. These results provide quantitative assessment of how mixing varies on timescales longer than a few weeks, clearly showing its controlling influence on seasonal cooling of SST in a critical oceanic regime.

Equatorial cold tongues in the Atlantic and Pacific are formed in part through diverging horizontal transport near the sea surface associated with large-scale wind patterns, which bring cool waters towards the ocean surface<sup>7,8</sup>. Maintaining cool SSTs in the presence of intense solar heating requires a combination of subsurface mixing and vertical advection to transport surface heat downward<sup>4,9–11</sup>. Limited measurements during the passage of a tropical instability wave (TIW) at 0, 140° W revealed a tenfold increase in subsurface turbulent heat flux<sup>12</sup>. This was sufficient to cool surface waters by 2 K per month, indicating that mixing alone has the potential to maintain the equatorial cold tongue, a conjecture supported by climatological evidence that sea surface cooling is enhanced by TIWs<sup>12</sup>.

Establishing general relationships that show how irreversible turbulent mixing influences patterns in large-scale (10,000 km) ocean phenomena has been notoriously difficult for two reasons. First, the delicate measurements required to quantify mixing have been limited to short shipboard campaigns (30 days) that target specific processes<sup>13–17</sup>. Although these have led to fundamental advances in our knowledge of ocean dynamics at a few locations and on timescales of a few weeks, such measurements are unable to determine whether changes in mixing on seasonal and interannual timescales might influence large-scale dynamics. Second, diagnostics of mixing in numerical model solutions of ocean circulation are ambiguous, because models grossly oversimplify their representation of mixing, which occurs on scales that are orders of magnitude smaller than the smallest spatial and shortest timescales resolved.

Here we directly quantify variations in mixing on long timescales using specialized instrumentation that we developed for use on oceanographic moorings<sup>18,19</sup>. Since late 2005, these sensors have provided near-continuous measurements of mixing below the Tropical Atmosphere–Ocean (TAO) buoy maintained by the National Ocean and Atmospheric Administration (NOAA) at 0, 140° W<sup>20</sup>.

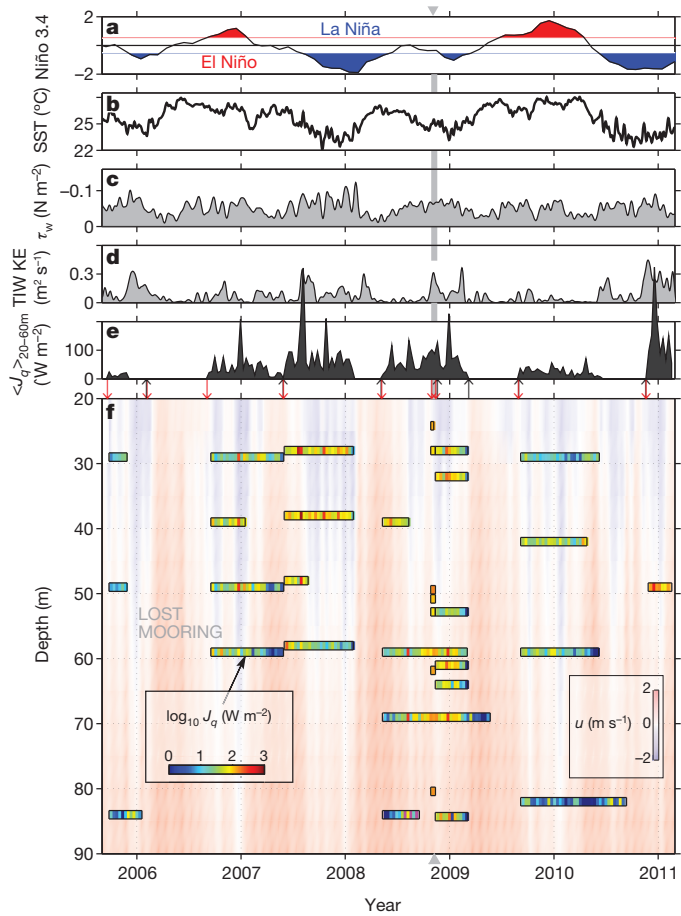


**Figure 1 | Six-year record of mixing at the TAO mooring at 0, 140° W.** **a**, Niño3.4 SST index, a measure of the relative strengths of El Niño and La Niña events<sup>28</sup>. **b**, SST. **c**, Wind stress,  $\tau_w$  (7-day averages). **d**, Squared meridional velocity at 40 m filtered at 12–33 days, taken as a proxy for kinetic energy in the tropical instability wave frequency band (TIW KE). **e**, Turbulent heat flux averaged over depths 20–60 m,  $\langle J_q \rangle_{20-60m}$ . **f**, Image plot of zonal currents (zonal velocity denoted  $u$ , eastward currents red, westward blue; see right inset colour scale). Coloured bars show depths and durations of  $\chi$ -pod deployments;  $\log_{10} J_q$  is indicated by the colour (10-day average, see left inset colour scale). Arrows at top of **f** show deployments (red) and recoveries (black) of moorings. Grey bars show period of comparison experiment with shipboard turbulence profiling instrumentation<sup>12,19</sup>.

<sup>1</sup>College of Earth, Ocean and Atmospheric Sciences, Oregon State University, Corvallis, Oregon 97331, USA. <sup>2</sup>NOAA/Pacific Marine Environmental Laboratory, Seattle, Washington 98115, USA.  
†Deceased.

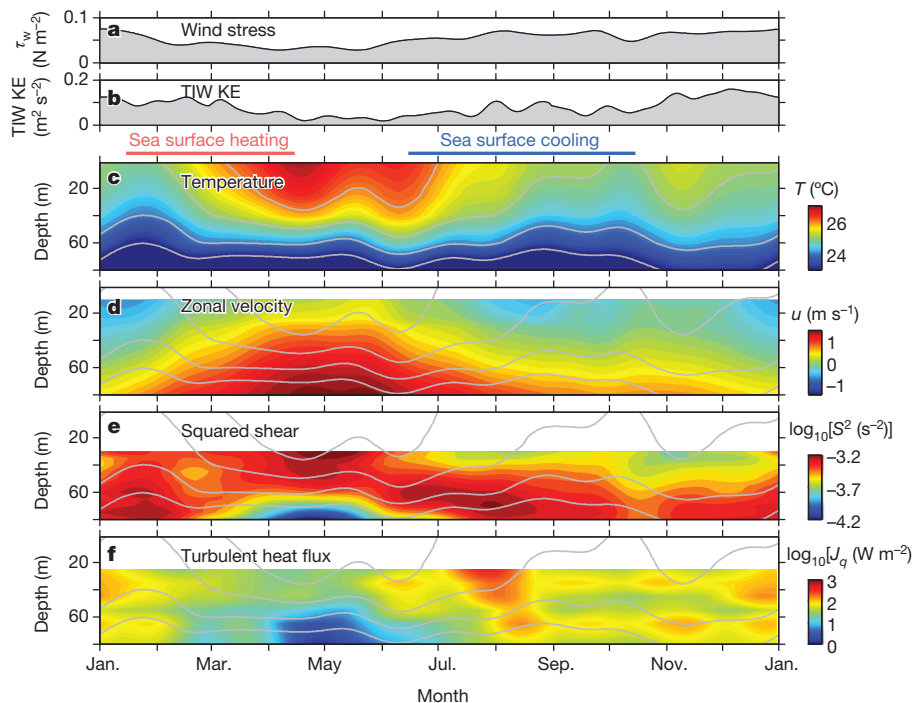


**Figure 2 | Annual cycles of upper-ocean vertical structure at 0, 140°W over the period 2005–11.** **a**,  $\tau_w$ ; **b**, TIW KE; **c**,  $T$ ; **d**, zonal velocity,  $u$ ; **e**,  $\log_{10}S^2$ , where  $S^2 = u_z^2 + v_z^2$ ; **f**,  $\log_{10}J_q$ . Velocities from upward-looking subsurface acoustic Doppler current profiler measurements at 270 m nominal depth go up to 30 m depth at 5 m vertical bin spacing. Point velocity measurements at 10 m depth extend velocities closer to the surface but are not used in estimation of  $S^2$ . Grey contours in **c–f** are isotherms, which are transferred onto **d–f** for reference.

This first multi-year time series of mixing is summarized in Fig. 1f together with other measures of larger-scale background influences (Fig. 1a–d). Considered together, these suggest patterns in mixing that span multiple depth ranges on timescales of weeks to months, contributing to a cyclic pattern of mixing on the seasonal timescale (Fig. 1f), and hint at longer-timescale patterns (for example, mixing is weaker during El Niño events than during La Niña events or neutral periods; Fig. 1a, e). Short-timescale variations associated with shear instabilities<sup>21,22</sup>, daily cooling<sup>13,14</sup> and weekly variations in surface winds<sup>13</sup> are hidden by our 10-day averaging. Our intent here is to establish the role of mixing on the seasonal cycle.

As a metric to quantify long-term patterns, we compute the turbulent heat flux ( $J_q$ ; coloured bars in Fig. 1f and defined in Methods) averaged over 20–60 m depth ( $\langle J_q \rangle_{20-60m}$ ; Fig. 1e). Over this depth range, turbulence fluctuations are closely related to coupled air-sea interactions, and to strong velocity gradients formed between the westward flowing near-surface South Equatorial Current (SEC) and the core of the Equatorial Undercurrent (maximum eastward flow near 100 m; 95% confidence interval CI = 70–145 m) are marginally stable, offering an additional energy source for mixing.

From monthly-averaged data,  $\langle J_q \rangle_{20-60m}$  is positively correlated with wind stress ( $r = 0.43$ , 95% CI = 0.15–0.64,  $P$ -value  $P = 0.004$ ) and TIW kinetic energy (KE;  $r = 0.59$ , 95% CI = 0.35–0.75,  $P = 0.00002$ ). However, it is not significantly correlated, on a monthly average, with any available measure of vertical stratification, shear, or their ratio, Ri (the gradient Richardson number, which defines the instability condition for stratified shear flows). Such correlations do exist in high-resolution measurements from targeted process experiments<sup>21,23</sup>, suggesting that the averaging over long periods hides the mechanistic relationships that drive the turbulence. Regardless, strong seasonal cycles exist in all flow properties of the equatorial cold tongue (Fig. 2), including clear correspondences between  $J_q$  shear and stratification. Warming of the upper 50 m in boreal spring coincides with reduced winds, weakening or disappearance of the westward flowing SEC, and reduced TIW KE;  $J_q$  is diminished throughout the water column. Increasing winds and TIW KE occur in late summer, following which the SEC reappears, the layer of high shear deepens,  $J_q$  increases and surface waters cool. Despite continued high wind stress ( $\tau_w$ ) in September,  $J_q$  weakens throughout the upper water column, as

does velocity shear in the upper 60 m. High  $\tau_w$  and high TIW KE accompany a secondary maximum in  $J_q$  late in the year.

The quantity  $\langle J_q \rangle_{20-60m}$  (Fig. 3a) exhibits an annual cycle that is significant at the 95% confidence level. Minima in April–May are a factor of 6 smaller than the maximum in August. The smallest values of  $\langle J_q \rangle_{20-60m}$  coincide with rising or maximum SST and the largest values with cooling SST.

We examine the heat budget of the surface mixed layer (with depth  $h$ ) to illustrate the importance of  $J_q$  to changes in SST. The net surface flux acting to heat or cool the mixed layer is  $J_q^0 - I^h$  (Fig. 3a), where  $J_q^0$  is the total surface flux from atmosphere to ocean and  $I^h$  is the intensity of short wave radiation penetrating below  $h$ .  $J_q^0$  is determined from the TropFlux analysis<sup>6</sup>,  $I^h$  is derived from an empirical formulation<sup>24</sup>, and  $h$  is determined from hourly temperature profile measurements on the TAO mooring (Supplementary Information). In the annual cycle,  $J_q^0 - I^h$  peaks in late boreal winter with a minimum in late boreal summer<sup>9</sup>. The critical seasonal modulation of  $J_q^0 - I^h$  is due in equal parts to modulations of solar radiation and latent cooling (a seasonal cycle of atmospheric flux components is included in Supplementary Information) but is partially offset by  $I^h$ , which is diminished in boreal summer when winds and mixing tend to increase  $h$ .

The heating and cooling rate of a fluid parcel due solely to vertical mixing is  $\rho C_p dT/dt = -dJ_q/dz$ , where  $\rho$ ,  $C_p$  and  $T$  are respectively the density, heat capacity and temperature of the fluid parcel,  $t$  is time and  $dJ_q/dz$  the vertical heat flux divergence across the fluid parcel. Across the surface mixed layer  $dJ_q/dz = (J_q^0 - I^h - J_q^h)/h$ , where  $J_q^h$  is the turbulent heat flux acting across the mixed layer base. If we assume that  $\langle J_q \rangle_{20-60m}$  is a reasonable estimator of  $J_q^h$ , then the sign of  $\langle J_q \rangle_{20-60m} - (J_q^0 - I^h)$  in Fig. 3a ought to reflect the sign of the observed cooling rate,  $dSST/dt$ . During February to May,  $J_q^0 - I^h > J_q^h$ , coincident with maximum sea surface heating. Conversely, from June to September,  $J_q^0 - I^h < J_q^h$ , coinciding with maximum sea surface cooling. The maximum observed cooling rate is  $<1\text{ K month}^{-1}$  while the heat flux divergence based on mixing alone contributes a maximum cooling of  $4\text{ K month}^{-1}$  (Fig. 3b).

The surface mixed layer heat budget discussed above considered a one-dimensional vertical balance. However, at the fixed point of observation, SST is also changed by horizontal advection<sup>25</sup>: gradients in temperature transported by surface currents cause a local change in temperature (see Supplementary Information). The sign of the zonal

advection ( $uT_x$ ) varies with that of the zonal surface currents ( $u$ ) because the negative sign of the zonal SST gradient ( $T_x$ ) is relatively constant. Meridional advection ( $vT_y$ ), largely due to TIWs, is a net heat source (Fig. 3b). Vertical advection (upwelling) brings cool fluid nearer the surface but mixing is required to modify SST. The sum of heat flux divergence and advection balances the observed heating rate (within 95% confidence limits) during strong sea surface cooling (July–September), but indicates greater heating than observed at other times.

Vertical profiles of  $J_q^h(z)$ , averaged on seasonal timescales (Fig. 4), show that the heat flux during June–August has significant vertical structure coincident with minimal  $J_q^0 - I^h$ , suggesting that the flux divergence acting across the sea surface may actually be larger than shown in Fig. 3b. It also emphasizes the distinctively weak turbulence throughout the upper 70 m in March–May, the period coinciding with maximal  $J_q^0 - I^h$ .

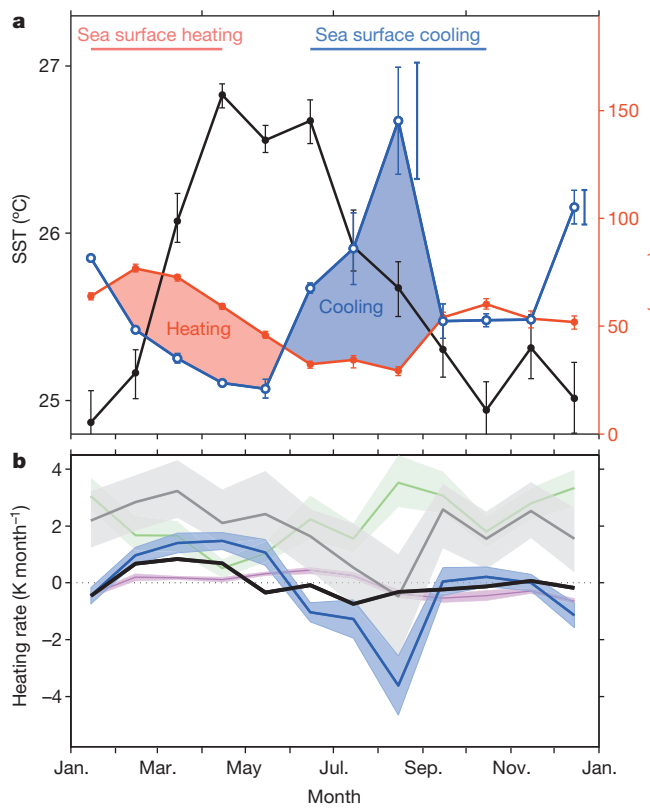


**Figure 3 | Annual cycles of SST and turbulence at 0, 140° W.** **a**, SST (black),  $\langle J_q \rangle_{20-60m}$  (blue) and that part of the surface heat flux that contributes to mixed layer heating ( $J_q^0 - I^h$ ) from TropFlux (red; <http://www.locean-ipsl.upmc.fr/tropflux/>). Averages are derived from the observations in Fig. 1. Error bars on SST and  $J_q^0 - I^h$  are 95% confidence limits on bootstrap estimates of means from daily values. Error bars on individual values of  $\langle J_q \rangle_{20-60m}$  represent the range based on two independent estimates of  $T_z$ . One estimate is computed from the temperature profile the sensor measures as it profiles the water column by surface-wave-induced motion coupled through the surface float. The second estimate uses temperature profiles from auxiliary temperature sensors distributed about that  $\chi$ -pod on the mooring, averaged hourly in time and differenced vertically over 10–20 m. The value of  $J_q$  plotted is the average of these two estimates. Natural variability is represented by 95% bootstrap confidence intervals on 15-min averages of  $J_q$  for the largest (August) value by the adjacent blue bar, and for all of the data by the blue bar adjacent to the December value. Details are included in Supplementary Information. **b**, Terms contributing to SST evolution. Black line,  $dSST/dt$ ; blue,  $1/(\rho C_p) dJ_q/dz$ ; red,  $uT_x$ ; green,  $vT_y$ ; grey,  $1/(\rho C_p) dJ_q/dz + uT_x + vT_y$ . Advection terms  $uT_x$ ,  $vT_y$  were computed from surface currents measured at the mooring and a revised SST product<sup>29</sup>. Uncertainties (shaded regions) are 95% bootstrap confidence limits on means computed from 30-day averages. Confidence limits on the turbulent heat flux divergence are based on reasonable ranges of  $h$  (Supplementary Information).

The finding that  $J_q^0 - I^h$  and  $J_q^h$  are each in quadrature with SST but out-of-phase with each other is a critical factor in defining the seasonal cycle of SST. The strong correlation between mixing and wind stress on the annual cycle, together with correlations found over shorter periods<sup>13</sup>, suggests the importance of the (predominantly easterly) wind in enhancing westward currents, thereby increasing velocity gradients and promoting shear instability, which is likely to be the root cause of turbulence in the upper equatorial ocean<sup>21,22,26</sup>. Higher winds also increase latent cooling, decreasing  $J_q^0 - I^h$  at the same times that mixing peaks.

These are, to our knowledge, the first long-term mixing measurements in the ocean that resolve the temporal intermittency and multi-year variability at a point of observation. Figure 3a clearly shows that observed seasonal sea surface heating and cooling coincide with the correct sign of the air–sea heat flux divergence. Subsurface mixing is the dominant sea surface cooling term and controls the SST cooling phase, but provides too little cooling to counter surface heating from the atmosphere plus advection during some parts of the year. It is possible that, at these times, the governing heat flux divergence is shallower than 20 m, as suggested by Fig. 4. It is also possible that spatial intermittency is important because the measured temperature of a fluid parcel is controlled by the cumulative sum of the mixing processes along its trajectory. Spatial gradients in temperature and currents are large, especially across the Equator. Gradients in mixing are unknown, but if they are proportionately large, then fluid parcels at the point of observation may have experienced a different history of mixing than observed.

This finding—that equatorial mixing is organized in a meaningful seasonal cycle—shows that the ocean’s microstructure (on scales of seconds to minutes and centimetres to metres) is clearly linked to, and at times dominates, particular aspects of the larger-scale dynamics. Extended measurements like these are intended to provide quantitative estimates of mixing on interannual timescales to improve our understanding of the El Niño/Southern Oscillation cycle and help to

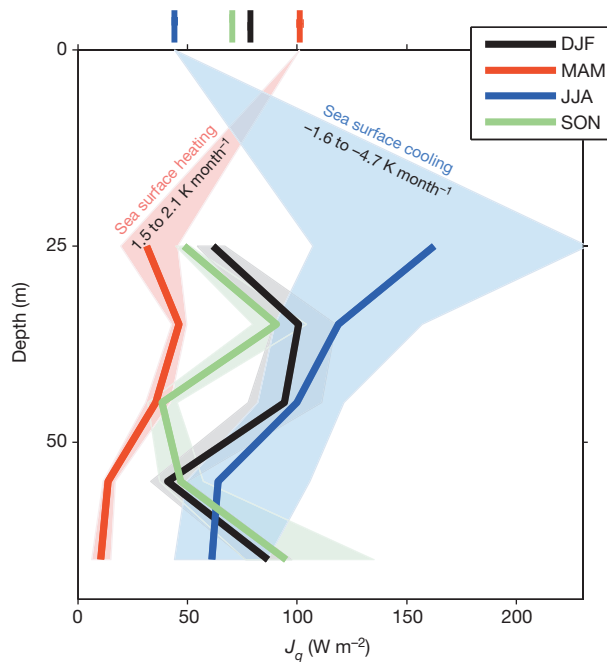


**Figure 4 | Seasonally averaged vertical profiles of turbulence heat flux.** Curves are shown for December–February (DJF); March–May (MAM); June–August (JJA) and September–November (SON). Positive heat flux indicates heating from above. Shading indicates 95% bootstrapped confidence limits on means based on 15-min averages. At top, values of  $J_q^0 - I^h$  in  $\text{W m}^{-2}$  are shown as vertical bars.

reduce the equatorial Pacific cold tongue bias that affects the mean state of many coupled ocean-atmosphere climate models<sup>3</sup>.

## METHODS SUMMARY

The vertical (more strictly, diapycnal) flux of heat by turbulence is represented by Fickian diffusion, enhanced by a turbulence diffusion coefficient,  $K_p = \chi_T T_z^2$  (ref. 27). The temperature variance dissipation rate ( $\chi_T$ ) is computed by scaling the temperature gradient spectrum measured by fast thermistors on small autonomous instruments (' $\chi$ -pods')<sup>18</sup> attached to oceanographic moorings and packaged with inertial navigation units to quantify the component of flow speed past the sensor that is due to wave-induced motions of the surface float<sup>19</sup>. The other component of the flow speed is the ocean current speed, measured separately by velocity sensors on the mooring. The vertical temperature gradient,  $T_z$ , is defined locally by the vertical motion of the sensor through the water or, on a larger scale, by additional temperature sensors on the mooring. The depth-dependent vertical heat flux caused by turbulence is  $J_q = -\rho C_p K_p T_z$ .

Received 14 March; accepted 3 June 2013.

Published online 24 July 2013.

1. Xie, S.-P. Satellite observations of cool ocean-atmosphere interaction. *Bull. Am. Meteorol. Soc.* **85**, 195–208 (2004).
2. Richter, I. & Xie, S.-P. On the origin of equatorial Atlantic biases in coupled general circulation models. *Clim. Dyn.* **31**, 587–598 (2008).
3. Wittenberg, A. T., Rosati, A., Lau, N. C. & Ploshay, J. J. GFDL's CM2 global coupled climate models. Part III: Tropical Pacific climate and ENSO. *J. Clim.* **19**, 698–722 (2006).
4. Jouanno, J., Marin, F., Du Penhoat, Y., Sheinbaum, J. & Molines, J.-M. Seasonal heat balance in the upper 100 m of the equatorial Atlantic ocean. *J. Geophys. Res.* **116**, C09003 (2011).
5. Xie, S. On the genesis of the equatorial annual cycle. *J. Clim.* **7**, 2008–2013 (1994).
6. Praveen Kumar, B., Vialard, J., Lengaigne, M., Murty, V. S. N. & McPhaden, M. J. TropFlux: air-sea fluxes for the global tropical oceans—description and evaluation. *Clim. Dyn.* **38**, 1521–1543 (2012).
7. Mitchell, T. P. & Wallace, J. M. The annual cycle in equatorial convection and sea surface temperature. *J. Clim.* **5**, 1140–1156 (1992).
8. Trenberth, K. E., Caron, J. M. & Stepaniak, D. P. The atmospheric energy budget and implications for surface fluxes and ocean heat transports. *Clim. Dyn.* **17**, 259–276 (2001).
9. Wang, B. & Fu, X. Processes determining the rapid reestablishment of the equatorial Pacific cold tongue/ITCZ complex. *J. Clim.* **14**, 2250–2265 (2001).
10. Wang, W. & McPhaden, M. J. The surface-layer heat balance in the equatorial Pacific ocean. Part I: mean seasonal cycle. *J. Phys. Oceanogr.* **29**, 1812–1831 (1999).
11. McPhaden, M. J., Cronin, M. F. & McClurg, D. C. Meridional structure of the seasonally varying mixed layer temperature balance in the eastern tropical Pacific. *J. Clim.* **21**, 3240–3260 (2008).
12. Moun, J. N. *et al.* Sea surface cooling at the Equator by subsurface mixing in tropical instability waves. *Nature Geosci.* **2**, 761–765 (2009).
13. Moun, J. N. & Caldwell, D. R. Local influences on shear flow turbulence in the equatorial ocean. *Science* **230**, 315–316 (1985).
14. Gregg, M. C., Peters, H., Wesson, J. C., Oakey, N. S. & Shay, T. J. Intensive measurements of turbulence and shear in the equatorial undercurrent. *Nature* **318**, 140–144 (1985).
15. Lien, R.-C., Caldwell, D. R., Gregg, M. C. & Moun, J. N. Turbulence variability in the central Pacific at the beginning of the 1991–93 El Niño. *J. Geophys. Res.* **100**, 6881–6898 (1995).
16. Inoue, R., Lien, R.-C. & Moun, J. N. Modulation of equatorial turbulence by a tropical instability wave. *J. Geophys. Res.* **117**, C10009 (2012).
17. Hummels, R. & Dengler, M. B. B. Seasonal and regional variability of upper ocean diapycnal heat flux in the Atlantic cold tongue. *Prog. Oceanogr.* **111**, 52–74 (2013).
18. Moun, J. N. & Nash, J. D. Mixing measurements on an equatorial ocean mooring. *J. Atmos. Ocean. Technol.* **26**, 317–336 (2009).
19. Perlin, A. & Moun, J. N. Comparison of thermal variance dissipation rates from moored and profiling instruments at the equator. *J. Atmos. Ocean. Technol.* **29**, 1347–1362 (2012).
20. McPhaden, M. J. *et al.* The tropical ocean-global atmosphere observing system: a decade of progress. *J. Geophys. Res.* **103**, 14,169–14,240 (1998).
21. Moun, J. N., Nash, J. D. & Smyth, W. D. Narrowband high-frequency oscillations at the equator. Part I: interpretation as shear instabilities. *J. Phys. Oceanogr.* **41**, 397–411 (2011).
22. Smyth, W. D., Moun, J. N., Li, L. & Thorpe, S. A. Shear instability, the descent of the diurnal mixing layer and the deep cycle of equatorial turbulence. *J. Phys. Oceanogr.* (submitted).
23. Zaron, E. D. & Moun, J. N. A new look at Richardson number mixing schemes for equatorial ocean modeling. *J. Phys. Oceanogr.* **39**, 2652–2664 (2009).
24. Ohlmann, J. C., Siegel, D. A. & Gautier, C. Ocean mixed layer radiant heating and solar penetration: a global analysis. *J. Clim.* **9**, 2265–2280 (1996).
25. Swenson, M. S. & Hansen, D. V. Tropical Pacific ocean mixed layer heat budget: the Pacific cold tongue. *J. Phys. Oceanogr.* **29**, 69–81 (1999).
26. Sun, C., Smyth, W. D. & Moun, J. N. Dynamic instability of stratified shear flow in the upper equatorial ocean. *J. Geophys. Res.* **103**, 10323–10337 (1998).
27. Osborn, T. R. & Cox, C. S. Oceanic fine structure. *Geophys. Fluid Dyn.* **3**, 321–345 (1972).
28. NOAA Commerce Department. NOAA gets U.S. consensus for El Niño/La Niña index, definitions. *NOAA press release NOAA 03–119* (2003); available at <http://www.noaanews.noaa.gov/stories/s2095.htm>.
29. Reynolds, R. W. *et al.* Daily high-resolution-blended analyses for sea surface temperature. *J. Clim.* **20**, 5473–5496 (2007).

**Supplementary Information** is available in the online version of the paper.

**Acknowledgements** This work was funded by the National Science Foundation (grants 0424133, 0728375 and 1256620). We thank M. Neely-Brown and R. Kreth, who were primarily responsible for construction, testing and maintenance of  $\chi$ -pods, and P. Freitag and NOAA's PMEL mooring group, who helped us to get started with these measurements. We also thank NOAA's NDBC group, who have continued to deploy our  $\chi$ -pods on TAO moorings. E. Shroyer, S. de Szoeke, K. Benoit-Bird and D. Chelton provided comments on the paper. This is PMEL contribution no. 3970. We dedicate this paper to the memory of our colleague and co-author A. Perlin, who passed away during final revisions, and to the memory of lab engineer R. Kreth.

**Author Contributions** J.N.M. wrote the paper. A.P. and J.N.M. did the analysis. J.D.N. has been part of this project since its inception and provided suggestions for analysis. M.J.M. provided advice on the large-scale context of these measurements. All authors contributed suggestions and text at the writing stage.

**Author Information** Reprints and permissions information is available at [www.nature.com/reprints](http://www.nature.com/reprints). The authors declare no competing financial interests. Readers are welcome to comment on the online version of the paper. Correspondence and requests for materials should be addressed to J.N.M. (moun@coas.oregonstate.edu).

# Feeding andesitic eruptions with a high-speed connection from the mantle

Philipp Ruprecht<sup>1</sup> & Terry Plank<sup>1</sup>

Convergent margin volcanism is ultimately fed by magmas generated in the mantle, but the connection between the mantle and the eruption at the surface is typically obscured by cooling, crystallization and magma mixing within the crust<sup>1–3</sup>. Geophysical techniques are also not very effective in the lower and middle crust, where seismic events are rare and resolution is generally poor<sup>4,5</sup>. It has thus been unclear how fast mantle-derived magmas transit the crust and recharge crustal magma chambers. Here we use diffusion modelling of nickel zonation profiles in primitive olivines from diverse primary melts<sup>6–10</sup> to show how mantle recharge may occur on timescales as short as eruptions themselves. In Irazú volcano in Costa Rica, magmas apparently ascend from their source region in the mantle through crust about 35 kilometres thick in just months to years, recharging hybrid basaltic andesites over the course of the eruption. These results show that large stratovolcanoes with shallow magma chambers<sup>11,12</sup> may still preserve the deep record of their mantle origin in olivine crystals. This approach—documenting magma ascent timescales from the mantle beneath a convergent margin stratovolcano—can be applied to other eruptions that record magma mixing with recharge melts. Signs of volcanic unrest are typically monitored at the surface or upper crust; new efforts should look deeper, tracking magma movement from the base of the crust to the surface in the months to years before eruptions.

The 1963–65 eruption of Irazú volcano, the largest stratovolcano in the Central American arc<sup>13</sup>, produced basaltic andesites that contain a remarkable diversity of olivine crystals, many of which still preserve chemical vestiges of their mantle origin. Nickel (Ni) and forsterite (Fo) variations (measured by laser-ablation inductively coupled plasma mass spectrometry, LA-ICPMS; see Methods) in olivines from the single 1963–65 eruption record as much variation as global and regional data sets<sup>6,7,10,14</sup> (Fig. 1). In particular, primitive magnesian olivines ( $>Fo_{88}$ ) have Ni concentrations that vary by a factor of about two. Such Ni variations at high, constant Fo contents are thought to be created during mantle melting—resulting from melting of distinct mantle lithologies (for example, pyroxenitic versus peridotitic mantle) and melting at distinct depths<sup>6–10</sup>. The large range in Ni concentrations at constant Fo content implies that distinct batches of mantle melts are supplied to Irazú volcano—even within a single eruption. The actual process that creates these variations is not as critical to this study as the timescale over which those variations would be erased. Upon crystallization, the Ni concentration in melt is controlled predominantly by growth of olivine alone. Other silicate phases (plagioclase and pyroxenes) later join the crystallization sequence and drive a shallower Ni–Fo trajectory (Fig. 1).

Such an evolutionary path of the magma is supported by other trace-element variations in olivine (see Supplementary Fig. 5 for Ca, Sc, Ti variations with Ni content). High Ni concentrations at intermediate Fo content reflect magma hybridization at shallow crustal levels during mixing of primitive mantle-derived magmas with evolved resident magmas and assimilation of foreign crystals (that is, xenocrysts; see Supplementary Information). Although shallow magma processes (such as magma mixing or prolonged residence in hybrid magmas) are

recorded in the majority of the olivine crystals, we focus on the magnesian olivines with variable Ni content because they provide insight into mantle recharge timescales.

We consider the magnesian olivines that are common in hybrid magmas of Irazú volcano<sup>15</sup> to be magmatic in origin and true phenocrysts (that is, crystals growing from the ascending primitive mantle melt that later mixes with resident magma in the shallow plumbing system). Their phenocrystic character is indicated by their texture (well-formed crystals with sharp, continuous crystal faces typical of growth from a melt), and trace-element compositions (see Supplementary Information). Even if they are mantle xenocrysts, however, they still constrain the timescale of ascent from the mantle.

Most olivines from the 1963–65 Irazú eruption record growth in a closed system magma, with melt evolving along a liquid line of descent (Fig. 2a, b). Some olivines (~15% of all analysed) show a more complex history of mixing between distinct primitive melts, with Ni zonation crossing multiple olivine fractionation curves (Fig. 2c, d). Retention of such distinct Ni zonation requires that mixing of these mantle melts must have been faster than the timescales of diffusive re-equilibration. Given the high Fo contents of the olivines that record this Ni zonation (many over 90% forsterite, Fo<sub>90</sub>, which is typical of mantle olivine), this mixing process requires deep crystallization in or near the mantle, or not far removed in time from the mantle history. Indeed, thermal arguments show how any crustal residence before mixing must be very short (less than a month) to both preserve the Ni zonation and prevent a decrease in Fo (see Supplementary Information).

Experimental studies constrain Ni diffusion in olivine<sup>16–18</sup> and enable us to calculate mixing-to-eruption timescales for these mantle melts (see Methods Summary). Some individual olivine crystals are reversely zoned in Ni, with reversals up to 1,000 p.p.m. at only slightly varying Fo (Fig. 3). In some cases the reversals correlate with chromium (Cr) and phosphorus (P) reversal, which put additional constraints on the crystallization and diffusion history of these olivines. Although diffusion rates of trivalent Cr in olivine are currently debated, P diffusion is known to be slow compared to Ni and it therefore records growth zoning<sup>18,19</sup>. Zonation bands that are narrower in P than Ni (Fig. 3d, f) indicate some diffusive re-equilibration of Ni, and this zonation can be used to constrain the mixing timescales of the primitive melts before eruption. Cr does not always correlate with Ni because (1) Ni possesses greater primary variation and (2) Cr in olivine may be affected by coprecipitation of spinels<sup>20</sup>.

Mixing-to-eruption timescales derived from one-dimensional Ni zoning profiles are short (months to a few years; see Fig. 4, Supplementary Table 1 and Methods for details of the calculation procedure). Calculated timescales are maximum estimates, whereas a Monte Carlo approach is used to generate probability density functions (PDFs) and estimate uncertainties. Maximum timescales of mixing before eruption are derived for 11 olivines with Ni reversals unambiguously related to mixing of two distinct mantle melts. Using a Ni diffusion coefficient ( $D_{Ni}$ ) at 1,200 °C (appropriate for the primitive melts that host these magnesian olivines) leads to average timescales of  $0.6^{+4.8}_{-0.4}$  years and  $0.3^{+2.3}_{-0.2}$  years for the earlier (IZ-10-11) and the later (IZ-10-13)

<sup>1</sup>Lamont-Doherty Earth Observatory of Columbia University, 61 Route 9W, Palisades, New York 10964, USA.

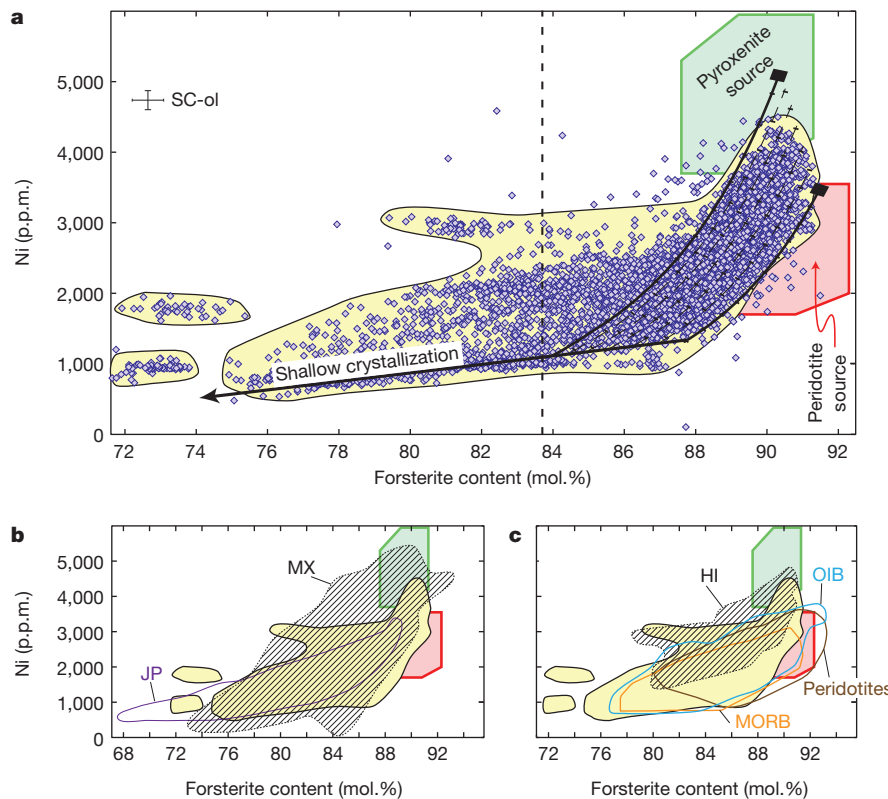


**Figure 1 | Compositional diversity in olivine phenocrysts.** **a**, Ni and forsterite contents measured by LA-ICPMS for 176 core-to-rim traverses (6,398 data points) in olivine phenocrysts from the 1963–65 Irazú eruption. Green and red fields are olivines calculated to be in equilibrium with pyroxenite and peridotite source compositions taken from ref. 10 as one possible source of primary melt variability. Fractionation curves (solid and dashed curves) for different primary melt compositions encompass the compositional diversity recorded in the most primitive olivines ( $>Fo_{88}$ ). Tick marks are 1% increments of olivine crystallization. External reproducibility is estimated by analysis of olivine grains of San Carlos USNM 111312/44 (SC-ol). The major-element fractionation path passes through melt inclusion compositions from ref. 26 and additional melt inclusions reported here. The high- and low-Ni fractionation curves assume 302 p.p.m. Ni at 8.08 wt% MgO and 247 p.p.m. at 9.53 wt% MgO in the melt, respectively. Each contour varies by an added 16.7% Ni in the melt

compared to the low-Ni liquid line of descent. At about 1,000 p.p.m. Ni the data diverge from the simple fractionation curves and follow a shallower trajectory associated with the shallow co-crystallization of plagioclase, pyroxene and olivine (see Supplementary Data for additional trace elements supporting this interpretation, and Supplementary Fig. 5). The vertical dotted line is the olivine composition in equilibrium with whole rocks<sup>11</sup> from the 1963–65 eruption assuming a partition coefficient  $K_D$  of 0.3. **b**, Irazú data (yellow shading) compared to the typical compositional variations observed in arc magmas represented here by data from Mexico<sup>7,10</sup> (MX, hatched, dotted outline) and Daisen Volcano in Japan<sup>14</sup> (JP, purple). **c**, Irazú data (yellow shading) compared to global compilations<sup>6</sup> for peridotites (brown), mid-ocean-ridge-basalt olivines (MORB, orange), Hawaiian olivines (HI, hatched, dotted outline), and other ocean-island-basalt olivines (OIB, blue).

erupted samples (see sample description for details of the stratigraphy). Given that calculated timescales are short compared to the time of volcanic activity (approximately 2 years), mantle-derived magmas were actively mixing deep in the plumbing system while the eruption was already in full swing and magma transit through the crust may have sped up as the eruption progressed—potentially as continuous magma extraction from mantle and ascent led to the establishment of a more transmissible crustal pathway over time. This raises the question of where the magmas mix and whether we can use such mixing records to extract transit times from the mantle to the surface of this large, active convergent margin stratovolcano.

The non-primitive character of many arc magmas, phase equilibria constraints combined with thermal considerations<sup>2</sup>, as well as the geo-barometry of gabbroic cumulates and volcanic mineral assemblages<sup>21</sup>, all suggest that mantle-derived melts may crystallize over a wide pressure range (typically 4–10 kbar) in the crust. In the case of Central America this pressure range represents the entire crustal column, assuming an average crustal density of  $2,830 \text{ kg m}^{-3}$  and that the Mohorovičić discontinuity (Moho) is 35 km deep<sup>12</sup>. Furthermore, the fact that the primitive Irazú olivines are  $>Fo_{88}$  suggests that they are the Mg-rich liquidus phase and therefore probably represent the earliest silicate crystallization, close to the mantle–crust interface, because the melts would evolve to low Mg/Fe ratios upon ascent, transient stalling and

cooling (see Supplementary Discussion). Thermodynamic<sup>22</sup> and pseudo-liquidus<sup>23</sup> phase calculations confirm olivine as a liquidus phase for pressures over 9 kbar, potentially co-crystallizing with orthopyroxene. However, the absence of high-magnesium-number (Mg#) orthopyroxene suggests that olivine is the primary liquidus phase throughout the crustal column.

Assuming magnesian olivine crystallization and mixing of primary mantle melts near the Moho, at 9 kbar depth (about 30 km deep), and given Ni diffusion timescales of the order of one year (Fig. 4), we calculate average crustal transport rates of 80 m per day for mantle magmas. Even if the upper 5–10 km are transited rapidly as part of the eruption process, lower and middle crustal transport rates would still be of the order of tens of meters per day (that is, 55 m per day, assuming 10 km at  $>0.1 \text{ m s}^{-1}$ , as for explosive eruptions<sup>24</sup>). It is also possible that mantle melts mix in the crust, but the high Fo contents that vary little across Ni zonation profiles (for example,  $>Fo_{90}$  in Fig. 3c) place tight constraints on the timescales involved. For example, as little as 35 °C cooling will drive olivine to drop one Fo unit<sup>22</sup>, and if this occurred before mixing, it would be observed. If melts ascend adiabatically, they may nearly parallel the olivine liquidus<sup>25</sup>, and thus could transit the crust chemically unmodified until they crystallize at the point of water-vapour saturation at 5–8 km depth (for the 1723 Irazú eruption<sup>26</sup>), where there is a clearly imaged low-velocity zone that probably represents

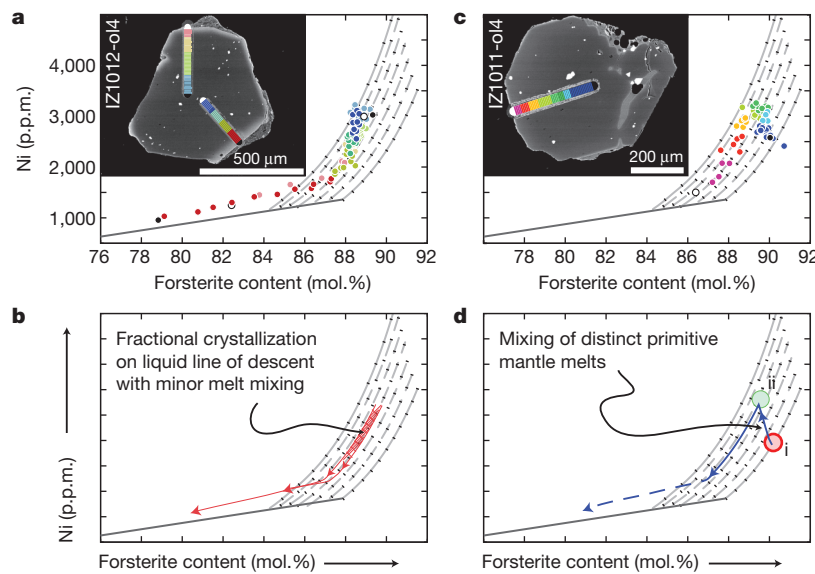


**Figure 2 | Nickel and forsterite zoning in olivine from Irazú volcano.** **a**, Ni versus forsterite variations for olivine phenocrysts that follow a single liquid line of descent. Colour coding in the crystal traverse ties the Ni–Fo data spatially to the image of the crystal. **b**, Conceptual evolution of olivines evolving along subparallel olivine fractionation trends. The two red curves show that crystals often diverge slightly from the calculated olivine-fractionation trend, suggesting minor melt mixing. The grey curves are the same fractionation

curves for different primary melt compositions with tick marks at 1% crystallization increments as in Fig. 1. **c**, Ni versus forsterite variations for olivine phenocrysts with strongly varying Ni concentrations at primitive Fo content, suggesting the involvement of distinct mantle-derived melts. **d**, Conceptual evolution of Ni in an olivine, recording two distinct primitive mantle melt compositions (i and ii).

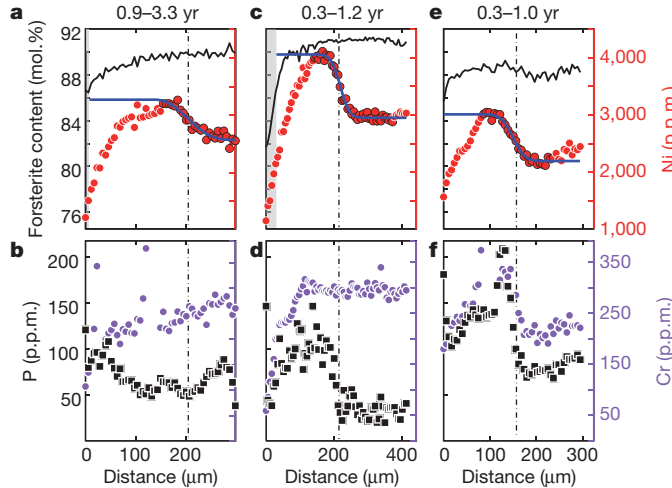


**Figure 3 | Representative zonation profiles for three magnesian olivine phenocrysts.** **a, b**, Sample IZ1011-014; **c, d**, Sample IZ1013-012; **e, f**, Sample IZ1013-0153. All olivines show Ni reversals that are modelled (blue line) by equation (1) and schematically displayed in Supplementary Fig. 8. All 11 olivines are shown in Supplementary Figs 6 and 7. The mixing-to-eruption timescales represent the mode of the probability density functions (PDFs) derived via a Monte Carlo approach where the lower and upper bound are calculated for 1,200 °C and 1,100 °C, respectively. Full uncertainties are given in Supplementary Table 1. We note that the displayed timescales for the best-fit diffusion profiles (blue line, lowest root-mean-square value among all Monte Carlo calculations) are typically in agreement with the estimates from maximum-probability estimates (Fig. 4). Only olivines with less well-defined PDF peaks show a shift to longer timescales in the best-fit estimate. In some cases the Ni reversal coincides with Cr and P zonation, whereas P zonation typically shows a sharper gradient consistent with very limited diffusive reequilibration<sup>19</sup>. Gaps in the Cr data are caused by partial ablation of Cr-spinels. The distance of crystal traverses is measured from the rim towards the centre of each grain.

a major magma storage zone beneath Irazú<sup>12,27</sup>. If this were the case, however, melts would ascend at even faster rates than the crustally averaged rates calculated above (55–80 m per day), because adiabatic ascent would require transport rates of over 1,000 m per day in a 2-m-wide, 25-km-long dike (see Supplementary Information). Thus, no matter at what depth the Ni clock is set, processes happen quickly before eruption. Mixing of mantle melts, ascent through the crust, hybridization in the upper crustal magma storage region, and final ascent in the conduit must all happen within months to years, within the two-year span of this eruption itself.

Recent studies have reported earthquake swarms in the lower crust that are ascribed to magma movement<sup>4,5,28,29</sup>. High-resolution depth location of these events in the western USA and Iceland reveals significant upward migration between swarms, of the order of a kilometre per week or per month, very similar to the rates estimated above for the 1963–65 Irazú eruption (that is, 50–100 m per day, or 1 km per 10–20 days). The comparison is not perfect, because most of these seismically active systems did not erupt, whereas Irazú did, and Irazú olivines record an integrated ascent over the entire crustal column that could include very rapid transit punctuated by brief stalling on the way to the surface. Nonetheless, the crystal records are consistent with the seismic observations and provide a new constraint for magma transport from the mantle to the surface underneath large stratovolcanoes.

Our results indicate that (1) distinct primary melts coexist and mix in the mantle beneath arc volcanoes. (2) These mantle-derived melts may stall only briefly in the crust with total crustal ascent timescales of the order of months to years. Thus, crustal processes<sup>30</sup> in some regions may be limited and our results establish (3) a direct connection between the mantle and shallow crustal magma chambers. Even though compositionally distinct magmas may mix and hybridize completely<sup>1,2</sup>, (4) olivines may retain chemical vestiges of their mantle history. A fairly homogenous basaltic andesite eruption like Irazú 1963–65 belies the rich diversity of olivines it contains, which record the magma's integrated history from the mantle to eruption. This is not an isolated occurrence; magma mixing, mafic magma recharge, and high Fo olivines are common to many stratovolcanoes above subduction zones<sup>31,32</sup>, and the approach we have outlined here may be applied generally. It

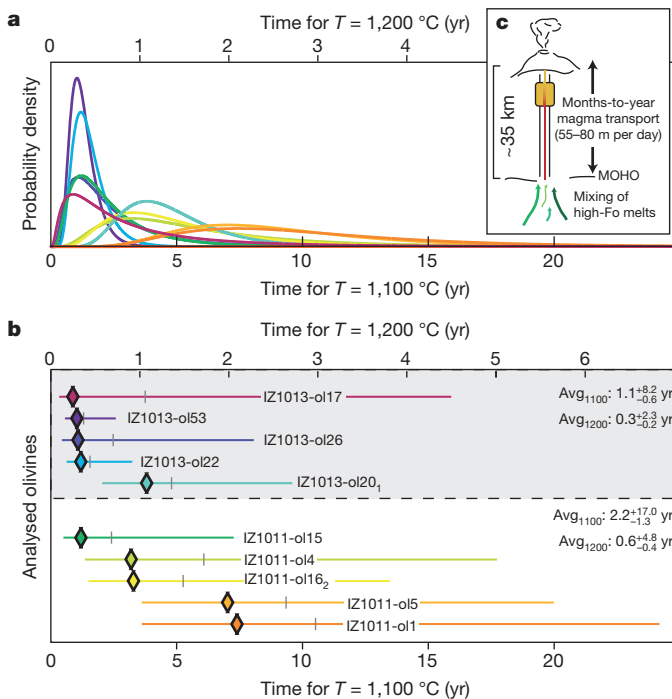


**Figure 4 | Mantle melt mixing-to-eruption timescales for all analysed olivines.** **a**, Relative PDFs for calculated mixing-to-eruption timescales at 1,100 °C and 1,200 °C (note the different time axes for the two end-member temperatures, which vary by a factor of  $\sim 3.5$ ). See Methods for additional information. Colours correspond to the different olivines in **b**. **b**, Compilation of the calculated timescales ordered by stratigraphic order (Supplementary Fig. 1) showing the 2-s confidence interval (coloured bars). Mode (diamonds) and mean (vertical bar) of the PDFs are shown. IZ1013-ol44 plots beyond the scale of the plot for both temperature calculations; the mode for the 1,100 °C and 1,200 °C calculations is 17.3 and 61.3 years, respectively (Supplementary Table 1). The five profiles shown for each crystal of each sample have been used to calculate average timescales ( $\text{Avg}_{1100}$  and  $\text{Avg}_{1200}$ ) for the rapid mixing-to-eruption timescales observed in the Irazú data set. Olivines from the later erupted sample IZ-10-13 record on average shorter timescales, suggesting a speeding up of magma ascent as pathways in the crust became more open during the progress of magma extraction and eruption at the surface. **c**, Conceptual diagram illustrating melt mixing at Moho depth followed by fast ascent (over a months-to-year period) to the surface. At shallow levels the mafic magmas mix with resident evolved magma in the shallow crust. See text for additional information. Green arrows represent distinct mantle melts pooling at the base of the crust. Once extracted from the mantle the primitive mixed magma (red) ascends through the crust until it interacts with a more evolved hybrid magma (orange) and erupts as such hybrid magma.

remains to be seen how many other stratovolcanoes like Irazú may be fed and possibly triggered by magma recharge directly from the mantle. Seismically recorded deformation in lower and mid-crustal levels<sup>4</sup> may be the first precursor of such fast-ascending mantle-derived melts.

## METHODS SUMMARY

The zoning of about 176 olivines from three tephra samples was studied using a combination of back-scattered electron microscopy and LA-ICPMS. Major- and minor-element compositions were analysed by electron microscopy (wavelength dispersive X-ray spectroscopy). Continuous zoning profiles of major (Fe-Mg) and trace elements were determined by LA-ICPMS. To account for diffusive anisotropy in olivine, lattice orientations of analysed olivine were characterized using electron back-scatter diffraction. Because the erupted magmas are hybrid in composition, we estimated temperatures of the primitive end-members using a combination of thermodynamic models and olivine-melt thermometry. Ni diffusion calculations were based on an analytical solution for a confined-planar interior source with constant boundary conditions<sup>33</sup> and uncertainty estimates for the timescales of mixing to eruption were generated using Monte Carlo simulations (Fig. 4). Initial and boundary conditions as well as parameters varied for the Monte Carlo simulations are summarized in Supplementary Fig. 8. Ni diffusivity was taken from

refs 16, 17 and 33. Presented timescales for mixing to eruption are conservative (maximum) estimates due to the use of a one-dimensional model that neglects volume diffusive re-equilibration, the assumption that zoning profiles are purely diffusive (no simultaneous growth or spatial smearing by the laser ablation analyses), and the low end of the temperature range (1,100–1,200 °C) chosen.

**Full Methods** and any associated references are available in the online version of the paper.

Received 29 March 2012; accepted 23 May 2013.

- Kent, A. J. R., Darr, C., Koleszar, A. M., Salisbury, M. J. & Cooper, K. M. Preferential eruption of andesitic magmas through recharge filtering. *Nature Geosci.* **3**, 631–636 (2010).
- Annen, C., Blundy, J. D. & Sparks, R. S. J. The genesis of intermediate and silicic magmas in deep crustal hot zones. *J. Petrol.* **47**, 505–539 (2006).
- Dungan, M. A., Wulfe, A. & Thompson, R. Eruptive stratigraphy of the Tatará-San Pedro complex, 36 °S, Southern Volcanic Zone, Chilean Andes: reconstruction method and implications for magma evolution at long-lived arc volcanic centers. *J. Petrol.* **42**, 555–626 (2001).
- Shelly, D. R. & Hill, D. P. Migrating swarms of brittle-failure earthquakes in the lower crust beneath Mammoth Mountain, California. *Geophys. Res. Lett.* **38**, L20307 (2011).
- White, R. S. et al. Dynamics of dyke intrusion in the mid-crust of Iceland. *Earth Planet. Sci. Lett.* **304**, 300–312 (2011).
- Sobolev, A. V., Hofmann, A. W., Sobolev, S. V. & Nikogosian, I. K. An olivine-free mantle source of Hawaiian shield basalts. *Nature* **434**, 590–597 (2005).
- Straub, S. M., LaGatta, A. B., Martin-Del Pozzo, A. L. & Langmuir, C. H. Evidence from high-Ni olivines for a hybridized peridotite/pyroxenite source for orogenic andesites from the central Mexican Volcanic Belt. *Geochem. Geophys. Geosyst.* **9**, Q03007 (2008).
- Wang, Z. & Gaetani, G. A. Partitioning of Ni between olivine and siliceous eclogite partial melt: experimental constraints on the mantle source of Hawaiian basalts. *Contrib. Mineral. Petrol.* **156**, 661–678 (2008).
- Li, C. & Ripley, E. M. The relative effects of composition and temperature on olivine-liquid Ni partitioning: statistical deconvolution and implications for petrologic modeling. *Chem. Geol.* **275**, 99–104 (2010).
- Straub, S. M. et al. Formation of hybrid arc andesites beneath thick continental crust. *Earth Planet. Sci. Lett.* **303**, 337–347 (2011).
- Alvarado, G. E. et al. Recent volcanic history of Irazú volcano, Costa Rica: alternation and mixing of two magma batches, and pervasive mixing. *Spec. Pap. Geol. Soc. Am.* **412**, 259–276 (2006).
- Dzierma, Y. et al. Imaging crustal structure in south central Costa Rica with receiver functions. *Geochem. Geophys. Geosyst.* **11**, Q08S26 (2010).
- Carr, M. J. et al. Element fluxes from the volcanic front of Nicaragua and Costa Rica. *Geochem. Geophys. Geosyst.* **8**, Q06001 (2007).
- Tamura, Y., Uehara, M. & Ishii, T. Primary arc basalts from Daisen volcano, Japan: equilibrium crystal fractionation versus disequilibrium fractionation during supercooling. *J. Petrol.* **41**, 431–448 (2000).
- Alvarado Induni, G. E. *Volcanology and Petrology of Irazú Volcano, Costa Rica* PhD thesis, 1–261 (Christian-Albrechts-Universität zu Kiel, 1993).
- Petry, C., Chakraborty, S. & Palme, H. Experimental determination of Ni diffusion coefficients in olivine and their dependence on temperature, composition, oxygen fugacity, and crystallographic orientation. *Geochim. Cosmochim. Acta* **68**, 4179–4188 (2004).
- Holzapfel, C., Chakraborty, S., Rubie, D. C. & Frost, D. J. Effect of pressure on Fe-Mg, Ni and Mn diffusion in (Fe,Mg<sub>1-x</sub>)<sub>2</sub>SiO<sub>4</sub> olivine. *Phys. Earth Planet. Inter.* **162**, 186–198 (2007).
- Spandler, C. & O'Neill, H. Diffusion and partition coefficients of minor and trace elements in San Carlos olivine at 1,300 °C with some geochemical implications. *Contrib. Mineral. Petrol.* **159**, 791–818 (2010).
- Milman-Barris, M. et al. Zoning of phosphorus in igneous olivine. *Contrib. Mineral. Petrol.* **155**, 739–765 (2008).
- Qian, Q., O'Neill, H. S. C. & Hermann, J. Comparative diffusion coefficients of major and trace elements in olivine at  $\sim 950$  °C from a xenocryst included in dioritic magma. *Geology* **38**, 331–334 (2010).
- Arculus, R. J. & Wills, K. J. A. The petrology of plutonic blocks and inclusions from the Lesser Antilles island arc. *J. Petrol.* **21**, 743–799 (1980).
- Ghiorso, M. S., Hirschmann, M. M., Reiners, P. W. & Kress, V. C. III. The pMELTS: a revision of MELTS for improved calculation of phase relations and major element partitioning related to partial melting of the mantle to 3 GPa. *Geochem. Geophys. Geosyst.* **3**, doi:10.1029/2001GC000217 (2002).
- Danyushevsky, L. V. & Plechov, P. Petrolog3: integrated software for modeling crystallization processes. *Geochem. Geophys. Geosyst.* **12**, Q07021 (2011).
- Rutherford, M. J. Magma ascent rates. *Rev. Mineral. Geochem.* **69**, 241–271 (2008).
- Weaver, S. L., Wallace, P. J. & Johnston, A. D. A comparative study of continental vs. intraoceanic arc mantle melting: experimentally determined phase relations of hydrous primitive melts. *Earth Planet. Sci. Lett.* **308**, 97–106 (2011).
- Benjamin, E. et al. High water contents in basaltic magmas from Irazú Volcano, Costa Rica. *J. Volcanol. Geotherm. Res.* **168**, 68–92 (2007).
- Lizarralde, D. et al. Crustal structure along the active Costa Rican volcanic arc. *Am. Geophys. Union Fall Mtg Abstr. T13A–2176* (2010).
- Klein, F. W. Earthquakes at Loihi Submarine Volcano and the Hawaiian Hot Spot. *J. Geophys. Res.* **87**, 7719–7726 (1982).

29. Tarasewicz, J., Brandsdóttir, B., White, R. S., Hensch, M. & Thorbjarnardóttir, B. Using microearthquakes to track repeated magma intrusions beneath the Eyjafjallajökull stratovolcano, Iceland. *J. Geophys. Res.* **117**, B00C06 (2012).
30. Costa, F. & Dungan, M. A. Short time scales of magmatic assimilation from diffusion modeling of multiple elements in olivine. *Geology* **33**, 837–840 (2005).
31. Sisson, T. W. & Bronto, S. Evidence for pressure-release melting beneath magmatic arcs from basalt at Galunggung, Indonesia. *Nature* **391**, 883–886 (1998).
32. Grove, T. L. *et al.* Magnesian andesite and dacite lavas from Mt. Shasta, northern California: products of fractional crystallization of H<sub>2</sub>O-rich mantle melts. *Contrib. Mineral. Petro.* **148**, 542–565 (2004).
33. Costa, F. & Morgan, D. in *Timescales of Magmatic Processes: From Core to Atmosphere* (eds Dosseto, A., Turner, S. P. & Van Orman, J. A.) 125–159 (Wiley-Blackwell, 2010).

**Supplementary Information** is available in the online version of the paper.

**Acknowledgements** We thank G. Alvarado for help during tephra sampling and S. Straub for discussions on olivine partitioning. The work was funded by a Feodor-Lynen Fellowship from the Alexander-von-Humboldt foundation to P.R. and NSF grant EAR 0948533 to T.P. This is Lamont-Doherty Earth Observatory contribution 7695.

**Author Contributions** P.R. designed the study and led the sampling, analytical, diffusion and thermal modelling efforts. P.R. and T.P. equally contributed to the discussions and interpretation of the data and both participated equally in the writing stages.

**Author Information** Reprints and permissions information is available at [www.nature.com/reprints](http://www.nature.com/reprints). The authors declare no competing financial interests. Readers are welcome to comment on the online version of the paper. Correspondence and requests for materials should be addressed to P.R. ([ruprecht@ldeo.columbia.edu](mailto:ruprecht@ldeo.columbia.edu)).

## METHODS

**Electron microprobe analyses.** Olivine mounts were imaged via back-scattered electrons with a Cameca SX100 electron microprobe at the American Museum of Natural History, New York. Quantitative crystal traverses and olivine-hosted melt inclusions were obtained by electron microprobe at the American Museum of Natural History using multiple spot analyses, performed at 15 kV accelerating voltage, 15–20 nA probe current, and beam size of 1–5  $\mu\text{m}$ . All elements (Si, Ti, Na, Mg, Fe, Mn, Cr, Al, P, K, Ca, Ni) were routinely measured for 20–30 s. Long counting times were only used when improved precision was necessary (that is, electron microprobe versus LA-ICPMS data comparison; Supplementary Fig. 4), in which counting times generally were extended to 60 s (Ti, Cr, Ni) and 120 s (Al, Ca). To minimize Na loss we measured Na using sub-counting (ten steps), while recording the zero-time intercept. Reference materials (olivine 174.1 (ref. 34) and augite 164905 (ref. 35) were reproduced to better than  $\pm 2\%$  relative error ( $1\sigma$ ) for major elements (Mg# to better than  $\pm 0.5\%$ ). Extended counting times for the comparison of electron microprobe and LA-ICPMS resulted in reproducible Ni (Ol174.1) and Cr (Aug16490) concentrations to within  $\pm 5\%$  and  $\pm 3\%$ , respectively. Olivine-hosted melt inclusions were analysed with a 10- $\mu\text{m}$  beam at 15-kV accelerating voltage with a composite measurement routine where Na was measured first at 4 nA for 20 s with a zero-time intercept. Other major and minor elements (Al, Mg, Si, K, P, Ti, Ca, Fe, Mn) were measured next at 10 nA with counting times varying between 20 s and 30 s on peak. Cl, S, and Cr were measured last at 40 nA with counting times of 60 s, 80 s and 30 s, respectively. Most elements of our reference material (Mangatolu Rift-ND7001,  $n = 3$ ) were reproducible to better than  $\pm 4\%$  (Si: 0.3%, Ti: 5.3%, Al: 0.3%, Cr: 7.9%, Fe: 1.4%, Mn: 22%, Mg: 2.0%, Ca: 0.8%, Na: 8.3%, K: 2.2%, P: 55%, S: 3.2%, Cl: 5.6%).

**Laser-ablation inductively coupled mass spectrometry.** Major- and trace-element traverses via LA-ICPMS were collected using a VG PQ ExCell and NewWave 196-nm ArF Eximer laser at Lamont-Doherty Earth Observatory. Olivine traverses were ablated as core-to-rim line scans using a 10–25- $\mu\text{m}$  laser spot rastering across the crystal at  $\sim 3 \mu\text{m s}^{-1}$  with frequency of 15 Hz and a power output of 70% ( $>10.5 \text{ J cm}^{-2}$  and  $>2.0 \text{ GW cm}^{-2}$ ). The ablated material was transported in a He-Ar atmosphere to the ICPMS. Each traverse was pre-ablated with a 25–50- $\mu\text{m}$  laser spot at 20% power output. Dwell times for major and minor elements in each cycle were 10 ms. Reference sample calibrations were performed using reference materials BHVO-1, BCR-1, and BIR-1. MgO served as internal reference element and data quality was monitored by measuring San Carlos olivine (USNM 111312/44). Elemental concentrations were corrected by normalizing data either to published concentrations for elements with accepted values in San Carlos olivine<sup>18,36–39</sup> or to an average calculated from the San Carlos measurements in our study that are within 1 s.d. of the average of all our San Carlos olivine runs (measurement sessions with large variations were omitted because there was a problem during the cross-calibration between pulse-counting and analogue mode that led to large uncertainties for some elements such as Ca, Sc and Mn; Supplementary Table 3). External reproducibility can be estimated from the scatter of individual San Carlos olivine traverses (Fig. 1). LA-ICPMS time series were processed with a Matlab code (developed by P.R.) that follows standard calibration techniques and calculates major- and trace-element concentrations for each individual time slice. To reduce the noise of the measured profiles, while providing detailed information on individual zones within each olivine, each reported datum is an average of five time slices (each slice 0.36 s and  $\sim 1.1 \mu\text{m}$ , and so each datum is 1.8 s and 5.4  $\mu\text{m}$ ). Reproducible results were obtained for a large suite of elements (Li, Mg, P, Ca, Sc, Ti, V, Cr, Mn, Fe, Co, Ni, Cu and Zn).

**Electron-backscattered diffraction.** Electron-backscattered diffraction measurements to determine olivine crystal orientations were performed on a Zeiss Supra 40VP scanning electron microscope, Oxford energy-dispersive X-ray spectroscopy and HKL electron back-scatter diffraction (EBSD) integrated system at the Marine Biological Laboratory in Woods Hole. Diffraction patterns were matched against a reference olivine lattice model and Euler angles were recorded for a rotation from the reference frame to the observed orientation.

**Ni diffusion modelling.** We use the one-dimensional analytical solution for a confined source in an infinite medium with fixed boundary conditions<sup>33</sup> to estimate timescales since mixing, assuming isothermal and isobaric diffusion and therefore a constant diffusion coefficient  $D$  for Ni in olivine:

$$C(x) = C_{\text{outer}} + 0.5(C_{\text{inner}} - C_{\text{outer}})(\text{erf}[(L - x)/(2Dt)^{0.5}] + \text{erf}[(L - x)/(2Dt)^{0.5}]) \quad (1)$$

where  $C_{\text{outer}}$  and  $C_{\text{inner}}$  are the initial Ni concentration profiles after instantaneous growth, separating a high outer Ni zone from a low inner Ni core at the location  $L$  of the concentration step away from the rim. Ni diffusion coefficients are calculated for constant temperature and pressure and a specific crystal lattice orientation,

where  $\alpha$ ,  $\beta$  and  $\gamma$  represent angles between profile direction and the crystallographic axes [100], [010] and [001], respectively<sup>16,17</sup>. The crystal lattice orientation was determined by EBSD (see above). Diffusion coefficients were calculated for a conservative temperature range (1,100–1,200 °C) consistent with pMELTS<sup>22</sup> using olivine-liquidus temperatures of back-calculated melt inclusion compositions (with 2–4 wt% H<sub>2</sub>O; Supplementary Table 2) and with other geothermometry estimates for Irazú magmas<sup>11</sup>. These temperatures are slightly higher than that (1,043–1,074 °C) previously reported for 1723 Irazú melt inclusions<sup>26</sup>, which are trapped in uniformly more iron-rich olivine compositions ( $<\text{Fo}_{87}$ ) than the olivines modelled here. Calculated at intermediate pressures (500 MPa) and oxygen fugacity of  $3.2 \times 10^{-10} \text{ Pa}$  the Ni diffusion coefficients range from  $1.34\text{--}8.06 \times 10^{-18} \text{ m}^2 \text{ s}^{-1}$  (at 1,100 °C) to  $4.75\text{--}28.5 \times 10^{-18} \text{ m}^2 \text{ s}^{-1}$  (at 1,200 °C)<sup>16,17,33</sup>. Our timescale calculations assume that zonation profiles are the result of diffusive re-equilibration only, occurring after instantaneous growth of a Ni-rich zone. Following this initial growth episode, we assume no additional growth occurred (until shallow fractional crystallization led to low-Fo rims) and Ni profile evolution was purely diffusive (that is, the chemical Pe number is small ( $<1$ ) where  $\text{Pe} = Vl/D$ , with  $V$ ,  $l$  and  $D$  being the growth rate, the half-width of the Ni reversal, and the Ni diffusion coefficient, respectively<sup>40</sup>). However, growth and diffusive re-equilibration may be synchronous where growth is more gradual, modifying the compositional gradients according to the moving boundary. For those large-Pe-number conditions, true diffusive timescales would be shorter because the half-width is widened by growth. Thus, our calculated timescales are maximum estimates. Comparison of existing Ni diffusion data for olivine<sup>16–18</sup> suggests that Ni diffusion is known to within a factor of 2. We have chosen to calculate the Ni diffusion coefficient  $D$  from the studies<sup>16,17</sup> that (1) give maximum timescales and (2) provide complete formulations for temperature and pressure dependence.

**Error analysis for timescale calculations.** Ni zonation profiles are subject to various complications, which we try to exclude whenever possible to minimize the uncertainties of our timescale calculations. Thus, we limit our timescale analysis to olivines that pass a series of data quality tests. We exclude crystals from our calculations (1) that lack lattice orientation measurements (via EBSD), (2) for which we have significant contamination from ablated mineral inclusions (that is, high Cr from Cr-spinel, correlating with entire high Ni reversal), (3) that have a Ni reversal only in more iron-rich olivines and extend beyond the ‘olivine fractionation corridor’ to lower Fo ( $<\text{Fo}_{88}$ ), and (4) that show only minor Ni variations (ANi  $<300 \text{ p.p.m.}$ ). Furthermore, we limit our analysis to olivines with Ni reversals because Ni variations due to changes in melt compositions are readily spotted in those crystals. Such Ni variations are less apparent in normally zoned olivine phenocrysts. We avoided cases where olivines show correlated Ni reversals with Fo reversal and the resulting Ni–Fo variations are parallel to olivine fractionation curves for Irazú (Fig. 1). In these crystals, distinguishing diffusion from growth effects is less certain and mixing along a liquid line of descent may only reflect thermal mixing in a thermally zoned magma body<sup>41,42</sup>. Given these restrictions, we find only 11 useful traverses (Fig. 4, Supplementary Figs 6 and 7; a total of 176 olivine traverses were measured) that show primary variations in trace elements at high Fo content and can be used for estimating magma transfer timescales. This emphasizes that many crystals ( $>100$ ) per sample have to be analysed to extract not only the mantle signature, but also the mixing relationships of such signatures, as most crystals do not preserve this early history and instead are overprinted (or crystallized later) by the shallow processes typical for arc andesites (such as at Irazú). A recent numerical study of crystal gathering and dispersal<sup>43</sup> shows how different crystals may record very different stages in a single mixing event, with some recording strong variations if they are near large chemical gradients, while others barely experience any significant compositional variation. Thus, continuous magma evolution and mixing of different batches quickly obscures the record of primitive mantle magma compositions.

Besides the process-related uncertainties (that is, growth versus diffusion versus fractional crystallization), more quantifiable uncertainties exist regarding the length of the laser profile and the orientation of the laser traverse with respect to the olivine lattice orientation. The laser ablation stage speed was set at  $3 \mu\text{m s}^{-1}$ . Comparison of the resulting laser track length with length measurements from backscattered-electron microprobe images indicates that the true stage speed is in good agreement (within 5%) of the measured value. A 5% underestimation of the stage speed results in 5% longer diffusion length scales. EBSD measurements are subject to uncertainty owing to misalignment of the reference lattice with the measured diffraction pattern. Repeat measurements suggest that crystal orientation determinations are generally robust (better than  $\pm 10^\circ$ ).

PDFs are derived via a Monte Carlo approach. Best-fit mixing-to-eruption timescales are calculated using equation (1) through minimization of the root mean square between model and measured concentration profiles (Fig. 3 and 4) while varying  $C_{\text{outer}}$ ,  $C_{\text{inner}}$ ,  $L$ ,  $\alpha$ ,  $\beta$  and  $\gamma$  between acceptable bounds (Supplementary Table 4). Best-fit timescales for all trials are combined into PDFs for each olivine,

providing an estimate of the uncertainties of the calculated timescales. We vary (1) the three angles (as mentioned above) by  $\pm 10^\circ$ , (2) the post- and pre-mixing equilibrium Ni concentration by  $\pm 100$  p.p.m. around an average value of the observed step, and (3) the location of the initial step by  $\pm 15$   $\mu\text{m}$ . A full summary of the different parameters used for the Monte Carlo approach is given in Supplementary Fig. 8 and listed in Supplementary Table 4. PDFs for each olivine crystal provide an estimate for fixed pressure–temperature conditions of diffusive re-equilibration (that is, 500 MPa and 1,100 °C); higher or lower assumed temperatures shift the results systematically to shorter or longer mixing timescales, respectively (Fig. 4).

34. White, R. W. Ultramafic inclusions in basaltic rocks from Hawaii. *Contrib. Mineral. Petrol.* **12**, 245–314 (1966).
35. Jarosewich, E., Gooley, R. & Husler, J. Chromium augite — a new microprobe reference sample. *Geostand. Newslett.* **11**, 197–198 (1987).
36. Taura, H., Yurimoto, H., Kurita, K. & Sueno, S. Pressure dependence on partition coefficients for trace elements between olivine and the coexisting melts. *Phys. Chem. Miner.* **25**, 469–484 (1998).
37. Jarosewich, E., Nelen, J. A. & Norberg, J. A. Reference samples for electron microprobe analysis. *Geostand. Newslett.* **4**, 43–47 (1980).
38. Norman, M. D. Melting and metasomatism in the continental lithosphere: laser ablation ICPMS analysis of minerals in spinel Iherzolites from eastern Australia. *Contrib. Mineral. Petrol.* **130**, 240–255 (1998).
39. Sobolev, A. V. *et al.* The amount of recycled crust in sources of mantle-derived melts. *Science* **316**, 412–417 (2007).
40. Ruprecht, P. & Cooper, K. M. Integrating the uranium-series and elemental diffusion geochronometers in mixed magmas from volcán Quizapu, Central Chile. *J. Petrol.* **53**, 841–871 (2012).
41. Couch, S., Sparks, R. S. J. & Carroll, M. R. Mineral disequilibrium in lavas explained by convective self-mixing in open magma chambers. *Nature* **411**, 1037–1039 (2001).
42. Ruprecht, P. & Wörner, G. Variable regimes in magma systems documented in plagioclase zoning patterns: El Misti stratovolcano and Andahua monogenetic cones. *J. Volcanol. Geotherm. Res.* **165**, 142–162 (2007).
43. Ruprecht, P., Bergantz, G. W. & Dufek, J. Modeling of gas-driven magmatic overturn: tracking of phenocryst dispersal and gathering during magma mixing. *Geochem. Geophys. Geosyst.* **9**, Q07017 (2008).

# The molecular logic for planarian regeneration along the anterior–posterior axis

Yoshihiko Umesono<sup>1,2</sup>†, Junichi Tasaki<sup>2</sup>, Yui Nishimura<sup>2</sup>, Martina Hrouda<sup>2</sup>, Eri Kawaguchi<sup>2</sup>, Shigenobu Yazawa<sup>2</sup>, Osamu Nishimura<sup>2</sup>, Kazutaka Hosoda<sup>2</sup>, Takeshi Inoue<sup>2</sup> & Kiyokazu Agata<sup>2</sup>

The planarian *Dugesia japonica* can regenerate a complete individual from a head, trunk or tail fragment via activation of somatic pluripotent stem cells<sup>1,2</sup>. About a century ago, Thomas Hunt Morgan attempted to explain the extraordinary regenerative ability of planarians by positing two opposing morphogenetic gradients of formative “head stuff” and “tail stuff” along the anterior–posterior axis<sup>3,4</sup>. However, Morgan’s hypothesis remains open to debate. Here we show that extracellular signal-related kinase (ERK) and Wnt/β-catenin signalling pathways establish a solid framework for planarian regeneration. Our data suggest that ERK signalling forms a spatial gradient in the anterior region during regeneration. The fibroblast growth factor receptor-like gene *nou-darake*<sup>5</sup> (which serves as an output of ERK signalling in the differentiating head) and posteriorly biased β-catenin activity<sup>6–8</sup> negatively regulate ERK signalling along the anterior–posterior axis in distinct manners, and thereby posteriorize regenerating tissues outside the head region to reconstruct a complete head-to-tail axis. On the basis of this knowledge about *D. japonica*, we proposed that β-catenin signalling is responsible for the lack of head-regenerative ability of tail fragments in the planarian *Phagocata kawakatsui*, and our confirmation thereof supports the notion that posterior β-catenin signalling negatively modulates the ERK signalling involved in anteriorization across planarian species. These findings suggest that ERK signalling has a pivotal role in triggering globally dynamic differentiation of stem cells in a head-to-tail sequence through a default program that promotes head tissue specification in the absence of posteriorizing signals. Thus, we have confirmed the broad outline of Morgan’s hypothesis, and refined it on the basis of our proposed default property of planarian stem cells.

The planarian *Dugesia japonica* has four distinct body regions arranged in an anterior to posterior sequence: head containing a brain and eyes (H), prepharyngeal (Pr), pharyngeal containing a pharynx (Ph), and tail (T) regions<sup>5,9–12</sup> (Fig. 1a) and possesses high regenerative ability<sup>13,14</sup>. After amputation, anterior-facing wounds form a head blastema, whereas posterior-facing wounds form a tail blastema, a phenomenon known as regeneration polarity. Thereafter, the complete anterior–posterior pattern regenerates within a week by filling in the prepharyngeal and pharyngeal regions between the head and tail<sup>15,16</sup>. This sequence of events requires appropriate activation of somatic pluripotent stem cells (neoblasts), the sole source of regenerative cells<sup>1,2</sup>.

Recent RNA interference<sup>17,18</sup> (RNAi) studies revealed that Wnt/β-catenin signalling regulates regeneration polarity in planarians<sup>6–8,19</sup>. RNAi of planarian β-catenin caused transformation of the tail region into a head-like region<sup>6,7,19</sup>. β-catenin presumably forms a decreasing tail-to-head activity gradient as a result of the expression of posterior Wnt genes<sup>8</sup>, as inferred from the expression pattern of *DjAbd-Ba*, a target *Hox* gene of posterior Wnt/β-catenin signalling in neoblast

progeny<sup>11,19</sup> (Fig. 1b), and accordingly fits the instructive role of the “tail stuff”. By contrast, no molecules have been reported to function as the “head stuff”.

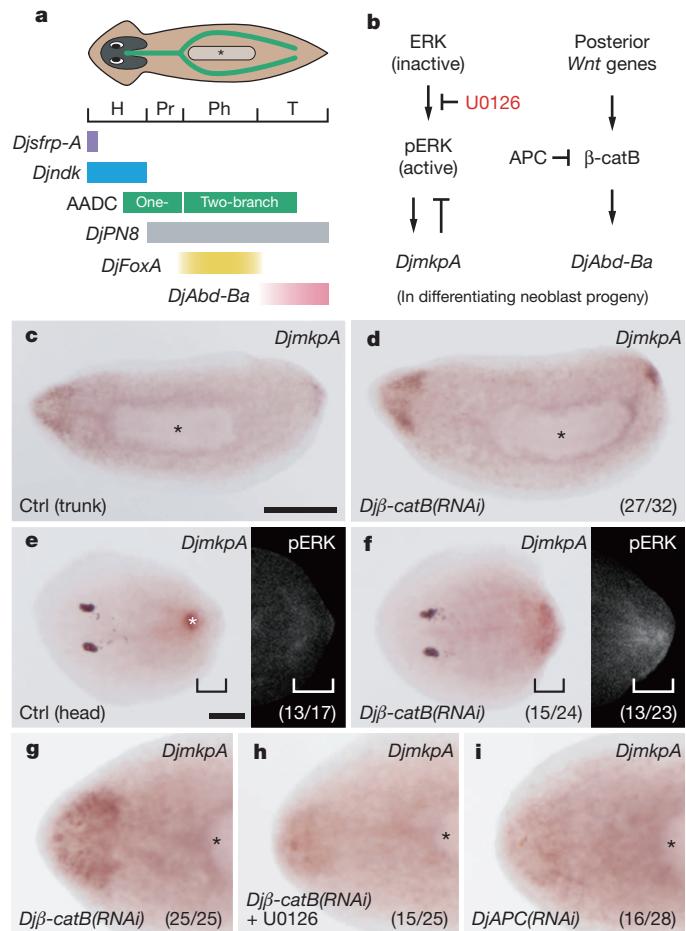


**Figure 1 | β-catenin signalling affects ERK signalling during regeneration.** **a**, Anterior–posterior regional subdivisions. **b**, Signalling pathways. **c–i**, *DjmkpA* expression at 3 days of regeneration (Re-3d). **c**, Control trunk fragment (30/30). **d**, *Djβ-catB(RNAi)* trunk fragment. **e**, Control head fragment. Strong *DjmkpA* expression occurred transiently in the tail blastema<sup>20</sup>, and then decreased at this time (26/26). White asterisk indicates *DjmkpA* expression in cells associated with pharynx regeneration (left). Most animals (13/17) showed no obvious pERK signals around posterior-facing wounds (bracket, right). **f**, *Djβ-catB(RNAi)* increased *DjmkpA* expression (left) and pERK level in the presumptive tail region (bracket, right). **g–i**, Regenerating head in trunk fragments. Black asterisks (**a**, **c**, **d** and **g–i**) indicate a pharynx. Anterior is to the left. Scale bars: **c**, 500 μm; **e**, 200 μm.

<sup>1</sup>RIKEN Center for Developmental Biology, 2-2-3 Minatojima-minamimachi, Chuo-ku, Kobe 650-0047, Japan. <sup>2</sup>Department of Biophysics, Graduate School of Science, Kyoto University, Kitashirakawa Oiwake-cho, Sakyō-ku, Kyoto 606-8502, Japan. †Present address: Department of Life Systems, Institute of Technology and Science, University of Tokushima, 2-1 Minami-Jyosanjima-cho, Tokushima 770-8506, Japan.

We previously reported that mitogen-activated protein kinase (MAPK)/extracellular signal-related kinase (ERK) signalling is highly activated at wounds and induces *DjmkaP*, a *D. japonica* MAPK phosphatase gene, in head and tail blastema cells (Fig. 1c); activated ERK (phosphorylated ERK; pERK) and *DjmkaP* form a negative feedback circuit that controls blastema cell differentiation (Fig. 1b), resulting in regeneration of the head or tail at a wound<sup>20</sup>. Thus, hitherto unknown links between ERK and posterior  $\beta$ -catenin signals might direct the appropriate differentiation of neoblasts to reconstruct a complete head-to-tail axis, and here we tested this possibility during regeneration of *D. japonica*.

To sensitively visualize ERK activation *in vivo*, we monitored *DjmkaP* expression. RNAi of *D. japonica*  $\beta$ -catenin<sup>19</sup> (*Dj $\beta$ -catB*) clearly increased *DjmkaP* expression in the presumptive regenerating tail via ERK activation (Fig. 1c–f). *Dj $\beta$ -catB* RNAi also increased *DjmkaP* expression in the regenerating head region via ERK activation (Fig. 1c, d) because this increase was strongly suppressed by treatment with MEK inhibitor U0126 (Fig. 1g, h), which inhibits ERK signalling<sup>20</sup> (Fig. 1b and Supplementary Fig. 1). Conversely, increased  $\beta$ -catB activity induced by RNAi of *D. japonica* *adenomatous polyposis coli* (*DjAPC*) strongly decreased *DjmkaP* expression in regenerating head (Fig. 1i) and interfered with head regeneration (Supplementary Fig. 2). These observations suggest that the posterior  $\beta$ -catenin signalling level may directly affect the ERK signalling level, and the absence of  $\beta$ -catenin signalling allows neoblasts to achieve the ERK activation necessary for head regeneration at anterior-facing wounds.

We next examined whether ERK signalling is also required for regeneration of the prepharyngeal and pharyngeal regions. U0126 (25  $\mu$ M) caused failure of head and tail regeneration (Fig. 2a, b and Supplementary Fig. 3) without affecting neoblast survival, as assayed by the expression of *DjipiwiA*, a neoblast-specific marker gene<sup>1</sup> (Supplementary Figs 1b and 4c). Such inhibitor treatment also prevented pharynx regeneration from both head and tail fragments (Fig. 2a, b and Supplementary Fig. 3), and blocked reconstruction of the single anterior gut branch from pre-existing gut tissues in regenerating tail fragments (Fig. 2a, b). Further analysis of regenerating tail fragments revealed that lower concentrations of U0126 (5–6.25  $\mu$ M) severely inhibited formation of both an anterior gut within the prepharyngeal region and a pharynx, but not head regeneration (Fig. 2c), suggesting that quantitative differences of ERK activity influence reconstruction of the anterior–posterior pattern. Quantitative reverse transcription–polymerase chain reaction (qRT–PCR) analysis revealed a decreasing head-to-tail gradient of *DjmkaP* expression in response to ERK activation, a pattern reversed compared with that of *DjAbd-Ba* expression (Fig. 2d). Indeed, a lower concentration of U0126 inhibited *DjmkaP* expression most strongly outside the head region (Fig. 2e, f), in the same region where severe regeneration defects occurred (Fig. 2c). Thus, graded ERK activation along the anterior–posterior axis may instruct the reconstruction of the prepharyngeal and pharyngeal regions between the head and tail.

*D. japonica nou-darake* (*Djndk*) encodes a fibroblast growth factor (FGF) receptor-like transmembrane protein, but lacks the cytoplasmic kinase domain characteristic of the FGF receptor family<sup>5</sup>. Our previous finding that *Djndk* RNAi induced ectopic differentiation of head tissues, such as eyes and brain cells, outside the head region<sup>5</sup>, a phenotype opposite to that of ERK inhibition, led us to test the relationship between ERK and *Djndk* for specifying the intermediate subdivisions along the anterior–posterior axis during regeneration.

We demonstrated that *de novo* expression of *Djndk* serves as an output of the ERK/*DjmkaP* feedback circuit in the differentiating head blastema (Supplementary Fig. 4). In control tail fragments at 3 days of regeneration, *DjmkaP* was highly expressed with a well-demarcated posterior end in the head region, and expressed at progressively lower levels towards the pharyngeal region (Fig. 3a). *Djndk* RNAi abolished the clearly defined boundary of *DjmkaP* expression between the head and prepharyngeal region (Fig. 3b), presumably due to increased

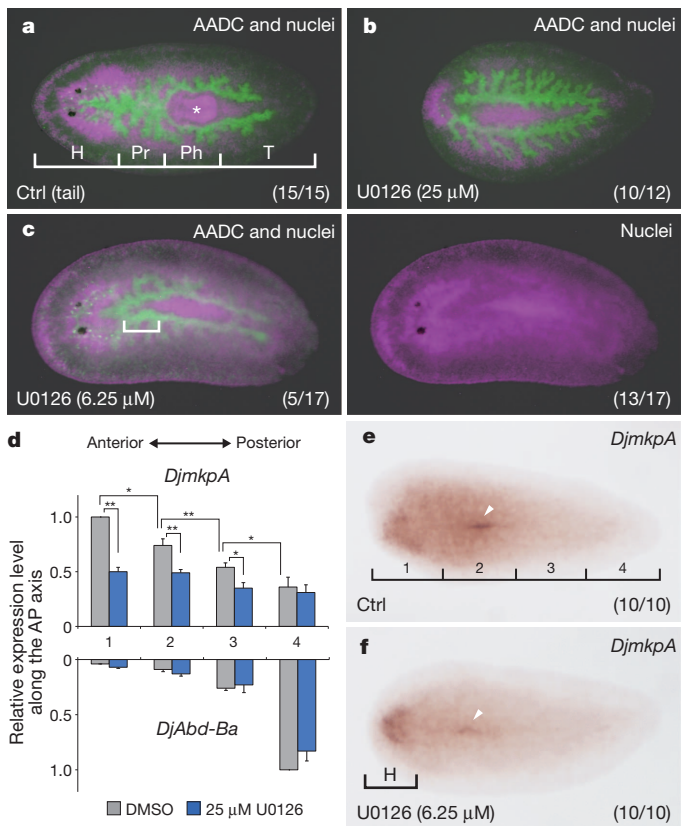


**Figure 2 | Effects of pharmacological ERK inhibition on anterior-posterior patterning during regeneration.** **a**, Control tail fragment at Re-7d (15/15). **b**, 25  $\mu$ M U0126 treatment blocked regeneration of the H, Pr and Ph regions at Re-7d, but allowed the regenerant to retain the two original posterior branches of the gut (10/12), as assayed by anti-AADC antibody staining (green), and caused failure to regenerate a pharynx (Hoechst 33342 staining (magenta) (12/12)). **c**, 6.25  $\mu$ M U0126 treatment caused the regenerant to have two gut branches in the presumptive Pr region (5/17; bracket, left), but left head regeneration normal at Re-7d (100% of animals,  $n = 17$ ). This treatment also caused failure to regenerate a pharynx (13/17, right). The brain in the H region and the pharynx (asterisk in **a**) are visualized by Hoechst 33342 staining (magenta). **d**, Relative gene expression levels at Re-3d, as determined by qRT–PCR. Regenerants were divided into quarters along the anterior–posterior (AP) axis and total RNA was isolated from each quarter. Bars show mean  $\pm$  s.d. of replicate qRT–PCR assays ( $n = 3$ ) of pooled RNA from each quarter of 12 animals (Student's *t*-test, \* $P < 0.05$ , \*\* $P < 0.01$ ). **e**, **f**, *DjmkaP* expression in control versus 6.25  $\mu$ M U0126-treated regenerants at Re-3d. Arrowheads indicate *DjmkaP* expression in cells associated with pharynx regeneration. Anterior is to the left.

*DjmkaP* expression in the prepharyngeal region. qRT–PCR confirmed that *Djndk* RNAi increased the ERK-dependent *DjmkaP* expression (Fig. 3c). Later, *Djndk* RNAi caused formation of ectopic head tissues predominantly in the prepharyngeal region<sup>5,14</sup> (Supplementary Fig. 5b) and marked loss of prepharyngeal identity<sup>9,16</sup> (Fig. 3d–f). These observations suggest that *Djndk* RNAi caused transformation of the prepharyngeal region into a head-like region through ERK activation in a non-cell autonomous manner. Moreover, *Djndk* RNAi rescued the loss-of-pharynx phenotype in a moderately ERK-deficient background (Fig. 3c, g–i). Thus, we speculate that *Djndk* might encode a protein that concentrates in the head region and binds to molecules secreted in that area (as yet unidentified) that promote ERK activation in neoblasts involved in anteriorization.

We also showed that posterior  $\beta$ -catenin signalling acts to specify the pharyngeal, but not prepharyngeal, region during head regeneration from tail fragments. *Dj $\beta$ -catB* RNAi decreased the posteriorly biased *DjAbd-Ba* expression (Fig. 2d), and conversely increased the expression of *DjmkaP* and *DjsfrpA* (a readout of ERK signalling in

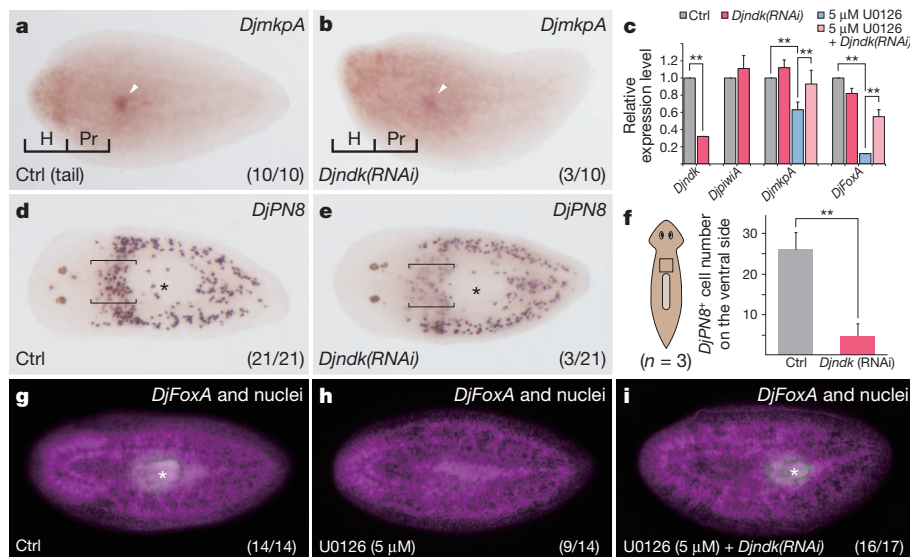


**Figure 3 | Effects of *Djndk* RNAi on anterior-posterior patterning during regeneration.** **a, b**, *DjmkpA* expression at Re-3d. Arrowheads indicate *DjmkpA* expression in cells associated with pharynx regeneration. **c**, Relative gene expression levels at Re-3d. Bars show mean  $\pm$  s.d. of replicate qRT-PCR assays ( $n = 3$ ) of pooled RNA from 15 animals (Student's *t*-test,  $*P < 0.05$ ,  $**P < 0.01$ ). **d, e**, Ventral view of *DjPN8* expression at Re-7d. Brackets indicate

*DjPN8* expression in the prepharyngeal region that was severely affected by *Djndk* RNAi. *Djndk* RNAi caused formation of an ectopic eye posterior to an original eye. **f**, The number of *DjPN8*<sup>+</sup> cells in the boxed area ( $n = 3$  animals in each assay; Student's *t*-test,  $**P < 0.01$ ). Error bars represent s.d. **g–i**, Staining with *DjFoxA* probe (green) and Hoechst 33342 nuclear staining (magenta) at Re-7d. Asterisks (**d, e** and **i**) indicate a pharynx. Anterior is to the left.

the head blastema<sup>20</sup>), suggesting that anterior ERK signalling was increased in *Djβ-catB(RNAi)* animals (Fig. 4a–c; Supplementary Fig. 6). However, these knockdown animals failed to form a pharynx rudiment at 3 days of regeneration (Fig. 4d, e), as assayed by the expression of *DjFoxA* (a marker for pharyngeal cells<sup>10</sup>). Combined 5 μM U0126 treatment and *Djβ-catB* RNAi additively decreased *DjFoxA* expression

(Fig. 4c), suggesting that interplay between ERK and posterior β-catenin signals is required to regenerate pharyngeal cells. At 7 days of regeneration, *Djβ-catB(RNAi)* animals showed roughly normal regeneration of the head and prepharyngeal regions (100% of animals,  $n = 30$ ) and ectopic fusion of the two posterior branches of the gut in the presumptive pharyngeal region (Fig. 4f), a phenotype opposite to

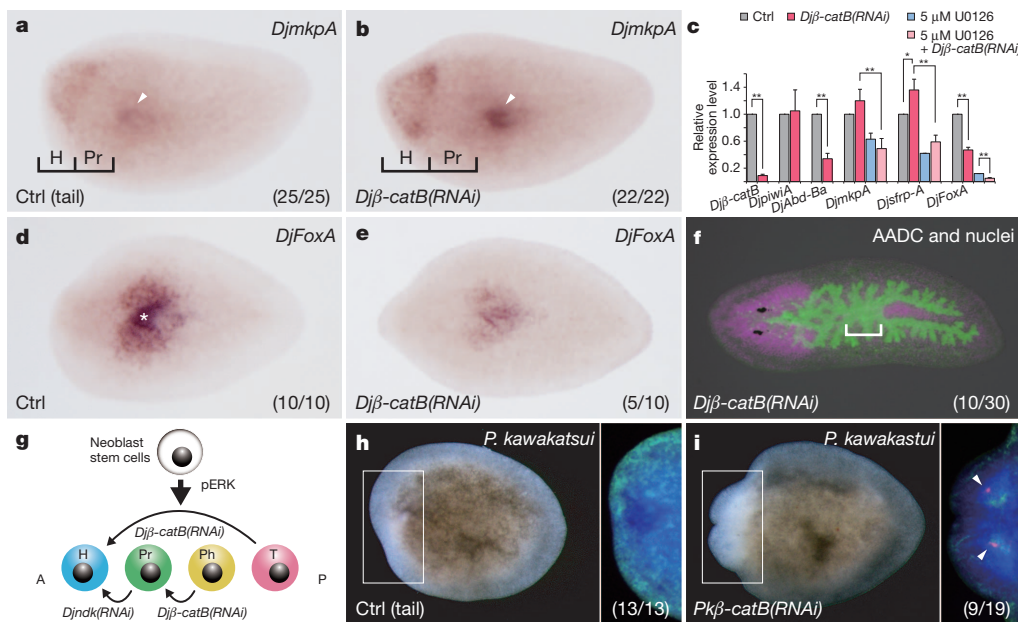


**Figure 4 | Phenotypes induced by RNAi of β-catenin in different planarian species.** **a, b**, *DjmkpA* expression at Re-3d. Arrowheads indicate *DjmkpA* expression in cells associated with pharynx regeneration. **c**, Relative gene expression levels at Re-3d. Bars show mean  $\pm$  s.d. of replicate qRT-PCR assays ( $n = 3$ ) of pooled RNA from 15 animals (Student's *t*-test,  $*P < 0.05$ ,  $**P < 0.01$ ). **d, e**, *DjFoxA* expression at Re-3d. Asterisk (**d**) indicates a pharynx rudiment. **f**, Staining with anti-AADC antibody (green) and Hoechst 33342 nuclear staining (magenta) at Re-7d. The *Djβ-catB(RNAi)* animal completely lacks a pharynx, and instead shows ectopic fusion of the two posterior gut branches (bracket). **g**, Molecular logic for planarian regeneration along the

anterior-posterior (A–P) axis. **h, i**, Left panels, control tail fragment of *Phagocata kawakatsu* at 19 days after amputation and a *Pkβ-catB(RNAi)* tail fragment at 16 days after amputation. Right panels, enlarged view of corresponding boxed areas in left panels. The *Pkβ-catB(RNAi)* animal regenerated a head-like structure, including a brain visualized by strong staining with Hoechst 33342 (blue) and with anti-synaptotagmin (SYT) antibody (green), and a paired cluster of photoreceptor cells visualized by anti-arrestin staining (magenta; arrowheads). The control animal failed to regenerate a head and showed high background signals of anti-SYT staining. Anterior is to the left.

that induced by ERK inhibition (Fig. 2c), at the expense of the pharynx structure. This suggests that *Djβ-catB* RNAi caused transformation of the pharyngeal region into a prepharyngeal-like region through ERK activation.

Altogether, our findings encourage us to refine Morgan's hypothesis at the cellular and molecular levels as follows. We showed that *Djndk* RNAi anteriorized the prepharyngeal region, and *Djβ-catB* RNAi anteriorized the pharyngeal and tail regions, with increases of ERK activity level in both cases, suggesting that regenerative cells are prone to undergo differentiation into head tissues in the absence of these two posteriorizing signals (Fig. 4g and Supplementary Fig. 5). Accordingly, we propose that neoblasts might follow a default program of differentiation into head tissues that is triggered by the activation of ERK and calls to mind the old description by Morgan in 1904 that "in the absence of polarity (i.e. posteriorizing signals) the new material (i.e. *de novo* pERK) produces a head" in *Planaria maculata*<sup>21</sup>. Thus, activated-ERK triggering of the default program might correspond to Morgan's "head stuff". To validate this, we will have to demonstrate the existence of a pERK gradient itself in planarians.

The ability to regenerate a head varies among planarian species<sup>22</sup>. In the planarian *Phagocata kawakatsui*, the tail region shows markedly reduced head-regenerative ability, whereas tail regeneration is normal (Fig. 4h and Supplementary Fig. 7). We reasoned that if head tissue differentiation is a default property of neoblasts in response to ERK activation not only in *D. japonica* but across planarian species (Supplementary Fig. 8), excessive posterior β-catenin signalling might be interfering with the ERK activation necessary for head regeneration from tail fragments of *P. kawakatsui*. Indeed, RNAi of *P. kawakatsui* β-cateninB (*Pkβ-catB*) enabled *de novo* regeneration of a head-like structure, including brain tissues and a pair of eyes, at anterior-facing wounds of tail fragments (9/19; Fig. 4i). Moreover, seven of these nine regenerants showed negative phototaxis<sup>23</sup> (a typical outcome of the function of the brain and eyes<sup>24</sup>), in contrast to regenerants from control tail fragments (0/13; Supplementary Fig. 9). Thus, we identified a genetic cause of the lack of head-regenerative capacity in this planarian species. We speculate that the balance between anterior ERK signalling and posterior β-catenin signalling may vary among planarian species, resulting in the drastic differences of their head-regenerative capacity.

In summary, we have not only integrated the concept of default differentiation of stem cells into head tissues into Morgan's hypothesis, but have also demonstrated that posterior Wnt/β-catenin signalling interferes with head tissue differentiation in planarians by overriding this default.

## METHODS SUMMARY

Planarian culture, drug treatments and quantitative RT-PCR<sup>20</sup>, behavioural assay<sup>23</sup>, gene silencing by RNA interference<sup>17,18</sup> and whole-mount *in situ* hybridization<sup>25</sup> were performed as reported. The *Pkβ-catB* gene sequence was obtained from transcriptome analysis of *P. kawakatsui* by next generation sequencing with a Roche 454 GS FLX Titanium. Based on the sequence data, a 1,300-base-pair complementary DNA fragment of *Pkβ-catB* was amplified from a cDNA library of non-regenerating intact planarians constructed in lambda ZAP II (Stratagene) using oligo(dT) primers, and used as a template to make double-stranded RNA. Whole-mount immunostaining is described in the Methods section.

**Full Methods** and any associated references are available in the online version of the paper.

Received 4 December 2012; accepted 7 June 2013.

Published online 24 July 2013.

- Shibata, N., Rouhana, L. & Agata, K. Cellular and molecular dissection of pluripotent adult somatic stem cells in planarians. *Dev. Growth Differ.* **52**, 27–41 (2010).

- Wagner, D. E., Wang, I. E. & Reddien, P. W. Clonogenic neoblasts are pluripotent adult stem cells that underlie planarian regeneration. *Science* **332**, 811–816 (2011).
- Morgan, T. H. "Polarity" considered as a phenomenon of gradation of materials. *J. Exp. Zool.* **2**, 495–506 (1905).
- Lawrence, P. A. Background to *bicoid*. *Cell* **54**, 1–2 (1988).
- Cebrià, F. et al. FGFR-related gene *nou-darake* restricts brain tissues to the head region of planarians. *Nature* **419**, 620–624 (2002).
- Gurley, K. A., Rink, J. C. & Sánchez Alvarado, A. β-Catenin defines head versus tail identity during planarian regeneration and homeostasis. *Science* **319**, 323–327 (2008).
- Petersen, C. P. & Reddien, P. W. *Smed-βcatenin-1* is required for anteroposterior blastema polarity in planarian regeneration. *Science* **319**, 327–330 (2008).
- Petersen, C. P. & Reddien, P. W. A wound-induced Wnt expression program controls planarian regeneration polarity. *Proc. Natl. Acad. Sci. USA* **106**, 17061–17066 (2009).
- Kobayashi, C., Nogi, T., Watanabe, K. & Agata, K. Ectopic pharynxes arise by regional reorganization after anterior/posterior chimera in planarians. *Mech. Dev.* **89**, 25–34 (1999).
- Koinuma, S., Umesono, Y., Watanabe, K. & Agata, K. Planaria *FoxA* (HNF3) homologue is specifically expressed in the pharynx-forming cells. *Gene* **259**, 171–176 (2000).
- Nishimura, K. et al. Position-specific and non-colinear expression of the planarian posterior (*Abdominal-B*-like) gene. *Dev. Growth Differ.* **43**, 177–184 (2001).
- Agata, K. & Umesono, Y. Brain regeneration from pluripotent stem cells in planarian. *Phil. Trans. R. Soc. Lond. B* **363**, 2071–2078 (2008).
- Umesono, Y. & Agata, K. Evolution and regeneration of the planarian central nervous system. *Dev. Growth Differ.* **51**, 185–195 (2009).
- Agata, K., Saito, Y. & Nakajima, E. Unifying principles of regeneration I: epimorphosis versus morphallaxis. *Dev. Growth Differ.* **49**, 73–78 (2007).
- Agata, K., Tanaka, T., Kobayashi, C., Kato, K. & Saitoh, Y. Intercalary regeneration in planarians. *Dev. Dyn.* **226**, 308–316 (2003).
- Sánchez Alvarado, A. & Newmark, P. A. Double-stranded RNA specifically disrupts gene expression during planarian regeneration. *Proc. Natl. Acad. Sci. USA* **96**, 5049–5054 (1999).
- Rouhana, L. et al. RNA interference by feeding in vitro-synthesized double-stranded RNA to planarians: methodology and dynamics. *Dev. Dyn.* **242**, 718–730 (2013).
- Yazawa, S., Umesono, Y., Hayashi, T., Tarui, H. & Agata, K. Planarian Hedgehog/Patched establishes anterior-posterior polarity by regulating Wnt signaling. *Proc. Natl. Acad. Sci. USA* **106**, 22329–22334 (2009).
- Tasaki, J. et al. ERK signaling controls blastema cell differentiation during planarian regeneration. *Development* **138**, 2417–2427 (2011).
- Morgan, T. H. The control of heteromorphosis in *Planaria maculata*. *Arch. Entw. Mech. Org.* **17**, 683–695 (1904).
- Agata, K. & Inoue, T. Survey of the differences between regenerative and non-regenerative animals. *Dev. Growth Differ.* **54**, 143–152 (2012).
- Inoue, T. et al. Morphological and functional recovery of the planarian photosensing system during head regeneration. *Zoolog. Sci.* **21**, 275–283 (2004).
- Takano, T. et al. Regeneration-dependent conditional gene knockdown (Readyknock) in planarian: demonstration of requirement for *Djsnap-25* expression in the brain for negative phototactic behavior. *Dev. Growth Differ.* **49**, 383–394 (2007).
- Umesono, Y., Watanabe, K. & Agata, K. A planarian *orthopedia* homolog is specifically expressed in the branch region of both the mature and regenerating brain. *Dev. Growth Differ.* **39**, 723–727 (1997).

**Supplementary Information** is available in the online version of the paper.

**Acknowledgements** We thank C. Hashimoto for discussions and comments. We also thank E. Nakajima and A. Alié for critical reading of the manuscript, Y. Saito for illustrations, and all of our other laboratory members for their help and encouragement. This work was supported by a Grant-in-Aid for Scientific Research on Innovative Areas to Y.U. (22124004), a Grant-in-Aid for Scientific Research on Innovative Areas to K.A. (22124001), a Grant-in-Aid for Creative Scientific Research to K.A. (17GS0318), Global COE Program A06 of Kyoto University, the Naito Foundation, a Sasakawa Scientific Research Grant, and a JSPS Research Fellowship to J.T.

**Author Contributions** Y.U. and K.A. designed the study. Y.U., J.T. and K.H. performed the study in *D. japonica*. S.Y., E.K. and O.N. performed *P. kawakatsui* transcriptome analysis. Y.U., J.T., Y.N. and M.H. performed the study in *P. kawakatsui*. T.I. performed behavioural assays. Y.U. wrote the paper.

**Author Information** Reprints and permissions information is available at [www.nature.com/reprints](http://www.nature.com/reprints). The authors declare no competing financial interests. Readers are welcome to comment on the online version of the paper. Correspondence and requests for materials should be addressed to Y.U. (umesono.yoshihiko@tokushima-u.ac.jp).

## METHODS

**Animals.** A clonal strain of the planarian *Dugesia japonica* derived from the Iruma River in Gifu prefecture, Japan, which is maintained in autoclaved tap water at 22–24 °C, was used in this study. An isolated colony of the planarian *Phagocata kawakatsui* derived from the Yogo Lake area in Shiga prefecture, Japan, which is maintained in autoclaved tap water at 16–18 °C, was used in this study. These planarians (about 8 mm in length) were starved for at least 1 week before experiments. They were transversely dissected into three pieces: head, trunk (including pharynx) and tail, and allowed to undergo regeneration.

**Treatment with a chemical inhibitor.** The MAPK/ERK kinase (MEK) inhibitor U0126 (Cell Signaling Technology) was dissolved in dimethyl sulphoxide (DMSO) and used at the indicated concentration(s) for each experiment. Amputated planarians were allowed to regenerate in tap water supplemented with the inhibitor or DMSO alone immediately after amputation for the indicated period of regeneration for each experiment.

**Identification of *P. kawakatsui*  $\beta$ -cateninB (*Pk $\beta$ -catB*) gene.** Transcriptome analysis of *P. kawakatsui* was performed by next generation sequencing with Roche 454 GS FLX Titanium. For this purpose, messenger RNA was isolated from 190 trunk fragments containing a pharynx and from 178 tail fragments. The *Pk $\beta$ -catB* gene sequence was obtained from the Roche 454 sequencing reads by using the full-length amino acid sequence encoded by the *D. japonica*  $\beta$ -catB gene as a query through tblastn search. A 1,300-bp cDNA fragment of *Pk $\beta$ -catB* was amplified from a cDNA library of non-regenerating intact planarians constructed in lambda ZAP II (Stratagene) using oligo(dT) primers and used in this study.

**RNA interference.** Double-stranded RNA (dsRNA) was synthesized essentially as previously described<sup>17,18</sup>. Sequences used to generate dsRNAs are shown in Supplementary Fig. 10. dsRNA was suspended in diethylpyrocarbonate (DEPC)-treated H<sub>2</sub>O. Intact planarians were injected with dsRNA every other day for a total of 2 times using a Drummond Scientific Nanoject II injector (Drummond Scientific Company). Control animals were injected with DEPC-treated H<sub>2</sub>O alone. In the case of *P. kawakatsui*, no injection was performed in control animals. One day after the last injection, planarians were amputated and allowed to undergo regeneration.

**Whole-mount *in situ* hybridization.** Animals were treated with 2% hydrochloric acid (HCl) in 5/8 Holtfreter's solution for 5 min at 4 °C and fixed in 5/8 Holtfreter's solution containing 4% paraformaldehyde and 5% methanol for less than 2 h at 4 °C. Hybridization and colour detection of digoxigenin (DIG)-labelled RNA probes were carried out as previously described<sup>25</sup>. A mixture of BCIP/NBT (5-bromo-4-chloro-3-indolyl-phosphate/nitro blue tetrazolium) (Roche), HNPP/Fast Red (Roche) or TSA Labelling (Molecular Probes) was used for colour development of the alkaline

phosphatase-conjugated anti-DIG antibody (Roche) or for detection of fluorescence.

**Whole-mount immunostaining.** Planarians were treated with 2% HCl in 5/8 Holtfreter's solution for 5 min at 4 °C and washed twice with 5/8 Holtfreter's solution at room temperature. They were then fixed with 5/8 Holtfreter's solution containing 4% paraformaldehyde and 5% methanol for less than 2 h at 4 °C. The fix solution supplemented with PhosSTOP phosphatase inhibitor (Roche) was used for the detection of phosphorylated protein. To lower the background, fixed planarians were treated with hybridization buffer for whole-mount *in situ* hybridization overnight at 55 °C. Fixed animals were blocked with 10% Blocking reagent (Roche) in PBST (phosphate buffered saline containing 0.1% Triton X-100) for 1 h at 4 °C, and then incubated with 1/1,000 diluted mouse anti-AADC<sup>12</sup>, 1/1,000 diluted mouse anti-DjPiwiA<sup>20</sup>, 1/200 diluted rabbit anti-phosphorylated histone H3 (Upstate Biotechnology), 1/1,000 diluted rabbit anti-phosphorylated ERK (pERK)<sup>20</sup>, 1/1,000 diluted mouse anti-synaptotagmin<sup>14</sup> or 1/1,000 diluted rabbit anti-arrestin<sup>14</sup> antibody overnight at 4 °C. The samples were washed with PBST for 30 min four times and signals were detected with 1/500 diluted Alexa Fluor 488- or 594-conjugated goat anti-mouse or anti-rabbit IgG (Invitrogen) in 10% goat serum in PBST overnight at 4 °C in the dark. pERK signals were detected with 1/500 diluted alkaline phosphatase-conjugated goat anti-rabbit IgG and HNPP/Fast Red (Roche). The samples were also incubated with 1/1,000 diluted Hoechst 33342 at the same time.

**Reverse transcription and quantitative RT-PCR analysis.** Total RNA was isolated from 15 whole tail fragments of *D. japonica* using Isogen LS (Nippon Gene). Twelve regenerating tail fragments of *D. japonica* were divided into quarters along the anterior–posterior axis and total RNA was also isolated from each quarter. In the case of *P. kawakatsui*, the stock of mRNA isolated for transcriptome analysis was used. First-strand cDNA was synthesized using a QuantiTect Reverse Transcription Kit (Qiagen). Quantitative analysis of the amount of each gene product was carried out as previously described<sup>20</sup> using an iCycler real-time PCR machine (Bio-Rad Laboratories). Measurements were normalized by the expression level of a constitutively transcribed housekeeping gene, *GAPDH*. The mean of three replicate qRT-PCR assays was reported. Oligonucleotide primer sequences used for the assays are listed in Supplementary Fig. 11.

**Behavioural assay.** Ten millilitres of planarian culture water (23 °C) was put in a 3-cm wide × 6-cm long × 1-cm deep quartz rectangular container painted black except for one clear end. A planarian was put into the container 1.5 cm from the clear end, and the container was exposed to 300 lx of white light from a horizontal position at the clear end of the container. Planarian behaviour was recorded using an overhead digital video camera (Sony) for 90 s.

# Restoration of anterior regeneration in a planarian with limited regenerative ability

James M. Sikes<sup>1†</sup> & Phillip A. Newmark<sup>1</sup>

Variability of regenerative potential among animals has long perplexed biologists<sup>1</sup>. On the basis of their exceptional regenerative abilities, planarians have become important models for understanding the molecular basis of regeneration<sup>2</sup>. However, planarian species with limited regenerative abilities are also found<sup>3,4</sup>. Despite the importance of understanding the differences between closely related, regenerating and non-regenerating organisms, few studies have focused on the evolutionary loss of regeneration<sup>5</sup>, and the molecular mechanisms leading to such regenerative loss remain obscure. Here we examine *Procotyla fluviatilis*, a planarian with restricted ability to replace missing tissues<sup>6</sup>, using next-generation sequencing to define the gene expression programs active in regeneration-permissive and regeneration-deficient tissues. We found that Wnt signalling is aberrantly activated in regeneration-deficient tissues. Notably, downregulation of canonical Wnt signalling in regeneration-deficient regions restores regenerative abilities: blastemas form and new heads regenerate in tissues that normally never regenerate. This work reveals that manipulating a single signalling pathway can reverse the evolutionary loss of regenerative potential.

Unlike more commonly studied planarians<sup>2</sup>, representatives of the family Dendrocoelidae regenerate heads only when amputated within the anterior third of the body, yet retain full posterior regeneration ability along the anterior-posterior axis (Fig. 1a, b and Supplementary Fig. 1)<sup>3,4</sup>. After amputation in regeneration-deficient tissues, *P. fluviatilis* fails to produce a blastema and never regenerates anterior structures (Fig. 1b and Supplementary Fig. 1). The stage at which regenerative processes fail in this animal is unknown. Planarian regeneration encompasses several processes, including wound healing to cover exposed tissues and allow signalling between the wound epidermis and underlying mesenchymal cells<sup>7</sup>, apoptosis<sup>8</sup>, and stem cell (neoblast) proliferation<sup>9</sup>. Following amputation, neoblast proliferation occurs in two waves: a systemic response shortly after amputation and a later burst near the wound site<sup>9</sup>. In addition, regenerating tissues re-establish proper axial polarity, using a number of conserved signalling pathways<sup>10–14</sup>. Subsequently, tissue outgrowth occurs as an undifferentiated mass of cells (the regeneration blastema) differentiates to replace lost structures<sup>15</sup>.

To identify the nature of regeneration failure in *P. fluviatilis*, we characterized several of these early regenerative processes following amputation in both regeneration-proficient (Reg<sup>+</sup>) and regeneration-deficient (Reg<sup>-</sup>) tissues. Histological staining and electron microscopy revealed that wound healing occurs properly following amputation in all tissues, regardless of regenerative potential (Fig. 1c, d). After amputation in Reg<sup>-</sup> tissues, biphasic cell division occurs in both Reg<sup>+</sup> and Reg<sup>-</sup> tissues (Fig. 1e, f and Supplementary Fig. 2). In addition, gut tissues seem to remodel<sup>16</sup> in fragments that fail to regenerate (Supplementary Fig. 1). These data show that early phases of the regenerative response occur, although Reg<sup>-</sup> tissues fail to form a blastema.

To assess whether axial polarity is re-established properly following amputation in Reg<sup>-</sup> tissues of *P. fluviatilis*, we characterized the spatio-temporal expression of homologues of *nou-darake* (*ndk*) and *sFRP1*, genes expressed specifically at the anterior of other planarian

species<sup>10,11,17</sup>. Both *Pfu-ndk* and *Pfu-sFRP1* are expressed at the anterior wound site shortly after amputation in Reg<sup>+</sup> tissue (Fig. 1g, i). However, the expression of these genes was reduced in Reg<sup>-</sup> tissue following injury (Fig. 1h, j), indicating that the initial failure of regeneration occurs at or upstream of axial re-polarization.

Because these polarity markers are not expressed appropriately following amputation in Reg<sup>-</sup> fragments, we sought to identify gene expression differences between Reg<sup>+</sup> and Reg<sup>-</sup> tissue after amputation. We generated a *de novo* *P. fluviatilis* transcriptome and used RNA sequencing (RNA-seq) to characterize transcripts from excised tissue fragments in Reg<sup>+</sup> and Reg<sup>-</sup> body regions 24 h post amputation (Fig. 2a). We performed parallel analyses on tissues excised from intact animals at identical body regions to account for regional differences in transcripts, thereby identifying changes resulting from amputation (Fig. 2a). Analysis of amputated versus intact tissues revealed that

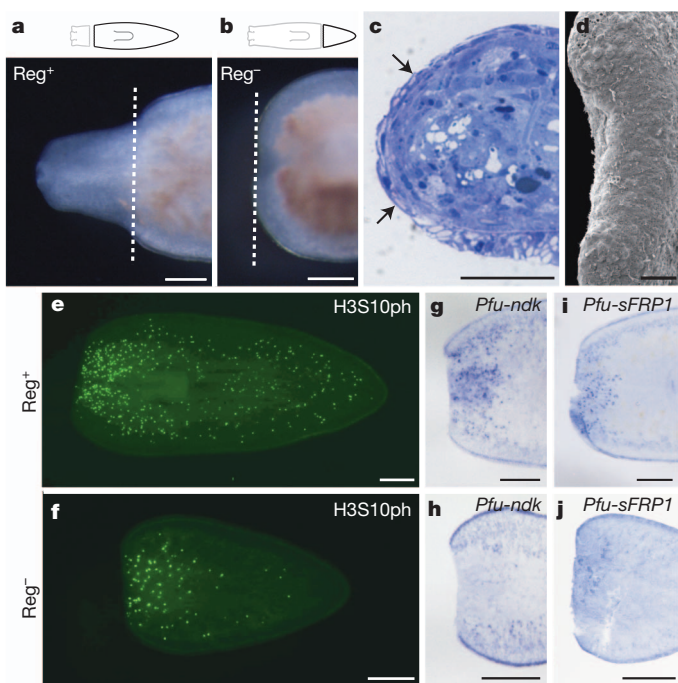


**Figure 1 | *Procotyla fluviatilis* fails to regenerate heads after amputation in posterior body regions.** a, b, Proficient and failed head regeneration 10 days after amputation in Reg<sup>+</sup> and Reg<sup>-</sup> regions, respectively ( $n = 25/25$ ). Dashed lines indicate amputation planes. c, d, Complete wound epithelium (arrows;  $n = 8/9$ ) and full wound closure ( $n = 7/8$ ) 48 h after amputation in Reg<sup>-</sup> tissue. Scale bar in d, 100  $\mu$ m. e, f, Mitotic activity 4 days after amputation in Reg<sup>+</sup> and Reg<sup>-</sup> tissues ( $n = 10/treatment$ ) assayed by phosphohistone H3 (H3S10ph) immunostaining. g–j, *Pfu-ndk* and *Pfu-sFRP1* expression 24 h after amputation in Reg<sup>+</sup> and Reg<sup>-</sup> tissues ( $n = 8/treatment$ ). Anterior is to the left. Scale bars, 250  $\mu$ m unless otherwise noted.

<sup>1</sup>Howard Hughes Medical Institute and Department of Cell and Developmental Biology, University of Illinois at Urbana-Champaign, Urbana, Illinois 61801, USA. <sup>†</sup>Present address: Department of Biology, University of San Francisco, San Francisco, California 94117, USA.

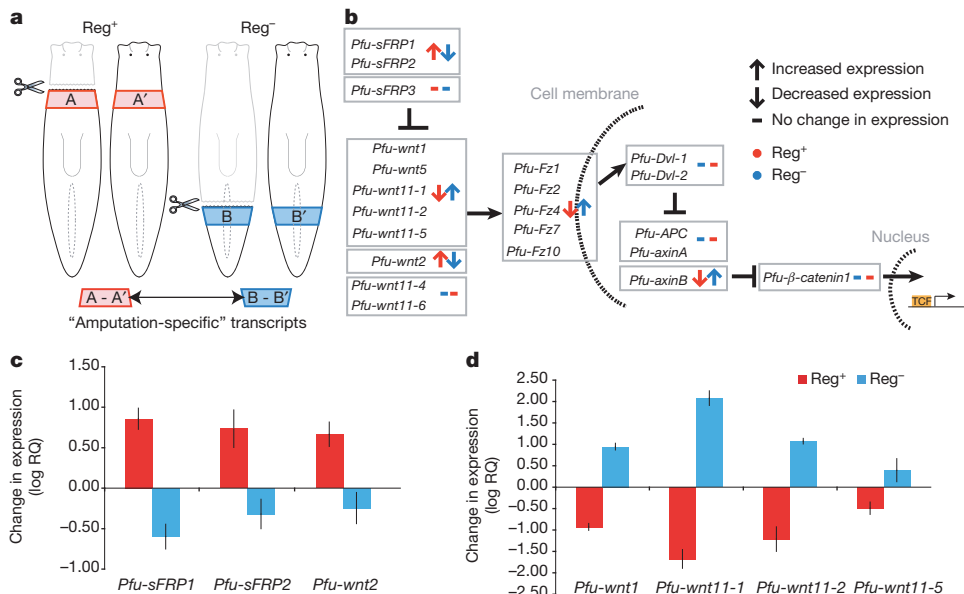


**Figure 2 | Comparative transcriptomics reveal differentially expressed genes following amputation in Reg<sup>+</sup> and Reg<sup>-</sup> tissues.** **a**, Experimental strategy to identify transcripts responsive to amputation in Reg<sup>+</sup> (red) and Reg<sup>-</sup> (blue) tissues. **b**, Alteration in expression levels of Wnt signalling components after amputation in Reg<sup>+</sup> (red) and Reg<sup>-</sup> (blue) tissues measured by RNA-seq.

10.7% of the assembled contigs (16,026/149,594) were significantly altered  $\geq$  twofold ( $P < 0.05$ ) after amputation in either Reg<sup>+</sup> or Reg<sup>-</sup> tissues. After collapsing contigs likely to be representing the same transcript based upon BLAST comparison similarity, we focused our analysis on 15,742 contigs that seem to be expressed differentially after amputation (based on the large number of contigs, many individual transcripts are likely to be represented by multiple contigs). Whereas a small number of contigs were simultaneously over- or under-represented in both conditions (74/15,742), many were over- or under-represented exclusively in either Reg<sup>+</sup> or Reg<sup>-</sup> fragments (14,288/15,742). Other contigs were over-represented in Reg<sup>+</sup> tissue and under-represented in Reg<sup>-</sup> tissue (537/15,742) or vice versa (842/15,742) (Supplementary Table 1). Upon close examination of transcripts over-represented in Reg<sup>-</sup> tissues and under-represented in Reg<sup>+</sup> tissues, we found that several represented genes were involved in Wnt signalling. Given the importance of Wnt signalling in defining anteroposterior polarity in other planarian species<sup>10,11,14</sup>, we focused on genes involved in this pathway.

RNA-seq revealed significant over-representation of many transcripts encoding Wnt ligands and receptors in Reg<sup>-</sup> tissues after amputation (Fig. 2b), with some transcripts, such as *Pfu-wnt11-1*, upregulated as much as  $\sim$ 400-fold relative to intact controls. These same transcripts were downregulated in Reg<sup>+</sup> tissues relative to their position-adjusted intact controls (Fig. 2b). In addition, homologues of Wnt inhibitors, such as *sFRP1* and *sFRP2* (ref. 18), were downregulated in Reg<sup>-</sup> tissues and upregulated in Reg<sup>+</sup> tissues (Fig. 2b). These patterns of gene expression were confirmed by quantitative PCR with reverse transcription (qRT-PCR) (Fig. 2c, d). *Pfu-β-catenin1*, the intracellular effector of Wnt signalling, was not expressed differentially following amputation in either tissue region (Fig. 2b), indicating that *Pfu-β-catenin1* expression is not responsive to wounding in either Reg<sup>+</sup> or Reg<sup>-</sup> tissues.

Because axial repolarization fails in Reg<sup>-</sup> tissues after amputation, we propose that upregulation of posteriorly expressed genes, including Wnt ligands, may inhibit signals that lead to proper anterior–posterior patterning and, thus, block regeneration. To test this hypothesis, we disrupted Wnt signalling using RNA interference (RNAi) to target *Pfu-β-catenin1*, the intracellular Wnt signalling effector. Remarkably, *Pfu-β-catenin1* RNAi resulted in blastema formation and regeneration

**c, d**, Changes in transcript levels based on relative quantification (RQ) of selected anterior- and posterior-specific Wnt signalling components after amputation in Reg<sup>+</sup> (red) and Reg<sup>-</sup> (blue) tissues relative to uncut controls measured by qRT-PCR. Error bars represent standard deviations.

of a complete head and brain in Reg<sup>-</sup> fragments as assayed by regeneration of the photoreceptors ( $n = 64/71$ ) (Fig. 3b, f), whereas control RNAi animals, injected with double-stranded RNA from a *ccdB* and *camR*-containing bacterial sequence, failed to form a blastema or neural structures (Fig. 3a, e). *Pfu-β-catenin1* RNAi also affected posterior regeneration with the formation of heads at posterior facing wounds (Supplementary Fig. 3), which has been observed in other planarian species<sup>10</sup>. Knocking down Wnts individually or in combination did not rescue Reg<sup>-</sup> tissue (Supplementary Table 2). *Pfu-β-catenin1* (RNAi) animals with rescued regeneration demonstrated anteriorly directed movements within 15 days after amputation (Supplementary Video 1), indicating complete and functional regeneration of the head. Rescue of regeneration in *Pfu-β-catenin1* (RNAi) animals reveals that Reg<sup>-</sup> tissues are competent to express the head regeneration program, but either lack signals required for re-establishment of axial polarity or these signals are inhibited.

In contrast, knockdown of *APC*, an inhibitor of *β-catenin* and Wnt signalling, also resulted in blastema formation, but led to regeneration of tails at anterior-facing wounds ( $n = 14/53$ , Fig. 3c, g), as observed in *Schmidtea mediterranea*<sup>10</sup>. These data indicate that altering gene expression to create either an anterior or posterior polarity cue within Reg<sup>-</sup> tissues can perpetuate downstream steps in regeneration, thereby allowing blastema formation and regeneration of heads or tails at anterior-facing wounds. Notum has recently been identified as a Wnt inhibitor expressed at anterior facing wounds in the planarian *S. mediterranea*<sup>19</sup>. However, *Pfu-notum* RNAi failed to initiate a similar posterior-regeneration program. To assay alterations in gene expression following regeneration rescue, we used qRT-PCR to characterize expression patterns of polarity genes following *Pfu-β-catenin1* RNAi and *Pfu-APC* RNAi (Fig. 3h). After amputation in *Pfu-β-catenin1* (RNAi) animals, both *Pfu-sFRP1* and *Pfu-ndk* were significantly upregulated, indicating that a latent anterior regeneration program is reactivated in Reg<sup>-</sup> tissues following *Pfu-β-catenin1* RNAi.

Our data provide important clues about mechanisms regulating regeneration. In a related Dendrocoelid species with reduced regenerative capacity, anterior regeneration ability in posterior fragments was rescued through grafting irradiated anterior tissue onto Reg<sup>-</sup> tissue<sup>20</sup>, suggesting that signals from differentiated anterior cells were sufficient to allow regeneration. Our results indicate that such signals

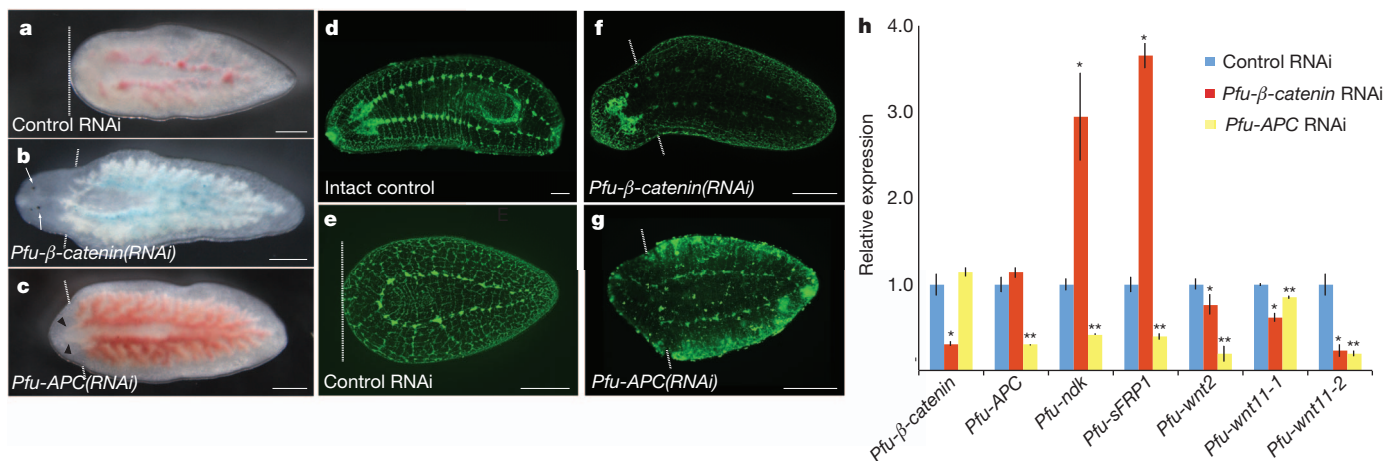


**Figure 3 | Disruption of Wnt signalling via RNAi rescues regeneration in Reg<sup>-</sup> tissues.** **a–c**, Posterior fragments 14 days after amputation in Reg<sup>-</sup> regions of control RNAi, *Pfu-β-catenin1(RNAi)*, and *Pfu-APC(RNAi)* animals. Black arrowheads, gut branches indicative of posterior fate; dashed lines, amputation planes; white arrows, eyespots. **d–g**, Nervous system in uncut and Reg<sup>-</sup> body regions of control RNAi, *Pfu-β-catenin1(RNAi)*, and *Pfu-APC(RNAi)* animals 28 days after amputation. Anterior is to the left. Scale bars, 250  $\mu$ m. **h**, Relative

transcript levels in Reg<sup>-</sup> tissue from *Pfu-β-catenin1(RNAi)*, *Pfu-APC(RNAi)* and control RNAi animals 48 h after amputation. Significant differences between control and experimental samples based on *P* values ( $<0.05$ ) from two-tailed unpaired *t*-test are shown. (\**Pfu-β-catenin1(RNAi)* versus control RNAi; \*\**Pfu-APC(RNAi)* versus control RNAi). Error bars represent standard deviations.

are involved in re-establishing anterior–posterior polarity. Recent efforts have identified many requirements for the regenerative response to wounding, including proliferation<sup>9</sup>, apoptosis<sup>8</sup> and cell signalling<sup>11,12,21</sup>, but the interrelationships between these processes are not yet well understood. Our data confirm that increased neoblast proliferation following amputation occurs independently of the re-establishment of anterior–posterior polarity (Fig. 1e, f and Supplementary Fig. 2)<sup>14</sup>. We have also shown that subsequent regenerative processes are inhibited until polarity is re-established. These observations suggest a checkpoint in the regeneration program that must be satisfied before downstream developmental processes can occur. Such a checkpoint would act as a vulnerable stage at which evolutionary modifications could alter regenerative potential.

Loss of regenerative ability would seem to carry a selective disadvantage, and possible causes for such losses have been the subject of much speculation<sup>1,5</sup>. Identification of aberrant Wnt signalling following amputation in Reg<sup>-</sup> tissues of *P. fluiatilis* suggests one mechanism limiting regeneration ability in planarians; however, we can only speculate about the driving force leading to regeneration loss. Unlike most planarians, *P. fluiatilis* is semelparous, reproducing only once, then dying within a single season<sup>6</sup>. Life-history studies have shown that semelparous species invest more in reproduction<sup>22</sup>, possibly at the expense of other developmental programs. Whereas highly regenerative, iteroparous planarian species resorb reproductive structures during periods of starvation<sup>23</sup> and following amputation<sup>24</sup>, semelparous species do not resorb testes after such events<sup>23,25</sup>. We speculate that the signals maintaining the reproductive system in semelparous planarians may perturb the proper re-establishment of polarity after amputation, providing a selective advantage for later reproductive potential. As a consequence, anterior regeneration ability has been limited.

Next-generation sequencing technologies and functional analyses facilitate research on understudied, yet biologically informative, non-model organisms. Expanding use of these technologies will help elucidate causes for limited regeneration in other animals, potentially identifying inhibitory signals that must be overcome to elicit a regenerative response after wounding. Given that perturbation of a single gene's function can rescue an entire regenerative program, identifying additional regeneration-inhibiting signals will increase our understanding of the evolution of regeneration loss and provide the intriguing prospect of restoring regenerative abilities in regeneration-deficient animals.

## METHODS SUMMARY

**In situ hybridization.** *In situ* hybridizations were performed using formaldehyde fixation as described previously<sup>26</sup> with minor modifications.

**Immunostaining.** Immunostaining was conducted as described previously<sup>27</sup> using anti-synapsin mouse monoclonal, anti-phospho-histone H3 (Ser10) rabbit monoclonal, goat anti-mouse Alexa-488, and goat anti-rabbit Alexa-488 antibodies.

**Histology and scanning electron microscopy.** Samples were initially prepared as described previously<sup>28</sup>. For histology, samples were sectioned and stained with toluidine blue. For scanning electron microscopy, samples were mounted on aluminium stubs and coated with Au/Pd.

**Transcriptome sequencing and RNA-seq.** Roche 454 pyrosequencing technology was used to sequence a reference transcriptome from the RNA of four intact *P. fluiatilis*. Reads were assembled *de novo* using iterations of SeqMan NGen and CLC Genomics. Solexa Illumina sequencing was performed on RNA extracted from excised tissues. Reads were mapped to the reference transcriptome using CLC Genomics as described previously<sup>29</sup>.

**Cloning.** Candidate genes were amplified via PCR from complementary DNA (Supplementary Table 3) and homology was assigned (Supplementary Fig. 4). PCR products were ligated with *Fam1105I*-digested pJC53.2 (ref. 30) and used to transform DH5 $\alpha$  *Escherichia coli* cells. To generate riboprobes, *in vitro* transcription reactions were performed with the appropriate RNA polymerase using standard approaches and the addition of digoxigenin-11-UTP.

**RNAi.** dsRNA was synthesized via *in vitro* transcription using amplified templates (Supplementary Fig. 5). dsRNA solution was mixed with dye and microinjected into the gut three times over the course of 1 week before amputation. As a negative control, animals were injected with dsRNA synthesized from the *ccdB*- and *camR*-containing insert of pJC53.2 (ref. 30).

**Quantitative RT-PCR.** cDNA was synthesized from RNA isolated as described for RNA-seq and used to conduct quantitative PCR. Three biological replicates were performed. Absolute quantities were determined for each gene and normalized to the endogenous level of *Pfu-actin*. The mean value for each treatment was then normalized to control conditions to determine the relative changes in expression.

**Full Methods** and any associated references are available in the online version of the paper.

Received 21 September 2012; accepted 21 June 2013.

Published online 24 July 2013.

1. Bely, A. E. Evolutionary loss of animal regeneration: pattern and process. *Integr. Comp. Biol.* **50**, 515–527 (2010).
2. Newmark, P. A. & Sánchez Alvarado, A. Not your father's planarian: a classic model enters the era of functional genomics. *Nature Rev. Genet.* **3**, 210–219 (2002).
3. Lillie, F. R. Notes on regeneration and regulation in planarians. *Am. J. Physiol.* **6**, 129–141 (1901).
4. Morgan, T. H. Notes on regeneration. *Biol. Bull.* **6**, 159–172 (1904).

5. Bely, A. E. & Nyberg, K. G. Evolution of animal regeneration: re-emergence of a field. *Trends Ecol. Evol.* **25**, 161–170 (2010).
6. Kenk, R. *Biota of Freshwater Ecosystems Identification Manual No. 1: Freshwater planarians (Turbellaria) of North America* (US Environmental Protection Agency, 1972).
7. Wenemoser, D., Lapan, S. W., Wilkinson, A. W., Bell, G. W. & Reddien, P. W. A molecular wound response program associated with regeneration initiation in planarians. *Genes Dev.* **26**, 988–1002 (2012).
8. Pellettieri, J. *et al.* Cell death and tissue remodeling in planarian regeneration. *Dev. Biol.* **338**, 76–85 (2010).
9. Wenemoser, D. & Reddien, P. W. Planarian regeneration involves distinct stem cell responses to wounds and tissue absence. *Dev. Biol.* **344**, 979–991 (2010).
10. Gurley, K. A., Rink, J. C. & Sánchez Alvarado, A.  $\beta$ -catenin defines head versus tail identity during planarian regeneration and homeostasis. *Science* **319**, 323–327 (2008).
11. Petersen, C. P. & Reddien, P. W. *Smed-Bcatenin-1* is required for anteroposterior blastema polarity in planarian regeneration. *Science* **319**, 327–330 (2008).
12. Yazawa, S., Umesono, Y., Hayashi, T., Tarui, H. & Agata, K. Planarian Hedgehog/Patched establishes anterior-posterior polarity by regulating Wnt signaling. *Proc. Natl. Acad. Sci. USA* **106**, 22329–22334 (2009).
13. Rink, J. C., Gurley, K. A., Elliott, S. A. & Sánchez Alvarado, A. Planarian Hh signaling regulates regeneration polarity and links Hh pathway evolution to cilia. *Science* **326**, 1406–1410 (2009).
14. Gurley, K. A. *et al.* Expression of secreted Wnt pathway components reveals unexpected complexity of the planarian amputation response. *Dev. Biol.* **347**, 24–39 (2010).
15. Reddien, P. W. & Sánchez Alvarado, A. Fundamentals of planarian regeneration. *Annu. Rev. Cell Dev. Biol.* **20**, 725–757 (2004).
16. Forsthöfel, D. J., Park, A. E. & Newmark, P. A. Stem cell-based growth, regeneration, and remodeling of the planarian intestine. *Dev. Biol.* **356**, 445–459 (2011).
17. Cebrià, F. *et al.* FGFR-related gene *nou-darake* restricts brain tissues to the head region of planarians. *Nature* **419**, 620–624 (2002).
18. Mii, Y. & Taira, M. Secreted Frizzled-related proteins enhance the diffusion of Wnt ligands and expand their signaling range. *Development* **136**, 4083–4088 (2009).
19. Petersen, C. P. & Reddien, P. W. Polarized *notum* activation at wounds inhibits Wnt function to promote planarian head regeneration. *Science* **332**, 852–855 (2011).
20. Stephan-Dubois, F. & Gilgenkrantz, F. Transplantation et régénération chez la planaire *Dendrocoelum lacteum*. *J. Embryol. Exp. Morphol.* **9**, 642–649 (1961).
21. Tasaki, J. *et al.* ERK signaling controls blastema cell differentiation during planarian regeneration. *Development* **138**, 2417–2427 (2011).
22. Calow, P. *Life Cycles. An Evolutionary Approach to the Physiology of Reproduction, Development and Ageing* (Chapman and Hall, 1978).
23. Romero, R. & Baguna, J. Quantitative cellular analysis of life-cycle strategies of iteroparous and semelparous triclad. *Fortschr. Zool.* **36**, 283–289 (1988).
24. Fedecka-Bruner, B. Etudes sur la régénération des organes génitaux chez la planaire *Dugesia lugubris* I. Régénération des testicules après destruction. *Bull. Biol. Fr. Belg.* **101**, 255–319 (1967).
25. Grassé, M. & Gardenghi, G. The involvement of cellular elements other than neoblasts in *Dendrocoelum lacteum* regeneration. *Boll. Zool.* **45**, 365–368 (1978).
26. Pearson, B. J. *et al.* A formaldehyde-based whole-mount *in situ* hybridization method for planarians. *Dev. Dyn.* **238**, 443–450 (2009).
27. Chong, T., Stary, J. M., Wang, Y. & Newmark, P. A. Molecular markers to characterize the hermaphroditic reproductive system of the planarian *Schmidtea mediterranea*. *BMC Dev. Biol.* **11**, 69 (2011).
28. Rouhana, L., Vieira, A. P., Roberts-Galbraith, R. H. & Newmark, P. A. PRMT5 and the role of symmetrical dimethylarginine in chromatoid bodies of planarian stem cells. *Development* **139**, 1083–1094 (2012).
29. Marioni, J. C., Mason, C. E., Mane, S. M., Stephens, M. & Gilad, Y. RNAseq: An assessment of technical reproducibility and comparison with gene expression arrays. *Genome Res.* **18**, 1509–1517 (2008).
30. Collins, J. J. III *et al.* Genome-wide analysis reveals a role for peptide hormones in regulating planarian germ line development. *PLoS Biol.* **8**, e1000509 (2010).

**Supplementary Information** is available in the online version of the paper.

**Acknowledgements** We thank Newmark laboratory members for comments, A. Vieira for technical assistance, A. Hernandez and the W. M. Keck Center for Comparative and Functional Genomics for sequencing assistance, and the National Forest Service, Illinois Department of Natural Resources, USA, and Montgomery County (Maryland) Department of Parks, USA, for field collection permits. We also thank A. Boney, J. Brubacher, T. Chong, M. Issigonis, H. Iyer and B. Lambrus for assistance in field collections. This work was supported by National Institute of General Medicine Sciences fellowship F32GM097921 (J.M.S.). P.A.N. is an investigator of the Howard Hughes Medical Institute.

**Author Contributions** Both authors contributed to the design of the experimental strategy. J.M.S. conducted all experiments, analysed the data and drafted the manuscript, which was critically reviewed and revised by P.A.N. Both authors discussed the results and commented on the final version of the manuscript.

**Author Information** Sequence read archive (SRA) data reported in this paper were deposited at NCBI as a BioProject under accession number PRJNA205293. RNA-seq analyses have been deposited in the NCBI Gene Expression Omnibus under accession number GSE48497. Reprints and permissions information is available at [www.nature.com/reprints](http://www.nature.com/reprints). The authors declare no competing financial interests. Readers are welcome to comment on the online version of the paper. Correspondence and requests for materials should be addressed to J.M.S. ([jsikes@usfca.edu](mailto:jsikes@usfca.edu)).

## METHODS

**Animal collection and culture.** *Procotyla fluviatilis* was collected from streams at Blockhouse Point Conservation Park (Maryland, USA) or the LaRue Pine Hills/Otter Pond Research Natural Area (Illinois, USA). Animals were maintained in the laboratory at 18 °C in Montjuich salts<sup>31</sup> and fed bi-weekly. Planarians were starved for 1 week before use.

**In situ hybridization.** *In situ* hybridizations were performed using the formaldehyde-based fixation procedure as described previously<sup>26</sup> with the following modifications. Planarians were killed in 8% *n*-acetyl cysteine for 5 min, fixed in 4% formaldehyde in PBSTX (PBS + 0.3% Triton X-100) for 25 min, and incubated in reduction solution for 5 min at room temperature. Samples were bleached in 6% H<sub>2</sub>O<sub>2</sub> for 1 h. Samples were imaged with a Leica M205A stereoscope.

**Immunostaining.** Immunostaining was conducted as described previously<sup>27</sup> using methacarn fixative. Primary antibody incubation was performed overnight at 4 °C at the following concentrations: anti-synapsin mouse monoclonal antibody (1:75; Developmental Studies Hybridoma Bank, catalogue no. 3C11), anti-phospho-histone H3 (Ser10) rabbit monoclonal antibody (1:1,000; Cell Signaling Technology, catalogue no. 3377). Animals were incubated in secondary antibody (goat anti-mouse Alexa-488, 1:400 or goat anti-rabbit, Alexa-488, 1:500; Molecular Probes, Invitrogen, catalogue no. A11029) overnight at 4 °C. Animals were mounted in Vectashield. Images were captured with Zeiss SteREO Lumar V12, Zeiss AxioZoomV16, and Zeiss LSM710 confocal microscopes.

**Histology and scanning electron microscopy.** Animals were fixed and prepared as previously described<sup>28</sup>. For histology, ethanol was gradually replaced with acetone, followed by infiltration with Araldite/Embed 812 (Electron Microscopy Sciences). Sections (1 µm) were collected on glass slides, dried over a heating plate, and stained with 1% toluidine blue for 10 s. Slides were mounted with Cytoseal 60 (Thermo Scientific) and imaged on a Nikon Eclipse TE200 inverted microscope. For scanning electron microscopy, once the samples reached 100% ethanol, they were critical-point dried using a Tousimis Samdri-PVT-3D, mounted on aluminium stubs, coated with Au/Pd using a Denton Desk II TSC turbo-pumped sputter coater and imaged on a Philips XL30 ESEM-FEG.

**Transcriptome sequencing and RNA-seq.** For sequencing the reference transcriptome, RNA from four random, intact *P. fluviatilis* adults was isolated using TRIzol (Invitrogen), DNase-treated, purified with an RNA Clean and Concentrator kit (Zymo Research), and submitted to the W. M. Keck Center for Comparative and Functional Genomics for Roche 454 pyrosequencing. Reads were assembled *de novo* using iterations of SeqMan NGen (DNASTAR) and CLC Genomics (CLCbio). For RNA-seq experiments, RNA was isolated from tissue fragments of five worms, each excised ~2 mm posterior to the amputation sites. Control RNA was purified from corresponding control fragments excised from intact animals at equivalent body regions as described above. Samples were submitted to the W. M. Keck Center for Comparative and Functional Genomics for Illumina sequencing. Reads were mapped to the reference transcriptome using CLC Genomics and compared as in ref. 29. Contigs with  $\geq 2$ -fold change and *P* value  $< 0.05$  (from two-sided unpaired *t*-tests) were used for detailed analysis. Selected contigs were screened to identify redundant contigs by using BLAST homology to the NCBI nr database to merge contigs with top hits to the same gene.

**Cloning.** To generate riboprobes, candidate genes were PCR amplified from cDNA generated from total RNA (iScript cDNA Synthesis Kit, Bio-Rad). For cDNA preparations, RNA was extracted using TRIzol Reagent (Invitrogen). For cloning, 2–3 µl of PCR product was ligated with 70 ng of Eam1105I-digested pJC53.2 (Rapid DNA Ligation kit, Roche)<sup>30</sup> and used to transform DH5 $\alpha$  *Escherichia coli* cells. *In vitro* transcriptions with the appropriate RNA polymerase were performed using standard approaches with the addition of digoxigenin-11-UTP (Roche). All primers used to amplify candidate genes are included in Supplementary Table 3.

**RNAi.** To generate dsRNA, templates cloned into pJC53.2 (ref. 30) were amplified with a modified T7 oligonucleotide (GGATCCTAATACGACTCACTATAGGG), purified using a DNA Clean & Concentrator kit (Zymo Research), and eluted in 15 µl of water. 10.5 µl of each PCR product (Supplementary Fig. 5) was used as template for *in vitro* transcription in a reaction containing 5 µl 100 mM mix of ribonucleotide triphosphates (rNTPs) (Promega), 1 µl high-yield transcription buffer (0.4 M Tris pH 8.0, 0.1 M MgCl<sub>2</sub>, 20 mM spermidine, 0.1 M DTT), 1 µl thermostable inorganic pyrophosphatase (New England Biolabs), 0.5 µl Optizyme recombinant RNase inhibitor (Fisher Scientific), and 2 µl T7 RNA polymerase. Samples were incubated at 37 °C for 12 h and then treated with RNase-free DNase (Fisher Scientific, catalogue number FP2231) and cleaned/concentrated via ammonium acetate precipitation. Synthesized RNA was then annealed by heating at 95 °C, 75 °C and 50 °C each for 3 min. dsRNA solution was mixed with dye and 65 nl (~1 µg µl<sup>-1</sup>) was microinjected into the gut of randomized adult planarians three times over the course of 1 week before amputation using a Nanoject II micromanipulator (Drummond Scientific). As a negative control, animals were injected with dsRNA synthesized from the *ccdB*- and *camR*-containing insert of pJC53.2 (ref. 30). Live (RNAi) animals were imaged and videos were captured with a Leica M205A.

**Quantitative RT-PCR.** To examine transcript levels following amputation in regeneration-proficient and regeneration-deficient tissues, RNA was extracted using TRIzol reagent from five random tissue fragments identical to those used for RNA sequencing. Following DNase treatment (DNA-free RNA Kit, Zymo Research), reverse transcription was performed (iScript cDNA Synthesis Kit) and quantitative PCR was conducted using Power SYBR Green PCR Master Mix (Applied Biosystems) and a 7900HT real-time PCR system (Applied Biosystems). Three biological replicates were performed and all samples were measured in triplicate to account for pipetting error. Absolute quantities of each transcript were determined for each gene and normalized to the level of *Pfu-actin* in each sample. The mean value for each amputated treatment was then normalized to the intact tissue fragments extracted from an identical axial position to determine the relative changes in expression due to amputation. For qRT-PCR of genes following RNAi experiments, the mean values of control RNAi and experimental (RNAi) samples were graphed independently without normalization to intact fragments. All primers used for these studies are included in Supplementary Table 3.

31. Cebria, F. & Newmark, P. A. Planarian homologues of *netrin* and *netrin receptor* are required for proper regeneration of the central nervous system and the maintenance of nervous system architecture. *Development* **132**, 3691–3703 (2005).

# Reactivating head regrowth in a regeneration-deficient planarian species

S.-Y. Liu<sup>1</sup>, C. Selck<sup>2</sup>, B. Friedrich<sup>2</sup>, R. Lutz<sup>2</sup>, M. Vila-Farré<sup>1</sup>, A. Dahl<sup>3</sup>, H. Brandl<sup>1</sup>, N. Lakshmanaperumal<sup>1</sup>, I. Henry<sup>1</sup> & J. C. Rink<sup>1,2</sup>

Species capable of regenerating lost body parts occur throughout the animal kingdom, yet close relatives are often regeneration incompetent<sup>1,2</sup>. Why in the face of ‘survival of the fittest’ some animals regenerate but others do not remains a fascinating question<sup>3</sup>. Planarian flatworms are well known and studied for their ability to regenerate from minute tissue pieces, yet species with limited regeneration abilities have been described even amongst planarians<sup>4</sup>. Here we report the characterization of the regeneration defect in the planarian *Dendrocoelum lacteum* and its successful rescue. Tissue fragments cut from the posterior half of the body of this species are unable to regenerate a head and ultimately die<sup>5</sup>. We find that this defect originates during the early stages of head specification, which require inhibition of canonical Wnt signalling in other planarian species<sup>6–8</sup>. Notably, RNA interference (RNAi)-mediated knockdown of *Dlac-β-catenin-1*, the Wnt signal transducer, restored the regeneration of fully functional heads on tail pieces, rescuing *D. lacteum*’s regeneration defect. Our results demonstrate the utility of comparative studies towards the reactivation of regenerative abilities in regeneration-deficient animals. Furthermore, the availability of *D. lacteum* as a regeneration-impaired planarian model species provides a first step towards elucidating the evolutionary mechanisms that ultimately determine why some animals regenerate and others do not.

The two current model planarian species, *Dugesia japonica*<sup>9</sup> and *Schmidtea mediterranea*<sup>10</sup>, were selected precisely because of their excellent regenerative abilities. Others amongst the many hundred planarian species worldwide<sup>11</sup> are regeneration deficient. We decided to address the mechanistic basis of such inter-species variation by example of the species *D. lacteum*, which has been reported to be incapable of regenerating heads from their posterior body half<sup>4,5</sup>. We found a *D. lacteum* population near Nottingham, UK, that adapted well to laboratory culture conditions and could be expanded via rounds of anterior amputations. Assaying our strain’s regenerative ability along the anterior-posterior axis confirmed lack of head regeneration from tail pieces (Fig. 1a) in specific contrast to the global head regeneration ability of *S. mediterranea* (Fig. 1b). Previous characterizations of the *D. lacteum* regeneration defect were limited by the methods available at the time<sup>4,12–14</sup>. Intermittently obtained molecular insights in the planarian model species suggested a comparative approach towards the molecular diagnosis of *D. lacteum*’s regeneration defect. To enable the identification and analysis of marker genes in *D. lacteum* and to obtain a mapping reference for RNA-sequencing (RNA-seq) experiments, we *de novo* assembled a *D. lacteum* transcriptome (Supplementary Fig. 1 and ref. 15). Our transcriptome provides a representative overview of the species’ protein coding genes, as indicated by the presence of orthologues to all 248 core eukaryotic genes<sup>16</sup> (Supplementary Fig. 2) or to all Wnt ligands and Fzd receptors known

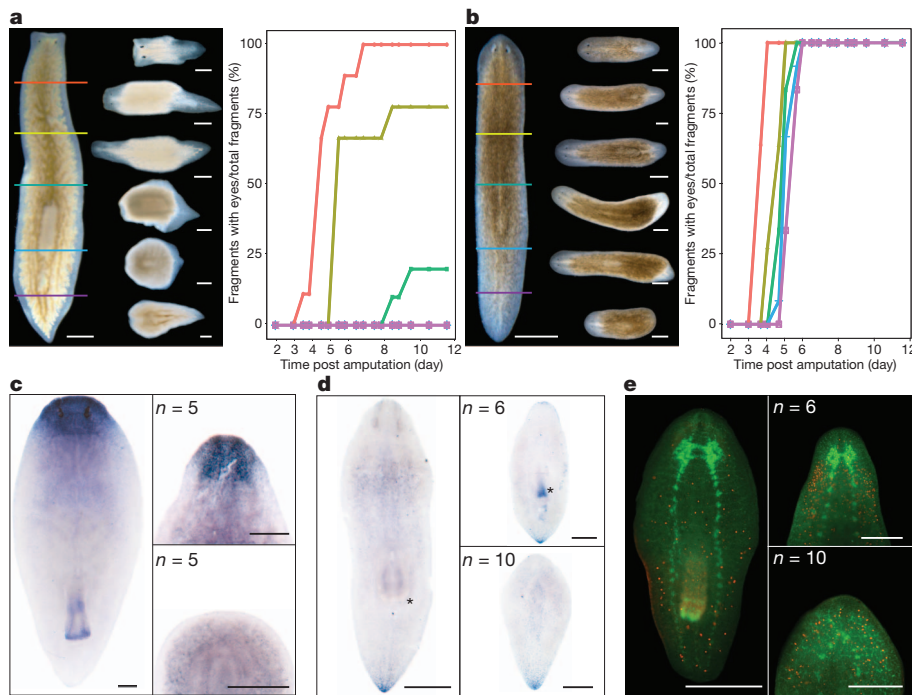


**Figure 1 | *D. lacteum* cannot regenerate heads posteriorly.** **a, b**, Transverse sections assaying regenerative abilities along *D. lacteum* (a) or *S. mediterranea* (b) anterior-posterior axis. Coloured lines indicate cutting planes, resulting fragments are shown 14 d.p.a. Graphs quantify head regeneration by timing of eye appearance in cohorts of 10 fragments, colour-coding as for cutting planes. **c**, Head marker *Dlndk* expression. **d**, Tail marker *Dlac-wnt11-2* expression. **e**, Brain/central nervous system (anti-synapsin, green) and mitoses (anti-H3P, red) immunostaining. Representative examples of uncut *D. lacteum* (left), head-regenerating trunk (top right) or regeneration-impaired tail pieces (bottom right) at 14 d.p.a., *n* as indicated. Asterisk, pharynx. Scale bars, 500  $\mu$ m.

<sup>1</sup>Max Planck Institute of Molecular Cell Biology and Genetics, Pfotenhauerstraße 108, 01307 Dresden, Germany. <sup>2</sup>DFG-Center for Regenerative Therapies Dresden (CRTD), Cluster of Excellence, Technische Universität Dresden, Fetscherstraße 105, 01307 Dresden, Germany. <sup>3</sup>Deep Sequencing Group-SFB655, DFG-Center for Regenerative Therapies Dresden (CRTD), Cluster of Excellence, Biotechnology Center (Biotec), Technische Universität Dresden, Fetscherstraße 105, 01307 Dresden, Germany.

from *S. mediterranea* (Supplementary Fig. 3a, b). Furthermore, we frequently find multiple distinct *D. lacteum* transcripts orthologous to a given *S. mediterranea* gene (for example, Supplementary Fig. 3c), indicating either high gene-specific haplotype divergence rates or multiple gene duplications in *D. lacteum*. Cloning and expression analysis of a planarian head marker<sup>17</sup> (*Dlac-ndk*) (Fig. 1c) and a tail marker<sup>18</sup> (*Dlac-wnt11-2*) (Fig. 1d) revealed that neither was expressed in tail pieces at 14 days post amputation (d.p.a.). Phospho-histone H3 (H3P) staining as proxy of stem cell activity<sup>19</sup> was present all along the anterior-posterior axis (Fig. 1e), confirming previous indications that stem cells are equally distributed along *D. lacteum*'s anterior-posterior axis<sup>4,12–14</sup>. Despite ectopic looping of ventral nerve cords instead of regenerating a bi-lobed brain (Fig. 1e), tail fragments survived for more than 3 months without ever displaying any overt signs of head regeneration (Supplementary Fig. 4). *D. lacteum*'s posterior head regeneration inability therefore probably originated from a specific defect in regeneration, rather than a kinetic delay.

Regeneration is a multistep process, entailing (1) appropriate wound responses, (2) cell proliferation/blastema formation and (3) blastema fate specification<sup>20</sup>. To delimit which of these processes might be compromised, we carried out detailed RNA-seq time-course experiments of head-regenerating wounds in the anterior body half ('trunk') versus non-regenerating wounds in the posterior body half ('tail') (Fig. 2a)<sup>15</sup>. A recent *S. mediterranea* study identified planarian early wound response genes<sup>21</sup>. All scoreable *D. lacteum* orthologues<sup>15</sup> showed remarkably consistent expression kinetics at trunk and tail wounds, indicating that *D. lacteum* tail pieces have a functional wound response (Fig. 2a). To assess whether blastema formation might be defective, we compared the accumulation of *Dlac-piwi-1*-expressing stem cells at wound sites and their mitotic activity<sup>19</sup>. As shown in Fig. 2b, the accumulation of *Dlac-piwi-1*<sup>+</sup> cells and elevation of H3P<sup>+</sup> cell numbers occurred to comparable extents at trunk and tail wounds during the first 3 d.p.a. Histological sections through the wound area at day 3 of regeneration revealed a gap in the basement membrane and the accumulation of small, undifferentiated cells (Fig. 2c), confirming successful blastema formation. Regeneration of the body edge, as assayed by *in situ* hybridization with the *D. lacteum* orthologue of *Smed-laminB*<sup>22</sup>, further suggested that tail-piece blastemas are functional and capable of replacing lost cell types (Supplementary Fig. 5). Thus, in agreement with previous studies<sup>12–14</sup>, these data demonstrate that the *D. lacteum* tail regeneration defect is not due to defective blastema formation.

To explore the remaining possibility of aberrant blastema fate specification, we systematically analysed the expression kinetics of a library of head and tail marker genes (Supplementary Table 1). Trunk wounds showed the expected upregulation of head markers above their low baseline expression at the amputation level (Fig. 3a, top), even though response kinetic differed from similar experiments in *S. mediterranea* (Supplementary Fig. 6). *In situ* hybridization (Supplementary Fig. 7) and independent quantitative PCR (Supplementary Fig. 8) confirmed the RNA-seq measurements. Remarkably, tail wounds failed to induce any of the head markers examined, not even the very early anterior fate markers *notum*<sup>23</sup> or *sFRP1* (ref. 6) (Fig. 3a, bottom). Concomitantly, *D. lacteum* tail pieces failed to downregulate markers of tail identity (Supplementary Table 1), again in sharp contrast to the rapid and sustained downregulation of these genes in head-regenerating *S. mediterranea* tail pieces cut at the same level (Fig. 3b). These results therefore demonstrate a twofold fate specification defect at *D. lacteum* tail wounds, (1) complete failure to establish anterior/head identity and (2) inappropriately maintained tail identity.

In planarians, head and tail identity are mutually exclusive due to opposite dependence on canonical Wnt signalling/β-catenin. Inhibition of β-catenin is necessary and sufficient for head induction, whereas activation of β-catenin is necessary and sufficient for tail specification<sup>6–8</sup>. Failed head establishment under sustained tail marker

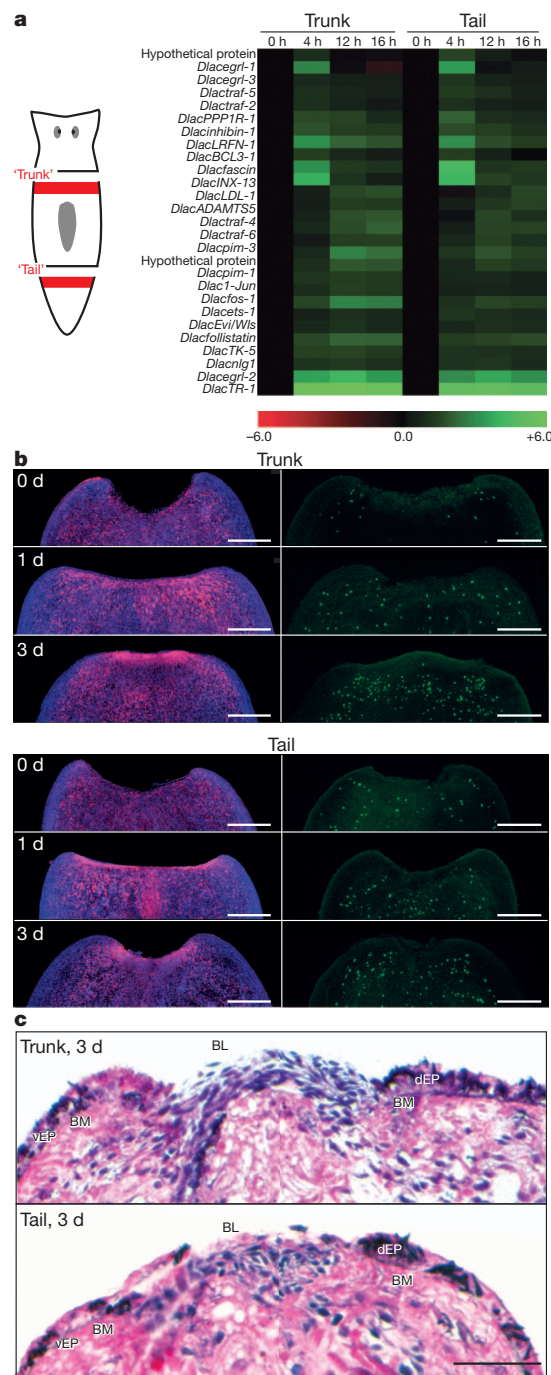


**Figure 2 | Posterior *D. lacteum* wounds form a blastema. a**, RNA-seq time-course analysis of wound response in trunk or tail. Heat map of log<sub>2</sub> fold-change relative to *t*<sub>0</sub> expression levels of the indicated genes. **b**, Accumulation of *Dlac-piwi-1*-expressing cells (red) at wounds of representative trunk or tail fragments (*n* = 4 per cohort) at indicated d.p.a., DAPI counterstaining (blue). Anti-H3P immunostaining (green, right) labels mitoses. Images are maximum projected confocal Z-stacks. Scale bar, 200 μm. **c**, Representative haematoxylin/eosin sagittal sections through trunk and tail wounds, 3 d.p.a. (*n* = 2). BL, blastema; BM, basement membrane; d/VEP, dorsal/ventral epithelium. Scale bar, 50 μm.

expression could therefore result both from inappropriately high levels of Wnt signalling and/or from insufficient Wnt inhibitory capacity. We adapted the double-stranded RNA (dsRNA) injection protocol from the planarian model species to functionally address these possibilities. Simultaneous targeting of the three Wnt ligands failing to downregulate in *D. lacteum* tail wounds (Fig. 3b) did not rescue

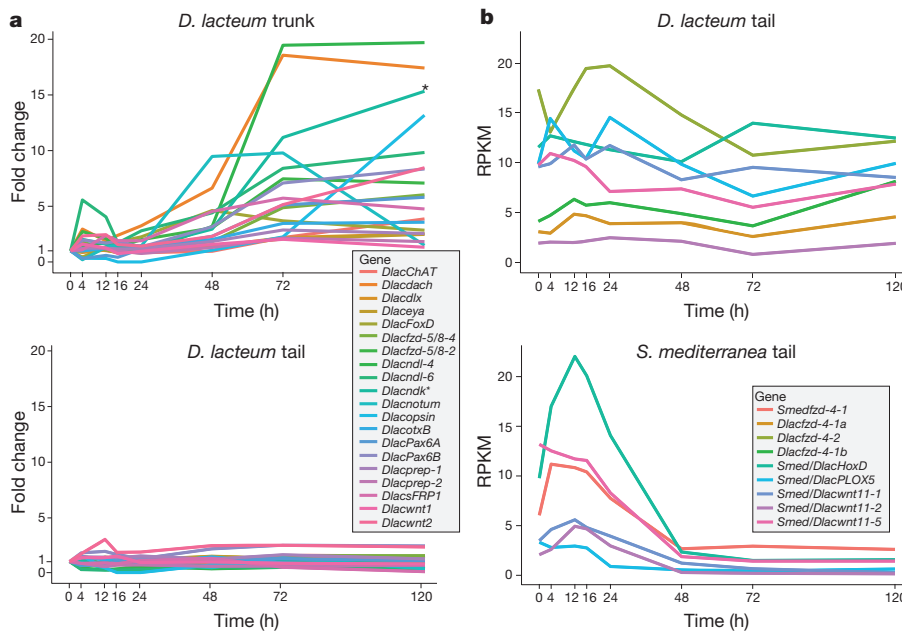


**Figure 3 | Posterior *D. lacteum* wounds cannot re-specify tissue identity.** **a**, RNA-seq time course of head marker genes in regenerating trunk (top) and regeneration-impaired tail wounds (bottom). Expression levels are graphed as fold-change relative to  $t_0$ , time points post amputation as indicated. Asterisk, *Dlac-ndk*. **b**, Comparative RNA-seq time course of tail marker genes in regeneration-impaired *D. lacteum* (top) and head-regenerating *S. mediterranea* tail wounds (bottom). Transcript abundances in reads per kilobase per million mapped reads (RPKM) are graphed without  $t_0$  normalization.

head regeneration, but interfered with tail formation at posterior-facing wounds (Supplementary Fig. 9). However, increasing pathway activity via targeting of the destruction complex member *Dlac-APC* induced tail regeneration (Supplementary Fig. 10), indicating that Wnt signalling levels were not constitutively posteriorizing at the amputation level and that at least the three tested Wnt ligands were not the cause of the head fate initiation failure. To test a possible contribution of insufficient Wnt-pathway inhibition to *D. lacteum*'s head regeneration defect, we specifically downregulated *Dlac-β-catenin1* (Supplementary Fig. 11). dsRNA injections induced ectopic heads on trunk pieces (Supplementary Fig. 12), but, remarkably, also rescued head regeneration in 16 out of 24 tail pieces (Fig. 4a). All heads scored as rescued were morphologically and behaviourally indistinguishable from heads regenerated at trunk amputations. Where examined, specimens showed normal head marker *Dlac-ndk* expression and morphologically normal bi-lobed brains (Fig. 4b). In contrast to headless controls, *Dlac-β-catenin1(RNAi)* tail pieces were able to feed (Fig. 4c), demonstrating the functionality of the heads. Rescued tail fragments at 3 months post amputation further showed the same anterior-posterior gradation of regenerative abilities as in control animals, demonstrating the rescue of global body plan patterning (Fig. 4d).

Our results therefore demonstrate that *D. lacteum* is not defective in regeneration *per se*, but in the choice of blastema identity. The outcome of *D. lacteum* tail-piece regeneration, that is, newly formed tissue devoid of anterior or posterior identity, looping of ventral nerve cords (Fig. 1) and expression of boundary marker (Supplementary Fig. 5) are strongly reminiscent of the “headless” phenotype previously described in *S. mediterranea*<sup>24–28</sup>. Jointly, these defects indicate a hierarchical structure of blastema fate specification, whereby the initiation of axial pole regeneration (head or tail)<sup>28</sup> requires further signals beyond those required for mere ‘repair’ of lateral wounds. Our data and previous results emphasize the central importance of β-catenin at this step, signifying head formation when inhibited and tail specification when activated. By failing to trigger the β-catenin switch, *D. lacteum* tail pieces fail to initiate pole regeneration and only carry out local damage repair. Interestingly, we found occasional *D. lacteum* escapees from such molecular deadlock that regenerated bona fide tails (Supplementary Fig. 13). Although consistent with a lack of Wnt inhibition in *D. lacteum* tail pieces (Fig. 3b), the low proportion of escapees emphasizes that this alone is not sufficient for robust tail fate establishment.

What prevents the binary choice capability of the β-catenin system from activating in *D. lacteum* tail pieces (or during normal damage repair) remains an open question. One possible explanation is the failed upregulation of the Wnt inhibitor *notum* in *D. lacteum* tails (Fig. 3a, Supplementary Fig. 14), which is critical in *S. mediterranea* head specification<sup>23</sup>. A further interesting observation is the greatly reduced induction of *wnt1* during the *D. lacteum* early wounding response (Supplementary Fig. 14). In *S. mediterranea*, *wnt1* expression increases rapidly and strongly at any wound<sup>18,29</sup> and contributes, at anterior

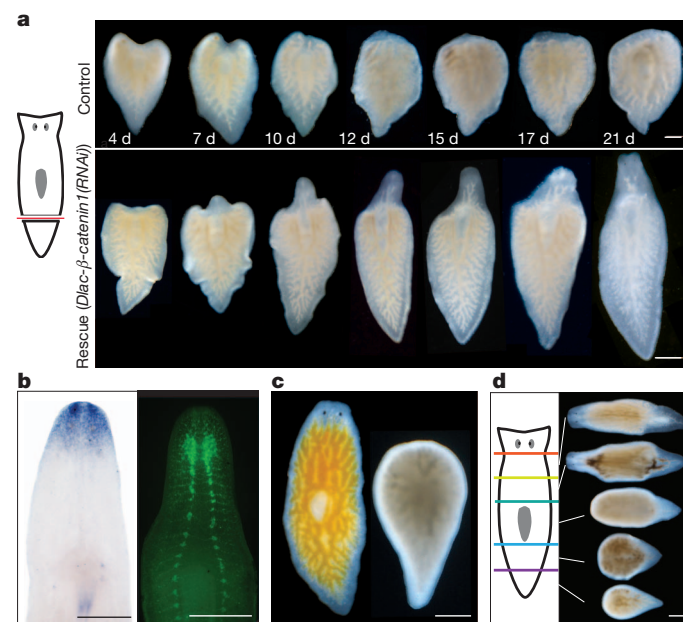


**Figure 4 | Rescue of the *D. lacteum* regeneration defect by β-catenin (RNAi).** **a**, Live images of a representative control (top) or *β-catenin1(RNAi)* tail piece (bottom) at indicated d.p.a. Rescue was observed in 16 out of 24 cases from two independent experiments. **b**, Rescued head marker expression (*Dlac-ndk*, left) and brain/central nervous system (anti-synapsin staining, right) in *β-catenin1(RNAi)* tail pieces ( $n = 3/3$ ). **c**, *β-catenin1(RNAi)* tail pieces (left), but not controls (right), ingest phenol-red-labelled food ( $n = 2/2$ ). **d**, Restoration of graded regeneration competence in rescued tail piece ( $n = 2/2$ ). Fragments in **b–d** were at 3 months post amputation. Scale bars, 500 μm.

facing wounds only, to *notum* upregulation as part of a negative feedback loop<sup>23</sup>. The functional significance of the polarity-independent Wnt1 response remains unclear, but our observations raise the interesting possibility that a Wnt signalling burst early in regeneration might prime the  $\beta$ -catenin system for subsequent fate choices, thus contributing to the robustness of regeneration in species that have it.

Overall, the fact that the global inhibition of a signalling pathway can reverse a species-specific regeneration defect remains astonishing. This result shows that rebuilding complex body parts may not always necessitate understanding and manipulation of myriad individual signals, but possibly a small number of network nodes only. Reactivating regeneration in species that, unlike *D. lacteum*, have entirely lost the ability, certainly constitutes a significantly greater challenge. However, our results provide a proof of principle towards the utility of comparative approaches in understanding and potentially rescuing species-specific regeneration defects.

## METHODS SUMMARY

**Transcriptome assembly, RNA-seq and cloning.** The Dresden *D. lacteum* (ddDlac) transcriptome was *de novo* assembled using Trinity<sup>15</sup> and comprises a total of 49,394 transcripts, with the half-point of the contig length distribution (N50) at 1,570 base pairs. For RNA-seq time courses, single replicates of poly-A selected RNA from dissected wound areas of 8 fragments/time point were sequenced to a depth of 20–30 million reads per time point and mapped to the ddDlac assembly<sup>15</sup>. For wound response analysis, *D. lacteum* orthologues of known *S. mediterranea* wound-response genes<sup>21</sup> were identified using reciprocal BLAST against the ddDlac assembly. All orthologues displaying >twofold upregulation for at least one time point and  $>0$  aligned reads at the zero time point were analysed. For marker analysis, *D. lacteum* transcripts were PCR-amplified from *D. lacteum* cDNA and cloned into pPR-T4P<sup>24</sup>. For primers, see Supplementary Table 2.

**In situ hybridization, immunohistochemistry and histology.** For details on *in situ* hybridizations, see ref. 15. Immunocytochemistry was done on post *in situ* hybridization animals, using rabbit anti-H3P (1:250, Millipore), mouse  $\alpha$ -synapsin (3C11, 1:10, Hybridoma Bank) and Alexa Fluor secondary antibodies. Histology specimens were killed and fixed with Bouin's solution, transferred to 70% ethanol and cleared in clove oil before paraffin embedding. 5  $\mu$ m sections were attached to gelatine-coated slides, stained in haematoxylin/eosin and mounted in DPX. All wide field images were taken on an IFMZ100 microscope (Nikon) equipped with a colour camera; confocal images on a Zeiss LSM700.

**Animal husbandry, RNAi and amputations.** *D. lacteum* were maintained at 20 °C in a defined salt solution and expanded using prepharyngeal bisection<sup>15</sup>, using specimens of < 12 mm length for experiments. Double-stranded RNA for injections were synthesized using templates of 750 bp PCR products with added T7 promoter sequences<sup>15</sup>. For primers, see Supplementary Table 2. dsRNA was injected into cold-immobilized *D. lacteum* three times every second day at 4  $\mu$ g  $\mu$ l<sup>-1</sup> final concentration before amputation 3 days post last injection.

**Full Methods** and any associated references are available in the online version of the paper.

Received 26 September 2012; accepted 25 June 2013.

Published online 24 July 2013.

1. Sánchez Alvarado, A. & Tsonis, P. A. Bridging the regeneration gap: genetic insights from diverse animal models. *Nature Rev. Genet.* **7**, 873–884 (2006).
2. Tanaka, E. M. Regeneration: if they can do it, why can't we? *Cell* **113**, 559–562 (2003).
3. Bely, A. E. & Nyberg, K. G. Evolution of animal regeneration: re-emergence of a field. *Trends Ecol. Evol.* **25**, 161–170 (2010).
4. Brøndsted, H. V. *Planarian regeneration* (Pergamon Press, 1969).
5. Morgan, T. H. Notes on regeneration. *Biol. Bull.* **6**, 159–172 (1904).
6. Gurley, K. A., Rink, J. C. & Sánchez Alvarado, A.  $\beta$ -catenin defines head versus tail identity during planarian regeneration and homeostasis. *Science* **319**, 323–327 (2008).

7. Petersen, C. P. & Reddien, P. W. *Smed- $\beta$ -catenin-1* is required for anteroposterior blastema polarity in planarian regeneration. *Science* **319**, 327–330 (2008).
8. Iglesias, M., Gómez-Skarmeta, J. L., Saló, E. & Adell, T. Silencing of *Smed- $\beta$ -catenin-1* generates radial-like hypercephalized planarians. *Development* **135**, 1215–1221 (2008).
9. Agata, K. & Watanabe, K. Molecular and cellular aspects of planarian regeneration. *Semin. Cell Dev. Biol.* **10**, 377–383 (1999).
10. Newmark, P. A. & Sánchez Alvarado, A. Not your father's planarian: a classic model enters the era of functional genomics. *Nature Rev. Genet.* **3**, 210–219 (2002).
11. Schockaert, E. R. *et al.* Global diversity of free living flatworms (Platyhelminthes, 'Turbellaria') in freshwater. *Hydrobiologia* **595**, 41–48 (2008).
12. Stéphan-Dubois, F. & Gilgenkrantz, F. Transplantation et régénération chez la planaire *Dendrocoelum lacteum*. *J. Embryol. Exp. Morphol.* **9**, 642–649 (1961).
13. Stéphan-Dubois, F. & Bautz, A. Étude histologique et cytologique des néoblastes et des cellules fixes du parenchyme chez des planaires *Dendrocoelum lacteum* privées de région antérieure. *Arch. Anat. Microsc. Morphol. Exp.* **64**, 75–89 (1975).
14. Sauzé-Monnot, M.-J. Étude ultrastructurale des néoblastes de *Dendrocoelum lacteum* au cours de la régénération. *J. Ultrastruct. Res.* **45**, 206–222 (1973).
15. See Methods section included in the HTML or PDF-versions of the manuscript for further detail.
16. Parra, G., Bradnam, K. & Korf, I. CEGMA: a pipeline to accurately annotate core genes in eukaryotic genomes. *Bioinformatics* **23**, 1061–1067 (2007).
17. Cebrià, F. *et al.* FGFR-related gene *nou-darake* restricts brain tissues to the head region of planarians. *Nature* **419**, 620–624 (2002).
18. Gurley, K. A. *et al.* Expression of secreted Wnt pathway components reveals unexpected complexity of the planarian amputation response. *Dev. Biol.* **347**, 24–39 (2010).
19. Rink, J. C. Stem cell systems and regeneration in planaria. *Dev. Genes Evol.* **223**, 67–84 (2013).
20. Tanaka, E. M. & Reddien, P. W. The cellular basis for animal regeneration. *Dev. Cell* **21**, 172–185 (2011).
21. Wenemoser, D., Lapan, S. W., Wilkinson, A. W., Bell, G. W. & Reddien, P. W. A molecular wound response program associated with regeneration initiation in planarians. *Genes Dev.* **26**, 988–1002 (2012).
22. Reddien, P. W., Bermange, A. L., Kicza, A. M. & Sánchez Alvarado, A. BMP signaling regulates the dorsal planarian midline and is needed for asymmetric regeneration. *Development* **134**, 4043–4051 (2007).
23. Petersen, C. P. & Reddien, P. W. Polarized *notum* activation at wounds inhibits Wnt function to promote planarian head regeneration. *Science* **332**, 852–855 (2011).
24. Rink, J. C., Gurley, K. A., Elliott, S. A. & Sánchez Alvarado, A. Planarian Hh signaling regulates regeneration polarity and links Hh pathway evolution to cilia. *Science* **326**, 1406–1410 (2009).
25. Beane, W. S., Morokuma, J., Adams, D. S. & Levin, M. A chemical genetics approach reveals H<sub>K</sub>-ATPase-mediated membrane voltage is required for planarian head regeneration. *Chem. Biol.* **18**, 77–89 (2011).
26. Felix, D. A. & Aboobaker, A. A. The TALE class homeobox gene *Smed-prep* defines the anterior compartment for head regeneration. *PLoS Genet.* **6**, e1000915 (2010).
27. Blassberg, R. A., Felix, D. A., Tejada Romero, B. & Aboobaker, A. A. PBX/extradenticle is required to re-establish axial structures and polarity during planarian regeneration. *Development* **140**, 730–739 (2013).
28. Chen, C.-C. G., Wang, I. E. & Reddien, P. W. *pbx* is required for pole and eye regeneration in planarians. *Development* **140**, 719–729 (2013).
29. Petersen, C. P. & Reddien, P. W. A wound-induced Wnt expression program controls planarian regeneration polarity. *Proc. Natl. Acad. Sci. USA* **106**, 17061–17066 (2009).

**Supplementary Information** is available in the online version of the paper.

**Acknowledgements** We thank H. Andreas for expert animal care and colleagues at the MPI-CBG for comments.

**Author Contributions** S.-Y.L., C.S., B.F., R.L. and M.V.-F. carried out experiments; A.D. contributed RNA sequencing; S.-Y.L., H.B., N.L. and I.H. carried out bioinformatics analyses; J.C.R. designed the experiments and wrote the manuscript.

**Author Information** The ddDlac transcriptome assembly is available at <http://publications.mpi-cbg.de/5330-site>. Time-course RNA-seq reads and named gene sequences have been deposited at GenBank/DBJ/EMBL under the accession numbers GAKU00000000 (*D. lacteum*) and GAKV00000000 (*S. mediterranea*). Reprints and permissions information is available at [www.nature.com/reprints](http://www.nature.com/reprints). The authors declare no competing financial interests. Readers are welcome to comment on the online version of the paper. Correspondence and requests for materials should be addressed to J.C.R. (rink@mpi-cbg.de).

## METHODS

**RNA-seq.** Total RNA was isolated using the TRIzol (Invitrogen) protocol described in the online supplement of ref. 30, quality controlled on a Bioanalyzer (Agilent), poly-A selected using Sera-Mag Oligo(dT) beads (Thermo Scientific) and processed for Illumina Sequencing (HiSeq 2000). Pooled intact and day 1–6 regenerating *D. lacteum* served as RNA source for ~400 million 100-bp paired-end reads; dissected wound areas at different regeneration stages (below) for the ~550 million 76-bp single-end reads.

**Transcriptome assembly.** The R2 mate pairs of paired-end reads were trimmed to 65 bp from 3' to 5' with the FASTX Trimmer (Toolkit version 0.0.13) due to poor sequence quality. All paired-end reads were further filtered with Cutadapt (version 0.9.5) and low-complexity reads were removed with a customized script. The remaining 354 million high-quality paired-end reads and 521 million 76-bp single-end reads from time-course experiments (below) were processed with Trinity<sup>31</sup>, version trinityrnaseq\_r2012-06-08, and assembled using default settings.

The 189,820 transcripts of the primary assembly were corrected for strand orientation using the directional bias in the single-end fraction of input reads. Directional reads were aligned against the assembly using Bowtie2<sup>32</sup> (version 2.1.0), and all transcripts with >70% of aligning reads in the forward direction (5' to 3') were reverse-complemented. Second, to correct for a class of assembly artefacts resulting in frame shifts, we re-mapped the input reads against the assembly, called putative insertions/deletions (InDels) using SAMtools mpileup<sup>33</sup>, filtered for InDel positions with an alternate allele frequency of greater than 75% and a minimum coverage of 8, and adjusted the resulting transcript sequences according to the replacement pattern suggested by SAMtools.

The primary transcriptome was annotated using the following tools: (1) Getorf from the EMBOSS tools suite<sup>34</sup> (v6.4) was used to detect open reading frames (ORF) longer than 100 nucleotides, allowing ORFs spanning one or both transcript bounds to not exclude fragmented transcripts. (2) Domains were predicted using InterProScan<sup>35</sup> 5 RC4 for all ORFs containing at least 40 amino acids. (3) Transcripts were searched against the RefSeq protein database, using BLASTX<sup>36</sup> (v2.2.27) with an *e*-value cutoff of 0.0001 and allowing for maximum 100 hits per transcript. Only high-scoring segment pairs (HSPs) with a query and subject coverage of at least 40% and a per cent similarity score of 40 or greater were retained for annotation purposes.

To generate an assembly subset enriched in cDNAs, we filtered the primary assembly on basis of conforming to any one of the following criteria: (1) ORF length longer than 225 nucleotides (75 amino acids); (2) presence of at least one predicted domain or (3) BLASTX homology to a RefSeq entry. In case of multiple transcripts variants, only the longest graph component was retained. The resulting Dresden *D. lacteum* (ddDlac) assembly comprises a total of 49,394 transcripts, with the half-point of the contig length distribution (N50) at 1,570 base pairs (see Supplementary Fig. 1).

**RNA-seq time course experiments.** 8 fragments per time point (0, 4, 12, 16, 24, 48, 72 and 120 h post amputation) were killed in 1% HCl for 1 min, washed with PBS 2×, transferred into RNAlater (Life Technologies) before dissection of the immediate wound area on a cold plate. Dissected tissue was transferred into TRIzol (Invitrogen) and RNA extraction/sequencing was carried out as above. Each time point was sequenced at a depth of 20–30 million single-end 76 bp reads, post-processed and aligned to the ddDlac assembly with bowtie<sup>32</sup> (version 0.12.7) using -m1 -v2 options. The number of aligned reads/transcript were converted to RPKM (reads per kilobase per million mapped reads), and, for fold-change normalization, divided by the RPKM value at the zero time point. Data analysis and graphing were done in R (version 2.15.3).

**Wound response analysis.** To compare the *D. lacteum* wound response to the published *S. mediterranea* data set<sup>21</sup>, the *S. mediterranea* wound response gene sequences were used to identify their *D. lacteum* orthologues using reciprocal BLAST against the ddDlac assembly. All orthologues showing >twofold

upregulation for at least one time point and > 0 mapped reads at the zero time point were included in the analysis.

**Gene identification and cloning.** *D. lacteum* orthologues of planarian marker genes were identified by reciprocal BLAST for *S. mediterranea*, *Schmidtea polychroa* or *Dugesia japonica* transcripts. cDNA fragments were PCR-amplified from *D. lacteum* cDNA and cloned into pPR-T4P<sup>24</sup>. For primers, see Supplementary Table 2.

**In situ hybridization, immunohistochemistry and histology.** *In situ* hybridizations were carried out essentially as described<sup>37</sup>, except that animals were killed in 500 mM MgCl<sub>2</sub> for 90 s before N-acetyl cysteine treatment and the reduction time was extended to 20 min. Immunocytochemistry was carried out on post *in situ* hybridization animals, using monoclonal rabbit anti-H3P (1:250, Millipore), monoclonal mouse anti-synapsin (3C11, 1:10, Hybridoma Bank) and Alexa Fluor-conjugated secondary antibodies raised in goat. For histology, the specimens were killed and fixed with Bouin's solution and stored in 70% ethanol. Fixed specimens were cleared in clove oil before paraffin wax embedding, sectioning (5 µm) and mounting on gelatine-coated slides. Sections were stained in haematoxylin/eosin and mounted in DPX. All wide-field images were taken on a IFM100 microscope (Nikon), equipped with a Ds-Fi1 colour camera (Nikon). Z-stacks were acquired on a Zeiss LSM700 confocal and maximum-projected using Fiji<sup>38</sup>.

**Animal husbandry, RNAi and amputations.** *D. lacteum* were maintained at 20 °C as described<sup>39</sup> and expanded using prepharyngeal bisection. Double-stranded RNA against *Dlac-β-catenin1*, *Dlac-APC*, *Dlac-wnt11-1*, -2, -5 and a planarian codon usage optimized *mCherry* sequence (negative control) were synthesized using 750 bp PCR products with added T7 promoter sequences as template (see Supplementary Table 2 for primer sequences). dsRNA synthesis was carried out as described<sup>40</sup>, but omitting the RNase III digestion. dsRNA was resuspended in RNase free water at a concentration of 4 µg µl<sup>-1</sup> and injected into cold-immobilized *D. lacteum* three times every second day. Injected animals were amputated 72 h after the last injection.

**qPCR.** RNA was extracted as described above and cDNA synthesis was done with the SuperScript III First-Strand Synthesis System (Invitrogen). qPCR was performed with Absolute QPCR SYBR Green Mix Plus ROX system (Thermo Scientific) according to the manufacturer's recommendations. See Supplementary Table 2 for primer information.

30. Eisenhoffer, G. T., Kang, H. & Sánchez Alvarado, A. Molecular analysis of stem cells and their descendants during cell turnover and regeneration in the planarian *Schmidtea mediterranea*. *Cell Stem Cell* **3**, 327–339 (2008).
31. Grabherr, M. G. et al. Full-length transcriptome assembly from RNA-Seq data without a reference genome. *Nature Biotechnol.* **29**, 644–652 (2011).
32. Langmead, B. & Salzberg, S. L. Fast gapped-read alignment with Bowtie 2. *Nature Methods* **9**, 357–359 (2012).
33. Li, H. et al. The sequence alignment/map format and SAMtools. *Bioinformatics* **25**, 2078–2079 (2009).
34. Rice, P., Longden, I. & Bleasby, A. EMBOSS: The European Molecular Biology Open Software Suite. *Trends Genet.* **16**, 276–277 (2000).
35. Quevillon, E. et al. InterProScan: protein domains identifier. *Nucleic Acids Res.* **33**, W116–W120 (2005).
36. Altschul, S. F., Gish, W., Miller, W., Myers, E. W. & Lipman, D. J. Basic local alignment search tool. *J. Mol. Biol.* **215**, 403–410 (1990).
37. Pearson, B. J. et al. Formaldehyde-based whole-mount *in situ* hybridization method for planarians. *Dev. Dyn.* **238**, 443–450 (2009).
38. Schindelin, J. et al. Fiji: an open-source platform for biological image analysis. *Nature Methods* **9**, 676–682 (2012).
39. Cebrià, F. & Newmark, P. A. Planarian homologs of *netrin* and *netrin receptor* are required for proper regeneration of the central nervous system and the maintenance of nervous system architecture. *Development* **132**, 3691–3703 (2005).
40. Buchholz, F., Kittler, R., Slabicki, M. & Theis, M. Enzymatically prepared RNAi libraries. *Nature Methods* **3**, 696–700 (2006).

# Dual-mode operation of neuronal networks involved in left-right alternation

Adolfo E. Talpalar<sup>1\*</sup>, Julien Bouvier<sup>1\*</sup>, Lotta Borgius<sup>1</sup>, Gilles Fortin<sup>2</sup>, Alessandra Pierani<sup>3</sup> & Ole Kiehn<sup>1</sup>

All forms of locomotion are repetitive motor activities that require coordinated bilateral activation of muscles. The executive elements of locomotor control are networks of spinal neurons that determine gait pattern through the sequential activation of motor-neuron pools on either side of the body axis<sup>1–4</sup>. However, little is known about the constraints that link left-right coordination to locomotor speed. Recent advances have indicated that both excitatory and inhibitory commissural neurons may be involved in left-right coordination<sup>5–7</sup>. But the neural underpinnings of this, and a possible causal link between these different groups of commissural neurons and left-right alternation, are lacking. Here we show, using intersectional mouse genetics, that ablation of a group of transcriptionally defined commissural neurons—the V0 population—leads to a quadrupedal hopping at all frequencies of locomotion. The selective ablation of inhibitory V0 neurons leads to a lack of left-right pattern at low frequencies, mixed coordination at medium frequencies, and alternation at high locomotor frequencies. When ablation is targeted to excitatory V0 neurons, left-right alternation is present at low frequencies, and hopping is restricted to medium and high locomotor frequencies. Therefore, the intrinsic logic of the central control of locomotion incorporates a modular organization, with two subgroups of V0 neurons required for the existence of left-right alternating modes at different speeds of locomotion. The two molecularly distinct sets of commissural neurons may constrain species-related naturally occurring frequency-dependent coordination and be involved in the evolution of different gaits.

V0 neurons, characterized by the early expression of the transcription factor *Dbx1* (refs 8, 9), represent a major class of commissural neurons in the ventral spinal cord, where the locomotor network is localized<sup>2</sup>. Previous experiments have shown that knockout of the *Dbx1* gene leads to an intermittent disruption of, but a preserved possibility for, left-right alternation during drug-induced locomotion *in vitro*<sup>10</sup>. These experiments also indicated an exclusive role for inhibitory commissural neurons in securing left-right alternation. Here, we tested *in vivo* and *in vitro* the possibility that transmitter-defined subsets of commissural neurons may condition left-right alternation at distinct locomotor frequencies using the *Dbx1*<sup>loxP-stop-loxP-DTA</sup> (*Dbx1*<sup>DTA</sup>; DTA, diphtheria toxin A)<sup>11</sup> mouse strain that allows conditional ablation of V0 cells. Crossing the *Dbx1*<sup>DTA</sup> line with generic Cre mouse lines led to lethal genotypes owing to breathing impairments<sup>12</sup>. However, when *Dbx1*<sup>DTA</sup> mice were mated with the *E1Ngn2::Cre* line<sup>13</sup>, where Cre is expressed in the spinal cord but has limited impact on the respiratory centres, *E1Ngn2::Cre;Dbx1*<sup>DTA</sup> pups survived<sup>14</sup>. Juvenile mutant animals (3–4 weeks) showed a pronounced quadrupedal hopping, with sequential synchronized lifting (phase values around 0 or 1) of the forelimbs followed by synchronized lifting of the hindlimbs (Fig. 1a, bottom, and Supplementary Video 1). This behaviour was never seen in age-matched wild-type mice at comparable frequencies of locomotion, in which alternating gait patterns (phase values around 0.5) dominated (Fig. 1a, top, and Supplementary Video 2).

The V0 population is composed of dorsal (V0<sub>D</sub>) and ventral (V0<sub>V</sub>) neuronal sub-classes that arise respectively from the dorsal (*Pax7*<sup>+</sup>) and ventral (*Pax7*<sup>-</sup>) subdomains of *Dbx1*-expressing (p0) progenitors<sup>8,9</sup>. We found that the E1 enhancer of *Ngn2* drives Cre expression in the majority of *Dbx1*<sup>+</sup> progenitors of both subdomains (Fig. 1b, c). Accordingly, *E1Ngn2::Cre;Dbx1*<sup>DTA</sup> embryos show a marked reduction in *Dbx1*<sup>+</sup> progenitors and *Evx1*-expressing neurons, which are a known V0<sub>V</sub> contingent (Fig. 1d, e), whereas adjacent progenitors (pd6, p1 and p2a) were spared (Supplementary Fig. 1). Together, these findings indicate that the quadrupedal hopping is due to a specific elimination of both V0<sub>D</sub> and V0<sub>V</sub> neurons.

To rule out the possibility that the *E1Ngn2::Cre;Dbx1*<sup>DTA</sup> phenotype may result in part from the loss of V0 neurons in supraspinal structures, we used isolated spinal cords from newborn mice (Fig. 1f), in which locomotor-like activity can be induced by the exogenous application of neuro-active substances such as NMDA (*N*-methyl-D-aspartate) and serotonin, or 5-hydroxytryptamine (5-HT). In such conditions, wild-type preparations show a typical pattern of hindlimb locomotor-like activity characterized by left (L)-right (R) alternation between corresponding flexor-related lumbar (L2) roots (LL2–RL2) and extensor-related lumbar 5 roots (LL5–RL5), and flexor–extensor alternation (LL2–LL5; RL2–RL5) (Fig. 1g, top; seen as phase values around 0.5 in circular plots in Fig. 1g, bottom). By contrast, preparations from *E1Ngn2::Cre;Dbx1*<sup>DTA</sup> animals (Fig. 1h, top) show rhythmic activity characterized by intrasegmental synchrony (phase values around 0 or 1) (LL2–RL2; LL5–RL5). Flexor–extensor alternation (LL2–LL5; RL2–RL5) was maintained with a larger spread of coordination around strict out-of-phase alternating activity as compared with wild-type mice ( $P < 0.001$ ; Fig. 1h, bottom). Further confirmation of the spinal origin of the *E1Ngn2::Cre;Dbx1*<sup>DTA</sup> phenotype came from examining *Hoxb8::Cre;Dbx1*<sup>DTA</sup> animals, in which Cre recombination is restricted to spinal segments caudal to cervical segment 4 (Supplementary Fig. 2a–c)<sup>15</sup>. These conditional mutants showed, as did the *E1Ngn2::Cre;Dbx1*<sup>DTA</sup> mice, a clear hopping phenotype both *in vivo* and *in vitro* (Supplementary Fig. 2d, e and Supplementary Video 3). The hopping phenotype was complete at the hindlimb level whereas episodes of alternation were still present in the forelimbs, reflecting the rostro-caudal gradient of *Hoxb8* expression. Together, these data show that major (*E1Ngn2::Cre;Dbx1*<sup>DTA</sup>) or complete (*Hoxb8::Cre;Dbx1*<sup>DTA</sup>) depletion of V0 neurons leads to a hopping locomotor phenotype that is due to changes in left-right alternating circuitries contained within the spinal cord. Although V0 neurons are not necessary for flexor–extensor alternation, their elimination may affect coordination because of long-range commissural projections in the lumbar spinal cord<sup>7</sup>.

When spontaneously moving with locomotor frequencies ranging from 2–10 Hz, juvenile wild-type mice either walk (lower end of frequencies) or trot (higher end of frequencies)<sup>16</sup> (Fig. 2a). At higher locomotor frequencies (>10 Hz) wild-type mice might gallop<sup>16</sup>. In the same range of locomotor frequencies at which wild-type mice show alternating gaits (walking/trotting), V0-ablated mice consistently

<sup>1</sup>The Mammalian Locomotor Laboratory, Department of Neuroscience, Karolinska Institutet, Stockholm S-17177, Sweden. <sup>2</sup>Neurobiology and Development, Centre National de la Recherche Scientifique, 91198 Gif-sur-Yvette, France. <sup>3</sup>Institut Jacques Monod, CNRS UMR 7592, Université Paris Diderot, Sorbonne Paris Cité, 75205 Paris Cedex, France.

\*These authors contributed equally to this work.

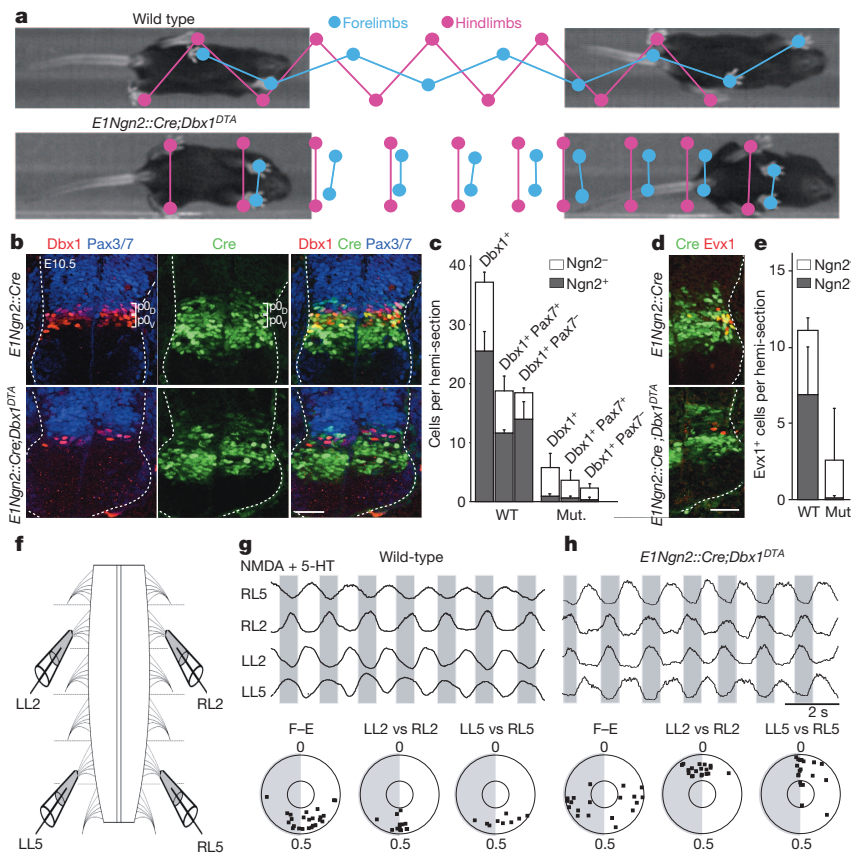


**Figure 1 | Ablation of V0 neurons leads to a hopping gait.** **a**, Locomotor pattern in freely moving wild-type and *E1Ngn2::Cre;Dbx1<sup>DTA</sup>* mutant mice. **b**, Partitioning of *Dbx1*<sup>+</sup> progenitors at E10.5 into dorsal (p0<sub>D</sub>: Pax7<sup>+</sup>) and ventral (p0<sub>V</sub>: Pax7<sup>-</sup>) subdomains, and co-expression of *E1Ngn2::Cre*, in both genotypes. Scale bar: 50  $\mu$ m. **c**, Corresponding quantifications (*E1Ngn2::Cre* (wild type; WT),  $N = 3$ ; *E1Ngn2::Cre;Dbx1<sup>DTA</sup>* (mutant; Mut.)  $N = 3$ , mean  $\pm$  standard deviation (s.d.)). **d**, *Evx1*<sup>+</sup> V0<sub>V</sub> interneurons and *E1Ngn2::Cre* expression in both genotypes at E10.5. Scale bar: 50  $\mu$ m. **e**, Corresponding quantifications (*E1Ngn2::Cre* (WT)  $N = 3$ ; *E1Ngn2::Cre;Dbx1<sup>DTA</sup>* (Mut.)  $N = 4$ , mean  $\pm$  s.d.). **f**, Ventral root recording configuration for *in vitro* experiments. **g**, **h**, Top, rectified recordings of locomotor-like pattern in left (L) and right (R) lumbar (L2) and 5 ventral roots of wild-type and *E1Ngn2::Cre;Dbx1<sup>DTA</sup>* mice. Bottom, corresponding circular plots showing the phase relationships LL2–RL2 (wild-type,  $N = 14$ ; *E1Ngn2::Cre;Dbx1<sup>DTA</sup>*,  $N = 19$ ), LL5–RL5 ( $N = 9$ ;  $N = 19$ ) and flexor (F)–extensor (E) ( $N = 24$ ;  $N = 20$ ).

showed a quadrupedal (*E1Ngn2::Cre;Dbx1<sup>DTA</sup>*, Fig. 2b) or hindlimb (*Hoxb8::Cre;Dbx1<sup>DTA</sup>*, Supplementary Fig. 2d) hopping gait. Similarly, isolated spinal cord preparations from *E1Ngn2::Cre;Dbx1<sup>DTA</sup>* (Fig. 2c, d) and *Hoxb8::Cre;Dbx1<sup>DTA</sup>* (Supplementary Fig. 2e) mice also produced hindlimb activity with left-right synchrony at all obtainable locomotor frequencies. These experiments show that ablation of V0 neurons leads to loss of left-right limb alternation along the entire locomotion frequency domain at which alternation is normally present.

Unlike in *Dbx1*-knockout mice<sup>10</sup>, left-right alternation could not be restored in *E1Ngn2::Cre;Dbx1<sup>DTA</sup>* mice by increasing the inhibitory network drive with uptake blockers of glycine and GABA ( $\gamma$ -aminobutyric acid) (Supplementary Fig. 3), showing that in the absence of V0 neurons normal alternating gait is not secured by other commissural pathways. These observations point to the differences between gene knockout strategies, in which targeted cells may acquire a different fate but may still be part of the network, and DTA-mediated ablation, which permanently removes the targeted cells. Moreover, the blockade of fast glycinergic and GABAergic inhibition in the presence of neuro-active drugs produced a left-right and flexor-extensor synchrony indistinguishable from that seen in wild-type mice (Supplementary Fig. 4), indicating that bilateral synchronization is mediated by a non-V0 commissural population.

The V0 population is composed of V0<sub>V</sub> and V0<sub>D</sub> subpopulations, and of excitatory and inhibitory contingents<sup>10</sup>, raising the question of how these molecularly and transmitter-defined populations are linked, and what their individual contributions are to left-right alternation. In the mouse lumbar ventral spinal cord, Pax7-derived V0<sub>D</sub> neurons constitute two-thirds of the V0 lineage and are predominantly GABAergic or glycinergic inhibitory neurons (Supplementary Fig. 5a–d). *Evx1*<sup>+</sup> V0<sub>V</sub> neurons constitute one-third of the V0 lineage (Supplementary Fig. 5b, c) and largely express *Vglut2*, the only vesicular glutamate transporter found in ventral spinal neurons<sup>17</sup>, and no inhibitory transmitter markers (Supplementary Fig. 5d–f). Therefore, the genetic partitioning

of p0 progenitors in mice leads to the production of excitatory (V0<sub>V</sub>, one-thirds) and inhibitory (V0<sub>D</sub>, two-thirds) subgroups of V0 neurons.

We first tested the role of the inhibitory, Pax7-derived, V0<sub>D</sub> neurons in bilateral coordination by partnering *Pax7::Cre<sup>18</sup>* with *Dbx1<sup>DTA</sup>* mice. This cross efficiently ablated p0<sub>D</sub> progenitors (Fig. 3a), whereas the p0<sub>V</sub>-derived *Evx1*<sup>+</sup> neurons (Fig. 3a, c) and the pd6, p1 and p2 progenitors were normally produced (Fig. 3b). *Pax7::Cre;Dbx1<sup>DTA</sup>* mutants die at birth from impaired breathing<sup>12</sup>, precluding any *in vivo* investigations. Nevertheless, hindlimb locomotor-like activity could be induced in isolated spinal cords from embryonic day (E)18.5 embryos (Fig. 3d). Mutant preparations did not show any coordinated locomotor-like activity below 0.20 Hz (Fig. 3e). At medium frequencies (0.20–0.45 Hz), left-right alternation coexisted with synchronous activity in flexor-related L2 roots, whereas the extensor-related L5 roots showed synchronization. At the highest obtainable frequencies ( $>0.45$  Hz), the flexor-related L2 ventral roots featured clear left-right alternation (Fig. 3e, middle). These trends in frequency–phase relationships were also seen when phase values were converted to a half-circle and weighted regression lines were fitted to the combined data sets (Supplementary Fig. 6a). The differences in L2 and L5 activity may reflect the greater robustness of left-right alternating circuits in the rostral compared with the caudal lumbar spinal cord<sup>19</sup>. These experiments show that the inhibitory V0<sub>D</sub> neurons are needed for left-right alternation at low frequencies but dispensable for alternation at the highest locomotor frequencies. In the absence of the V0<sub>D</sub> population, the remaining commissural neurons do not sustain persistent alternation at medium-range frequencies, leading to the presence of both intrasegmental alternation and synchrony.

We next assessed the role of the excitatory V0<sub>V</sub> commissural neurons by crossing *Dbx1<sup>DTA</sup>* with *Vglut2::BAC-Cre* (*Vglut2::Cre*) mice<sup>17</sup>. Cre expression was found in one-third of *Dbx1*-derived V0 neurons, predominantly in *Evx1*<sup>+</sup> V0<sub>V</sub> neurons (Supplementary Fig. 5c–f). Accordingly, *Vglut2::Cre;Dbx1<sup>DTA</sup>* animals lacked most *Evx1*<sup>+</sup> V0<sub>V</sub>

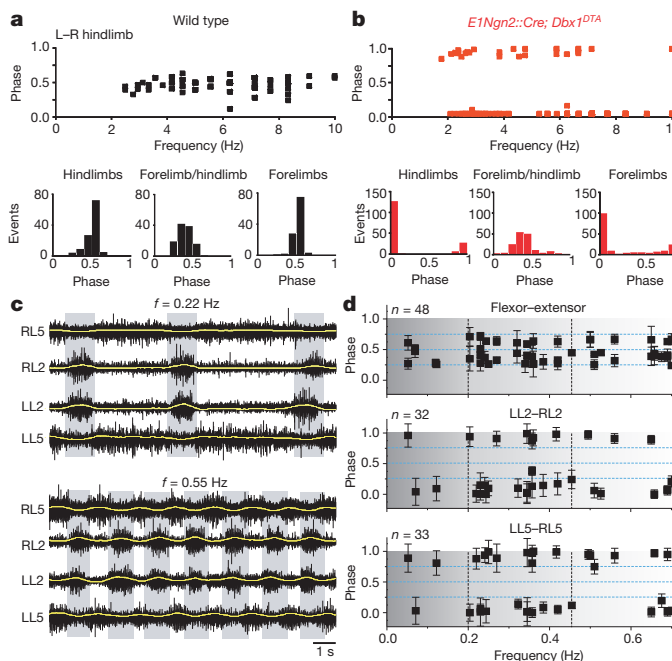


**Figure 2 | V0-deleted mice hop at all locomotor frequencies.** **a, b**, Locomotor gait in wild-type and *E1Ngn2::Cre; Dbx1<sup>DTA</sup>* mice. Top, frequency–phase relationship of wild-type (**a**;  $N = 3$ ) and *E1Ngn2::Cre; Dbx1<sup>DTA</sup>* (**b**;  $N = 4$ ) mice. Bottom, phase histograms between indicated pairs of limbs. **c**, Ventral root recordings during drug-induced locomotor-like activity in postnatal day (P)0–P1 *E1Ngn2::Cre; Dbx1<sup>DTA</sup>* preparations at different frequencies (obtained by changing the concentrations of locomotor-inducing drugs). Raw ventral root recordings shown in black with superimposed rectified and integrated signals in yellow (same in Figs 3d and 4d). **d**, Corresponding frequency–phase plots where each square represents the mean phase of a significantly oriented phase vector ( $N = 11$ ). Error bars show angular dispersion. The different scales of grey indicate low- ( $<0.2$  Hz), intermediate- (0.20–0.45 Hz) and high-frequency ( $>0.45$  Hz) regimes here and in Figs 3e and 4e.

neurons (Supplementary Fig. 7a and Fig. 4a) but there was no change in the number of the adjacent Di6, V2a and V1/V0<sub>D</sub> neurons (Supplementary Fig. 7b, c). We did not exclude a possible effect on the small population of Dbx1-derived Pitx2-expressing neurons<sup>20</sup>. Importantly, the main respiratory populations were spared, allowing *in vivo* analysis. Juvenile mutant animals showed either a left–right alternating or hopping hindlimb gait in a frequency-dependent manner: an alternating

pattern was present at low locomotor frequencies (2–4 Hz) and a hopping gait at high frequencies (4–10 Hz) (Fig. 4b, c and Supplementary Video 4). The forelimbs maintained left–right alternation at all speeds. This frequency-dependent locomotor phenotype was recapitulated *in vitro*, with locomotor-like activity showing a hindlimb ‘hopping’ pattern at the higher and alternation at the lower frequencies (Fig. 4d, e and Supplementary Fig. 6b). At intermediate frequencies, flexor-related L2 and extensor-related L5 ventral roots showed either alternation or synchrony (Fig. 4d, e). Flexor–extensor alternation was close to normal at all frequencies. Blockade of fast inhibition in these animals resulted in bilateral synchronization (Supplementary Fig. 4c). Thus, glutamatergic V0 neurons are necessary for hindlimb alternation at high locomotor frequencies but dispensable at low locomotor frequencies. By contrast, at the forelimb level, V0<sub>V</sub> neurons are dispensable for alternation at all frequencies, suggesting that V0<sub>D</sub> neurons may be the dominant alternating system in the forelimb locomotor network.

Using both *in vivo* and *in vitro* experiments, we have identified V0 commissural neurons as necessary for alternating gaits in mice. Together with previous studies on Dbx1-independent commissural neurons<sup>21,22</sup>, our study points to a role for distinct commissural pathways in ensuring different modes of left–right locomotor coordination. V0 neurons seem to be the major executors necessary for left–right alternating gaits, whereas other non-V0 commissural neurons promote synchrony and presumably secure galloping at high speeds of locomotion in intact mice.

The V0 alternating network relies on distinct molecularly defined populations that enforce alternation at the low and high ends of the alternating locomotor frequency domain. Studies in newborn rodents<sup>5,7</sup> have revealed that contralateral inhibition of motor neurons can be mediated both directly, by inhibitory commissural neurons, and indirectly, via excitatory commissural neurons acting on local inhibitory interneurons. The present study elucidates the genetic underpinning and shows the functional expression of this dual organization of the alternating locomotor network, and opposes the generally held notion that left–right alternation is mediated by inhibitory commissural neurons alone<sup>1,10,23</sup>. The implication is that the configuration of the left–right alternating locomotor network changes with speed. The inhibitory V0<sub>D</sub> neurons are recruited first, during slow locomotion, followed by excitatory V0<sub>V</sub> neurons recruited at higher frequencies. It is conceivable that at intermediate frequencies of locomotion the two systems are active simultaneously. Such speed-dependent changes in recruitment order have been described in zebrafish for classes of excitatory interneurons driving motor neurons during swimming movements<sup>24,25</sup>. The network switch described here is in accord with findings in mice

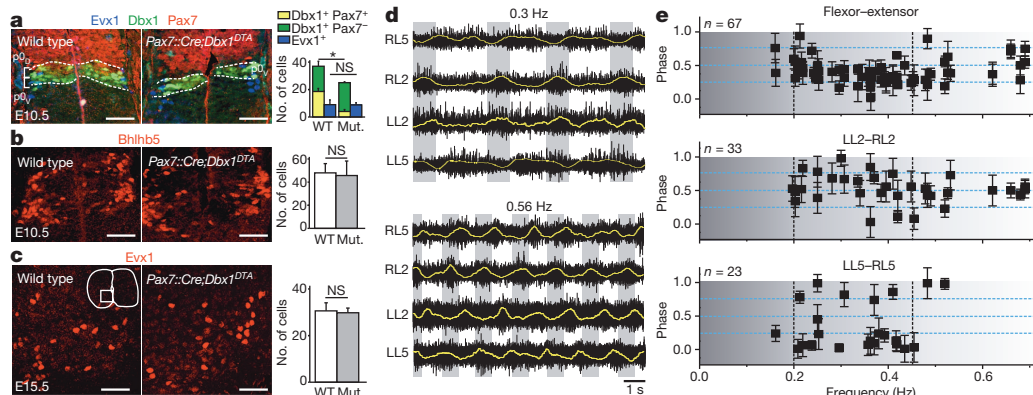


**Figure 3 | V0<sub>D</sub>-deleted mice show a lack of alternation at low frequencies and alternation at high frequencies.** **a**, Pax7-expressing dorsal Dbx1<sup>+</sup> progenitors ( $p0_D$ ) are ablated in *Pax7::Cre; Dbx1<sup>DTA</sup>* mutants (Mut.) as compared with wild type (WT), whereas the ventral  $p0_V$  ( $p0_V$ , Pax7<sup>–</sup>) neural progenitors and the V0<sub>V</sub> neurons expressing Evx1 are spared ( $N = 3$  in each group, mean  $\pm$  s.d.). NS, not significant. **b**, The expression of Bhlhb5, a marker for pd6, p1 and p2a progenitors at E10.5 (ref. 30), is preserved in *Pax7::Cre; Dbx1<sup>DTA</sup>* mutant mice. **c**, V0<sub>V</sub> Evx1<sup>+</sup> neurons are spared in *Pax7::Cre; Dbx1<sup>DTA</sup>* mutant mice at E15.5 (wild type,  $N = 3$ ; *Pax7::Cre; Dbx1<sup>DTA</sup>*,  $N = 3$ ; mean  $\pm$  s.d.). **a–c**, Scale bars: 50  $\mu$ m. **d**, Ventral root recordings during drug-induced locomotor-like activity in E18.5 *Pax7::Cre; Dbx1<sup>DTA</sup>* preparations at different frequencies. **e**, Corresponding frequency–phase plots ( $N = 21$ ). Error bars show angular dispersion.

*Dbx1<sup>DTA</sup>* mutant mice (wild type,  $N = 4$ ; *Pax7::Cre; Dbx1<sup>DTA</sup>*,  $N = 4$ ; mean  $\pm$  s.d.) **c**, V0<sub>V</sub> Evx1<sup>+</sup> neurons are spared in *Pax7::Cre; Dbx1<sup>DTA</sup>* mutant mice at E15.5 (wild type,  $N = 3$ ; *Pax7::Cre; Dbx1<sup>DTA</sup>*,  $N = 3$ ; mean  $\pm$  s.d.). **a–c**, Scale bars: 50  $\mu$ m. **d**, Ventral root recordings during drug-induced locomotor-like activity in E18.5 *Pax7::Cre; Dbx1<sup>DTA</sup>* preparations at different frequencies. **e**, Corresponding frequency–phase plots ( $N = 21$ ). Error bars show angular dispersion.

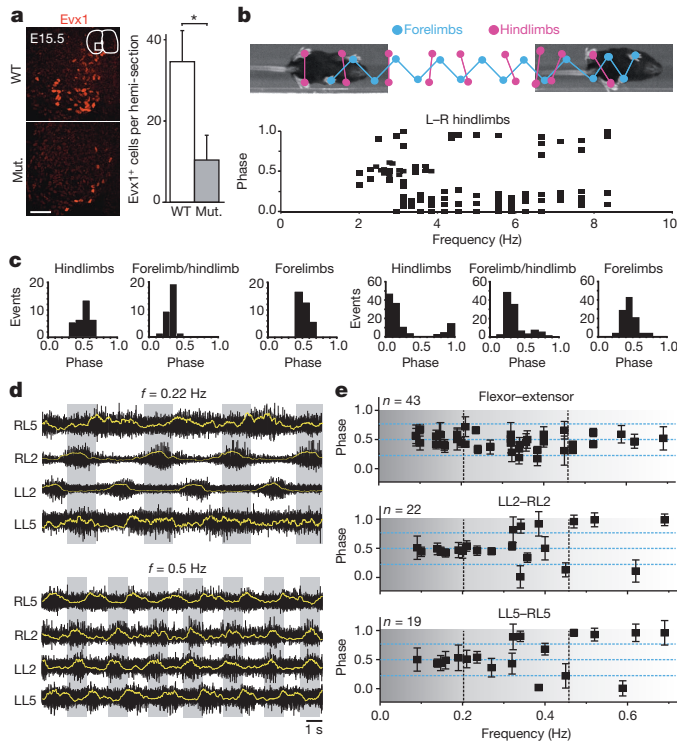


**Figure 4 | Deletion of excitatory  $V0_v$  neurons causes hopping at high locomotor frequencies but preserves alternation at lower frequencies.** **a**,  $V0_v$  ( $Evx1^{+}$ ) neurons in E15.5 wild-type (WT;  $N = 3$ ) and  $Vglut2::Cre; Dbx1^{DTA}$  mutant (Mut.;  $N = 3$ ) lumbar spinal cord (scale bar: 50  $\mu$ m; mean  $\pm$  s.d.). **b**, Locomotor pattern at medium to high frequencies and frequency–phase relationship of hindlimbs (bottom) in  $Vglut2::Cre; Dbx1^{DTA}$  mice. **c**, Phase histograms between the indicated pairs of limbs at low (2–4 Hz; three panels to the left) and high (4–10 Hz; three panels to the right) frequencies. **d**, Ventral root recordings during drug-induced locomotor-like activity in P0–P1  $Vglut2::Cre; Dbx1^{DTA}$  preparations at different frequencies. **e**, Corresponding frequency–phase plots ( $N = 12$ ). Error bars show angular dispersion.

that ipsilaterally projecting V2a excitatory neurons project to  $V0_v$  neurons<sup>26</sup> and that V2a-ablated mice hop<sup>27</sup> at higher frequencies. These findings suggest that ensembles of neurons are selected as modules<sup>28</sup> at different speeds of locomotion.

The  $Dbx1/Evx1$  transcription factors seem to be phylogenetically conserved<sup>29</sup>, and a modular system similar to the one described here may be found in other vertebrates with alternating gait. Moreover, during evolution bipedal and quadrupedal hopping have developed in a number of species and some strains of rodents, suggesting that this change in locomotor behaviour may be carried by a loss, partial or complete, of the  $V0$ -determined alternating system.

## METHODS SUMMARY

All experiments were approved by the local ethical committee. For full details of methods used, including detailed information about mice lines, the *in vivo* and *in vitro* locomotor recordings and analysis, statistical analysis and protocols for immunohistochemical analysis, see Methods.

**Full Methods** and any associated references are available in the online version of the paper.

Received 11 October 2012; accepted 13 May 2013.

Published online 30 June 2013.

1. Grillner, S. The motor infrastructure: from ion channels to neuronal networks. *Nature Rev. Neurosci.* **4**, 573–586 (2003).
2. Kiehn, O. Locomotor circuits in the mammalian spinal cord. *Annu. Rev. Neurosci.* **29**, 279–306 (2006).
3. Goulding, M. Circuits controlling vertebrate locomotion: moving in a new direction. *Nature Rev. Neurosci.* **10**, 507–518 (2009).

4. Grillner, S. & Jessell, T. M. Measured motion: searching for simplicity in spinal locomotor networks. *Curr. Opin. Neurobiol.* **19**, 572–586 (2009).
5. Quinlan, K. A. & Kiehn, O. Segmental, synaptic actions of commissural interneurons in the mouse spinal cord. *J. Neurosci.* **27**, 6521–6530 (2007).
6. Jankowska, E. Spinal interneuronal networks in the cat: elementary components. *Brain Res. Rev.* **57**, 46–55 (2008).
7. Butt, S. J. & Kiehn, O. Functional identification of interneurons responsible for left-right coordination of hindlimbs in mammals. *Neuron* **38**, 953–963 (2003).
8. Moran-Rivard, L. *et al.*  $Evx1$  is a postmitotic determinant of  $V0$  interneuron identity in the spinal cord. *Neuron* **29**, 385–399 (2001).
9. Pierani, A. *et al.* Control of interneuron fate in the developing spinal cord by the progenitor homeodomain protein  $Dbx1$ . *Neuron* **29**, 367–384 (2001).
10. Lanuza, G. M., Gosgnach, S., Pierani, A., Jessell, T. M. & Goulding, M. Genetic identification of spinal interneurons that coordinate left-right locomotor activity necessary for walking movements. *Neuron* **42**, 375–386 (2004).
11. Bielle, F. *et al.* Multiple origins of Cajal-Retzius cells at the borders of the developing pallium. *Nature Neurosci.* **8**, 1002–1012 (2005).
12. Bouvier, J. *et al.* Hindbrain interneurons and axon guidance signaling critical for breathing. *Nature Neurosci.* **13**, 1066–1074 (2010).
13. Berger, J. *et al.*  $E1-Ngn2::Cre$  is a new line for regional activation of cre recombinase in the developing CNS. *Genes* **40**, 195–199 (2004).
14. Teissier, A. *et al.* A novel transient glutamatergic population migrating from the pallial–subpallial boundary contributes to neocortical development. *J. Neurosci.* **30**, 10563–10574 (2010).
15. Witschi, R. *et al.*  $Hoxb8::Cre$  mice: a tool for brain-sparing conditional gene deletion. *Genesis* **48**, 596–602 (2010).
16. Serradj, N. & Jamon, M. The adaptation of limb kinematics to increasing walking speeds in freely moving mice 129/Sv and C57BL/6. *Behav. Brain Res.* **201**, 59–65 (2009).
17. Borgiusti, L., Restrepo, C. E., Leao, R. N., Saleh, N. & Kiehn, O. A transgenic mouse line for molecular genetic analysis of excitatory glutamatergic neurons. *Mol. Cell. Neurosci.* **45**, 245–257 (2010).
18. Keller, C., Hansen, M. S., Coffin, C. M. & Capecchi, M. R.  $Pax3::Fkhr$  interferes with embryonic  $Pax3$  and  $Pax7$  function: implications for alveolar rhabdomyosarcoma cell of origin. *Genes Dev.* **18**, 2608–2613 (2004).
19. Kjaerulff, O. & Kiehn, O. Distribution of networks generating and coordinating locomotor activity in the neonatal rat spinal cord *in vitro*: a lesion study. *J. Neurosci.* **16**, 5777–5794 (1996).
20. Zagoraiau, L. *et al.* A cluster of cholinergic premotor interneurons modulates mouse locomotor activity. *Neuron* **64**, 645–662 (2009).
21. Zhang, Y. *et al.* V3 spinal neurons establish a robust and balanced locomotor rhythm during walking. *Neuron* **60**, 84–96 (2008).
22. Andersson, L. S. *et al.* Mutations in DMRT3 affect locomotion in horses and spinal circuit function in mice. *Nature* **488**, 642–646 (2012).
23. Roberts, A., Li, W. C., Soffe, S. R. & Wolf, E. Origin of excitatory drive to a spinal locomotor network. *Brain Res. Rev.* **57**, 22–28 (2008).
24. McLean, D. L. & Fethjo, J. R. Spinal interneurons differentiate sequentially from those driving the fastest swimming movements in larval zebrafish to those driving the slowest ones. *J. Neurosci.* **29**, 13566–13577 (2009).
25. Ausborn, J., Mahmood, R. & El Manira, A. Decoding the rules of recruitment of excitatory interneurons in the adult zebrafish locomotor network. *Proc. Natl. Acad. Sci. USA* **109**, E3631–E3639 (2012).
26. Crone, S. A. *et al.* Genetic ablation of V2a ipsilateral interneurons disrupts left-right locomotor coordination in mammalian spinal cord. *Neuron* **60**, 70–83 (2008).
27. Crone, S. A., Zhong, G., Harris-Warrick, R. & Sharma, K. In mice lacking V2a interneurons, gait depends on speed of locomotion. *J. Neurosci.* **29**, 7098–7109 (2009).
28. Jordan, L. In *Neurobiological Basis of Human Locomotion* (ed. Shimamura, M.) 3–21 (Japan Scientific Societies, 1991).
29. Suster, M. L. *et al.* A novel conserved  $evx1$  enhancer links spinal interneuron morphology and cis-regulation from fish to mammals. *Dev. Biol.* **325**, 422–433 (2009).
30. Liu, B. *et al.* Selective expression of  $Bhlhb5$  in subsets of early-born interneurons and late-born association neurons in the spinal cord. *Dev. Dyn.* **236**, 829–835 (2007).

**Supplementary Information** is available in the online version of the paper.

**Acknowledgements** This work was supported by the Söderberg Foundation, Swedish Research Council and European Research Council. J.B. is an EMBO fellow. We thank H. U. Zeilhofer for donating the  $Hoxb8::Cre$  mouse strain, S. Karaz, A. C. Westerdahl and P. Löw for extensive genotyping, L. Lundfeld for participating in early experiments, N. Sleiers for participating in the *in vivo* experiments, and P. L. Ruffault for providing mouse tissue. We thank colleagues for discussing different aspects of our study.

**Author Contributions** O.K., A.E.T., L.B. and J.B. contributed to the conception and design of the study. A.E.T. performed electrophysiological experiments, J.B. performed anatomical experiments and both analysed the data. L.B. carried out and analysed the *in vivo* experiments. A.P. engineered the  $Dbx1^{DTA}$  mice and detected the hopping phenotype in the  $E1Ngn2::Cre; Dbx1^{DTA}$  mice. G.F. provided mice and fixed tissue. O.K. supervised all aspects of the work. All authors discussed the results and participated in writing the manuscript.

**Author Information** Reprints and permissions information is available at [www.nature.com/reprints](http://www.nature.com/reprints). The authors declare no competing financial interests. Readers are welcome to comment on the online version of the paper. Correspondence and requests for materials should be addressed to O.K. (ole.kiehn@ki.se).

## METHODS

All experiments were approved by the local ethical committee and performed in accordance with European guidelines for the care and use of laboratory animals. The following transgenic lines have been described previously: *Pax7::Cre*<sup>18</sup>, *E1Ngn2::Cre*<sup>13</sup>, *Vglut2::Cre*<sup>17</sup>, *Dbx1*<sup>lox-STOP-lox-DTA</sup> (*Dbx1*<sup>DTA</sup>)<sup>11</sup>, *Dbx1*<sup>nlslacZ</sup> (ref. 9); *Glyt2-GFP*<sup>31,32</sup>, *GAD67-GFP*<sup>32,33</sup>, *Hoxb8::Cre*<sup>15</sup>. All animals were genotyped after the experiments with gene-specific primers.

**In vivo locomotor analysis.** All *in vivo* data were recorded using a TSE MotoRater system that captures the natural movement of animals on a runway. The animals were allowed to walk or run freely in a glass-walled corridor and recorded by high-speed camera at 100–200 frames per second. For each mouse, runs from at least three independent recordings were analysed using the Clickjoint software. The first and the last step in a run and episodes with frequencies lower than 2 strides per second were not included in the analysis. Phase values were calculated as the time of the swing onset of a limb related to the step cycle length of the reference limb in that particular step cycle. One step cycle corresponds to the time from swing onset until the next swing onset.

**In vitro experiments.** Mice aged E18.5 (*Pax7::Cre*; *Dbx1*<sup>DTA</sup>) or newborn mice aged 1–2 days were used in all experiments. The embryonic state was called E0.5 on the morning of plug detection. For analyses at E18.5, fetuses were surgically removed from pregnant mice, cooled, decapitated and eviscerated before the brainstem and spinal cord were isolated in ice-cold low calcium Ringer's solution (oxygenated 95% O<sub>2</sub>, 5% CO<sub>2</sub>) that contained (in mM): 111 NaCl, 3 KCl, 11 glucose, 25 NaHCO<sub>3</sub>, 3.7 MgSO<sub>4</sub>, 1.1 KH<sub>2</sub>PO<sub>4</sub>, 0.25 CaCl<sub>2</sub> (pH 7.4). Newborn animals were anaesthetized with isoflurane and dissected as described previously<sup>34</sup>. The isolated spinal cord was transferred to a recording chamber that was continuously perfused with normal Ringer's solution and contained (in mM): 111 NaCl, 3 KCl, 11 glucose, 25 NaHCO<sub>3</sub>, 1.25 MgSO<sub>4</sub>, 1.1 KH<sub>2</sub>PO<sub>4</sub>, 2.5 CaCl<sub>2</sub> oxygenated 95% O<sub>2</sub>, 5% CO<sub>2</sub> to obtain a pH of 7.4. All recordings were done at room temperature (22–24 °C).

**In vitro recording of locomotor activity and analysis.** Locomotor activity was recorded with suction electrodes attached to the L2 and L5 lumbar roots on either side of the cord. The ventral root activity was band-pass filtered at 100 Hz to 1 kHz. The signal was sampled using Axoscope 10 (Molecular Devices) at 1–2 kHz. Data points for analysing cycle periods and phases were taken after the locomotor activity had stabilized 10–15 min after the initial burst of activity. Locomotor wave onsets were automatically detected and calculated based on the intersection between the smoothed traces with a horizontal line running through the centre of the trace. The cycle periods of the reference trace were normalized to a scale of 360 degrees, with the onset of a locomotor burst in the reference ventral root corresponding to a phase value of 0° and the onset of the next burst corresponding to a phase value of 360°. The phase delay of the period cycle onset with respect to the reference was calculated for test traces. Epochs of at least 20 consecutive phase values were taken from a sample of at least 70 consecutive phase values. Flexor–extensor and left–right coordination were evaluated with circular statistics (see ref. 34), in which the vector direction gives the preferred mean phase of the activity, and the length of the vector ( $\mathbf{r}$ ) the precision of the phase.  $P$  values greater than 0.05 as determined by Rayleigh's test were considered non-significant. The angular dispersions (a variance measure) were calculated from  $\mathbf{r}$  values and plotted as error bars<sup>35</sup>. Values for frequency–phase plots in the *Vglut2::Cre;Dbx1*<sup>DTA</sup> and *Pax7::Cre;Dbx1*<sup>DTA</sup> mice were also generated using the Spinalcore software<sup>36</sup> (using Morlet wavelet algorithms) to obtain frequencies and phases. The condition for inclusion in these frequency–phase plots was that each of the samples ( $n$ ) involves at least two significantly oriented vector relationships between activities in the ventral roots (LL2–RL2 and/or LL5–RL5 (left–right), and LL2–LL5 and/or RL2–RL5 (flexor–extensor)). The Watson–Williams test for circular data was used to compare conditions<sup>35</sup>.

The different locomotor frequencies for the *in vitro* experiments were obtained by varying the concentrations of locomotor-inducing drugs (5-HT in combination with NMDA)<sup>34</sup>. We classified frequency–phase data in groups according to their locomotor frequency: high frequency,  $f > 0.45$  Hz; medium frequency,  $0.45 \geq f \geq 0.2$  Hz; and low frequency,  $f < 0.2$  Hz. These arbitrary limits were set to include half and double the average locomotor frequencies obtained during drug-induced locomotor-like activity wild-type mice.

Linear fits were produced to correlate changes in the phase to changes in the locomotor frequency (Supplementary Fig. 6). To make these calculations possible,

the circular data in Fig. 3e and Fig. 4e were converted to semi-circular coordinates assuming a central symmetry of data and bimodality for the two opposite states: alternation (0.5 turn) and synchrony (0.0 turn). Thus, concentration of the angle distribution within the 0.0–0.5 range forces the direction of angular variance to contribute to the linear fit<sup>37</sup>. Having done this conversion, the weighted linear fits using means and semi-circular dispersion data were calculated by the least mean squares method on circular data (Supplementary Fig. 6). Significance of the correlation was additionally assessed with the Spearman's rank correlation,  $r_s$ , a test not requiring normal distribution of the two variables.

**Drugs.** NMDA was used in combination with 5-HT to induce locomotor-like activity *in vitro*. GABA<sub>A</sub> and glycine receptors were blocked with picrotoxin (10  $\mu$ M) and strychnine (0.5  $\mu$ M), respectively. Sarcosine (100  $\mu$ M) and nipeptic acid (120  $\mu$ M) were used to block glycine and GABA uptakes, respectively. All drugs were purchased from Sigma.

**Immunohistochemistry.** Whole embryos (E10.5) or isolated lumbar spinal cords (E15.5 to newborn) were fixed for 2 h in 4% (wg/vol) paraformaldehyde in phosphate-buffered saline (PBS), rinsed in PBS, cryoprotected in 30% (wg/vol) sucrose in PBS overnight, and embedded in OCT mounting medium. Transverse sections (16- $\mu$ m thick for E10.5/E12.5, or 20  $\mu$ m for E15 to postnatal day 1) were obtained on a cryostat. Sections were incubated overnight at 4 °C with one or several of the following primary antibodies diluted in PBS supplemented with 5% (vol/vol) fetal bovine serum and 0.5% (wg/vol) Triton X-100: rabbit anti-Dbx1 (1:10,000), chicken anti-GFP (Aves Labs 1020; 1:2,000), chicken anti- $\beta$ -Gal (abcam 9361; 1:1,000), guinea pig anti-Evxl1 (1:4,000), goat anti-Pax3/7 (Santa Cruz 7748; 1:200), rabbit anti-Cre (1:8,000, gift from G. Shutz<sup>17</sup>), guinea pig anti-Bhlhb5 (1:20,000, gift from B. Novitch<sup>38</sup>), guinea pig or rabbit anti-Lbx1 (1:10,000, gift from C. Birchmeier<sup>39</sup>), rabbit anti-GABA (1:1,000, Sigma), sheep anti-Chx10 (1:500, Chemicon), and rabbit anti-Pax2 (1:300, Covance). Secondary antibodies were obtained from Jackson Immunoresearch or Invitrogen and incubated for 1 h at room temperature. Slides were rinsed, mounted in Vectashield medium and scanned on a LSM5 confocal microscope (Zeiss Microsystems) using a  $\times 20$  or a  $\times 40$  objective. Multiple channels were scanned sequentially to prevent fluorescence bleedthrough and false-positive signals. A contrast enhancement and a noise reduction filter were applied in Adobe Photoshop for publication images.

**Cellular counts.** For experiments at E10.5, five to ten non-adjacent cryo-sections, encompassing 300 to 600  $\mu$ m of the hindlimb bud area, were counted. For experiments at E15.5–E16.5, five to ten non-adjacent sections spanning the rostral lumbar spinal cord (T13 to L3) were counted. Neurons expressing the makers of interest were counted on the same side, using raw z-stack confocal images obtained with the  $\times 40$  objective and spanning the entire thickness of the sections. Counts were done manually with the help of the cell-counter plug-in in ImageJ. Cellular counts per section were averaged (or expressed as percentages) per individual animal, and the grand mean (or grand mean percentage)  $\pm$  standard deviation was calculated across animals to produce cells per hemi-section (or percentage) column plots summarizing anatomical staining in the figures.

31. Zeilhofer, H. U. *et al.* Glycinergic neurons expressing enhanced green fluorescent protein in bacterial artificial chromosome transgenic mice. *J. Comp. Neurol.* **482**, 123–141 (2005).
32. Restrepo, C. E. *et al.* Transmitter-phenotypes of commissural interneurons in the lumbar spinal cord of newborn mice. *J. Comp. Neurol.* **517**, 177–192 (2009).
33. Tamamaki, N. *et al.* Green fluorescent protein expression and colocalization with calretinin, parvalbumin, and somatostatin in the GAD67-GFP knock-in mouse. *J. Comp. Neurol.* **467**, 60–79 (2003).
34. Talpalar, A. E. & Kiehn, O. Glutamatergic mechanisms for speed control and network operation in the rodent locomotor CPG. *Front Neural Circuits* **4**, 1–14 (2010).
35. Zar, J. H. *Biostatistical Analysis* (Prentice-Hall, 1974).
36. Mor, Y. & Lev-Tov, A. Analysis of rhythmic patterns produced by spinal neural networks. *J. Neurophysiol.* **98**, 2807–2817 (2007).
37. Mahan, R. P. *Circular Statistical Methods: Applications in Spatial and Temporal Performance Analysis. Special Research Report #16*. (United States Army Research Institute for the Behavioral and Social Sciences, ARI Press, 1991).
38. Skaggs, K., Martin, D. M. & Novitch, B. G. Regulation of spinal interneuron development by the Olig-related protein Bhlhb5 and Notch signaling. *Development* **138**, 3199–3211 (2011).
39. Müller, T. *et al.* The homeodomain factor lbx1 distinguishes two major programs of neuronal differentiation in the dorsal spinal cord. *Neuron* **34**, 551–562 (2002).

# AID stabilizes stem-cell phenotype by removing epigenetic memory of pluripotency genes

Ritu Kumar<sup>1</sup>, Lauren DiMenna<sup>2</sup>, Nadine Schrode<sup>3</sup>, Ting-Chun Liu<sup>1</sup>, Philipp Franck<sup>1</sup>, Silvia Muñoz-Descalzo<sup>3</sup>, Anna-Katerina Hadjantonakis<sup>3</sup>, Ali A. Zarrin<sup>4</sup>, Jayanta Chaudhuri<sup>2</sup>, Olivier Elemento<sup>5</sup> & Todd Evans<sup>1</sup>

The activation-induced cytidine deaminase (AID; also known as AICDA) enzyme is required for somatic hypermutation and class switch recombination at the immunoglobulin locus<sup>1</sup>. In germinal-centre B cells, AID is highly expressed, and has an inherent mutator activity that helps generate antibody diversity<sup>2</sup>. However, AID may also regulate gene expression epigenetically by directly deaminating 5-methylcytosine in concert with base-excision repair to exchange cytosine<sup>3</sup>. This pathway promotes gene demethylation, thereby removing epigenetic memory. For example, AID promotes active demethylation of the genome in primordial germ cells<sup>4</sup>. However, different studies have suggested either a requirement<sup>5</sup> or a lack of function<sup>6</sup> for AID in promoting pluripotency in somatic nuclei after fusion with embryonic stem cells. Here we tested directly whether AID regulates epigenetic memory by comparing the relative ability of cells lacking AID to reprogram from a differentiated murine cell type to an induced pluripotent stem cell. We show that *Aid*-null cells are transiently hyper-responsive to the reprogramming process. Although they initiate expression of pluripotency genes, they fail to stabilize in the pluripotent state. The genome of *Aid*-null cells remains hypermethylated in reprogramming cells, and hypermethylated genes associated with pluripotency fail to be stably upregulated, including many MYC target genes. Recent studies identified a late step of reprogramming associated with methylation status<sup>7</sup>, and implicated a secondary set of pluripotency network components<sup>8</sup>. AID regulates this late step, removing epigenetic memory to stabilize the pluripotent state.

The path to pluripotency involves multiple steps that can be more or less efficient, and this can be modelled in transcription-factor-induced reprogramming<sup>9</sup>. Reprogrammed induced pluripotent stem cell (iPSC) clones initially retain methylation patterns that may reflect an epigenetic memory of the source lineage<sup>10,11</sup>. To test directly the function of AID in reprogramming, we prepared tail-tip fibroblasts (TTFs) from *Aid*-knockout or control sibling mice. Before reprogramming, the fibroblasts appeared morphologically identical (Supplementary Fig. 1a), and were transduced equivalently with lentivirus encoding the four human 'Yamanaka' reprogramming transcription factors<sup>12</sup>: OCT4, KLF4, SOX2 and cMYC (OKSM; Supplementary Fig. 1b). Expression levels of exogenous human OCT4 72 h after infection (before induction of the endogenous murine gene) were equivalent, showing that lack of AID does not affect expression vector function (Supplementary Fig. 1c). Exogenous transcription factor expression was subsequently equivalently repressed in wild-type and *Aid*-null transduced cells (Supplementary Fig. 1d). Using quantitative polymerase chain reaction with reverse transcription (RT-qPCR) assays, transcript levels for *Aid* were not reliably detected above background in wild-type TTFs. However, after 1 week of reprogramming, transcripts were readily measured in wild-type cells, increasing as much as tenfold during the reprogramming process (Supplementary Fig. 2).

Initial reprogramming steps include the induction of proliferation and a change in the morphology of fibroblasts to smaller and rounder cells<sup>13</sup>. We found that cells lacking AID are initially hyper-responsive to reprogramming factors. The change in morphology was more rapid in *Aid*<sup>-/-</sup> cells, beginning at 2 days after transduction. After 4 days, *Aid*<sup>-/-</sup> cells were rounded and smaller than *Aid*<sup>+/+</sup> cells (Fig. 1a). A higher fraction of *Aid*<sup>-/-</sup> cells stained positive for SSEA1, an early marker for pluripotency<sup>14</sup> (Fig. 1b). At day 7, more *Aid*-null cells expressed NANOG compared with controls (Fig. 1c), correlating with modestly higher transcript levels for several pluripotency genes before the first week of reprogramming (Fig. 1d). Consistent with the molecular data, at 2 weeks the *Aid*-null cells consistently generated more early colonies than wild-type cells (sixfold more colonies on average over six independent experiments). Thus, *Aid*-null fibroblasts are hyper-responsive to reprogramming, even though the growth curves for uninfected wild-type and *Aid*-null cells were indistinguishable (Supplementary Fig. 3a). Rather, the enhanced expression of pluripotency markers in *Aid*<sup>-/-</sup> cells suggests that AID normally helps to stabilize the differentiated state, creating a barrier to the initial process of reprogramming. When the *Aid*<sup>-/-</sup> fibroblasts were passaged before transduction, this hyper-responsiveness was no longer seen (Supplementary Fig. 3b), suggesting

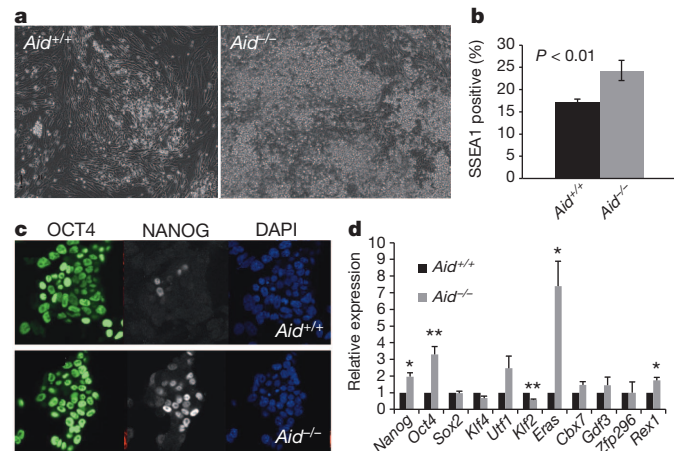


**Figure 1 | Cells lacking AID are initially hyper-responsive to transcription-factor-based reprogramming.** **a**, *Aid*<sup>+/+</sup> and *Aid*<sup>-/-</sup> fibroblasts after 4 days of OKSM transduction. Note the more rounded appearance of null cells. Original magnification,  $\times 10$ . **b**, Cells positive for SSEA1 after 4 days of OKSM transduction, determined by flow cytometry. **c**, Immunostaining with anti-OCT4 and anti-NANOG antibodies after 1 week of OKSM transduction. Original magnification,  $\times 40$ . **d**, Relative transcript levels of pluripotency genes determined by qPCR after 4 days of OKSM transduction. For each gene, transcript levels were normalized to *Aid*<sup>+/+</sup> cells set to a value of 1. Data represent the mean  $\pm$  standard error of the mean (s.e.m.) from three independent experiments (\* $P < 0.05$ , \*\* $P < 0.01$ ).

<sup>1</sup>Department of Surgery, Weill Cornell Medical College, New York, New York 10065, USA. <sup>2</sup>Immunology Program, Sloan-Kettering Institute, Memorial Sloan Kettering Cancer Institute, New York, New York 10065, USA. <sup>3</sup>Developmental Biology Program, Sloan-Kettering Institute, Memorial Sloan Kettering Cancer Institute, New York, New York 10065, USA. <sup>4</sup>Genentech, South San Francisco, California 94080, USA. <sup>5</sup>Institute for Computational Biomedicine, Weill Cornell Medical College, New York, New York 10065, USA.

that passive removal of epigenetic marks through DNA replication can normalize the initial response to OKSM.

Although there were more cells, no obvious differences were observed at 2 weeks in the morphologies of iPSC-like colonies derived from *Aid*<sup>-/-</sup> cells compared with *Aid*<sup>+/+</sup> cells, and both stained positive for the pluripotency marker NANOG (Supplementary Fig. 4). However, by 4 weeks the colonies derived from *Aid*<sup>-/-</sup> fibroblasts were flattened with less defined edges (Fig. 2a). We tracked individual iPSC-like colonies and observed many *Aid*<sup>-/-</sup> colonies that appeared pluripotent at 3 weeks but showed a differentiated morphology at 4 weeks (Fig. 2b). At 3 weeks, the *Aid*<sup>-/-</sup> colonies showed a 'patchy' NANOG pattern, and by 4 weeks most colonies were differentiated, with few NANOG<sup>+</sup> cells (Fig. 2c). This highly reproducible phenomenon was never observed for colonies derived from *Aid*<sup>+/+</sup> cells, which retained their iPSC morphology and NANOG expression throughout the 4 weeks (Fig. 2d, e). The colonies derived from *Aid*<sup>-/-</sup> cells showed a progressive decline in the frequency of cells expressing SSEA1 (Fig. 2d) and OCT4 (Fig. 2e). The same results were observed using mouse embryonic fibroblasts (MEFs), as the *Aid*-null cells failed to maintain a pluripotent iPSC phenotype (Supplementary Fig. 5). The stabilization of pluripotency was equally effective in wild-type cells (and ineffective in *Aid*-null cells) regardless of whether constitutively expressed or doxycycline-inducible OSKM cassettes were used (Supplementary Fig. 6a).

Using either wild-type or *Aid*-null cells, the expression of OKSM using a doxycycline-inducible vector for only 6 days was insufficient to generate pluripotent colonies. OKSM expression for 9, 12, 21 or 28 days was sufficient to generate pluripotent colonies, showing a 'dose response' in the wild-type fibroblasts, but was equally ineffective for generating stable pluripotent cells from *Aid*-null cells at the 4-week time point (Supplementary Fig. 6b, c). When AID was expressed along with OKSM during initial reprogramming stages, this failed to rescue pluripotency (data not shown). However, when OKSM-transduced *Aid*-null cells were secondarily infected with an AID-expressing retrovirus

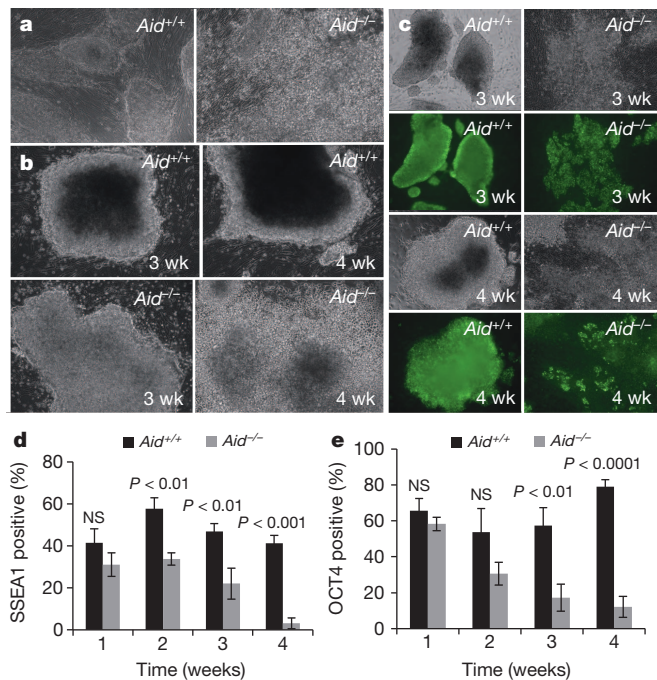


**Figure 2 | AID stabilizes pluripotency.** **a**, *Aid*<sup>-/-</sup> cells lose ES-cell-like morphological characteristics 4 weeks after OKSM transduction. **b**, *Aid*<sup>-/-</sup> iPSC-like colonies progressively lose this phenotype. wk, weeks. **c**, Mutant cells lose NANOG expression. **a–c**, Original magnification,  $\times 10$ . **d, e**, Cells that stained positive for SSEA1 (**d**) or OCT4 (**e**) were measured by flow cytometry after 1, 2, 3 or 4 weeks of OKSM transduction;  $n = 3$  independent experiments, error bars denote standard deviation. NS, not significant.

after 1 week (Supplementary Fig. 7a, b), there was a partial but statistically significant rescue of pluripotency markers stabilized at the 4-week time point. Because the rescue was not complete we cannot rule out additional molecular mechanisms, beyond AID, that also contribute to the stabilization of pluripotency. Expression of AID in wild-type cells further enhanced the stable expression of pluripotency markers at 4 weeks (Supplementary Fig. 7c). As *Nanog* is syntenic with the *Aid* locus, an independent set of experiments used fibroblasts derived from an *Aid*-knockout strain in which the *neoR* gene was deleted<sup>15</sup>. These 'clean' knockout cells also failed to derive stable iPSC colonies (data not shown).

It was previously reported that iPSCs derived from different cell types retain an epigenetic memory of their somatic phenotype<sup>10,11</sup>. We tested whether genome replication through passaging could stabilize a pluripotent phenotype even in the absence of AID. We generated iPSC-like colonies and isolated 13 *Aid*<sup>+/+</sup> and 12 *Aid*<sup>-/-</sup> colonies (clones) at 3 weeks that appeared pluripotent by morphology. After three passages (p3) all the clones, regardless of genotype, retained iPSC-like morphology and stained positive for OCT4 and NANOG (Fig. 3a). However, between p7 and p10, 5 out of 12 *Aid*<sup>-/-</sup> clones failed to retain pluripotency and differentiated (Fig. 3b). All 13 *Aid*<sup>+/+</sup> colonies and the other 7 *Aid*<sup>-/-</sup> clones that were stable beyond p10 retained pluripotency until at least p50. All iPSC clones that retained morphology beyond p10 formed embryoid bodies equivalently and could differentiate into cells expressing smooth muscle actin (mesoderm),  $\beta$ III tubulin (ectoderm) and  $\alpha$ -fetoprotein (endoderm), regardless of *Aid* genotype (Fig. 3c). In an independent set of experiments, wild-type and *Aid*-null clones were picked and either maintained in culture as colonies or passaged. The non-passaged wild-type-derived clones maintained a pluripotent morphology, whereas the *Aid*-null cells differentiated. With passaging, 60% of the *Aid*-null clones were able to maintain a pluripotent morphology (Supplementary Fig. 8).

Thus, although AID is not essential for reprogramming, an important transition occurs at around 3 weeks that is assisted by AID to stabilize the pluripotent phenotype. We considered whether the previously described DNA-demethylating role of AID might be at least partially responsible for this phenotypic stabilization. We profiled the epigenome by carrying out reduced-representation bisulphite sequencing (RRBS) in *Aid*-null and control cells after 3 weeks of

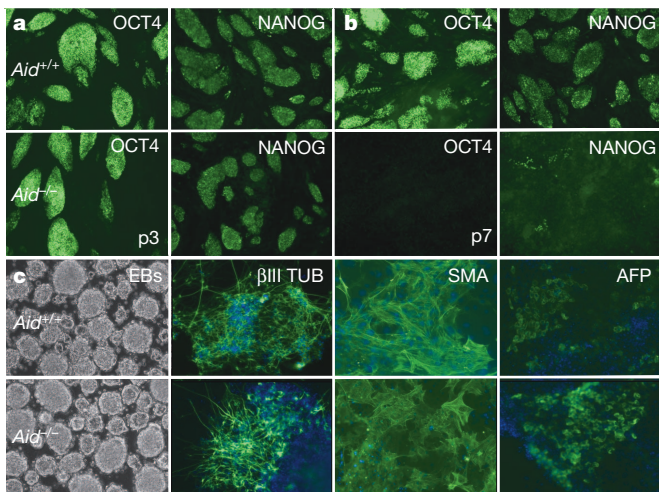


**Figure 3 | Cells lacking AID reprogram inefficiently, but those that do are pluripotent.** **a, b**, Immunostaining of iPSC colonies isolated 3 weeks after OKSM transduction and passaged three times (**a**) or seven times (**b**) before staining. In this example, the null cells failed to form stable iPSCs. **c**, Stable iPSC clones were passaged more than ten times. In this case (unlike in **b**) the passaged *Aid*-null cells maintained NANOG expression (data not shown) and generate embryoid bodies (EBs) that differentiate into cells positive for smooth muscle actin (SMA),  $\beta$ III tubulin ( $\beta$ III TUB) and  $\alpha$ -fetoprotein (AFP). Original magnification,  $\times 10$ .

reprogramming. We observed global DNA hypermethylation in the *Aid*-null cells (Supplementary Fig. 9a), when we considered either total CpGs or differentially methylated regions (DMRs). DNA hypermethylation occurs preferentially near RGYW motifs (Supplementary Fig. 9b), the characteristic DNA-targeting sites for AID (45% of the hypermethylated CpGs). Notably, as AID targets gene bodies, the hypermethylated regions are enriched in gene bodies, even though RRBS is biased towards capturing CpG-rich promoter and enhancer regions (Supplementary Fig. 9c).

Transcript profiles comparing the original, pre-transduced fibroblasts from *Aid*<sup>+/+</sup> and *Aid*<sup>-/-</sup> embryos closely match (Supplementary Fig. 10a). By contrast, many genes fail to be upregulated in the mutant cells during reprogramming (Fig. 4a, b and Supplementary Fig. 10b). The genes that fail to be upregulated during reprogramming are highly enriched ( $P < 1 \times 10^{-10}$ ) in the gene set showing hypermethylation in *Aid*-null cells (Fig. 4c). Of note, genes that are upregulated during reprogramming in both wild-type and *Aid*-null cells are also enriched in hypermethylated genes ( $P < 1 \times 10^{-14}$ ), suggesting that many genes overcome the loss of AID during reprogramming. Among the set of hypermethylated genes, in *Aid*-null cells there is a failure to upregulate a set of secondary pluripotency genes, including *Rex1* (also known as *Zfp42*), *Gdf3*, *Dnmt3l*, *Cbx7*, *Zfp296*, *Dnmt1*, *Apobec1* and *Tet3* (Fig. 4d). This expression data correlates well with the RRBS data, which was validated by MassArray bisulphite sequencing (Supplementary Fig. 11), and is consistent with a failure of this downstream network to be demethylated at late stages of reprogramming. Comparing the gene set of hypermethylated underexpressed genes to public embryonic stem (ES)-cell chromatin immunoprecipitation and massively parallel DNA sequencing (ChIP-seq) data sets revealed a marked enrichment of cMYC target genes in reprogramming cells lacking AID (Supplementary Fig. 12). According to qPCR data there was no difference in *cMyc* transcript levels in wild-type or *Aid*-null cells at any point in the reprogramming process (data not shown). Furthermore, enhanced levels of cMYC, achieved by retroviral transduction starting at 1 week of reprogramming, failed to stabilize pluripotency in *Aid*-null cells (Supplementary Fig. 13), suggesting that

cMYC access to key target pluripotency genes (due to hypermethylation) rather than cMYC levels *per se* may be a limiting step for stabilization of the network.

Individual iPSC-like clones were isolated at 2 weeks and expanded to evaluate global methylation patterns for each individual clone. Hypermethylation patterns in the *Aid*-null clones were highly consistent with data obtained from bulk colony analysis. On the basis of genome-wide DNA methylation profiles (with the genome binned for 100 kb regions), *Aid*-null or wild-type clones cluster according to genotype (Supplementary Fig. 14a). Regions that were hypermethylated in the *Aid*-null bulk analysis tended to be hypermethylated in the *Aid*-null clones (Supplementary Fig. 14b). In fact, 66% of bulk hypermethylated DMRs were also hypermethylated in DNA derived from the isolated clones ( $P < 1 \times 10^{-151}$ ). Methylation differences found previously for the secondary pluripotency genes were largely validated by MassArray bisulphite sequencing of DNA (Supplementary Fig. 14c), and most of the hypermethylated genes were expressed in the *Aid*-null clones at significantly lower levels compared with levels in wild-type clones (Supplementary Fig. 14d).

Altogether, our results show that active demethylation through AID-dependent cytosine deamination is important for stabilizing a genetic network controlling stem-cell phenotype. AID is not essential for reprogramming, because cells lacking AID can form stable pluripotent iPSCs, either through a passive demethylation process facilitated by DNA replication, or perhaps through compensation from related members of the APOBEC family<sup>16</sup>. A recent study suggested that loss of AID affects transcription-factor-induced reprogramming only by an early acute short hairpin RNA (shRNA)-dependent depletion<sup>17</sup>, but did not report the 'iPSC' phenotype beyond 3 weeks, when we show that *Aid*-null cells eventually fail to stabilize as pluripotent. Unless passaged, *Aid*-null cells always fail to reprogram. RNA-seq profiles of *Aid*-null cells after 4 weeks of reprogramming cluster with fibroblast samples (data not shown), and qPCR analysis validates significant upregulation of fibroblast-associated genes in the *Aid*-null samples (Supplementary Fig. 15), consistent with an epigenetic memory for fibroblast fate that fails to be fully removed during reprogramming in

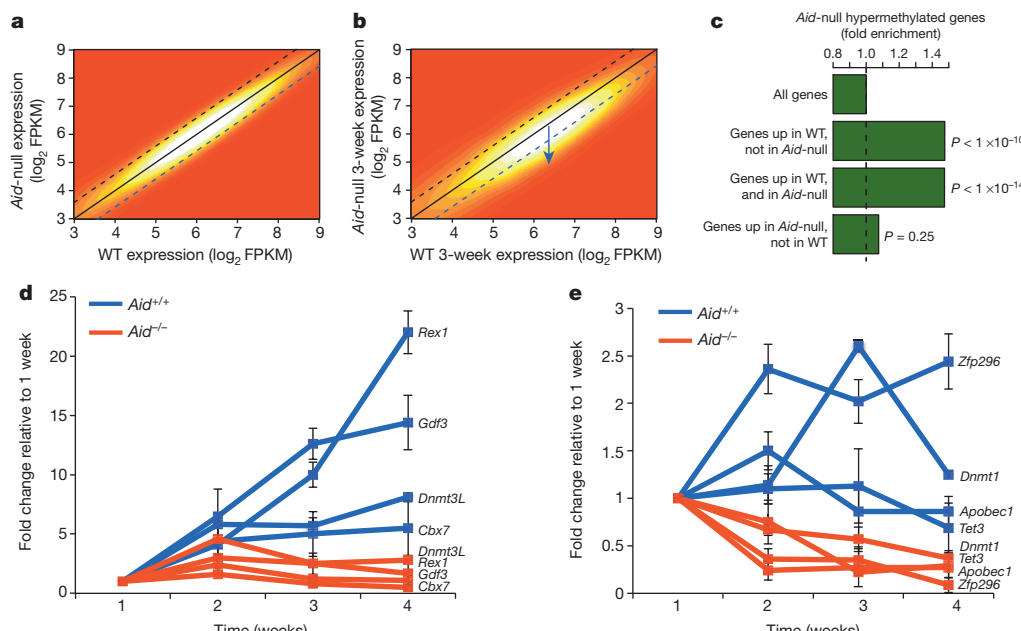


**Figure 4 | Cells lacking AID fail to activate expression of hypermethylated pluripotency genes.** **a**, In the original, pre-transduced fibroblasts few differentially expressed genes are off the diagonal. FPKM, fragments per kilobase of transcript per million fragments mapped; WT, wild type. **b**, Many genes are underexpressed in *Aid*-null cells 3 weeks after transduction. **c**, Fold

enrichment for hypermethylated genes in *Aid*-null cells. All  $P$  values were calculated using the hypergeometric distribution. **d**, Transcript levels for hypermethylated pluripotency genes during reprogramming, comparing wild-type cells (blue lines) with *Aid*-null cells (red lines). Data represent the mean  $\pm$  s.e.m. from three independent experiments.

the absence of AID. The function of AID for transition to a stable pluripotent phenotype may be relevant during embryogenesis, as *Aid*-knockout strains have small litters. We found that ES-cell lines could be established from *Aid*-null blastocysts, and these appeared by morphology and staining patterns to be normal (Supplementary Fig. 16). However, the efficiency of ES-cell-line derivation was markedly reduced (17/28 embryos, 60.7%) compared with congenic wild-type embryos (21/24, 87.5%;  $P < 0.03$  by chi-squared analysis).

Although there is much promise for the use of iPSCs for disease modelling and cellular therapies<sup>18</sup>, there remains concern about whether iPSC genomes are damaged through the process of reprogramming<sup>19–21</sup>. AID, which has natural mutator activity, is activated during reprogramming, and mediates demethylation in gene bodies including secondary pluripotency genes that encode proto-oncogenes. Although inefficient, we showed that iPSCs could be generated in the absence of AID, removing epigenetic memory marks through an AID-independent mechanism. Retaining epigenetic memory, in the absence of AID, might be useful for promoting efficiency of differentiation towards parental lineage fate. Furthermore, if AID-independent reprogramming lessens the mutation load, it could provide a safer strategy for the generation of iPSCs for cellular therapies.

## METHODS SUMMARY

TTFs were prepared using 0.2% collagenase; MEFs were prepared from embryonic day (E)13.5 embryos. Intracellular immunostaining was performed after fixing the cells with 4% paraformaldehyde. Surface staining was done without fixing the cells. Complementary DNA was prepared using Superscript III and qPCR was performed (primers listed in Supplementary Table 1) using SYBR green and a Roche LightCycler 480 II. All data were from at least three independent experiments. Enhanced RRBS was performed as described<sup>22</sup> and bisulphite reads were aligned to the bisulphite-converted mm9 genome using Bismark<sup>23</sup>. We achieved very high coverage by sequencing one full Illumina lane ( $\sim 200$  M, 51 bp reads) per sample. For bulk colonies, the wild-type and *Aid*-null samples (at 3 weeks) were analysed with RRBS that covered 1.96 M and 1.82 M CpGs, respectively, with at least 10 $\times$  coverage (with  $>1.62$  M CpGs in common between the two runs). 1.52 M and 1.59 M CpGs had  $\geq 20\times$  coverage in wild-type and *Aid*<sup>−/−</sup> cells, respectively. 1.17 M and 1.32 M CpGs had  $\geq 50\times$  coverage, respectively. Differentially methylated CpGs were identified using the Fisher exact test with Benjamini–Hochberg correction for multiple testing. DMRs were defined as containing at least five differentially methylated CpGs and a total methylation difference of more than 10%. Paired-end RNA-seq libraries were constructed as described<sup>24</sup> and sequenced using an Illumina HiSeq2000. Reads were aligned to mm9 using TopHat and gene expression levels were quantified using Cufflinks, using upper-quartile and GC-content normalizations. Fold changes of 1.5 with fragments per kilobase of transcript per million fragments mapped (FPKM)  $> 5$  in at least one condition were used to derive differentially expressed genes. MassArray EpiTYPER analysis was performed on selected regions identified as hypermethylated by RRBS. PCR primers (Supplementary Table 2) were designed to probe amplicons using EpiDesigner (<http://www.epidesigner.com/>). Bisulphite conversion and MassArray analysis were performed as previously described<sup>22</sup>. Metadata for all RRBS experiments are given in Supplementary Table 3. Methylation differences were calculated at each CpG and boxplot analysis was performed at each interrogated region. All statistical analyses were performed using the R software package.

**Full Methods** and any associated references are available in the online version of the paper.

Received 14 August 2012; accepted 13 May 2013.

Published online 26 June 2013.

1. Muramatsu, M. *et al.* Class switch recombination and hypermutation require activation-induced cytidine deaminase (AID), a potential RNA editing enzyme. *Cell* **102**, 553–563 (2000).

2. Chaudhuri, J. *et al.* Transcription-targeted DNA deamination by the AID antibody diversification enzyme. *Nature* **422**, 726–730 (2003).
3. Bhutani, N., Burns, D. M. & Blau, H. M. DNA demethylation dynamics. *Cell* **146**, 866–872 (2011).
4. Popp, C. *et al.* Genome-wide erasure of DNA methylation in mouse primordial germ cells is affected by AID deficiency. *Nature* **463**, 1101–1105 (2010).
5. Bhutani, N. *et al.* Reprogramming towards pluripotency requires AID-dependent DNA demethylation. *Nature* **463**, 1042–1047 (2010).
6. Foshay, K. M. *et al.* Embryonic stem cells induce pluripotency in somatic cell fusion through biphasic reprogramming. *Mol. Cell* **46**, 159–170 (2012).
7. Polo, J. M. *et al.* A molecular roadmap of reprogramming somatic cells into iPSCs. *Cell* **151**, 1617–1632 (2012).
8. Buganim, Y. *et al.* Single-cell expression analyses during cellular reprogramming reveal an early stochastic and a late hierachic phase. *Cell* **150**, 1209–1222 (2012).
9. Meissner, A. Epigenetic modifications in pluripotent and differentiated cells. *Nature Biotechnol.* **28**, 1079–1088 (2010).
10. Kim, K. *et al.* Epigenetic memory in induced pluripotent stem cells. *Nature* **467**, 285–290 (2010).
11. Polo, J. M. *et al.* Cell type of origin influences the molecular and functional properties of mouse induced pluripotent stem cells. *Nature Biotechnol.* **28**, 848–855 (2010).
12. Sommer, C. A. *et al.* Induced pluripotent stem cell generation using a single lentiviral stem cell cassette. *Stem Cells* **27**, 543–549 (2009).
13. Smith, Z. D., Nachman, I., Regev, A. & Meissner, A. Dynamic single-cell imaging of direct reprogramming reveals an early specifying event. *Nature Biotechnol.* **28**, 521–526 (2010).
14. Brambrink, T. *et al.* Sequential expression of pluripotency markers during direct reprogramming of mouse somatic cells. *Cell Stem Cell* **2**, 151–159 (2008).
15. Sun, Y. *et al.* Critical role of activation induced cytidine deaminase in experimental autoimmune encephalomyelitis. *Autoimmunity* **46**, 157–167 (2013).
16. Conticello, S. G. The AID/APOBEC family of nucleic acid mutators. *Genome Biol.* **9**, 229 (2008).
17. Bhutani, N. *et al.* A critical role for AID in the initiation of reprogramming to induced pluripotent stem cells. *FASEB J.* **27**, 1107–1113 (2012).
18. Robinton, D. A. & Daley, G. Q. The promise of induced pluripotent stem cells in research and therapy. *Nature* **481**, 295–305 (2012).
19. Gore, A. *et al.* Somatic coding mutations in human induced pluripotent stem cells. *Nature* **471**, 63–67 (2011).
20. Hussein, S. M. *et al.* Copy number variation and selection during reprogramming to pluripotency. *Nature* **471**, 58–62 (2011).
21. Mayshar, Y. *et al.* Identification and classification of chromosomal aberrations in human induced pluripotent stem cells. *Cell Stem Cell* **7**, 521–531 (2010).
22. Akalin, A. *et al.* Base-pair resolution DNA methylation sequencing reveals profoundly divergent epigenetic landscapes in acute myeloid leukemia. *PLoS Genet.* **8**, e1002781 (2012).
23. Krueger, F. & Andrews, S. R. Bismark: a flexible aligner and methylation caller for Bisulfite-Seq applications. *Bioinformatics* **27**, 1571–1572 (2011).
24. Mortazavi, A., Williams, B. A., McCue, K., Schaeffer, L. & Wold, B. Mapping and quantifying mammalian transcriptomes by RNA-Seq. *Nature Methods* **5**, 621–628 (2008).

**Supplementary Information** is available in the online version of the paper.

**Acknowledgements** We thank G. Mostoslavsky for the gift of reprogramming vectors. A. Melnick provided advice and consultation. We are grateful to T. Honjo for AID-knockout mice, and N. Papavasiliou for assistance in designing genotyping PCR primers. The Epigenomics Core Facility of Weill Cornell Medical College carried out the bisulphite sequencing and provided consultation. This study was supported by National Institutes of Health grant HL056182 (T.E.), AI072194 (J.C.) and National Science Foundation CAREER grant 1054964 (O.E.).

**Author Contributions** R.K. conceived the study, carried out experiments, and wrote the manuscript. L.D., N.S., T.-C.L., P.F. and S.M.-D. carried out experiments. A.A.Z. and A.-K.H. provided essential reagents and expertise. J.C. conceived the study and wrote the manuscript. O.E. conceived the study, carried out computational and informatics analyses, and wrote the manuscript. T.E. conceived the study and wrote the manuscript.

**Author Information** All RNA-seq and RRBS data have been deposited in the Gene Expression Omnibus under accession GSE46700. Reprints and permissions information is available at [www.nature.com/reprints](http://www.nature.com/reprints). The authors declare no competing financial interests. Readers are welcome to comment on the online version of the paper. Correspondence and requests for materials should be addressed to T.E. (tre2003@med.cornell.edu).

## METHODS

**Summary.** Intracellular immunostaining was performed after fixing the cells with 4% paraformaldehyde. Surface staining was done without fixing the cells. All data were from at least three independent experiments. Enhanced RRBS was performed as described<sup>22</sup> and bisulphite reads were aligned to the bisulphite-converted mm9 genome using Bismark<sup>23</sup>. We achieved very high coverage by sequencing one full Illumina lane (~200 M, 51 bp reads) per sample. For bulk colonies, the wild-type and *Aid*-null samples (at 3 weeks) were analysed with RRBS that covered 1.96 M and 1.82 M CpGs, respectively, with at least 10× coverage (with >1.62 M CpGs in common between the two runs). 1.52 M and 1.59 M CpGs had ≥20× coverage in wild-type and *Aid*<sup>-/-</sup> cells, respectively. 1.17 M and 1.32 M CpGs had ≥50× coverage, respectively. Differentially methylated CpGs were identified using the Fisher exact test with Benjamini–Hochberg correction for multiple testing. DMRs were defined as containing at least five differentially methylated CpGs and a total methylation difference of more than 10%. Paired-end RNA-seq libraries were constructed as described<sup>24</sup> and sequenced using an Illumina HiSeq2000. Mass-Array EpiTYPER analysis was performed on selected regions identified as hypermethylated by RRBS. PCR primers (Supplementary Table 2) were designed to probe amplicons using EpiDesigner (<http://www.epidesigner.com/>). Bisulphite conversion and MassArray analysis were performed as previously described<sup>22</sup>. Metadata for all RRBS experiments are given in Supplementary Table 3. Methylation differences were calculated at each CpG and boxplot analysis was performed at each interrogated region. All statistical analyses were performed using the R software package.

**Mice.** *AID*-deficient (*Aid*<sup>-/-</sup>) mice were a gift from T. Honjo. Some of the reprogramming experiments were performed on the *Aid*<sup>-/-</sup> and *Aid*<sup>+/+</sup> littermates derived by crossing *Aid*<sup>+/+</sup> mice, and for some of the experiments wild-type BALB/c mice were purchased from the Jackson Laboratory. Reprogramming experiments were performed on tail fibroblasts obtained from seven *Aid*<sup>-/-</sup> and seven *Aid*<sup>+/+</sup> age-matched mice (four littermates and three non-littermates, each). We observed similar results when comparing littermates or the purchased mice. Mice or embryos used for MEFs were genotyped by PCR. All animals were maintained according to the guidelines for animal welfare of the Memorial Sloan-Kettering Research Animal Resource Center.

**Preparation of fibroblasts.** For preparation of tail fibroblasts either whole tails or tail tips were collected from age-matched adult *Aid*<sup>+/+</sup> and *Aid*<sup>-/-</sup> mice (age range, 3–8 weeks). Tails or tail tips were minced using a razor blade/scalpel after washing with PBS. For preparation of MEFs, *Aid*<sup>+/+</sup> males and *Aid*<sup>-/-</sup> females were time mated and E13.5 embryos were collected. Embryos were washed several times and extra care was taken to prevent maternal cross contamination. After removing the head and all internal organs embryos were minced using a razor blade/scalpel. Minced tails or embryos were washed twice with DMEM (Cellgro) containing 10% FBS (Gemini Bio Products), 1 mM L-glutamine (Cellgro), 100 U ml<sup>-1</sup> penicillin (Cellgro) and 10 µg ml<sup>-1</sup> streptomycin (Cellgro), and dissociated using 0.2% collagenase from *Clostridium histolyticum* (Sigma) at 37 °C for 4 h (tails) or 2 h (embryos) with continuous shaking. Dissociated cells were filtered through a 70-µm cell strainer (BD falcon) and washed two times with DMEM containing 10% FBS and plated on 0.1% gelatin- (Cellgro) coated tissue culture plates. Fibroblasts were cultured in DMEM containing 10% FBS, 1 mM L-glutamine, 100 U ml<sup>-1</sup> penicillin and 100 µg ml<sup>-1</sup> streptomycin and media was replaced daily. After passaging two times, fibroblasts were frozen in media containing 10% DMSO, 40% FBS and 50% DMEM. Generally, p2 fibroblasts were used for the reprogramming experiments, unless indicated otherwise. Genotype was confirmed by PCR. Primers for wild type, F: 5'-GGTCCCGAGTCTGAGATGTA; R: 5'-CAACGTGGCGTCCAAACAGGC; for knockout, F: 5'-CTGCCAACCTGA TGTCTTGA; R: 5'-AACCAAGCCTATGCCTACAGC.

**Production of lentiviruses and retroviruses.** Reprogramming virus was produced by transfection of a single lentiviral stem cell cassette (STEMCCA) in HEK293T cells using polyethylenimine (PEI) (Polysciences). STEMCCA (constitutive) expresses all four human factors (OCT4, KLF4, SOX2, cMYC), using a single elongation factor 1α (EF1α) promoter within a lentiviral vector using a combination of 2A peptide and internal ribosome entry site (IRES) strategies. Both constitutive and doxycycline-inducible STEMCCA vectors were used for the reprogramming studies. For the doxycycline-inducible system, fibroblasts were treated with doxycycline (1 µg ml<sup>-1</sup>) starting 1 day after transduction for 2 weeks. Lentiviruses were produced using a five-plasmid transfection system with STEMCCA transfected together with four expression vectors encoding the packaging proteins Gag-Pol, Rev and Tat, and the G protein of the vesicular stomatitis virus (VSV). Five vectors were incubated in DMEM with 0.06% PEI for 20 min and then transferred to the plates containing 80% confluent HEK293T cells. Transfection was performed in FBS (10%) containing media. After 5 h media was replaced with fresh media. Viral supernatant was collected after 48 h and spun at 3,000 r.p.m. to remove dead cells and filtered through a sterile syringe filter with

0.45 µm polyethersulfone membrane (VWR international). Ectopic expression of wild-type AID or catalytically mutant AID was achieved using retroviral vectors as described previously<sup>25</sup>. Retroviruses were produced by co-transfected the vector with the packaging plasmid pCL-ECO in HEK293T cells. The cMYC overexpression experiments were achieved using retroviral vector pMXs-c-Myc (Addgene, 13375). pMXs-c-Myc was co-transfected with vector encoding VSVg in GP2-293 cells to collect functional virus.

**Transduction with lentiviruses.** Five-hundred-thousand fibroblasts were plated in one well of a gelatin-coated 6-well tissue culture plate. After 6 h, 1 ml of viral supernatant containing 8 µg ml<sup>-1</sup> polybrene (Millipore) was added to the fibroblast-containing wells. For every experiment, *Aid*<sup>-/-</sup> and *Aid*<sup>+/+</sup> fibroblasts were infected at the same time with an identical titre of virus, prepared for each experiment from the same batch. Viral supernatant was removed after 12 h of infection and fresh media containing DMEM, 10% FBS, 1 mM L-glutamine, 100 U ml<sup>-1</sup> penicillin and 10 µg ml<sup>-1</sup> streptomycin was added. After 1 day media was replaced by mouse embryonic stem-cell (MES) media containing DMEM, 20% ES-cell-compatible FBS (Gemini Bio Products), LIF (2% conditioned medium) and 1.5 × 10<sup>-4</sup> M monothioglycerol (MTG; Sigma), 1 mM L-glutamine, 100 U ml<sup>-1</sup> penicillin and 10 µg ml<sup>-1</sup> streptomycin. Cells were maintained in the same media. In some of the experiments cells were transferred to mitotically inactivated MEF feeders after 2 days of transduction. Approximately 30,000–50,000 cells were transferred to one well of a feeder-containing 6-well plate. Isolated iPSC colonies were always cultured on feeders. All the cells were kept at 37 °C in a humidified environment at 5% CO<sub>2</sub>.

**Immunostaining.** Immunostaining was performed on fixed cells (4% PFA in BBS with 1 mM CaCl<sub>2</sub>, 15 min) washed and blocked for 30 min in BBT-BSA buffer (BBS with 0.5% BSA, 0.1% Triton and 1 mM CaCl<sub>2</sub>). Cells with primary antibodies were incubated overnight at 4 °C at the following dilutions: anti-NANOG (eBiosciences 14-5761, 1:100, 5 µg ml<sup>-1</sup>) and anti-OCT4 (Santa Cruz 5279, 1:100, 2 µg ml<sup>-1</sup>). Cells were washed and blocked in BBT-BSA and then incubated with Alexa-conjugated secondary antibodies (1:500, from Molecular Probes). Vectashield-DAPI was used as a mounting medium. Images were acquired using a Zeiss LSM 510-Meta confocal microscope or a Zeiss epifluorescence microscope with AxioVision software. For flow cytometric analysis cells were trypsinized, fixed with 4% PFA for 20 min, blocked for 1 h and then stained in suspension. SSEA1 (Santa Cruz, 1:100) staining was performed on unfixed cells. Cells were analysed on a BD-Accuri C6 flow cytometer (BD Biosciences) using CFlow Plus software.

**RT-qPCR.** Cells were trypsinized and collected in Trizol reagent (Life technologies). Total RNA extraction was done using the RNeasy Mini Kit (Qiagen). The cDNA was synthesized using the SuperScript III First-Strand Synthesis System (Invitrogen). RT-qPCR was performed on three experimental replicates using SYBR green Master I (Roche). Data were generated on a LightCycler 480 II (Roche) and analysed using LightCycler 480 software. qPCR data was calculated based on the mean of three experimental replicates. All quantifications were normalized to an endogenous *Gadph* control. The relative quantification value for each target gene was compared to the calibrator for that target gene. All the primers used for qPCR spanned introns (Supplementary Table 1).

**In vitro differentiation.** For embryoid body formation, iPSCs were passaged two times on feeder-free gelatin-coated culture dishes. 5 × 10<sup>5</sup> iPSCs were plated on a 10-cm low attachment dish. Embryoid bodies were cultured for 6 days in MES media without LIF, and media was changed every other day. For mesodermal differentiation, embryoid bodies were replated on gelatin-coated dishes and cultured for another 7 days in the same media. For neural differentiation, embryoid bodies were cultured in media containing DMEM F-12 (Cellgro), 0.5% N2 (Gibco) and 0.5% B27 (Gibco) supplements, 1 mM L-glutamine, 1% non-essential amino acids (Gibco) and 1.5 × 10<sup>-4</sup> M monothioglycerol for another 3 days, after which embryoid bodies were seeded onto gelatin-coated dishes with the same media, plus 10 µM retinoic acid (Sigma) for another 4 days. For endoderm differentiation, embryoid bodies were replated onto gelatin-coated dishes in MES media lacking LIF but containing 0.5% FBS and 50 ng ml<sup>-1</sup> Activin (R&D) for 7 days. For all differentiation cultures, media was changed daily.

**ES-cell derivation from blastcyst-stage mouse embryos.** *Aid*<sup>-/-</sup> males and *Aid*<sup>-/-</sup> females (or congenic wild-type pairs as controls) were time mated and E3.5 blastocyst-staged embryos were collected in M2 media according to standard protocols<sup>26</sup>. Embryos were placed on mitotically inactivated MEFs<sup>27</sup> in knockout DMEM (Gibco) containing 15% knockout serum replacement (KSR; Gibco), 2 mM L-glutamine, 0.1 mM β-mercaptoethanol, 0.1 mM non-essential amino acids, 1 mM sodium pyruvate, 100 U ml<sup>-1</sup> penicillin and 100 µg ml<sup>-1</sup> streptomycin, 1,000 U ml<sup>-1</sup> LIF, 1 µM PD032501 (ERK inhibitor) and 3 µM CHIR99021 (inhibitor of GSK3B). After embryos attached, media was replaced every other day. After 10–11 days an outgrowth could be observed and was dissociated in 0.25% trypsin/EDTA using a mouth-controlled drawn glass pipette. Trypsin was inactivated by adding knockout

DMEM (Gibco) containing 15% ES-cell-compatible FBS, 2 mM L-glutamine, 0.1 mM  $\beta$ -mercaptoethanol, 0.1 mM non-essential amino acids, 1 mM sodium pyruvate, 100 U ml<sup>-1</sup> penicillin and 100  $\mu$ g ml<sup>-1</sup> streptomycin, 1,000 U ml<sup>-1</sup> LIF, 1  $\mu$ M PD0325901 and 3  $\mu$ M CHIR99021. From this point onwards the culture was maintained in the same media on mitotically inactivated MEFs. Media was replaced every other day. After 3–5 days ES-cell-like colonies were observed and passaged at 70% confluence. Stable ES-cell lines were validated by passaging a minimum of ten times without loss of pluripotent morphology or marker expression.

**Genomic analysis.** RRBS was performed as described<sup>22</sup> and bisulphite reads were aligned to the bisulphite-converted mm9 using Bismark<sup>23</sup>. Differentially methylated CpGs were identified using the Fisher exact test with Benjamini–Hochberg correction for multiple testing. We defined DMRs as regions containing at least five differentially methylated CpGs, where contiguous differentially methylated CpGs are separated by 250 bp or less, and for which the total methylation change between wild-type and *Aid*-null cells is 10% or more (calculated using all CpGs within the considered region including those that were not called as differentially methylated). The distribution of DMR lengths was as follows. For hypermethylated DMRs, average, 222 bp; median, 190 bp; minimum, 10 bp; maximum, 4,081 bp. For the lower number of hypomethylated DMRs, we observed the following statistics: average, 229 bp; median, 188 bp; minimum, 19 bp; maximum, 1,250 bp. Paired-end RNA-seq libraries were constructed as previously described<sup>24</sup> and sequenced using an Illumina HiSeq2000. Reads were aligned to mm9 using TopHat and gene

expression levels were quantified using Cufflinks, using upper-quartile and GC-content normalizations. Twofold changes with FPKM > 5 in at least one condition were used to derive differentially expressed genes. All statistical analyses were performed using the R software package. The meta-data for all RBBS data are provided in Supplementary Table 3.

**Quantitative DNA methylation analysis by mass spectrometry.** The level of DNA methylation for specific genes was measured using a MALDI-TOF mass spectrometry based method (EpiTYPER; Sequenom) as previously described<sup>28</sup>. Briefly, 1  $\mu$ g of DNA was treated with sodium bisulphite using the EZ methylation kit (Zymo-Research). The treatment converts non-methylated cytosines into uracil, leaving methylated cytosines unchanged. PCR amplification, addition of SAP solution and Transcription/RNase A cocktails were performed according to the protocol provided by Sequenom and the mass spectra were quantified by the EpiTYPER analyser. Amplicons probed are given in Supplementary Table 2.

25. Vuong, B. Q. et al. Specific recruitment of protein kinase A to the immunoglobulin locus regulates class-switch recombination. *Nature Immunol.* **10**, 420–426 (2009).
26. Nagy, A., Gertsenstein, M., Vintersten, K. & Behringer, R. *Manipulating the Mouse Embryo: A Laboratory Manual* 3rd edn (Cold Spring Harbor, 2003).
27. Joyner, A. L. *Gene Targeting: A Practical Approach* 2nd edn (Oxford Univ. Press, 2000).
28. Ehrich, M. et al. Quantitative high-throughput analysis of DNA methylation patterns by base-specific cleavage and mass spectrometry. *Proc. Natl Acad. Sci. USA* **102**, 15785–15790 (2005).

# A stable transcription factor complex nucleated by oligomeric AML1–ETO controls leukaemogenesis

Xiao-Jian Sun<sup>1</sup>, Zhanxin Wang<sup>2</sup>, Lan Wang<sup>3,4</sup>, Yanwen Jiang<sup>5</sup>, Nils Kost<sup>6</sup>, T. David Soong<sup>7</sup>, Wei-Yi Chen<sup>1</sup>, Zhanyun Tang<sup>1</sup>, Tomoyoshi Nakadai<sup>1</sup>, Olivier Elemento<sup>7</sup>, Wolfgang Fischle<sup>6</sup>, Ari Melnick<sup>5</sup>, Dinshaw J. Patel<sup>2</sup>, Stephen D. Nimer<sup>3,4</sup> & Robert G. Roeder<sup>1</sup>

Transcription factors are frequently altered in leukaemia through chromosomal translocation, mutation or aberrant expression<sup>1</sup>. AML1–ETO, a fusion protein generated by the t(8;21) translocation in acute myeloid leukaemia, is a transcription factor implicated in both gene repression and activation<sup>2</sup>. AML1–ETO oligomerization, mediated by the NHR2 domain, is critical for leukaemogenesis<sup>3–6</sup>, making it important to identify co-regulatory factors that ‘read’ the NHR2 oligomerization and contribute to leukaemogenesis<sup>4</sup>. Here we show that, in human leukaemic cells, AML1–ETO resides in and functions through a stable AML1–ETO-containing transcription factor complex (AETFC) that contains several haematopoietic transcription (co)factors. These AETFC components stabilize the complex through multivalent interactions, provide multiple DNA-binding domains for diverse target genes, co-localize genome wide, cooperatively regulate gene expression, and contribute to leukaemogenesis. Within the AETFC complex, AML1–ETO oligomerization is required for a specific interaction between the oligomerized NHR2 domain and a novel NHR2-binding (N2B) motif in E proteins. Crystallographic analysis of the NHR2–N2B complex reveals a unique interaction pattern in which an N2B peptide makes direct contact with side chains of two NHR2 domains as a dimer, providing a novel model of how dimeric/oligomeric transcription factors create a new protein-binding interface through dimerization/oligomerization. Intriguingly, disruption of this interaction by point mutations abrogates AML1–ETO-induced haematopoietic stem/progenitor cell self-renewal and leukaemogenesis. These results reveal new mechanisms of action of AML1–ETO, and provide a potential therapeutic target in t(8;21)-positive acute myeloid leukaemia.

AML1–ETO consists of the DNA-binding (RUNT) domain of the haematopoietic transcription factor AML1 (also known as RUNX1) and four conserved domains (NHR1–4) of ETO (also known as RUNX1T1)<sup>2</sup>. These domains differentially contribute to AML1–ETO activities in regulating cell proliferation, differentiation and survival<sup>2</sup>. In particular, the NHR2-mediated oligomerization of AML1–ETO has been shown to be critical for leukaemogenesis<sup>3–6</sup>. Although oligomerization endows AML1–ETO with a DNA-binding preference for duplicated AML1 sites<sup>7</sup>, it is important to explore the possibility that oligomerization might also affect cofactor recruitment and function. AML1–ETO is generally thought to act as a transcriptional repressor by recruiting corepressors (for example, NCOR and HDAC proteins) to AML1 target genes<sup>8–10</sup>, or by interacting and interfering with other transcription factors (for example, ETS family proteins, C/EBP $\alpha$ , GATA1 and E proteins)<sup>11–17</sup>. In relation to its functions in gene activation, AML1–ETO also can recruit the coactivators p300 (ref. 18) and PRMT1 (ref. 19). Beyond these indications of dynamic AML1–ETO interactions with diverse proteins, it has been unclear whether AML1–ETO resides in any stable multiprotein

complex(es) that might endow it with new properties that lead to altered regulatory events and corresponding cellular functions.

To identify a natural AML1–ETO-containing complex in leukaemic cells, we used patient-derived Kasumi-1 cells and an antigen-purified anti-ETO antibody that showed high specificity and affinity (Supplementary Fig. 2a, b). The absence of wild-type ETO in Kasumi-1 cells<sup>20</sup> allowed selective isolation of AML1–ETO from derived nuclear extracts, which contained most of the AML1–ETO (Supplementary Fig. 2c). Using a high-stringency buffer to preclude weak or non-specific interactions, we isolated the stable AETFC complex, whose components were identified by SDS–polyacrylamide gel electrophoresis (SDS–PAGE) (Fig. 1a) and mass spectrometry (Supplementary Fig. 3a), and confirmed by immunoblot (Fig. 1b). These components include the AML1-binding partner CBF- $\beta$ , E proteins HEB and E2A, the haematopoietic E-box-binding transcription factor LYL1 (but not its homologue SCL; also known as TAL1), the LIM-domain protein LMO2 and its interacting partner LDB1. Although interactions between some of these factors (or their homologues) have been implicated in a related GATA1–SCL–E2A–LMO2–LDB1 complex in erythrocytes<sup>21</sup>, their connection with AML1–ETO in AML is unknown. A gel-filtration analysis indicated that they form a stable, high-molecular-weight complex (Supplementary Fig. 3b). We then used baculovirus vectors to reconstitute AETFC and to characterize the pairwise interactions within AETFC (Supplementary Fig. 3c, d). The results revealed an interaction network (Fig. 1c) in which several strong interactions link all the components one by one and probably have a major role in AETFC assembly, although some weak interactions may further stabilize the complex.

To assess potentially joint functions of the AETFC components, we performed a chromatin immunoprecipitation coupled with massively parallel DNA sequencing (ChIP-seq) analysis of AML1–ETO, HEB, E2A and LMO2 in Kasumi-1 cells and validated some binding events by ChIP coupled with quantitative polymerase chain reaction (ChIP-qPCR)—for example, on the well-established *CSF1R FIRE*<sup>22</sup> and *SPI1 URE*<sup>23</sup> enhancers. Comparison of their binding sites and enrichment scores indicated a genome-wide co-localization and a correlation of binding strengths, and suggested that the interactions between the components facilitate their binding to the genome (Fig. 1d and Supplementary Fig. 4a–d). Sequence analysis of AML1–ETO-binding regions revealed that both AML1 sites and E-boxes (recognized by E proteins and other basic helix-loop-helix (bHLH) transcription factors including LYL1) were overrepresented (Supplementary Fig. 4e, f), suggesting that, in addition to direct binding to DNA through the RUNT domain, AML1–ETO also binds to DNA indirectly through its interaction with the E-box-binding AETFC components.

To investigate the role of AETFC in regulating gene expression and leukaemogenesis, we performed gene knockdown in Kasumi-1 cells<sup>24</sup>

<sup>1</sup>Laboratory of Biochemistry and Molecular Biology, The Rockefeller University, New York, New York 10065, USA. <sup>2</sup>Structural Biology Program, Sloan-Kettering Institute, Memorial Sloan-Kettering Cancer Center, New York, New York 10065, USA. <sup>3</sup>Molecular Pharmacology and Chemistry Program, Sloan-Kettering Institute, Memorial Sloan-Kettering Cancer Center, New York, New York 10065, USA. <sup>4</sup>Sylvester Comprehensive Cancer Center, Miller School of Medicine, University of Miami, Miami, FL 33136, USA. <sup>5</sup>Division of Hematology and Medical Oncology, Department of Medicine, Weill Cornell Medical College, New York, New York 10065, USA. <sup>6</sup>Laboratory of Chromatin Biochemistry, Max Planck Institute for Biophysical Chemistry, 37077 Göttingen, Germany. <sup>7</sup>Institute for Computational Biomedicine, Weill Cornell Medical College, New York, New York 10065, USA.

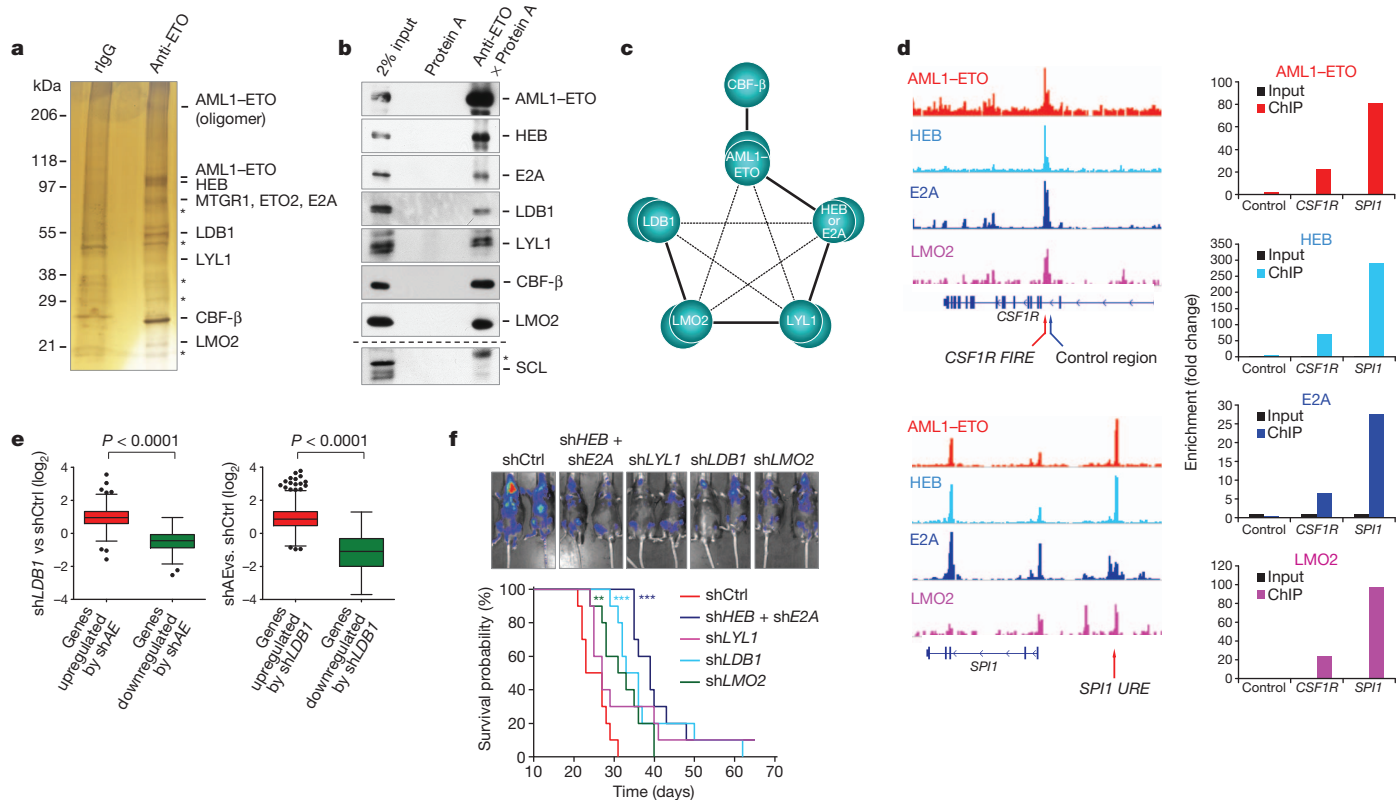


**Figure 1 | AML1-ETO resides in and functions through AETFC.** **a**, SDS-PAGE and silver staining of AETFC isolated from Kasumi-1 nuclear extract. Asterisks, non-specific bands. rIgG, rabbit immunoglobulin G. **b**, Co-immunoprecipitation and immunoblot confirmation of AETFC components. Asterisk, IgG signal. **c**, Schematic of interactions within AETFC. Thick and thin lines denote strong and weak interactions, respectively. Double spheres denote

potential homodimerization of components. **d**, ChIP-seq and ChIP-qPCR analyses of AETFC components on *CSF1R* and *SPI1*. **e**, Correlation between AE and LDB1 in regulating gene expression. shCtrl, control shRNA. **f**, Knockdown of AETFC components delays AE9a-induced leukaemogenesis in mice, indicated by representative bioluminescent imaging (top) and survival curves (bottom;  $n = 10$ ;  $***P < 0.001$ ;  $**P < 0.01$ ).

and in a mouse leukaemic model induced by AML1-ETO9a (AE9a), a leukaemogenic, truncated form of AML1-ETO<sup>25</sup>. First of all, individual knockdowns of AETFC components (but not SCL) significantly decreased some other components at the protein level but not at the messenger RNA level (Supplementary Fig. 5a, b), suggesting a mutual stabilization mechanism within AETFC. Interestingly, SCL mRNA was downregulated by knockdown of any AETFC component (Supplementary Fig. 5b). Because the 3' haematopoietic enhancer of *SCL*<sup>26</sup> is bound by AETFC (Supplementary Fig. 5c), *SCL* is probably a direct target gene of AETFC. In an extension of this observation, global ChIP-seq and RNA-seq analyses revealed that the genes up- and downregulated by one AETFC component were similarly regulated by others (Fig. 1e and Supplementary Fig. 5d). These analyses led to the identification of a set of genes that are both directly bound and cooperatively regulated by AETFC components (Supplementary Fig. 5e and Supplementary Tables 1, 2). We next showed that knockdowns of AETFC components considerably delayed leukaemogenesis in mice (Fig. 1f and Supplementary Fig. 6), indicating a requirement for AETFC components in AML1-ETO-mediated leukaemogenesis. Notably, double knockdown of HEB and E2A most markedly delayed leukaemogenesis, which is consistent with the primary importance of these two E proteins in AETFC assembly/stabilization (Fig. 1c and Supplementary Fig. 5a, f).

To investigate further the function and mechanism of these two E proteins in AETFC, we performed co-immunoprecipitation experiments with a series of deletion mutants of AML1-ETO and HEB, as well as a GST pull-down assay with isolated domains. These analyses clearly established multivalent interactions between AML1-ETO and E proteins and, interestingly, showed that the functionally critical NHR2 domain mediates not only oligomerization but also an interaction with E proteins (Supplementary Fig. 7; ref. 16). We next took

several steps to clarify the relationship between NHR2 oligomerization and the NHR2-E-protein interaction. First, we found that the multisite NHR2 mutation m7, which disrupts NHR2 oligomerization<sup>4</sup>, also completely disrupts the NHR2-E-protein interaction (Fig. 2a, b). Second, we performed an exhaustive screening of NHR2 mutations and found that NHR2 oligomerization and the NHR2-E-protein interaction involve different surfaces of the NHR2  $\alpha$ -helix (Fig. 2a-d). Accordingly, we identified point mutations that specifically disrupt the NHR2-E-protein interaction (Fig. 2b) but not NHR2 oligomerization, as indicated by co-immunoprecipitation (Supplementary Fig. 8) and gel-filtration (Fig. 2c) assays. Third, we found that the mutant-wild-type AML1-ETO heterodimer, unlike the wild-type homodimer, failed to bind HEB( $\Delta$ AD1) (Fig. 2e), indicating that a single wild-type AML1-ETO in the dimer is unable to bind HEB( $\Delta$ AD1) and, thus, that NHR2 oligomerization is required for the NHR2-E-protein interaction.

To clarify further the mechanism of E-protein recognition of the NHR2 oligomer, we first mapped the N2B region in HEB. As a result, we identified a novel, 18-amino-acid N2B motif that is required for the NHR2 interaction (Fig. 3a, b and Supplementary Fig. 9). A subsequent X-ray crystallographic analysis of the NHR2-N2B complex showed that NHR2 formed a tetrameric  $\alpha$ -helical bundle<sup>4</sup> with four N2B peptides bound on two symmetrically related surfaces with 1:1 stoichiometry (Fig. 3c and Supplementary Fig. 10a). After an independent validation of the directionality and register of the bound N2B peptide (Supplementary Fig. 10b, c), we demonstrated that a given N2B binds to a narrow surface channel created by two NHR2 helices, with P191 and S192 of N2B inserted deeply into a surface pocket (Fig. 3d). Notably, P191 of N2B interacts through hydrogen bonding with S522 from one NHR2 helix, while S192 and V194 form hydrogen bonds with E501 and H504, respectively, from another NHR2 helix

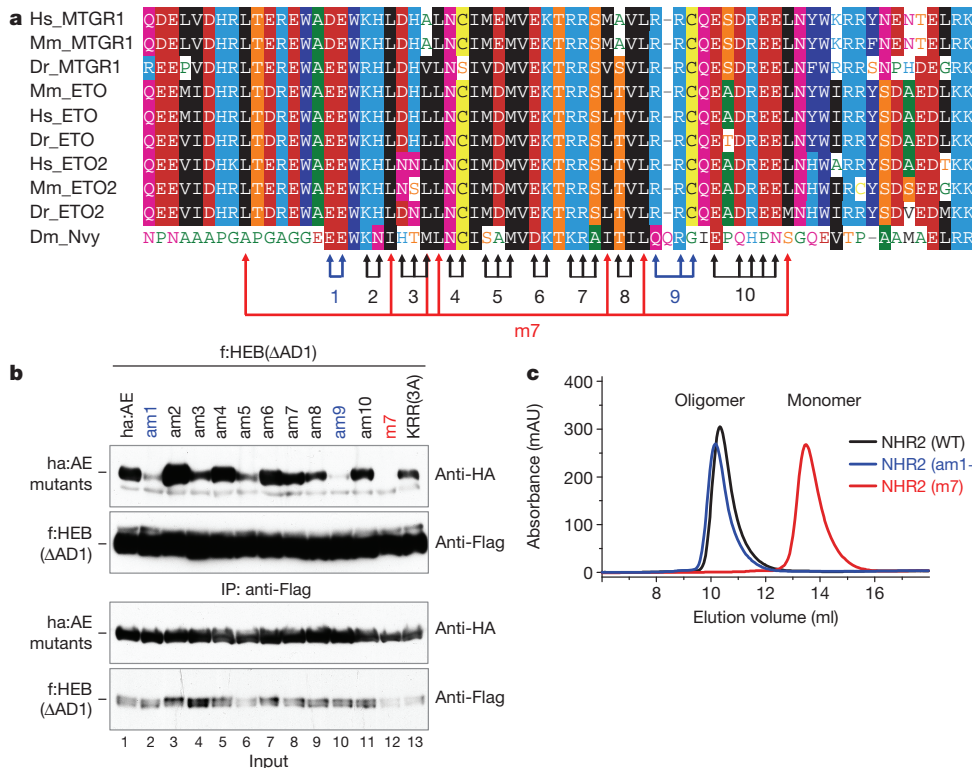


**Figure 2 | The oligomerized AML1-ETO NHR2 domain mediates a specific interaction with E proteins. a, Alignment of the NHR2 of ETO family proteins. Arrows denote residues mutated to alanine in mutants am1–am10, which were screened in this study, and the m7 mutant that disrupts NHR2 oligomerization<sup>4</sup>. Hs, human; Mm, mouse; Dr, zebrafish; Dm, fruit fly. b, Identification of mutations that disrupt the interaction between AE and HEB(ΔAD1). f, Flag tag; ha, HA tag. c, Gel-filtration profiles of wild-type (WT) and mutant NHR2. Wild-type NHR2 and am1+9 NHR2 were eluted as oligomers, and the m7 mutant was eluted as a monomer. d, Distinct surfaces of the NHR2  $\alpha$ -helix mediate oligomerization and the E-protein interaction. e, NHR2 oligomerization is required for the NHR2-E-protein interaction. Mutant-mutant-AE homodimer (lanes 1, 4), mutant-wild-type heterodimer (lanes 2, 5) and wild-type-wild-type homodimer (lanes 3, 6) were formed in 293T cells by co-expression of wild-type AE and NHR2-mutated AE (XX) that fails to interact with HEB(ΔAD1), and their abilities to bind to HEB(ΔAD1) were determined by co-immunoprecipitation. IP, immunoprecipitant.**

mutant was eluted as a monomer. **d**, Distinct surfaces of the NHR2  $\alpha$ -helix mediate oligomerization and the E-protein interaction. **e**, NHR2 oligomerization is required for the NHR2-E-protein interaction. Mutant-mutant-AE homodimer (lanes 1, 4), mutant-wild-type heterodimer (lanes 2, 5) and wild-type-wild-type homodimer (lanes 3, 6) were formed in 293T cells by co-expression of wild-type AE and NHR2-mutated AE (XX) that fails to interact with HEB(ΔAD1), and their abilities to bind to HEB(ΔAD1) were determined by co-immunoprecipitation. IP, immunoprecipitant.

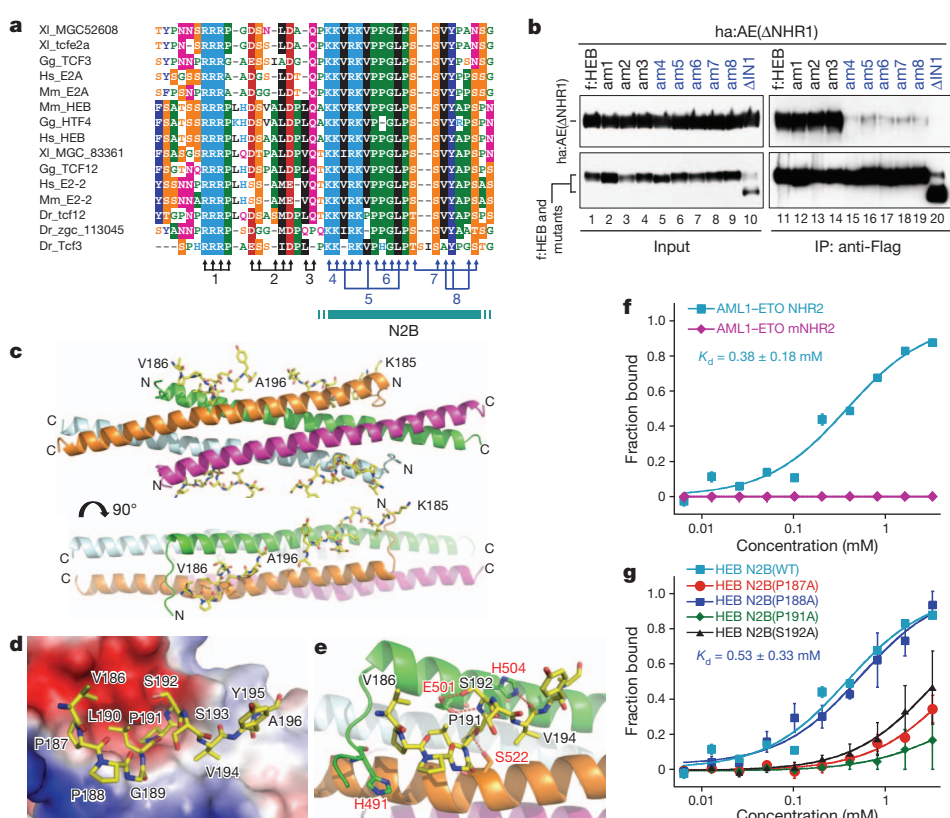


**Figure 3 | Structural details of the NHR2-N2B interaction. a, Alignment of the N2B regions of vertebrate E proteins. Arrows denote residues mutated to alanine in mutants am1–am8. Gg, chicken; Xl, frog. b, Identification of the N2B motif by co-immunoprecipitation. c, Side (top) and look-down (bottom) ribbon views of the structure of the complex between the N2B(177–200) peptide and the tetrameric-helical bundle of NHR2. The N2B peptide is shown in stick representation, and the NHR2 helices in ribbon representation. d, Positioning of the N2B peptide on the electrostatic surface of the NHR2 tetramer. e, One N2B peptide interacts with two NHR2 helices through hydrogen bonds. f, g, Fluorescence-polarization analysis of the binding between NHR2 and a shorter N2B(182–196) peptide, comparing wild-type (WT) and indicated mutants of NHR2 (f) and N2B (g).  $n = 3$ ; mean  $\pm$  standard deviation (s.d.).**

(Fig. 3e). This unique interaction pattern confirms the results of the cell-based assay (Fig. 2e) by showing, unequivocally, that two dimerized NHR2 helices are required for the N2B interaction. To verify the binding specificity further, we made mutations in NHR2 and in a shorter N2B(182–196) peptide, and determined their interactions using fluorescence polarization assays. The results showed that the binding of such a short N2B peptide to NHR2 is relatively weak but highly specific, as the mutation in NHR2 (mNHR2; Supplementary Fig. 11a) completely abolished the binding (Fig. 3f). Reciprocally, single mutations of the key residues P187, P191 or S192 of N2B also significantly reduced the binding, whereas mutation of the less important P188 residue had very little effect (Fig. 3g).

To study the biological relevance of the AML1–ETO–E-protein interactions in leukaemogenesis, we introduced the mNHR2 mutation that specifically disrupts the NHR2–N2B interaction without affecting NHR2 oligomerization (Figs 2c, 3f and Supplementary Fig. 11a, b), as well as the mNHR1 mutation that blocks the NHR1–AD1 interaction<sup>27</sup>. Effects of the NHR1 and NHR2 mutations on AML1–ETO function were initially analysed with the human CD34<sup>+</sup> haematopoietic stem/progenitor cell (HSPC) self-renewal assay<sup>28</sup>. Although AML1–ETO and the mNHR1, mNHR2 and mNHR1+2 mutants exhibited comparable expression levels in transduced CD34<sup>+</sup> cells (Supplementary Fig. 11c), mNHR2 significantly impaired the ability of AML1–ETO to maintain CD34<sup>+</sup> cells (Fig. 4a). We also measured the frequencies of functional HSPCs using cobblestone-area-forming cell (CAFC) and long-term culture-initiating cell (LTC-IC) assays. Notably, mNHR2 significantly reduced the CAFC and LTC-IC colonies in both assays, whereas mNHR1 showed relatively mild effects and no clear synergy between mNHR1 and mNHR2 was evident (Fig. 4b, c). These results suggest that the NHR2–N2B interaction, rather than simply acting additively with the NHR1–AD1 interaction to increase binding affinity, may act as a conformational switch within AETFC (Supplementary Fig. 1a) and thus contribute to AML1–ETO-enhanced HSPC self-renewal. By contrast, these mutations showed no effect on AML1–ETO activities in differentiation inhibition (Supplementary Fig. 12) and cell growth arrest (data not shown). To exclude the possibility that mNHR2 may affect interactions other than the E-protein interaction, we designed (based on the structure) another NHR2 mutation (mNHR2S) that effected a similar loss of E-protein binding but differed completely in sequence from mNHR2. Nevertheless, mNHR2 and mNHR2S showed similar effects in HSPC self-renewal and differentiation (Supplementary Fig. 13), indicating that these effects were specifically caused by disruption of the NHR2–N2B interaction.

To determine whether these interactions are also required for leukaemogenesis *in vivo*, we used the mouse leukaemic model<sup>25</sup> involving transplantation of mouse HSPCs transduced with wild-type and mutated AE9a. In this assay, mice carrying AE9a–mNHR2 showed a significant delay in leukaemogenesis compared with AE9a mice. First, AE9a–mNHR2 mice showed a significantly lower white-blood-cell count than AE9a mice (Fig. 4d), consistent with peripheral blood morphology (Supplementary Fig. 14a). Second, mNHR2 mice had a lower percentage of c-Kit<sup>+</sup>/Mac-1<sup>-</sup>/GFP<sup>+</sup> leukaemic blast cells in their peripheral blood (Supplementary Fig. 14b, c). Third, undifferentiated leukaemic cells were enriched in AE9a mice but not in mNHR2 mice (Fig. 4e). Last, mNHR2 mice survived significantly longer than AE9a mice (Fig. 4f). The mNHR1 mutation again showed relatively mild effects in suppressing leukaemogenesis in mice. Taken together, both human HSPC and mouse transplantation assays clearly showed that the NHR2–N2B interaction is required for AML1–ETO-mediated leukaemogenesis. Given that the extremely high stability of the NHR2 oligomer makes its therapeutic targeting very challenging<sup>4</sup>, the NHR2–N2B interaction potentially offers a new target.

In contrast to previously reported dynamic interactions of various proteins with AML1–ETO under overexpression conditions, this study provides a direct and unbiased analysis of natural AML1–ETO in leukaemic cells, and identifies an endogenous stable complex (AETFC). The

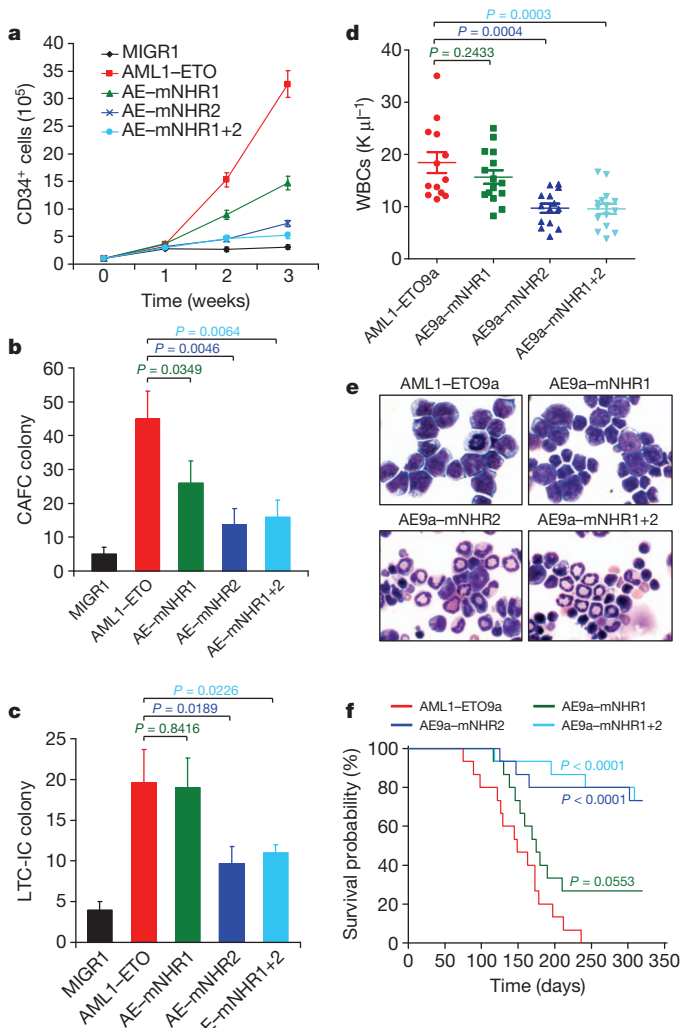


**Figure 4 | Role of the AML1-ETO-E-protein interactions in human HSPC self-renewal and mouse leukaemogenesis.** **a**, Effects of AE and derived mutants in the maintenance of human CD34<sup>+</sup> cells. **b**, CAFC assays measuring the frequency of functional HSPCs in cells transduced with AE or derived mutants. **c**, LTC-IC assays measuring the frequency of functional HSPCs after long-term *in vitro* culture of cells transduced with AE or derived mutants. **a–c**,  $n = 3$ ; mean  $\pm$  s.d. **d**, Effects of AE9a and derived mutants in mouse leukaemogenesis, as indicated by white blood cell (WBC) count of peripheral blood at 4 months after transplantation. **e**, Morphological analysis of mouse bone marrow cells. Original magnification,  $\times 1,000$ . **f**, Kaplan–Meier survival curves of the mice ( $n = 15$ ).

multiple components in AETFC offer opportunities for the recruitment of AML1–ETO to a variety of target genes and for the regulation of gene expression through context-dependent functional interactions with diverse transcriptional coactivators and corepressors (Supplementary Figs 1, 15; further discussion in Supplementary Information). In leukaemic cells, most, if not all, AML1–ETO probably resides in and functions through AETFC, because (1) knockdown of other AETFC components destabilizes AML1–ETO, (2) many AML1–ETO-regulated genes are likewise co-occupied and co-regulated by AETFC components, and (3) knockdowns of AETFC components significantly impair leukaemogenesis. Consistent with the observation that HEB and E2A have essential roles in AETFC assembly and stabilization, and in leukaemogenesis, the direct AML1–ETO–E-protein interaction is shown to be required for leukaemogenesis. Among the two defined AML1–ETO–E-protein interaction sites, surprisingly, the NHR2–N2B interaction, which requires oligomerization of NHR2, is necessary and sufficient for AML1–ETO-mediated leukaemogenesis (further discussed in Supplementary Information). Oligomerization of transcription factors has been known to be

an important regulatory mechanism for modulating their DNA-binding specificity and affinity; and a choice of different oligomerizing partners also contributes to the selective recruitment of cofactors<sup>29,30</sup>. The unique NHR2–N2B interaction provides a novel model in which oligomeric transcription factors use their oligomerization domains to create a new protein-binding interface. Thus, this study reveals new mechanisms of action of oligomerized AML1–ETO in leukaemogenesis, and provides potential therapeutic possibilities.

## METHODS SUMMARY

Kasumi-1 cells were grown in 12-litre spinner flasks (BellCo) and the nuclear extract was prepared with our standard high-salt extraction method. Complex purification was performed in a high stringency buffer (containing 300 mM KCl and 0.1% NP-40). The Bac-to-Bac Baculovirus Expression Systems (Invitrogen) was used to reconstitute the complex in Sf9 cells. ChIP was performed with a dual cross-linking method, and ChIP- and RNA-seq were performed following Illumina protocols. The short hairpin RNA (shRNA) targeting the AML1–ETO fusion site was designed as previously described<sup>24</sup>; and other lentiviral shRNA sets were purchased from Open Biosystems. The co-immunoprecipitation assay was performed in a buffer containing 300 mM NaCl and 1% Triton X-100. Purified N2B peptide and NHR2 domain were mixed at a 1:1 ratio and crystals of the complex were grown by the hanging-drop method. Human HSPC self-renewal and differentiation assays<sup>18,28</sup>, and mouse leukaemogenesis assays<sup>35</sup>, were performed as previously described.

**Full Methods** and any associated references are available in the online version of the paper.

Received 17 December 2012; accepted 13 May 2013.

Published online 30 June 2013.

- Look, A. T. Oncogenic transcription factors in the human acute leukemias. *Science* **278**, 1059–1064 (1997).
- Peterson, L. F. & Zhang, D. E. The 8;21 translocation in leukaemogenesis. *Oncogene* **23**, 4255–4262 (2004).
- Minucci, S. *et al.* Oligomerization of RAR and AML1 transcription factors as a novel mechanism of oncogenic activation. *Mol. Cell* **5**, 811–820 (2000).
- Liu, Y. *et al.* The tetramer structure of the Nervy homology two domain, NHR2, is critical for AML1–ETO's activity. *Cancer Cell* **9**, 249–260 (2006).
- Kwok, C., Zeisig, B. B., Qiu, J., Dong, S. & So, C. W. Transforming activity of AML1–ETO is independent of CBF $\beta$  and ETO interaction but requires formation of homo-oligomeric complexes. *Proc. Natl. Acad. Sci. USA* **106**, 2853–2858 (2009).
- Yan, M., Ahn, E. Y., Hiebert, S. W. & Zhang, D. E. RUNX1/AML1 DNA-binding domain and ETO/MTG8 NHR2-dimerization domain are critical to AML1–ETO9a leukaemogenesis. *Blood* **113**, 883–886 (2009).
- Okumura, A. J., Peterson, L. F., Okumura, F., Boyapati, A. & Zhang, D. E. t(8;21)(q22;q22) fusion proteins preferentially bind to duplicated AML1/RUNX1 DNA-binding sequences to differentially regulate gene expression. *Blood* **112**, 1392–1401 (2008).
- Gelmetti, V. *et al.* Aberrant recruitment of the nuclear receptor corepressor-histone deacetylase complex by the acute myeloid leukemia fusion partner ETO. *Mol. Cell. Biol.* **18**, 7185–7191 (1998).
- Lutterbach, B. *et al.* ETO, a target of t(8;21) in acute leukemia, interacts with the N-CoR and mSin3 corepressors. *Mol. Cell. Biol.* **18**, 7176–7184 (1998).
- Wang, J., Hoshino, T., Redner, R. L., Kajigaya, S. & Liu, J. M. ETO, fusion partner in t(8;21) acute myeloid leukemia, represses transcription by interaction with the human N-CoR/mSin3/HDAC1 complex. *Proc. Natl. Acad. Sci. USA* **95**, 10860–10865 (1998).
- Westendorf, J. J. *et al.* The t(8;21) fusion product, AML1–ETO, associates with C/EBP $\alpha$ , inhibits C/EBP $\alpha$ -dependent transcription, and blocks granulocytic differentiation. *Mol. Cell. Biol.* **18**, 322–333 (1998).
- Mao, S., Frank, R. C., Zhang, J., Miyazaki, Y. & Nimer, S. D. Functional and physical interactions between AML1 proteins and an ETS protein, MEF: implications for the pathogenesis of t(8;21)-positive leukemias. *Mol. Cell. Biol.* **19**, 3635–3644 (1999).
- Elagib, K. E. *et al.* RUNX1 and GATA-1 coexpression and cooperation in megakaryocytic differentiation. *Blood* **101**, 4333–4341 (2003).
- Zhang, J., Kalkum, M., Yamamura, S., Chait, B. T. & Roeder, R. G. E protein silencing by the leukemogenic AML1–ETO fusion protein. *Science* **305**, 1286–1289 (2004).
- Gardini, A. *et al.* AML1/ETO oncoprotein is directed to AML1 binding regions and co-localizes with AML1 and HEB on its targets. *PLoS Genet.* **4**, e1000275 (2008).
- Guo, C., Hu, Q., Yan, C. & Zhang, J. Multivalent binding of the ETO corepressor to E proteins facilitates dual repression controls targeting chromatin and the basal transcription machinery. *Mol. Cell. Biol.* **29**, 2644–2657 (2009).
- Martens, J. H. *et al.* ERG and FLI1 binding sites demarcate targets for aberrant epigenetic regulation by AML1–ETO in acute myeloid leukemia. *Blood* **120**, 4038–4048 (2012).
- Wang, L. *et al.* The leukemogenicity of AML1–ETO is dependent on site-specific lysine acetylation. *Science* **333**, 765–769 (2011).
- Shia, W. J. *et al.* PRMT1 interacts with AML1–ETO to promote its transcriptional activation and progenitor cell proliferative potential. *Blood* **119**, 4953–4962 (2012).
- Miyoshi, H. *et al.* The t(8;21) translocation in acute myeloid leukemia results in production of an AML1–MTG8 fusion transcript. *EMBO J.* **12**, 2715–2721 (1993).
- Wadman, I. A. *et al.* The LIM-only protein Lmo2 is a bridging molecule assembling an erythroid, DNA-binding complex which includes the TAL1, E47, GATA-1 and Ldb1/NLI proteins. *EMBO J.* **16**, 3145–3157 (1997).
- Follows, G. A. *et al.* Epigenetic consequences of AML1–ETO action at the human c-FMS locus. *EMBO J.* **22**, 2798–2809 (2003).
- Huang, G. *et al.* PU.1 is a major downstream target of AML1 (RUNX1) in adult mouse hematopoiesis. *Nature Genet.* **40**, 51–60 (2008).
- Heidenreich, O. *et al.* AML1/MTG8 oncogene suppression by small interfering RNAs supports myeloid differentiation of t(8;21)-positive leukemic cells. *Blood* **101**, 3157–3163 (2003).
- Yan, M. *et al.* A previously unidentified alternatively spliced isoform of t(8;21) transcript promotes leukemogenesis. *Nature Med.* **12**, 945–949 (2006).
- Sanchez, M. *et al.* An SCL 3' enhancer targets developing endothelium together with embryonic and adult haematopoietic progenitors. *Development* **126**, 3891–3904 (1999).
- Park, S. *et al.* Structure of the AML1–ETO eTAFH domain–HEB peptide complex and its contribution to AML1–ETO activity. *Blood* **113**, 3558–3567 (2009).
- Mulloy, J. C. *et al.* The AML1–ETO fusion protein promotes the expansion of human hematopoietic stem cells. *Blood* **99**, 15–23 (2002).
- Amoutzias, G. D., Robertson, D. L., Van de, P. Y. & Oliver, S. G. Choose your partners: dimerization in eukaryotic transcription factors. *Trends Biochem. Sci.* **33**, 220–229 (2008).
- Funnell, A. P. & Crossley, M. Homo- and heterodimerization in transcriptional regulation. *Adv. Exp. Med. Biol.* **747**, 105–121 (2012).

**Supplementary Information** is available in the online version of the paper.

**Acknowledgements** We thank N. A. Speck and J. H. Bushwell for providing the AML1–ETO m7 plasmid, and R. Baer for providing anti-SCL antibodies. This work was supported by National Institutes of Health (NIH) grants CA163086 (R.G.R.), CA129325 (R.G.R.), CA113872 (R.G.R.) and CA166835 (S.D.N.), Starr Cancer Consortium grant I5-A554 (R.G.R., D.J.P. and S.D.N.), Leukemia and Lymphoma Society (LLS) SCOR grants 7013-02 (R.G.R. and S.D.N.) and 7132-08 (R.G.R., A.M. and D.J.P.), and Rockefeller University Center for Clinical and Translational Science Pilot Project grant UL1RR024143 from NIH (X.-J.S.). X.-J.S. was a Starr Cancer Consortium Visiting Fellow. L.W. was an Empire State Stem Cell Scholar and an LLS Fellow. Y.J. was an American Society of Haematology Scholar. W.-Y.C. was an LLS Fellow. D.J.P. was supported by funds from the Abby Rockefeller Mauze Trust and the Maloris Foundation.

**Author Contributions** X.-J.S. and R.G.R. conceived the project. R.G.R. supervised the biochemical studies. S.D.N. supervised the leukaemia pathological studies. D.J.P. supervised the structural studies. A.M. supervised the genomic studies. X.-J.S., Z.W., L.W., Y.J., N.K., T.D.S., W.-Y.C., Z.T., T.N., O.E. and W.F. performed the experiments and analysed the data. X.-J.S. and R.G.R. wrote the paper.

**Author Information** ChIP-seq and RNA-seq data have been deposited in the Gene Expression Omnibus under accession GSE43834. The crystal structure of the NHR2–N2B complex has been deposited in the Protein Data Bank under accession 4JOL. Reprints and permissions information is available at [www.nature.com/reprints](http://www.nature.com/reprints). The authors declare no competing financial interests. Readers are welcome to comment on the online version of the paper. Correspondence and requests for materials should be addressed to R.G.R. (roeder@rockefeller.edu).

## METHODS

**Protein purification and mass spectrometry.** Kasumi-1 cells were grown in 12-litre spinner flasks (BellCo) and the nuclear extract was prepared by our standard high-salt extraction method<sup>31</sup>. A custom anti-ETO antibody (Covance) was developed against a C-terminal peptide of ETO and purified with a recombinant protein. Complex purification was performed in buffer BC300 (20 mM Tris, pH 7.3, 300 mM KCl, 0.2 mM EDTA and 20% glycerol) plus 0.1% NP-40. Eluted proteins were separated by SDS-PAGE and visible bands on the gel were sliced separately and subjected to liquid chromatography coupled with tandem mass spectrometry (LC-MS/MS) analysis. For immunoblots, the following antibodies were used: ETO (Santa Cruz; sc-9737), HEB (Santa Cruz; sc-357), E2A (Santa Cruz; sc-763), LDB1 (Santa Cruz; sc-1198), LYL1 (Abcam; ab30334), CBF- $\beta$  (Pierce; PA1-317), LMO2 (Abcam; ab81988) and SCL (a gift from R. Baer).

**Gel filtration.** The antigen-eluted complex was subjected to gel filtration with a Precision Column PC 3.2/30 that was pre-packed with Superose 6 and connected to an AKTA FPLC system (GE Healthcare). A Superdex 75 column (GE Healthcare) was used to determine the oligomeric states of wild-type and mutant AML1-ETO NHR2.

**Reconstitution of protein complex.** The Bac-to-Bac Baculovirus Expression Systems (Invitrogen) was used to generate recombinant baculoviruses containing each AETFC component. Reconstituted protein complexes were purified from Sf9 insect cells co-infected with different baculoviruses.

**ChIP and ChIP-seq.** Antigen-purified anti-ETO antibody and antibodies against HEB (Santa Cruz; sc-357), E2A (Santa Cruz; sc-763) and LMO2 (Abcam; ab81988) were used for ChIP and ChIP-seq assays. ChIP was performed with a dual cross-linking method. ChIP-seq libraries were constructed following the Illumina protocol and sequenced on the Illumina Genome Analyzer II. Peak-calling/annotation and consensus sequence analyses were performed with ChIPseeker<sup>32</sup>, CisFinder<sup>33</sup> and Cisgenome<sup>34</sup>.

**shRNA knockdown.** The shRNA against AML1-ETO was designed to target the fusion site<sup>24</sup>. Other lentiviral shRNA sets were purchased from Open Biosystems. Virus preparation and cell infection were performed according to the manufacturer's protocol. Knockdown efficiencies were analysed by RT-qPCR and/or immunoblot at 4 days after infection.

**RNA-seq.** Kasumi-1 cells with knockdowns of AETFC components were harvested at 4 days after infection and RNA was extracted with TRIzol Reagent (Invitrogen). Libraries were generated using the TruSeq RNA Sample Preparation Kit (Illumina) and sequenced with Illumina HiSeq2000. The reads were aligned with TopHat and then processed with an in-house program to calculate the reads per kilobase per million reads (RPKM) value for each gene following published methods<sup>35</sup>.

**Cell transfection and co-immunoprecipitation.** 293T cells were transfected using Lipofactamine 2000 (Invitrogen). Cell lysis and co-immunoprecipitation were performed with T/G lysis buffer (20 mM Tris-HCl, pH 7.5, 300 mM NaCl, 50 mM NaF, 2 mM EDTA, 1% Triton X-100 and 20% glycerol), and proteins were analysed by immunoblot.

**GST pull-down.** GST-tagged proteins were expressed in *Escherichia coli* and purified with Glutathione Sepharose 4B (GE Healthcare). The <sup>35</sup>S-labelled prey proteins were synthesized with the TNT Quick Coupled Transcription/Translation System (Promega). Pull-down assays were performed with NETN buffer (20 mM Tris-HCl, pH 8.0, 100 mM NaCl, 1 mM EDTA and 0.5% NP-40), followed by SDS-PAGE and autoradiography analyses.

**Co-expression of N2B fragment and NHR2 domain.** The His-Sumo-tagged N2B(100–219) fragment of HEB and the GST-tagged NHR2(482–551) domain of AML1-ETO were co-expressed in *E. coli* and purified by GST or His pull-down. By serial truncation of N2B from both ends, a short N2B(177–200) peptide was

shown to retain its binding affinity for NHR2, and this N2B fragment was used for crystallization trials.

**Crystallization and structure determination.** Purified N2B(177–200) peptide and NHR2(486–548) domain were mixed at around 1:1 ratio and subjected to crystallization trials. Crystals of the complex were grown by the hanging-drop method at 20 °C in buffer containing 0.1 mM Tris (pH 8.5) and 20% ethanol. A 2.9 Å resolution data set of the complex was collected on beamline 24ID-E at the Advanced Photon Source, Argonne National Laboratory. The initial model was solved by molecular replacement using the free NHR2 structure as the search model. The validation of the directionality and register of the bound N2B peptide were performed with the selenomethionine-labelling method following the introduction of V186M, V194M and corresponding double mutations.

**Fluorescence-polarization-based measurements.** Peptides were labelled with fluorescein at the N terminus. Fluorescence-polarization assays were carried out and analysed using FP buffer (10 mM TEA, 20 mM NaCl, pH 7.4)<sup>36</sup>. Titration series of protein in 10 µl volume and containing 100 nM fluoresceinated peptide in 384-well plates were read multiple times on a Plate Chameleon II plate reader (HIDEX Oy).

**Human HSPC self-renewal and differentiation.** CD34<sup>+</sup> cells were purified from human cord blood samples using the MACS CD34 Isolation Kit (Miltenyi Biotec). After expansion, cells were infected with MIGR1-derived retroviruses. GFP<sup>+</sup>/CD34<sup>+</sup> cells were sorted and grown in basic or differentiation medium and replated weekly. Numbers of HSPC and differentiated cells were determined by cell counting and flow cytometry. For the CAFC assays, CD34<sup>+</sup> cells were co-cultured on an MS-5 monolayer and demi-depopulated weekly. The cobblestone areas were scored at week 5. For LTC-IC assays, the cells were plated at week 6 in methylcellulose with cytokines, and the colony numbers were scored 14 days after seeding<sup>18,28</sup>.

**Mouse fetal liver transplantation and leukaemogenesis assays.** Mouse fetal liver HSPCs were infected with MIGR1-derived retroviruses and cultured in X-VIVO medium (Lonza) with cytokines. Recipient mice were lethally irradiated and transduced fetal liver cells were transplanted into recipient mice by tail-vein injection. Leukaemia development was determined by complete blood count, flow cytometry and morphological analyses of peripheral blood and bone marrow cells<sup>25</sup>. The overall survival of the mice was analysed by the Kaplan-Meier method, and the statistical significance was evaluated by the logrank test. For bioluminescent imaging of leukaemia in mice<sup>37</sup>, AE9a leukaemic cells were transduced with MSCV-Luciferase PGK-hygro (Addgene). On injection of the substrate of luciferase, D-Luciferin, bioluminescent imaging was performed using an IVIS100 imaging system. For gene knockdown assays in the mouse model, a mouse leukaemic cell line was generated from the spleen of the mice bearing AE9a-induced leukaemia. These cells were infected with shRNA lentiviruses, selected by puromycin and injected into recipient mice to generate leukaemia.

31. Dignam, J. D., Lebovitz, R. M. & Roeder, R. G. Accurate transcription initiation by RNA polymerase II in a soluble extract from isolated mammalian nuclei. *Nucleic Acids Res.* **11**, 1475–1489 (1983).
32. Giannopoulou, E. G. & Elemento, O. An integrated ChIP-seq analysis platform with customizable workflows. *BMC Bioinformatics* **12**, 277 (2011).
33. Sharov, A. A. & Ko, M. S. Exhaustive search for over-represented DNA sequence motifs with CisFinder. *DNA Res.* **16**, 261–273 (2009).
34. Ji, H. et al. An integrated software system for analyzing ChIP-chip and ChIP-seq data. *Nature Biotechnol.* **26**, 1293–1300 (2008).
35. Mortazavi, A., Williams, B. A., McCue, K., Schaeffer, L. & Wold, B. Mapping and quantifying mammalian transcriptomes by RNA-Seq. *Nature Methods* **5**, 621–628 (2008).
36. Jacobs, S. A., Fischle, W. & Khorasanizadeh, S. Assays for the determination of structure and dynamics of the interaction of the chromodomain with histone peptides. *Methods Enzymol.* **376**, 131–148 (2004).
37. Zuber, J. et al. Mouse models of human AML accurately predict chemotherapy response. *Genes Dev.* **23**, 877–889 (2009).

# Reshaping of the conformational search of a protein by the chaperone trigger factor

Alireza Mashaghi<sup>1</sup>, Günter Kramer<sup>2</sup>, Philipp Bechtluft<sup>1</sup>, Beate Zachmann-Brand<sup>2</sup>, Arnold J. M. Driessens<sup>3</sup>, Bernd Bukau<sup>2</sup> & Sander J. Tans<sup>1</sup>

Protein folding is often described as a search process, in which polypeptides explore different conformations to find their native structure. Molecular chaperones are known to improve folding yields by suppressing aggregation between polypeptides before this conformational search starts<sup>1,2</sup>, as well as by rescuing misfolds after it ends<sup>1,3</sup>. Although chaperones have long been speculated to also affect the conformational search itself—by reshaping the underlying folding landscape along the folding trajectory<sup>4,5</sup>—direct experimental evidence has been scarce so far. In *Escherichia coli*, the general chaperone trigger factor<sup>6–8</sup> (TF) could play such a role. TF has been shown to interact with nascent chains at the ribosome<sup>9,10</sup>, with polypeptides released from the ribosome into the cytosol<sup>11</sup>, and with fully folded proteins before their assembly into larger complexes<sup>12</sup>. To investigate the effect of TF from *E. coli* on the conformational search of polypeptides to their native state, we investigated individual maltose binding protein (MBP) molecules using optical tweezers. Here we show that TF binds folded structures smaller than one domain, which are then stable for seconds and ultimately convert to the native state. Moreover, TF stimulates native folding in constructs of repeated MBP domains. The results indicate that TF promotes correct folding by protecting partially folded states from distant interactions that produce stable misfolded states. As TF interacts with most newly synthesized proteins in *E. coli*, we expect these findings to be of general importance in understanding protein folding pathways.

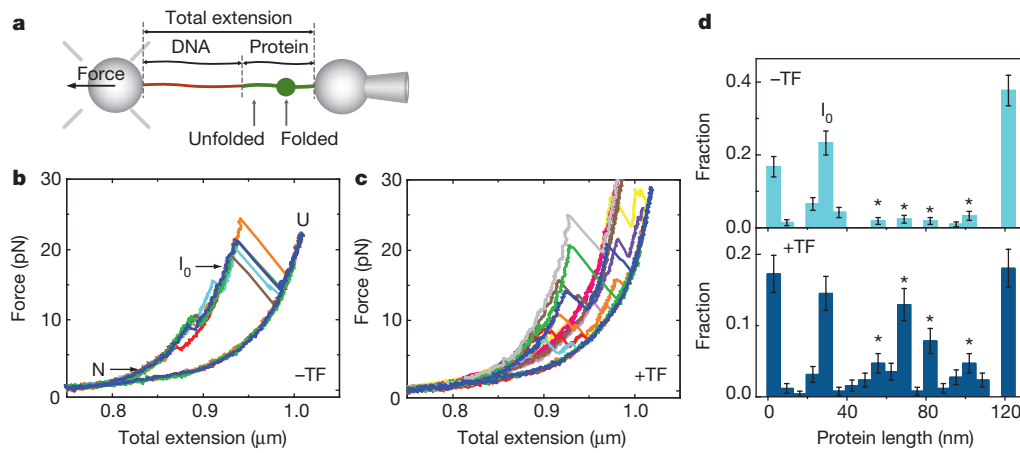


**Figure 1 | TF promotes partial protein folds.** **a**, Schematic diagram of the setup. MBP (green) is tethered between two beads: one (right) is held on a position-controlled micropipette; the other (left) is held by an optical trap that allows force detection. At the amino terminus, MBP is attached to a bead by a 920-nm-long DNA tether (orange) via streptavidin–biotin linkages. The DNA is attached to the bead using antibody–digoxigenin linkages. At the carboxy terminus, MBP is attached to a bead via an antibody–myc-tag connection. **b**, Stretching–relaxation experiments in the absence of TF. The force–extension data shows a frequently visited intermediate state I<sub>0</sub> in between the fully folded

Atomic force microscopes and optical tweezers can be used to study protein folding at the single-molecule level<sup>13,14</sup>. By pulling proteins at their ends while accurately monitoring lengths and forces, one can directly observe partially folded states that are only transiently stable, and follow transitions between them. This method has been used primarily to investigate isolated proteins<sup>15,16</sup> or proteins that interact with metal ions<sup>17</sup> or ligands<sup>18,19</sup>, but rarely to address how folding is affected by chaperones<sup>20</sup>. Here we investigate how the chaperone trigger factor (TF) influences the folding of two proteins: the single-domain MBP, which folds efficiently in isolation, and an MBP repeat construct, which has a high tendency to misfold. This approach made it possible to distinguish how TF affects the folding transitions within one domain and misfolding between domains.

In the absence of any chaperone, stretching MBP molecules with optical tweezers (Fig. 1a and Supplementary Fig. 1) results in a simple unfolding pattern in the force–extension domain that involves two transitions<sup>20</sup> (Fig. 1b). When the force reached 10 pN on average, the measured total protein length had increased by 28 nm, indicating the unfolding of a polypeptide segment of that length. The remaining structure unfolded completely at around 22 pN, yielding the full MBP length of 120 nm. After relaxation to zero force, the polypeptide chain was allowed to refold for 5 s. Subsequent stretching typically showed either a fully folded or fully unfolded state, as evidenced by a curve similar to the first or by a curve lacking unfolding features

state N and the unfolded state U. **c**, Stretching–relaxation experiments in the presence of TF (1 μM), indicating frequently visited additional stable states of intermediate protein length. **d**, Protein length distribution of stable states without (light blue) and with (dark blue) TF, as derived from the force–extension data. Lengths are determined by fitting to the worm-like chain model<sup>29</sup>. Error bars,  $\pm 1$  s.d. The native, I<sub>0</sub> and fully extended states correspond to lengths of about 0 nm, 28 nm and 120 nm. The number of times a state with a certain length is visited is indicated as a fraction of the total number of visits to all states. See main text for meaning of asterisks.

<sup>1</sup>FOM institute AMOLF, Science Park 104, 1098 XG Amsterdam, The Netherlands. <sup>2</sup>Zentrum für Molekulare Biologie der Universität Heidelberg (ZMBH), DKFZ-ZMBH Allianz, Im Neuenheimer Feld 282, Heidelberg 69120, Germany. <sup>3</sup>Department of Molecular Microbiology, Groningen Biomolecular Sciences and Biotechnology Institute and the Zernike Institute for Advanced Materials, University of Groningen, Nijenborgh 7, 9749 AG Groningen, The Netherlands.

(refolding rate  $\sim 0.7 \text{ s}^{-1}$ ), in line with a two-state folding process<sup>20</sup>. Analysis of many stretching curves showed that a small fraction displayed additional protein states that were visited briefly (for less than 1 s) during unfolding (9% of observed states,  $N = 215$ ). In the distribution of protein lengths, these states are seen as four small but significant peaks between 40 and 110 nm (indicated by asterisks in Fig. 1d), which are consistent with partially folded states observed previously during atomic force microscope unfolding of MBP and truncated MBP constructs<sup>21</sup>. Thus, a number of partially folded MBP states can be transiently stable during unfolding in the absence of chaperone.

In the presence of TF (1  $\mu\text{M}$ , Methods) the first stretching curves were unchanged, but subsequent stretching and relaxation data were quite different (Fig. 1c). The intermediate protein lengths that were rare without chaperone were now observed frequently and for longer times (of the order of seconds). Consequently, the four additional peaks in the distribution of observed lengths were substantially higher (Fig. 1d, asterisks). The peaks were distinct, suggesting that in different experiments the protein chains repeatedly adopted similar structures. The broadness of some peaks, and the small unfolding transitions observed occasionally (Supplementary Fig. 2), did indicate small structural variations. Overall, the increased peak heights indicated that TF promoted the presence of partially folded states. The correspondence in peak positions (Fig. 1d, asterisks) suggested that they contained elements of the MBP native state.

To probe interactions within the TF-promoted partial folds, we considered how they were disrupted by force. Disruption occurred in discrete steps at high force, consistent with the unfolding of partial folds that exhibit tertiary structure. In contrast, if the polypeptide were sequestered on TF without tertiary structure, disruption would be

expected to occur gradually. We found that with TF the unfolding force of partial folds was almost twice that without (15 versus 27 pN on average, Fig. 2a). Some unfolding forces exceeded even 40 pN, which is significantly higher than the force at which the native state unfolds without chaperone (22  $\pm$  5 pN). These data indicate that TF either bound the partial folds directly, or that it simultaneously bound the two non-folded polypeptide segments directly flanking the folded structure. Stabilization by TF thus seems to have similarities with the stabilization of fully folded proteins by ligand binding<sup>19</sup>. Unfolding of the partial folds could be triggered by (partial) TF dissociation. This scenario would be consistent with reported TF-substrate lifetimes<sup>22–24</sup>, which are of similar order (between 0.1 and 100 s) to that of the stretching experiments (several seconds).

The protection against forced unfolding suggests that TF may also stabilize partial folds in the absence of force, and thus affect folding to the native state. To address this issue, we analysed folding transitions during the 5-s waiting periods at zero force in the presence of TF, by comparing protein lengths before and after this period (Fig. 2b–e). Sometimes, the protein length increased (14%,  $N = 33$ ; Supplementary Fig. 2) or remained constant (22%; Fig. 2d, experiment 2), indicating that the folded structure had unfolded or remained stable, respectively. Most often however (64%) the protein length decreased, indicating that a larger part of the protein chain had become folded. We observed the full range of these refolding transitions: from unfolded to an intermediate length (Fig. 2e, experiment 2), from an intermediate length to a shorter one (Fig. 2c, experiment 2), and from a shorter one onwards to the native length (Fig. 2c experiment 4 and Fig. 2b experiment 2). Given the 5-s waiting period, the average lifetime of TF-promoted partial folds is thus of the order of seconds<sup>25</sup>. These visits to partial folds thus significantly decrease the overall folding rate,

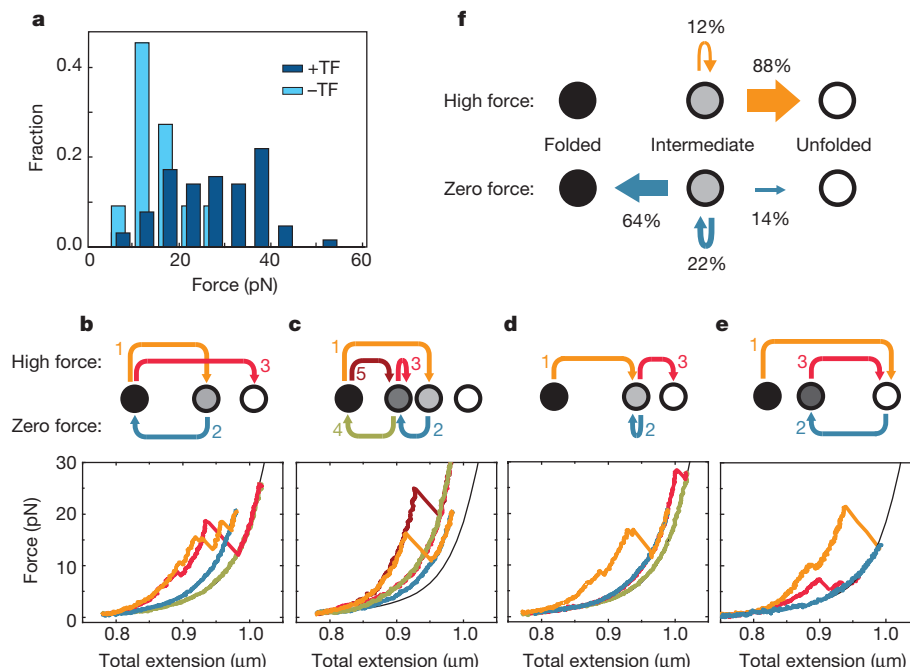


**Figure 2 |** TF stabilizes partial folds and mediates folding transitions.

a, Distribution of forces maximally sustained by partial MBP folds (protein lengths between 40 and 110 nm). In the presence (dark blue) of TF the forces are higher than in its absence (light blue), indicating protection against forced unfolding. b–e, Transitions between folded states with TF. In the diagrams (top), circles represent protein states, with white the fully extended state and black the most compact state. Arrows represent transitions between these states during stretching (high force) or relaxation followed by waiting at zero force for 5 s (zero force). Numbers indicate the order of experiments. Graphs (bottom) show force–extension curves, with the colours corresponding to the arrows shown in diagrams above. At high force, proteins typically unfold but can also

remain intact (c, experiment 3). At zero force, the data show the full spectrum of folding transitions: from unfolded to intermediate (e, experiment 2), from intermediate to another intermediate (c, experiment 2), and from intermediate to native (c, experiment 4, and b, experiment 2), as evidenced by subsequent characteristic unfolding pattern (b, experiment 3). The protein length can also remain unchanged (d, experiment 2). For clarity, the stretching–relaxation behaviour of fully unfolded protein with DNA tether is indicated by a black line. f, Average probabilities of decreasing, maintaining or increasing the protein length in the stretching (high force) and relaxation (zero force) experiments with TF, starting from any intermediate MBP fold (b–e).

consistent with bulk studies<sup>11,22,26</sup>. The partially folded states were not observed when pulling from zero force in the absence of TF, suggesting they were either visited too briefly during refolding at zero force, or did not form at all. In the absence of applied force, TF thus transiently stabilized partial folds, resulting in a step-wise refolding via these partial folds. To test the generality of these central findings, we performed a similar set of experiments on a different substrate, namely the protein luciferase, which gave comparable results (Supplementary Fig. 6).

Two main lines of evidence indicate that TF-mediated folding leads to the native structure. First, we found MBP function is restored after chemical denaturing and refolding in the presence of TF in a bulk assay, as tested by amylose binding (Fig. 3a). Second, after unfolding by force and relaxation, subsequent stretching experiments displaying the characteristic two-step native unfolding pattern indicated that MBP had natively refolded (Fig. 2b experiment 3). Once MBP is folded natively, we find that it binds TF only weakly or not at all. This can be seen in the optical tweezers experiments, where the first stretching curve showed the same unfolding pattern and unfolding force—with or without TF. In bulk, a column retardation assay further confirmed this lack of interaction (Fig. 3c). Partial folds do interact with TF (Fig. 2a). To confirm this in a bulk assay, we purified MBP constructs that are truncated and thus cannot form the full MBP native state but can form partially folded structures (Fig. 3b). TF indeed bound these truncates in column retardation assays, in contrast to the full-length MBP (Fig. 3c). TF-truncate binding was also evidenced by a suppression of heat-induced aggregation (Fig. 3d). Overall, the data confirm

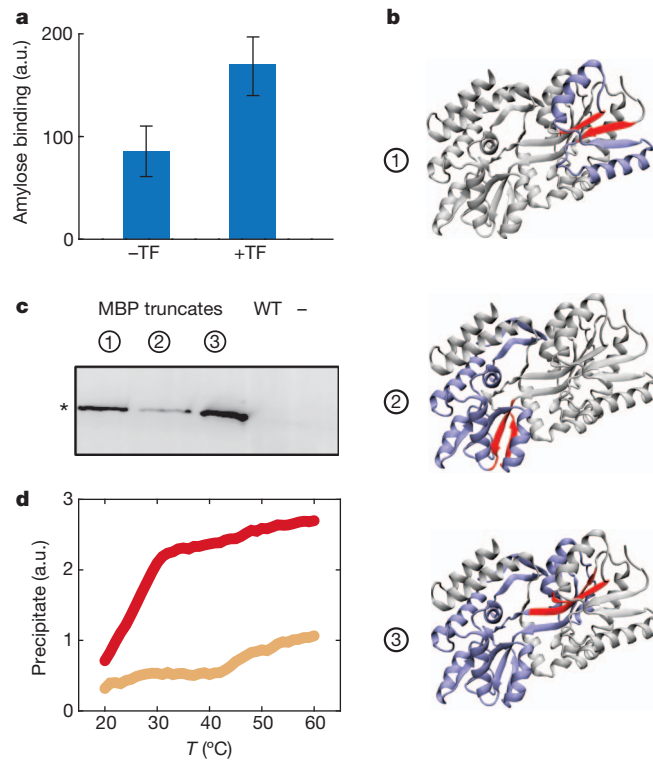


**Figure 3 | TF binds partially folded states, not the native state.** **a**, Bulk refolding and functional assay of MBP. Indicated is the amount of protein specifically bound to amylose, a mimic of the natural MBP substrate maltose, after chemical denaturation and subsequent refolding without and with TF (see Methods). a.u., arbitrary units. **b**, Constructed MBP truncates 1–3 in purple and red, with red indicating their C and N termini (see Methods, Supplementary Figs 3 and 4). **c**, TF binding to MBP truncates. All three MBP truncates bind TF, natively folded MBP (wild type; WT) does not. See Methods. **d**, Thermal aggregation assay. Displayed is an Fourier transform infrared (FTIR) signal that indicates the amount of precipitated MBP truncate 3 (**b**) as a function of temperature, in the absence (red) and presence (orange) of TF (see Methods).

that TF binds partial folds along the folding pathway until it reaches the native state.

We surmised that TF association could be particularly beneficial for complex multi-domain proteins, which can suffer from misfolding interactions between domains<sup>27</sup>. To test this hypothesis, we performed stretching experiments on a construct composed of four MBP repeats (MBP<sub>4</sub>). When unfolded MBP<sub>4</sub> was relaxed in the absence of chaperone, subsequent stretching typically showed it had become as compact as native MBP<sub>4</sub> but it failed to unfold<sup>20</sup> (Fig. 4a). This suggested that tight misfolding interactions had formed between domains. When unfolding did occur, the length increases were typically more than one full-length domain (370 residues). This large step-size indicated the disruption of interactions between domains, though less tight than observed without chaperone. Occasionally we observed signatures of native-like folds involving just one domain, as characterized by unfolding forces below 30 pN and length changes smaller than one MBP repeat. Overall, we found that the major part of the protein chain (73% on average,  $N = 41$  stretching curves) was involved in tight (35%) or weak (38%) misfolding interactions, and the rest (27%) in native interactions (Fig. 4b). These data indicate a strong tendency for MBP<sub>4</sub> to misfold.

In the presence of TF, the first stretching curve on fresh MBP<sub>4</sub> was similar to curves without TF. However, subsequent stretching of the same construct after relaxation showed marked differences (Fig. 4a). Strikingly, with TF present, although weak misfolding interactions were still substantial (35%), the tight misfolds that failed to unfold were only rarely observed (less than 4%). The majority of the protein chain was now involved in native unfolding signatures (61%,  $N = 55$ , Fig. 4b). As a result, over 10 unfolding–refolding cycles on one construct could sometimes be followed, contrasting with a maximum of 3

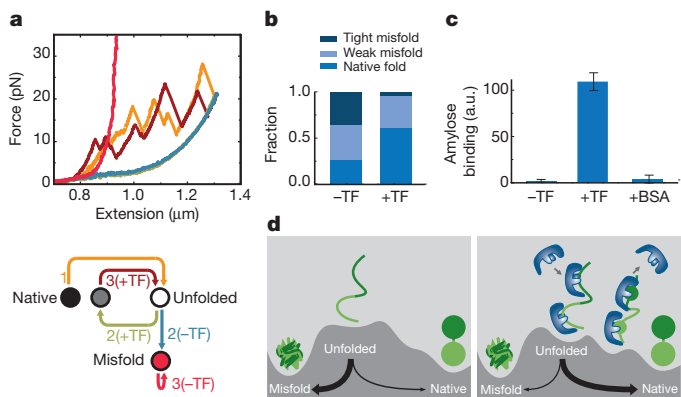


**Figure 4 | TF suppresses misfolding between domains.** **a**, Force–extension curves for a four MBP repeat construct, with and without TF (1  $\mu$ M). See Fig. 2 legend for description of diagram under. Without TF: after unfolding (experiment 1, orange), relaxation (2, blue), waiting at zero force for 5 s, stretching (3, bright red) shows no unfolding, indicating tight misfolding interactions between domains. With TF: after unfolding (not shown) and relaxation (2, green), waiting at zero force, stretching (3, dark red) showed extension changes characteristic of native interactions (for example, at  $\sim 1.23$   $\mu$ m) and weak non-native interactions (at  $\sim 1.10$   $\mu$ m), but no tight ones. **b**, Misfolded and folded fractions with and without TF. Indicated are the fractions of the polypeptide length involved in native, weak and tight misfolding interactions (see main text). Data are derived from multiple force–distance curves ( $N = 41$  without,  $N = 55$  with TF). **c**, Bulk refolding and functional assay of the multi-domain protein. Indicated is the amount of protein specifically bound to amylose, after chemical denaturation and subsequent refolding without and with TF, and with the protein BSA (Methods, Supplementary Fig. 4). **d**, Cartoon of folding landscape reshaping by TF. Left, without chaperone, interactions between domains leads to efficient misfolding. Right, the stabilization of partial folds by TF can be seen as a deepening or formation of energy valleys. The barrier heights to misfolds are increased more than to native folds, in line with the promotion of local over distant interactions along the polypeptide.

cycles due to tight misfolding in the absence of TF. We further probed native refolding of MBP<sub>4</sub> in a bulk assay, which showed that in the absence of chaperone MBP<sub>4</sub> failed to refold to a functional state, whereas the presence of TF restored native folding, as shown by a more than tenfold increase in amylose binding ability (Fig. 4c, Methods). A control experiment in which bovine serum albumin (BSA) was used instead of TF again led to misfolding and an inability to bind amylose, indicating that the effect of TF is not caused by aspecific interactions. We note that although vectorial synthesis and co-translational folding may in principle also suppress misfolding between domains<sup>28</sup>, interactions with TF delay folding until nascent chain lengths are well beyond the average size of one domain<sup>26</sup>. Thus, the propensity of TF to promote native folding within domains while suppressing long range interactions is of central importance to *de novo* protein folding.

The results may be summarized by considering the underlying folding energy landscape (Fig. 4d). By binding and protecting partial folds, TF induces energy valleys or deepens existing ones, and hence directs folding pathways along these states towards native folds and away from misfolds. In contrast, the chaperone SecB binds only non-folded polypeptide, in a manner that suppresses folding altogether<sup>20</sup>. The ability of TF to combine binding with folding could stem from its highly flexible structure and heterogeneous surface<sup>6</sup>. These features may allow TF to interact dynamically with substrates as they fold, either by remaining partially bound when folding transitions occur, or by unbinding fully. Interestingly, the data suggest a simple mechanism by which TF resolves the generic chaperone challenge of distinguishing native folding from misfolding: by interacting with a restricted region of the polypeptide, TF could effectively promote local native contacts by shielding this region from misfolding interactions with distant regions, hence allowing shielded domains to fold quasi-independently from the rest. Given the minimal requirements for this mechanism, it is intriguing to consider whether it is employed by other chaperone systems as well.

Our study has shown that the conformational search of a polypeptide for its native state can be influenced directly by a chaperone. The generic interaction between chaperones and proteins suggests that this chaperone-induced reshaping of the folding energy landscape is of general importance to our understanding of protein folding.

## METHODS SUMMARY

Expression and purification of MBP and MBP<sub>4</sub> constructs, DNA linker and bead preparation, and the characteristics of the optical tweezers have been described previously<sup>20</sup>. Expression and purification of TF is described in Methods. Bulk refolding of MBP<sub>4</sub> was assayed by chemical denaturing, followed by refolding in the presence or absence of TF, testing of the ability to bind amylose resin, and quantification of protein amounts by SDS-PAGE, Coomassie staining and densitometric analysis using the analysis software Image Gauge (Methods). To test the affinity of TF for MBP partial folds, N-terminally biotinylated MBP truncates (Supplementary Fig. 4) were engineered, purified (Methods), immobilized on Streptactin Sepharose and incubated with purified TF. Bound TF was eluted and detected by western blotting using TF-specific polyclonal antibodies (Methods).

**Full Methods** and any associated references are available in the online version of the paper.

Received 5 December 2012; accepted 14 May 2013.

Published online 7 July 2013.

1. Hartl, F. U., Bracher, A. & Hayer-Hartl, M. Molecular chaperones in protein folding and proteostasis. *Nature* **475**, 324–332 (2011).
2. Kramer, G., Boehringer, D., Ban, N. & Bukau, B. The ribosome as a platform for co-translational processing, folding and targeting of newly synthesized proteins. *Nature Struct. Mol. Biol.* **16**, 589–597 (2009).

3. Sharma, S. K., De los Rios, P., Christen, P., Lustig, A. & Goloubinoff, P. The kinetic parameters and energy cost of the Hsp70 chaperone as a polypeptide unfoldase. *Nature Chem. Biol.* **6**, 914–920 (2010).
4. Dobson, C. M. Protein folding and misfolding. *Nature* **426**, 884–890 (2003).
5. Bartlett, A. I. & Radford, S. E. An expanding arsenal of experimental methods yields an explosion of insights into protein folding mechanisms. *Nature Struct. Mol. Biol.* **16**, 582–588 (2009).
6. Hoffmann, A., Bukau, B. & Kramer, G. Structure and function of the molecular chaperone Trigger Factor. *Biochim. Biophys. Acta* **1803**, 650–661 (2010).
7. Wegrzyn, R. D. & Deuerling, E. Molecular guardians for newborn proteins: ribosome-associated chaperones and their role in protein folding. *Cell. Mol. Life Sci.* **62**, 2727–2738 (2005).
8. Merz, F. et al. Molecular mechanism and structure of Trigger Factor bound to the translating ribosome. *EMBO J.* **27**, 1622–1632 (2008).
9. Ferbitz, L. et al. Trigger factor in complex with the ribosome forms a molecular cradle for nascent proteins. *Nature* **431**, 590–596 (2004).
10. Kramer, G. et al. L23 protein functions as a chaperone docking site on the ribosome. *Nature* **419**, 171–174 (2002).
11. Agashe, V. R. et al. Function of trigger factor and DnaK in multidomain protein folding: increase in yield at the expense of folding speed. *Cell* **117**, 199–209 (2004).
12. Martinez-Hackert, E. & Hendrickson, W. A. Promiscuous substrate recognition in folding and assembly activities of the trigger factor chaperone. *Cell* **138**, 923–934 (2009).
13. Borgia, A., Williams, P. M. & Clarke, J. Single-molecule studies of protein folding. *Annu. Rev. Biochem.* **77**, 101–125 (2008).
14. Fisher, T. E., Marszalek, P. E. & Fernandez, J. M. Stretching single molecules into novel conformations using the atomic force microscope. *Nature Struct. Biol.* **7**, 719–724 (2000).
15. Cecconi, C., Shank, E. A., Bustamante, C. & Marqusee, S. Direct observation of the three-state folding of a single protein molecule. *Science* **309**, 2057–2060 (2005).
16. Fernandez, J. M. & Li, H. Force-clamp spectroscopy monitors the folding trajectory of a single protein. *Science* **303**, 1674–1678 (2004).
17. Jakobi, A. J., Mashaghi, A., Tans, S. J. & Huizinga, E. G. Calcium modulates force sensing by the von Willebrand factor A2 domain. *Nature Commun.* **2**, 385 (2011).
18. Junker, J. P., Ziegler, F. & Rief, M. Ligand-dependent equilibrium fluctuations of single calmodulin molecules. *Science* **323**, 633–637 (2009).
19. Cao, Y., Balamurali, M. M., Sharma, D. & Li, H. A functional single-molecule binding assay via force spectroscopy. *Proc. Natl. Acad. Sci. USA* **104**, 15677–15681 (2007).
20. Bechtluft, P. et al. Direct observation of chaperone-induced changes in a protein folding pathway. *Science* **318**, 1458–1461 (2007).
21. Bertz, M. & Rief, M. Mechanical unfoldings as building blocks of maltose-binding protein. *J. Mol. Biol.* **378**, 447–458 (2008).
22. Maier, R., Scholz, C. & Schmid, F. X. Dynamic association of trigger factor with protein substrates. *J. Mol. Biol.* **314**, 1181–1190 (2001).
23. Kaiser, C. M. et al. Real-time observation of trigger factor function on translating ribosomes. *Nature* **444**, 455–460 (2006).
24. Lakshmiapathy, S. K., Gupta, R., Pinkert, S., Etchells, S. A. & Hartl, F. U. Versatility of trigger factor interactions with ribosome-nascent chain complexes. *J. Biol. Chem.* **285**, 27911–27923 (2010).
25. Park, S., Klein, T. E. & Pande, V. S. Folding and misfolding of the collagen triple helix: Markov analysis of molecular dynamics simulations. *Biophys. J.* **93**, 4108–4115 (2007).
26. Hoffmann, A. et al. Concerted action of the ribosome and the associated chaperone trigger factor confines nascent polypeptide folding. *Mol. Cell* **48**, 63–74 (2012).
27. Han, J. H., Batey, S., Nickson, A. A., Teichmann, S. A. & Clarke, J. The folding and evolution of multidomain proteins. *Nature Rev. Mol. Cell Biol.* **8**, 319–330 (2007).
28. Jaenicke, R. Stability and folding of domain proteins. *Prog. Biophys. Mol. Biol.* **71**, 155–241 (1999).
29. Marko, J. F. & Siggia, E. D. Stretching DNA. *Macromolecules* **28**, 8759–8770 (1995).

**Supplementary Information** is available in the online version of the paper.

**Acknowledgements** Work in the laboratory of S.J.T. is part of the research programme of the Stichting voor Fundamenteel Onderzoek der Materie (FOM), which is financially supported by the Nederlandse Organisatie voor Wetenschappelijke Onderzoek (NWO). Work in the laboratory of B.B. and G.K. is supported by grants from the Deutsche Forschungsgemeinschaft (SFB 638, FOR967). We are grateful to M. Meyer for his support in performing and analysing FTIR experiments. We thank T. Shimizu, L. Guilbride, M. Dogterom and members of the Tans group for critical reading of the manuscript.

**Author Contributions** S.J.T. and A.M. conceived and designed the research; P.B., A.J.M.D. and B.Z.-B. designed and purified the MBP protein constructs; A.M. and P.B. performed the optical tweezers experiments; G.K. and B.Z.-B. purified the TF and MBP truncates and performed the bulk refolding experiments; A.M. and S.J.T. analysed the data; and A.M., G.K., B.B. and S.J.T. wrote the paper.

**Author Information** Reprints and permissions information is available at [www.nature.com/reprints](http://www.nature.com/reprints). The authors declare no competing financial interests. Readers are welcome to comment on the online version of the paper. Correspondence and requests for materials should be addressed to S.J.T. (tans@amolf.nl).

## METHODS

**Contact map with high-energy contact regions.** The 3D conformation of MBP (PDB 1jw4) can be represented in a symmetrical, square, Boolean adjacency matrix ( $A_{ij}$ ) of pairwise, inter-residue contacts.  $A_{ij}$  was constructed using a threshold of 7 Å in spatial distance between the residue's C $\alpha$  atoms. Nearest neighbour contacts, with a distance  $d(A_{ij}, A_{kl}) = ((i - k)^2 + (j - l)^2)^{1/2}$  of less than 2, were considered to form a single contact region. The shortest range interactions, between residues spaced less than 20 residues along the polypeptide, were not considered. The stability of the contact regions was crudely estimated by summing empirical Thomas–Dill energies<sup>30</sup> of all the residue–residue contacts within that region. The residues involved in the 5 most stable contact regions are indicated in red in Supplementary Fig. 4. These contact residues define the ends of a sub-structure, as indicated in purple in Supplementary Fig. 4. 4 of the 5 sub-structures are nested, such that for instance one large sub-structure (Supplementary Fig. 4e) encompasses 3 other sub-structures (Supplementary Fig. 4b–d). One of the stable sub-structures is independent of the others (Supplementary Fig. 4a). One may consider that two independent sub-structures are present simultaneously, and either interact and thus form one larger fold (for example, Supplementary Fig. 4a and e, which together form the core state), or do not interact, giving two distinct folds.

**TF expression and purification.** TF with a Ulp1-cleavable N-terminal His<sub>6</sub>-SUMO tag was expressed from vector pCA528-tig in *E. coli* BL21 DE3Atig::Kan by induction with 1 mM isopropyl-1-thio-β-D-galactopyranoside at 30 °C. The protein was purified using Ni-IDA matrix (Protino, Macherey-Nagel); eluted material was supplemented with His<sub>6</sub>-Ulp1 protease, dialysed overnight, and contaminants were removed by incubation with Ni-IDA matrix and subsequent anion-exchange chromatography (Resource Q, GE Healthcare).

**Bulk MBP and MBP<sub>4</sub> refolding assay.** 2.5 μM MBP<sub>4</sub> and 10 μM MBP were denatured by incubation in RF buffer (50 mM HEPES-KOH, pH 7.5, 100 mM KCl, 5 mM MgCl<sub>2</sub>) containing 8 M urea at 37 °C for 12 h and subsequently for 5 min at 60 °C. Samples were diluted 1:10 in RF buffer in the absence or presence of TF (2 μM) in a final volume of 50 μl and incubated for 15 min at 30 °C. Forty microlitres amylose magnetic beads (NEB) equilibrated in RF buffer were added and samples were incubated at 4 °C for 15 min. Resin was washed four times in 1 ml RF buffer and bound MBP or MBP<sub>4</sub> was eluted by resuspending the resin in 40 μl RF buffer containing 20 mM maltose followed by centrifugation and collection of the supernatant. Samples were subjected to SDS-PAGE followed by silver staining (Supplementary Fig. 5). Protein bands corresponding to the MBP proteins were quantified using Image Gauge (Fujifilm Science Lab).

**Expression and purification of N-terminally biotinylated MBP truncates.** N-terminally biotinylated MBP fragments were expressed as hybrid proteins consisting of an Ulp1-cleavable N-terminal His<sub>10</sub>-SUMO tag followed by a TEV protease-cleavage site, an AviTag (Avidity, LCC), which is biotinylated *in vivo*, and the respective MBP fragment. Proteins were expressed in *E. coli* BL21 cells harbouring pBirAcm, an IPTG inducible plasmid with an extra copy of the *birA* gene encoding biotin ligase (Avidity, LCC) in LB medium supplemented with

20 mg l<sup>-1</sup> biotin, 20 mg l<sup>-1</sup> kanamycin, 10 mg l<sup>-1</sup> chloramphenicol, 0.2% glucose. Cells were lysed in denaturing buffer D containing 20 mM Tris-HCl pH 7.5, 0.2 M NaCl, 8 M urea, the lysate was incubated at room temperature for 1 h, cleared from cell debris by centrifugation at 35,000g for 30 min and incubated with Ni-IDA matrix (Protino, Macherey-Nagel) for 30 min. The matrix was washed extensively with buffer D followed by several washing steps in refolding buffer R (20 mM Tris-HCl pH 7.5, 0.2 M NaCl, 1 M urea) and finally buffer MBP (20 mM Tris-HCl pH 7.5, 0.2 M NaCl). Hybrid proteins were eluted in buffer MBP containing 500 mM imidazole. The eluate was supplemented with His<sub>6</sub>-Ulp1 protease, dialysed overnight in 20 mM Tris-HCl pH 7.5, 0.2 M NaCl, 10% glycerol, and remaining contaminants (His<sub>6</sub>-Ulp1 protease and His<sub>10</sub>-SUMO) were removed by incubation with Ni-IDA matrix.

**Interaction studies of TF with MBP and MBP truncates.** Saturating amounts of N-terminally biotinylated MBP or MBP truncates were immobilized by incubation with 150 μl Streptactin Sepharose (IBA) for 15 min at 4 °C in MBP buffer (20 mM Tris-HCl pH 7.5, 0.2 M NaCl). Unbound protein was removed by repetitive washing steps using MBP buffer. TF interaction with immobilized MBP or MBP truncates was studied by a one-hour incubation with purified TF (5 μM) at room temperature followed by 5 times washing for 5 min in MBP buffer supplemented with 0.1% NP40. Bound TF was eluted by boiling in SDS sample buffer (125 mM Tris-HCl pH 6.8, 3% SDS, 3% β-mercaptoethanol, 0.01% bromophenol blue, 10% glycerol) for 5 min. Detection of TF was done by standard western blotting procedure using TF-specific polyclonal antibodies from rabbit (custom made by Charles River Laboratories).

**FTIR measurements.** An MBP truncate (residues 57–267, see Supplementary Fig. 4e) was purified as described above except that hybrid protein was directly digested while bound to the IDA matrix by overnight incubation with the His<sub>6</sub>-Ulp1 protease in buffer MBP (20 mM Tris-HCl pH 7.5, 0.2 M NaCl). The eluate containing the biotinylated MBP truncate free of the SUMO-tag and the protease (both were His-tagged and remained bound to the affinity matrix) was concentrated using Vivaspin concentrators (Sartorius) to a concentration of 2 mg ml<sup>-1</sup> and dialysed overnight at 4 °C in 20 mM Tris-HCl pH 7.5, 0.2 M NaCl, 10% glycerol. For FTIR measurements, purified TF and the MBP truncate were dialysed in separate dialysis bags in the same buffer container to exclude any buffer differences. After dialysis, concentrations of TF and MBP fragment were determined using the Biorad Protein Assay and FTIR measurements were performed at 1:1 stoichiometry at protein concentrations of approximately 30 μM. FTIR spectra were taken from 20 to 60 °C using Bruker Tensor27 instrumentation equipped with BioATRCell II. For each spectrum, 60 scans were conducted over a range from 3,000 to 1,000 cm<sup>-1</sup>. Between each series of scans, temperature was raised by 1 °C followed by an equilibration time of 2 min. Spectra were corrected by subtraction of the background water spectrum, compensated for water vapour, and analysed by determining the area under the amide I band.

30. Thomas, P. D. & Dill, K. A. An iterative method for extracting energy-like quantities from protein structures. *Proc. Natl. Acad. Sci. USA* **93**, 11628–11633 (1996).

# Structural basis for the inhibition of bacterial multidrug exporters

Ryosuke Nakashima<sup>1</sup>, Keisuke Sakurai<sup>1</sup>, Seiji Yamasaki<sup>2</sup>, Katsuhiko Hayashi<sup>2</sup>, Chikahiro Nagata<sup>3</sup>, Kazuki Hoshino<sup>3</sup>, Yoshikuni Onodera<sup>3</sup>, Kunihiko Nishino<sup>4</sup> & Akihito Yamaguchi<sup>1,2</sup>

**The multidrug efflux transporter AcrB and its homologues are important in the multidrug resistance of Gram-negative pathogens<sup>1,2</sup>. However, despite efforts to develop efflux inhibitors<sup>3</sup>, clinically useful inhibitors are not available at present<sup>4,5</sup>. Pyridopyrimidine derivatives are AcrB- and MexB-specific inhibitors that do not inhibit MexY<sup>6,7</sup>; MexB and MexY are principal multidrug exporters in *Pseudomonas aeruginosa*<sup>8–10</sup>. We have previously determined the crystal structure of AcrB in the absence and presence of antibiotics<sup>11–13</sup>. Drugs were shown to be exported by a functionally rotating mechanism<sup>12</sup> through tandem proximal and distal multisite drug-binding pockets<sup>13</sup>. Here we describe the first inhibitor-bound structures of AcrB and MexB, in which these proteins are bound by a pyridopyrimidine derivative. The pyridopyrimidine derivative binds tightly to a narrow pit composed of a phenylalanine cluster located in the distal pocket and sterically hinders the functional rotation. This pit is a hydrophobic trap that branches off from the substrate-translocation channel. Phe 178 is located at the edge of this trap in AcrB and MexB and contributes to the tight binding of the inhibitor molecule through a  $\pi$ – $\pi$  interaction with the pyridopyrimidine ring. The voluminous side chain of Trp 177 located at the corresponding position in MexY prevents inhibitor binding. The structure of the hydrophobic trap described in this study will contribute to the development of universal inhibitors of MexB and MexY in *P. aeruginosa*.**

Members of the resistance-nodulation-division (RND) family of transporters, which include AcrB, are tripartite complexes composed of an inner membrane transporter, a membrane fusion protein and an outer membrane channel<sup>14,15</sup>. Among the RND transporters, AcrAB-TolC and its homologues (including MexAB-OprM and MexXY-OprM) are essential for intrinsic antibiotic tolerance and bacterial survival during infection<sup>16,17</sup>. Most clinically isolated *P. aeruginosa* strains with multidrug-resistance phenotypes overexpress MexAB and/or MexXY<sup>18</sup>. Over the last decade, various compounds have been randomly screened and subsequently modified to inhibit these efflux transporters<sup>3,19</sup>. Among them, two groups of effective inhibitors, the derivatives of Phe-Arg  $\beta$ -naphthylamide (PA $\beta$ N)<sup>19,20</sup> and *tert*-butyl thiazolyl aminocarboxyl pyridopyrimidine<sup>6,7</sup>, are the most commonly investigated. However, both groups of inhibitors are still in preclinical development<sup>4</sup>. Although the competitive inhibitor PA $\beta$ N exhibits a broad synergistic effect with antibiotics against multidrug-resistant *P. aeruginosa*<sup>19</sup>, its toxicity is probably due to the induction of membrane dysfunction<sup>20,21</sup>. However, pyridopyrimidine derivatives do not cause membrane dysfunction and have almost no antibiotic activity. These derivatives are AcrAB-TolC- and MexAB-OprM-specific inhibitors<sup>6</sup>, but they do not inhibit MexXY-OprM, which is the main reason why pyridopyrimidine derivatives are not useful as clinical drugs to target multidrug-resistant *P. aeruginosa*. Among pyridopyrimidine derivatives, [[2-{{((3R)-1-{{8-[(4-*tert*-butyl-1,3-thiazol-2-yl)amino]carbonyl}-4-oxo-3-[(E)-2-(1H-tetrazol-5-yl)vinyl]-4H-pyrido[1,2-a]pyrimidin-2-yl}piperidin-3-yl}oxy]carbonyl}amino]ethyl](dimethyl) ammonio]

acetate (D13-9001 (ref. 7), which we refer to as AcrAB/MexAB-specific inhibitor of pyridopyrimidine derivative (ABI-PP) in this manuscript (Supplementary Fig. 1), is an efficient inhibitor and has a relatively high water solubility<sup>7</sup>. Unlike PA $\beta$ N<sup>21</sup>, ABI-PP is hardly exported by efflux transporters (Supplementary Fig. 2). ABI-PP binds to purified AcrB and MexB proteins, but not to purified MexY protein (Supplementary Fig. 3b). The binding of a distal-binding drug to purified exporter proteins was competitively inhibited by ABI-PP, but the binding of a proximal-binding drug was not affected (Supplementary Fig. 4b), indicating that ABI-PP binds to the distal pocket. ABI-PP binding was not affected by either drug. However, ABI-PP potentiates the activities of a wide variety of drugs and toxic compounds including both distal- and proximal-binding drugs against MexAB-OprM-expressing cells, but fails to enhance the effects of these drugs against MexXY-OprM-expressing cells (Supplementary Fig. 5). The purpose of this study was to determine the structural basis of the inhibition of efflux transporters by determining the crystal structure of AcrB and MexB bound to the pyridopyrimidine derivative ABI-PP. Our work will provide a structural basis for designing a universal inhibitor of multidrug efflux transporters. Although bound PA $\beta$ N was detected in the AcrB(N109A) mutant<sup>22</sup>, the physiological importance of the structure is not clear<sup>23</sup>. The structures reported in this manuscript represent, to our knowledge, the first examples of physiologically important asymmetric structures of efflux transporters bound to inhibitors.

We solved the crystal structure of AcrB with bound ABI-PP at a resolution of 3.05 Å (Fig. 1a, b). ABI-PP binds to a narrow pit composed of a phenylalanine cluster in the distal pocket of the binding monomer (Fig. 1c and Supplementary Fig. 6a). The hydrophobic *tert*-butyl thiazolyl aminocarboxyl pyridopyrimidine (TAP) moiety is surrounded by phenylalanine residues, including F136, F178, F610, F615 and F628. The pyridopyrimidine ring and thiazolyl ring strongly interact with F178 and F628, respectively, through  $\pi$ – $\pi$  stacking interactions. However, the tetrazole ring and the piperidine aceto-amino ethylene ammonio-acetate (PAEA) moiety interact with ionic and/or hydrophilic residues including N274, R620, Q176 and S180 in addition to aliphatic residues including I277 and L177 (Fig. 1c). Figure 1d and e present cutaway views of the distal binding pockets with bound ABI-PP superimposed with bound minocycline and doxorubicin. Figure 1d provides a view towards the channel's exit and Fig. 1e provides a view towards the entrance from the proximal pocket<sup>13</sup>. As shown in these figures, minocycline<sup>12</sup> and doxorubicin<sup>24</sup> are bound in the substrate-translocation channel from the entrance to the exit. The ethyl tetrazole group and the PAEA moiety of ABI-PP are also located in the substrate-translocation channel and almost overlap with the minocycline and doxorubicin molecules. Q176, L177 and I277 interact with both doxorubicin and ABI-PP. N274, R620 and S180 interact with both minocycline and ABI-PP. However, the TAP moiety is deeply inserted into a narrow phenylalanine-rich trap that branches off of the substrate-translocation channel.

<sup>1</sup>Department of Cell Membrane Biology, Institute of Scientific and Industrial Research, Osaka University, Ibaraki, Osaka 567-0047, Japan. <sup>2</sup>Graduate School of Pharmaceutical Sciences, Osaka University, Suita, Osaka 565-0871, Japan. <sup>3</sup>Daichi Sankyo Co. Ltd, 16-13, Kita-Kasai 1-Chome, Edogawa-ku, Tokyo 134-8630, Japan. <sup>4</sup>Laboratory of Microbiology and Infectious Diseases, Institute of Scientific and Industrial Research, Osaka University, Ibaraki, Osaka 567-0047, Japan.

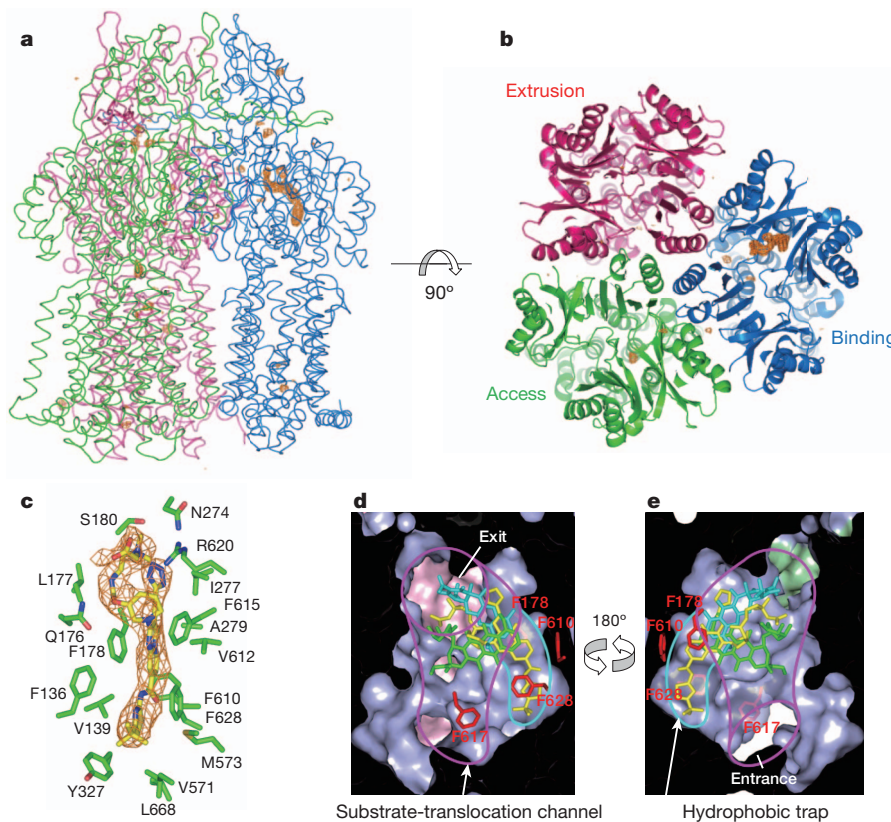


**Figure 1 | Crystal structure of the inhibitor-bound AcrB trimer.** Three AcrB monomers are shown in blue, red and green to indicate the binding, extrusion and access monomers, respectively. The difference Fourier map ( $F_{\text{inhibitor}} - F_{\text{free}}$ ) contoured at  $3.5\sigma$  (a and b) and  $3.0\sigma$  (c) is represented by an orange mesh. This colour scheme is used in all other figures. a, The side view of the entire structure of the ABI-PP-bound AcrB trimer. b, Cutaway view of the head-piece

from the distal side of the cell. c, Close-up view of the ABI-PP-binding site. Carbon atoms of ABI-PP and amino acid residues are shown in yellow and green, respectively. d, e, Cutaway views of the distal drug-binding pocket towards the exit (d) and the entrance (e). Bound minocycline<sup>12</sup> (blue) and doxorubicin<sup>24</sup> (green) are superimposed.

We also solved the crystal structures of MexB bound by ABI-PP at  $3.15\text{ \AA}$  (Fig. 2a, b) and drug-free MexB at  $2.7\text{ \AA}$  (Supplementary Fig. 7). As illustrated in the close-up view (Fig. 2c and Supplementary Fig. 6b), the ABI-PP binding site in MexB is similar to the site in AcrB. The hydrophobic TAP moiety is inserted into the narrow hydrophobic trap surrounded by F136, F178, F610, F615, F628 and F573. The hydrophilic tetrazole ring interacts with D274, R620 and K151. The conformations of these two ABI-PP moieties are almost the same as their conformations in AcrB. However, the conformation of the PAEA moiety in MexB is different from that in AcrB; specifically, this moiety extends towards R128 in MexB (Fig. 2c), but it is bent between the piperidine ring and the aceto-amino ethylene ammonio-acetate group in AcrB (Fig. 1c). As shown in Fig. 2d–f, the distal pocket is separated into two parts: a relatively hydrophilic substrate-translocation channel and a hydrophobic trap. The channel has sufficient space for multisite drug binding, and the trap forms a deep and narrow fissure. Our crystal structure of drug-free MexB (Supplementary Fig. 7) is largely identical to the structure determined at  $3.0\text{ \AA}$  in ref. 25. In our structure, the electron density corresponding to an entire molecule of *n*-dodecyl- $\beta$ -D-maltoside (DDM) in the distal pocket is evident (Supplementary Fig. 8a) and the bound DDM partially overlaps with the bound ABI-PP in the narrow hydrophobic trap (Supplementary Fig. 8b, c).

The crystal structure of MexY has not yet been solved. However, we constructed a homology model of MexY (using SWISS-MODEL<sup>26</sup>) on the basis of the ABI-PP-bound AcrB/MexB structure. Figure 3 shows a close-up view of the ABI-PP-binding region. The most notable difference between AcrB/MexB and MexY in this region is that the position of F178 in AcrB and MexB at the edge of the hydrophobic trap (Fig. 3a,

b) is occupied by W177 in MexY (Fig. 3c). The voluminous indolyl side chain hinders the binding of ABI-PP to this trap, which may be the reason why ABI-PP does not inhibit MexY. We constructed the AcrB(F178W) mutant and solved its structure (Fig. 3d and Supplementary Fig. 12a), which revealed that the indolyl side chain of W178 hindered ABI-PP binding, as in MexY. Therefore, to determine the effect of steric hindrance at this position on the inhibitory activity, we constructed the mutants MexY(W177F), MexB(F178W) and AcrB(F178W) using site-directed mutagenesis. Mutagenesis did not affect the expression levels of any of the proteins (Supplementary Fig. 9). Although the AcrB(F178A) mutation causes a decrease in antibiotic resistance<sup>27</sup>, the F178W mutation in AcrB and MexB and the W177F mutation in MexY did not alter the antibiotic resistance pattern (Supplementary Table 2), suggesting that these mutations may not cause conformational changes in the substrate-translocation channel.

The inhibitory effect of ABI-PP on efflux transporters was measured by examining its effect on cell growth and its ability to prevent the accumulation of doxorubicin in *Escherichia coli* cells (Fig. 4). In the absence of antibiotics, the growth rates of wild-type and mutant AcrB-, MexB- and MexY-expressing cells were similar to each other and were unaffected by the addition of ABI-PP (Supplementary Fig. 10). Wild-type *E. coli* cells are resistant to erythromycin, whereas *acrB*-deficient *E. coli* cells are highly sensitive to this drug (Fig. 4a), indicating that the intrinsic tolerance of *E. coli* to erythromycin is due to efflux by the AcrAB-TolC system. The quenching of doxorubicin fluorescence was prevented in wild-type *E. coli* cells by the AcrAB-TolC system, but the fluorescence in *acrB*-deficient and *acrB/tolC*-deficient cells was quenched due to the accumulation of doxorubicin in the cells (Fig. 4f). In wild-type

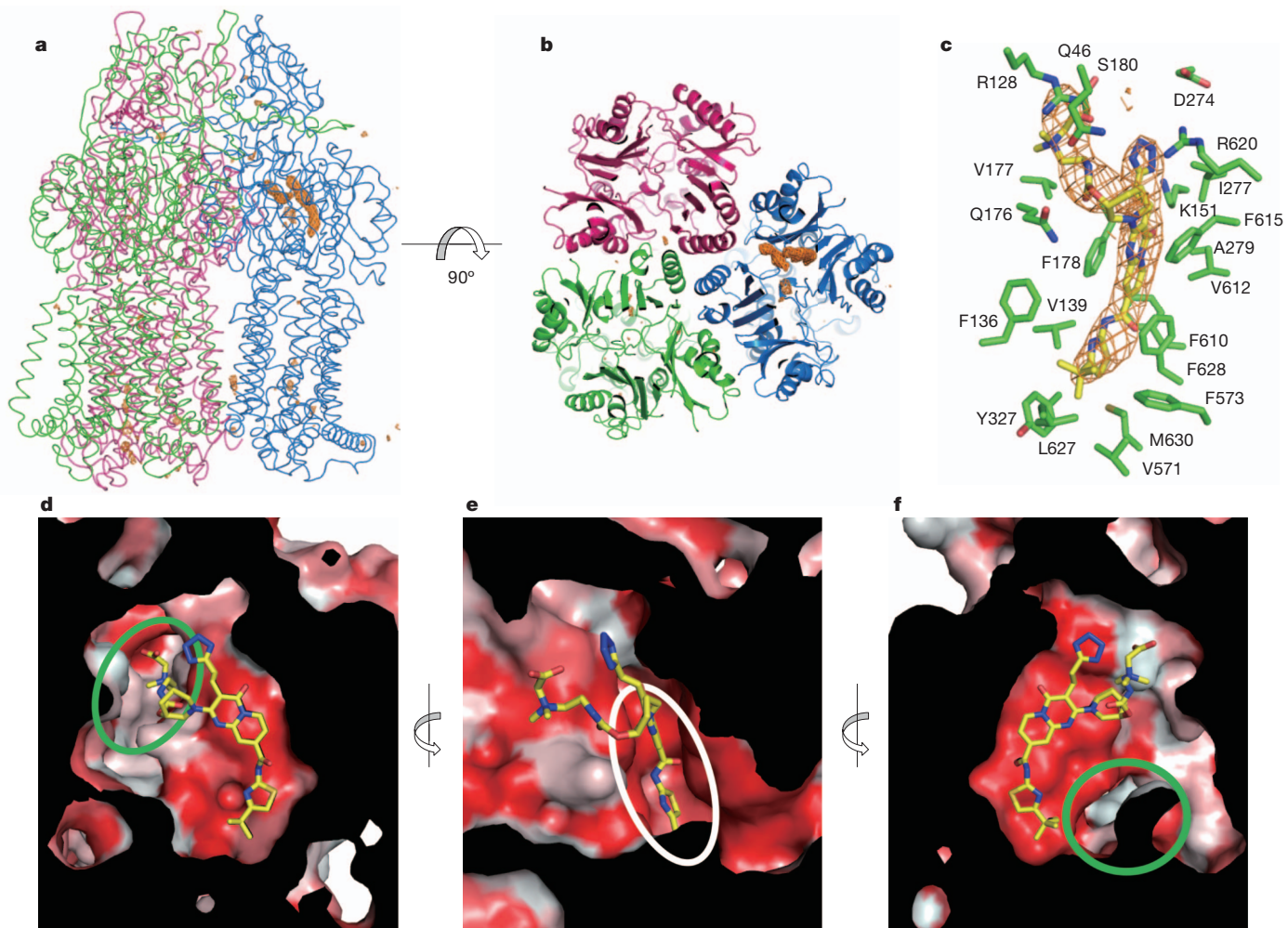


**Figure 2 | Crystal structure of the inhibitor-bound MexB trimer.** **a**, Entire structure of the ABI-PP-bound MexB trimer. **b**, Cutaway view of the head-piece of the ABI-PP-bound MexB. The  $F_0 - F_c$  omit map is represented by an orange mesh, contoured at  $3.0\sigma$  (**a** and **b**). **c**, Close-up stereo view of the ABI-PP-binding site of MexB as shown in Fig. 1c, except that the electron density map of ABI-PP is calculated as an  $F_0 - F_c$  omit map contoured at  $3.0\sigma$  because

drug-free MexB binds a detergent molecule. **d–f**, Cutaway view of the distal drug-binding pocket of the ABI-PP-bound MexB towards the exit (green oval; **d**), looking down the hydrophobic trap (white oval) from the substrate-translocation channel (**e**) and towards the entrance (green oval; **f**). The hydrophobicity of the inner wall of the pocket is coloured according to Eisenberg's hydrophobicity scale.

AcrB-expressing cells, cell growth was inhibited by ABI-PP in the presence of erythromycin (Fig. 4b) and fluorescence quenching was increased by ABI-PP (Fig. 4g), indicating that AcrB was inhibited by ABI-PP. By contrast, in wild-type MexY-expressing cells, cell growth and fluorescence quenching were not affected by ABI-PP (Fig. 4d, i), indicating that MexY was not inhibited by ABI-PP. The doxorubicin fluorescence in the MexY-expressing cells may have been somewhat quenched even in the absence of ABI-PP (Fig. 4i) because MexY is not able to completely prevent doxorubicin accumulation. The degree to which the growth of AcrB(F178W)-expressing cells was inhibited by ABI-PP was considerably decreased (Fig. 4c), and the quenching of doxorubicin fluorescence was completely prevented, even in the presence of ABI-PP (Fig. 4h), indicating that the AcrB(F178W) mutant is no longer inhibited by ABI-PP. By contrast, the growth of the MexY(W177F)-expressing cells was inhibited by ABI-PP (Fig. 4e), and the degree of quenching was increased by ABI-PP (Fig. 4j), indicating that the MexY(W177F) mutant is inhibited by ABI-PP. These results clearly indicate that the presence of a voluminous side chain at the edge of the hydrophobic trap in MexY reduces the inhibitory activity of ABI-PP.

However, in the case of MexB, the F178W mutation caused no change in the inhibitory activity of ABI-PP, as evidenced by the ABI-PP-induced inhibition of cell growth and the accumulation of doxorubicin (Supplementary Fig. 11). To reveal the reason for the

difference between AcrB(F178W) and MexB(F178W) with respect to the response to ABI-PP, we determined the crystal structures of these mutants. The overall structures of AcrB(F178W) and MexB(F178W) were almost the same as the wild-type structures of AcrB and MexB, respectively. A close-up view of the hydrophobic trap showed that the indolyl side chain of W178 in the AcrB mutant protrudes into the narrow space of the hydrophobic trap (Supplementary Fig. 12a), whereas the indolyl side chain of W178 in the MexB mutant does not protrude towards the hydrophobic trap (Supplementary Fig. 12b), because that space is partially occupied by a DDM molecule, as in the wild-type MexB. We succeeded in determining the crystal structure of ABI-PP-bound MexB(F178W). ABI-PP was actually detected in the hydrophobic trap, as in the wild-type MexB (Supplementary Fig. 12c). The indolyl ring of W178 fits into a position that is capable of forming  $\pi-\pi$  interactions with the pyridopyrimidine ring without large conformational change relative to the ABI-PP-free structure. By contrast, in the case of AcrB(F178W) and MexY, such conformation of the indolyl ring seems to be impossible because of the steric hindrance with V139 and I138, respectively (Supplementary Fig. 13). When these residues were replaced by alanine, the resulting mutants, AcrB(F178W/V139A) and MexY(I138A), became inhibited by ABI-PP (Supplementary Fig. 14). These results clearly indicate that the sensitivity of exporters to ABI-PP depends on the space of the inhibitor-binding pit.

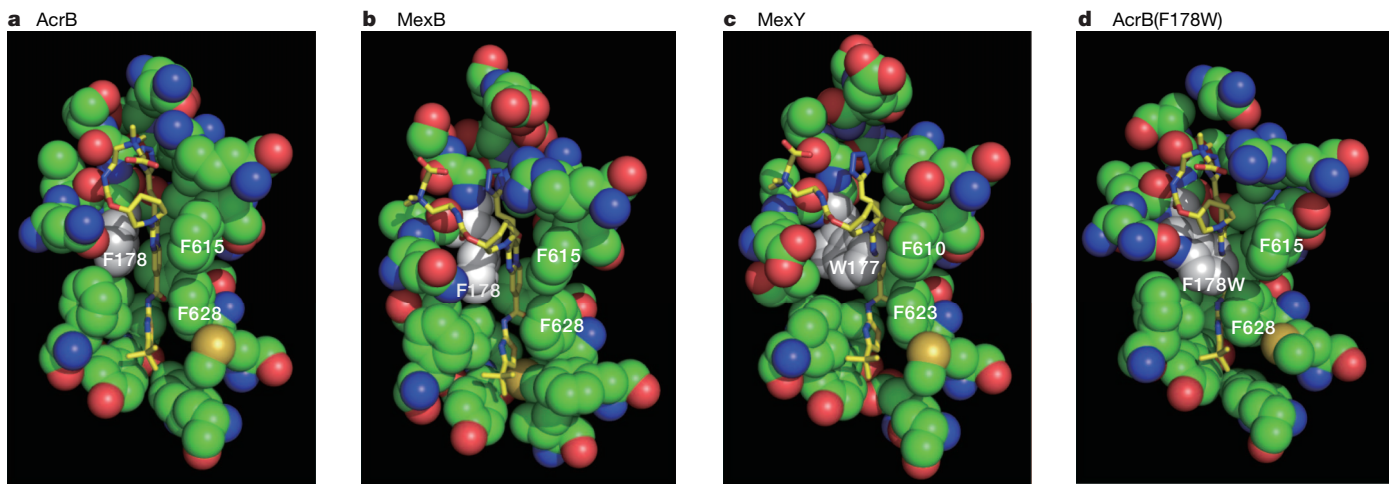


**Figure 3 | Comparison of the close-up views of the inhibitor-binding site of multidrug efflux transporters.** The amino acid residues around this site are depicted using the space-filling model. The phenyl and indolyl side chains of F178 and W177 are shown in white. **a**, AcrB. **b**, MexB. **c**, Homology model of MexY overlapped with MexB-bound ABI-PP. The alignment of AcrB,

MexB and MexY was generated by GENETYX (v9, GENETYX). The homology model of MexY was calculated using SWISS-MODEL<sup>26</sup>.

**d**, AcrB(F178W) overlapped with AcrB-bound ABI-PP. In this panel, W178 is shown in white.

In this study, we found that ABI-PP is deeply inserted into a hydrophobic trap that branches off of the substrate-translocation channel in the distal binding pocket of AcrB/MexB. This trap is rich in phenylalanine residues, which do not directly interact with the exported drugs but have been shown to indirectly affect drug binding by site-directed mutagenesis<sup>27</sup> and molecular dynamics simulations<sup>28</sup>. ABI-PP is not exported by AcrB/MexB. ABI-PP binds tightly to this trap and inhibits the functional rotation mechanism<sup>12</sup> of AcrB/MexB monomers. Therefore, it potentiates the activities of all of the antibiotics exported by AcrB/MexB not only distal-binding drugs but also proximal-binding

drugs. By contrast, ABI-PP does not inhibit MexY because the voluminous side chain of W177 is located in this trap. The inhibitor specificity is determined by the small difference in the amount of space in the hydrophobic trap. Several classes of AcrB/MexB inhibitors have been developed but their mechanisms of action remain largely unknown. This study represents the first success, to our knowledge, in solving the inhibitor-bound structures of AcrB/MexB. The development of clinically useful inhibitors for multidrug efflux transporters is of key importance because such agents might make existing antibiotics more effective. This study provides detailed insight into the mechanism

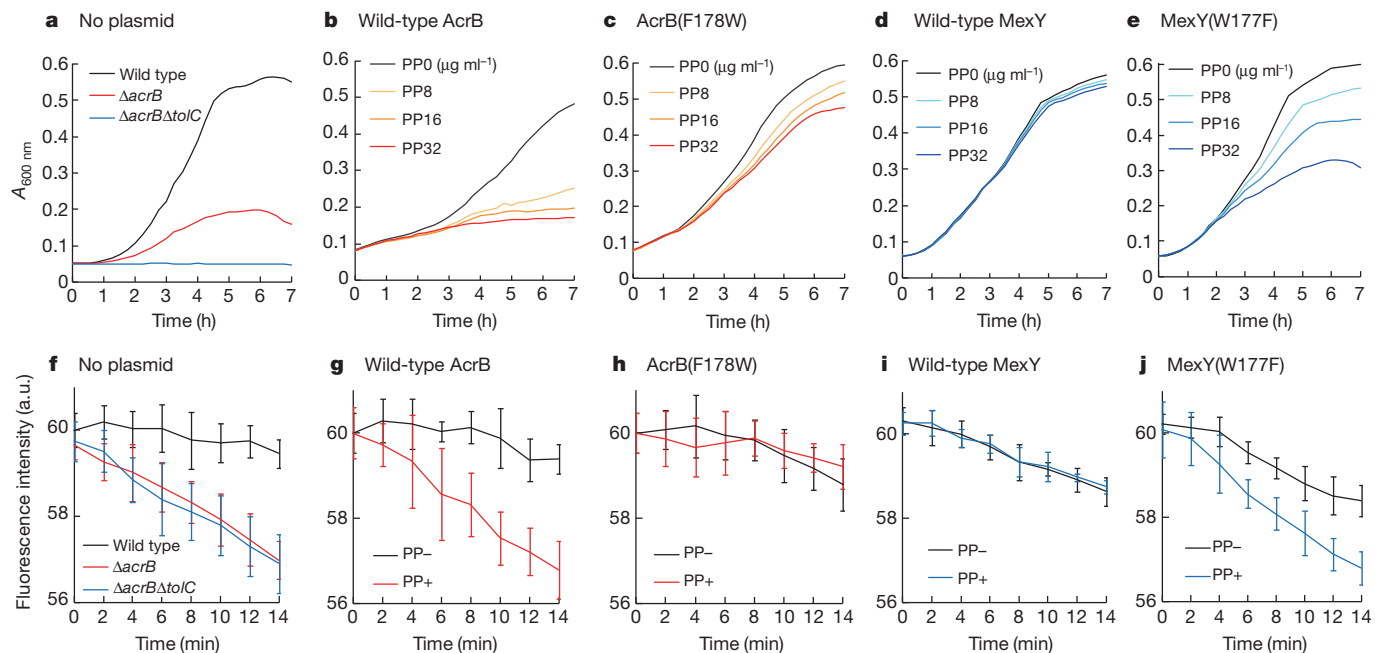


**Figure 4 | The inhibitory effect of ABI-PP.** **a**, The growth of wild-type, *acrB*-deficient and *acrB/tolC*-deficient *E. coli* cells in the presence of 6  $\mu\text{g ml}^{-1}$  erythromycin. **b–e**, The growth of *E. coli* cells expressing wild-type AcrB (**b**), AcrB(F178W) (**c**), wild-type MexY (**d**) and MexY(W177F) (**e**) in the presence of 6  $\mu\text{g ml}^{-1}$  (**b**, **c**) or 16  $\mu\text{g ml}^{-1}$  (**d**, **e**) erythromycin and various concentrations of ABI-PP (depicted as PP in panels). These tests were repeated three times. **f–j**, Quenching of doxorubicin fluorescence due to the

accumulation in *E. coli* cells. **f**, The effect of *acrB* and/or *tolC* deletion. **g–j**, The effect of ABI-PP (28.6  $\mu\text{M}$ ) in *E. coli* cells expressing wild-type AcrB (**g**), AcrB(F178W) (**h**), wild-type MexY (**i**) and MexY(W177F) (**j**). The data and error bars correspond to the mean values of three independent experiments and the  $\pm$  standard deviation, respectively. a.u., arbitrary units.

by which the inhibitor ABI-PP acts on RND transporters, and our results will promote the structure-based development of universal inhibitors that inhibit both MexB and MexY.

## METHODS SUMMARY

**Crystallization and structural determination of inhibitor-bound AcrB and MexB.** C2 crystals of ABI-PP-bound AcrB and drug-free AcrB(F178W) were generated (see Methods) using dodecanoyl sucrose and the structures were solved at resolutions of 3.05 and 3.60 Å, respectively. P1 crystals of drug-free and ABI-PP-bound MexB and drug-free and ABI-PP-bound MexB(F178W) were generated (see Methods) using DDM, and the structures were solved at resolutions of 2.70, 3.15, 3.30 and 3.00 Å, respectively (Supplementary Table 1).

**Full Methods** and any associated references are available in the online version of the paper.

Received 27 June 2012; accepted 13 May 2013.

Published online 30 June 2013.

1. Poole, K. Multidrug resistance in Gram-negative bacteria. *Curr. Opin. Microbiol.* **4**, 500–508 (2001).
2. Nikaido, H. & Pages, J. M. Broad-specificity efflux pumps and their role in multidrug resistance of Gram-negative bacteria. *FEMS Microbiol. Rev.* **36**, 340–363 (2011).
3. Lomovskaya, O. & Watkins, W. Inhibition of efflux pumps as a novel approach to combat drug resistance in bacteria. *J. Mol. Microbiol. Biotechnol.* **3**, 225–236 (2001).
4. Lomovskaya, O. & Bostian, K. A. Practical applications and feasibility of efflux pump inhibitors in the clinic—A version for applied use. *Biochem. Pharmacol.* **71**, 910–918 (2006).
5. Pages, J. M. & Amaral, L. Mechanisms of drug efflux and strategies to combat them: challenging the efflux pump of Gram-negative bacteria. *Biochim. Biophys. Acta* **1794**, 826–833 (2009).
6. Nakayama, K. et al. MexAB-OprM-specific efflux pump inhibitors in *Pseudomonas aeruginosa*. Part 1: discovery and early strategies for lead optimization. *Bioorg. Med. Chem. Lett.* **13**, 4201–4204 (2003).
7. Yoshida, K. et al. MexAB-OprM-specific efflux pump inhibitors in *Pseudomonas aeruginosa*. Part 7: highly soluble and *in vivo* active quarternary ammonium analogue D13–9001, a potential preclinical candidate. *Bioorg. Med. Chem. Lett.* **15**, 7087–7097 (2007).
8. Masuda, N. et al. Contribution of the MexX-MexY-OprM efflux system to intrinsic resistance in *Pseudomonas aeruginosa*. *Antimicrob. Agents Chemother.* **44**, 2242–2246 (2000).
9. Sobel, M. L., McKay, G. A. & Poole, K. Contribution of the MexXY multidrug transporter to aminoglycoside resistance in *Pseudomonas aeruginosa* clinical isolates. *Antimicrob. Agents Chemother.* **47**, 3202–3207 (2003).
10. Hocquet, D., Nordmann, P., Garch, F. E., Cabanne, L. & Plesiat, P. Involvement of the MexXY-OprM efflux system in emergence of ceftazidime resistance in clinical strains of *Pseudomonas aeruginosa*. *Antimicrob. Agents Chemother.* **50**, 1347–1351 (2006).
11. Murakami, S., Nakashima, R., Yamashita, E. & Yamaguchi, A. Crystal structure of bacterial multidrug efflux transporter AcrB. *Nature* **419**, 587–593 (2002).
12. Murakami, S., Nakashima, R., Yamashita, E., Matsumoto, T. & Yamaguchi, A. Crystal structure of a multidrug transporter reveal a functionally rotating mechanism. *Nature* **443**, 173–179 (2006).
13. Nakashima, R., Sakurai, K., Yamasaki, S., Nishino, K. & Yamaguchi, A. Structures of the multidrug exporter AcrB reveal a proximal multisite drug-binding pocket. *Nature* **480**, 565–569 (2011).
14. Tikhonova, E. B. & Zgurskaya, H. I. AcrA, AcrB and TolC of *Escherichia coli* form a stable intermembrane multidrug efflux complex. *J. Biol. Chem.* **279**, 32116–32124 (2004).
15. Symmons, M. F., Bokma, E., Koronakis, E., Hughes, C. & Koronakis, V. The assembled structure of a complete tripartite bacterial multidrug efflux pump. *Proc. Natl Acad. Sci. USA* **106**, 7173–7178 (2009).
16. Poole, K. & Srikumar, R. Multidrug efflux in *Pseudomonas aeruginosa*: components, mechanisms and clinical significance. *Curr. Top. Med. Chem.* **1**, 59–71 (2001).
17. Nikaido, H. & Zgurskaya, H. I. AcrB and related multidrug efflux pumps of *Escherichia coli*. *J. Mol. Microbiol. Biotechnol.* **3**, 215–218 (2001).
18. Aeschlimann, J. R. The role of multidrug efflux pumps in the antibiotic resistance of *Pseudomonas aeruginosa* and other gram-negative bacteria. Insights from the Society of Infectious Diseases Pharmacists. *Pharmacotherapy* **23**, 916–924 (2003).
19. Lomovskaya, O. et al. Identification and characterization of inhibitors of multidrug resistance efflux pumps in *Pseudomonas aeruginosa*: novel agents for combination therapy. *Antimicrob. Agents Chemother.* **45**, 105–116 (2001).
20. Askoura, M., Mottawea, W., Abujamel, T. & Tahler, I. Efflux pump inhibitors (EPIs) as new antimicrobial agents against *Pseudomonas aeruginosa*. *Libyan J. Med.* **6**, 5870–5877 (2011).
21. Matsumoto, Y. et al. Evaluation of multidrug efflux pump inhibitors by a new method using microfluidic channels. *PLoS ONE* **6**, e18547 (2011).
22. Yu, E. W., Aires, J. R., McDermott, G. & Nikaido, H. A periplasmic drug-binding site of the AcrB multidrug efflux pump: a crystallographic and site-directed mutagenesis study. *J. Bacteriol.* **187**, 6804–6815 (2005).
23. Takatsuka, Y., Chen, C. & Nikaido, H. Mechanism of recognition of compounds of diverse structures by the multidrug efflux pump AcrB of *Escherichia coli*. *Proc. Natl Acad. Sci. USA* **107**, 6559–6565 (2010).
24. Eicher, T. et al. Transport of drugs by the multidrug transporter AcrB involves an access and a deep binding pocket that are separated by a switch-loop. *Proc. Natl Acad. Sci. USA* **109**, 5687–5692 (2012).
25. Sennhauser, G., Bokowska, M. A., Briand, C. & Grutter, M. G. Crystal structure of the multidrug exporter MexB from *Pseudomonas aeruginosa*. *J. Mol. Biol.* **389**, 134–145 (2009).
26. Kiefer, F., Arnold, K., Künzli, M., Bordoli, L. & Schwede, T. The SWISS-MODEL Repository and associated resources. *Nucleic Acids Res.* **37**, D387–D392 (2009).
27. Bohnert, J. A. et al. Site-directed mutagenesis reveals putative substrate binding residues in the *Escherichia coli* RND efflux pump AcrB. *J. Bacteriol.* **190**, 8225–8229 (2008).
28. Vargiu, A. V. et al. Effect of the F610A mutation on substrate extrusion in the AcrB transporter: explanation and rationale by molecular dynamics simulations. *J. Am. Chem. Soc.* **133**, 10704–10707 (2011).

**Supplementary Information** is available in the online version of the paper.

**Acknowledgements** We thank T. Nakae for providing the plasmids encoding *mexB*, *mexY*, *mexAB-oprM* and *mexXY-oprM*. We also thank N. Kato for discussion regarding the organic chemistry of the inhibitor that was investigated in this study. Our diffraction data were collected using Osaka University's BL44XU beamline at SPring-8, which was equipped with an MX225-HE CCD detector (Rayonix) and was financially supported by the Academia Sinica and the National Synchrotron Radiation Research Center (Taiwan). We thank K. Harada for assistance with the liquid chromatography–tandem mass spectrometry assay. This work was supported by CREST from the Japan Science and Technology Agency, the Program for the Promotion of Fundamental Studies in Health Sciences of the National Institute of Biomedical Innovation and Grants-in-Aid from the Ministry of Education, Culture, Sports, Science and Technology of Japan.

**Author Contributions** R.N., K.S., K.Hayashi and C.N. performed the crystallographic analysis. S.Y. and K.N. performed the molecular biological and biochemical analyses. K.Hoshino and Y.O. prepared the inhibitor. A.Y. designed the research and wrote the manuscript.

**Author Information** The coordinates for ABI-PP-bound AcrB, drug-free MexB, and ABI-PP-bound MexB have been deposited in the Protein Data Bank under accession numbers 3W9H, 3W9I and 3W9J, respectively. Reprints and permissions information is available at [www.nature.com/reprints](http://www.nature.com/reprints). The authors declare no competing financial interests. Readers are welcome to comment on the online version of the paper. Correspondence and requests for materials should be addressed to A.Y. (akihito@sanken.osaka-u.ac.jp).

## METHODS

**Preparation of membrane proteins.** Histidine-tagged AcrB was expressed from the plasmid pAcBH in the *E. coli* strain JM109 and prepared as previously described<sup>13</sup>. AcrB(F178W) was expressed from pAcBHF178W in the *acrA/acrB*-deficient *E. coli* strain W3104 and prepared using a method similar to that for wild-type AcrB. For MexB and MexB(F178W) overexpression, we used the plasmids pUCP20-B<sub>His</sub> (provided by T. Nakae<sup>29</sup>) and pUC118mexB F178W (pUC118 DNA, Takara Bio), respectively, and the protein was expressed with a carboxy-terminal polyhistidine tag in the wild-type and *acrB*-deficient *E. coli* strain MG1655, respectively. Bacteria were grown to an  $A_{580}$  nm of 0.7 at 37 °C and MexB expression was induced with 0.1 mM isopropyl- $\beta$ -D-1-thiogalactopyranoside for 4 h. The cells were disrupted with a high-pressure homogenizer (APV 1000, SPX) equipped with a sample cooling unit at 180 MPa and the membrane fractions were collected by ultracentrifugation at 158,000g for 90 min. The purified membrane fractions were solubilized in buffer A (20 mM Tris-HCl (pH 7.5), 300 mM NaCl and 10% glycerol) containing 1.5% DDM (D316, Dojindo). The solubilized protein mixture was centrifuged for 1 h at 172,000g, and the supernatant was applied to a Ni Sepharose Fast Flow column (GE Healthcare) pre-equilibrated with buffer A containing 0.05% DDM. The column was washed using buffer A plus DDM containing 25 mM imidazole (pH 7.5) and subsequently washed with 140 mM imidazole. MexB was eluted with 350 mM imidazole. Purified MexB was concentrated using an Amicon stirred cell (Model 8010, Millipore) and exchanged into buffer composed of 10 mM Tris-HCl (pH 7.5), 50 mM NaCl and 0.05% DDM with three concentration-dilution steps. Finally, the proteins were concentrated to approximately 30 mg ml<sup>-1</sup>.

**Crystallization.** Crystals of AcrB complexed with ABI-PP were prepared as previously described<sup>13</sup> with an inhibitor:protein molar ratio of 5:1. Crystals of AcrB(F178W) were prepared in a manner similar to that of the wild-type protein. MexB crystals were grown at 25 °C using the hanging drop vapour diffusion method. The protein solution (25 mg ml<sup>-1</sup>) was mixed with an equal volume of reservoir solution containing 50 mM Na acetate-HCl (pH 5.5), 300 mM NaCl and 26% (v/v) polyethylene glycol 400 (conditions similar to those in ref. 25). Crystals appeared within 5 days and were collected after a further 5 days. Crystals of MexB(F178W) were prepared using a method similar to that for the wild-type protein, except that *n*-octyl- $\beta$ -D-thioglucoside was used as an additive. Crystals of MexB complexed with ABI-PP were prepared using a method similar to that for AcrB. Cryoprotection was achieved by increasing the polyethylene glycol 400 concentration to 40% (v/v) in three steps. The crystals were flash frozen in liquid nitrogen or cryostream (100 K).

**Crystallographic analysis.** Each data set was collected using the BL44XU beamline at SPring-8 with an MX225-HE CCD detector (Rayonix) at 100 K. The diffraction data were processed and scaled using the HKL2000 (ref. 30) package. The crystals belonged to the C2 space group (AcrB and AcrB(F178W)) and the P1 space group (free and inhibitor-bound MexB), and the cell dimensions are listed in Supplementary Table 1. Other crystallographic analysis procedures were performed as described previously<sup>13</sup>.

**Site-directed mutagenesis.** The *acrB* gene was amplified from *E. coli* MG1655 (ref. 31) genomic DNA using the *Eco*\_*acrB*-*F*\_SalI (5'-CGCGTCGACAGTCT TAACTTAAACAGGAGC-3') and *Eco*\_*acrB*-*R*\_SphI (5'-CGCGCATGCTCAA

TGGTGATGGTGATGATGACAGTATGGCT-3') primers, which introduce SalI and SphI restriction sites at each end of the amplified fragment (underlined in the primer sequences above). This PCR product was cloned into the SalI and SphI sites of the pBAD33 vector<sup>32</sup> to produce the pBADacrB plasmid. Point mutations were introduced using mutagenic primers to create the F178W (TTC→TGG) and V139A (GTT→GCG) substitutions. The pMexAB<sup>his</sup>M and pMexXY<sup>his</sup>M plasmids were kindly provided by T. Nakae<sup>33</sup>. Point mutations were introduced using mutagenic primers to create the MexB(F178W) (TTC→TGG), MexY(W177F) (TGG→TTT) and MexY(I138A) (ATC→GCG) substitutions. The constructed plasmids were sequenced using a 3100-Avant Genetic Analyzer (Applied Biosystems) to ensure the presence of the desired mutation.

**Erythromycin susceptibility tests in the presence of ABI-PP.** Single colonies of *E. coli*  $\Delta$ acrB/pBADacrB,  $\Delta$ acrB $\Delta$ tolC/pMexAB<sup>his</sup>M and  $\Delta$ acrB $\Delta$ tolC/pMexXY<sup>his</sup>M strains were inoculated into 2 ml of Luria-Bertani (LB) broth. Cultures were grown overnight at 37 °C, and  $2 \times 10^7$  colony-forming units ml<sup>-1</sup> bacteria were inoculated into 200  $\mu$ l of LB broth containing erythromycin (6  $\mu$ g ml<sup>-1</sup> for AcrB-expressing cells, 2  $\mu$ g ml<sup>-1</sup> for MexAB-OprM-expressing cells and 16  $\mu$ g ml<sup>-1</sup> for MexXY-OprM-expressing cells) in the presence of various concentrations of ABI-PP and 10 mM arabinose. Bacterial growth was measured using 96-well plates and a Versa Max microplate reader (Molecular Devices).

**Doxorubicin efflux assay.** Overnight cultures of *E. coli* were diluted in LB broth to achieve a cell density of  $10^7$  cells ml<sup>-1</sup>. The cells were grown under aerobic conditions at 37 °C in the presence of 10 mM arabinose as an inducer until  $A_{600\text{ nm}} = 0.3$  was reached. The cells were then collected, washed twice with 100 mM potassium phosphate buffer (pH 7.5 containing 5 mM MgSO<sub>4</sub>) and re-suspended in the same buffer to adjust the  $A_{600}$  to 18. Each assay was performed in 96-well black flat-bottom plates (Iwaki) using a final cell volume of 100  $\mu$ l, and doxorubicin (Sigma-Aldrich) was added to a final concentration of 28.6  $\mu$ M. For the inhibition assay, 28.6  $\mu$ M ABI-PP was added. The fluorescence of doxorubicin was measured using an SH-8100 microplate reader (Corona Electric) with excitation set at 480 nm and emission at 600 nm. The fluorescence intensity decreased in a time-dependent manner owing to the accumulation of doxorubicin in the cells, and the decrease in fluorescence intensity was prevented when doxorubicin was expelled by an efflux pump.

29. Eda, S., Maseda, H. & Nakae, T. An elegant means of self-protection in Gram-negative bacteria by recognizing and extruding xenobiotics from the periplasmic space. *J. Biol. Chem.* **278**, 2085–2088 (2003).
30. Otwowski, Z. & Minor, W. Processing of X-ray diffraction data collected in oscillation mode. *Methods Enzymol.* **276**, 307–326 (1997).
31. Blattner, F. R. et al. The complete genome sequence of *Escherichia coli* K-12. *Science* **277**, 1453–1462 (1997).
32. Guzman, L. M., Belin, D., Carson, M. J. & Beckwith, J. Tight regulation, modulation, and high-level expression by vectors containing the arabinose PBAD promoter. *J. Bacteriol.* **177**, 4121–4130 (1995).
33. Mokhov, V. V., Mokhova, E. I., Akama, H. & Nakae, T. Role of the membrane fusion protein in the assembly of resistance-nodulation-cell division multidrug efflux pump in *Pseudomonas aeruginosa*. *Biochem. Biophys. Res. Commun.* **322**, 483–489 (2004).

# Unusual base pairing during the decoding of a stop codon by the ribosome

Israel S. Fernández<sup>1</sup>, Chyan Leong Ng<sup>1,†</sup>, Ann C. Kelley<sup>1</sup>, Guowei Wu<sup>2</sup>, Yi-Tao Yu<sup>2</sup> & V. Ramakrishnan<sup>1</sup>

During normal translation, the binding of a release factor to one of the three stop codons (UGA, UAA or UAG) results in the termination of protein synthesis. However, modification of the initial uridine to a pseudouridine ( $\Psi$ ) allows efficient recognition and read-through of these stop codons by a transfer RNA (tRNA), although it requires the formation of two normally forbidden purine–purine base pairs<sup>1</sup>. Here we determined the crystal structure at 3.1 Å resolution of the 30S ribosomal subunit in complex with the anticodon stem loop of tRNA<sup>Ser</sup> bound to the  $\Psi$ AG stop codon in the A site. The  $\Psi$ A base pair at the first position is accompanied by the formation of purine–purine base pairs at the second and third positions of the codon, which show an unusual Watson–Crick/Hoogsteen geometry. The structure shows a previously unsuspected ability of the ribosomal decoding centre to accommodate non-canonical base pairs.

The genetic code normally requires Watson–Crick base pairing at the first two positions of the codon–anticodon helix, and tolerates certain specific mismatches at the third (wobble) position. The structural basis for this was apparent when three universally conserved bases in the A site of the small (30S) ribosomal subunit were shown to change conformation to monitor Watson–Crick geometry at the first two base pairs in the minor groove of the codon–anticodon helix, while leaving the wobble position relatively unconstrained<sup>2</sup>. These interactions result in additional binding energy that is used to induce global conformational changes that facilitate the hydrolysis of GTP by the elongation factor EF-Tu<sup>3–5</sup>, as was predicted by earlier kinetic data<sup>6</sup>. However, recently it was shown that modification of the uridine in stop codons to  $\Psi$  (Fig. 1a) allowed  $\Psi$ AA and  $\Psi$ AG to code for serine or threonine and  $\Psi$ GA to code for phenylalanine or tyrosine<sup>1</sup>.

To understand how the normally forbidden base pairs in such recoding can be accepted by the ribosome, we determined the crystal structures of the anticodon stem loops (ASLs) of tRNA<sup>Ser</sup> and tRNA<sup>Phe</sup> bound to the modified stop codons  $\Psi$ AG and  $\Psi$ GA, respectively, in the A site of the 30S subunit, as well as the crystal structure of the most common bacterial tRNA<sup>Ser</sup> bound to  $\Psi$ AG in the entire 70S ribosome.

We first showed that nonsense suppression by  $\Psi$  also occurs in bacteria. We constructed three synthetic messenger RNAs encoding a 6×-histidine tag at the amino terminus and a Flag tag at the carboxy terminus (Fig. 1b, top). The three mRNAs contain either an amber stop (UAG), a glutamine sense (CAG) or a pseudouridylated amber ( $\Psi$ AG) codon inserted just before the Flag tag. After *in vitro* translation, anti-6×-histidine immunoblotting revealed that the three constructs are translated at the same level (Fig. 1b, bottom left). The anti-Flag immunoblot had a signal comparable to background when the normal UAG amber codon was present, showing that normal termination occurred and the downstream Flag sequence was not translated (Fig. 1b, bottom right). However, the presence of the  $\Psi$ AG amber codon increased the signal from the Flag tag to a level comparable to that of the CAG sense codon, showing that the substitution of U by  $\Psi$  results in a strong read-through of the amber stop codon in bacteria, as previously reported in eukaryotes<sup>1</sup>. Given the conservation of the

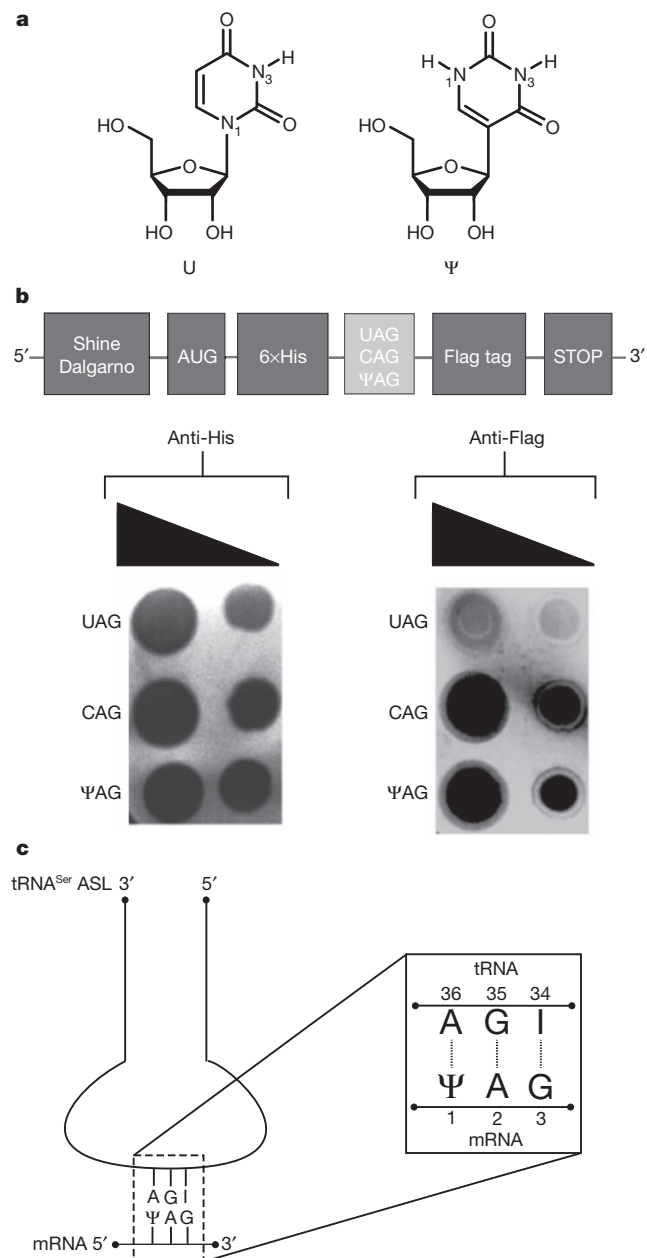


**Figure 1 | Chemical differences between uridine and pseudouridine, and experimental set-up.** a, Uridine (U; 1-β-D-ribofuranosyluracil) and pseudouridine (Ψ; 5-β-D-ribofuranosyluracil). b, Top, diagram of the three synthetic mRNA constructs designed for the *in vitro* nonsense suppression experiment in bacteria. Bottom, anti-His and anti-Flag immunoblot analysis of the *in vitro* translation assays in *Escherichia coli*. c, The tRNA<sup>Ser</sup> ASL and mRNA used in this study.

<sup>1</sup>MRC Laboratory of Molecular Biology, Cambridge CB2 0QH, UK. <sup>2</sup>Department of Biochemistry and Biophysics, University of Rochester Medical Center, 601 Elmwood Avenue, Rochester, New York 14642, USA. <sup>†</sup>Present address: Institute of Systems Biology, Universiti Kebangsaan Malaysia, 43600 UKM Bangi, Selangor, Malaysia.

decoding centre, it is likely that the recoding also specifies the same amino acids as previously established in eukaryotes.

As recoding and the decoding centre are both conserved across the two kingdoms, we determined the structure of the ASL for the yeast tRNA<sup>Ser</sup>, which has an IGA anticodon ([http://gtrnadb.ucsc.edu/Sacc\\_cere/](http://gtrnadb.ucsc.edu/Sacc_cere/)) (Fig. 1c) bound to a modified  $\Psi$ AG stop codon in the 30S subunit, as previously described for cognate tRNA<sup>2</sup> (Supplementary Methods and Supplementary Table 1).

The codon and the ASL could clearly be seen in difference Fourier maps (Fig. 2a), allowing an unambiguous determination of the conformation of the bases involved (Fig. 2b). The overall conformations of the  $\Psi$ AG codon and ASL in the A site are very similar to those observed previously for phenylalanine-codon-ASL pairs in both the 30S subunit<sup>2,3</sup> and the intact 70S ribosome<sup>7</sup>. However, the details of each of the codon-anticodon base pairs are markedly different, and reveal how the ribosome facilitates the decoding of a normally non-cognate tRNA.

At the first position, the  $\Psi$ 1 of the codon and A36 of the tRNA form the expected Watson-Crick base pair (Fig. 2b, left, and Fig. 3a). The N1 of  $\Psi$  is exposed to solvent and does not form an additional interaction with either the ASL or the ribosome. The minor groove of this base pair is recognized by A1493 of the decoding centre (Fig. 3a). However, unlike in normal decoding (Fig. 3d), the electron density for A1493 is consistent with a *syn* rather than an *anti* conformation (Supplementary Fig. 1).

In the second position, the A2 of the codon adopts a *syn* conformation that forms two hydrogen bonds via its Hoogsteen edge<sup>8</sup> with the Watson-Crick edge of G35 of the ASL (Fig. 2b, centre, and Fig. 3b). Interestingly, the C1'-C1' distance of 10.9 Å in this non-canonical base pair is not much greater than the distance of 10.5 Å found in a canonical pyrimidine-purine base pair with Watson-Crick geometry<sup>2</sup>. Presumably this difference is small enough to allow the base pair to be accommodated in the decoding centre of the ribosome. Surprisingly, despite the completely different type of base pair, the conformation

and interactions of the ribosomal bases A1492 and G530 are very similar to those seen in normal decoding (Fig. 3b, e).

Yeast tRNA<sup>Ser</sup> has an inosine in the third (wobble) position of the anticodon<sup>9</sup>. In suppression of a  $\Psi$ AG codon, the inosine would have to make a previously unknown I-G base pair, which would bring the two normally repulsive O6 groups close together. As in the second position, this unusual base pair is formed by a *syn* conformation of G3 making a single hydrogen bond via its Hoogsteen face with the Watson-Crick edge of I34 of the ASL (Fig. 2b, right, and Fig. 3c). The potential electrostatic repulsion between the O6 atoms on G3 and I34 is overcome by coordination of both atoms with what is probably a magnesium ion, thus stabilizing the base pair.

To determine the generality of these interactions, we determined two additional structures. The first was that of bacterial tRNA<sup>Ser</sup> with a CGA anticodon, bound to mRNA in the entire 70S ribosome. Here, only the second base pair involves a purine-purine mismatch, which adopts the same Hoogsteen/Watson-Crick geometry as seen in the 30S ribosome (Supplementary Table 1 and Supplementary Fig. 2a, c). We also determined the structure of the 30S subunit with a  $\Psi$ GA codon bound to the ASL of tRNA<sup>Ph</sup> containing a GAA anticodon (Supplementary Table 1 and Supplementary Fig. 2b), as it was shown that  $\Psi$ GA could be decoded by phenylalanine<sup>1</sup>. The same type of base pairing is seen, including the *syn* conformation of A1493 at the first position and the Hoogsteen/Watson-Crick interactions at the second and third positions. Because the third position here involves a GA pair instead of an IG, there are two hydrogen bonds and there is no coordinating magnesium ion. These structures show that the unusual Hoogsteen/Watson-Crick base pairs for purine-purine mismatches are seen for both bacterial and eukaryotic tRNAs implicated in the recoding of stop codons, and in the context of both 30S subunits and the 70S ribosome.

The structure of tRNA<sup>Ser</sup> ASL bound to the unmodified UAG codon in the 30S subunit (data not shown; Protein Data Bank (PDB) accession

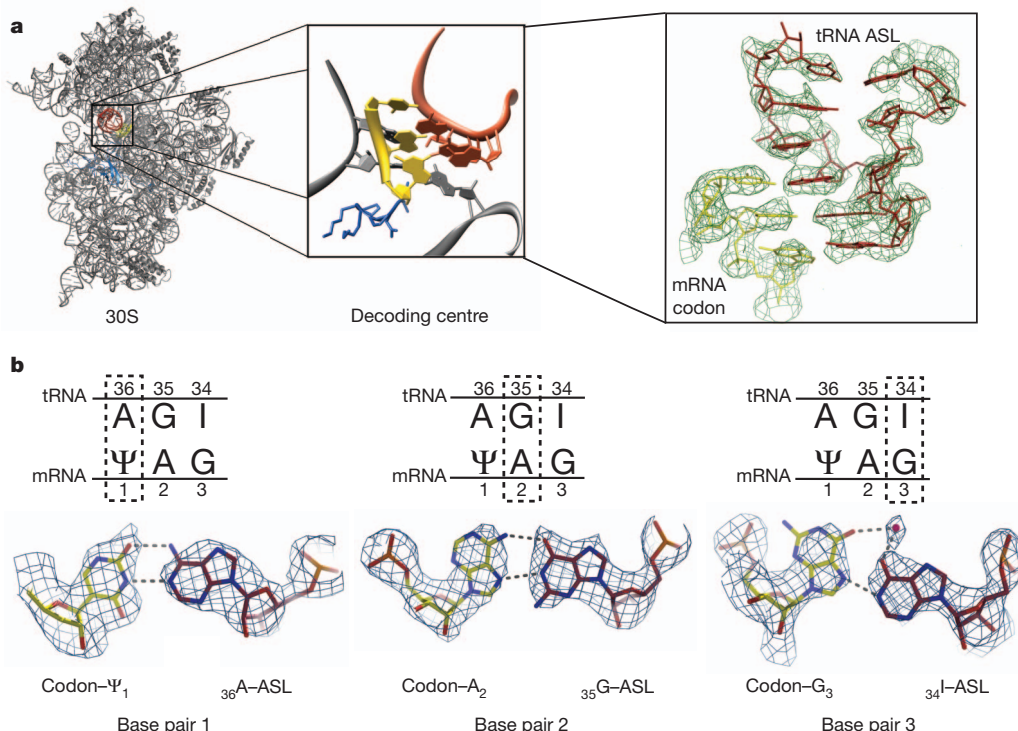


**Figure 2 | Overall and detailed view of the base pairs involved in the codon-anticodon interaction.** a, Overview of the 30S subunit and detail of the 30S decoding site with the  $\Psi$ AG-ASL-tRNA<sup>Ser</sup>. The ASL of tRNA<sup>Ser</sup> is depicted in red, the  $\Psi$ AG codon in yellow, the 16S rRNA in grey and the S12 protein in blue. Right, unbiased difference Fourier density for the ASL and codon. b, The

base pairs for the codon-anticodon interaction are shown with boxes over the first (left), second (middle) and third (right) positions; the actual structures of the base pair is shown below in unbiased difference Fourier maps contoured at  $1.5\sigma$ . Subscripts indicate residue numbers.

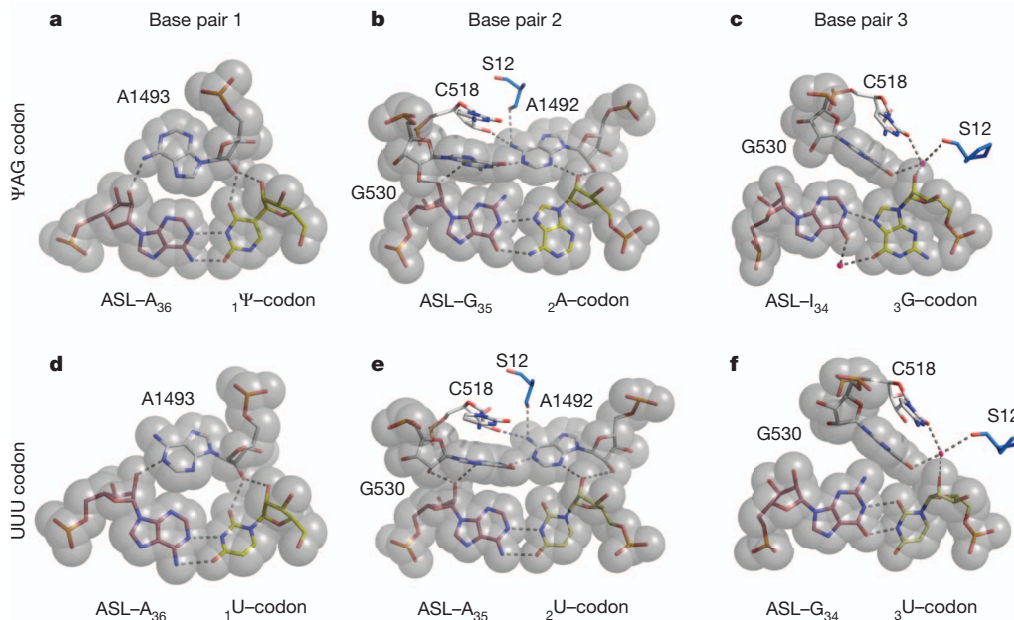


**Figure 3 | Interaction of ribosomal bases with the codon–anticodon base pairs.** Details of base pairing for the first, second and third positions of the  $\Psi$ AG–ASL-tRNA $^{\text{Ser}}$  structure with the ribosomal bases involved in minor-groove recognition shown on the top (a–c). For comparison, the corresponding

4K0K) was identical within coordinate error to that with the  $\Psi$ AG codon. This suggests that any difference in the decoding properties must come from differences in the stability of the final complex due to  $\Psi$ , rather than differences in structure.

This work shows how the normally forbidden codon–anticodon pairs that would be involved in recoding by  $\Psi$ -containing stop codons are accommodated in the ribosomal decoding centre.

At the first codon position, the *syn* conformation of A1493 facilitates a possibly tighter interaction with the minor groove of the Watson–Crick  $\Psi$ A pair (Fig. 3a) than the commonly seen *anti* conformation (Fig. 3d). The Watson–Crick/Hoogsteen base pairs at the second and third positions seen here have also been observed in canonical duplex DNA<sup>10</sup>, showing that the energetic difference between canonical and Hoogsteen pairs is small enough for the latter to be observed as a transient feature. However, during decoding, the ribosomal bases A1492 and G530 were suggested to recognize specifically Watson–Crick-pairing geometry at the second position<sup>2</sup> (Fig. 3e). Nevertheless, the same interactions can be formed with the Watson–Crick/Hoogsteen base pair described here (Fig. 3b), presumably because its width is similar and the interactions are with the 2'-OH groups of the riboses of the codon–anticodon base pair rather than with the bases themselves. It is likely that these interactions are not as favourable as for a canonical Watson–Crick base pair. However, suppression of stop codons by tRNAs requires only that they are able to outcompete release factors; they do not have to be as efficient as cognate tRNAs on sense codons.

It is not apparent why the  $\Psi$  modification should facilitate binding of a non-cognate tRNA. The additional hydrogen-bond donor N1 of  $\Psi$ , which is not present in U (Fig. 1a), is exposed to solvent and does not make additional interactions with the ribosome or ligands.  $\Psi$  in RNA has been shown to result in an increased stabilization of helices without noticeable changes in structure<sup>11,12</sup>. Understanding how  $\Psi$  results in increased stabilization of helices will require both high-resolution data on model systems as well as computational and biochemical studies. Determining the effect of  $\Psi$  on the rate constants of various steps in decoding<sup>6</sup>, or on efficiency of termination, will also help to clarify its role.

In principle, modification of sense codons could also lead to alternative forms of recognition. In this context it is interesting that a  $\Psi$  in the

positions of the codon–anticodon base pairs of a phenylalanine UUU codon with its cognate ASL anticodon from a previous study<sup>2</sup> are shown on the bottom (d–f). Subscripts indicate residue numbers.

anticodon of a tRNA leads to altered coding of a sense codon<sup>13</sup>. Finally, our results show that the decoding centre of the ribosome has a previously unsuspected plasticity that under certain circumstances allows alternative non-canonical base pairing, thereby allowing an expansion of the genetic code.

## METHODS SUMMARY

A combination of *in vitro* transcribed and chemically synthesized RNAs were used to generate the three mRNA versions used in the *in vitro* translation assays in *E. coli*. Aliquots of the *in vitro* translation reactions were spotted onto nitrocellulose membranes and probed with monoclonal anti-His or anti-Flag antibodies<sup>14</sup>. Crystallization of 30S ribosomal subunits and their complex formation with tRNA ASLs and hexanucleotide mRNAs were done as previously reported<sup>2</sup>. An initial round of refinement with REFMAC<sup>15</sup> using only the 30S subunit or the empty 70S ribosome as starting models to avoid any model bias, clearly showed additional differences in density that could be attributable to mRNA and tRNA, or to ASL, as shown in Fig. 2.

**Full Methods** and any associated references are available in the online version of the paper.

**Received 19 October 2012; accepted 15 May 2013.**

**Published online 30 June 2013.**

1. Karijolich, J. & Yu, Y.-T. Converting nonsense codons into sense codons by targeted pseudouridylation. *Nature* **474**, 395–398 (2011).
2. Ogle, J. M. *et al.* Recognition of cognate transfer RNA by the 30S ribosomal subunit. *Science* **292**, 897–902 (2001).
3. Ogle, J. M., Murphy, F. V., Tarry, M. J. & Ramakrishnan, V. Selection of tRNA by the ribosome requires a transition from an open to a closed form. *Cell* **111**, 721–732 (2002).
4. Schmeing, T. M. *et al.* The crystal structure of the ribosome bound to EF-Tu and aminoacyl-tRNA. *Science* **326**, 688–694 (2009).
5. Voorhees, R. M., Schmeing, T. M., Kelley, A. C. & Ramakrishnan, V. The mechanism for activation of GTP hydrolysis on the ribosome. *Science* **330**, 835–838 (2010).
6. Pape, T., Wintermeyer, W. & Rodnina, M. V. Complete kinetic mechanism of elongation factor Tu-dependent binding of aminoacyl-tRNA to the A site of the *E. coli* ribosome. *EMBO J.* **17**, 7490–7497 (1998).
7. Selmer, M. *et al.* Structure of the 70S ribosome complexed with mRNA and tRNA. *Science* **313**, 1935–1942 (2006).
8. Leontis, N. B. & Westhof, E. Geometric nomenclature and classification of RNA base pairs. *RNA* **7**, 499–512 (2001).
9. Sprinzl, M., Horn, C., Brown, M., Ioudovitch, A. & Steinberg, S. Compilation of tRNA sequences and sequences of tRNA genes. *Nucleic Acids Res.* **26**, 148–153 (1998).

10. Nikolova, E. N. *et al.* Transient Hoogsteen base pairs in canonical duplex DNA. *Nature* **470**, 498–502 (2011).
11. Davis, D. R., Veltri, C. A. & Nielsen, L. An RNA model system for investigation of pseudouridine stabilization of the codon-anticodon interaction in tRNA<sup>Lys</sup>, tRNA<sup>His</sup> and tRNA<sup>Ψ</sup>. *J. Biomol. Struct. Dyn.* **15**, 1121–1132 (1998).
12. Yarian, C. S. *et al.* Structural and functional roles of the N1- and N3-protons of Ψ at tRNA's position 39. *Nucleic Acids Res.* **27**, 3543–3549 (1999).
13. Tomita, K., Ueda, T. & Watanabe, K. The presence of pseudouridine in the anticodon alters the genetic code: a possible mechanism for assignment of the AAA lysine codon as asparagine in echinoderm mitochondria. *Nucleic Acids Res.* **27**, 1683–1689 (1999).
14. Huang, C., Wu, G. & Yu, Y.-T. Inducing nonsense suppression by targeted pseudouridylation. *Nature Protocols* **7**, 789–800 (2012).
15. Winn, M. D., Murshudov, G. N. & Papiz, M. Z. Macromolecular TLS refinement in REFMAC at moderate resolutions. *Methods Enzymol.* **374**, 300–321 (2003).

**Supplementary Information** is available in the online version of the paper.

**Acknowledgements** We thank D. Hall and G. Winter for help and advice with data collection at beamline I04, Diamond Light Source; T. Tomizaki at beamline X06SA for help with data collection at the Swiss Light Source; and A. McCarthy at beamline ID14-4, ESRF, where screening and initial data collection were done. We thank

M. Härtlein for the gift of an overproducing tRNA<sup>Ser</sup> clone, M. Torrent for advice on yeast tRNA abundance, and G. Murshudov for advice and help with data analysis and refinement. V.R. was supported by the UK Medical Research Council (grant U105184332), a Programme Grant and Senior Investigator Award from the Wellcome Trust, the Agouron Institute and the Louis-Jeantet Foundation. Y.-T.Y. was supported by a grant from the National Institutes of Health (GM104077), and by the University of Rochester CTS award (UL1TR000042) from the National Center for Advancing Translational Sciences of the National Institutes of Health. I.S.F. was supported by a postdoctoral fellowship from the Fundacion Ramon Areces.

**Author Contributions** I.S.F. carried out the crystallographic experiments and analysis and helped write the paper. G.W. did the *in vitro* translation assays. C.L.N. helped with crystallographic data collection. A.C.K. made the 30S subunits, 70S ribosome and tRNA<sup>Ser</sup>, and Y.-T.Y. and V.R. oversaw the project and helped write the paper.

**Author Information** The coordinates and structure factors have been deposited in the PDB under accessions 4JV5, 4JYA, 4KOK (30S) and 4KOL, 4KOM, 4KOP, 4K0Q (70S). Reprints and permissions information is available at [www.nature.com/reprints](http://www.nature.com/reprints). The authors declare no competing financial interests. Readers are welcome to comment on the online version of the paper. Correspondence and requests for materials should be addressed to V.R. (ramak@mrc-lmb.cam.ac.uk) or Y.-T.Y. (YiTao\_Yu@URMC.Rochester.edu).

## METHODS

**Bacterial *in vitro* translation assay.** Reporter mRNAs were synthesized essentially as described previously<sup>1</sup>. Briefly, we generated a DNA template using overlap-extension PCR. The template thus generated contained a T7 promoter, followed sequentially by a Shine–Dalgarno (SD) sequence, a His6 tag, a termination codon (TAG) and a Flag tag (see Fig. 1), with the sequence:

5'-GGGAGAGGAGGCAACGACATGCCGCCACCACCACCAACCAC  
GCCGGCGCCGAACAGAAGGAAGAACCGCGAG(T/C/Ψ)AGGACTACA  
AGGACGACGACGACAAGGCCTAG-3'.

*In vitro* transcription with T7 RNA polymerase was used to generate the reporter mRNA transcript containing an authentic termination codon (UAG) immediately upstream of the Flag tag. Using the same strategy, we also generated a control mRNA transcript, where a CAG sense codon replaced the UAG codon. In addition, oligonucleotide-mediated two-piece splint ligation was used to generate another mRNA containing a YAG codon in place of the UAG or CAG codon, as described previously<sup>1</sup>. The 5' half RNA was *in vitro* transcribed, ending with GAG at its 3' end. The 3' half RNA was chemically synthesized, beginning with ΨAG at its 5' end. The two RNA fragments were aligned through hybridization with a complementary bridging oligodeoxynucleotide, and ligated by T4 DNA ligase. Thus, all three mRNA transcripts have the same sequence, except for the codon immediately upstream of the Flag tag (UAG, CAG or ΨAG).

**Translation in bacterial cell lysate and dot-blot analysis of proteins.** *In vitro* translation was carried out in a 37-μl reaction using *E. coli* cell lysate (Cosmo Bio Co) according to the manufacturer's instructions. Immediately after the reaction, dot-blot analysis was performed as described<sup>1</sup>. Briefly, small aliquots of the reaction (2.5 μl and 2.5 μl of a fivefold dilution) were spotted onto the nitrocellulose membrane, and probed with a monoclonal anti-His antibody (H-3; Santa Cruz Biotechnology) or a monoclonal anti-Flag antibody (M2; Sigma-Aldrich). Goat anti-mouse IgG (H+L)-alkaline phosphatase conjugate (Bio-Rad) was then used as a secondary antibody. His and Flag signals were visualized using 1-Step NBT/BCIP (Pierce).

**Crystallization.** For 30S experiments, the ASLs of tRNAs and the hexanucleotide mimics of mRNA with the sequence 5'-ΨAGΨAG-3' (for ASL<sup>Ser</sup>) or 5'-ΨGAΨGA-3' (for ASL<sup>Phe</sup>) were chemically synthesized (Dharmacon). The ASLs

were designed with an extra G26–C44 base pair to improve stability. The tRNA<sup>Ser</sup> was produced and purified as previously reported<sup>16</sup>.

*Thermus thermophilus* 30S ribosomal subunits were purified, crystallized and cryoprotected as previously described<sup>2,7</sup>. In the 30S experiments, crystals were soaked for 48 h in cryoprotection buffer containing 100 μM of the mRNA and 100 μM of the ASL, and then flash frozen in liquid nitrogen. In the case of the ASL for tRNA<sup>Phe</sup> with a ΨAG codon, the addition of paromomycin to 100 μM in the cryoprotection buffer improved diffraction from about 3.7 Å to 3.1 Å, so that structure was solved in the presence of paromomycin. However, within the limits of resolution, no difference was seen in the conformation of the decoding centre. For the 70S experiment, a complex of the ribosome with mRNA, tRNA<sup>fMet</sup> in the P site and tRNA<sup>Ser</sup> in the A site was crystallized as previously described<sup>7</sup>. The chemically synthesized mRNA was identical to that previously used, except for a ΨAG codon in the A site.

**Data collection and refinement.** Data were collected at the Diamond Light Source, beamline I04, integrated and scaled with XDS<sup>17</sup> and refined using REFMAC<sup>18</sup>. Visualization and model building was done with COOT<sup>19</sup>. An initial round of rigid body refinement using the published structure of the *T. thermophilus* 30S (PDB accession 1FJF) or the 70S ribosome (PDB accessions 2WH1 and 2WH2) was followed by restrained maximum-likelihood refinement. A final 'jelly body' refinement in REFMAC<sup>18</sup> further lowered the R factor and also significantly improved the quality of the maps. The mRNA and ASL or tRNA were clearly seen in difference Fourier maps. The final model including the ligands and conformational changes in the ribosome was refined as earlier. The density for a solvent atom adjacent to the O6 of G and I at the third base pair was assigned to a Mg<sup>2+</sup> ion based on its coordination and the fact that a water molecule at this position refined to an abnormally low B factor. All figures were drawn using PyMOL<sup>20</sup>.

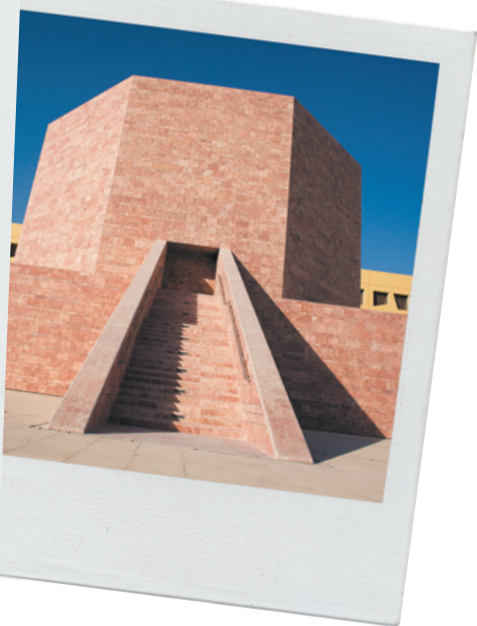
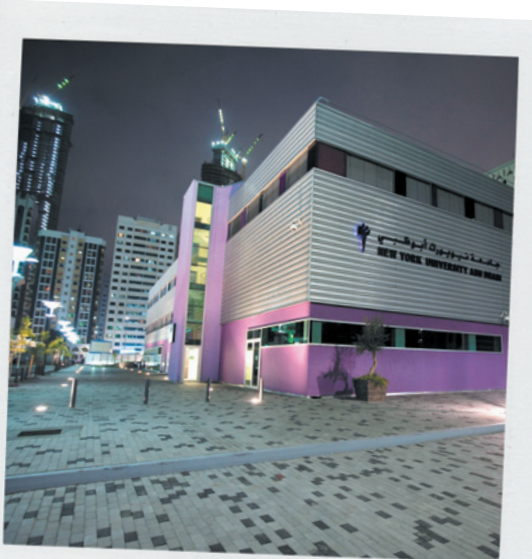
16. Borel, F., Hartlein, M. & Leberman, R. *In vivo* overexpression and purification of *Escherichia coli* tRNA<sup>Ser</sup>. *FEBS Lett.* **324**, 162–166 (1993).
17. Kabsch, W. *XDS. Acta Crystallogr. D* **66**, 125–132 (2010).
18. Murshudov, G. N. et al. REFMAC5 for the refinement of macromolecular crystal structures. *Acta Crystallogr. D* **67**, 355–367 (2011).
19. Emsley, P., Lohkamp, B., Scott, W. G. & Cowtan, K. Features and development of Coot. *Acta Crystallogr. D* **66**, 486–501 (2010).
20. DeLano, W. L. The PyMOL Molecular Graphics System. <http://www.pymol.org> (2006).

# CAREERS

**COLUMN** Scientists must learn to promote their work without hyping it **p.113**

**PUBLISHING** Trendy topics tend to drive physics research, says study **p.113**

 **NATUREJOBS** For the latest career listings and advice [www.naturejobs.com](http://www.naturejobs.com)



Research institutions in Saudi Arabia, the United Arab Emirates and Qatar are offering opportunities to foreign researchers.

## RELOCATING

# Middle Eastern promise

*Countries on the Arabian Peninsula are vying to attract young scientists to their universities.*

BY QUIRIN SCHIERMEIER

**W**hen Diego Cuadros told fellow scientists that he was moving to Qatar, they looked at him in disbelief. What, they asked, did he hope to gain from doing research in a small Arab emirate, fabulously rich in oil and gas but with no noteworthy tradition in science? What if he became totally disconnected from the collaborations, colleague networks and scientific expertise that could facilitate his career success?

But Cuadros, a Colombian-born epidemiologist who was finishing his PhD at the University of Kentucky in Lexington, knew what he was getting into. He had come across papers by Laith Abu-Raddad, a public-health researcher at Weill Cornell Medical College in Qatar (WCMC-Q) — the Doha branch of Weill Cornell Medical College in New York — and had become interested in Abu-Raddad's

research on diabetes and other illnesses. He also knew that his chances of getting funding in the United States after his PhD were slim. In 2010, he asked about postdoctoral opportunities at the WCMC-Q, and Abu-Raddad invited him for a two-month summer internship. Cuadros liked what he saw during his brief stay in Qatar — and, when Abu-Raddad later offered him a postdoctoral position, he packed his bags and returned to the Middle East.

Nineteen months on, Cuadros is glad that he made the move. “I get all the support I could wish for and I can focus 100% on my malaria project,” he says, noting that the emirate provides ample resources for research, travel, equipment procurement and housing. For the first time in his career, he is managing his own research money — a three-year, US\$100,000 grant from the Junior Scientists Research Experience Program of the Qatar National Research Fund. Thanks to generous travel

support from Abu-Raddad and the university, he can regularly attend conferences in Asia, Europe and North America. And he does not feel isolated in Doha. The capital's Education City, a large science and technology compound launched in 1998 with government support, hosts branches of several US and British universities, including Texas A&M University, Carnegie Mellon University and University College London. “I feel better-connected here than I did in the United States,” says Cuadros.

## KNOWLEDGE IS POWER

Qatar is not the only aspiring science hub on the Arabian Peninsula. Aware that their oil wells will run dry sooner or later, and that a knowledge economy may be key to future prosperity, Saudi Arabia and the United Arab Emirates (UAE) have launched their own ambitious efforts to become well regarded in international science and higher education. ▶

► Saudi Arabia's English-speaking King Abdullah University of Science and Technology (KAUST) in Thuwal, which graduated its first cohort of PhD students last December, prides itself on having several dozen leading Western researchers on its faculty. The UAE's New York University Abu Dhabi (NYUAD) attracts science students from around the world to its undergraduate courses (it has no official PhD programmes yet), and the Paris-Sorbonne University Abu Dhabi offers programmes in the humanities and social sciences.

The past decade or so also has seen several futuristic science campuses rising among the sand dunes, complete with new labs, lucrative funding opportunities (Qatar spends around 2.8% of its gross domestic product, or \$1 billion, on research and higher education each year, and KAUST has a \$10-billion endowment) and generous pay that is generally on a par with US salaries. Money often comes directly from institutions, meaning that researchers spend little energy drumming up external grants.

The region is replete with partnerships meant to draw in expertise and infrastructure from other countries. The Masdar Institute of Science and Technology in Abu Dhabi is collaborating with the Massachusetts Institute of Technology in Cambridge on research into energy and sustainability, and into biofuel for aviation. Kourosh Salehi-Ashtiani, a systems biologist formerly at Harvard Medical School in Boston, Massachusetts, began his research there on algae metabolism with a grant from the US Department of Energy. He is now working at the NYUAD, and collaborating with people at the University of Virginia in Charlottesville.

However, institutions have plenty of catching up to do in terms of recruitment and amassing expertise. The NYUAD plans to substantially expand its science and maths programmes and to hire faculty members next year, after it moves to a spacious new campus on Saadiyat Island. Since January, KAUST has recruited in biosciences and materials sciences.

A stint at a lab in the Gulf can be a valuable addition to a Western scientist's CV, hinting at personal flexibility, open-mindedness and a willingness to take on a certain level of risk. But anyone considering the move must remember that the scientific environment is still new, says Khaled Machaca, associate dean for research at the WCMC-Q. Although

funding opportunities are ample and new talent is welcome, foreign researchers will need to be patient about under-developed infrastructure. When Salehi-Ashtiani arrived at the NYUAD in February 2011, he found that his laboratory was nothing but empty benches. He says it took several weeks to get to know local suppliers for the most urgently needed reagents and pieces of equipment — from high-throughput sequencers to photo bioreactors and microarrays.

"Don't expect to find what you're used to," says Machaca. For all their modern conveniences and regional charms, Doha and Abu Dhabi have little to offer in the way of nightlife such as concerts, clubs or trendy bars. And the local institutions are too new and unproven to have the reputation or traditions of the University of Oxford or Harvard. "If you're looking for a research environment identical to the one you leave behind, the Gulf region is probably not what you're after," continues Machaca. "But if you have a bent for adventure and thrive on the new and exciting, it might be exactly the right place for you." Teething troubles, he says, are not unusual in a barely ten-year-old campus on the periphery of the scientific world. But government bureaucracy and research administrators are getting more experienced and efficient, and productive research is possible.

#### RECRUITMENT DRIVE

In 2009, Abu-Raddad left a tenure-track position at the Fred Hutchinson Cancer Research Centre in Seattle, Washington, and moved to Qatar, eager to be closer to his native Jordan and tempted by the no-strings-attached funding at the WCMC-Q. "I gave myself one year to try out how things might work here," he says. His expectations were easily surpassed: he won \$6 million in grants for hepatitis and HIV projects from the Qatar National Research Fund, and hired six research specialists (temporary workers who are typically locally trained graduate students) whom he found to be exceptionally gifted. He decided to stay.

Recruiting high-calibre postdocs was a challenge at first, he says. Many baulked at a stint in the Middle East. But most faculty members at KAUST and branch universities in the region are now being recruited from abroad, and early-career researchers have followed, keen to take advantage of the funding — and incentives such as free or inexpensive on-campus housing, free public transport and zero taxes. In the past few years, Abu-Raddad has recruited postdocs from Colombia, Japan, Hong Kong and the United States. In all, there are currently around 50 foreign postdocs at the WCMC-Q, up from 5 in 2009. And the trends are similar elsewhere: in the first half of this year, KAUST recruited 15 assistant, associate and full professors from abroad.

The NYUAD's planned campus move will create more than 200 faculty and postdoc positions at all levels of experience, says Pance Naumov, a chemist who moved from Japan to

Abu Dhabi last year. Salehi-Ashtiani says that when he advertised a job five years ago, only a handful of people applied. Now he receives several speculative applications per week.

Abu-Raddad says that he has chosen his postdocs carefully: anyone who thinks that a research stay in the Middle East is a nice,

relaxed way to make a good salary and polish their CV is mistaken. "I'm expecting my group members to be just as hard-driven as they would need to be to pursue a career in the United States, Europe or Japan," he says. "That research is still relatively new here doesn't mean that things are more easy-going. Getting something started from the ground up requires, in fact, extra stamina and self-motivation."

Laith Abu-Raddad

Those who do venture to the Middle East have plenty to gain. Doha and Abu Dhabi — like neighbouring Dubai — have large expatriate populations, and so have acquired a multicultural identity that makes it relatively easy for foreigners to settle. English is spoken fluently, crime is low and hanging out in restaurants or cafes or on the beach on a Saturday night is commonplace. Religiously ultra-conservative Saudi Arabia is far more restrictive in terms of gender equality and in some other regards — alcohol is forbidden, for example (it is legal but restricted in the UAE and Qatar). However, KAUST operates as a mixed-gender campus and there are no Saudi religious police on its grounds. Women may mingle with men and drive cars while on campus, and need not wear Islamic dress unless they leave the grounds, at which point they must dress modestly.

Women's rights are also restricted in Qatar, where men enjoy privileged status under federal law, and to a lesser degree in the UAE. Cuadros advises anyone considering relocating to the Gulf to go on an exploratory trip or undertake an on-site internship first. His wife, plant physiologist Maria Torres, started postdoctoral research on the date genome at the WCMC-Q in June; she had high hopes, but was also nervous. "When I first arrived in Qatar, I was prepared to find a place that would challenge my cultural boundaries," she says. But she has seen a mixture of cultures, languages and opinions in the lab. "Surprisingly, my experience has not been that removed from my life as a PhD student in the United States." ■

**Quirin Schiermeier** is *Nature's* Germany correspondent.



***"I feel better-connected here than I did in the United States."***

Diego Cuadros



***"Getting something started from the ground up requires self-motivation."***

Laith Abu-Raddad

# COLUMN

# Too much hype

Scientists have to promote their work. But they should fight the pull to oversell it, says **Monika Maleszewska**.

**J**if you had asked me a few years ago what makes a scientist, I would have said curiosity. Now, after almost three years pursuing my PhD, I would probably say political skills. Genuine curiosity does indeed make a good scientist, but the ability to promote one's work makes a successful one.

No matter how driven they are, researchers need more than expertise and bright ideas: they need money. Young scientists seeking funding must be ready to enter a world for which their degrees have not prepared them — a world of administrative and funding-agency politics, in which they must promote their ideas to gain attention and receive grants. But they also must take care to avoid crossing the line between promotion and hype.

In the competitive and expensive world of modern science, researchers cannot afford to toil away on their own. Lone-wolf scientists might have their own vision of innovative, cutting-edge research that will reap rewards. But they will probably struggle to procure enough funding to do that work. A hybrid approach might be to secure money through grant applications for 'fashionable' work (with a pinch of hype where necessary), and to hope that the resulting funding will, somewhere along the way, let the visionary scientist pursue his or her dream project — the one that really has an impact.

As a young scientist learning to navigate these issues, I often hear the following advice: communicate more effectively. If your project is in basic science or is difficult to understand, people say, make it simpler. Nicer. Easier to digest. Yet scientists thrive on precision. So sometimes, when pressed to make our projects sound simpler and more attractive, we choose hype as an easy way out.

Fashionable keywords, which change almost seasonally, help our projects to sound more relevant to the current trends. Society expects science to have applications, so we readily slip in some socially relevant perspective. A bit of exaggeration about expected results or future uses does not bother our consciences, as long as we perceive it as unbridled enthusiasm. ■

A skilful presentation and a positive attitude can make a huge difference in how a scientist's work is perceived. Give two PhD students the same set of data to present, and



one may put the audience to sleep with dry delivery, whereas the other might spark a vigorous discussion, perhaps winning a collaborator.

Yet despite being under constant pressure as we climb the ranks of academia, scientists must learn to navigate the blurred line between hype and savvy promotion. Young researchers who frequently exaggerate the implications of their findings or make hasty conclusions risk harming their reputations and losing the trust of their colleagues.

I often wish that scientists had the luxury of being able to do basic research just because it is interesting. But reviewers sometimes gravitate towards the projects that provide direct solutions to burning problems, rather than to basic projects with no clear applications. We must give basic projects a chance, especially because breakthroughs are hard to anticipate. That basic science might be closer to a meaningful application than anyone expects.

In the competitive world of scientific funding, researchers often have no choice but to hone their political skills and manage public relations for their research. Ideally, they will be able to do this without taking too much time away from the science. What's clear is that budding researchers must learn how to promote their work, and perhaps even become trendsetters — without resorting to hype. ■

**Monika Maleszewska** is a graduate student in regenerative medicine at the University of Groningen in the Netherlands.

## PUBLISHING

### Fashion rules in physics

Physicists are fad-followers who often pursue the fields with the highest number of recently published papers, says a study (T. Wei *et al.* *Sci. Rep.* **3**, 2207; 2013). The metareview, of around 320,000 articles published by the American Physical Society's Physical Review journals from 1976 to 2009, also found that papers with many authors, which are common in some areas of physics, tend to be on 'hot' research topics. Working in a hot field can be a good strategy, says lead author Jinshan Wu, a physicist at Beijing Normal University, because it can increase citations, attention from peers and research funding. But, he notes, the scientific community can suffer if leaders are not exploring new directions.

## EUROPEAN UNION

### Grant popularity soars

A 50% spike in demand for European Research Council (ERC) Starting Grants has pulled this year's success rate down to 9%, and is likely to lead to changes in some eligibility requirements. ERC president Helga Nowotny says that the increase — to 3,329 applications this year, of which 287 were successful — is attributable in part to research-budget cuts in some European nations. The ERC, based in Brussels, will consider lengthening the period between resubmissions to reduce the flow of applications, she adds. Starting Grants, now in their sixth year, fund researchers who finished their doctorate in the past 2–7 years. This year, the ERC spent nearly €400 million (US\$527 million) on the awards, which are worth up to €2 million each and last for up to five years.

## FUND-RAISING

### Art sales fund science

Sales of stylized scientific images, including micrographs of human-heart and mouse-brain cells, are helping to pay for early-career researchers to travel. Proceeds from an art fair and website ([go.nature.com/aakuwa](http://go.nature.com/aakuwa)) have raised some US\$30,000 so far, enough to send 60 graduate students and postdocs from the University of Michigan in Ann Arbor to conferences. And there is another benefit: "We started this as a fund-raiser, but it turns out to be an awesome public-outreach tool," says Deborah Gumucio, founder of the Michigan Center for Organogenesis, which runs the Bio-Artography project. "People come into our fair booth and we can talk to them about pluripotent stem cells."

# COLUMN

# Too much hype

Scientists have to promote their work. But they should fight the pull to oversell it, says **Monika Maleszewska**.

**J**if you had asked me a few years ago what makes a scientist, I would have said curiosity. Now, after almost three years pursuing my PhD, I would probably say political skills. Genuine curiosity does indeed make a good scientist, but the ability to promote one's work makes a successful one.

No matter how driven they are, researchers need more than expertise and bright ideas: they need money. Young scientists seeking funding must be ready to enter a world for which their degrees have not prepared them — a world of administrative and funding-agency politics, in which they must promote their ideas to gain attention and receive grants. But they also must take care to avoid crossing the line between promotion and hype.

In the competitive and expensive world of modern science, researchers cannot afford to toil away on their own. Lone-wolf scientists might have their own vision of innovative, cutting-edge research that will reap rewards. But they will probably struggle to procure enough funding to do that work. A hybrid approach might be to secure money through grant applications for 'fashionable' work (with a pinch of hype where necessary), and to hope that the resulting funding will, somewhere along the way, let the visionary scientist pursue his or her dream project — the one that really has an impact.

As a young scientist learning to navigate these issues, I often hear the following advice: communicate more effectively. If your project is in basic science or is difficult to understand, people say, make it simpler. Nicer. Easier to digest. Yet scientists thrive on precision. So sometimes, when pressed to make our projects sound simpler and more attractive, we choose hype as an easy way out.

Fashionable keywords, which change almost seasonally, help our projects to sound more relevant to the current trends. Society expects science to have applications, so we readily slip in some socially relevant perspective. A bit of exaggeration about expected results or future uses does not bother our consciences, as long as we perceive it as unbridled enthusiasm. ■

A skilful presentation and a positive attitude can make a huge difference in how a scientist's work is perceived. Give two PhD students the same set of data to present, and



one may put the audience to sleep with dry delivery, whereas the other might spark a vigorous discussion, perhaps winning a collaborator.

Yet despite being under constant pressure as we climb the ranks of academia, scientists must learn to navigate the blurred line between hype and savvy promotion. Young researchers who frequently exaggerate the implications of their findings or make hasty conclusions risk harming their reputations and losing the trust of their colleagues.

I often wish that scientists had the luxury of being able to do basic research just because it is interesting. But reviewers sometimes gravitate towards the projects that provide direct solutions to burning problems, rather than to basic projects with no clear applications. We must give basic projects a chance, especially because breakthroughs are hard to anticipate. That basic science might be closer to a meaningful application than anyone expects.

In the competitive world of scientific funding, researchers often have no choice but to hone their political skills and manage public relations for their research. Ideally, they will be able to do this without taking too much time away from the science. What's clear is that budding researchers must learn how to promote their work, and perhaps even become trendsetters — without resorting to hype. ■

**Monika Maleszewska** is a graduate student in regenerative medicine at the University of Groningen in the Netherlands.

## PUBLISHING

### Fashion rules in physics

Physicists are fad-followers who often pursue the fields with the highest number of recently published papers, says a study (T. Wei *et al.* *Sci. Rep.* **3**, 2207; 2013). The metareview, of around 320,000 articles published by the American Physical Society's Physical Review journals from 1976 to 2009, also found that papers with many authors, which are common in some areas of physics, tend to be on 'hot' research topics. Working in a hot field can be a good strategy, says lead author Jinshan Wu, a physicist at Beijing Normal University, because it can increase citations, attention from peers and research funding. But, he notes, the scientific community can suffer if leaders are not exploring new directions.

## EUROPEAN UNION

### Grant popularity soars

A 50% spike in demand for European Research Council (ERC) Starting Grants has pulled this year's success rate down to 9%, and is likely to lead to changes in some eligibility requirements. ERC president Helga Nowotny says that the increase — to 3,329 applications this year, of which 287 were successful — is attributable in part to research-budget cuts in some European nations. The ERC, based in Brussels, will consider lengthening the period between resubmissions to reduce the flow of applications, she adds. Starting Grants, now in their sixth year, fund researchers who finished their doctorate in the past 2–7 years. This year, the ERC spent nearly €400 million (US\$527 million) on the awards, which are worth up to €2 million each and last for up to five years.

## FUND-RAISING

### Art sales fund science

Sales of stylized scientific images, including micrographs of human-heart and mouse-brain cells, are helping to pay for early-career researchers to travel. Proceeds from an art fair and website ([go.nature.com/aakuwa](http://go.nature.com/aakuwa)) have raised some US\$30,000 so far, enough to send 60 graduate students and postdocs from the University of Michigan in Ann Arbor to conferences. And there is another benefit: "We started this as a fund-raiser, but it turns out to be an awesome public-outreach tool," says Deborah Gumucio, founder of the Michigan Center for Organogenesis, which runs the Bio-Artography project. "People come into our fair booth and we can talk to them about pluripotent stem cells."

# THE BEST OF US

*It's no game.*

BY LEE HALLISON

**W**ind howled over blackened trees as Ginja picked her way to me over broken highway lumps. A tough cookie, the kind that sometimes broke. Hard to judge on the first day. On the other hand, soft ones didn't even get to try. Like the boy I'd refused yesterday? He had no idea the favour I'd done his sorry ass.

I train recruits for scavenger duty. If this one passed the first-day test, she was in luck. I hadn't always been a teacher, but I'd be god-damned if I wasn't a good one.

"Ears hurt," Ginja complained when she reached the bus. The wind out here was painful, a never-ending screech, as if Earth itself was moaning. The nearly useless helmets we wore had way-too-thin ear pads and faceplates that barely protected us from the sharp debris and swirling dust.

Faded lettering across the tilted bus announced "Panorama Tours!" Ginja set her half-filled sack by the left wheel. The bus seemed stable. Two wheels on the cracked asphalt, two in a long furrow in the bare median strip.

I swung my rifle butt into the Greyhound's door. The glass shattered. I reached in and yanked the inner handle. A musty-sour smell wafted over us as I opened the door.

The wind dropped as I climbed in. Ginja stepped up. This was the moment when some would-be scavengers freaked out.

"Look at all this stuff!"

Hand luggage was strewn in the aisle. Skeletons draped with decayed clothing slumped in the seats.

"Yes, a good haul." She'd do. I shifted my rifle to the side to let her by.

Vehicles sometimes hosted rats or feral dogs. This bus seemed empty, so I pointed the rifle down — but stayed ready. I wasn't about to break my track record. My trainees came back.

"Stinks!" Ginja pulled her faceplate back down. She reached over the driver's headless skeleton and yanked the window open.

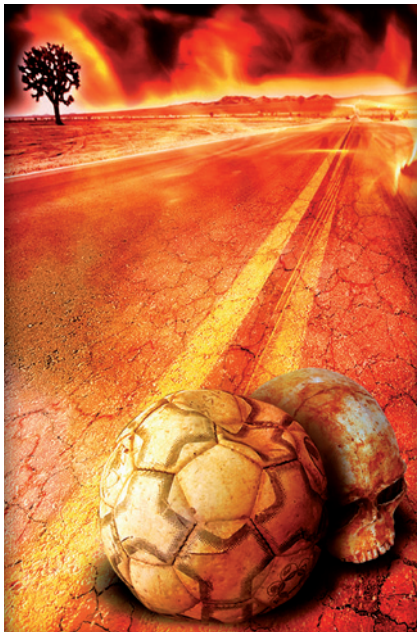
"Jeez, shut it! Are you stupid?" I yelled. She pushed, but the frame stuck. Now we were in a mini-windstorm inside a bus filled with dead people's dust. Maybe I was mistaken. Tough was good but smart was better.

I forced the window closed.

"Ask me before you do shit. Wind comes from this side. If you need air, open one on the lee side."

She nodded, worry that she'd blown it written on her face. I ignored her dismay and told her what to search for. I'd stay up front as guard.

"Batteries, books, all electronics and toys," I said. "Any medicines or creams, even open tubes. Clothing if it looks strong, check for quality — thin or torn-up stuff ain't worth



saving. Pass on food. It won't be good anymore."

"Even cans?" She unzipped a large athletic-style bag.

"Nobody brought food cans on tours. Use your brains."

She picked up a skull that was resting on a purse snuggled between two bony knees. Before I could stop her, she opened a lee-side window and tossed it out.

"Hey! No desecrating the dead. That's important."

"Surviving is important. Finding stuff to haul back is important. Where does giving a shit fit in?" Ginja stood, skinny arms akimbo, chin out.

"Being human, that's where."

She snorted but didn't throw away any more body parts. She worked quickly, tossing a mobile phone and a cosmetics bag into the growing pile in the aisle, then pulled a black leather duffel from underneath the seat.

A small "oh" drew my attention away from the windows.

Ginja held up a dirty white ball.

"Soccer."

"Yeah, so?"

"My brother played soccer. That could have been him." She looked at the seated skeleton.

I stayed quiet, letting her chew on the idea.

She set the ball on the pile. Gently, though, and her hand lingered. I looked out front, giving her space. I wondered, idly curious, if she would break this soon.

She coughed and pulled out a shopping bag, dumping the papers it held. I heard a scritch from the back and turned to see a fat furry shape streak over a seatback.

"Rat! Get behind me!"

Ginja jumped up and we swivelled around each other in the narrow aisle. The rats were fearless, vicious and carried disease our meagre antibiotics couldn't fight. I aimed the rifle and waited. Soon enough, it poked a head up and stared at me. I let it nose up higher and squeezed the trigger.

Ginja yelled at the echoing boom and we both fell back a bit. I'd seen the blood spray. I kept the gun aimed towards the back and motioned to her pile.

"Grab it, we'd better get out. Gunshot might bring the curious."

Her face was ashen. She stepped around me, squatted down and scooped her finds into the shopping bag. The soccer ball rolled slowly away and she looked up at me.

"Yeah, sure, get it."

She duck-walked towards the ball and grabbed it before it got too far. She squeezed it to her chest, her lip trembling. She jabbed her chin at the disarrayed skeletons.

"All these people. Oh, jeez. They're all people!"

I cocked my head.

"What did you think they were?"

She shuddered, stuck the ball in the bag and stood up.

"Stupid, I know."

"No, you're not stupid. It's hard to care and it's hard not to care."

As she reached the front steps, she turned.

"Cap?" She blinked as if something were in her eyes. "Do we have time to bury them?"

We didn't, but I was pleased. The best of us knew just exactly what we were doing.

I passed her, of course. ■

**Lee Hallison** is a writer living in the Pacific Northwest. She blogs at [leehallison.com](http://leehallison.com).